PREMIER REFERENCE SOURCE

Advanced Solar Cell Materials, Technology, Modeling, and Simulation

Laurentiu Fara & Masafumi Yamaguchi

Advanced Solar Cell Materials, Technology, Modeling and Simulation

Laurentiu Fara
Polytechnic University of Bucharest, Romania
& Academy of Romanian Scientists, Romania

Masafumi Yamaguchi
Toyota Technological Institute (TTI), Nagoya, Japan

ENGINEERING
SCIENCE REFERENCE

Managing Director: Lindsay Johnston
Senior Editorial Director: Heather A. Probst
Book Production Manager: Sean Woznicki
Development Manager: Joel Gamon
Development Editor: Myla Merkel
Assistant Acquisitions Editor: Kayla Wolfe
Typesetter: Nicole Sparano
Cover Design: Nick Newcomer

Published in the United States of America by
Engineering Science Reference (an imprint of IGI Global)
701 E. Chocolate Avenue
Hershey PA 17033
Tel: 717-533-8845
Fax: 717-533-8661
E-mail: cust@igi-global.com
Web site: http://www.igi-global.com

Library of Congress Cataloging-in-Publication Data

Advanced solar cell materials, technology, modeling, and simulation / Laurentiu Fara and Masafumi Yamaguchi, editors.
p. cm.
Includes bibliographical references and index.
Summary: “Featuring a premiere cast of the leading photovoltaic scientists from around the globe, this book addresses the fundamental challenges in the field and examines the basic fundamental limitation of photovoltaic conversion”--Provided by publisher.
ISBN 978-1-4666-1927-2 (hardcover) -- ISBN 978-1-4666-1928-9 (ebook) -- ISBN 978-1-4666-1929-6 (print & perpetual access) 1. Photovoltaic cells--Materials. 2. Solar cells--Materials. 3. Photovoltaic cells--Design and construction. 4. Solar cells--Design and construction. 5. Photovoltaic power generation. I. Fara, Laurentiu. II. Yamaguchi, Masafumi, 1946-
TK8322.A38 2012
621.31’244--dc23

2012004966

British Cataloguing in Publication Data
A Cataloguing in Publication record for this book is available from the British Library.

Editorial Advisory Board

Table of Contents

Detailed Table of Contents

Section 2
Quantum Well Solar Cells

Quantum well solar cells with p-i-n structure are presented. The physical processes in multiple quantum well solar cells, the materials commonly used for photovoltaic applications, and technological aspects are analyzed. The quantum confinement effect produces resonant energy levels located in the valence and conduction bands of well layers. In addition, it produces energy quantum confinement levels located in the energy band gap of both well and barrier layers. The absorption on both resonant and quantum confinement levels leads to an extension of the internal quantum efficiency in near infrared domain. Several structures with different absorbers from 3-5 and 4 groups are described and discussed. Various technological and design solutions, such as multiple quantum well solar cells with graded band gap, with tandem configurations, with strain-balanced structure, and strain-balanced structure improved with nanoparticles deposited atop are analyzed. The cell parameters are discussed and related to the materials and technology.

In this chapter, the authors present the modelling and simulation of the multi-layered quantum well solar cells as well as the simulated results of this model. The quantum confinement of a semiconductor induces new energy levels, located in the band gap, as well as resonant levels located in the conduction and valence bands. These levels allow supplementary absorption in the visible and near infrared range. The quantum efficiency of the supplementary absorption is calculated within the infinite rectangular quantum well approximation. As the absorption excites carriers in the gap of each layer, even a small absorption significantly increases the photocurrent (by photoassisted tunneling) and, therefore, the cell efficiency. The results of the simulation are presented for the internal quantum efficiency of the transitions between the resonant levels of GaAs, as well as the internal quantum efficiency of the transitions between the confinement levels for GaAs and $Al_xGa_{1-x}As$. New directions for the research of quantum well solar cells are indicated.

The analytical modelling of bulk and quantum well solar cells is reviewed. The analytical approach allows explicit estimates of dominant generation and recombination mechanisms at work in charge neutral and space charge layers of the cells. Consistency of the analysis of cell characteristics in the light and in the dark leaves a single free parameter, which is the mean Shockley-Read-Hall lifetime. Bulk PIN cells are shown to be inherently dominated by non-radiative recombination as a result of the doping related non-radiative fraction of the Shockley injection currents. Quantum well PIN solar cells on the other hand

are shown to operate in the radiative limit as a result of the dominance of radiative recombination in the space charge region. These features are exploited using light trapping techniques leading to photon recycling and reduced radiative recombination. The conclusion is that the mirror backed quantum well solar cell device features open circuit voltages determined mainly by the higher bandgap neutral layers, with an absorption threshold determined by the lower gap quantum well superlattice.

Section 3
Hybrid and Polymer Solar Cells

Conventional solar cells are usually manufactured from silicon, an inorganic material. This type of solar cell has a high efficiency, up to 40%, but these cells are using very expensive materials of a high purity and energy intensive processing techniques. This chapter is dedicated to a critical presentation of hybrid solar cells. They are a combination of both organic and inorganic nanostructure materials and, therefore, combine the properties and advantages of their components. Unfortunately, so far, the hybrid solar cells have a low conversion efficiency of the sunlight, 6-7% (Kim, et al., 2007).

Currently, the active materials used for the fabrication of solar cells are mainly inorganic. Materials such as silicon (Si), gallium-arsenide (GaAs), cadmium-telluride (CdTe), and cadmium-indium-selenide (CIS). Nevertheless, the large production cost for the silicon solar cells is one of the major drawback in this field. This chapter is dedicated to a critical presentation of another type of photovoltaics, called polymer, or plastic, solar cell technology. Polymer solar cells have attracted significant attention in the past few years due to their potential of providing environmentally safe, lightweight, flexible, and efficient solar cells.

Modelling and simulation of organic (polymer, dye sensitized, and nanotube) solar cells is discussed. High J-V theoretical curves, the calculation of key parameters, and also the relative influence of different parameters on the cell operation, are evidenced and analyzed. On this basis, the authors obtain information on the optimization of the solar cell design and manufacturing.

Section 4
High Efficiency Solar Cells

The concept underlying the hot carrier solar cell is to slow the rate of photo-excited carrier cooling to allow time for the carriers to be collected while they are still at elevated energies ("hot"), and thus allowing higher voltages to be achieved from the cell. Significant reduction in carrier cooling has been observed in Quantum Well (QW) nano-structures at very high illumination intensities due to a "phonon bottleneck" mechanism. With the phononic gaps in nano-structures, the optical phonon lifetime can be prolonged by blocking the main phonon decay from optical branches to acoustical branches (such as the Klemens or Ridley decay channels). Si-based hot carrier cell is a very active topic and Si-Ge nano-structures are especially interesting for the application, as their fabrication process is well developed. In this chapter, the authors first analyse the operation of a hot carrier solar cell and lay down the general principles. They then discuss the opportunity of phonon engineering to improve the phonon bottleneck. Finally, they present how these can be modeled in nanostuctures comprising several thousand atoms, where true 3D phonon dispersion relations for Si-Ge nano-structures are obtained using first principles methods. The effects of the nano-structure size and geometry on the phonon dispersion relations are investigated. The possible phonon decay processes in the nano-structures are discussed and compared with the bulk crystal materials. The performance of calculated nano-structures on the hot carrier solar cell is evaluated with the acquired knowledge of phonon modes.

Luminescent Solar Concentrators (LSCs) offer a way of making Photovoltaic (PV) systems more attractive through reduced energy costs, the possibility of application in cloudy regions, and improved building integration. LSCs collect light over a large area and concentrate it, both spatially and spectrally, onto solar cells at the edges of the device, such that the total cell area required to generate a specific power is reduced. Since the solar cells constitute the more expensive component in the system, this leads to cost reductions. Unlike conventional geometric concentrators, LSCs do not require solar tracking and can collect diffuse as well as direct sunlight. The current research challenges lie in increasing the efficiency of the LSC and extending it to larger areas to make it commercially viable. In this chapter, the authors outline the mode of operation of the LSC, with particular regard to cost considerations and device geometry. They then review recent approaches aiming to increase device efficiency and, finally, introduce their versatile raytrace approach to modelling the LSC. The model is utilised here to investigate tapered LSC designs and rationalise the optimal geometry and configuration for planar LSCs.

Foreword

The speed and scale of the current deployment by the photovoltaic industry is truly astonishing. This current success is the culmination of the sustained technological improvement that has occurred over the past 30 years, such as seeing first the 20%, then 30%, and now even the 40% photovoltaic conversion efficiency barrier broken. While these developments have been truly remarkable, only rarely have photovoltaic developments been recognized in mainstream science and engineering circles.

It is somewhat surprising that the development in photovoltaics has not garnered more attention when one considers that solar electric energy demand has grown by an average 30% per annum over the past 20 years. This demand has been fuelled by rapidly declining costs and prices. This decline in cost has been driven by economies of manufacturing scale, manufacturing technology improvements, and the aforementioned improvement in the efficiency of solar cells. This decline in costs can be seen in the fact that installed photovoltaic system prices have decreased in Europe by 50% in the last 5 years.

The photovoltaic revolution has in many ways mirrored the microelectronic revolution, except in its transparency to most consumers. The irony is that the advances in photovoltaics and the long-term positive impacts that they hold for the health of our planet may be far more important than the viral explosion of the next electronic gadget.

One of the very attractive features is that the photovoltaic story is truly an international one. Without the essential contribution of many nations and regions across the globe, the state of this industry and its technology could not be where it is today. From its earliest beginnings in fundamental chemistry and physics labs in Europe, to the modern silicon "solar cell" developed in the industrial labs in the U.S., to its early adoption of in Japan, and later in an even much greater deployment scale in Germany and throughout Europe, to today's surge in manufacturing in China and throughout southeast Asia, it has truly been an international confluence of forces that has made the solar revolution possible.

The question is how can the photovoltaic industry continue to grow and develop and help the worldwide community continue to meet one of the greatest challenges of our time, the development of ubiquitous, environmentally friendly, and affordable electrical energy generation. The answer undoubtedly lies in capturing the same elements that have allowed this technology to get where it is today: specifically, harvesting the talents of scientists around the globe in the development of new lower cost earth abundant photovoltaic materials, new methods of photon management, and even more novel paradigms in photovoltaic conversion.

The editors of *Advanced Solar Cell Materials, Technology, Modeling, and Simulation*, Laurentiu Fara and Masafumi Yahaguchi, have assembled a premiere cast of the leading photovoltaic scientists from around the globe who are indeed working at the very cutting edge of photovoltaic technology to address the fundamental challenges in the field. This book examines the basic fundamental limitation

of photovoltaic conversion, and describes how we can simulate the essential mechanisms using fundamental models to both better understand these mechanisms and to evaluate new methodologies. It then goes on to look at some of the new materials, approaches, and device and system designs. Finally, new paradigms in photovoltaic conversion using quantum confinement, as well as light and thermal management, are considered.

The development of the materials and concepts and analytical tools discussed in this book will be essential to the future of the photovoltaics industry. It is from these developments that the future breakthroughs in performance and corresponding cost reduction will come. Although the speed and scale of today's photovoltaic deployment is truly remarkable, we have not reached any sort of a limit—a limit of where we can be or where we need to be in order to meet the growing demand for energy. Further improvements in cost and performance will allow the industry to not only meet the new demands for energy, but to start to displace the non-renewable forms of electrical energy production so damaging to our planet.

Ryne P. Raffaelle
Rochester Institute of Technology, USA

Ryne P. Raffaelle *is the Vice President for Research and Associate Provost at Rochester Institute of Technology (RIT). Prior to his current position, he served as the Director of the National Center for Photovoltaics at the National Renewable Energy Lab of the U.S. Department of Energy, from 2009 through 2011. Before joining NREL, Dr. Raffaelle was the Academic Director for the Golisano Institute for Sustainability at RIT. He is also the Emeritus Director of the NanoPower Research Laboratory, a laboratory that he founded at RIT in 2001. He currently holds appointments as a Professor of Physics, Imaging Science, Microsystems Engineering, and Sustainability. As a professor, he has been responsible for more than $20 million in research grants in photovoltaics, batteries, and nanomaterials research. His career includes working as a visiting scientist at the NASA-Glenn Research Center; the NASA Lewis Research Center; and at Oak Ridge National Laboratory. He was a Professor of Physics and Space Sciences at the Florida Institute of Technology from 1992-1999. Dr. Raffaelle has authored or co-authored over 200 refereed publications and books. He is the Managing Editor of Progress in Photovoltaics published by Wiley Interscience. He is currently serving on the organizing committee for the IEEE Photovoltaics Specialists Conference, is a member of the AIAA Technical Committee on Aerospace Power, and is a member of the IEC/IEEE Joint Project Team (JPT) 62659 (IEEE 1784). He has a Ph.D. in Physics from University of Missouri-Rolla, and Bachelor of Science and Master of Science degrees in Physics from Southern Illinois University.*

Preface

Photovoltaic power generation technology is one of the most promising options for a sustainable energy future. A permanent interest, both of research and the solar cell industry, has increased the efficiency and dropped the cost of producing 1 kW. In this way, four generations of solar cells have been developed.

The majority of solar cells that exist on the market belong to the first generation of solar cells, based on silicone mono-crystalline. These products are based on silicon wafers, either single-crystalline or a lower-grade multi-crystalline wafers. The production volume is growing with the focus on improving the efficiency and reducing the cost. One of the high-efficiency technologies is based on "buried contact" solar cells. Another technology is based on high-performance silicon-on-glass.

The second generation of solar cells has the objective of reducing the production cost by using polycrystalline silicone or different semiconductors (CdTe, CuIn, Se_2) thin films. Large-scale commercialization of these products leads to a completely different manufacturing cost structure compared to the wafer-based products.

The solar cells from the third generation allow for high-efficiency, while remaining cheap (Green, 2006). There are three options of these solar cells, based on the utilization of nanotechnologies:

- The first option is based on *Quantum Well Solar Cells*. Keith Barnham and his co-workers from the Imperial College of Science, Technology and Medicine, London, United Kingdom, have developed such solar cells by interleaving 50 slices of InGaAs (Barnham, et al., 2001). They have demonstrated the possibility of obtaining an efficiency of 17% for concentrated solar radiation with a concentration ratio of 300.
- The second option is based on the development of *Sensitized Organic Dye Solar Cells* as well as *Polymer Solar Cells.* The best efficiency of such solar cells was 11%, reported by Michael Gratzel (O'Regan & Gratzel, 1991). These solar cells are 3-4 times cheaper than the first generation. The efficiency of the polymer solar cells is 10-11%.
- The third one is based on the *Quantum Dot Solar Cells.* The Martin Green Group, from the New South Wales University, Sidney, Australia, successfully developed the first solar cells of this type. This technology offers an efficiency of 20-30%. However, in order to become commercial, 10 to 15 years are still required.

The fourth generation of solar cells was launched and uses composite materials.

The third and fourth generations of solar cells are potentially able to overcome the Schockley-Quiesser conversion efficiency (Shockley & Queisser, 1961) of 31% at l-sun and 41% under concentration for

single bandgap solar cells. The third generation systems include multi-layer, multi-junction (tandem) solar cells made of thin film Si or III-V compounds, while new developments include intermediate bands and hot carrier solar cells.

Taking into account this approach, the book, which is dedicated especially to the third generation of solar cells, is structured on five sections, namely:

- **Section 1: Basic Topics:** Chapter 1, **"**New Trends in Solar Cells," and Chapter 2, "Physical Limitations of Photovoltaic Conversion"
- **Section 2: Quantum Well Solar Cells:** Chapter 3, "Quantum Well Solar Cells: Physics, Materials, and Technology," Chapter 4, "Quantum Confinement Modeling and Simulation for Quantum Well Solar Cells," Chapter 5, "Analytical Models of Bulk and Quantum Well Solar Cells and Relevance of the Radiative Limit"
- **Section 3: Hybrid and Polymer Solar Cells:** Chapter 6, "Hybrid Solar Cells: Materials and Technology," Chapter 7, "Polymer Solar Cells," Chapter 8, "Organic Solar Cells: Modeling and Simulation"
- **Section 4: High Efficiency Solar Cells:** Chapter 9, "Super High Efficiency Multi-Junction Solar Cells and Concentrator Solar Cells," Chapter 10, "Quantum Dot Solar Cells," Chapter 11, "Intermediate Band Solar Cells: Modeling and Simulation," Chapter 12, "Phononic Engineering for the Hot Carrier Solar Cells"
- **Section 5: Luminescent Solar Concentrators: Prospects and Strategies for Advanced Solar Cells:** Chapter 13, "The Luminescent Solar Concentrator: Advances, Optimization, and Outlook, Chapter 14, "Prospects and Strategy of Development for Advanced Solar Cells**"**

The main goal of this book is to concentrate and present the main results obtained in research regarding materials, technology, modeling, and simulation of different types of advanced solar cells.

The book is targeted at experts from universities and research organizations (engineers, physicists, chemists), as well as young professionals (PhD students, master students, engineers, physicists, chemists, as well as under-graduate students from the terminal years in physics, chemistry, material sciences, optical and electrical engineering) interested in advanced solar cells. The book could be used also by specialized companies in order to consider the development trends and market opportunities for advanced solar cells.

The editors would like this book to become a building block in the progress of PV conversion of solar energy and, in this way, to a sustainable development society.

Laurentiu Fara
Polytechnic University of Bucharest, Romania & Academy of Romanian Scientists, Romania

Masafumi Yamaguchi
Toyota Technical Institute (TTI), Japan

Section 1

Basic Topics

Chapter 1
New Trends in Solar Cells

Masafumi Yamaguchi
Toyota Technological Institute (TTI), Japan

Laurentiu Fara
Polytechnic University of Bucharest, Romania & Academy of Romanian Scientists, Romania

ABSTRACT

Photovoltaic (PV) power generation technology is one of the most promising renewable energy technologies because of the possibility of solving environmental problems and limited sources of energy. In order to realize widespread deployment of solar photovoltaics and contribute to further development in civilization, further development in the science and technology of PV is very important. That is, further improvements in conversion efficiencies and reliability and lowering the cost of solar cells and modules are necessary. Regarding conversion efficiencies of solar cells, because there is the Shockley–Queisser conversion efficiency limit of 31% at 1-sun and 41% under concentration for single bandgap solar cells, several approaches to overcome the Shockley–Queisser limit should be made. This book will provide readers some guidance to overcome the limit. This chapter presents the current status of solar cells and new trends in solar cells from the viewpoint of conversion efficiency.

INTRODUCTION

Photovoltaics (PV) is the technology that generates electrical power from mainly semiconductors, recently from organic and other materials, when they are illuminated by photons. PV power generation technology is one of the most promising renewable energy technologies because of possibility of solving environmental problems and limited sources for energy. Table 1 shows sustainable potentials of renewable energy sources presented by N. S. Lewis (2005). From the 1.2×10^5 TW (the Solar constant is 1.76×10^5 TW) of solar energy that strikes the earth's surface, a practical sitting-constrained terrestrial global solar power potential value is about 600 TW. Thus, for a 10% efficient solar farm, at least 60 TW of power could be supplied from terrestrial solar energy resources. Therefore, solar energy is the only renewable energy resource that has enough terrestrial energy potential to satisfy a 20 TW or more carbon-free supply.

DOI: 10.4018/978-1-4666-1927-2.ch001

According to the world energy vision 2100 recommended by WBGU (German Advisory Council on Global Change) (WBGU, 2003) as shown in Figure 1, solar electricity, including PV, is expected to become a major energy source with a share of about 20% in 2050 and about 70% in the total energy of the world in 2100. Thus becoming the major energy resource in the world because of its resource potential and clean energy. That means PV will play an important role in contributing to solving global environmental problems as the major energy resource in the world. In order to realize such a vision, further development in science and technology of PV is very important. That is, further improvements in conversion efficiencies and reliability, and lowering cost of solar cells and modules are necessary. Regarding conversion efficiencies of solar cells, because there is the Shockley-Queisser conversion efficiency limit (Shockley & Queisser, 1961) of 31% at 1-sun and 41% under concentration for single bandgap solar cells, several approaches to overcome the Shockley-Queisser limit should be made. This book will provide readers some guidance to overcome the limit.

This chapter presents the current status of solar cells and new trends in solar cells from the viewpoint of conversion efficiency.

CURRENT STATUS OF VARIOUS SOLAR CELLS

Dissemination of PV systems has been advanced and solar cell module productions have also been significantly increased in the world as a result of R&D and national government and regional government programs. Such a rapid growth in PV system installation in the world needs production of large-scale PV systems. That means necessity for development of higher efficiency and lower cost solar cell modules. Table 2 shows characteristics of various types of solar cells developed for terrestrial applications. Although crystalline Si solar cells are mainly used for terrestrial power applications, various types of solar cells are studied and developed. This section presents the current status of various types of solar cells.

Table 1. Sustainable potentials of renewable energy sources (Lewis, 2005)

Renewable Energies	Theoretical Potential (TW)	Technically Feasible Potential (TW)	Economically Feasible Potential (TW)
Hydro Electric	4.6	1.5	0.9
Geothermal	30	11.6	
Ocean Energy	2.7		
Wind	50		2
Biomass	20	5-7	3
Solar Photo-voltaics	$1.2x10^5$	600	60

Crystalline Si Solar Cells

Even crystalline Si solar cells, solar cells are very sensitive to defects, impurities, surface, and interface in solar cell materials. Figure 2 shows calculated results for changes in conversion efficiencies of single crystal Si solar cells as a function of minority-carrier lifetime and surface recombination velocity. Key issues for achieving higher efficiencies are reduction in bulk recombination loss, reduction in carrier recombination loss at surface and interface, passivation of crystalline grain boundary, and defects in grains, gettering of heavy metal impurities, reduction in optical reflection loss at surface, reduction in series resistance and parallel resistance, carrier confinement, and photon confinement. R&D trends in the field of crystalline Si solar cells and materials are rear surface junction, hetero junction structures, thinner Si wafer, effective utilization of low-grade Si such as Solar Grade (SOG)-Si and Metallurgical Grade (MG)-Si.

Figure 1. Transforming the global energy mix: the exemplary until 2050/2100 (WBGU, 2003)

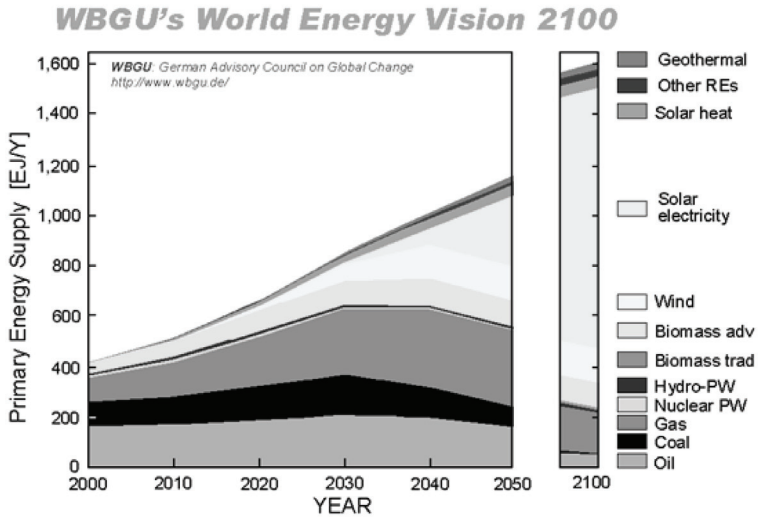

Table 3 shows efficiency table of crystalline Si, thin film Si, CIGS, CdTe, 3-5 compounds and concentrator, dye-sensitized, and organic solar cells reported in "Progress in Photovoltaics" (Green, Emery, Hishikawa, & Warta, 2011). The highest efficiencies achieved in laboratories are 25.0% for single crystalline Si and 20.4% for poly crystalline Si solar cells.

Thin Film Si Solar Cells

Thin-film Si solar cells has great potential for low cost solar cells because of thin films, usage of low cost substrate, lower processing temperature, and easy production of large area solar cells. However, there are problems to be solved. One is lower efficiencies with 7-8% for amorphous Si (a-Si) solar cell modules compared to that (15-18%) for single crystalline Si solar cell modules and that (13-16%) for poly crystalline Si solar cell modules. Another one is degradation of a-Si solar cells under light illumination condition.

a-Si/micro-crystalline Si 2-junction tandem cells with small area of 1cm^2 and modules with area of 91cm x 45.5cm have recorded 15.0% and 13.5%, respectively. a-Si/a-SiGe/nc-Si 3-junction tandem solar cells with small area of 0.25cm^2 have reached initial efficiency of 15.4% and stabilized efficiency of 13.3%, respectively. As problems to be solved in the field of thin film Si solar cells and modules, there are understanding and reducing light degradation of a-Si solar cells, improvements in material quality of middle and bottom cell materials, development of higher stabilized efficiency thin film Si solar cell modules with efficiency of more than 15%, development of low-cost glass substrates with transparent conductive oxide layer, and development of low-cost process technologies such as high-speed thin film deposition, patterning, and so on.

CdTe Solar Cells

CdTe solar cells are expected as low cost and high efficiency solar cells. CdTe solar cells with small area of 0.845cm^2 and modules with area of 4874cm^2 have recorded 16.7% and 10.9%, respectively. The First Solar, Inc. has developed low cost mass production technologies of CdTe solar cell modules with cost of $0.87/W and is producing

Table 2. Characteristics of various types of solar cells developed for terrestrial and space applications. Conversion efficiencies for various solar cells are the highest values achieved in laboratories.

	Materials	Conversion Efficiency (%)	Efficiency Potential (%)	Radiation Resistance	Reliability	Cost	Application Area
1	Single crystal Si	25.0	28.9	Fair	Good	Fair	Terrestrial Space
	Poly crystal Si	20.4	28.9	Fair	Good	Fair	Terrestrial
2	Amorphous Si	14.5	17.5	Fair	Fair	Fair	Terrestrial
	Micro-crystal Si	15.2	23.5	Fair	Fair	Fair	Terrestrial
	CdTe	16.7	20	Fair	Fair	Fair	Terrestrial
	$CuInGaSe_2$	20.3	23.5	Excellent	Fair	Fair	Terrestrial
3	Concentrator 3-5 Tandem	41.6	> 50	Fair	Good	Fair	Terrestrial
Space	GaAs	27.6	30	Good	Good	Expensive	Space
	InP	22.1	30	Excellent	Good	Expensive	Space
	3-5 Tandem	35.8	> 40	Good	Good	Expensive	Space
New	Dye-sensitized	11.2	17.5	?	Poor	?	?
	Organic	8.3	16	?	Poor	?	?

Figure 2. Calculated results for changes in conversion efficiencies of single crystal Si solar cells as a function of minority-carrier lifetime and surface recombination velocity S

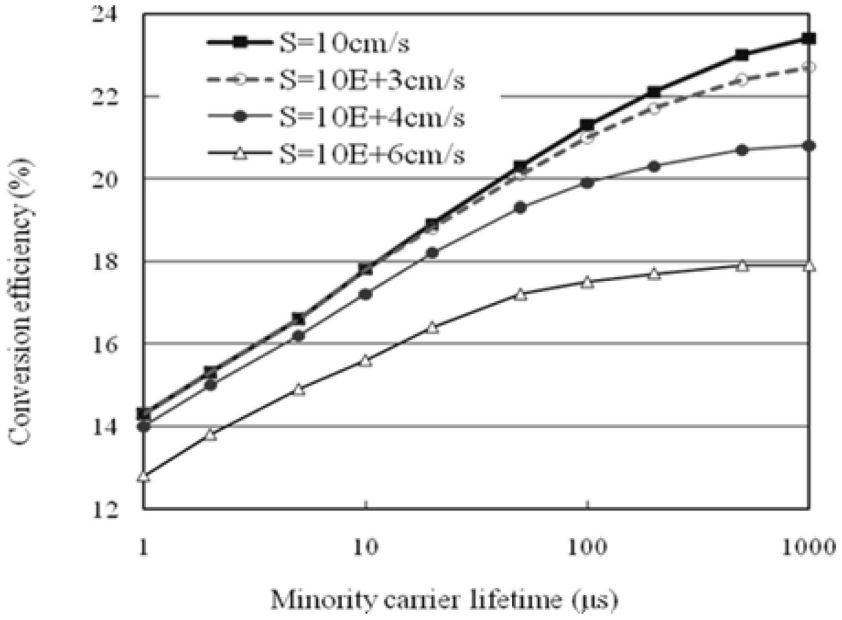

low cost CdTe solar cell modules. Figure 3 shows conversion efficiencies of CdTe and CIGS solar cells and modules versus area of solar cells and modules. Improving conversion efficiency of large area CdTe solar cell modules is very important for CdTe solar cell modules because their efficiencies decrease with increase in their area. As problems to be solved in the field of CdTe solar cells and modules, there are standardization of absorber layer and production equipments, improvement in large area module efficiency of more than 15%, development in stable rear contacts, development of thin active layer solar cells, and understanding and controlling properties of CdTe related materials and interfaces.

$CuInGaSe_2$ Solar Cells

CIGS ($CuInGaSe_2$) solar cells are also expected as low cost and high efficiency solar cells. CIGS solar cells with small area of 0.5cm^2 and modules with area of 30cm x 30cm have recorded 20.3% and 15.22%, respectively. As shown in Figure 3, improving conversion efficiency of large area CIGS solar cell modules is also very important. As problems to be solved in the field of CIGS solar cells and modules, there are improvement in large area module efficiency of more than 15%, development of Cd free solar cells and modules, development of thin active layer solar cells, improvements in stoichiometry and uniformity of absorber and buffer layers, standardization of absorber layer and production equipments, and understanding and controlling properties and interfaces of CIGS related materials and buffer layers.

3-5 Compound Multi-Junction and Concentrator Solar Cells

3-5 compound Multi-Junction (MJ) and concentrator solar cells have great potential for space and terrestrial applications because they have high efficiency potential of more than 50% and superior radiation-resistance. As a result of developing wide bandgap InGaP double hetero structure tunnel junction for sub-cell interconnection, InGaAs middle cell lattice-matched to Ge substrate, and InGaP-Ge heteroface structure bottom cell, 38.9% efficiency at 489-suns AM1.5 have been demonstrated with InGaP/InGaP/Ge 3-junction solar cells (Takamoto, Kaneiwa, Imaizumi, & Yamaguchi, 2005). Most recently, 41.6% efficiency at 364-suns has been reported with InGaP/GaAs/Ge 3-junction concentrator cells by Spectrolab (King, et al., 2009) as shown in Figure 4. Figure 4 shows chronological improvements in best research-cell efficiencies summarized by Kazmerski (2009). 35.8% efficiency at 1-sun AM1.5G has also been reported with inverted epitaxially grown InGaP/GaAs/InGaAs 3-junction solar cells by Sharp (Yoshida, Agui, Nakaido, Murasawa, Juso, Sasaki, & Takamoto, 2011). Details of fundamental issues, present status, and future prospects of 3-5 compound MJ and concentrator solar cells will be presented in Chapter 4.

Dye-Sensitized and Organic Solar Cells

Dye-sensitized and organic solar cells are expected as low cost solar cells. However, current efficiencies obtained with small area dye-sensitized and organic solar cells are 11.5% and 8.3%, respectively and it must be necessary for those cells to realize more 15% in order to commercialize those cells in widespread applications. Therefore, further development of science and technologies in dye-sensitized and organic solar cells is very important for the end.

Trends in Conversion Efficiency Improvements and Cost Reduction of Solar Cells

Increasing conversion efficiencies of solar cells has huge positive impacts throughout the entire value chain and means less materials, less glass and other module materials, and less installation

Table 3. Efficiency table of crystalline Si, thin film Si, CIGS, CdTe, dye-sensitized, and organic solar cells reported in "progress in photovoltaics"

Classification	Effic. (%)	Area (cm^2)	Voc (V)	Jsc (mA/cm^2)	FF (%)	Test Centre (date)	Description
Si (single crystal)	25.0±0.5	4.00(da)	0.706	42.7	82.8	Sandia(3/99)	UNSW
Si (multicrystal)	20.4±0.5	1.002(ap)	0.664	38.0	80.9	NREL(5/04)	FhG-ISE
a-Si	9.6±0.3	1.070(ap)	0.859	17.6	63.0	NREL(4/03)	U.Neuchatel
a-Si/nc-Si /nc-Si(tandem)	12.5±0.7	0.27(da)	2.011	9.11	68.4	NREL(3/09)	United Solar stabilized
a-Si/mc-Si (tandem)	11.9±0.8	1.227	1.346	12.92	68.5	NREL(8/10)	Oerlikon
a-Si/mc-Si (tandem)	11.7±0.4	14.23(ap)	5.462	2.99	71.3	AIST(9/04)	Kaneka
CIGS	20.3±0.6	0.5015(ap)	0.740	35.4	77.5	FhG-ISE(6/10)	ZSW
CdTe	16.7±0.5	1.032(ap)	0.845	26.1	75.5	NREL(9/01)	NREL
GaAs	27.6±0.8	0.9989(ap)	1.107	29.6	84.1	NREL(11/10)	Alta Devices
InP	22.1±0.7	4.02(t)	0.878	29.5	85.4	NREL(4/90)	Spire
GaInP/GaInAs /Ge 3-J (concentration)	41.6±2.5 364-suns	0.3174(da)	3.192	1.696A	88.74	NREL(8/09)	Spectrolab
InGaP/GaAs /InGaAs 3-J (1-sun)	35.8±1.5	0.880(ap)	3.012	13.9	86.3	AIST(9/09)	Sharp
Dye-sensitized	11.2±0.3	0.219(ap)	0.736	21	72.2	AIST(3/06)	Sharp
Organic polymer	8.3±0.3	1.031(ap)	0.816	14.46	70.2	NREL(11/10)	Konarka

(da)=designated illumination area, (ap)=aperture area, (t)=total area.

Figure 3. Conversion efficiencies of CdTe and CIGS solar cells and modules vs. area of solar cells and modules

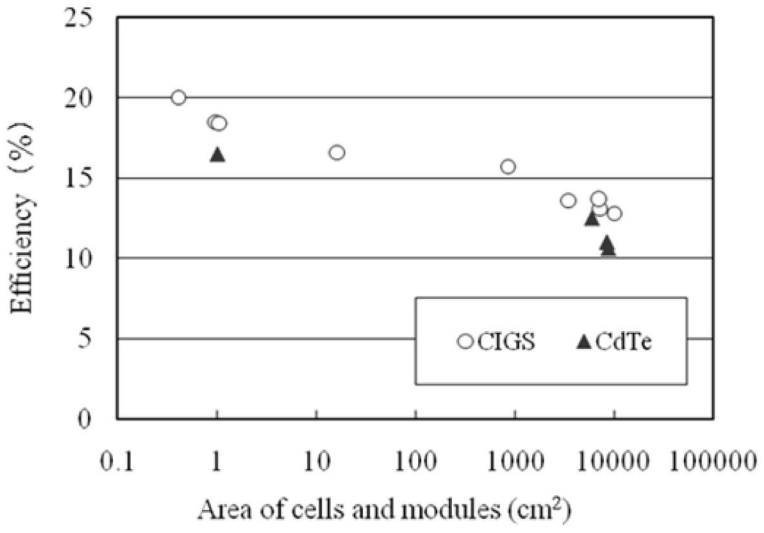

Figure 4. Chronological improvements in best research-cell efficiencies

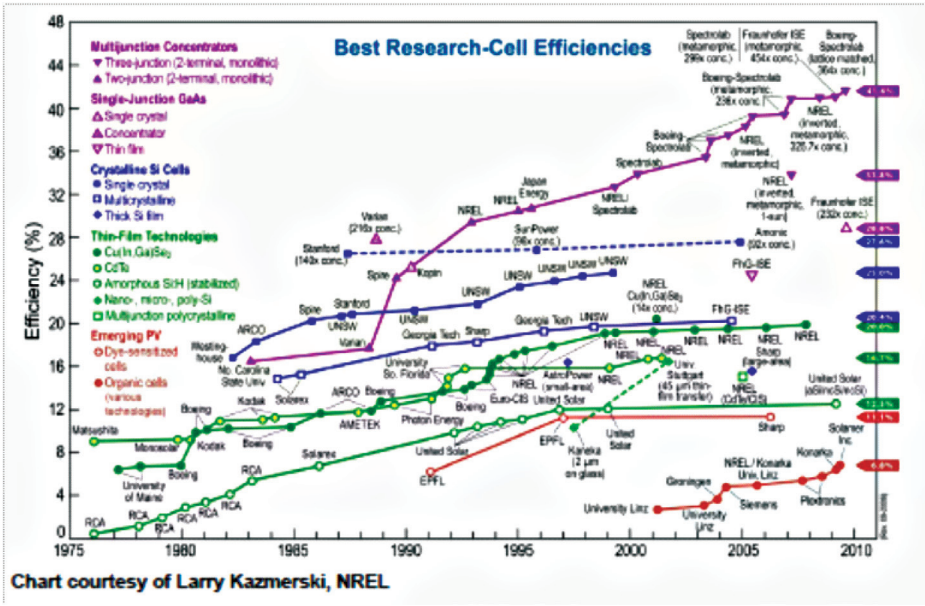

cost. Although many R&Ds for various types of solar cells have been carried out and improvements in their conversion efficiencies have been achieved, conversion efficiencies of almost all the solar cells are expected to have limitations. Figure 5 shows future efficiency predictions of various solar cells (original idea by Professor A. Goetzberger [Goetzberger, Luther, & Willeke, 2001] and modified by M. Yamaguchi [Yamaguchi, 2004]). According to efficiency predictions shown in Figure 5, limiting efficiencies are predicted to be 28.9%, 23.5%, 23.5%, 17.5%, and 16% for crystalline Si, thin-film Si, CIGS as well as CdTe, dye-sensitized and organic solar cells, respectively. On the other hands, because 41.6% efficiency has been realized with concentrator InGaP/InGaAs/Ge 3-junction solar cells, concentrator 4-junction or 5-junction solar cells have great potential for realizing super high-efficiency of over 50%. In addition, developing new types of solar cells based on new materials and new concepts is also very important to overcome conversion efficiency limitations.

Cost reduction of solar cell modules is also very important for large-scale penetration of PV as a primary energy source. Figure 6 shows comparison of the projected module price with an extension of the historical experience curve (Swanson, 2006). According to the historical experience curve, a price of $1.40/W will be obtained in 2012. A module price of $1.40/W, coupled with a system price of twice ($2.80/W) should result in a cost-effective grid-connected market in many locations. That means that crystalline Si is expected to be still the dominant technology in 10 years. As low cost mass production technologies of CdTe solar cell modules with cost of $0.87/W has already been developed, there must well be several thin-film technologies that are rapidly gaining market share. In addition, concentrator PV is also expected to contribute to large-scale power generation systems. Dye-sensitized, organic, and new types of solar cells may also have great potential for their further lowering cost.

Figure 5. Future efficiency predictions of various solar cells

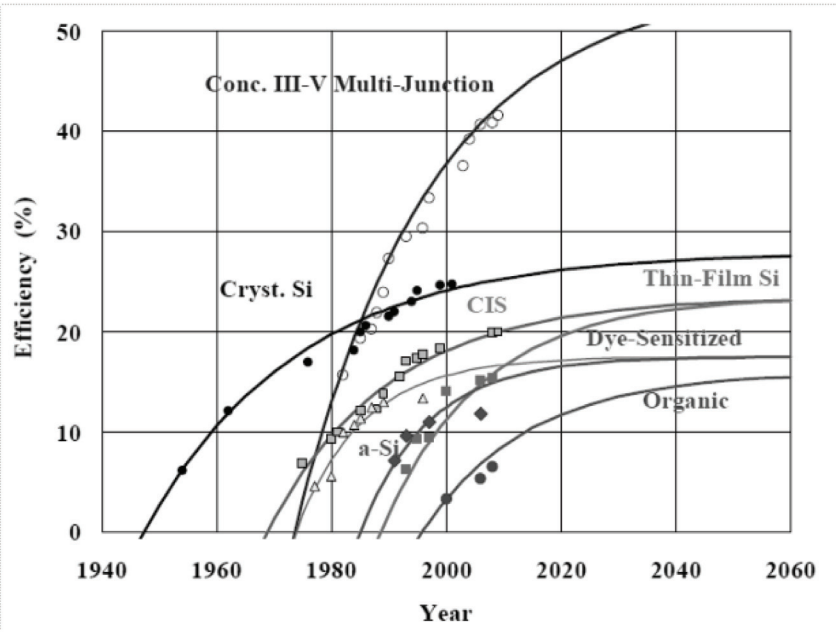

NEW TRENDS IN SOLAR CELLS

Third generation solar cells proposed by M. Green (2003) are solar cells that are potentially able to overcome the Shockley–Queisser conversion efficiency limit (Shockley & Queisser, 1961) of 31% at 1-sun and 41% under concentration for single bandgap solar cells. This includes a range of alternatives to the so-called "first generation solar cells" (which are solar cells made of semiconducting p-n junctions) and "second generation solar cells" (based on reducing the cost of first generation cells by employing thin film technologies). Common third-generation systems include multi-layer multi-junction (tandem) solar cells made of thin-film Si or 3-5 compounds, while more theoretical developments include intermediate bands, hot-carrier effects and other multiple-carrier ejection.

3-5 Compound Multi-Junction Solar Cells

3-5 compound Multi-Junction (MJ) and concentrator solar cells have great potential of more than 50% as shown in Figure 6 because 41.6% efficiency at 364-suns with InGaP/GaAs/Ge 3-junction concentrator cells by Spectrolab and 35.8% efficiency at 1-sun AM1.5G with inverted epitaxially grown InGaP/GaAs/InGaAs 3-junction solar cells by Sharp have already been achieved.

One of the most realistic approaches to overcome the Shockley–Queisser conversion efficiency limit (Shockley & Queisser, 1961) of 31% at 1-sun and 41% under concentration for single bandgap solar cells is the 3-5 compound MJ and concentrator solar cells. Table 4 shows theoretical conversion efficiencies of MJ solar cells at 1-sun and under concentration in ideal case. As shown in Table 4, 3-5 compound Multi-Junction (MJ) and concentrator solar cells have great potential of more than 50%.

Figure 6. Comparison of the projected module price with an extension of the historical experience curve

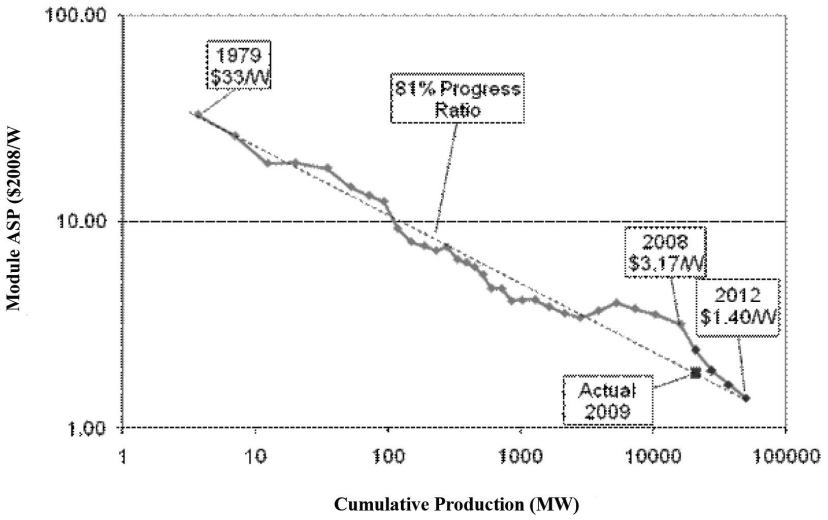

Figure 7 shows concepts for increasing conversion efficiency of 3-5 compound multi-junction solar cells in the future (Luther, Bett, Burger, & Dimroth, 2006). This section presents new approaches for high-efficiency 3-5 compound MJ and concentrator solar cells.

Lattice-Mismatched InGaP/InGaAs/Ge 3-Junction Solar Cells

Conversion efficiency of InGaP/(In)GaAs/Ge based multi-junction solar cells has been improved up to 31-32% at AM1.5G by considering the lattice matching between sub cell layers and Ge substrate. However, because the present band-gap InGaP/InGaAs combination is far from the optimum combination for the AM1.5 spectra, the lattice-mismatched system should be studied in order to realize high efficiencies. Efficiencies up to 39% are possible under ideal band-gap combination with In composition 0.16 of $In_xGa_{1-x}As$ middle cell. Figure 8 shows conversion efficiency potential and lattice-mismatching of InGaP/InGaAs/Ge 3-junction solar cells as a function of In content of the InGaAs middle cell. The lattice-mismatched InGaP/InGaAs/Ge system should be studied in order to realize high efficiencies of about 39% at 1-sun AM1.5G.

However, strain-induced dislocations and defects are thought to degrade solar cell properties in lattice-mismatched system. The effects of graded buffer layer and Thermal Cycle Annealing (TCA) upon solar cell properties, dislocation behavior and other physical properties in lattice-mismatched $In_xGa_{1-x}As$ middle cells have been studied (Sasaki, Arafune, Lee, Ekins-Daukes, Tanaka, Ohshita, & Yamaguchi, 2006).

Significant reduction in misfit dislocation density in the lattice mismatched InGaAs cells has been observed after thermal cycle annealing, and as the cycle number is increased the reduction is greater. High quality InGaAs films with a dislocation density of $3\text{-}5x10^5$ cm^{-2} with high minority-carrier lifetime of about 8ns have been obtained using only thermal cycle annealing with a TCA temperature of 800^0C. As a result of dislocation density reduction by TCA, improvements in minority-carrier lifetime (measured by the photo-

Table 4. Theoretical efficiencies of multi-junction solar cells in ideal case

Number of junction	Conversion efficiency under 1-sun	Conversion efficiency under concentrator
1	30.8%	40.8%
2	42.9%	55.7%
3	49.3%	63.8%
4	68.2%	86.8%

Table 5. Efficiency potential (ideal case) of 3rd generation PV technologies

Concept	Year proposed	Conversion efficiency in ideal case
Multi-junction (tandem)	1955	86.8%
Multiple excitation	1972	85.4%
Hot carrier	1981	86.2%
Multi band (intermediate band)	1997	86.8%
Quantum well	1990	60%
Impurity band PV	1960	63%

luminescence decay method) and Voc of InGaAs middle cells were obtained (Sasaki, Arafune, Lee, Ekins-Daukes, Tanaka, Ohshita, & Yamaguchi, 2006). Although 31.7% efficiency with lattice-mismatched InGaP/InGaAs/Ge 3-junction cell without TCA (Voc=0.74V) has been obtained, over 33% at 1-sun by using higher Voc InGaAs middle cells has not yet been obtained. More than 33% by using 0.775V middle cell is expected to be obtained and 35% will be achieved if one realize 0.83V middle cell. For concentrator cells, 40% will be realized by using 0.775V middle cell and 42% will be achieved if one realize 0.83V middle cell as shown in Figure 9.

Most recently, world-record efficiency under 1-sun has been demonstrated with InGaP/GaAs/InGaAs 3-junction solar cell by Sharp. By optimizing buffer layer, 36.9% (Jsc=14.05 mA/cm^2, Voc=3.006 V, FF=0.875) efficiency metamorphic 3-junction InGaP/GaAs/InGaAs solar cells have been achieved by Yoshida, Agui, Nakaido, Murasawa, Juso, Sasaki, and Takamoto (2011), as shown in Figure 10.

New (In)GaAsN Material for 4- and 5-Junction Applications

Although 31.7% at 1-sun AM1.5G with InGaP/InGaAs/Ge 3-junction cell has been attained, it is necessary to develop new material such as InGaAsN (Kurtz, Myers, & Olson, 1997) with a bandgap energy of 1.04eV in order to realize 4- or 5-junction cells with efficiencies of more than 40% or 50% as shown in Figure 11. In addition,

Figure 7. Concepts for increasing conversion efficiency of 3-5 compound multi-junction solar cells in the future (Luther, Bett, Burger, & Dimroth, 2006)

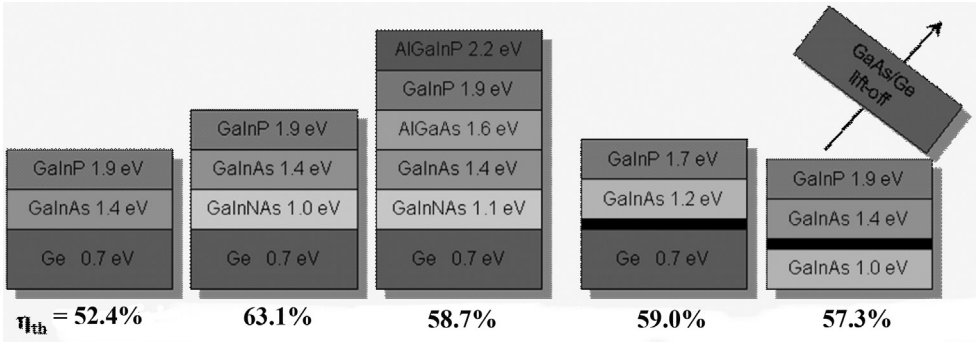

Figure 8. Conversion efficiency potential and lattice mismatching of InGaP/InGaAs/Ge 3-junction solar cells as a function of in content of the InGaAs middle cell

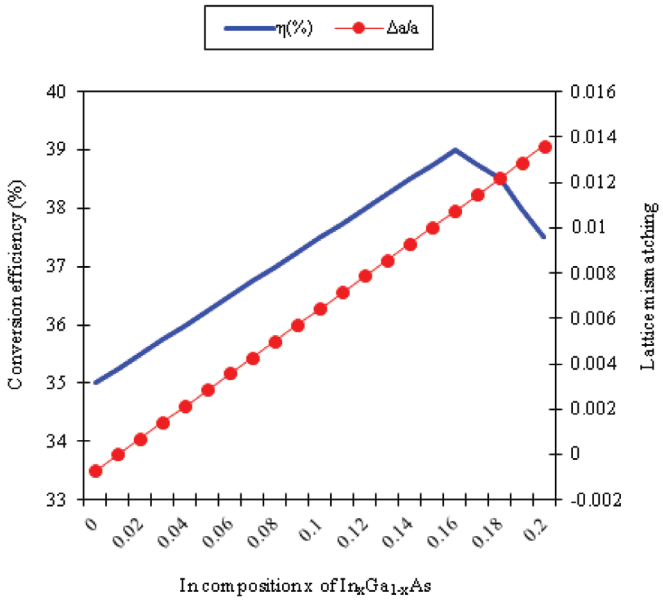

1eV energy gap material should be lattice-matched to Ge and GaAs. InGaAsN is one of appropriate materials for 4- or 5-junction solar cell configuration because this material has 1eV band gap and is lattice-matched to GaAs and Ge. However, present InGaAsN single-junction solar cells have been inefficient because of low minority-carrier lifetime due to N-related recombination centers such as N-H-V_{Ga} and $(N\text{-}As)_{As}$ and low electron mobility due to alloy scattering and non-homogeneity of N.

Figure 12 shows changes in minority-carrier (electron) diffusion length of GaAsN films as a function of N concentration (Kurtz, Johnston, Geisz, Friedman, & Ptak, 2005) and calculated acceptor concentration dependent of minority-carrier diffusion length in GaAsN with changing minority-carrier mobility μ. Acceptor concentration N_a dependence of minority-carrier diffusion length L were calculated by the following equations:

$$L = \sqrt{\mu \tau kT / q} \qquad (1)$$

$$\tau = 1 / BN_a \qquad (2)$$

where, τ is minority-carrier lifetime, k is Boltzamann constant, q is electronic charge, B is radiative recombination coefficient and $B = 2x10^{-10} cm^3 / s$ in GaAs was used in the calculation. The minority-carrier diffusion length in GaAsN is found to decrease very quickly with the addition of nitrogen as shown in Figure 12. Nitrogen in GaAsN seems to act as a shallow acceptor impurity and the larger change in electron diffusion length likely reflects the larger change in minority carrier mobility (Yamaguchi, et al., 2008).

Since the minority carrier diffusion length of this alloy is very short, the effect of InGaAsN intrinsic layer in p-GaAs/i-n-InGaAsN heterojunction solar cells fabricated by atomic hydrogen-assisted Molecular Beam Epitaxy (MBE) has been investigated. Figure 13 shows a structure and External Quantum Efficiencies (EQEs) of p-GaAs/i-n-InGaAsN heterojunction solar cells with varying intrinsic layer thickness, made by

Figure 9. Voc of InGaAs middle cells and 3-junction cell efficiency vs. bandgap of InGaAs

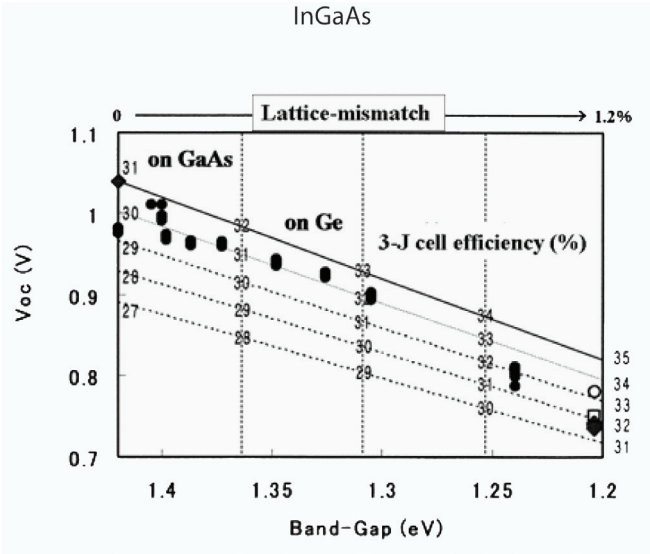

Figure 10. Current (I)-voltage (V) curve of 36.9% 3-junction cell

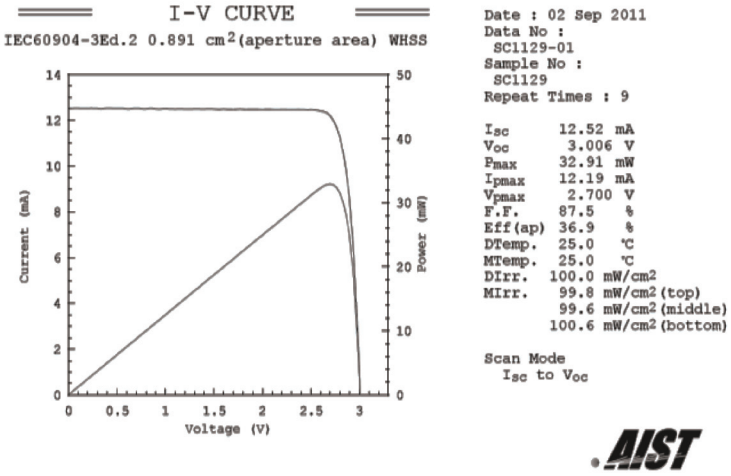

using atomic-H assisted RF-MBE. In order to increase photo current generation in poor quality InGaAsN sub-cells, p-i-n structure was used. As shown in the figure, the insertion of i-layer results in the overall improvements of EQE. As a result, it is thought that minority-carrier diffusion length is equivalently improved from less than 100 nm to 600 nm by inserting i-layer. Figure 14 shows current-voltage curve of a p-GaAs/i-n-InGaAsN heterojunction solar cell with i-layer thickness of 600 nm. With an optimized i-layer thickness of 600nm, 11.27% efficiency has been obtained (Miyashita, Shimizu, Kobayashi, Okada, & Yamaguchi, 2006).

Figure 11. Theoretical efficiency mapping as a function of top cell and 3rd cell layer bandgap energies for 4-junction solar cells

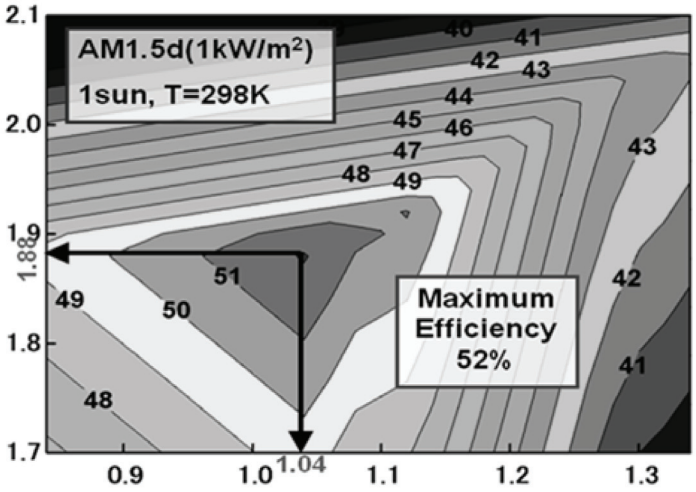

New Concepts

Third generation solar cells proposed by M. Green (2003) are solar cells that are potentially able to overcome the Shockley-Queisser conversion efficiency limit (Shockley & Queisser, 1961) of 31% at 1-sun and 41% under concentration for single bandgap solar cells. In addition to multi-layer multi-junction (tandem) solar cells described earlier, third-generation systems include intermediate bands, hot-carrier effects and other multiple-carrier ejection.

Figure 15 shows efficiency cost per unit area regimes for the three generations of technology. Since cost studies of any thin-film to date have shown large volume costs below US$100/m^2 are likely to be attained, this would seem a reasonable prospect for third generation thin-films. If efficiency double that thought reasonable for mature single junction thin-film modules of circa 15% can be obtained, this results in exceptionally low costs per peak Watt, US$0.33/Wp for this example.

As shown in Table 5, several ideas (Marti & Luque, 2003) have been proposed to overcome the Shockley-Queisser conversion efficiency limit. Although conversion efficiencies predicted in ideal case shown are 85-87% for multiple excitation, hot carrier, intermediate band concepts, realistic conversion efficiencies to be obtained for solar cells by using the above concepts may be less than 55% by considering possible efficiency based on the realistic multi-junction (tandem) concept.

The “hot carrier” cell approach is thought to be one of the most elegant approaches suggested for producing high performance cells. Basically, light is absorbed in an absorber region with photogenerated carriers extracted before they have the chance to thermalize with the lattice. Not only does this prevent the normal cell thermalization loss, but it means that the semiconductor bandgap no longer has to play a role in “stopping the rot” in carrier relaxation. Figure 16 shows calculations of the limiting efficiency of hot carrier cells (Nozik, 2002) as a function of carrier temperature showing the high performance available in principle,

Figure 12. Changes in minority-carrier (electron) diffusion length of GaAsN films as a function of N concentration and calculated acceptor concentration dependence of minority-carrier diffusion length in GaAsN with changing minority-carrier mobility μ

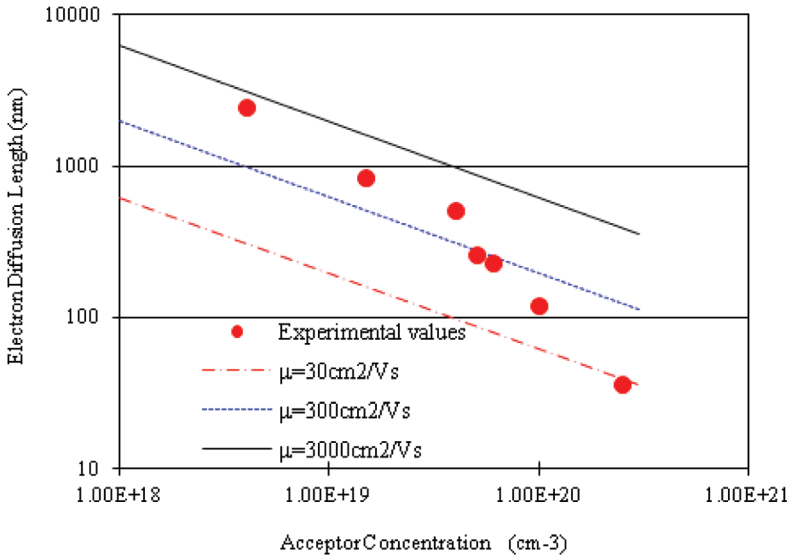

Figure 13. A structure and external quantum efficiencies (EQEs) of p-GaAs/i-n-InGaAsN heterojunction solar cells with varying intrinsic layer thickness, made by using atomic-H assisted RF-MBE

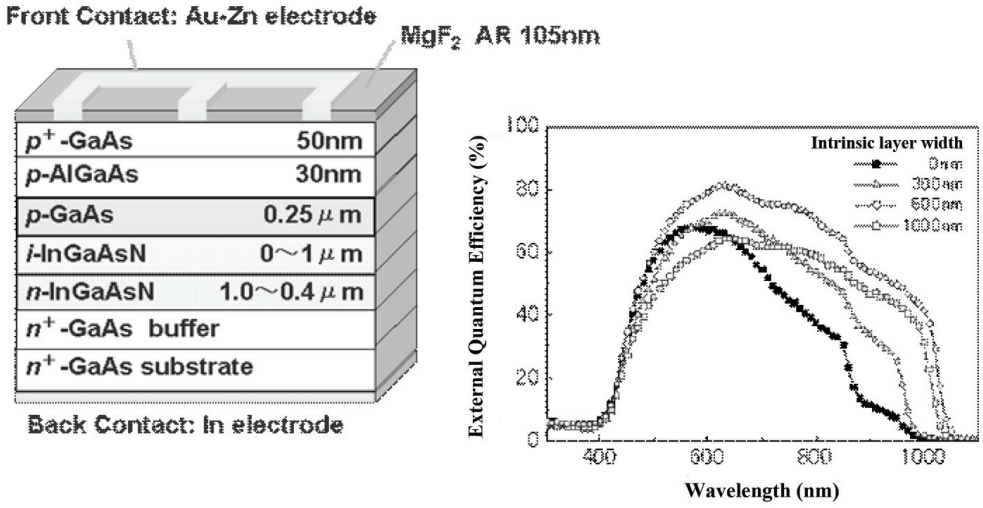

approaching that of an infinite stack of tandem cells. The requirement for reaching efficiencies as high as in Figure 16 is that energy relaxation times by phonon emission and radiative recombination lifetimes must be comparable in magnitude in this region. Alternatively, photon absorption has to occur over distances comparable to hot carrier relaxation lengths. This will require both slowing of energy relaxation processes and acceleration of radiative recombination rates. Although low dimensional structures may have the ability to do both, further development of science and technology such as photon absorber materials, selective energy contact, extraction of carriers and so forth in the hot carrier solar cell concept.

Another suggestion to improve solar cell performance is the "intermediate band concept" (Luque & Marti, 1997) as shown in Figure 17.

Figure 14. Current-voltage curve of a p-GaAs/i-n InGaAsN hetero-junction cell with intrinsic layer width of 600nm

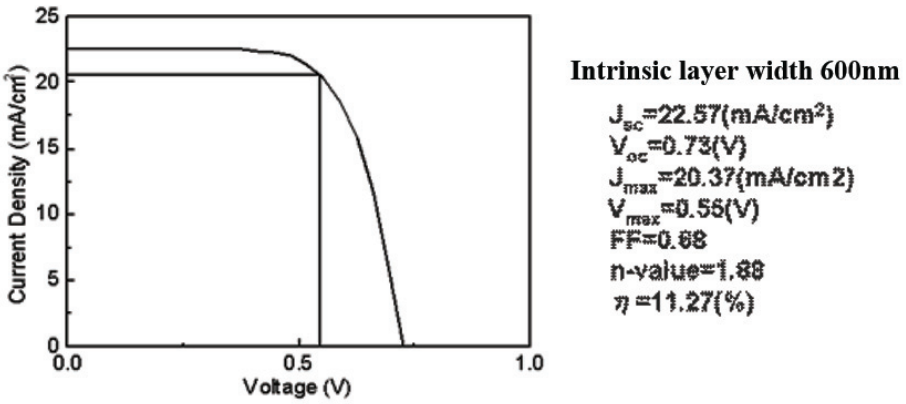

Figure 15. Efficiency/cost regimes for the three photovoltaic generations (Green, 2003)

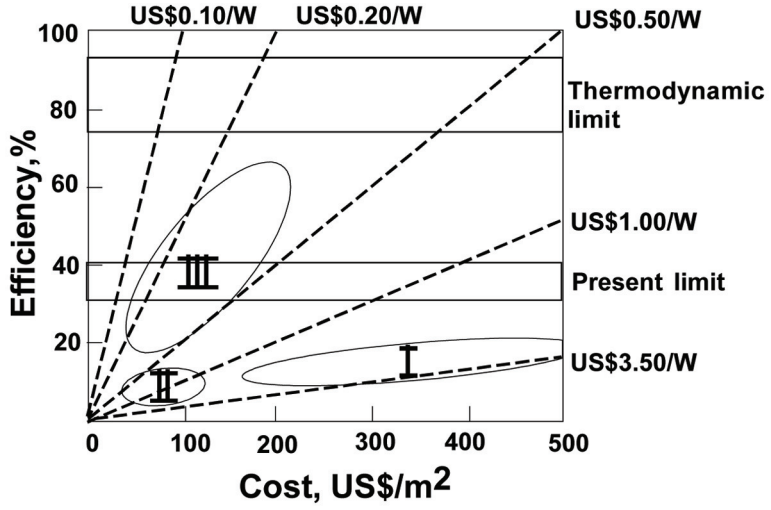

Figure 16. Limiting efficiency of hot carrier cells as a function of bandgap and carrier temperature (Nozik, 2002). The lowermost curve corresponds to that for a conventional cell.

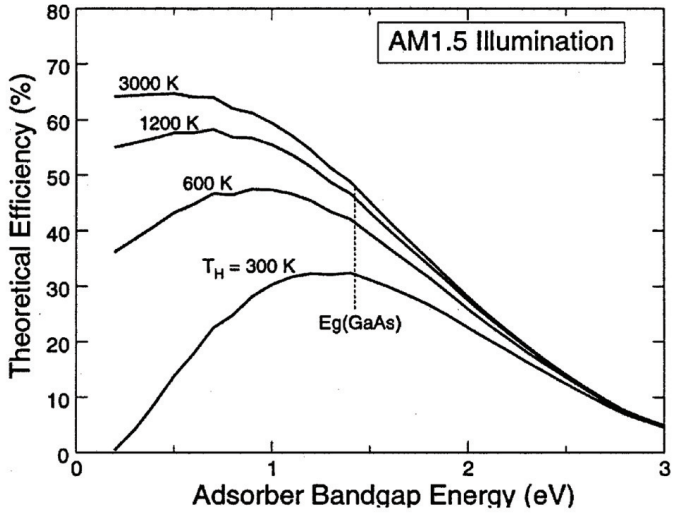

Figure 18 shows maximum efficiency of the Intermediate (IB) solar cell as a function of the lowest of the bandgaps and for the optimum bandgap (Luque & Marti, 1997). The limiting efficiency of single gap solar cells and of a tandem of two solar cells connected in series is also shown for comparison. In the case of 3 band configuration, IB solar cells with Ec-Ev=1.9eV, Ec-IB=1.2eV and IB-Ev=0.7eV (Ec: conduction band minimum, Ev: valence band maximum) are predicted to be 63%. Although low dimensional structures such as quantum dot structures may have the ability to do both, further development of science and technology in the IB solar cell concept.

In the following section, some approaches for solar cells by using quantum wells and quantum dots are presented.

Quantum Well Solar Cells

The Multi-Quantum Well (MQW) solar cells (Barnham & Duggan, 1990) have attracted attention for high efficiency, however, the reported results are lower than the calculated values. In order to achieve higher carrier collection efficiencies out of QWs thereby minimizing recombination losses, Potentially Modulated (PM) MQW structure has been proposed (Okada & Shiotsuka, 2005). Figure 19 shows schematic energy band diagram of 2-step potentially modulated QW and related photoluminescence. In PM-QWs, radiative recombination rates inside QWs are expected to be reduced as a consequence of spatial separation of carriers. Further, higher escape rates of carriers out of QWs can be realized.

Figure 20 shows schematic structure and I-V curve of a PM-QW solar cell made by atomic H-assisted MBE. By using 3-step QWs, dark current was reduced and External Quantum Efficiencies (EQE) in the wavelength regions of 650-850 nm and the longer wavelength region above 900 nm are improved compared to those of 2-step PM-QWs and conventional QWs. 3-step InGaAs/GaAs PM-MQW solar cell has shown projected efficiency of 18.27% that is higher than 16.56% of conventional QW solar cell.

Figure 17. Representation of the p-i-n structure solar cell and simplified band structure of an intermediate-band material

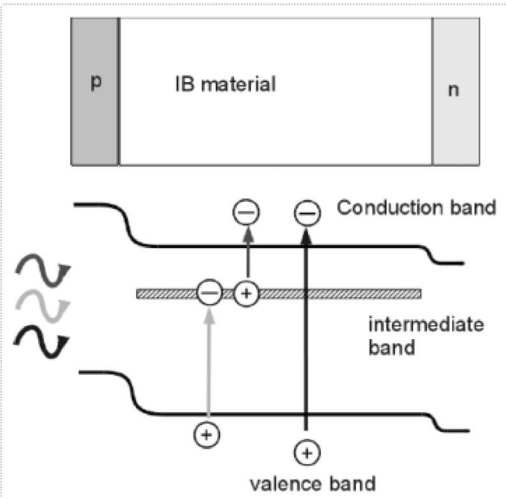

Quantum Dot Solar Cells

Quantum Dot (QD) solar cells have also attracted attention as possible photon utilization. If QDs are periodically distributed in space leading to the formation of an intermediate band rather than a multiplicity of discrete levels, efficiency enhancements around 60% are theoretically predicted in such intermediate band solar cells (Luque & Marti, 1997), which ideally incorporate three-dimensional (3D) quantum dot superlattice.

By taking advantage of spontaneous self-assembly or self-organization mechanism of coherent 3D islanding during growth, known as Stranski-Krastanow (S-K) growth mode in lattice-mismatched epitaxy, In(Ga)As QDs with dot diameter of 63-70 nm and size uniformity of 12-14% have successfully been fabricated on GaAs or InP (311)B substrate as shown in Figure 21. Superior size uniformity and laterally ordered structure of QDs has been achieved by using high-index GaAs or InP substrate as shown in this Atomic Force Microscope (AFM) image. In order to increase effective dot density by multiplayer stacking of QDs, strain-compensation growth technique in which compressive strain due to InAs QDs is compensated by tensile strain induced by InGaAlAs spacer layer as shown in Figure 21. Figure 21 also shows schematic of InAs QD solar cell fabricated by MBE on InP substrate.

Figure 22a shows External Quantum Efficiency (EQE) of 30-multilayer QD solar cells in near-infrared region with strain-compensating spacer layer thickness of 20 and 40 nm. EQE is found to depend on space thickness. Although the sample with spacer thickness of 10 nm showed poor structural and optical property, the best EQE response was obtained for the sample with 20 nm spacer layer due to smooth thermal escape and sequential collection of carriers from QDs before recombination. Figure 22b shows projected I-V

Figure 18. Maximum efficiency of the intermediate solar cell as a function of the lowest of the bandgaps and for the optimum bandgap. The limiting efficiency of single gap solar cells and of a tandem of two solar cells connected in series is also shown for comparison.

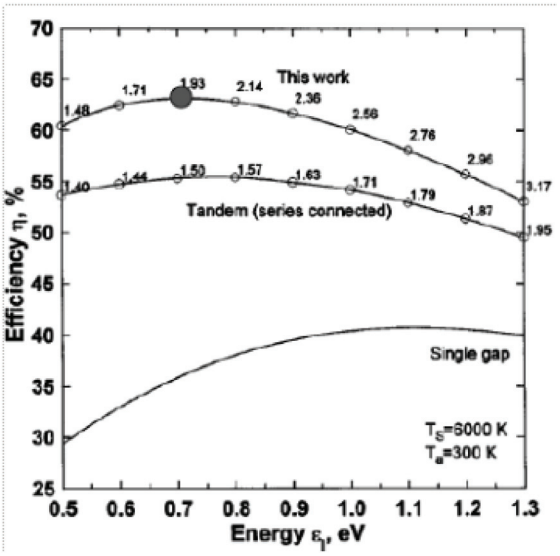

Figure 19. Schematic energy band diagram of 2-step potentially modulated QW and related photoluminescence

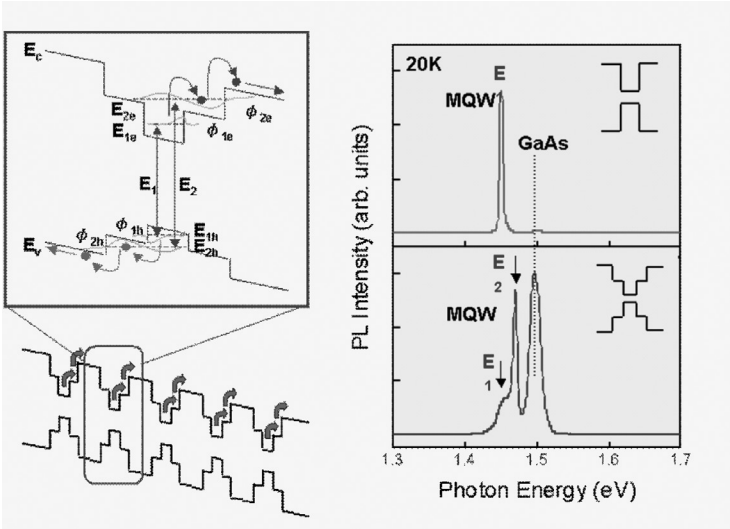

Figure 20. Schematic structure and I-V curve of a PM-QW solar cell made by atomic H-assisted MBE

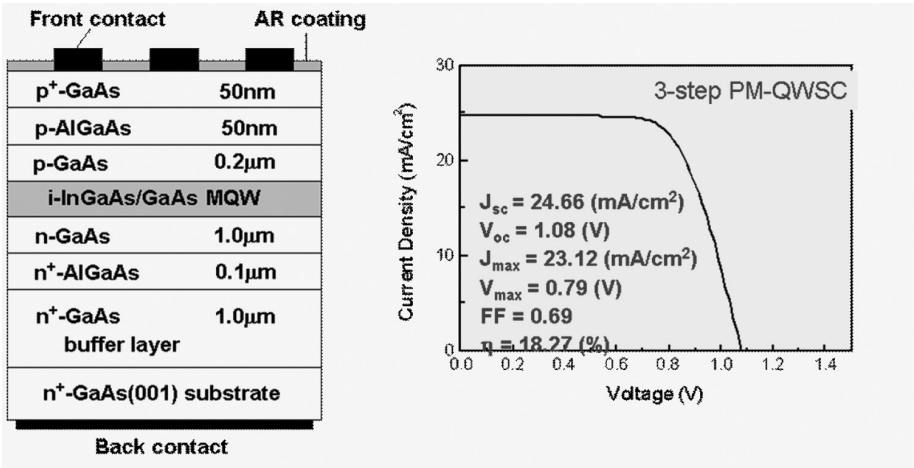

curve of InAs QD solar cell with spacer layer thickness of 20 nm. Efficiencies of the QD cells with space layer thickness of 20nm and 40 nm were 3.82% and 7.65%, respectively (Okada, Shiotsuka, Komiyama, Akahane, & Ohtani, 2005). The Present QD cell performance is thought to be limited by large series resistance and current leakage.

SUMMARY

Photovoltaic (PV) power generation technology is one of the most promising renewable energy technologies because of the possibility of solving environmental problems and limited sources for energy. In order to realize widespread deployment of solar photovoltaics and contribute to further

Figure 21. In(Ga)As quantum dots on GaAs(311)B and In(Ga)As dot cell fabricated on InP (311)B substrate

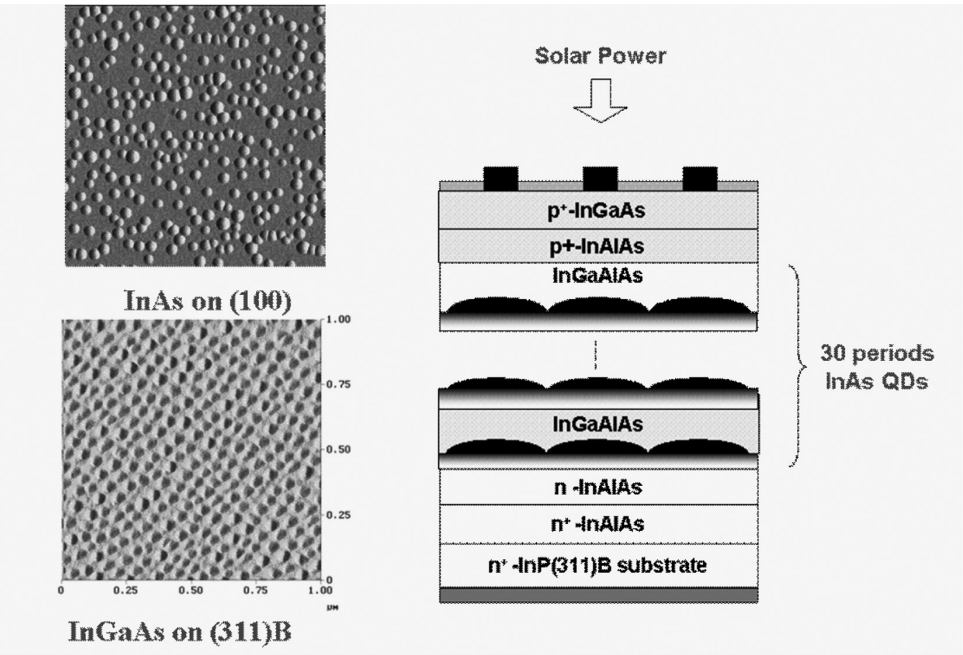

Figure 22. (a) External quantum efficiency (EQE) of 30-multilayer QD solar cells in near-infrared region with strain-compensating spacer layer thickness of 20 and 40 nm, (b) projected I-V curve of InAs QD solar cell with spacer layer thickness of 20 nm

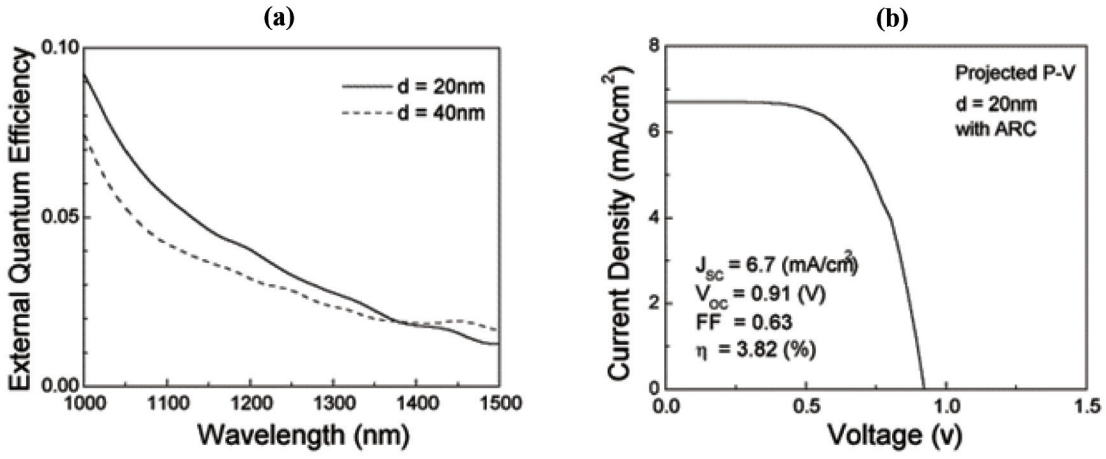

development in civilization, further development in science and technology of the PV is very important. That is, further improvements in conversion efficiencies and reliability, and lowering cost of solar cells and modules are necessary. Regarding conversion efficiencies of solar cells, because there is Shockley-Queisser conversion efficiency limit of 31% at 1-sun and 41% under concentration for single bandgap solar cells, several approaches to overcome the Shockley-Queisser limit should be made. This book will provide readers some guidance to overcome the limit. This chapter presents the current status of solar cells and new trends in solar cells from the viewpoint of conversion efficiency.

Although many R&D for various types of solar cells has been carried out and improvements in their conversion efficiencies have been achieved, conversion efficiencies of almost all the solar cells are expected to have limitations. Limiting efficiencies are expected to be 28.9%, 23.5%, 23.5%, 17.5%, and 16% for crystalline Si, thin-film Si, CIGS as well as CdTe, dye-sensitized and organic solar cells, respectively. On the other hands, because 41.6% efficiency has been realized with concentrator InGaP/InGaAs/Ge 3-junction solar cells, concentrator 4-junction or 5-junction solar cells have great potential for realizing super high-efficiency of over 50%. In addition, developing new types of solar cells based on new materials and new concepts is also very important to overcome conversion efficiency limitations. In addition to multi-layer multi-junction (tandem) solar cells, third-generation PV systems include intermediate bands, hot-carrier effects and other multiple-carrier ejection. Although conversion efficiencies in ideal case shown are 85-87% for multiple excitation, hot carrier, intermediate band concepts, realistic conversion efficiencies to be obtained for solar cells by using the above concepts may be less than 55% by considering possible efficiency based on the realistic multi-junction (tandem) concept. However, further R&D for new materials and new concepts is necessary to challenge to overcome the Shockley-Queisser limit.

REFERENCES

Barnham, K. W. J., & Duggan, G. (1990). Ideal theory of quantum solar cells. *Journal of Applied Physics*, *67*, 3490. doi:10.1063/1.345339

Green, M. (2003). *Third generation photovoltaics: Advanced solar energy conversion*. Berlin, Germany: Springer Science Business Media.

Goetzberger, A., Luther, J., & Willeke, G. (2001). Technical digest. In *Proceedings of the 12th International Photovoltaic Science and Engineering Conference*. Taejon, Japan: KIER.

Kazmerski, L. (2009). *Best research-cell efficiencies*. NREL.

King, R. R., Boca, A., Hong, W., Liu, X.-Q., Bhusari, D., & Larrabee, D. … Karam, N. H. (2009). A photovoltaic system with three solar cells and a band-stop optical filter. In *Proceedings of the 24th European Photovoltaic Solar Energy Conference*. Munich, Germany: WIP.

Kurtz, S. R., Johnston, S. W., Geisz, J. F., Friedman, D. J., & Ptak, A. J. (2005). Paper. In *Proceedings of the 31st IEEE Photovoltaic Specialists Conference*. New York, NY: IEEE.

Kurtz, S. R., Myers, D., & Olson, J. M. (1997). Paper. In *Proceedings of the 26th IEEE Photovoltaic Specialists Conference*. New York, NY: IEEE.

Lewis, N. S. (2005). *Characterization and analysis of InGan photovailic devices*. Paper presented at the 31st IEEE Photovoltaic Specialists Conference. Miami, FL.

Luque, A., & Marti, A. (1997). Increasing the efficiency of ideal solar cells by photon induced transmissions at intermediate levels. *Physical Review Letters*, *78*, 5014. doi:10.1103/PhysRevLett.78.5014

Luther, J., Bett, A. W., Burger, B., & Dimroth, F. (2006). Paper. In *Proceedings of the 21st European Photovoltaic Solar Energy Conference*. Munich, Germany: WIP.

Martí, A., & Luque, A. (Eds.). (2003). *Next generation photovoltaics: High efficiency through full spectrum utilization*. Bristol, UK: Institute of Physics Publishing.

Miyashita, N., Shimizu, Y., Kobayashi, N., Okada, Y., & Yamaguchi, M. (2006). Paper. In *Proceedings of the 4th World Conference on Photovoltaic Energy Conversion.* New York, NY: IEEE.

Nozik, A. J. (2002). Quantum dot solar cells. *Physica E, Low-Dimensional Systems and Nanostructures*, *14*, 115. doi:10.1016/S1386-9477(02)00374-0

Okada, Y., & Shiotsuka, N. (2005). Paper. In *Proceedings of the 31st IEEE Photovoltaic Specialists Conference*. New York, NY: IEEE.

Okada, Y., Shiotsuka, N., Komiyama, H., Akahane, K., & Ohtani, M. (2005). Paper. In *Proceedings of the 20th European Photovoltaic Solar Energy Conference*. Munich, Germany: WIP.

Sasaki, T., Arafune, K., Lee, H. S., Ekins-Daukes, N. J., Tanaka, S., Ohshita, Y., & Yamaguchi, M. (2006). Effects of thermal cycle annealing on reduction of deficit density on lattice-mismatched InGaAS solar cells. *Physica B, Condensed Matter*, *376-377*, 626. doi:10.1016/j.physb.2005.12.158

Shockley, W., & Queisser, H. J. (1961). Detailed balance limit of p-n junction solar cells. *Journal of Applied Physics, 32,* 510. Green, M. A., Emery, K., Hishikawa, Y., & Warta, W. (2011). Solar cell efficiency tables. *Progress in Photovoltaics: Research and Applications*, *19*, 84.

Swanson, R. M. (2006). A vision for crystalline silicone photovoltaics. *Progress in Photovoltaics: Research and Applications*, *14*, 443. doi:10.1002/pip.709

Takamoto, T., Kaneiwa, M., Imaizumi, M., & Yamaguchi, M. (2005). InGaP/GaAs-based multijunction solar cells. *Progress in Photovoltaics: Research and Applications*, *13*, 495. doi:10.1002/pip.642

WBGU. (2003). *World in transition: Towards sustainable energy systems*. London, UK: Earthsan.

Yamaguchi, M. (2004). Paper. In *Proceedings of the 19th European Photovoltaic Solar Energy Conference*. Munich, Germany: WIP.

Yamaguchi, M., Nishimura, K., Sasaki, T., Suzuki, H., Arafune, K., & Kojima, N. (2008). Novel materials for high-energy III-V multi-junction solar cells. *Solar Energy*, *82*, 173. doi:10.1016/j.solener.2007.06.011

Yoshida, A., Agui, T., Nakaido, K., Murasawa, K., Juso, H., Sasaki, K., & Takamoto, T. (2011). Technical digest. In *Proceedings of 21st International Photovoltaic Science and Engineering Conference*. Fukuoka, Japan: Photovoltaic Science and Engineering.

Chapter 2
Physical Limitations of Photovoltaic Conversion

Laurentiu Fara
Polytechnic University of Bucharest, Romania & Academy of Romanian Scientists, Romania

Masafumi Yamaguchi
Toyota Technological Institute (TTI), Japan

ABSTRACT

This chapter presents the factors that are included in the expression of the conversion efficiency of a solar cell. These factors are upper limited, and that is why the conversion efficiency could not exceed certain critical values. The chapter analyzes thermodynamic limitations, correction introduced by the atmosphere, Shockley-Quiesser limitations (based on the detailed energy balance), as well as additional limitations. Then it discusses ways to improve the conversion efficiency and future research directions.

THERMODYNAMIC LIMITATIONS

One factor limiting the conversion efficiency is the thermodynamic efficiency. A solar cell converts the sun's thermal radiation into electricity. Therefore, thermodynamic laws may restrict the efficiency to lower values of Carnot efficiency:

$$\eta_T^{(C)} = 1 - \frac{T_c}{T_S} \tag{1}$$

where T_S is the sun's temperature and T_c is the cell's temperature. The sun is usually considered as a blackbody with temperature of 6000 K and the solar cell is considered to be in thermal equilibrium with the environmental temperature, so

DOI: 10.4018/978-1-4666-1927-2.ch002

that $\eta_T^{(C)} = 95\ \%$. In reality, the sun is composed of plasma, so its behavior is closer to the thermal one of a metal, resulting in $T_S \approx 5800$ K. On the other hand, the solar cell is warmer than the environment (due to processes that are occurring in it), so that we can take $T_C \approx 320$ K and the yield falls to 94.5%. However, such a value is very high.

A closer analysis of the thermodynamic efficiency must take into account the thermal radiation laws. If we use the blackbody model, both for the Sun, and for the cell, and consider the cell in thermal equilibrium with the environment, we obtain the Landsberg yield (Markvart & Castañer, 2003; Landsberg & Badescu, 1998):

$$\eta_T^{(L)} = 1 - \frac{4}{3}\frac{T_c}{T_S} + \frac{1}{3}\left(\frac{T_c}{T_S}\right)^4 \tag{2}$$

A more precise calculation requires the cell's temperature evaluation when the Sun and the environment are in a thermodynamic equilibrium. Considering the heat exchange between the Sun and solar cell using the blackbody's laws, and the one between the environment and the cell corresponding to thermal contact, Müser obtained the heat balance equation, $4T_c^5 - 3T_aT_c^4 - T_aT_S^4 = 0$:

$$\eta_T^{(M)} = \left[1 - \left(\frac{T_c}{T_S}\right)^4\right]\left(1 - \frac{T_a}{T_c}\right) \tag{3}$$

and the yield value of 85.6% (Markvart & Castañer, 2003; Badescu & Landsberg, 1998). The heat radiation corrections of metals reduce this value down to about 85.2%.

A particular problem which will be discussed again in the next paragraph refers to the Earth's atmosphere selective absorption . This moves the solar spectrum, giving the appearance of lower temperatures (the blackbody model, this apparent temperature is $5767\ \mathrm{K}$), leading to $\eta_T^{(C)} = 94,8\ \%$, $\eta_T^{(L)} = 93,1\ \%$, $\eta_T^{(M)} = 85,4\ \%$ (the metal heat radiation corrections reduce these values by about 0.4%).

When it comes to space applications, the situation changes. Here the environmental temperature is almost 0 K, and the cell losses appear only by thermal radiation. Even if we consider the cell isothermal and the circuit open, the cell temperature is:

$$T_c = \left(\frac{\Omega}{2\pi}\right)^{1/4} T_S = \sqrt{\frac{R_S}{\sqrt{2}D_{SP}}}T_S = 331\ \mathrm{K} \tag{4}$$

($\Omega = 6{,}8\cdot10^{-5}$ Sr is the solid angle under the Sun is seen from Earth, $R_S = 696\cdot10^3$ km is the Sun's radius and $D_{SP} = 149{,}6\cdot10^6$ km is the Sun – Earth distance), so that the previously calculated yield decreases by about 0.1% . A more accurate calculation leads to a decrease of 0.2%. It can be seen that these corrections are insignificant.

CORRECTIONS INTRODUCED BY THE ATMOSPHERE

The Sun's spectrum is not exactly that of a blackbody (or metal). The solar photosphere and chromosphere introduce absorption lines (Fraunhofer lines), modifying the energy distribution. The Earth's atmosphere introduces more corrections, because of its much lower temperature, the existence of molecules (absorption bands instead of lines), the refractive index induced by the air currents oscillations, the water vapours and the thermal fluctuations, and the diffusion produced by dust and other matter (Fahrenbrunch, Bube, 1983; Smestad, 2002).

It is estimated that in ideal conditions (clean air, normal incidence), the solar spectrum in space (denoted AM 0 - 0 atmospheric mass), with full radiance of 1365 W/m^2, is reduced to 70% of its full radiance (taking into account absorption

Equation 5.

$$\eta_{SQ}^{(l)} = \left(x_g \int_{x_g}^{\infty} \frac{x^2 dx}{e^x - 1} \right) \Bigg/ \left(\int_0^{\infty} \frac{x^3 dx}{e^x - 1} \right) \equiv \frac{x_g \int_{x_g}^{\infty} f_{RT}(x)\, dx}{\int_0^{\infty} x f_{RT}(x)\, dx}, \quad x_g = \frac{E_g}{k_B T_S} \tag{5}$$

bands), plus 7% diffused light—1 AM, with about 1000 W/m^2.The full radiance of AM 1 is virtually equal to that of a blackbody temperature of 5767 K. Usually in order to take into account various factors, a lower range like AM 1.5 is used, it represents two thirds of AM 1 (700 W/m^2)—about half of AM 0. The radiance calculation took into account the full solid angle under which the Sun can be seen from Earth. At normal incidence, it introduces a factor $f\Omega = \Omega / \pi \approx 2.16 \bullet 10^{-5}$ in the ratio of full radiance emitted by the Sun and that received by the cell.

When it comes to space applications, AM 1.5 should be replaced with AM 0 and the same cell produces two times more energy than on Earth. As a result, for space applications is not intended primarily a higher conversion efficiency, but a lower mass / power ratio and a larger reliability in space conditions (high vacuum, ambient temperature of 0K, large temperature gradients between the illuminated face and the shadowed one, hard radiation, etc.).

DETAILED ENERGY BALANCE

The first self-consistent calculation of the conversion efficiency, based on the detailed energy balance of the solar cells was performed by Shockley and Queisser (Shockley & Queisser, 1961). They have assessed the behavior of a p-n junction, in which only appear radiative recombination phenomena, exposed to the thermal radiation of a blackbody. In this case, we can define a yield limit by the relationship in Equation 5, where E_g is the forbidden bandwidth (gap) of the used semiconductor. The $\eta_{SQ}^{(l)} = \eta_{SQ}^{(l)}(x_g)$ dependence is shown in the Figure 1.

It is noted that the yield limit is the maximum for the following equation:

$$x_{gm} f_{RT}(x_{gm}) = \int_{x_{gm}}^{\infty} f_{RT}(x)\, dx \tag{6}$$

Equation (6) admits as solution $x_{gm} \approx 2{,}17$, $E_g \approx 1{,}12$ eV, the obtained yield is 44%. Note: $x_{gSi} \approx 2{,}2$ ($E_{gSi} = 1{,}14$ eV).

This calculation is completed by assessing three additional factors.

Figure 1. The dependence of the limit yield gap semiconductor (Shockley & Queisser, 1961)

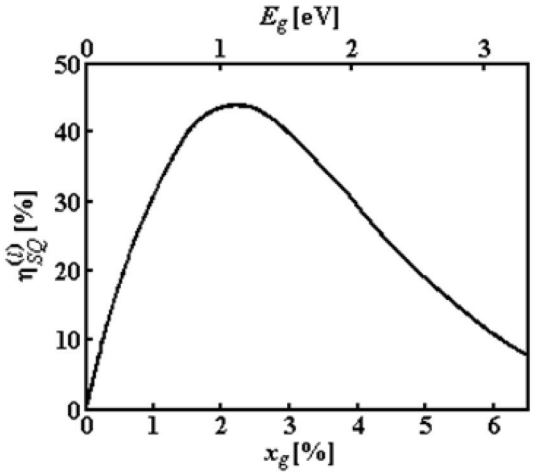

Equation 7.

$$v \equiv eU_{cd}/E_g = \frac{x_c}{x_g}\ln\left[\frac{f_r f_\Omega}{2x_c^3}\left(\int_{x_g}^{\infty}\frac{x^2dx}{e^x-1}\right)\Bigg/\left(\int_{x_g/x_c}^{\infty}\frac{x^2dx}{e^x-1}\right)\right],\ x_c = \frac{T_c}{T_S} \tag{7}$$

- The first one is the external quantum efficiency $\eta_Q^{(e)}(\lambda) = A_\lambda \eta_Q^{(i)}(\lambda)$, where A_λ is the junction's absorption and $\eta_Q^{(i)}$ is the internal quantum efficiency; $\eta_Q^{(i)}$ represents the probability that an absorbed photon (with energy greater than E_g) generates an electron-hole pair. Shockley and Queisser have taken for simplicity $\eta_Q^{(i)} = 1$ and assumed cell absorbance equal to that of a blackbody($A_\lambda = 1$), so $\eta_Q^{(e)} = 1$.
- The second one (see Equation 7) is the ratio between the open circuit's voltage and the gap one.

In this relationship, fr is the proportion of the recombination current that is given by the radioactive recombination (also taken equal to 1 for simplicity).

The third factor is the form factor,

$$FF \equiv U_M I_M / U_{cd} I_{sc} \tag{8}$$

where I_{sc} the short circuit current is, and U_M, I_M represent the maximum voltage and current for the power supplied in the external circuit.

If we consider $z_{cd} = eU_{cd}/k_B T_c$, $z_M = eU_M/k_B T_c$, and an ideal diode (no serial or parallel resistance and the ideality factor is 1),the maximum power requirement cut is $z_{cd} = z_M + \ln(1+z_M)$. Then the form factor becomes:

$$FF = \frac{z_M^2}{\left[1+z_M-\exp(-z_M)\right]\left[z_M+\ln(1+z_M)\right]} \tag{9}$$

With these factors, the conversion efficiency becomes:

$$\eta_{SQ} = \eta_{SQ}^{(l)} \cdot v \cdot FF \tag{10}$$

The maximum conversion efficiency given by (10) is 31.2%, for $x_g \approx 2{,}5$.. This value is close not only the crystalline silicon, but also to those of amorphous silicon, GaAs, Cu_2S, and a few other combinations. For crystalline silicon $\eta_{SQ} \approx 30\%$.

It must be taken into account that for obtaining the Formula (10) several important approximations have been made.

In the first approximation, the blackbody radiation was used instead of AM 1.5; Luque (Luque & Araújo, 1990) replaced the yield limit $\eta_{SQ}^{(l)}$ given by (5) in Equation 11.

Where

Equation 11.

$$\eta_L^{(l)} = \left(x_g\int_{x_g}^{\infty}N_f(x)\,dx\right)\Bigg/\left(\int_0^{\infty}xN_f(x)\,dx\right) \equiv x_g\int_{x_g}^{\infty}n_f(x)\,dx \tag{11}$$

$$x = \frac{hc}{k_B T_S \lambda} \tag{12}$$

$N_f(x)$ represents the AM 1.5 number of photons for the wavelength λ, and

$$n_f(x) = \frac{N_f(x)}{\int_0^\infty x N_f(x)\,dx} \tag{13}$$

This limit does not exceed 37.5% efficiency. The situation may be improved, if optical concentrators could be used, by increasing the number of photons incident on the cell in comparison to the geometric value.

A second approximation was to consider the internal quantum efficiency as ideal. This is not true. Internal quantum efficiency depends on the absorption and on the wavelength of the absorbed photon and may represent a percentage for certain wavelengths. A rigorous calculation should take this into account.

A third approximation was to neglect the absorbance. This may represent a major correction, reducing the conversion efficiency at less than half of the ideal value. To improve the situation, textured entrance surfaces and back reflective layers are used (Möller, 1993), this increase over the photons in the cell and enhance the absorption.

The fourth one was to neglect the non-radiative processes. This can dramatically reduce cell efficiency. But there are exceptions. The Auger effect can multiply the number of electrons generated by a photon and thus increase efficiency.

Finally, the last approximation was to consider an ideal diode. Experience shows that such a situation can never be found. Moreover, experimentally was proved that it is unnecessary to use efficient optical concentrators, because the efficiency tends to a saturation value with the increasing incident light flux.

ADDITIONAL FACTORS LIMITING THE CONVERSION EFFICIENCY

We will not discuss, in detail, the calculation of internal quantum efficiency, because it depends on the type of material from which the cell is made (Bardeen, Blatt, & Hall, 1956; Ryvkin, 1964; Tauc, Grigorovici, & Vancu, 1966; Kireev, 1975; Sze, 1981; Bube, 1992; Munteanu, 2003). By a proper choice of the material a 90% internal quantum efficiency can be obtained In order to assess the external quantum efficiency is necessary to know the absorbance. If we consider as known the input and output reflectance from the layer:

$$R_\lambda^{(in)} = \frac{\left(n_\lambda - n_\lambda^{(in)}\right)^2 + \kappa_\lambda^2}{\left(n_\lambda + n_\lambda^{(in)}\right)^2 + \kappa_\lambda^2}, \qquad R_\lambda^{(out)} = \frac{\left(n_\lambda - n_\lambda^{(out)}\right)^2 + \kappa_\lambda^2}{\left(n_\lambda + n_\lambda^{(out)}\right)^2 + \kappa_\lambda^2} \tag{14}$$

(n_λ, κ_λ being the real and imaginary part of the complex refractive index of the active layer and $n_\lambda^{(in)}$, $n_\lambda^{(out)}$ being the input and output refractive indices) and the absorption coefficient $\alpha_\lambda = 4\pi\kappa_\lambda/\lambda$, the absorbance for a normal incidence on a layer of d thickness (see Equation 15).

Another important factor is the collecting factor η, representing the fraction of electron-hole pairs generated by photons with a λ wavelength separated by a barrier and collected by the electrodes. This factor has a complicated expression. When it comes to thick active layers, this expression can be approximated as:

$$\eta_c \approx \left(\frac{\alpha_\lambda L_p}{1+\alpha_\lambda L_p} + \frac{\alpha_\lambda L_n}{1+\alpha_\lambda L_n}\right)\exp\left(-\alpha_\lambda d\right) \tag{16}$$

Equation 15.

$$A_\lambda = \frac{\left(1-R_\lambda^{(in)}\right)\left[1+R_\lambda^{(out)}\exp\left(-\alpha_\lambda d\right)\right]\left[1-\exp\left(-\alpha_\lambda d\right)\right]}{1-R_\lambda^{(in)}R_\lambda^{(out)}\exp\left(-2\alpha_\lambda d\right)} \tag{15}$$

It seems that this correction can be quite important.

Shockley and Queisser analysis refers to the ideal diode. A real diode has a number of additional parameters. The p and n regions preclude an ohmic resistance (series) R_s, due to the interaction of carriers with phonons and impurities. This resistance reduces the voltage at the junction of the diode's terminals. There are junction surface currents (equivalent to a parallel resistance R_p). A similar effect is introduced by the formation of inversion layers at the diode's contacts (more metal-semiconductor junctions).In addition, under strong injection (or another method that generates no equilibrium), the effect of voltage on the junction is changed by a factor γ, called the ideality factor. As a result, the equation that describes the operation of the diode in the dark is:

$$I = I_s\left\{\exp\left[\frac{e\left(U-R_sI\right)}{\gamma k_BT}\right]-1\right\}+\frac{U-R_sI}{R_p} \tag{17}$$

In the presence of the light a photovoltaic voltage is generated, usually described as a current source in parallel with the junction (the illumination current I_l is proportional to the integral after the wavelength of the product between the incident light flux, the external quantum efficiency and the collecting factor), so the Equation (15) becomes:

$$I = I_L - I_s\left\{\exp\left[\frac{e\left(U+R_sI\right)}{\gamma k_BT}\right]-1\right\}-\frac{U+R_sI}{R_p} \tag{18}$$

where U is the terminal voltage of the diode ($U = R_{ext}I$, R_{ext} being the load resistance of the outside circuit). From this equation, we find that the open circuit voltage and short circuit current satisfy default relations:

$$I_s\left[\exp\left(\frac{eU_{cd}}{\gamma k_BT}\right)-1\right]+\frac{U_{cd}}{R_p} = I_L \tag{19}$$

$$I_s\left[\exp\left(\frac{eR_sI_{sc}}{\gamma k_BT}\right)-1\right]+\left(1+\frac{R_s}{R_p}\right)I_{sc} = I_L \tag{20}$$

Considering the diode ideal ($R_s = 0$, $R_p = \infty$, γ = 1), these relations become:

$$I_{sc} = I_L,\ \ I_s\left[\exp\left(\frac{eU_{cd}}{k_BT}\right)-1\right] = I_L \tag{21}$$

Comparing these relations, we see that can introduce two subunit factors:

$$I_{sc} \equiv \beta_I I_L,\ \ U_{cd} \equiv \beta_U\frac{k_BT}{e}\ln\left(\frac{I_L}{I_s}+1\right) \tag{22}$$

Combining all these factors and taking into account the relations (11)÷(13) the solar cell conversion efficiency is obtained:

$$\eta = \eta_T^{(M)}vFF\beta_I\beta_U x_g\int_{x_g}^{\infty} n_f\left(x\right)A_x\eta_Q^{(i)}\left(x\right)\eta_c\left(x\right)dx \tag{23}$$

Comparing this result with Shockley's and Queisser's results, one sees that the value obtained is reduced below 20% for a conventional monocrystalline silicon cell. Furthermore, after mounting the cell into a PV module the efficiency is reduced by a technical factor (determined by encapsulation, external circuit, etc.), leading to the values obtained experimentally.

WAYS TO IMPROVE THE CONVERSION EFFICIENCY

In order to improve the conversion efficiency of the solar cells, we must take into account each factor in the Equation (23). We begin with the absorbance. The (15) relation shows that the absorbance depends exponentially on the thickness of the active layer. On the other hand, only pairs generated in the field barrier can be separated, so that what really counts is the thickness of the junction. This can be substantially increased if the classical p-n junction is replaced with a p-i-n junction, which introduces an intrinsic layer between p and n regions, in the barrier field (Crandall, 1983). This design can improve conversion efficiency up to 50% of its value. In addition, the photons movement through the active area may increase significantly when using back reflective surface and input surface is textured in order to multiply the possible paths of the photons.

As seen from above, the second factor is the collecting factor. It depends on two phenomena: the existence of a heavy field barrier—that can be achieved by doping increasing - and a small number of recombination centers - so few defects and impurities. If the first part is easily achievable, the second one requires special manufacturing conditions. This explains why the in laboratory created cells have achieved much higher conversion efficiency (and cost prices) than those produced industrially.

The β_I and β_U factors also depend on the construction of the diode and require detailed studies. There are many variants, most kept confidential.

The form factor depends nonlinear on the cell parameters. Its expression is complicated even if we only consider the radiative recombination. Usually, cells with different parameters are built in the laboratory and then optimize the parameters. It should be mentioned that the form factor and the conversion efficiency are not the same for the same maximum values of the parameters.

The ratio between the open circuit's voltage and the gap one (voltage greater than the barrier one) depends on the recombination types and (logarithmically) on the incident light flux. The more recombination we have, the more the ratio decreases. On the other hand, the ratio can be increased if we have an Auger effect, which multiplies the number of carriers. These effects occur only when there are high-energy carriers—"hot" electrons. It is true that in such cells thermal equilibrium between electrons and the crystalline network does not exist, this is why thermal efficiency decreases, but as we have seen, small changes in thermal efficiency are, therefore, less important. Optical concentrators are used to increase the light flow, which can introduce a multiplicative factor ranging up to several hundred.

The most important factors are the internal quantum efficiency and the limit yield. The internal quantum efficiency depends essentially on the type of used material. The internal quantum efficiency is higher in semiconductors with indirect gap, but they usually have a non-radiative recombination. Therefore, it was tried to replace silicon with GaAs chalcogenic compounds. Improvements made so far do not offset the cost increase. Another improvement was the introduction of quantum granules. These replace the energy band structure with a level structure. Under these conditions, the non-radiative recombination is significantly reduced, which compensates a lower efficiency.

Regarding the limit yield, it depends mainly on the gap's value. In order to extend the absorption field there are several options. The first option was the use of amorphous materials with band tails (Carlson & Wronski, 1976; Hubin & Shah, 1995; Schiff, 2003). This option did not give the expected results due to the instability of the material and especially the great number of recombination centers. A second option was a design of multiple series junctions, with the gap decreasing as departing from the front surface. The light that is not absorbed by the first junction is absorbed by the following one. By combining this structure with a textured front surface, mounting a rear reflector, and using an optical concentrator, 42% conversion efficiency was obtained (at laboratory scale). The last option was the development of intermediate-band junctions. These were achieved using nanomaterials. The absorption band extends the range without introducing non-radiative recombination and reducing the radiative ones (increasing the collecting factor). And this cell type reached a conversion efficiencies of around 30% (at laboratory scale).

An alternative to the conversion efficiency growth is the solar cell cost reduction. This is why studying organic solar cells is very important. They are very cheap, thin, flexible, and easy to handle. In contrast, the conversion efficiency has (so far) values below 10%. Obviously, the optimal solution is depending on the intended application.

On the other hand, one sees that the drastic limitations of the Shockley-Queisser model can be overcome.

FUTURE RESEARCH DIRECTIONS

Although many R&D for various types of solar cells has been carried out and improvements in their conversion efficiencies have been achieved, conversion efficiencies of almost all the solar cells are expected to have limitations. Limiting efficiencies are expected to be 28.9%, 23.5%, 23.5%, 17.5%, and 16% for crystalline Si, thin-film Si, CIGS as well as CdTe, dye-sensitized and organic solar cells, respectively. On the other hands, because 41.6% efficiency has been realized with concentrator InGaP/InGaAs/Ge 3-junction solar cells, concentrator 4-junction or 5-junction solar cells have great potential for realizing super high-efficiency of over 50%. In addition, developing new types of solar cells based on new materials and new concepts is also very important to overcome conversion efficiency limitations. In addition to multi-layer multi-junction (tandem) solar cells, third-generation PV systems include intermediate bands, hot-carrier effects and other multiple-carrier ejection. Although conversion efficiencies in ideal case shown are 85-87% for multiple excitation, hot carrier, intermediate band concepts, realistic conversion efficiencies to be obtained for solar cells by using the above concepts may be less than 55% by considering possible efficiency based on the realistic multi-junction (tandem) concept. However, further R&D for new materials and new concepts is necessary to challenge to overcome the Shockley-Queisser limit.

REFERENCES

Bardeen, J., Blatt, F. J., & Hall, L. H. (1956). Paper. In *Proceedings of Atlantic City Photoconductivity Conference*. Atlantic City, NJ: John Wiley and Chapman and Hall.

Bube, R. H. (1992). *Photoelectronic properties of semiconductors*. Cambridge, UK: Cambridge University Press.

Carlson, D. E., & Wronski, C. R. (1976). Amorphous silicon solar cell. *Applied Physics Letters*, *28*, 671. doi:10.1063/1.88617

Chitre, S. R. (1978). A high volume cost efficient production macrostructuring process. In *Proceedings of the 14th IEEE 25th IEEE Photovoltaic Specialists Conference*, (pp. 152-154). Washington, DC: IEEE Press.

Crandall, R. S. (1983). Physics of amorphous silicon alloy p-i-n solar cells. *Journal of Applied Physics*, *54*, 7176. doi:10.1063/1.331955

Emery, K., Burdik, J., Cayem, Y., Dunlavy, D., Field, H., Koposki, B., & Moriarty, T. (1996). Paper. In *Proceedings of the 25th IEEE Photovoltaic Specialists Conference,* (pp. 1275-1278). New York, NY: IEEE Press.

Fahrenbrunch, A. L., & Bube, R. H. (1983). *Fundamentals of solar cells*. New York, NY: Academic Press.

Fara, L., Mitroi, M. R., Cincu, C., Iancu, V., Zaharia, C., & Fara, S.…. Iancu, M. (2009). *Physics and technology of solar cells and PV systems.* Bucharest, Romania: Romanian Scientists Academy Publishing House.

Fara, L., Mitroi, M. R., Iancu, V., Milescu, G., & Noaje, G. (2008). *Modeling and numerical simulation of nanostructured solar cells*. Bucharest, Romania: Punct Publishing House.

Green, M. A. (1986). *Solar cells: Operating principles, technology and system applications*. Kensington, Australia: University of NSW.

Green, M. A. (1992). *Solar cells: Operating principles, technology and system applications*. Kensington, Australia: University of NSW.

Hu, C., & White, R. M. (1983). *Solar cells: From basic to advanced systems*. New York, NY: McGraw-Hill.

Hubin, J., & Shah, A. V. (1995). Effect of the recombination function on the collection in a p-i-n solar cell. *Philosophical Magazine B*, *72*, 589. doi:10.1080/01418639508240314

King, D. L., Kratochvil, J. A., & Boyson, W. E. (1997). Paper. In *Proceedings of the 26th IEEE Photovoltaic Specialists Conference*, (pp. 1183-1186). Anaheim, CA: IEEE Press.

Kireev, P. S. (1975). *Semiconductor physics*. Moscow, Russia: Mir.

Landsberg, P. T., & Badescu, V. (1998). Solar energy conversion: List of efficiencies and some theoretical considerations, part 1: Theoretical considerations. *Progress in Quantum Electronics*, *22*(4), 211–240. doi:10.1016/S0079-6727(98)00012-3

Markvart, T., & Casta, ñer, L. (Eds.). (2003). *Practical handbook of photovoltaics – Fundamentals and applications*. Oxford, UK: Elsevier.

Möller, H. J. (1993). *Semiconductors for solar cells*. Boston, MA: Artech House.

Munteanu, I. (2003). *Solid state physics*. Bucharest, Romania: Bucharest University Publishing House.

Radziemska, E. (2003). The effect of temperature on the power drop in crystalline silicon solar cells. *Renewable Energy*, *28*(1), 1–12. doi:10.1016/S0960-1481(02)00015-0

Ryvkin, S. M. (1964). *Photoelectric effects in semiconductors*. New York, NY: Consultant Bureau.

Schiff, E. A. (2003). Low mobility solar cells: A device physics primer with applications to amorphous silicon. *Solar Energy Materials and Solar Cells*, *78*, 567–595. doi:10.1016/S0927-0248(02)00452-X

Shockley, W., & Queisser, H. J. (1961). Detailed balance limit of efficiency of p-n junction solar cells. *Journal of Applied Physics*, *32*, 510. doi:10.1063/1.1736034

Smestad, G. P. (2002). *Optoelectronics of solar cells*. Bellingham, UK: SPIE Press. doi:10.1117/3.446028

Sze, S. M. (1981). *Physics of semiconductor devices* (2nd ed.). New York, NY: John Wiley & Sons.

Tauc, J., Grigorovici, R., & Vancu, A. (1966). Optical properties and electronic structure of amorphous germanium. *Physica Status Solidi*, *15*, 627–637. doi:10.1002/pssb.19660150224

Yablonovitch, E., & Cody, G. D. (1982). Intensity enhancement in textured optical sheets for solar cells. *IEEE Transactions on Electron Devices*, *29*, 300–305. doi:10.1109/T-ED.1982.20700

Section 2

Quantum Well Solar Cells

Chapter 3
Quantum Well Solar Cells: Physics, Materials and Technology

Magdalena Lidia Ciurea
National Institute of Materials Physics, Romania

Ana-Maria Lepadatu
National Institute of Materials Physics, Romania

Ionel Stavarache
National Institute of Materials Physics, Romania

ABSTRACT

Quantum well solar cells with p-i-n structure are presented. The physical processes in multiple quantum well solar cells, the materials commonly used for photovoltaic applications, and technological aspects are analyzed. The quantum confinement effect produces resonant energy levels located in the valence and conduction bands of well layers. In addition, it produces energy quantum confinement levels located in the energy band gap of both well and barrier layers. The absorption on both resonant and quantum confinement levels leads to an extension of the internal quantum efficiency in near infrared domain.

Several structures with different absorbers from 3-5 and 4 groups are described and discussed. Various technological and design solutions, such as multiple quantum well solar cells with graded band gap, with tandem configurations, with strain-balanced structure, and strain-balanced structure improved with nanoparticles deposited atop are analyzed. The cell parameters are discussed and related to the materials and technology.

DOI: 10.4018/978-1-4666-1927-2.ch003

INTRODUCTION

Solar energy represents a clean, renewable energy (Myong, 2007). As solar light is at our disposal, it represents a primary source of abundant clean energy. The internal quantum efficiency close to 100% in bulk heterojunction Solar Cells (SCs) (Park, et Al., 2009) makes SCs promising candidates among renewable energy sources. Almost 100% internal quantum efficiency means that every absorbed photon produces a separated electron-hole pair and that all these carriers are collected at the electrodes. The role of SCs is to convert the solar energy into electrical energy. In a semiconductor one photon absorption generates an electron-hole pair. These non-equilibrium carriers do not comply with the equilibrium statistics; therefore, they recombine after their lifetime. During their lifetime, the non-equilibrium carriers move through an external circuit, and their energy can be utilized. This is a simplified functioning principle of a solar cell.

The first aspect that has to be analyzed generally in SCs, and particularly, in Quantum Well (QW) SCs is light absorption. The calculation of the absorption coefficient ($\alpha(\lambda)$) is essential for the modeling of solar cells. The main absorption phenomenon is the band-to-band absorption that generates an electron-hole pair. There are two types of semiconductors, with direct or indirect energy band gap, considering the position of the conduction band minimum (E_c) related to the valence band maximum (E_v) in the $\vec{k}$ wave vector space. The most of 3-5 (GaAs) and 2-6 (CdTe) semiconductors have a direct gap, while the semiconductors from group 4 (C, Si, and Ge) have an indirect gap. The calculus of the absorption coefficient depends on the gap type (direct or indirect), and on both values of the orbital quantum number (l) for the valence band and conduction one. The absorption coefficient is found by determining the absorption rate and by evaluating the Einstein coefficients (Iancu, Mitroi, & Fara, 2009; Ciurea & Iancu, 2010; Iancu, Mitroi, Lepadatu, Stavarache, & Ciurea, 2011). Besides the band-to-band absorption, one should take into account the excitonic and inter-band absorption, and also the absorption on free charge carriers, impurities, phonons, and defects.

To achieve higher conversion efficiencies, multi-bandgap absorber systems such as multiple QWs and Superlattice (SL) were proposed (Barnham, & Duggan, 1990).

In the third generation of solar cells, nanomaterials based SCs have to be included. In QW SCs, for the first time, the idea of extending the spectral absorption appeared (Barnham, & Duggan, 1990). This idea was confirmed by the first experimental application, which used a *p-i-n* cell with an intrinsic region (*i*) in a $GaAs/Al_{0.3}Ga_{0.7}As$ multi-layered structure (Barnham, et al., 1991). Since the 1990s, the solar cells with multi-layered structures have been intensively studied (Anderson, 1995; Lynch, et al., 2005; Kirchartz, et al., 2009; Munteanu & Autran, 2011).

Usually, the layers have thicknesses from tens to hundreds of nanometers. The last ones are actually submicronic structures, and therefore, at these thicknesses, the quantum effects are weak. However, they are named quantum well structures, even if the consecrated terminology is of multi-layered photovoltaic cells.

Only recently, multi-layered cells with proper quantum sizes—less than 10 nm (multi-layered photovoltaic cells with quantum wells) were studied (Kirchartz, et al., 2009; Berghoff, et al., 2010; Munteanu & Autran, 2011). Indeed, the quantum effects at low size (less than about 20 interatomic distances, approximately 5 nm) become dominant, so that the continuous band structure is replaced by a discrete spectrum or at most with a quasiband structure due to quantum confinement effects (Nishida, 2005; Ciurea, et al.,

2006; Ciurea & Iancu, 2010). Even the momentum conservation law is no longer valid (Heitmann, et al., 2004) at these sizes.

QW SCs as well as quantum dots SCs are based on the advantages offered by the low dimensional systems (Ciurea & Iancu, 2007, 2010). In low dimensional systems, the light absorption domain is extended, and densities of states are modified by restricting the size at least on one direction to the order of magnitude of the electron wave function. In addition, the thermalization can be reduced. (Myong, 2007; Iancu, et al., 2011). These systems are 0D (quantum dots), 1D (nanowires), and 2D (nanolayers which can be described by quantum wells). A low dimensional structure has a nanometric size on at least one direction. At low size one has a strong quantum confinement effect, while the nature of the material type plays a secondary role (Ciurea, Iancu, & Stavarache, 2006; Ciurea, et al., 2006; Ciurea & Iancu, 2010). Another contribution is given by the increased role of surface interface, described by the ratio between the numbers of atoms located at the surface/interface (N_S^δ) of a low dimensional system (0D, 1D, 2D) and the total number of atoms (N). Thus, $N_S^\delta / N = 2(3-\delta)a/d_\delta$, where δ is the system dimensionality (0, 1, or 2), a is the mean interatomic distance and d_δ is the minimum size of the low dimensional structure (Ciurea & Iancu, 2010). Let us analyze GaAs which has the interatomic distance in the interval between $a_{(100)}$ = 0.2877 nm and $a_{(111)}$ = 0.2448 nm. If we consider for simplicity of calculus a = 0.25 nm value, it results $N_S^\delta / N = 50\%$ for dots with a diameter of d_0 = 3 nm, nanowires with a diameter of d_1 = 2 nm and layers with a thickness of d_2 = 1 nm. If d_δ = 5 nm, then the corresponding ratios are: $\left(N_S^\delta / N\right)_0 = 30\ \%$ for a quantum dot system, $\left(N_S^\delta / N\right)_1 = 20\ \%$ for a nanowire system, and $\left(N_S^\delta / N\right)_2 = 10\ \%$ for a quantum well system.

PHYSICAL PROCESSES IN QUANTUM WELL SOLAR CELLS

The multi-layered photovoltaic cells are divided in cells with multiple QWs (Barnham, et al., 2002; Aeberhard & Morf, 2008) and cells with SL (Varonides, 2008; Munteanu & Autran, 2011) depending on the thickness of the barrier layer (Myong, 2007). If the number of layers is big enough and if the layers are thin enough, the resonant levels are replaced with resonant bands (SL structure) (Iancu, Mitroi, & Fara, 2009). The criterion of thickness is not sufficient; one has to consider also the periodicity and number of layers, for the same reason as those defining the quantum sizes. The thickness of the layers becomes critical only at high values (submicronic domain), because the wave functions describing the localized states in each quantum well no longer overlap.

It is known that the multi-layered structure introduces resonant quantum levels in the conduction and valence bands of films with relatively small gap (Harrison, 2005). When the barrier layers (having larger energy gap) are thin enough to permit the superposition of electrons and holes wave functions on the resonant levels and also when the layers are periodically arranged and sufficiently numerous, then the resonant levels form mini-bands, equivalent to the formation of energy bands in a crystal. In this case a superlattice is formed. If the arrangement of layers is not completely periodic, the mini-bands are not clearly separated (similarly with the amorphous materials) or if the number of the layers is too small, instead of mini-bands, quasimini-bands can form.

The energy band diagrams of the *p-i-n* type single junction multiple QW and SL solar cells under an external bias V are already well known (e.g. Myong, 2007; Iancu, Mitroi, & Fara, 2009, see Chapter 8). They are illustrated in Figure 1. Both structures, the multiple QW and SL structures, consist of alternate layers of two (or more)

Figure 1. The energy band structure of p-i-n solar cells with: (a) multiple QW and (b) SL under applied bias V (continuous lines—resonant levels and bands and dashed lines—quantum confinement levels) (adapted from Iancu, Mitroi, & Fara. 2009, see chapter 8)

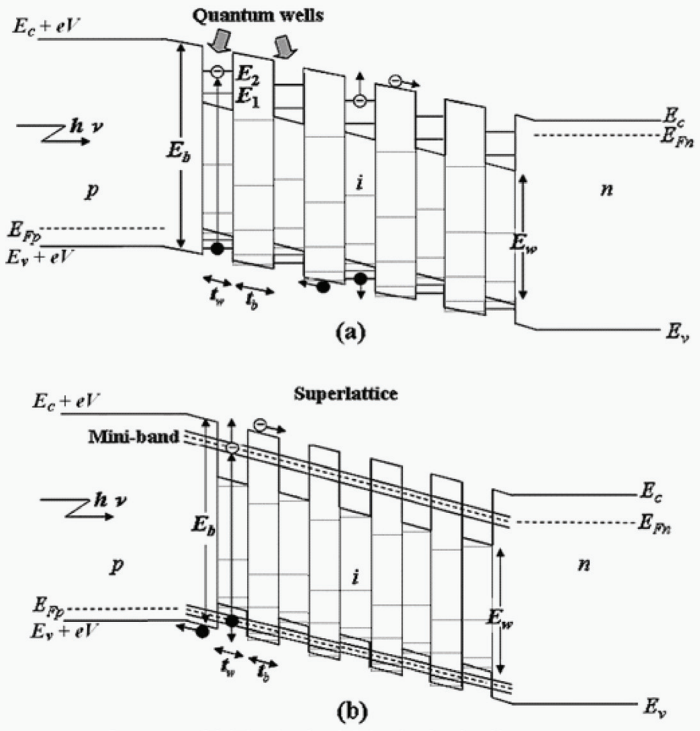

different semiconductors with different band gaps. The first layer represents the host layer in the intrinsic region and has a wider band gap (E_b) and thickness t_b, and it is named the barrier layer. The second layer, named well layer, has a narrower band gap (E_w) and thickness t_w. The sequence of these layers in the structure always begins and ends with the barrier layer. For multiple QW structures, the thickness of the well is of 5 – 10 nm, thin enough to form quantized energy states inside. The barrier thickness is usually below 100 nm. One can observe that, besides the resonant levels or minibands from the conduction and valence bands, there are also quantum confinement levels located in the band gap of both well and barrier layers (Ciurea, et al., 1998; Harrison, 2005; Ciurea, et al., 2006; Iancu, Mitroi, & Fara, 2009; Ciurea & Iancu, 2010).

An important parameter which validates if a material is appropriate for SC application is the internal quantum efficiency, $\eta_Q^{(i)}(\lambda)$. The internal quantum efficiency represents the ratio between the number of generated electron-hole pairs and the number of the absorbed photons, and depends on the absorbed wavelength (λ). It is given by the formula:

$$\eta_Q^{(i)}(\lambda) = \frac{8\pi\hbar B_{if}(\lambda)}{cS} \tag{1}$$

where $\hbar$ is the reduced Planck constant, $B_{ij}(\lambda)$ is the Einstein absorption coefficient, c is the speed of light, S is the area of the surface, normal to the incident direction of the light flux. Experimentally, one measures the current flowing in the external circuit of the device per incoming photon, this ratio

representing the external quantum efficiency. In the following, we will refer to the internal quantum efficiency only.

The absorption rate (R_λ) at a given wavelength depends on the square modulus of the matrix element of the Hamiltonian ($|H_{fi}|^2$) corresponding to the transition between the initial (i) and final (f) states:

$$R_\lambda = (2\pi / h)\left|H_{fi}\right|^2 \delta(\Delta\varepsilon - hc / \lambda) \text{ or}$$
$$R_\lambda = (\lambda / h^2 c)\left|H_{fi}\right|^2 = (\lambda^2 / 2\pi c) B_{if}(\lambda) w_\lambda \quad (2)$$

with w_λ as the spectral-volumic density of the absorbed radiation energy.

The contributions of resonant levels as well as of quantum confinement levels are given by the relations (1) and (2) (Iancu, Mitroi, & Fara, 2009). For the evaluation of matrix elements of the interaction Hamiltonian between electrons and electromagnetic field, the wave functions of electron between the initial and the final states have to be known. The simplest description of quantum confinement process is given by the infinite rectangular quantum well model (Iancu & Ciurea, 1998; Ciurea, et al., 1998; Ciurea, et al., 2006; Lepadatu, et al., 2010). More refined investigations use a finite rectangular quantum well. However, it was proved that the infinite rectangular quantum well model is a good approximation for quantum confinement process in the limits of the experimental errors (Iancu & Ciurea, 1998; Ciurea, et al., 2006).

Let us consider the case of multiple QW SCs, where 2D layers with nanometric thickness (t) are described by the infinite rectangular quantum well approximation. The thickness t is either t_w for well layer or t_b for barrier layer. In the most cases, these layers are plane, parallel with the crystalline planes. Then, the electron Hamiltonian can be exactly separated as a sum of two parts: one is Bloch-type, parallel with the layer surface, leading to a 2D band structure, and the orthogonal one can be described with an infinite rectangular quantum well, leading to quantum confinement levels. Therefore, the electron energy has the form:

$$\varepsilon^{2D} = \varepsilon = \varepsilon_n\left(k_x, k_y\right) + \left[\left(2\pi^2\hbar^2\right)\Big/\left(m_\perp^* t^2\right)\right] p^2, \quad (3)$$

where $\varepsilon_n(k_x, k_y)$ represents the 2D band energy, $m_\perp^*$ is the transversal effective mass (the effective mass on the confinement direction), and $p > 0$ is a natural number.

The quantum confinement energy levels are located in the band gap (at 0 K, the fundamental quantum confinement level, and the energy level corresponding to the valence band maximum are occupied, so that they must coincide). Therefore, we will shift the zero of the quantum confinement energy and we will measure it from the top of the valence band:

$$\begin{aligned}\varepsilon &= \left[\varepsilon_n\left(k_x, k_y\right) + \left(2\pi^2\hbar^2\right)\Big/\left(m_\perp^* t^2\right)\right] \\ &+ \left[\left(2\pi^2\hbar^2\right)\Big/\left(m_\perp^* t^2\right)\right]\left(p^2 - 1\right) \\ &\equiv \varepsilon_n^{(s)}\left(k_x, k_y\right) + \varepsilon_{p-1}.\end{aligned} \quad (4)$$

Here $\varepsilon_n^{(s)}\left(k_x, k_y\right)$ is the shifted band energy and ε_{p-1} is the quantum confinement energy level with the quantum number p (with $\varepsilon_0 \equiv 0$).

The modeling of the 2D structures takes into consideration the change of the band gap from the well layer to the barrier one, and so on in the subsequent layers. The well layers are described by quantum wells and introduce quantum confinement levels in the conduction and valence bands. These levels are named resonant levels, and they contribute to the optical properties and do not contribute to the electrical transport properties. Therefore, they are not proper quantum confinement levels. A complete analysis of the behavior of a low dimensional system requires to take into

account both quantum confinement levels and resonant ones.

In the following, we will evaluate the contribution of the quantum confinement levels and resonant ones to the functioning of QW SCs (Iancu, Mitroi, & Fara, 2009; Ciurea & Iancu, 2010). In order to calculate the internal quantum efficiency for the absorption on these levels, the matrix element of the interaction Hamiltonian has to be first calculated. The most probable interaction Hamiltonian is the electrical dipole one.

$$H_{fi} = -\frac{2}{t} e \int_0^t \vec{E} \cdot \vec{r} \sin\frac{p_f \pi z}{t} \sin\frac{p_i \pi z}{t} dz \tag{5}$$

where p_i and p_f are natural non-zero numbers (e is the elementary charge, $e > 0$). The absorption rate is given by the relation (3.2). For an absorption rate different from zero, meaning to have absorption, the matrix element of the Hamiltonian H_{fi} must be different from zero, too.

In order to calculate the matrix elements, it is necessary to take into account if the electric field $\vec{E}$ is parallel with or perpendicular on the layer. We consider a square QW (well layer) with lateral size L. At a normal incidence, meaning that $\vec{E}$ is parallel with the layer, the matrix element of the electric dipole interaction Hamiltonian is $H_{fi} = e \cdot E_{x,y} \cdot L/2$, where the quantum selection rule $p_f = p_i$ was considered. This matrix element describes the transition between resonant levels from the valence and the conduction bands. If the field is orthogonal on the layer, then the matrix element is $e \cdot E_{x,y} \cdot t/2$ also with $p_f = p_i$, meaning that transitions between resonant states take place.

The matrix element is given by a different formula for transitions between quantum confinement levels existing in the band gap, as it follows:

$$H_{fi} = \frac{eE_z t}{\pi^2} \left[\frac{1-(-1)^{p_f - p_i}}{(p_f - p_i)^2} - \frac{1-(-1)^{p_f + p_i}}{(p_f + p_i)^2} \right] \tag{6}$$

In this case, H_{fi} is non-null if and only if $p_f - p_i = 2p - 1$.

The solar light is not polarized, therefore $E_{||} = E_{\perp} = E/\sqrt{2}$ Then, for transitions between resonant symmetric levels in the well layer, the absorption rate is:

$$R_{\lambda} = \frac{\pi e^2 \langle E^2 \rangle}{\hbar} \left[L^2 \left(1 - \frac{\sin^2\theta}{4\beta_w} \right) + t_w^2 \frac{\sin^2\theta}{4\beta_w} \right] \delta\left(\Delta\varepsilon - \frac{hc}{\lambda} \right) \tag{7}$$

where θ is the external incidence angle, β_w is the relative permittivity of the well layers and $\Delta\varepsilon = hc/\lambda = \varepsilon_w + \pi^2\hbar^2/2m_{||w}^* t_w^2$, with ε_w as the corresponding gap and $m_{||w}^* = \left(1/m_{||ew}^* + 1/m_{||hw}^*\right)^{-1}$ the excitonic effective mass in the well.

If we consider the transitions between the top of the valence band ($p_i = 1$) and the quantum confinement levels in the well layer, the absorption rate can be written as:

$$R_{\lambda_p} = \frac{512 e^2 t_w^2 \langle E^2 \rangle}{\pi^3 \hbar \beta_w} \cdot \frac{p^2 \sin^2\theta}{\left(4p^2 - 1\right)^4} \delta\left(\Delta\varepsilon_p - \frac{hc}{\lambda_p} \right) \tag{8}$$

with

$$\Delta\varepsilon_p = hc/\lambda_p = \left[\left(\pi^2\hbar^2\right) / \left(2m_{\perp w}^* t_w^2\right) \right] \cdot \left(4p^2 - 1\right)$$

and the constants (t_w and β_w) correspond to the well layer. Similar relation describes the transitions between the top of the valence band ($p_i = 1$) and the quantum confinement levels in the barrier layer (replacing w index with b one).

The internal quantum efficiency can be determined from relation (1) where S is replaced by L^2. Then, for the case of transitions between resonant symmetric levels in the well layer, it results:

$$\eta_Q^{(i)}(\lambda) = \frac{8\pi^2 e^2}{c\hbar\beta_0\beta_w}\left[\left(1-\frac{\sin^2\theta}{4\beta_w}\right)+\frac{t_w^2}{L^2}\frac{\sin^2\theta}{4\beta_w}\right] \tag{9}$$

where β_0 is the vacuum permittivity and β_w is the relative permittivity of the well layers. For transitions from the top of the valence band to the quantum confinement levels in the well layer, the internal quantum efficiency is:

$$\eta_Q^{(i)}(\lambda_p) = \frac{4096e^2}{\pi^2 c\hbar\beta_0\beta_w^2}\times\frac{t_w^2}{L^2}\frac{p^2\sin^2\theta}{\left(4p^2-1\right)^4} \tag{10}$$

From the comparison between Equations (9) and (10) it results that the internal quantum efficiency for transitions between resonant levels is several orders of magnitude greater than the internal quantum efficiency for transitions between the valence band maximum and the quantum confinement levels.

It has to be remarked that in a multilayer structure, the resonant levels are located in the layers with smaller gap (well layers), while the quantum confinement levels appear in both well and barrier layers.

As Mazzer et al. (2006) evidenced in the spectral response of external quantum efficiency at zero bias, the light absorption on resonant levels is extended to longer wavelengths in the near infrared domain in comparison with the bulk absorption. They used samples formed by 50 wells of $In_xGa_{1-x}As$ inserted into tensile strained $GaAs_{1-y}P_y$ barrier regions. The near infrared extension is dependent on the materials used. In addition, the absorption on quantum confinement levels is also extended to near infrared domain. From the above formulas, (9) and (10), it results that the internal quantum efficiency is also dependent on both size and used geometry, so that by tuning them, it can be increased.

An important problem for the third generation SCs, i.e. for multiple QW SCs, is given by the trapping processes. The trapping centers are mainly due to the misfit or stress (Ciurea, et al., 2011) between the layers of multiple QW SCs, and therefore they are located at the surface/interface (Ciurea, 2008). The shallow trapping centers are discharged at the work temperature of cell and they do not play an important role. The deep ones create a frozen-in electric field (Ciurea, Iancu, & Mitroi, 2007; Ciurea, 2008; Ciurea, et al., 2011) which adds itself to the barrier field, and in this way it can increase or decrease the cell efficiency. These effects can be beneficial or not, depending on the trapped carrier sign.

MATERIALS AND TECHNOLOGY FOR QUANTUM WELL SOLAR CELLS

A QW SC has intermediate properties between the properties of heterojunction cells and those of tandem cells. In heterojunction cells, the current is given by the sum of currents generated in both materials, and the voltage is controlled by the material with the lowest band gap. In tandem cells the voltage is a sum of sub-cells contribution, but current is controlled by the worst sub-cell (Mazzer, et al., 2006).

The multiple QW SCs have two advantages, one of them being the effective band gap that is lower than the energy gap of the barrier layer, E_b. This is due to the quantum mechanical effect. Consequently, the light absorption domain of multiple QW SCs is extended to longer wavelengths. Another advantage is the enhanced well number (N_w) that leads to the increase of the short-circuit current and thus, to an improved quantum efficiency (Bushnell, 2005). An increase of the quantum efficiency is also produced by the absorption of extra photons. The carriers, photogenerated in this way, will escape to the adjacent barrier layer under the built-in potential from the depletion

layer, thus contributing with an extra current. The efficiency at room temperature due to the escape carriers is relatively high (Barnham, et al., 1991).

The maximum value of the quantum efficiency calculated for *p-i-n* type multiple QW SC is about 63% (Barnham, et al., 2002). The maximum predicted theoretical power conversion efficiencies are in the interval between 44.5% and more than 63% (Wei, et al., 2007). The highest experimental value achieved is 28.3% under AM1.5D 416 X for single-junction QW SCs (Adams, et al., 2010).

As absorbers are necessary lattice-matched materials in order to avoid the defect formation and therefore the degradation of the SC photovoltaic properties. So that, the materials used as barrier or well layers and their thicknesses must be carefully selected in order to reduce the formation of dislocations. As lattice-matched multiple QW absorbers, successful candidates are the compounds from group 3-5 and elements or alloys from group IV (C or Si/Ge). An important problem to be solved in a SC is to have an optimal collecting of charge carriers from QWs and an optimal open circuit voltage V_{oc} (in order to minimize the reduction of V_{oc}). For this, a big enough electric field across the intrinsic region is usually required ($E \sim 30$ kV/cm or greater), that can be accomplished if the *p-i-n* diode is sufficiently thin (Alemu, Coaquira, & Freundlich, 2006). Another condition is to have barriers with energy of 0.20 – 0.45 eV or less, over which the carriers to be thermally or optically excited (Alemu, Coaquira, & Freundlich, 2006). By a suitable choosing of the material for well and barrier layers, this condition is satisfied. For example, in a SC structure with an intrinsic region thickness of 250 nm, the electric field across the *i* region was estimated to be 48 kV/cm in equilibrium, while at maximum power operating voltage of ~ 0.4 V, the electric field is 32 kV/cm (Derkacs, et al., 2008).

The conventional growth techniques for multiple QW structures are metal-organic vapor-phase epitaxy (Ekins-Daukes, et al., 1999; Bushnell, 2005), plasma enhanced chemical vapor deposition (Berghoff, et al., 2010), chemical beam epitaxy (Alemu, et al., 2006; Freundlich, et al., 2007), molecular beam epitaxy (Barnham, et al., 1991; Okada, et al., 2005). One main advantage of chemical beam epitaxy for photovoltaic applications is the ability to grow films at higher rates than those of molecular beam epitaxy (Freundlich, et al., 2007).

The SCs can be fabricated by changing the alloy composition or the well thickness of well and barrier layers (Barnham & Duggan, 1990; Tran, et al., 2002; Prażmowska, et al., 2007). These SCs are named graded band gap multiple QW SCs, and they absorb the incident light more efficiently. There are three types of band-gap gradation commonly used, namely normal, reverse and double

Figure 2. Band-gap profiling: (a) without gradation; (b) normal; (c) reverse; (d) double (adapted from Prażmowska, et al., 2007)

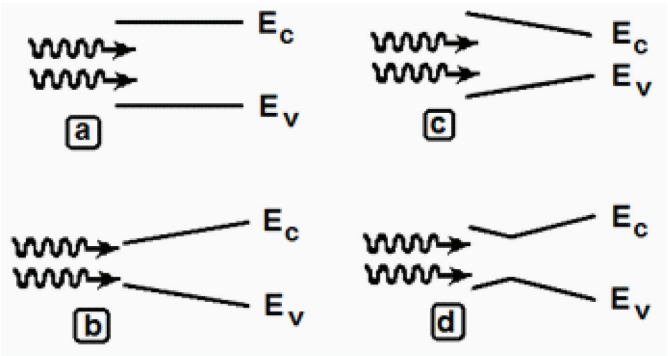

Figure 3. (a) Sketch of the energy band structure of GaAsP/InGaAs strain-balanced multiple QW SC (adapted from Ekins-Daukes, et al., 1999; Mazzer, et al., 2006); (b) crystal structure of the strain-balanced QW SC (adapted from Mazzer, et al., 2006)

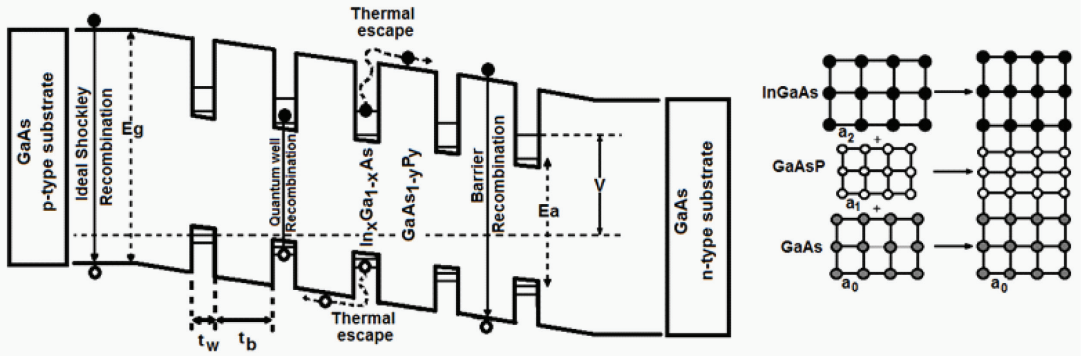

gradation as one can see in Figure 2 (Adapted from Prażmowska, et al., 2007).

Another possibility to achieve a good absorption at any (visible) Sun position of non-normal incidence is to use a refractive grating (Iancu, Mitroi, & Fara, 2009).

In order to provide higher conversion efficiencies, the multiple QW tandem SCs were fabricated. They are composed of stacked unit cells in series, that guide the incident light to appropriate absorbers leading to a higher conversion efficiency. A tandem SC contains at least two cells: a top cell that receives light first and absorbs higher energy photons (UV and VIS) and a bottom cell that receives light transmitted through the first cell. The bottom cell, made of a material with smaller bandgap, converts transparency losses of the top cell, and therefore, absorbs lower energy (longer wavelength radiation). Even for cells with low quantum efficiency, the tandem cell is the optimum solution (Adams, et al., 2011); thus, they overcome the fundamental limitation of a single cell.

Analysis of the photovoltaic response of the InP/InAsP multiple QW SCs exposed to proton irradiation shows their radiation hardness (Walters, et al., 2000), meaning that they are appropriate for space applications. Another application of multiple QW SCs is the conversion of the heat radiation from combustion processes into electricity (Rohr, et al., 2002).

GaAs has a band gap of 1.42 eV which is rather high because for a good efficiency it is necessary a bandgap of about 1.1 eV at 1 sun and relatively high concentration (Barnham, et al., 2006). Extension of the spectral range of high efficiency GaAs cells can be achieved if strain-balanced QW SCs are used (Mazzer, et al., 2006). In a strain-balanced QW SC the lattice-mismatch limitation is overcome by matching of the compressive strain in the InGaAs wells with the tensile strain in GaAsP barriers (Ekins-Daukes, et al., 1999). These SCs with different numbers of QWs were prepared by the metal-organic vapor-phase epitaxy method (Bushnell, et al., 2005). The well layers were incorporated into intrinsic region *i* of a *p-i-n* diode fabricated on GaAs wafer. A sketch of the energy band structure of a strain-balanced QW SC is presented in Figure 3a (adapted from Ekins-Daukes, et al., 1999; Mazzer, et al., 2006). Figure 3b shows the individual crystal structure of InGaAs, GaAsP and GaAs, and the matched crystal structure that forms a strain-balanced QW SC. As base, a GaAs layer doped with Si was used and as emitter, a C doped one. The well layers were made by nanometric layers of $In_xGa_{1-x}As$ (with low band gap and high lattice constant). These were strain compensated with $GaAs_{1-y}P_y$ barriers

(higher band-gap and lower lattice constant). The alloy compositions, (given by x and y), and well and barrier thicknesses (t_b and t_w) are adjusted to minimize the formation of dislocations. Thus, the QWs are compressively strained, while the barriers are tensile strained. A Si_3N_4 antireflection layer was deposited. The devices were characterized by measuring dark *I–5* and light *I–5* characteristics. The quantum efficiency and reflectance were also obtained. The authors conclude that these strain-balanced QW SCs have a reduced dark current and a significantly reduced number of dislocations in the active region. In addition, these devices may tune the short-circuit current of the cell by varying the QWs number. The reported efficiency is 26% ± 1% under AM1.5d at around 200 × concentration obtained on a structure with 50 shallow well cells. Lynch et al. demonstrated that the increasing of N_w induces an increase in recombination (Lync, et al., 2005). Due to the small decrease of the absorption at short λ with the increase of N_w, the authors showed that the cell efficiency decreases as N_w increases from 20.7% to 19.2%.

There is an alternative way to decrease the GaAs band gap, and consequently to fabricate strain-balanced QW SC structures (King, et al., 2003). King and co-workers proposed the growth of strain-balanced QW SC structure on a relaxed virtual substrate. The disadvantage is the producing of dislocations into the material.

Derkacs et al. (2008) succeeded to improve the performance of QW SCs by integrating dielectric or metallic nanoparticles within the semiconductor device. They deposited dielectric or metallic nanoparticles on the top of the semiconductor device, in order to scatter the incident light. The light scattering permits a better transmission of photons into the active layers and coupling of normally incident light into lateral optically confined waveguide layers within multiple QWs. Consequently, the absorption of photons is increased, together with photocurrent generation, and therefore the power conversion efficiency is also increased.

Figure 4. Sketch of the InP/$In_{1-x}Ga_xAs_yP_{1-y}$ multiple QW p-i-n SC structure (adapted from Derkacs, Chen, Matheu, Lim, Yu, & Yu, 2008)

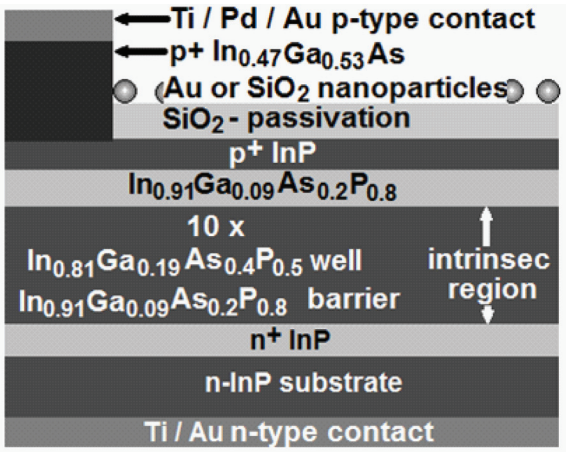

The multiple QW *p-i-n* SC structure of InP/$In_{1-x}Ga_xAs_yP_{1-y}$, fabricated by Derkacs et al., is sketched in Figure 4. The *n*-type electrode consists of a S doped InP substrate, while the intrinsic region *i* consists of $In_{0.81}Ga_{0.19}As_{0.4}P_{0.6}$ well layers alternating with $In_{0.91}Ga_{0.09}As_{0.2}P_{0.8}$ barrier layers for ten periods. The *p*-type electrode is formed from two layers, subsequently deposited, one being *p*-type InP and the other one *p*-type $In_{0.47}Ga_{0.53}As$. An active window region was defined using photolithography. The top $In_{0.47}Ga_{0.53}As$ contact layer was then removed from the window and a SiO_2 surface passivation layer was sputtered over the active window area. Au or SiO_2 nanoparticles were deposited atop the semiconductor device. The *n*-type Ohmic contacts have a large-area (typically 1 cm^2) and they were formed using Ti/Au metallization deposited by electron-beam evaporation. *p*-type contacts were then formed using Ti/Pd/Au metallization and a standard lift-off process.

Using SiO_2 or Au nanoparticles, the short-circuit current density increases with 12.9% or 7.3%, respectively, in comparison with the device fabricated without nanoparticles deposited on the top. In addition, the power conversion efficiency increases with 1% when SiO_2 nanoparticles were

deposited and with 1% only, when Au nanoparticles were used.

An alternative QW SC is made by 3–5 diluted nitride-based multiple QW (GaAsN/GaAs) SCs (Freundlich, et al., 2007). The structures were fabricated by chemical beam epitaxy. The dependence of external quantum efficiency on bias shows that the photogenerated carriers are incompletely collected from the well layers.

Rölver et al. presents the results obtained on Si/SiO_x QW structures (Al/Si–QW/Pt and Al/Si–QW/Al) fabricated by remote plasma enhanced chemical vapour deposition, followed by a rapid thermal annealing in N_2 at 1100 ^oC (Rölver, et al., 2008; Berghoff, et al., 2010). They implemented these structures in order to explore the potential for third generation Si based tandem SCs. They used two geometries, one with standard vertical contacts, and another one being an innovative approach, with lateral charge transport parallel to Si/SiO_2 interfaces. The authors stated that the lateral geometry enables to avoid inefficient tunneling processes through the insulating barrier material. It was found that the lateral transport parallel to Si/SiO_2 interface is four orders of magnitude more efficient compared to the vertical transport. Also, in the same geometry, a strong decrease of the $\mu \cdot \tau$ product, between the mobility and the carrier lifetime, with the decrease of well layer thickness was evidenced. The authors concluded that an important improvement of $\mu \cdot \tau$ values, necessary for an efficient energy conversion, could be achieved by minimizing the influence of Schottky barrier present in the investigated structures.

CONCLUSION AND FUTURE RESEARCH DIRECTIONS

In this chapter, we have presented the main physical processes that take place in multiple quantum well solar cells with *p-i-n* structure, the materials with appropriate properties for photovoltaic applications, and the aspects related to the technology used to implement these devices.

The quantum confinement effect produces resonant energy levels located in the valence and conduction bands of the well layers. In addition, it produces energy quantum confinement levels located in the energy band gap of both well and barrier layers. The absorption on resonant levels as well as on quantum confinement levels leads to an extension of the internal quantum efficiency in the near infrared domain.

In a quantum well solar cell with *p-i-n* structure, the alternative well and barrier layers are deposited inside the intrinsic *i* zone of the *p-i-n* structure. The number of pair of well and barrier layers has to be carefully selected in order to obtain quantum well solar cells with efficient conversion parameters.

The quantum well solar cells have several advantages that allow improving the cell parameters. Thus, the light absorption is extended to longer wavelengths in the near infrared domain. This near infrared extension is dependent on the materials used to implement the quantum well solar cell. The quantum efficiency is dependent on both size and used geometry, so that by tuning both sizes of well and barrier layers, it can be increased.

In order to avoid the formation of defects a lattice-matched material is necessary. Thus, strain-balanced multiple quantum well solar cells solve this problem. In addition, the choice of the method to deposit the layers is of great importance to fabricate good quality layers.

For an efficient absorption of the incident light, a multiple quantum well solar cell with graded band gap has been invented by patents. The graded band gap can be achieved by changing the alloy composition and the thickness of the quantum well layers. An open interesting idea is the deposition of nanoparticle layers on the top of the $InP/In_{1-x}Ga_xAs_yP_{1-y}$ quantum well structure that increases the photon absorption. Light scattering on these nanoparticles permits a better transmission of photons into the active

layers and coupling of normally incident light into lateral optically confined waveguide layers within the multiple quantum wells. The collection of the photogenerated carriers is also important for the parameters of quantum wells solar cells, so that an improvement of the collection geometry is necessary.

Tandem SCs overcome the fundamental limitation of a single cell. The top cell from tandem SC converts the high-energy photons (UV and VIS), while the bottom cell, made of a material with smaller bandgap, converts transparency losses of the top cell. Even, for the cells with low quantum efficiency, the tandem cell is the optimum solution.

The maximum theoretical power conversion efficiency is predicted in the interval between 44.5% and more than 63%. The highest experimental value achieved is 28.3% under AM1.5D 416 X for single-junction quantum well solar cells.

ACKNOWLEDGMENT

This work was partially supported by the Romanian National Authority for Scientific Research through the CNCS – UEFISCDI Contract No. 471/2009 (ID 918/2008).

REFERENCES

Adams, J. G. J., Browne, B. C., Ballard, I. M., Connolly, J. P., & Chan, N. L. A., Ioannides, A., … Ekins-Daukes, N. J. (2011). Recent results for single-junction and tandem quantum well solar cells. *Progress in Photovoltaics: Research and Applications*, *19*(7), 865–877. doi:10.1002/pip.1069

Adams, J. G. J., Elder, W., Hill, G., Roberts, J. S., Barnham, K. W. J., & Ekins-Daukes, N. J. (2010). Higher limiting efficiencies for nanostructured solar cells. In B. Witzigmann, F. Henneberger, Y. Arakawa, & M. Osinski (Eds.), *Proceedings of the SPIE Photonics West 2010 Conference*, (Vol 7597), (pp. 759705-759705-9). Bellingham, WA: SPIE.

Aeberhard, U., & Morf, R. H. (2008). Microscopic nonequilibrium theory of quantum well solar cells. *Physical Review B: Condensed Matter and Materials Physics*, *77*(12), 125–343. doi:10.1103/PhysRevB.77.125343

Alemu, A., Coaquira, J. A. H., & Freundlich, A. (2006). Dependence of device performance on carrier escape sequence in multi-quantum-well p-i-n solar cells. *Journal of Applied Physics*, *99*(8), 84–506. doi:10.1063/1.2191433

Anderson, N. G. (1995). Ideal theory of quantum-well solar-cells. *Journal of Applied Physics*, *78*(3), 1850–1861. doi:10.1063/1.360219

Barnham, K. W. J., Ballard, I., Bessière, A., Chatten, A. J., Connolly, J. P., & Ekins-Daukes, N. J. … Malik, M. A. (2006). Quantum well solar cells and quantum dot concentrator. In T. Soga (Ed.), *Nanostructured Materials for Solar Energy Conversion,* (pp. 517-537). Amsterdam, The Netherlands: Elsevier.

Barnham, K. W. J., Ballard, I., Connolly, J. P., Ekins-Daukes, N. J., Kluftinger, B. G., Nelson, J., & Rohr, C. (2002). Quantum well solar cells. *Physica E, Low-Dimensional Systems and Nanostructures*, *14*(1-2), 27–36. doi:10.1016/S1386-9477(02)00356-9

Barnham, K. W. J., Braun, B., Nelson, J., Paxman, M., Button, C., Roberts, J. S., & Foxon, C. T. (1991). Short-circuit current and energy efficiency enhancement in a low-dimensional structure photovoltaic device. *Applied Physics Letters*, *59*(1), 135–137. doi:10.1063/1.105553

Barnham, K. W. J., & Duggan, G. (1990). A new approach to high-efficiency multi-band-gap solar-cells. *Journal of Applied Physics*, *67*(7), 3490–3493. doi:10.1063/1.345339

Berghoff, B., Suckow, S., Rölver, R., Spangenberg, B., Kurz, H., Sologubenko, A., & Mayer, J. (2010). Quantum wells based on Si/SiO_x stacks for nanostructured absorbers. *Solar Energy Materials and Solar Cells*, *94*(11), 1893–1896. doi:10.1016/j.solmat.2010.06.033

Bushnell, D. B., Tibbits, T. N. D., Barnham, K. W. J., Connolly, J. P., Mazzer, M., & Ekins-Daukes, N. J. (2005). Effect of well number on the performance of quantum-well solar cells. *Journal of Applied Physics*, *97*(12), 124–908. doi:10.1063/1.1946908

Ciurea, M. L. (2008). Trapping phenomena in nanocrystalline semiconductors . In Korkin, A., & Rosei, F. (Eds.), *Nanoelectronics and Photonics* (pp. 191–222). New York, NY: Springer. doi:10.1007/978-0-387-76499-3_8

Ciurea, M. L., Baltog, I., Lazar, M., Iancu, V., Lazanu, S., & Pentia, E. (1998). Electrical behaviour of fresh and stored porous silicon films. *Thin Solid Films*, *325*(1-2), 271–277. doi:10.1016/S0040-6090(98)00429-5

Ciurea, M. L., & Iancu, V. (2007). Why the energy levels observed in electrical transport, phototransport and photoluminescence are different? In *Proceedings of CAS 2007: International Semiconductor Conference,* (pp. 41-44). New York, NY: IEEE Press.

Ciurea, M. L., & Iancu, V. (2010). Quantum confinement in nanometric structures . In Baleanu, D., Guvenc, Z. B., & Machado, J. A. T. (Eds.), *New Trends in Nanotechnology and Fractional Calculus Applications* (pp. 57–67). Berlin, Germany: Springer. doi:10.1007/978-90-481-3293-5_5

Ciurea, M. L., Iancu, V., & Mitroi, M. R. (2007). Trapping phenomena in silicon-based nanocrystalline semiconductors. *Solid-State Electronics*, *51*(10), 1328–1337. doi:10.1016/j.sse.2007.07.002

Ciurea, M. L., Iancu, V., & Stavarache, I. (2006). Quantum confinement modeling of electrical and optical processes in nanocrystalline silicon. *Journal of Optoelectronics and Advanced Materials*, *8*(6), 2156–2160.

Ciurea, M. L., Lazanu, S., Stavarache, I., Lepadatu, A.-M., Iancu, V., & Mitroi, M. R. (2011). Stress-induced traps in multilayered structures. *Journal of Applied Physics*, *109*(1), 13–717. doi:10.1063/1.3525582

Ciurea, M. L., Teodorescu, V. S., Iancu, V., & Balberg, I. (2006). Electronic transport in $Si\text{-}SiO_2$ nanocomposite films. *Chemical Physics Letters*, *423*(1-3), 225–228. doi:10.1016/j.cplett.2006.03.070

Derkacs, D., Chen, W. V., Matheu, P. M., Lim, S. H., Yu, P. K. L., & Yu, E. T. (2008). Nanoparticle-induced light scattering for improved performance of quantum-well solar cells. *Applied Physics Letters*, *93*(9), 91–107. doi:10.1063/1.2973988

Ekins-Daukes, N. J., Barnham, K. W. J., Connolly, J. P., Roberts, J. S., Clark, J. C., Hill, G., & Mazzer, M. (1999). Strain-balanced GaAsP/InGaAs quantum well solar cells. *Applied Physics Letters*, *75*(26), 4195–4197. doi:10.1063/1.125580

Freundlich, A., Fotkatzikis, A., Bhusal, L., Williams, L., Alemu, A., & Zhu, W. (2007). 3-5 dilute nitride-based multi-quantum well solar cell. *Journal of Crystal Growth*, *301-302*, 993–996. doi:10.1016/j.jcrysgro.2006.11.256

Harrison, P. (2005). *Quantum wells, wires, and dots: Theoretical and computational physics of semiconductor nanostructures*. Chichester, UK: John Wiley & Sons. doi:10.1002/0470010827

Heitmann, J., Müller, F., Yi, L. X., Zacharias, M., Kovalev, D., & Eichhorn, F. (2004). Excitons in Si nanocrystals: Confinement and migration effects. *Physical Review B: Condensed Matter and Materials Physics*, *69*(19), 195–309. doi:10.1103/PhysRevB.69.195309

Iancu, V., & Ciurea, M. L. (1998). Quantum confinement model for electric transport phenomena in fresh and stored photoluminescent porous silicon films. *Solid-State Electronics*, *42*(10), 1893–1896. doi:10.1016/S0038-1101(98)00160-9

Iancu, V., Mitroi, M. R., & Fara, L. (2009). Modeling of multi-layered quantum well photovoltaic cells. *University Politehnica of Bucharest Scientific Bulletin-Series A-Applied Mathematics and Physics*, *71*(4), 53–62.

Iancu, V., Mitroi, M. R., Lepadatu, A.-M., Stavarache, I., & Ciurea, M. L. (2011). Calculation of the quantum efficiency for the absorption on confinement levels in quantum dots. *Journal of Nanoparticle Research*, *13*(4), 1605–1612. doi:10.1007/s11051-010-9913-6

King, R. R., Fetzer, C. M., Colter, P. C., Edmondson, K. M., Law, D. C., & Stavrides, A. P. … Karam, N. H. (2003). Lattice-matched and metamorphic GaInP/GaInAs/Ge concentrator solar cells. In *Proceedings of 3rd World Conference on Photovoltaic Energy Conversion*, (Vols A-C), (pp. 622-625).Tokyo, Japan: WCPEC-3.

Kirchartz, T., Seino, K., Wagner, J.-M., Rau, U., & Bechstedt, F. (2009). Efficiency limits of Si/SiO_2 quantum well solar cells from first-principles calculations. *Journal of Applied Physics*, *105*(10), 104–511. doi:10.1063/1.3132093

Lepadatu, A.-M., Stavarache, I., Ciurea, M. L., & Iancu, V. (2010). The influence of shape and potential barrier on confinement energy levels in quantum dots. *Journal of Applied Physics*, *107*(3), 33–721. doi:10.1063/1.3284083

Lynch, M. C., Ballard, I. M., Bushnell, D. B., Connolly, J. P., Johnson, D. C., & Tibbits, T. N. D. (2005). Spectral response and I-V characteristics of large well number multi quantum well solar cells. *Journal of Materials Science*, *40*(6), 1445–1449. doi:10.1007/s10853-005-0580-4

Mazzer, M., Barnham, K. W. J., Ballard, I. M., Bessiere, A., Ioannides, A., & Johnson, D. C. (2006). Progress in quantum well solar cells. *Thin Solid Films*, *511*, 76–83. doi:10.1016/j.tsf.2005.12.120

Munteanu, D., & Autran, J. L. (2011). Modeling of energy bands in ultra-thin layer quantum nanostructures for solar cell applications. *Journal of Non-Crystalline Solids*, *357*(8-9), 1884–1887. doi:10.1016/j.jnoncrysol.2010.11.112

Myong, S. Y. (2007). Recent progress in inorganic solar cells using quantum structures. *Recent Patents on Nanotechnology*, *1*(1), 67–73. doi:10.2174/187221007779814763

Nishida, M. (2005). Electronic structure of silicon quantum dots: Calculations of energy-gap redshifts due to oxidation. *Journal of Applied Physics*, *98*(2), 23–705. doi:10.1063/1.1985978

Okada, Y., Shiotsuka, N., & Takeda, T. (2005). Potentially modulated multi-quantum wells for high-efficiency solar cell applications. *Solar Energy Materials and Solar Cells*, *85*(2), 143–152. doi:10.1016/j.solmat.2004.04.013

Park, S. H., Roy, A., Beaupre, S., Cho, S., Coates, N., & Moon, J. S. (2009). Bulk heterojunction solar cells with internal quantum efficiency approaching 100%. *Nature Photonics*, *3*(5), 297–303. doi:10.1038/nphoton.2009.69

Prażmowska, J., Paszkiewicz, R., Korbutowicz, R., Wośko, M., & Tłaczała, M. (2007). Solar cells conversion efficiency enhancement techniques. *Optica Applicata*, *37*(1-2), 93–99.

Rohr, C., Connolly, J. P., Ekins-Daukes, N., Abbott, P., Ballard, I., & Barnham, K. W. J. (2002). InGaAs/InGaAs strain-compensated quantum well cells for thermophotovoltaic applications. *Physica E, Low-Dimensional Systems and Nanostructures*, *14*(1-2), 158–161. doi:10.1016/S1386-9477(02)00369-7

Rölver, R., Berghoff, B., Bätzner, D., Spangenberg, B., Kurz, H., Schmidt, M., & Stegemann, B. (2008). Si/SiO_2 multiple quantum wells for all silicon tandem cells: Conductivity and photocurrent measurements. *Thin Solid Films*, *516*(20), 6763–6766. doi:10.1016/j.tsf.2007.12.087

Tran, D., Vendura, G. J., Jr., Jones, W. L., & Rezek, E. A. (2002). *Solar cell used in satellites and space stations, has intermediate semiconductor layers whose bandgaps transitions from smaller energy state to larger energy state*. Patent US6437233-B1. Washington, DC: US Patent Office.

Varonides, A. C. (2008). Quantum size effects in amorphous Si superlattice solar cells. *Renewable Energy*, *33*(2), 273–276. doi:10.1016/j.renene.2007.05.033

Walters, R. J., Summers, G. P., Messenger, S. R., Freundlich, A., Monier, C., & Newman, F. (2000). Radiation hard multi-quantum well InP/InAsP solar cells for space applications. *Progress in Photovoltaics: Research and Applications*, *8*(3), 349–354. doi:10.1002/1099-159X(200005/06)8:3<349::AID-PIP326>3.0.CO;2-Z

Wei, G. D., Shiu, K. T., Giebink, N. C., & Forrest, S. R. (2007). Thermodynamic limits of quantum photovoltaic cell efficiency. *Applied Physics Letters*, *91*(22), 223–507. doi:10.1063/1.2817753

Chapter 4
Quantum Confinement Modeling and Simulation for Quantum Well Solar Cells

Laurentiu Fara
Polytechnic University of Bucharest, Romania & Academy of Romanian Scientists, Romania

Mihai Razvan Mitroi
Polytechnic University of Bucharest, Romania

ABSTRACT

In this chapter, the authors present the modeling and simulation of the multi-layered quantum well solar cells as well as the simulated results of this model. The quantum confinement of a semiconductor induces new energy levels, located in the band gap, as well as resonant levels located in the conduction and valence bands. These levels allow supplementary absorption in the visible and near infrared range. The quantum efficiency of the supplementary absorption is calculated within the infinite rectangular quantum well approximation. As the absorption excites carriers in the gap of each layer, even a small absorption significantly increases the photocurrent (by photoassisted tunneling) and, therefore, the cell efficiency. The results of the simulation are presented for the internal quantum efficiency of the transitions between the resonant levels of GaAs, as well as the internal quantum efficiency of the transitions between the confinement levels for GaAs and $Al_xGa_{1-x}As$. New directions for the research of quantum well solar cells are indicated.

INTRODUCTION

The "*quantum well*" photovoltaic cells were first proposed in 1990 (Barnham & Duggan, 1990), based on the idea that the use of the quantum wells could improve the photovoltaic cells by extending their spectral response, as well as by increasing the photocurrent. One year later, this idea was experimentally proved by using a $GaAs/Al_xGa_{1-x}As$ multi-layered structure (Barnham, et al., 1991). From this moment on, the use of the Multi-Layered Photovoltaic (MLPV) cells became one of the most used approaches for a high efficiency PV cell. Generally, such cells are *p-i-n* type diodes, with the intrinsic region formed by a multilayered

DOI: 10.4018/978-1-4666-1927-2.ch004

structure (Paxman, et al., 1993; Anderson, 1995; Connolly, 1997; Raisky, et al., 1999; Green, 2000; Barnham, et al., 2002; Anderson, 2002; Abbott, 2003; Sato, et al., 2005; Jani, et al., 2005; Norman, et al., 2005; Myong, 2007; Hong, et al., 2007). Most of these cells have layers of tens or even hundreds of nanometer thickness, so that the quantum effects are reduced; nevertheless they are also called in some texts "quantum well" PV cells (see for instance Ref. 5). However, MLPV cells with real quantum sizes (Multi-Layered Quantum Well Photovoltaic—MLQWPV) are also studied (Myong, 2007; Hong, et al., 2007).

The E 2456-06 ASTM International Standard "Terminology for Nanotechnology" states that sizes between 0.1 and 1 μm are to be called "submicronic," while the prefix "*nano*" is to be used for sizes between 1 nm and 100 nm only. On the other hand, an analysis of the quantum effects proves that the quantum size appears under about 20 interatomic distances (e.g. about 5 nm), where the band structure is replaced by an energy level structure and the momentum conservation law is no longer valid (Heitmann, et al., 2004; Fara, et al., 2007).

The true quantum well photovoltaic cells use the special advantages of the low dimensional systems, where at least one size is at quantum scale. This leads to two important contributions.

- The first contribution is a strong Quantum Confinement (QC) effect. Indeed, at this size, it was proved that the material nature role is secondary with respect to the QC (Iancu, et al., 1998; Iancu, et al., 2006).
- The second contribution is the increased role of the surface/interface. The area/volume ratio is $1/d$, where d is the minimum size, so that, at quantum sizes, this ratio is greater than 2×10^8 m^{-1}. Then, the cells are classified with respect to their dimensionality in 2D, 1D, 0D and fractals. The MLPV (and the Multi-Layered Quantum Well Photovoltaic—MLQWPV) cells are 2D. In literature, they are divided in Multiple Quantum Wells (MQW) and Superlattice (SL) systems (Connolly, 1997; Myong, 2007), the difference being based on the barrier layer thickness (Myong, 2007). However, this interpretation is not correct. The SL structures replace the resonant levels from the conduction and valence bands of the "quantum wells" with resonant bands. This is not correlated with the barrier thickness, but with the total number of layers, for reasons similar with those that define the quantum size (Heitmann, et al., 2004; Fara, et al., 2007). In the following, only MQW structures will be considered.

We have to mention the recent results obtained regarding plasmonic solar cells which have important prospects for the future. They use nanoparticles to benefit from plasmonic effect in order to improve absorption and finally, the solar cell current response (Catchpole, 2008).

The aim of this chapter is to model MLQWPV cells in order to find out how to improve them. Section 2 deals with the QC effects. Section 3 calculates the quantum efficiency of a layer and discusses the optical improvements of the cells. Section 4 summarizes all the simulation results.

QUANTUM CONFINEMENT EFFECTS

As we have stated, the MLQWPV cells have a *p-i-n* structure, with a multi-layered *i* region (e.g. GaAs/$Al_xGa_{1-x}As$). It is well known that the band gap difference between the layers acts like a quantum well and induces the appearance of resonant levels in both the conduction and valence bands (MQW structure). These levels improve the absorption and therefore increase the cell efficiency. If the number of layers is big enough, the resonant levels are replaced with resonant bands (SL structure). An example of both structures, under an external bias V, is presented in Figure 1

Figure 1. (a) MQW and (b) SL p-i-n structures under applied bias V. Solid lines—the resonant levels (a) and bands (b); dotted lines—the QC levels

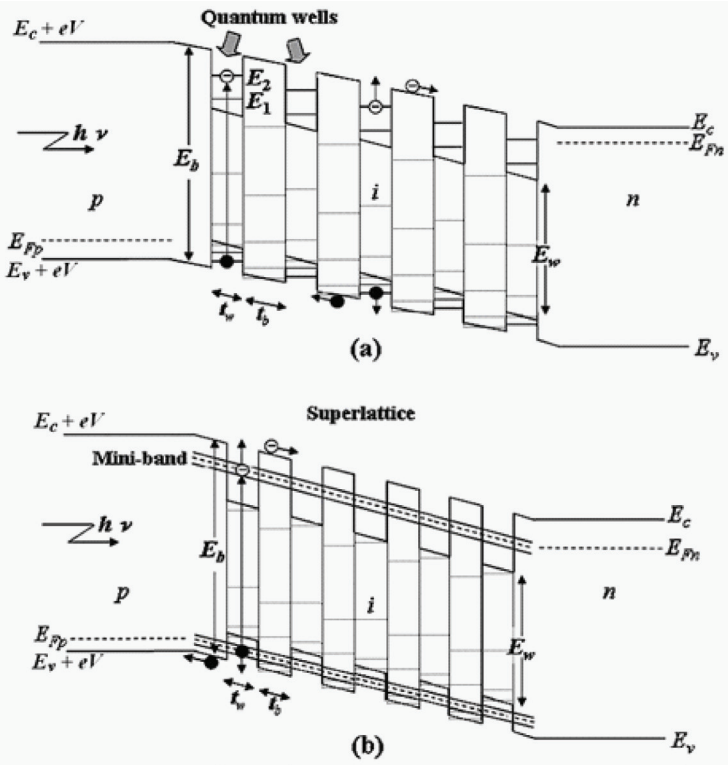

(adapted from Jani, et al., 2005). E_w, t_w and E_b, t_b are the gaps and thicknesses of the quantum well and barrier layers, respectively. For MLQWPV cells, both t_w and t_b are of the order of 5 ÷ 10 nm.

Several studies (Iancu & Ciurea, 1998; Iancu, et al., 2006; Pana, et al., 2006) proved that the main Quantum Confinement (QC) effect consists in the introduction of QC levels in the band gap. Indeed, the surface/interface of a low dimensional system acts like the wall of a quantum well. The analysis of different shapes proved that the rectangular quantum well is good enough for the description of the QC effects.

There are two more problems to analyze.

- The first one is the depth of the potential well. We have found that, for rectangular quantum wells, deeper than 2 eV and larger than 1 nm, the differences between the first three levels in the finite well and the infinite well with the same width is less than 2.5% (Iancu & Ciurea, 1998), so that the use of the Infinite Rectangular Quantum Well (IRQW) approximation does not exceed the experimental errors. As the relative error is proportional with $t\sqrt{U}$, where U is the potential well depth, it results that the IRQW approximation does not lead to errors greater than about 5% for any known MQW or SL structure.
- The second problem is the location of these additional energy levels. As at absolute zero temperature the maximum energy of an electron in a semiconductor corresponds with the top of the valence band, the fundamental quantum confinement level should be located at this energy value. This means

that the QC levels must be located in the band gap.

The electron energy has the expression:

$$E = \varepsilon_{n\vec{k}} + \frac{2\pi^2\hbar^2}{m_t^* t^2} p^2 = \left(\varepsilon_{n\vec{k}} + \frac{2\pi^2\hbar^2}{m_t^* t^2}\right) + \frac{2\pi^2\hbar^2}{m_t^* t^2}\left(p^2 - 1\right) \equiv \varepsilon_{n\vec{k}}^{(s)} + E_{p-1} \quad (1)$$

where $\varepsilon_{n\vec{k}}^{(s)}$ is the shifted 2D band energy, $E_{p\text{-}1}$ is the QC level energy $(E_0 \equiv 0)$, m_t^* is the transversal effective electron mass, and t the layer thickness. These QC levels induce supplementary absorption in the visible and near infrared range. It is important to remark that these levels appear in both narrow and wide gap layers. At the same time, one can see from Figure 1. that, at convenient bias value, some levels from the consecutive quantum well and barrier layers have practically the same energy value (differences under $k_B T$). This strongly increases the tunneling rate through the junction.

INTERNAL QUANTUM EFFICIENCY MODELING

This model (Iancu, et al., 2009) does not take into account the band-to-band absorption, but only the absorption induced by the resonant levels and by the QC levels from the gap. This model calculates the Einstein absorption coefficients for one layer; the coefficients have the following expressions:

$$B_\lambda = \frac{\pi e^2 L^2}{\hbar^2 \varepsilon_0 \varepsilon_{rw}}\left[\left(1 - \frac{\sin^2\theta}{4\varepsilon_{rw}}\right) + \frac{t_w^2}{L^2}\frac{\sin^2\theta}{4\varepsilon_{rw}}\right] \quad (2)$$

for transitions between resonant symmetric levels in the quantum well and:

$$B_{\lambda_p} = \frac{512\, e^2 L^2}{\pi^3 \hbar^2 \varepsilon_0 \varepsilon_{rw,b}^2} \cdot \frac{t_{w,b}^2}{L^2} \frac{p^2 \sin^2\theta}{\left(4p^2 - 1\right)^4} \quad (3)$$

for transitions between the top of the valence band and the QC levels.

The internal quantum efficiency is related to the Einstein absorption coefficient by the relation:

$$\eta = \frac{8\pi\hbar}{c L^2} B \quad (4)$$

so that we obtain:

$$\eta_\lambda = \frac{8\pi^2 e^2}{c\hbar\varepsilon_0 \varepsilon_{rw}}\left[\left(1 - \frac{\sin^2\theta}{4\varepsilon_{rw}}\right) + \frac{t_w^2}{L^2}\frac{\sin^2\theta}{4\varepsilon_{rw}}\right] \quad (5)$$

for the transitions between resonant symetric levels in the quantum well and:

$$\eta_{\lambda_p} = \frac{4096\ e^2}{\pi^2 c\hbar\varepsilon_0 \varepsilon_{rw,b}^2} \cdot \frac{t_{w,b}^2}{L^2} \frac{p^2 \sin^2\theta}{\left(4p^2 - 1\right)^4} \quad (6)$$

for the transitions between the top of the valence band and the QC levels.

One can observe that the internal quantum efficiency for the transitions between the top of the valence band and the QC levels is several orders of magnitude smaller than the one for transitions between resonant symmetric levels in the quantum well. However, the excitation of even a few carriers in the band gap, on QC levels that are practically equal between the different layers (due to a conveniently chosen bias), leads to a photo-assisted tunneling and significantly increases the photocurrent.

Figure 2. Schematics of a p-i-n MLQWPV cell with refraction grating

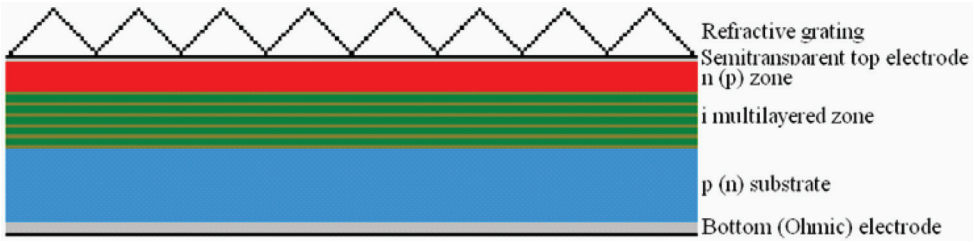

In order to ensure a non-normal incidence for any (visible) position of the sun, we suggest the placement of refraction grating made from parallel prisms on the front surface of the cell (see Figure 2), the prism edges being oriented in the East-West direction.

In this case, in Equations ((2) ÷ (3), (5) ÷ (6)), $\sin^2\theta$ must be replaced with Equation 7 (Iancu, et al., 2009).where α is the prism angle, n_p is the refraction index of the prism, and θ (as previous) is the incidence angle (the angle of the light beam with the normal to the layer surfaces).

As the prism refraction index is always smaller than the semiconductor refraction indexes, there is no risk of internal total reflection in any layer.

SIMULATION RESULTS

Solar Cells Dimensions and Material Data

Based on the Equations (10), (11) and (12) simulations have been carried out for cells with the dimension of $L = 2.5\,cm$ and the well thickness of $t_w = 10\,\text{nm}$.

The analysed materials were GaAs and $Al_xGa_{1-x}As$, where x is the Al concentration that ranges within the interval $[0,1]$. For this materials ε_r has the following expression (Catchpole & Polman, 2008):

$$\varepsilon_r = (6.3 + 19\cdot x)\cdot\left\{f(\chi) + \frac{f(\chi_0)}{2}\left(\frac{a_0}{b_0}\right)^{\frac{3}{2}}\right\} + (9.4 - 10.2\cdot x) \tag{8}$$

where:

$$f(\chi) = \frac{2 - \sqrt{1+\chi} - \sqrt{1-\chi}}{\chi^2};$$

$$\chi = \frac{h\,c}{a_0};$$

$$\chi_0 = \frac{h\,c}{b_0};$$

$$a_0 = 1.425 + 1.155\cdot x + 0.37\cdot x^2;$$

$$b_0 = 1.765 + 1.115\cdot x + 0.37\cdot x^2,$$

Equation 7.

$$\sin^2\theta + \delta\sin^2\theta = \frac{1+\cos\alpha}{2}\left\{n_p^2 - \cos\alpha - (1-\cos\alpha)\sin^2\theta - \right.$$
$$\left. - \sqrt{(1-\cos\alpha)\left[2n_p^2 - 1 - \cos\alpha - (1-\cos\alpha)\sin^2\theta\right]}\right\} \neq 0 \tag{7}$$

h is the Planck constant, c is the light velocity, ε_0 is the vacuum absolute permittivity.

The material constants utilises: for GaAs: energy gap: $E_g = 1.424\,eV$, effective mass of electron: $m_e^* = 0.067 \cdot m_e$, effective mass of gap: $m_g^* = 0.62 \cdot m_e$, for $Al_xGa_{1-x}As$: effective mass of electron - $m_e^* = (0.067 + 0.083 \cdot x) \cdot m_e$, and m_e - mass of electron.

The $Al_xGa_{1-x}As$ band gap in correlation with x is given by the Equations (9) and (10) (Catchpole & Polman, 2008):

$$E_g = 1.424 + 1.247x \tag{9}$$

for $x \leq 0.45$:

$$E_g = 1.9 + 0.125x + 0.143x^2 \tag{10}$$

for $x > 0.45$.

Simulation of the Internal Quantum Efficiency for the Transitions between the Resonant Levels for GaAs

The internal quantum efficiency of the transition between the resonant levels for GaAs was simulated based on the relation (5). The dependences on prism refraction index and on incidence angle can be seen in Figures 3 and 4.

According to Figures 3 and 4 the internal quantum efficiency - η_λ for the transitions between resonant levels in the GaAs:

- Has very high values ~ 75%;
- Increases with the increasing prism angle - α;
- Decreases with the increasing prism index and the angle of incidence.

Simulation of the Internal Quantum Efficiency for the Transitions between the Confinement Levels for GaAs

Taking into account, Figure 5, based on the Equations (11) and (12), we can determine the internal quantum efficiency for the transitions between the confinement levels for GaAs in correlation with the prism's refraction index and the prism angle.

According to Figures 5a and 5b, the internal quantum efficiency - η_{λ_p} of the transitions between the confinement levels GaAs:

- Decreases with the increasing prism angle - α;
- Increases with the increasing of the incidence angle;
- Increases with the increasing of the prism's refraction index .

Simulation of the Internal Quantum Efficiency for the Transitions between the Confinement Levels for $Al_xGa_{1-x}As$

Taking into account the Figures 6 and 7, and based on the Equation (6), we can determine the internal quantum efficiency for the transitions between the confinement levels for $Al_xGa_{1-x}As$ in correlation with the prism's refraction index and the prism angle.

According to Figures 6 and 7 the internal quantum efficiency - η_{λ_p} of the transitions between the confinement levels $Al_xGa_{1-x}As$:

- Decreases with the increasing prism angle - α;
- Increases with the increasing of the incidence angle;
- Decreases with the increasing of the prism's refraction index;
- Increases with the increase of the aluminium amount.

Figure 3. (a) Internal quantum efficiency for the transitions between resonant levels in GaAs quantum well versus the prism refraction index, for different values of the incidence angle – θ (□ $\theta = \pi / 12$; ▲ $\theta = \pi / 6$; ⋄ $\theta = \pi / 4$; • $\theta = \pi / 3$), the prism angle - $\alpha = \pi / 6$. (b) Internal quantum efficiency for the transitions between resonant levels in GaAs quantum well versus the prism refraction index, for different values of the incidence angle – θ (□ $\theta = \pi / 12$; ▲ $\theta = \pi / 6$; ⋄ $\theta = \pi / 4$; • $\theta = \pi / 3$), the prism angle - $\alpha = \pi / 3$.

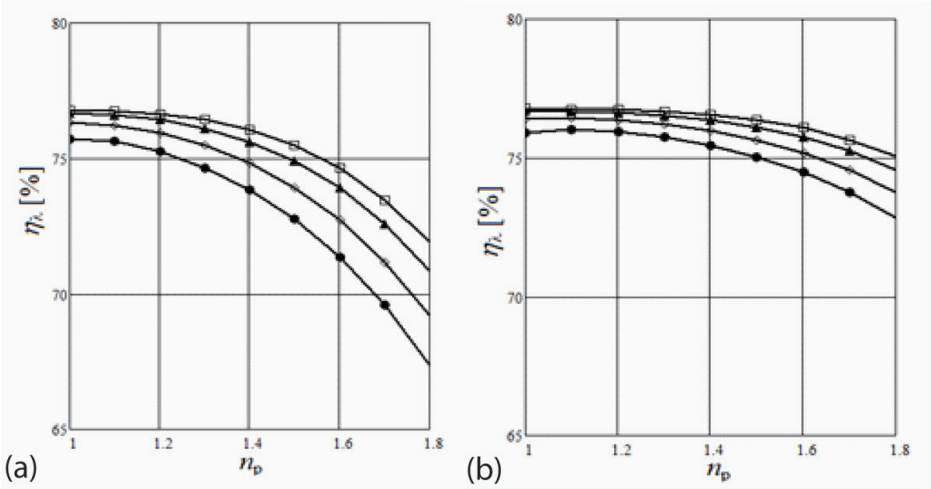

Figure 4. (a) Internal quantum efficiency for the transitions between resonant levels in GaAs quantum well versus incidence angle, for different values of the prism refraction index – n_p (□ $n_p = 1.2$; ▲ $n_p = 1.4$; ⋄ $n_p = 1.6$; • $n_p = 1.8$), the prism angle - $\alpha = \pi / 6$. (b) Internal quantum efficiency for the transitions between resonant levels in GaAs quantum well versus incidence angle, for different values of the prism refraction index – n_p (□ $n_p = 1.2$; ▲ $n_p = 1.4$; ⋄ $n_p = 1.6$; • $n_p = 1.8$), the prism angle - $\alpha = \pi / 3$.

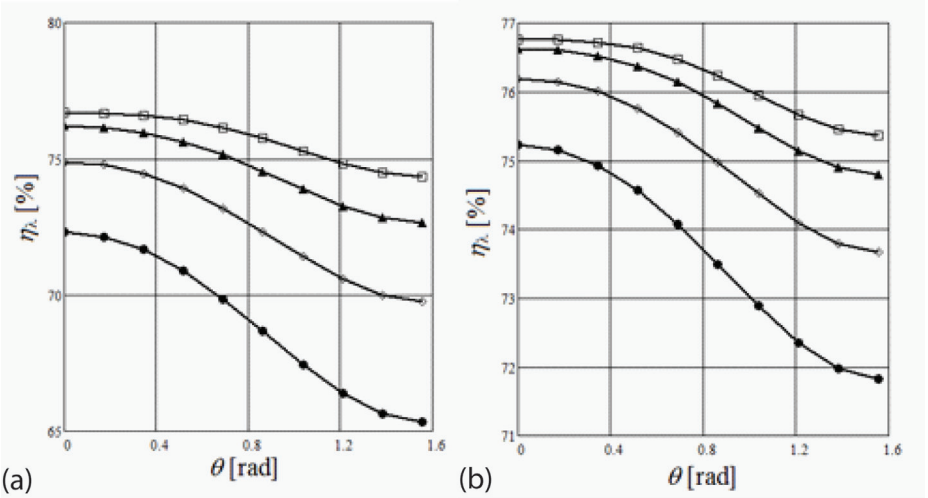

Figure 5. (a) Internal quantum efficiency for the transitions between confinement levels for GaAs versus the the incidence angle, for different values of prism refraction index – n_p (□ $n_p = 1.2$; ▲ $n_p = 1.4$; ⋄ $n_p = 1.6$; • $n_p = 1.8$), the prism angle $\alpha = \pi / 6$. (b) Internal quantum efficiency for the transitions between confinement levels for $Al_xGa_{1-x}As$ versus the prism refraction index, for different values of of Al concentration – x (□ $n_p = 1.2$; ▲ $n_p = 1.4$; ⋄ $n_p = 1.6$; • $n_p = 1.8$), the prism angle $\alpha = \pi / 3$.

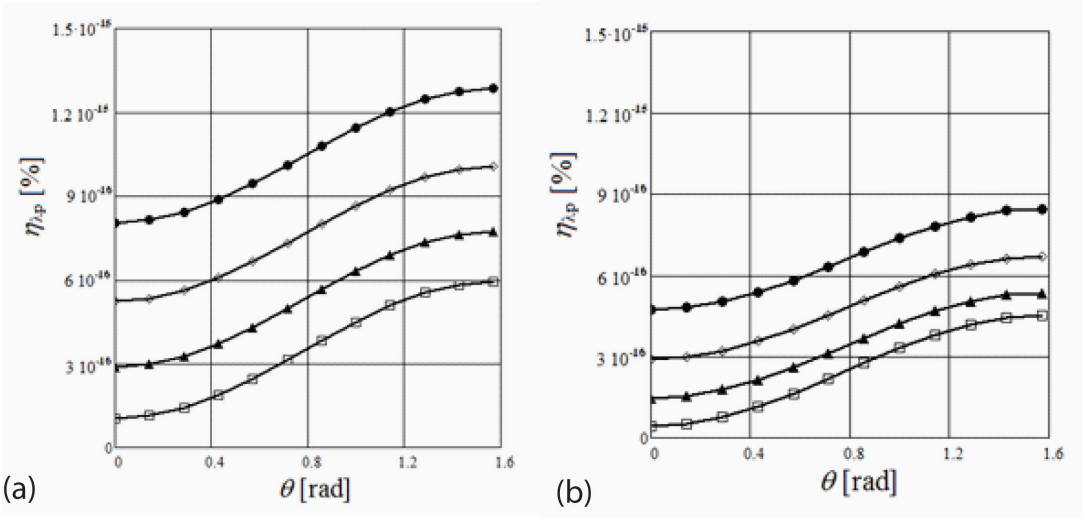

Figure 6. (a) Internal quantum efficiency for the transitions between confinement levels for $Al_xGa_{1-x}As$ versus the prism refraction index, for different values of Al concentration – x (□ $x = 0.1$; • $x = 0.2$; ⋄ $x = 0.4$; ▲ $x = 0.6$), the prism angle $\alpha = \pi / 6$. (b) Internal quantum efficiency for the transitions between confinement levels for $Al_xGa_{1-x}As$ versus the prism refraction index, for different values of Al concentration – x (□ $x = 0.1$; • $x = 0.2$; ⋄ $x = 0.4$; ▲ $x = 0.6$), the prism angle $\alpha = \pi / 3$.

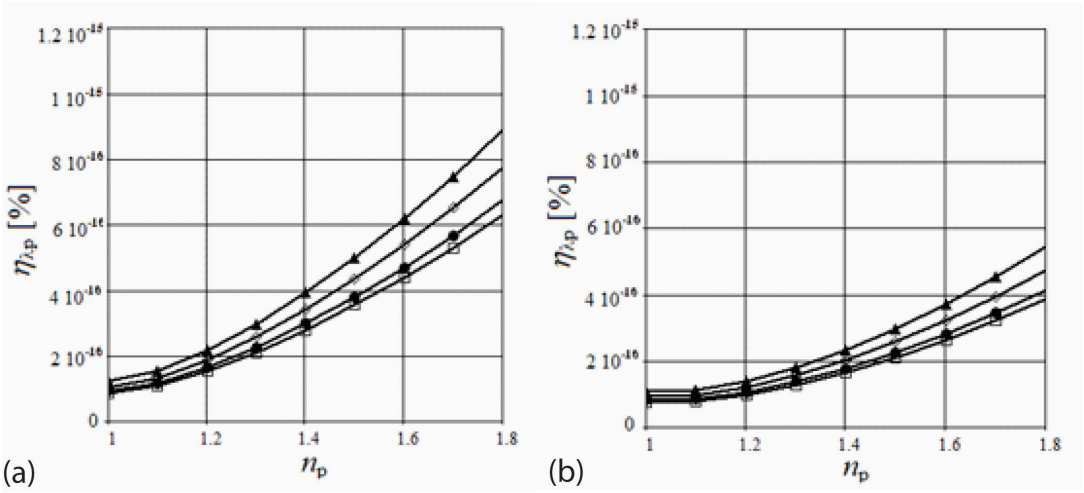

Figure 7. (a) Internal quantum efficiency for the transitions between confinement levels for $Al_xGa_{1-x}As$ versus the incidence angle, for different values of the Al concentration – x (□ $x = 0.1$; • $x = 0.2$; ◊ $x = 0.4$; ▲ $x = 0.6$), the prism angle $\alpha = \pi / 6$, $n_p = 1.6$. (b) Internal quantum efficiency for the transitions between confinement levels for $Al_xGa_{1-x}As$ versus the incidence angle, for different values of the Al concentration – x (□ $x = 0.1$; • $x = 0.2$; ◊ $x = 0.4$; ▲ $x = 0.6$), the prism angle $\alpha = \pi / 3$, $n_p = 1.6$.

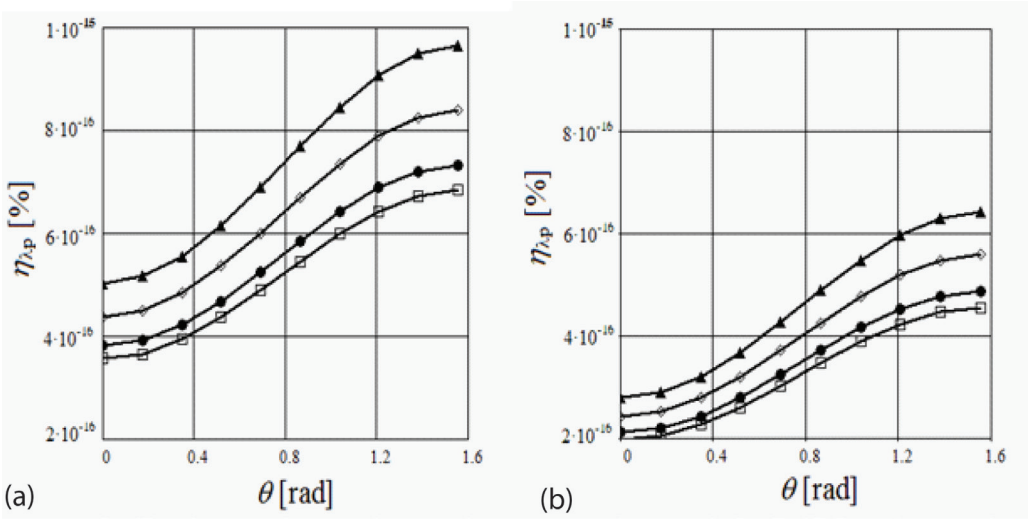

We remark the following:

- The internal quantum efficiency of the transitions between the confinement levels is lower for $Al_xGa_{1-x}As$ compared to the GaAs (Figures 5, 6, and 7);
- The internal quantum efficiency of the transitions between the confinement levels has very small values compared to the internal quantum efficiency between the resonant levels (Figures 3, 4, and 7).

Although, the internal quantum efficiency of the transitions between the confinement levels has very small values, the emergence of electrons in the gap increases significantly the photocurrent through the photo-assisted tunneling.

CONCLUSION

We have proved that the QC introduces energy levels not only in the conduction and valence bands (resonant levels), but also in the band gaps (QC levels). The corresponding energy values can be estimated from IRQW approximation with a good precision. On this basis, the quantum efficiency of the absorption for transitions between resonant or QC levels were calculated. A refraction grating was proposed in order to ensure good absorption conditions at any Sun position. Such an adaption could provide to the present MLQWPV cells several advantages over the classical PV cells: increased efficiency, wider spectral response, increased controllability. The simulated curves for the transition between the resonant levels as well as the transition between the confinement levels were presented and discussed.

The modeled and simulated results would allow an improved design of the quantum well solar cells.

FUTURE RESEARCH DIRECTIONS

A very good candidate for high efficiency QWSC is represented by GaAsP/GaInAs. The radiative recombination dominates the dark-current at high concentration levels, C=200 (Mazzer, et al., 2006). The dark-current can be reduced by photon-recycling effects. The suppression of radiative recombination could be also exploited to increase the efficiency of QWSC under high concentrations.

There were identified two candidate material systems for QDSC—Quantum Dot Solar Cells (Dahal, Bremner, & Honsberg, 2010)—with efficiencies greater than 50%. The first one is $InP_{0.07}Sb_{0.13}$ QDs with $Al_{0.57}In_{0.43}As$ barriers; it has a limiting efficiency up to 58% under C=1000. The other candidate material QD barrier is represented by $InAs_{0.41}P_{0.59}$ QDS with $Al_{0.50}In_{0.50}As$; It has a limiting efficiency of 53% under C=1000. The second candidate could be preferred to the first one.

REFERENCES

Abbott, P. (2003). *Characterisation of quantum well solar cells for low temperature thermophotovoltaic applications*. Ph.D. Thesis. London, UK: University of London.

Agachi, S. (1985). GaAs, AlAs, and $Al_xGa_{1-x}As$@B: Material parameters for use in research and device applications. *Journal of Applied Physics*, *58*(3).

Anderson, N. G. (1995). Ideal theory of quantum well solar cells. *Journal of Applied Physics*, *78*, 1850–1861. doi:10.1063/1.360219

Anderson, N. G. (2002). On quantum well solar cell efficiencies. *Physica E, Low-Dimensional Systems and Nanostructures*, *14*(1-2), 126–131. doi:10.1016/S1386-9477(02)00376-4

Barnham, K. W. J., Ballard, I., & Connolly, J. P. (2002). Quantum well solar cells. *Physica E, Low-Dimensional Systems and Nanostructures*, *14*(1-2), 27–36. doi:10.1016/S1386-9477(02)00356-9

Barnham, K. W. J., Braun, B., Nelson, J., & Paxman, M. (1991). Short-circuit current and energy efficiency enhancement in a low-dimensional structure photovoltaic device. *Applied Physics Letters*, *59*, 135–137. doi:10.1063/1.105553

Barnham, K. W. J., & Duggan, G. (1990). A new approach to high-efficiency multi-band-gap solar cells. *Journal of Applied Physics*, *67*, 3490–3493. doi:10.1063/1.345339

Catchpole, K. R., & Polman, A. (2008). Plasmonic solar cells. *Optics Express*, *16*(26), 21793–21800. doi:10.1364/OE.16.021793

Connolly, J. P. (1997). *Modeling and optimising GaAs/$Al_xGa_{1-x}As$ multiple quantum well solar cells*. Ph.D. Thesis. London, UK: University of London.

Dahal, S. N., Bremner, S. P., & Honsberg, C. (2010). Identification of candidate material systems for quantum dot solar cells including the effect of strain. *Progress in Photovoltaics: Research and Applications*, *18*(4), 233–239.

Fara, L., Iancu, V., Mitroi, M. R., & Nistor, E. (2007). *Physical bases of the nanotechnologies, applications and perspectives*. Bucharest, Romania: Punct.

Green, M. A. (2000). Prospects for photovoltaic efficiency enhancement using low-dimensional structures. *Nanotechnology*, *11*, 401–405. doi:10.1088/0957-4484/11/4/342

Heitmann, J., Müller, F., & Yi, L. X. (2004). Excitons in Si nanocrystals: Confinement and migration effects. *Physical Review B: Condensed Matter and Materials Physics*, *69*, 195–309. doi:10.1103/PhysRevB.69.195309

Hong, Z. R., Maennig, B., & Lessmann, R. (2007). Improved efficiency of zinc phthalocyanine/C60 based photovoltaic cells via nanoscale interface modification. *Applied Physics Letters*, *90*, 230–505. doi:10.1063/1.2739364

Iancu, V., & Ciurea, M. L. (1998). Quantum confinement model for electric transport phenomena in fresh and stored photoluminescent porous silicon films. *Solid-State Electronics*, *42*(1), 1893–1896. doi:10.1016/S0038-1101(98)00160-9

Iancu, V., Ciurea, M. L., & Stavarache, I. (2006). Quantum confinement modeling of electrical and optical processes in nanocrystalline silicon. *Journal of Optoelectronics and Advanced Materials*, *8*(6), 2156–2160.

Iancu, V., Fara, L., & Mitroi, M. R. (2009). Modeling of multi-layered quantum well photovoltaic cells. *Scientific Bulletin, Series A . Applied Mathematics and Physics*, *71*(4), 53–62.

Jani, O., Honsberg, C., Asghar, A., et al. (2005). Characterization and analysis of InGaN photovoltaic devices. In *Proceedings of the 31st IEEE Photovoltaic Specialists Conference.* Orlando, FL: IEEE Press.

Mazzer, M., Barnham, K. W. J., & Ballard, I. M. (2006). Progress in quantum well solar cells. *Thin Solid Films*, *511-512*, 76–83. doi:10.1016/j.tsf.2005.12.120

Myong, S. Y. (2007). Recent progress in inorganic solar cells using quantum structures. *Recent Patents on Nanotechnology*, *1*, 67–73. doi:10.2174/187221007779814763

Norman, A. G., Hanna, M. C., Dippo, P., et al. (2005). InGaAs/GaAs QD superlattices: MOVPE growth, structural and optical characterization and application in intermediate-band solar cells. In *Proceedings of the 31st IEEE Photovoltaic Specialists Conference.* Orlando, FL: IEEE Press.

Pana, O., & Giurgiu, L. M., Darabont, et al. (2006). Core-shell effects in granular perovskite manganites. *Journal of Physics and Chemistry of Solids*, *67*(1-3), 624–627. doi:10.1016/j.jpcs.2005.10.148

Paxman, M., Nelson, J., & Braun, B. (1993). Modeling the spectral response of the quantum well solar cell. *Journal of Applied Physics*, *74*, 614–621. doi:10.1063/1.355275

Raisky, O. Y., Wang, W. B., & Alfano, R. R. (1999). Resonant enhancement of the photocurrent in multiple-quantum-well photovoltaic devices. *Applied Physics Letters*, *74*, 129–131. doi:10.1063/1.122972

Sato, Y., Yamagishi, K., & Yamashita, M. (2005). Multilayer structure photovoltaic cells. *Optical Review*, *12*, 324–327. doi:10.1007/s10043-005-0324-3

Chapter 5
Analytical Models of Bulk and Quantum Well Solar Cells and Relevance of the Radiative Limit

James P. Connolly
Universidad Politécnica de Valencia, Spain

ABSTRACT

The analytical modeling of bulk and quantum well solar cells is reviewed. The analytical approach allows explicit estimates of dominant generation and recombination mechanisms at work in charge neutral and space charge layers of the cells. Consistency of the analysis of cell characteristics in the light and in the dark leaves a single free parameter, which is the mean Shockley-Read-Hall lifetime. Bulk PIN cells are shown to be inherently dominated by non-radiative recombination as a result of the doping related non-radiative fraction of the Shockley injection currents. Quantum well PIN solar cells on the other hand are shown to operate in the radiative limit as a result of the dominance of radiative recombination in the space charge region. These features are exploited using light trapping techniques leading to photon recycling and reduced radiative recombination. The conclusion is that the mirror backed quantum well solar cell device features open circuit voltages determined mainly by the higher bandgap neutral layers, with an absorption threshold determined by the lower gap quantum well superlattice.

INTRODUCTION

Despite great advances in physical understanding, in materials, and in fabrication, and despite reaching efficiencies over 40%, just two routes to higher efficiencies have been comprehensively studied. The first is the multi-junction cell concept, which reduces thermalisation losses. The second is the use of light concentration, reducing the solid angle for light emission towards the minimum, which is the angle for light acceptance (de Vos, 1992). The current interest in novel phenomena, often involving nanostructures, is part of the effort to go beyond these early ideas.

DOI: 10.4018/978-1-4666-1927-2.ch005

This chapter investigates generation and loss mechanisms in bulk and quantum well solar cells, with emphasis on developing physical understanding via analytical models, rather than more accurate but less revealing numerical methods. The designs studied are bulk PIN cells contrasted with Quantum Well Solar Cells (QWSCs), complementing other nanostructured designs reviewed in other chapters.

The quantum well solar cell (QWSC, Figure 1) is a *p-i-n* or *n-i-p* solar cell design with Quantum Wells (QWs) in the undoped intrinsic *i* region (Barnham & Duggan, 1990). Carrier escape studies show efficient field assisted thermal escape of the order of picoseconds, for carrier lifetimes of several nanoseconds (Nelson, Paxman, Barnham, Roberts, & Button, 1993). Early Quantum Efficiency (QE) modeling (Paxman, et al., 1993) further shows that escape efficiency is essentially 100%. More recent theoretical work by Tsai and Tsai (2009) confirms this while showing that escape times must be at least two orders of magnitude shorter than recombination lifetimes for a net efficiency again to be achievable.

Consequently, however, it is clear that this efficient collection requires that the field be maintained across the wells. The nominally undoped wells and barriers however inevitably contain a net background doping level, corresponding to a fixed charge density, which increasingly degrades the built in field, the wider the Multiple Quantum Well (MQW) superlattice is grown. This brings us to the first design issue with these cells, which is the practical upper limit on total intrinsic region thickness *Xi* and corresponding limit on absorbing MQW thickness that may be fabricated. This materials quality dependent limit may extend well over 1μm, and even in direct gap quantum wells makes this system well suited to light trapping techniques, as we will see in subsequent sections.

More recent analytical models by Rimada, Hernàndez, Connolly and Barnham (2007) have followed a similar analytical methodology confirming early results that an MQW can enhance efficiency in non-ideal, high bandgap cells, but do not demonstrate an advantage for ideal material. The MQW bandgap together with near unit collection efficiency leads to a net increase in short circuit current (ISC). This increase in Isc however is accompanied by an increase in recombination in the low gap well regions, as discussed in some detail by Anderson (1995) for example.

Bearing this in mind, the first non-trivial advantage of the QWSC is one of materials. The alternation of thin barrier and well regions allows the use of alternating tensile and compressive materials: this is the strain balancing technique (Barnham, et al., 2006) allowing a much wider range of materials to be explored without dislocations. This variation is the strain balanced SB-QWSC, illustrated in Figure 1 with the strain balanced quantum well superlattice or SB-MQW.

The second potential advantage is the result of the materials inhomogeneity and consequent departure from the homogeneous pn junction picture of solar cells. The difference in carrier properties and carrier dynamics between wells and barriers have led to much discussion concerning the quasi-equilibrium concentration of carriers in the wells and barriers. In particular, the possibility of suppressed quasi-Fermi levels in the wells and higher carrier temperatures has been investigated by studies of steady state luminescence, as reviewed by Barnham *et al.* (2006) and developed by Connolly *et al.* (2007).

Finally, the geometry of the QWSC introduces a further inhomogeneity that demonstrably leads to efficiency enhancement, which is the inhomogeneous luminescence from bulk and quantum well layers, and its potential exploitation for reduced recombination losses in practical devices.

In order to investigate this, the following sections review an analytical QWSC model allowing estimation of different loss mechanisms in a QWSC, and comparing and contrasting these with the case of bulk solar cells.

Figure 1. The strain balanced quantum well solar cell (SB-QWSC) structure. Alternating strain balanced wells and barriers of gaps Egw, Egb make up the intrinsic region of total width Xi, which is sandwiched between p and n doped layers of width Xp, Xn, and bandgap Eg, with an optional higher bandgap window layer. Widths are not to scale, and typical QWSCs contain some tens of QW periods.

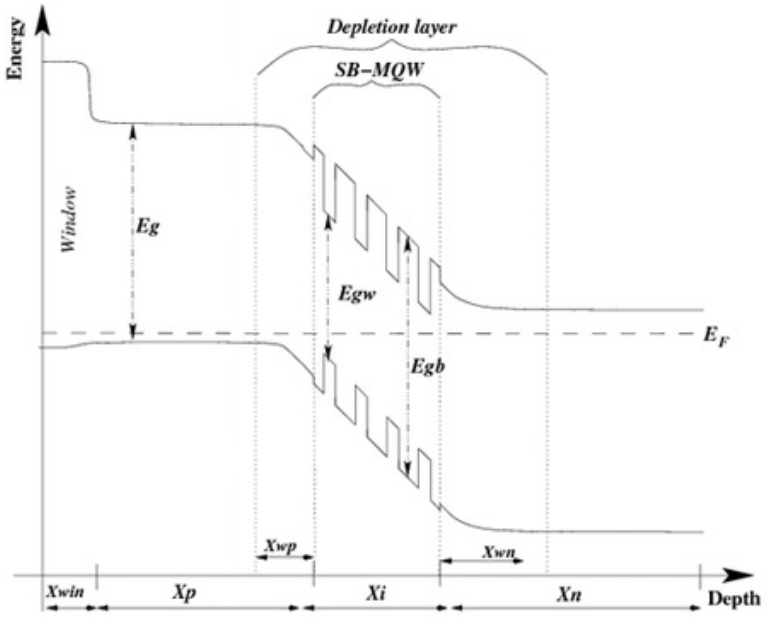

ANALYTICAL MODEL

The modeling methodology uses analytical solutions to allow explicit description of physical phenomena. The use of analytical methods rather than more exact numerical methods allows development of greater physical understanding. This comes at the expense, however, of accuracy and generality as a result of approximations required. This method is chosen since the prime focus is developing understanding rather than optimising devices, for which numerical methods are preferred. The modeling we develop nevertheless focusses on quantitative modeling of experimental data, and measured data is preferred to ab initio calculation of parameters wherever possible.

In this section, we will describe the components of the model SOL starting with notes on the description of structural and physical cell parameters which includes quantum well density of states and absorption coefficient calculations. These notes lay the foundation of the QE calculation first reported by Paxman *et al.* (1993) and followed by the integration of non-radiative (Connolly, et al., 2000) and radiative (Connolly, et al., 2004) mechanisms and finally light trapping and photon recycling elements (Connolly, et al., 2007).

The method makes use of the complementarity of generation and recombination phenomena. This complementarity typically fixes all sample parameters except the non radiative lifetime. For example the QE determines cell absorption and charge-neutral layer minority carrier lifetimes, which in turn quantitatively determine radiative and non-radiative recombination currents.

Concerning the structures, we make the common assumptions of homogeneous composition in doped and intrinsic layers, the depletion approximation in the Space-Charge Region (SCR), and 100% photogenerated carrier collection in the SCR.

The first cell characteristic simulated is the Spectral Response (SR), yielding the cell QE and short circuit current (ISC) for a given spectrum. The fit to the QE determines the recombination characteristics independently in charge neutral and space-charge regions. This determines the radiative and non-radiative recombination currents in these regions as a function of applied bias.

The overall photocurrent is simply expressed in terms of superposition, adding photocurrent to the dark current in order to ascertain the light current characteristic.

Bulk and Quantum Well Model

The materials of interest are the $Al_{(x)}Ga_{(1-x)}As$ and $In_{(x)}Ga_{(1-x)}As_{(y)}P_{(1-y)}$ families and their binary, ternary and quaternary compounds. For the modeling reviewed here, the materials parameters of their materials in the bulk rely exclusively on the rich literature in this field (Vurgaftman & Meyer, 2001; EMIS datareviews series 1990 no. 2, EMIS datareviews series 1991 no. 6; Adachi, 1994, 1992; Madelung, 1996).

The quantum well parameters are calculated in the finite square well picture under the effective mass approximation as described in detail by Nelson (Nelson, et al., 1999) and references therein. We summarise and extend the method here in order to define assumptions and relevant parameters.

The wells we are interested in are significantly greater than the lattice periodicity allowing us to use the envelope function approximation. We further assume that the wavefunction in the un-confined plane of the well and in the growth direction are decoupled, such that the confinement may be assumed one-dimensional and the effective mass may be assumed equal to the growth-direction value. The problem is then that of the one-dimensional solution of the Schrödinger equation for a finite square well.

The well depth is evaluated from the bandgap and band offsets of barrier and well materials in the bulk, and the masses of the three carriers estimated where possible from the literature and calculated from k.p methods otherwise (Lynch, et al., 2006). In the envelope function approximation, the effective Shrödinger equation takes the form:

$$\left[-\frac{h^2}{8\pi m^*}\nabla^2 + V(x)\right]\varphi(x) = E_n\varphi(x) \tag{1}$$

for the envelope function φ, carrier effective mass m^*, potential V and energy level E_n at position x. The boundary conditions, after Bastard (1988), are continuity of well and barrier wavefunctions at the well-barrier interface x_i, and continuity of the gradient of the wavefunctions at the same interface:

$$\begin{aligned} &\varphi_W(x_i) = \varphi_B(x_i), \\ &\frac{1}{m_W^*}\frac{\partial}{\partial x}\varphi_W(x_i) = \frac{1}{m_B^*}\frac{\partial}{\partial x}\varphi_B(x_i) \end{aligned} \tag{2}$$

Solving of the Schrödinger equation Equation (1) subject to these boundary conditions (2) gives even and odd solutions:

$$\begin{aligned} &\frac{k}{m_W^*}\tan(kL/2) = -\frac{c}{m_W^*}, \\ &\frac{k}{m_W^*}\cot(kL/2) = -\frac{c}{m_W^*} \end{aligned} \tag{3}$$

in terms of wave vector k, well width L and extinction coefficient c which is found by solving equations 5.3 numerically. This yields bound electron and whole wave functions in the well described by potential profile V(x). The result-

Equation 5.

$$\alpha(\omega) = \frac{4\pi e^2}{ncm^2\omega}\sum_i\sum_f \left|< \varphi_{v,i} \mid \varphi_{c,f} >\right|^2 \left(\frac{\pi\mu^*_{i,f}}{h^2}\right)\left|e.M_{CV}\right|^2 \times\sum_i\left(\left|f_i\right|^2 \delta(\frac{h\omega}{2\pi} - E_i) + \Theta\left(\frac{h\omega}{2\pi} - E_g - E_i\right)\right) \quad (5)$$

ing absorption coefficient is found from Fermi's Golden Rule defining the probability of transitions from initial to final bound states with an additional excitonic factor f_i accounting for electron-hole Coulomb interaction

$$\mid f_i \mid^2 = \frac{R_{CV}}{(1-\nu)^3} \quad (4)$$

in terms of the effective Rydberg for the material R_{CV} and v the bi-dimensionality of the exciton. Finally, the absorption for wells of index n at angular frequency ω (see Equation 5).

Where μ^*_{CV} is the reduced effective mass for initial i to final f states, m the free electron mass, and M_{CV} is the bulk conduction to valence band matrix element, defined for light and heavy hole transitions by:

$$\left|eM^{hh}_{CV}\right|^2 = 3\left|eM^{lh}_{CV}\right|^2 = \frac{E_P}{4m} \quad (6)$$

Ep in eV expresses the interband Kane matrix element, and is a known tabulated materials parameter (Vurgaftman, 2001).

The quantum well modeling introduces two free fitting parameters, which are the excitonic strength and broadening ν and the absolute well absorption strength scaling all transitions and accounting for uncertainties in effective densities of states and systematic uncertainties in the model.

Photocurrent

The methodology yielding the photocurrent follows standard methods described by Hovel (1975) for example. It differentiates between photogenerated carrier collection mechanisms in diffusion dominated charge neutral layers and drift dominated space-charge layers.

Charge Neutral Photocurrent

In the charge neutral layers, the Spectral Response (SR) is calculated as a function of wavelength by solving drift dominated transport and continuity equations. Cell dimensions are defined in Figure 1. The doping densities and known intrinsic carrier densities of the homogeneous *p* and *n* layers define the depletion widths x_{wp} and x_{wn} by analytically solving Poisson's equation in terms of fixed charge density only in the depletion approximation.

The SR calculation method used is standard (Hovel, 1975) and is briefly summarised here for completeness for a *p-i-n* structure. The generation at position x and photon wavelength λ of incident light flux F and front surface reflectivity R is:

$$G(x,\lambda) = F(1-R)e^{-\alpha x} \quad (7)$$

in homogeneous material with absorption coefficient α(λ). In the absence of an electric field in the charge neutral layer, current transport is diffusive only. The generalisation to a structure with a planar back surface mirror as discussed below is a straightforward in terms of an infinite

geometric sum of optical paths determining the total generation rate.

Current continuity defines the minority carrier densities n_p and p_n in *p* and *n* layers respectively as follows:

$$\frac{d^2 n_p}{dx^2} = \frac{n_p}{L_n^{\,2}} - \frac{G(x)}{D_n} \tag{8a}$$

$$\frac{d^2 p_n}{dx^2} = \frac{p_n}{L_p^{\,2}} - \frac{G(x)}{D_p} \tag{8b}$$

where L_n and L_p minority carrier diffusion lengths and D_n and, D_p minority carrier diffusion constants in *p* and *n* layers respectively. Equations 8a and 8b are solved analytically for the p layer subject to minority carrier current density Jn at front surface position x_w (see Figure 1) determined by a surface recombination velocity *Sn*, and the depletion approximation at the SCR of vanishing minority carrier concentration due to the built-in junction potential:

$$j_n(x) = qS_n n_p(x) \left(\mathrm{x} = \mathrm{x_{win}}\right) \tag{9a}$$

$$n_p(x) = 0 \quad \left(\mathrm{x} = \mathrm{x_{win}} + \mathrm{x_p} - \mathrm{x_{wp}}\right) \tag{9b}$$

Similarly for the n layer the boundary conditions at the SCR and at the back surface in terms of minority hole current density J_p and recombination velocity S_p are

$$j_p(x) = qS_p p_n(x) \left(\mathrm{x} = \mathrm{x_w} + \mathrm{x_p} + \mathrm{x_i} + \mathrm{x_{wn}}\right) \tag{10a}$$

$$p_n(x) = 0 \quad \left(\mathrm{x} = \mathrm{x_w} + \mathrm{x_p} + \mathrm{x_i} + \mathrm{x_n}\right) \tag{10b}$$

Equations 8a,b, 9a,b, and 10a,b provide analytical solutions for the electron and hole minority carrier profiles in *p* and *n* layers. The SR is then given by the minority carrier density gradient at the *p* and *n* depletion edges respectively. The QE is defined by the SR as the number of charge carriers collected as a fraction of the incident photon flux at a given wavelength.

Generalising to more than a single layer neutral regions follows the same solution methods. The solution piecewise across all homogeneous layers is found using the same boundary conditions (9a,b), (10,a,b) with additional boundary conditions at each interface between charge neutral layers of continuous charge density and current continuity. The model here uses a single homogeneous base layer and a dual layer emitter in order to include minor short wavelength contributions from the window layer.

In terms of the methodology, we have set out the solutions in order to explicitly define the variables that are set by the SR calculation and data fitting. The surface recombination velocities and transport parameters have similar effects on the SR, but these effects are nevertheless distinguishable if the corresponding losses are significant. That is, a high surface recombination velocity tends to reduce short wavelength response, whereas a short diffusion length reduces photocurrent more evenly over the entire wavelength range. As such, the QE fitting can reliably determine both high surface recombination velocities and low diffusion lengths particularly in the case of cells with poor performance.

Similarly, both parameters become less distinguishable in the case of good quality cells. However, this lesser accuracy applies to cases where the transport losses are negligible. It therefore has little effect on the QE, and on further calculations of recombination currents as we shall see further in the discussion.

Space Charge Region Photocurrent

The SR in the space charge region is calculated in the depletion approximation assuming infinite mobility and drift dominated transport, following

work by Paxman *et al*. (1993) showing that carriers photogenerated in the Space Charge Region (*SCR*) are collected with close to 100% efficiency as long as the background doping in the i-region is low enough that the built-in field is maintained across the i-region at the operating point. The calculation of the QE of bulk, barrier, and QWs, therefore, reduces to integrating the generation rate across the SCR. The barrier absorption coefficient is again extrapolated from available data in the literature and shifted in energy according to strain, if present (Barnham, et al., 2006).

The QW absorption is calculated as described above using effective masses for electrons, and light and heavy holes estimated from k.p calculations for strained material, and values from the literature for unstrained material (Lynch, et al., 2006). The excitonic strength and broadening, which are growth-dependent parameters, are variables to be fitted to the SR in the well but which which nonetheless remain relatively constant in good material.

Dark Current

Charge Neutral Layer Shockley Injection

The QE modeling, as we have seen, determines values of the minority carrier transport and surface recombination. We can therefore define the Shockley injection current density J_S over the junction in terms of these parameters (Nell & Barnett, 1987) as Equation 11 where n_{ip}, n_{in} are the *p* and *n* intrinsic carrier concentrations, N_A, N_D the *p* and *n* doping concentrations, *Dn*, *Dp* minority carrier diffusion constants, and other terms have their usual meaning.

Equation 11 includes surface recombination expressed as the diffusion of injected carriers towards the surface of *p* and *n* charge neutral layers.

Space Charge Region Non-Radiative Recombination

Calculation of non-radiative recombination via defects in the space charge region follows work developed by Shockley, Read, and Hall (Shockley & Read, 1952; Hall, 1952), adapted to QWSC structures by Nelson *et al.* (1999) and further developed as a function of bias for strained materials (Connolly, et al., 2000; Lynch, et al., 2006). The formalism describes the non-radiative recombination rate *U* via mid-gap trapping centres at position *x* in the space charge region as:

$$U_{SRH} = \frac{pn - n_i^{\,2}}{\tau_n(p + p_t) + \tau_p(n + n_t)} \tag{12}$$

Equation 11.

$$J_S(V) = q\left(e^{\frac{qV}{K_B T}} - 1\right)\left[\begin{array}{l} \dfrac{n_{ip}^{\,2}}{N_A}\dfrac{D_n}{L_n}\left(\dfrac{\dfrac{S_n L_n}{D_n}\cosh\dfrac{x_p}{L_n} + \sinh\dfrac{x_p}{L_n}}{\dfrac{S_n L_n}{D_n}\sinh\dfrac{x_p}{L_n} + \cosh\dfrac{x_p}{L_n}}\right) \\ + \dfrac{n_{in}^{\,2}}{N_D}\dfrac{D_p}{L_p}\left(\dfrac{\dfrac{S_p L_p}{D_p}\cosh\dfrac{x_n}{L_p} + \sinh\dfrac{x_n}{L_p}}{\dfrac{S_p L_p}{D_p}\sinh\dfrac{x_n}{L_p} + \cosh\dfrac{x_n}{L_p}}\right) \end{array}\right] \tag{11}$$

where τ_n, τ_p are electron and hole capture lifetimes, and trap densities p_t and n_t are calculated for the dominant mid-gap traps. Carrier densities *n(x)* and *p(x)* vary according to local potential and local densities of states at position x, across the space charge region (Connolly *et al.* 2000). The calculation is therefore an integral across depleted sections of the p-doped and n-doped layers, barrier, and quantum wells. The non-radiative depletion layer dark current density J_{SRH} is then the integral of U over the regions for which the electron and hole Fermi levels separate, namely intrinsic layer width x_i and p and n depletion widths x_{wp} and x_{wn}.

$$J_{SRH} = \int_{x_p - x_{wp}}^{x_p + x_i + x_{wn}} U_{SRH} dx \tag{13}$$

Hole and electron capture lifetimes are assumed equal in QW and barrier regions and in the absence of deviation from expected dark-current idealities as we shall see in the modeling section. All other parameters are as defined by, and consistent with, the QE calculation.

This method therefore introduces a single free fitting parameter, which is the non radiative carrier capture lifetime in the space-charge region, the others being constrained as we have seen.

Radiative Recombination

The generalised Planck equation expresses light emitted by a grey-body as a function of absorption, geometry, and chemical potential or quasi-Fermi level separation of recombining species. Nelson *et al.* (1999) expressed the electroluminescence of QWSC devices of cylindrical geometry and Connolly *et al.* (2007) extended the formalism to include light trapping and photon recycling.

The generalised Planck equation defines the total luminescent flux from a radiative emitter as an integral over the photon energy as:

$$J_{RAD} = \int_0^\infty \left(q \frac{2n^2}{h^3 c^2} \left(\frac{E^2}{e^{(E - q\Delta\phi)/kT} - 1} \right) \int_S a(E, \theta, s) dS \right) dE \tag{14}$$

where n is the refractive index of the grey body, $\Delta\varphi$ is the quasi-Fermi level separation, and the other symbols have their usual meanings. The radiative current is the integral of this flux over all energies. The absorptivity *a(E,θ,s)* is the line integral along the optical path of radiation at angle q with the normal exiting or entering surface S.

In the two-dimensional case of the QWSC with front and back surfaces allowing light emission, three paths are possible at both interfaces. A beam striking a surface may be totally internally reflected at angles of incidents greater than the critical angle giving a first internal reflection. For lesser angles, it may be partially reflected, giving a second internal beam, or transmitted.

Tracking these possible absorption and emission pathways allows us to express the total internal sum of light beams analytically as a geometrical sum, where we neglect coherent beams and interference effects, which is a good assumption for the device dimensions (including substrates) considered. The corresponding integral of the absorptivity a defines the total absorptivity over the emitting volume α_s which is therefore given as the combination of internal and external geometric sums over all angles (Connolly, et al., 2007) and takes the form in Equation 15 where d is the total material thickness, R_f and R_b the front and back surface reflectivities for energy E, and A_F and A_B the front and back surface areas. We note the three terms corresponding to total internal reflection, partial internal reflection, and emission through the back surface.

In the Planck grey body formalism, the different contributions to the luminescence inside the emitting volume contribute separately to the overall luminescence. Therefore, we define well, barrier, and charge neutral net absorptivities. The Planck formalism describes the emitting grey

Equation 15.

$$\begin{aligned}
\alpha_S &= \int_S a(E,\theta)dS \\
&= 2\pi A_F \left(\int_{\cos\theta_C}^{1} \frac{(1-e^{\alpha d\sec(\theta)})(R_F-1)(e^{\alpha d\sec(\theta)}+R_B)}{e^{2\alpha d\sec(\theta)}-R_B R_F}\cos(\theta)d(\cos\theta) \right) \\
&+2\pi A_B \left(\int_{\cos\theta_C}^{1} \frac{(1-e^{\alpha d\sec(\theta)})(R_B-1)(e^{\alpha d\sec(\theta)}+R_F)}{e^{2\alpha d\sec(\theta)}-R_B R_F}\cos(\theta)d(\cos\theta) \right) \\
&+2\pi A_B \left(\int_{0}^{\cos\theta_C} \frac{e^{\alpha d\sec(\theta)}(R_B-1)(e^{\alpha d\sec(\theta)}-e^{-\alpha d\sec(\theta)})}{R_B-e^{2\alpha d\sec(\theta)}}\cos(\theta)d(\cos\theta) \right)
\end{aligned} \tag{15}$$

body as a point source allows us to separate the contributions from different regions in the cell confined between the front and back surface. We can therefore define barrier, well, and charge-neutral absorbances $\alpha_{s_{Well}}$, $\alpha_{s_{Bulk}}$ and $\alpha_{s_{CN}}$ by analogy with Equation 15. well and recombination current density corresponding to the net radiative emission from the combined grey body can be expressed as:

$$\begin{aligned}
J_{Rad} &= \int_0^{\infty} \left[\begin{array}{l} \left(\dfrac{\alpha_{s_{CN}}}{e^{(E-q\Delta\phi_{CN})/kT_{CN}}-1} \right) + \\ \left(\dfrac{\alpha_{s_{Bulk}}}{e^{(E-q\Delta\phi_{Bulk})/kT_{Bulk}}-1} \right) + \\ \left(\dfrac{\alpha_{s_{Well}}}{e^{(E-q\Delta\phi_{Well})/kT_{Well}}-1} \right) \end{array} \right] dE \\
&= J_{Rad}^{CN} + J_{Rad}^{Bulk} + J_{Rad}^{Well}
\end{aligned} \tag{16}$$

in terms of quantum well and bulk quasi-Fermi level separations $\Delta\varphi_{CN}$ $\Delta\varphi_{Bulk}$ and $\Delta\varphi_{Well}$, and carrier temperatures T_{CN}, T_{Bulk} and T_{Well}.

The terms J_{Rad}^{CN}, J_{Rad}^{Bulk}, and J_{Rad}^{Well} enable us to explicitly estimate the radiative recombination current from bulk, well as a function of cell geometry and absorption coefficients, subject to knowledge of the quasi-Fermi level separations and temperatures.

In this work, we will assume an equal carrier temperature in all regions. We also assume a constant quasi-Fermi level in well and barrier material, equal to the applied bias. The situation in the charge-neutral layers is more delicate, depending on position and on illumination. An exact solution could be obtained by numerical solution of coupled transport and Poisson equations. In the spirit of analytical solutions considered in this chapter, however, we fall back on another limiting case, which is the case of high mobility in thin charge-neutral layers, or equivalently, diffusion lengths greater than the charge neutral width. In this case, the injected minority carrier concentration remains close to its value at the depletion edge throughout the charge-neutral layer, and the resulting quasi-fermi level separation remains approximately constant across the charge-neutral width as assumed by Araujo and Martí (1994) for example. In addition to compatibility with these other authors in the field, this assumption is made because it represents the maximum value that the radiative recombination can attain in the charge neutral limit, and therefore sets an upper limit, or best case, for the radiative efficiency of the structures considered.

The Shockley injection we have mentioned (Equation 11) combines radiative and non-radiative mechanisms in charge neutral layers. We can now combine the upper radiative limit with the Shockley injection in order to explicitly obtain the lowest possible non-radiative recombination rate in the charge-neutral layers which we define as:

$$J_S^{CN}(V) = J_S - J_{Rad}^{cn} \tag{17}$$

This upper limit for the non-radiative recombination in the charge-neutral layers, combined with the non-radiative SRH rate in the space-charge region gives us the lower limit of non-radiative recombination in the solar cell, including surface recombination. We can therefore define a bias dependent radiative efficiency as the ratio of radiative to total dark current as follows:

$$\eta_{RAD}(V) = \frac{J_{Rad}}{J_{SRH} + J_{Rad} + J_S^{cn}} \tag{18}$$

It is worth emphasising that this is an upper limit on the radiative efficiency of devices, and that devices closest to achieving this limit will be those devices with short diffusion lengths compared with relevant charge neutral widths. We will see in subsequent sections that the most interesting consequences of this analysis occur for the more efficient devices with good minority carrier transport.

Light Current and Efficiency

The sum of contributions from charge neutral *p*, and *n* zones, and space charge regions gives the total photocurrent density J_{PH}. This defines the external quantum efficiency including reflection loss (QE) as ratio of collected carriers to number of incident photons at a given wavelength, that is, the probability that a photon incident on the solar cell gives rise to a charge carrier collected at the cell terminal.

Finally, the light current density under applied bias, assuming superposition of light and dark currents is given by:

$$J_L(V) = J_{PH} - (J_S + J_{SRH} + J_{RAD}) \tag{19}$$

where we use the photovoltaic sign convention of positive photocurrent.

This light IV enables us in the standard manner (see for example Nelson, 2003) to evaluate solar cell figures of merit such as the short circuit current $J_{SC} = J_L(0)$, the maximum power point V_{mp}, and fill factor FF. Effects of parasitic resistance are included when modeling real data in the usual manner, that is, a series resistance defining a junction bias, and a parallel resistance and associated shunt current reducing the photocurrent.

Discussion

Having sketched the modeling methodology and the separate analytical solutions that, together, describe the overall solar cell performance, the links between the physical phenomena described merit some attention. Firstly, the QE modeling determines all cell parameters except space-charge SRH lifetime. That is, it sets the band structure, absorption profiles, majority carrier densities, and minority carrier transport properties.

The band structure and resulting carrier concentration profiles, together with minority carrier transport determine the Shockley injection current (11) across the built in potential.

The carrier densities injected across the SCR in turn determine the SRH non-radiative recombination current (13) with the introduction of a free parameter, which is the non-radiative capture lifetime.

The majority carrier densities and minority carrier transport determine Shockley injection (11) as a function of applied bias by diffusion across the built in potential. The same carrier concentration profiles as a function of position across the SCR

determine the non radiative SRH recombination profiles (13) with the addition of the non-radiative lifetime as single free parameter, which is a sensitive function of growth conditions. This approach has been found to fit data well for biases up to the open circuit voltage (Connolly, et al., 2007).

These drift-diffusion profiles are consistent with quasi-Fermi level separations determining the luminescence, which again are determined by the applied bias.

The Shockley Injection current includes both radiative and non-radiative contributions since both are subsumed into a single minority carrier lifetime or diffusion length. Therefore, the SRH calculation applies only to the SCR region, as does the radiative recombination current.

For luminescence calculations, however, the radiative calculation applies to the entire structure in those cases where the diffusion length is comparable or greater than the relevant charge-neutral layer thickness. This is always the case in the high purity material considered, where the dopant species are the only significant defects. A noteworthy feature of this approach is that modeling the QE of the samples uniquely determines all recombination mechanisms except the non-radiative recombination in the SCR. This being determined by a single lifetime, the model therefore fixes excitonic characteristics and minority carrier transport that might otherwise be free parameters. The electroluminescence spectra and hence the radiative contribution to the dark-current are also reproduced essentially without adjustable parameters.

The conclusion, we come to after this overview of the interdependence of the analytical solutions is that this analytical approach describes recombination mechanisms in detail with no free parameters in the limit of dominant radiative recombination. The reason for this is the linking physical processes common to photogeneration and recombination mechanisms. This explicit description made possible with analytical solutions methods comes at some cost in accuracy resulting from the approximations required. The following analyses of experimental data investigate show whether the understanding gained is justified.

RADIATIVE LIMITS OF BULK VS. QWSC

We now investigate bulk PIN and QWSC cases to examine the operating limits of these two structures. Both PIN and SB-QWSC structures are fabricated by MOVPE. The dimensions are similar but for the SB-MQW layer and can be summarised as follows: the PIN consists of a 43nm $Al_{0.7}Ga_{0.3}As$ cap on a 0.5μm GaAs p-type emitter, a 0.9μm intrinsic GaAs layer and finally a 2μm GaAs n-type base layer. The MQW sample consists of a slightly higher bandgap $Al_{0.8}Ga_{0.2}As$ cap, also of width 43nm. This is grown on a slightly thinner 0.4μm GaAs p-type emitter, a 1.46μm intrinsic GaAs layer and finally a 2μm GaAs n-type base layer. The SB-MQW system is made up of $In_{0.11}Ga_{0.89}As$ wells of width 95A, compressively strained between $InGa_{0.911}P_{.089}$ tensile strained barriers of width 196A.

These structures are not optimal structures for conversion efficiency, being instead designed for minimal parasitic resistance effects together with a intrinsic region width ensuring efficient carrier collection at bias up to high bias approaching flat band. As a result, they both comprise a high metallisation and shading fraction, which are 70% and 40% for the PIN and QWSC solar cell devices respectively. In addition, the number of wells in the QWSC sample is not the highest that has been manufactured, leading to a non-optimum number of wells. The following discussion therefore will not address specific performance issues, focusing instead on the limiting behaviour we have discussed earlier.

Bulk and Quantum Well Cells

The QE modeling and data for the bulk PIN is shown in Figure 2a, showing a good fit to the data overall. The photocurrent contributions are broken down into *n* and *p* doped layer response, including the depleted sections of these layers, and the intrinsic or nominally undoped layer. The contributions show the expected dominance of the front-most p layer, particularly at short wavelengths, followed by the intrinsic n-type base layer, in order of decreasing light intensity as a function of depth.

The QE of the QWSC in Figure 3a shows the same features as the PIN for emitter and base regions. The more intricate contribution from the wells merits some discussion. The wells are deeper than might be expected from the bulk bandgaps once strain shifts on the band-gap energy are taken into account, which, in this case shift the barriers upwards by about 50meV to 1.59eV or 782nm, and wells down by about 40meV to 1.26eV. Confinement increases the effective well gap to approximately 1.33eV or 926nm. The structure visible from the dominant bulk GaAs band-edge at 874nm to the strained barrier gap at 782nm is the higher quantum well bound states identified by the model as heavy whole states with just one light whole state lightly bound at the top of the well. The peaks visible in the intrinsic *i* region response are therefore bound excitonic states of heavy hole and electronic states identified by the model but not reported in detail here.

The main conclusions we draw from the model is the illusory nature of the apparent close agreement between bulk and QWSC responses, since it masks the fine detail that may be revealed by explicit evaluation of the response of the different regions making up the solar cells.

The PIN recombination current is shown in Figure 2b, from approximately half a typical Voc in order to see better the high bias behaviour. As described above, we see the non-radiative Shockley-Read-Hall (SRH) marked by the empty crosses dominating at lower bias, with an modelled ideality of n=1.81 which is a striking match for the data, showing to what extent the common assumption of 2 is approximate.

The higher bias regime above 1V sees a change in slope which, although masked by the onset of series resistance, is clearly and very closely modelled by the explicitly non-radiative contribution to the Shockley injection current marked by the triangles, with an ideality of n=1. The final contribution is the upper limit or maximum possible radiative current from the cell is indicated by the empty circles. The assumption of upper limit of radiative efficiency does not lead to a visible overestimation of the dark current, despite the radiative current clearly approaching a few percent of the total dark current at high bias.

This last point is underlined by the explicit radiative efficiency (Equation 5.18) shown on the right hand axis. The bulk PIN cell is of sufficient quality to approach 20% radiative efficiency at high bias, which quantifies the extent to which this cell approaches the ideal limit. This important point shows that an ideality tending towards 1 cannot be taken to mean radiative dominance, as a consequence of the analysis we have presented which breaks down the Shockley injection current into radiative and non radiative components.

Returning to the QWSC in Figure 3b, we observe the same trend from an SRH dominated regime with a slightly smaller ideality of n=1.78 again closely matching the data, to a regime of ideality n=1 looking remarkably similar to the PIN case. The fundamental difference however is clearly shown by the model: in the QWSC case, the contribution from the radiative recombination limit is slightly over an order of magnitude greater than the explicitly non-radiative Shockley injection recombination current. The corresponding radiative efficiency for this case reaches 76% at high bias.

The important result of this analysis is that PIN bulk cells and QWSCs operate in different physical limits despite apparently similar dark

Figure 2. QE data and model for (a) the bulk GaAs PIN and (b) dark current fit together with radiative efficiency peaking at 21% at flat band, and active area efficiency 21.0%

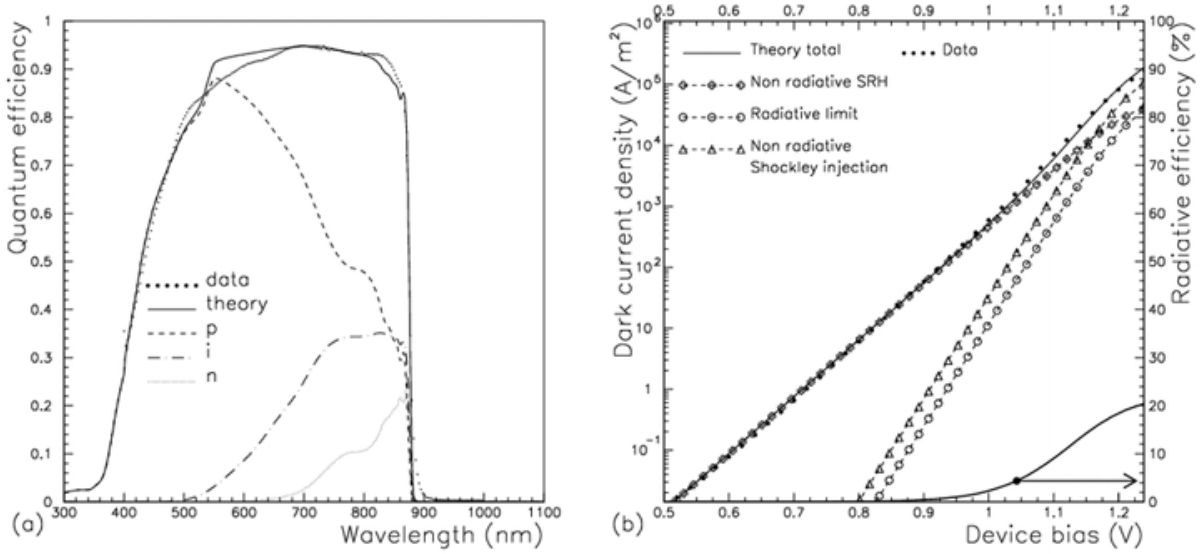

Figure 3. (a) QE data and model for a QWSC PIN with GaAs barriers and GaInas well and (b) dark current fit together with radiative efficiency peaking at 75% at flat band and active area efficiency 22.5%

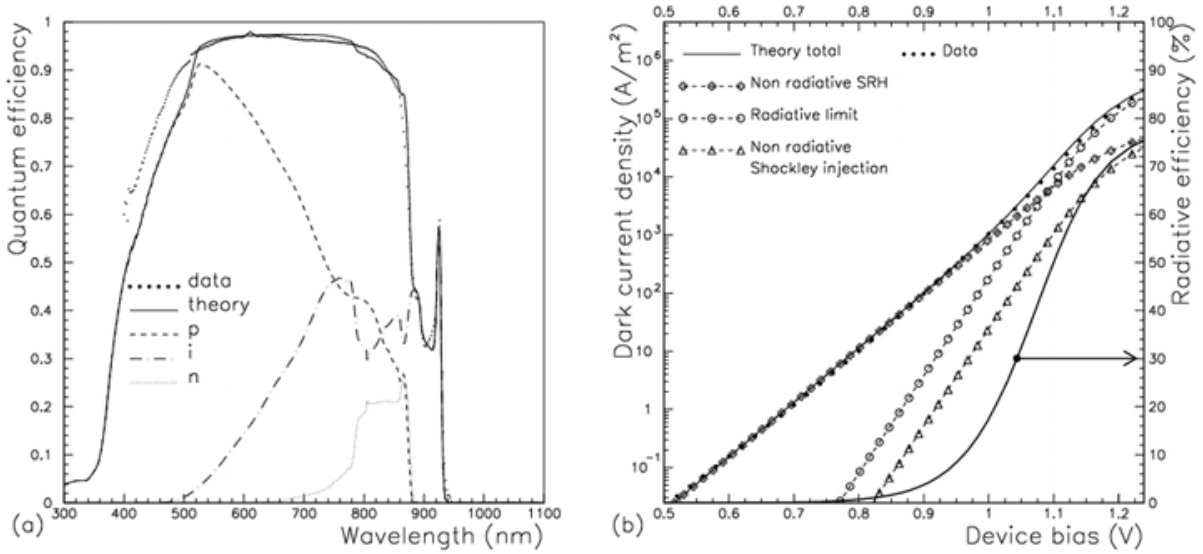

current characteristics. The QWSC, radiatively dominated at biases above 1.05V, operates closer to the fundamental efficiency limit than the PIN cell, which this analysis shows is dominated by non-radiative recombination in the ideality 1 regime. This must be qualified, however: as we have mentioned earlier, the structures are not optimal. As a result, it is a fortuitous consequence of material quality that the total dark current QWSC and bulk PIN devices are nearly equal, underlining the point made in the introduction concerning the greater importance of dominant carrier transport and recombination mechanisms rather than explicit performance issues.

Having established this powerful notion of radiative dominance, we now focus on the obvious flip side, which is that the radiative dominance comes at the price of increased recombination. This draws attention back to the magnitude of the corresponding increase in photocurrent, which is not, in this non-optimal design, sufficient to counterbalance the increased recombination rate. As a result, the bulk PIN cell, despite its less ideal, non-radiatively dominated recombination characteristic, is nevertheless the more efficient design simply because of the high absorption coefficient maintained to just a few nanometers in wavelength above the band-edge. In this specific case, however, the QWSC does perform more efficiently than the bulk cell due to secondary considerations, which are first the slightly better window and emitter design, and the better anti-reflection coating response for the QWSC.

This conclusion emphasises the introductory remarks on the non-ideal design of each cell and drawing attention to the physical regime the cells operate under rather than the conversion efficiency of each device. It furthermore echoes the observation made in the introduction regarding the relatively low well number, and resulting low well QE, with the first absorption continuum of just 33%, which, in turn, raises the issue of light trapping for increased absorption and consequences for the operating regime we shall cover next.

The strong conclusion however is that design specific issues apart, the QWSC is fundamentally a radiatively dominated design in a sense that the bulk PIN cannot be, unless non optimum, low doping levels are adopted in order to reduce the Shockley injection current. This demonstrates a promising high efficiency characteristic of this design.

Mirrors and Restricted Emission, or Photon Recycling

The previous section has emphasised the MQW low absorption as a weak point in the QWSC design. This problem is common to other thin film solar cell technologies however, and may be addressed by a range of geometric solutions such as textured surfaces and light management increasing the optical path length. Of these, the first and simplest solution is the back surface mirror as used in thin film solar cell photovoltaics, which is sufficient to illustrate the specific phenomenological features of the QWSC in the light of the analysis we have described. Coating surfaces with mirrors traps light and reduces light loss, but furthermore restricts light emission. The major advantage of this restricted emission, as we will see, in that coating a surface with a mirror cuts off the emission of light through that surface. As such, an ideal cell is one with the angle of light acceptance limited to the solid angle subtended by the spectral source, the sun, as described by de Vos (1992) and references therein, and complemented by Araujo and Martí (1994). This concept is closely related to photon recycling, differing by the increased absorptivity implied by photon recycling. In the ideal limit of an opaque cell and minimal spectral acceptance solid angle, the two concepts give the same radiatively limited efficiency.

In the case of a bulk PIN cells and QWSCs, the main difference is the transparence of the neutral regions. In the QWSC cell, the neutral layers are transparent to light emitted by the wells, whereas the bulk cell neutral layers of the bulk PIN are ef-

ficient absorbers of the *i* region emission. We will consider both QWSC and bulk PIN cells fabricated on substrates transparent to the luminescence in order to focus the description on the interaction between the active layers and the luminescence, rather than the less fundamental interaction with the substrate. We choose unit back reflectivity R_b=1 for similar reasons, but the results described apply to arbitrary non-zero back reflectivities.

Considering first the bulk PIN cell, Figure 4a shows the modelled QE with a back mirror and, for reference, the same data as in Figure 2a. Given the high absorption coefficient of GaAs, the bulk cell absorbs nearly all incident light on the first pass. As a result, the QE with a back mirror shows only a slight increase in QE for wavelengths within a few nm of the band-edge, where the absorption coefficient is weakest. The dark current modeling in Figure 4b however shows a marked difference to Figure 2b, in that a strong reduction in radiative current is seen, whilst the non-radiative Shockley injection and Shockley-Read-Hall space-charge region currents are unchanged. The radiative efficiency therefore is reduced to slightly less than one percent as shown by the arrow on Figure 4b. This is a consequence of the reduced net luminescence to the back surface, since that luminescence is reflected back into the cell by the back mirror according to equation 5.15. The second term in that expression relating to partial transmission through the back surface is reduced, while the third term relating to total transmission through the back surfaces vanishes for unit back reflectivity R_b=1. The net result is a reduction in the bulk PIN dark current, which is however relatively minor given the non-radiative dominated character of this cell. The practical advantage of the back surface mirror is, as might be expected for this opaque and non-radiatively dominated cell, relatively minor: The modelled efficiency increases marginally from 21% to 21.3% consistently with the minor impact on cell performance.

Figure 4. Bulk PIN case QE theory (a) with back surface mirror compared with reference data without mirror, showing a negligible increase in QE near the band-edge. A similar dark current comparison (b) shows reduced radiative recombination, and hence a radiative efficiency peaking at just 1% at flat band. The mirror increases efficiency marginally from 21.0% to 21.3%.

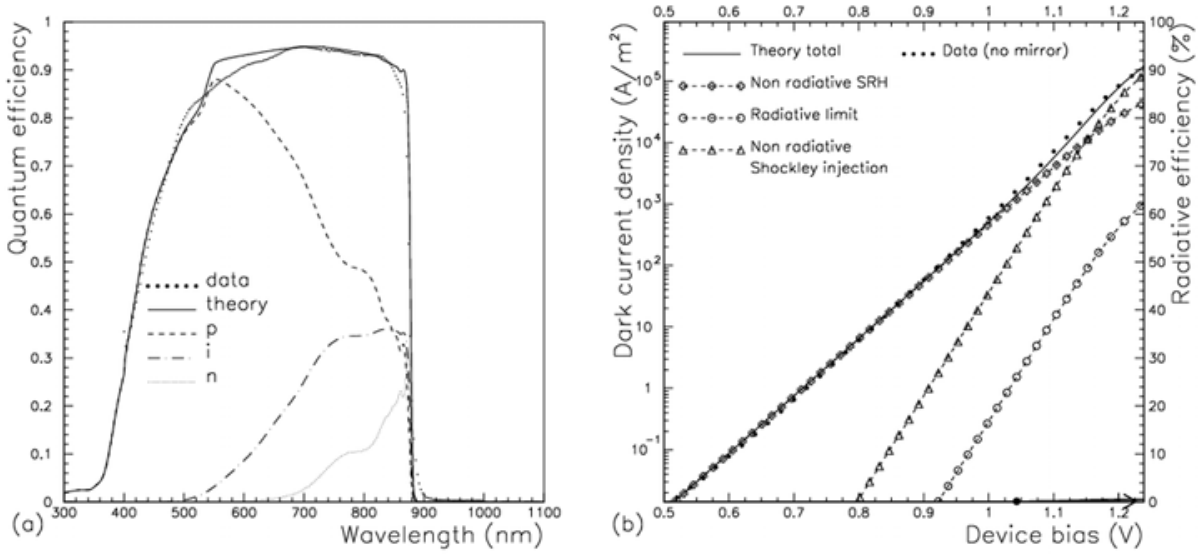

Figure 5. SB-QWSC case (a) QE theory with back mirror compared with reference data without mirror showing significantly increased well response. The dark current theory (b) shows the mirrored SB-QWSC high bias dominated by the neutral layer non-radiative Shockley injection current, and a radiative efficiency of the order of 12%. The SB-QWSC mirrored dark current is dominated by the higher bandgap charge-neutral. The mirror increases efficiency from 22.5% to 23.3%.

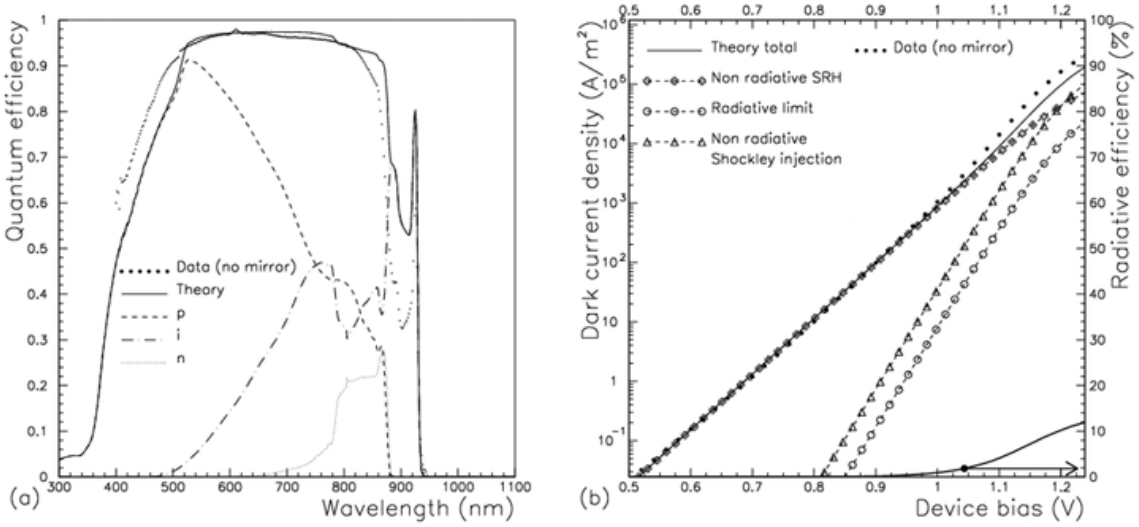

Figure 5a shows the corresponding effect on the QE of the QWSC. The quantum wells with the help of the mirror increase the short circuit current by 7% compared with a bulk control where wells and barriers are replaced by bulk GaAs, to 300.5A/m2 active area density under global spectrum AM1.5G. This furthermore represents a 3% increase over the QWSC case mentioned in the previous section without a mirror. It is clear, however, that the absolute level remains well short of the bulk QE, a level the quantum well must achieve in order to approach the radiative efficiency limits that it tends towards.

Concerning the radiative efficiency limit, Figure 5b shows a striking reduction of dark current and a reversion to explicitly non-radiatively dominated Shockley injection dominance. The addition of the back surface mirror has the effect of reducing the luminescence by cutting off radiative losses towards the back of the cell. Neglecting emission in the small in-plane solid angle, the only remaining net loss path is though the small escape cone through the front of the solar cell, typically of some 17 degrees. The removal of the much greater 180-degree loss angle at the back surface translates as a reduction of approximately an order of magnitude in net radiative recombination that can occur. The balance of luminescence, which is still inevitable emitted via the Planck grey-body law, is re-absorbed, leading to re-emission, and so on, according to the formalism developed earlier in Equation (15): This, in the dark, is equivalent to photon recycling, and is the mechanism whereby the back surface mirror transforms the QWSC from a radiatively dominated device to a non-radiatively dominated device.

Although at the first glance this appears a step backward, the comparison of Figures 5b and 2b shows us that the QWSC with a back mirror is in fact dominated by the explicitly non radiative Shockley injection recombination rate in the

charge neutral layers at sufficiently high bias, or equivalently, high current levels, such that SRH recombination no longer dominates. Such current levels are routinely achieved by cells operated under concentration of a few hundred suns as reviewed by Barnham *et al.* (2010). The consequence is that the QWSC can be operated in a regime where the fundamental absorption edge is determined by the space charge region, but the recombination mechanism remains determined by the higher bandgap charge neutral regions.

This important result is the second key advantage of the QWSC introduced earlier in this chapter, and suggested by Barnham and Duggan (1990). This analysis however pins down this conceptual disconnect between absorption edge and dominant recombination mechanism to the case where non-radiative recombination is present. More precisely, the ideal radiative case of pure, defect free material will show no such dominance of charge neutral recombination current, since this will have been reduced to a radiative level determined by its gap. In this case, the cell will return to being dominated by the fundamentally greater radiative recombination current from the lower gap region. This limiting case, however, is clearly not one in which a working solar cell, which requires defects (dopants) in order to set up the built-in potential at the root of photovoltaic action.

In light of these points, it is clear that that the disconnect between observed dark current dominance by the higher gap bulk regions remains consistent with theoretical work that has suggested that the structure, while remaining subject to the generalised Planck law and corresponding efficiency limits, might offer routes to higher efficiency (de Vos, 1992; Araujo & Martí, 1994).

We conclude with a mention of experimental results reported by Johnson *et al.* (2007). This work has reported the observation of the phenomenon of reduced radiative recombination in SB-QWSCs with Bragg reflectors incorporated at the back of the cell, and demonstrate the dark current reductions of the order of those reported here.

CONCLUSION

Solar cell efficiency potential remains far greater than the best achieved in the lab. The analytical model described in this chapter helps shed light on this by linking the solar cell performance in the light and in the dark, and using this to ascertain the dominant losses responsible for non-dealities. The set of approximations enabling this analytical methodology make it all the more important to minimise the free parameters. Consequently, the comparison of data and model crucial in determining what conclusions can justifiably be made. The model described satisfies both these conditions: the only free parameter is the Shockley-Read-Hall lifetime in the space-charge region, and furthermore, the modelled SRH ideality of slightly less than 2 agrees well with experiment.

The more interesting high bias regime of ideality one corresponding to higher efficiency concentrator current level is, however, free of any fitting parameters. Close agreement between model and experiment is seen in both bulk and quantum well cases.

In this higher bias ideality one regime, which is the focus of this chapter, some remarkable behaviour is revealed by comparing bulk and quantum well samples. The modeling and resulting analysis shows allows explicit estimates of the bias-dependent radiative efficiency of both classes of device.

It first transpires that the bulk device is non-radiatively dominated despite the transition from dark current ideality slightly below 2 to Shockley injection ideality 1. The radiative fraction in this high quality GaAs cell is only of the order of 20% at most, as the cell approaches flat band. The QWSC in the same regime is shown to be approximately 75% dominated by radiative recombination.

The analysis of samples with back surface mirrors reveals a quite different operational regime. The bulk PIN cell performance remains relatively unchanged, as expected for a nearly opaque structure, which is dominated by non-radiative

recombination. The QWSC however changes radically. First, the photocurrent increase is significant, which is a consequence of the low well absorption, and emphasising why light trapping is important for these structures. Secondly, and more significantly, the QWSC changes from a radiatively dominated to a non-radiatively dominated regime. Examination of the contributions to the recombination current from the different regions of the cell shows that the net radiative recombination is suppressed by an order of magnitude through a combination of photon recycling and restriction of emission solid angle. As a result, the explicitly non-radiative part of the Shockley injection current dominates the dark current. In other words, the dark current is primarily determined by the higher bandgap bulk charge neutral layers, rather than by the lower MQW layer.

The startling conclusion of this is that the Voc of the mirror backed QWSC is partly decoupled from the absorption edge. That is, the open circuit voltage of the mirror backed QWSC is determined by the high gap charge neutral layers, while the absorption edge is determined by the lower gap quantum well region. This is the original idea proposed by Barnham and Duggan (1990), albeit in a more restricted sense, in that this only holds true for doped, and therefore non-radiatively dominated structures: in a structure where only radiative recombination is present, both PIN and QWSC designs revert to the Planck grey-body radiative limit, but without, however, the benefit of a doped junction to enable photovoltaic action and carrier collection.

REFERENCES

Adachi, S. (1992). *Physical properties of III – V semiconductor compounds: InP, InAs, GaAs, GaP, InGaAs, and InGaAsP*. New York, NY: Wiley. doi:10.1002/352760281X

Adachi, S. (1994). *GaAs and related materials: Bulk semiconducting and superlattice properties*. Singapore: World Scientific.

Anderson, N. G. (1995). Ideal theory of quantum well solar cells. *Journal of Applied Physics*, *78*(3), 1850–1861. doi:10.1063/1.360219

Araujo, G. L., & Marti, A. (1994). Absolute limiting efficiencies for photovoltaic energy conversion. *Solar Energy Materials and Solar Cells*, *33*, 213. doi:10.1016/0927-0248(94)90209-7

Barnham, K. W. J., Ballard, I., Bessiere, A., Barnham, K. W. J., Ballard, I., & Bessiere, A. … Malik, M. A. (2006). Quantum well solar cells and quantum dot concentrators. In T. Soga (Ed.), *Nanostructured Materials for Solar Energy Conversion*, (pp. 517 – 538). London, UK: Elsevier.

Barnham, K. W. J., Ballard, I. M., Browne, B. C., Connolly, J. P., Ekins-Daukes, N. J., & Fuhrer, M.….. Rohr, C. (2010). Recent progress in quantum well solar cells. In L. Tsakalakos (Ed.), *Nanotechnology for Photovoltaics,* (pp. 187-210). New York, NY: CRC Press.

Barnham, K. W. J., & Duggan, G. (1990). A new approach to multi bandgap solar cells. *Journal of Applied Physics*, *67*, 3490. doi:10.1063/1.345339

Bastard, G. (1988). *Wave mechanics applied to semiconductor heterostructures*. Paris, France: Editions de Physique.

Connolly, J. P., Ballard, I. M., Barnham, K. W. J., Bushnell, D. B., Tibbits, T. N. D., & Roberts, J. S. (2004). Efficiency limits of quantum well solar cells. In *Proceedings of the 19th European Photovoltaic Solar Energy Conference*, (pp. 355-359). Paris, France: EU PVSEC.

Connolly, J. P., Johnson, D. C., Ballard, I. M., Barnham, K. W. J., Mazzer, M., & Tibbits, T. N. D… Calder, C. (2007). Mirrored strain-balanced quantum well concentrator cells in the radiative limit. In *Proceedings of the ICSC-4*, (pp. 21-24). ICSC.

Connolly, J. P., Nelson, J., Barnham, K. W. J., Ballard, I., Roberts, C., Roberts, J. S., & Foxon, C. T. (2000). Simulating multiple quantum well solar cells. In *Proceedings of the 28th IEEE Photovoltaic Specialists Conference*, (pp. 1304-1307). Anchorage, AK: IEEE Press.

de Vos, A. (1992). *Endoreversible thermodynamics of solar energy conversion*. Oxford, UK: Oxford University Press.

Hovel, H. J. (1975). *Semiconductors and semimetals*. New York, NY: Academic Press.

INSPEC. (1990). *Properties of gallium arsenide* (2nd ed.). New York, NY: John Wiley.

INSPEC. (1991). *Properties of indium phosphide*. New York, NY: John Wiley.

Johnson, D. C., Ballard, I. M., Barnham, K. W. J., Connolly, J. P., Mazzer, M., & Bessière, A. (2007). Observa.tion of photon recycling in strain-balanced quantum well solar cells . *Applied Physics Letters*, *90*, 213–505. doi:10.1063/1.2742334

Lynch, M. C., Ballard, I. M., Bessiere, A., Johnson, D. C., Stavrinou, P. N., & Barnham, K. W. J. … Calder, C. (2006). Modeling the confined carrier states in multi quantum well solar cells. In *Proceedings of the 4th World Conference on Photovoltaic Energy Conversion*, (pp. 67-70). Hawaii, HI: IEEE.

Madelung, O. (Ed.). (1996). *Semiconductors - Basic data*. Berlin, Germany: Springer Verlag. doi:10.1007/978-3-642-97675-9

Nell, M. E., & Barnett, A. M. (1987). The spectral p-n junction model for tandem solar-cell design. *IEEE Transactions on Electronic Devices, 34*(2).

Nelson, J. (2003). *The physics of solar cells*. London, UK: Imperial College Press.

Nelson, J., Ballard, I., Barnham, K., Connolly, J. P., Roberts, J. S., & Pate, M. (1999). Effect of quantum well location on single quantum well p–i–n photodiode dark currents. *Journal of Applied Physics*, *86*(10). doi:10.1063/1.371609

Nelson, J., Paxman, M., Barnham, K. W. J., & Roberts, J. S., & Button. (1993). Steady-state carrier escape from single quantum wells, C. *IEEE Journal of Quantum Electronics*, *29*(6), 1460–1468. doi:10.1109/3.234396

Paxman, M., Nelson, J., Barnham, K. W. J., Braun, B., Connolly, J. P., & Button, C. (1993). Modeling the spectral response of the quantum well solar cell. *Journal of Applied Physics*, *74*, 614. doi:10.1063/1.355275

Rimada, J. C., Hernandez, L., Connolly, J. P., & Barnham, K. W. J. (2007). Conversion efficiency enhancement of AlGaAs quantum well solar cells. *Microelectronics Journal*, *38*, 513–518. doi:10.1016/j.mejo.2007.03.007

Shockley, W., & Read, W. T. (1952). Statistics of the recombinations of holes and electrons. *Physical Review*, *87*, 835. doi:10.1103/PhysRev.87.835

Tsai, C.-Y., & Tsai, C.-Y. (2009). Effects of carrier escape and capture processes on quantum well solar cells: A theoretical investigation. *IET Optoelectronics*, *3*(6), 300–304. doi:10.1049/iet-opt.2009.0027

Vurgaftman, I., & Meyer, J. R. (2001). Using JPF1 format. *Journal of Applied Physics*, *89*(11), 5815–5875. doi:10.1063/1.1368156

Section 3

Hybrid and Polymer Solar Cells

Chapter 6
Hybrid Solar Cells: Materials and Technology

Corneliu Cincu
Polytechnic University of Bucharest, Romania

Aurel Diacon
Polytechnic University of Bucharest, Romania

ABSTRACT

Conventional solar cells are usually manufactured from silicon, an inorganic material. This type of solar cell has a high efficiency, up to 40%, but these cells are using very expensive materials of a high purity and energy intensive processing techniques. This chapter is dedicated to a critical presentation of hybrid solar cells. They are a combination of both organic and inorganic nanostructure materials and, therefore, combine the properties and advantages of their components. Unfortunately, so far, the hybrid solar cells have a low conversion efficiency of the sunlight, 6-7% (Kim, et al., 2007).

INTRODUCTION

Hybrid photovoltaic cells, classified as the third and fourth generation solar cells, are a mix of nanostructures of both organic (p-type conjugated polymers, photosensitive dyes, carbon nanotubes, etc.) and inorganic (nanostructures or nanoparticles of TiO_2, ZnO, PbS, PbSe, CdTe, $CuInS_2$, $CuInSe_2$, etc.) materials.

One of the materials (organic component) acts as the photon absorber. In contrast to inorganic semiconductors, photo excitation of organic semiconductors results in a strongly bounded electron-hole pair, called an exciton (Ginger & Greenham, 1999b). These electron-hole pairs are only effectively separated at an interface between a p-type (electron-donating) material and n-type (electron-accepting) material represented by the inorganic component of a hybrid solar cell, Figure 1.

DOI: 10.4018/978-1-4666-1927-2.ch006

Figure 1. Energy (E) diagram at the interface donor/acceptor in a hybrid solar cell

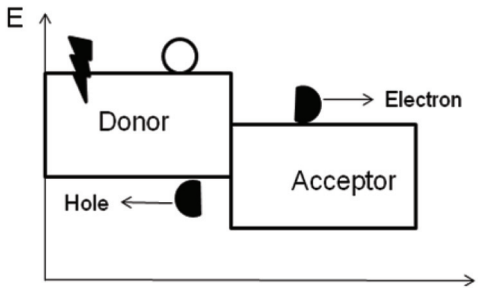

In order to have a favourable charge transfer at the interface, the following condition must be satisfied (Ginger & Greenham, 1999b): E_A^A-E_A^D>$U_{D,}$ where E_A is the electron affinity, U is the columbic binding energy of the exciton on the donor and superscript A refers to the acceptor and superscript D refers to the donor. For the exciton binding energy in commonly used organic materials (polymers, oligomers, small molecules, carbon nanotubes) the value ranges from 0.3 eV to 1.4 eV, which is considerably higher than the binding exciton energy for inorganic semiconductor materials, 0.02-0.04 eV (Scheblykin, Yartsev, Pullerits, Gulbinas, & Sundström, 2007). In order to dissociate the exciton in a bulk organic medium, the thermal energy at room temperature (≈0.025 eV) is not sufficient, therefore the exciton dissociation is possible only at the interface between the donor and the acceptor materials with favorable HOMO and LUMO energy levels.

The difference between the LUMOs (or conductive band) of the donor and acceptor will compensate the energy required for the dissociation and the transfer of the electron (Saunders & Turner, 2008). After charge separation, the carriers (electrons and holes) are transported to the electrodes through a percolation network.

The exciton generated in polymer has a time scale from one picosecond to one nanosecond (Shaw, Ruseckas, & Samuel, 2008) and the diffusion length (at average distance an exciton can diffuse through material before its annihilation by recombination) is short in polymers (5-10 nm) (Ginger & Greenham, 1999b). Only the exciton generated within this length close to an acceptor would contribute to the photocurrent of the cells. For this reason, the hybrid solar cells often use a nanostructured interpenetrating network of donor and acceptor materials (bulk heterojunction) with an enhanced interfacial area where the excitons are separated into charge carriers (Saunders & Turner, 2008). The bulk heterojunction concept allows for more interfacial contact between the organic (donor) and inorganic (acceptor) materials than the phase separated bi-layer heterojunction.

Hybrid solar cells have some advantages over the other types of photovoltaics (first and second-generation cells) (Gledhill, Scott, & Gregg, 2005; Huynh, Dittmer, & Alivisatos, 2002; McGehee, 2009; Ong & Levitsky, 2010):

- Hybrid nanocomposite mixtures combine the advantages of both type of materials: the solution processing of organic semiconductors with the high charge-carriers mobility and light absorption at longer wavelengths if inorganic semiconductors;
- The existence of an organic component allows hybrid solar cells to be superior over conventional semiconducting photovoltaics in terms of cost efficiency, scalable wet processing, and the variety of organic materials, lightweight, and flexibility. Moreover, the recent progress in advanced semiconducting nanostructures in combination with polymers and/or organic nanomaterials, such as fullerenes and carbon nanotubes, opens new opportunities to overcome the 8-10% barrier of light conversion efficiency for hybrid solar cells in the near future (Li, et al., 2009; Ong, Euler, & Levitsky, 2010).

Figure 2. Classification of hybrid solar cells

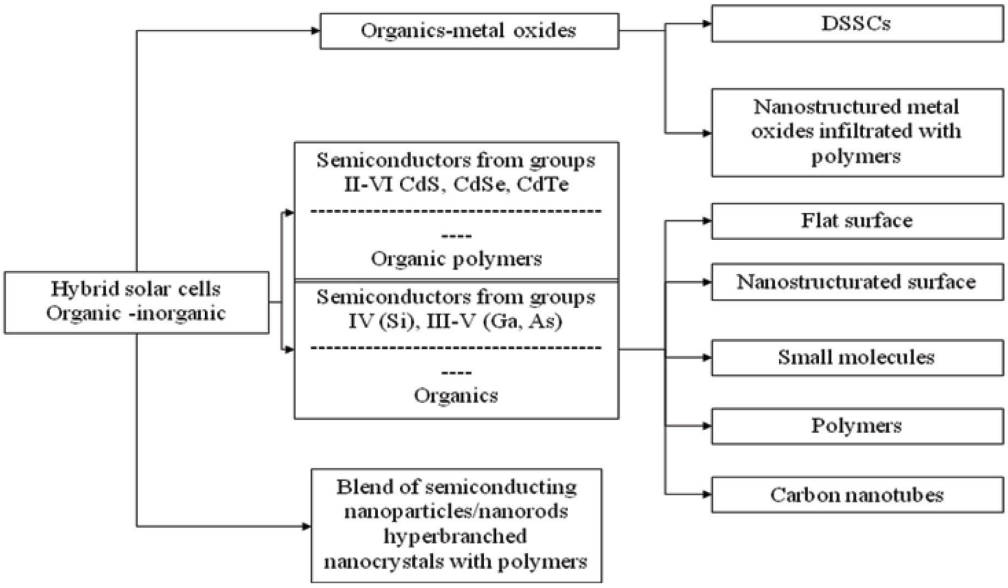

CLASSIFICATION OF HYBRID SOLAR CELLS

The hybrid solar cells classification depends on the nature and morphology of organic and inorganic components and it is presented in the Figure 2 (Ong & Levitsky, 2010).

DYE SENSITIZED SOLAR CELL

To date, Dye Sensitized Solar Cells (DSSCs) are the most studied hybrid solar cell (Gledhill, et al., 2005; Grätzel, 2003). Vlachopoulos, Liska, Augustynski, and Graetzel (1988) reported energy conversion from dye sensitized TiO_2 electrode immersed in an electrolyte, titanium dioxide being a n-type wide band gap semiconductor and transparent for visible light. This system has a low light absorption coefficient because the dye is adsorbed on a flat surface of the TiO_2 electrode. O'Regan and Grätzel (1991), used a nanoporous TiO_2 electrode which enhances the photoactive interface by order of magnitude (200-300 m^2/g for nanoporous TiO_2 as compared to approximately 10 m^2/g of flat single crystal) and the effective light absorption increased drastically. DSSC (Grätzel type) is composed of:

1. A nanoporous metal oxide (TiO_2, NiO, ZnO) infiltrated with sensitized dye molecules (Ru complexes or other organic dyes) and deposited on Transparent Conductive Oxide (TCO) electrode,
2. Electrolyte containing I^-/I_3^- redox system filling the pores of the metal oxide,
3. A platinum counter electrode (Grätzel, 2005) (Figure 3).

After the absorption of a photon, the excited electron within the sensitizer dyer is transferred to the conduction band of TiO_2. Electrons diffuse in the nanoporous metal oxide to TiO_2/TCO interface, where they are extracted to external load. In the same time, the resulting dye cations are reduced by the redox system (Figure 4).

Figure 3. Structure of DSSC

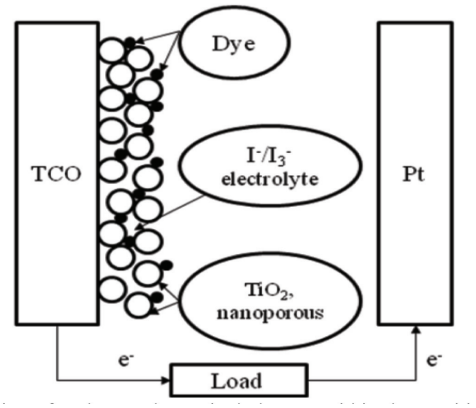

The process can be characterized by Incident Photon-to-Current Conversion Efficiency (IPCE) which is determined by Light-Harvesting Efficiency (LHE), Charge Injection Efficiency (CIE), and Charge Collection Efficiency (CCE). LHE is the ration of the amount of absorbed photons to that of incoming photons and depends on the absorption coefficient of the dye and the density or the thickness of absorbed dye on the nanoporous electrode.

CIE is determined by the potential difference between the conduction band edge of TiO_2 and LUMO of the dye, acceptor density in TiO_2 and spatial distance between the surfaces of TiO_2 and the dye.

The diffusion length of electrons in TiO_2 (L) influences CCE and the thickness of the TiO_2 electrode must be less than L. The length L is defined as:

$$L = (Dt)^{1/2}$$

where D electron diffusion coefficient and τ is electron lifetime in nanoporous TiO_2.

For a Grätzel type cell with nanoporous TiO_2 electrode and Ru complex dyes, 10-30 μm thickness (L) is required to achieve high LHE values (Grätzel, 2004).

In order to enhance the cell efficiency many different dyes have been studied, such as porphyrins (Mao, et al., 1998), phthalocyanines (Diacon, et al., 2010; Nazeeruddin, Humphry-Baker, Gratzel, & Murrer, 1998), coumarins (Rehm, et al., 1996), transition metal complexes (Halme, 2002; Polo, Itokazu, & Murakami Iha, 2004), perylene, cyanines, and azulene (O'Regan, et al., 2008).

The best results were obtained using the dyes with general structure ML_2X_2, where L is 2,2'-bipyridil-4-4' dicarboxylic acid, M-Ru or OS metals and X is a halide, cyanide or thiocyaninde. A comparative study (O'Regan, et al., 2008) regarding the role of different dyes used as sensitizers in DSSC into the value of V_{oc} explains why none of others dyes have surpassed the best ruthenium bipyridyl dyes (e.g., N719). In this case, the LUMO level of the dyes overlaps on the conduction band of TiO_2, which explains the fast electron transfer at the interface dye-TiO_2 and a higher efficiency.

Due to the presence of the liquid electrolyte there are some problems with sealing and long-term stability of the cell.

The liquid electrolyte has been replaced by different solid or gel-like electrolytes and the results reported in the literature include true hole conductors (p-type inorganic semiconductors and p-type semiconductors) or ionic conductors (elastomeric or gel-like electrolytes containing iodine) (Diacon, et al., 2010; Halme, 2002).

Krüger et al. (2001) reported a moderate efficiency of 2.56% using a true hole conductor (spirobifluorene), Cao, Oskam, and Searson (1995) obtained cell efficiencies of 3-5% with a polymer gel electrolyte and Kubo et al. (2001) obtained cell efficiency of gel electrolyte cell up to 5.91%. Diacon, = et al. (2010) have obtained some promising results by replacing the liquid electrolyte with a low T_g polymer containing quaternary ammonium salts in the pending chain and nanocrystalline particles embedded in the polymer matrix.

Figure 4. Scheme of charge generation, transport and interfacial transfer in DSSC

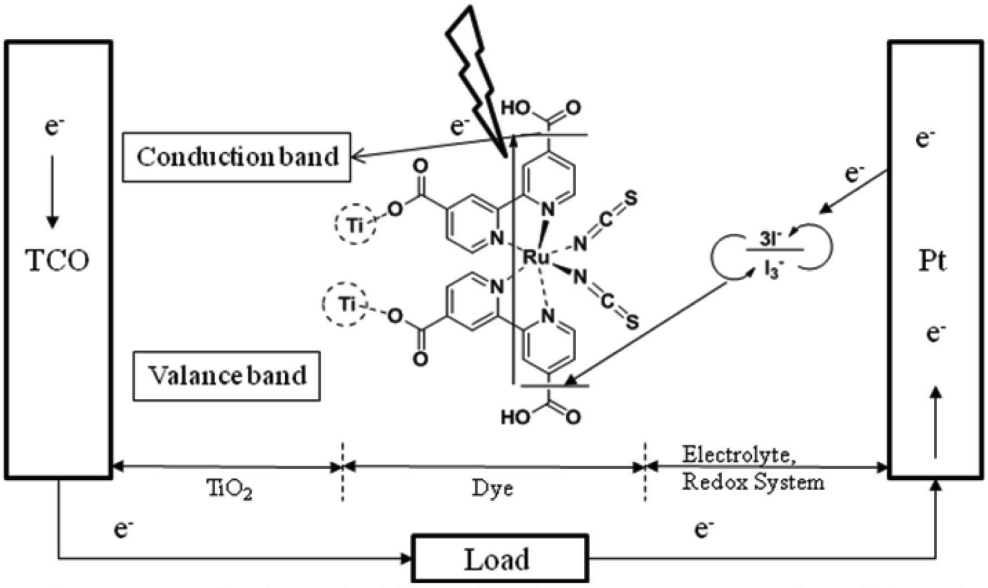

Toshiba Corporation prepared a cell with 7.3% efficiency using a polymer gel electrolyte consisting of imidazolium derivates, iodide and gelators with controllable viscosity (Murai, Mikoshiba, Sumino, & Hayase, 2002).

Other modifications of the initial DSSC composition have been reported (Mori & Yanagida, 2006). In order to avoid the sublimation of I_2 and corrosion effect of the system I^-/I_3^-, alternative redox complexes have been suggested: cobalt complexes, cooper complexes, SeCN etc. Different counter cations have been studied such as Li^+, 1, 2-dimethyl-3-propyl-imidazolium iodide, 4-tert-butyl pyridine etc., when I^-/I_3^- is used.

The energy conversion efficiency was also correlated with some characteristics of the nanoporous TiO_2 electrode: crystalline structure, shape, porosity and diameter of the particles, the cross-sectional area of the necks between nanoparticles, TiO_2 surface treatment by various thin metal oxide layer, etc.

The overall efficiency of a DSSC can be increased by the sensitization of nanoporous TiO_2 using CdS, CdSe and PbS, PbSe nanoparticle quantum dots which enlarge the spectral range of the absorbed light (Prabakar, Seo, Son, & Kim, 2009).

In the classical DSSC with Ru complex and I^-/I_3^- redox system a platinum counter electrode is used, but for mass production, platinum would be replaced with other materials, such as graphite, aluminium or poly(3,4-ethylene-dioxythiophene) (PEDOT). Graphite has not the same performance as platinum whereas PEDOT shows equivalent ability with platinum.

By replacing the liquid electrolyte in Grätzel's cell with a solid charge transport materials (p-type semiconductor or organic semiconductor), a solid-state DSSC is obtained avoiding the leakage of electrolyte. In this type of cell (Günes & Sariciftci, 2008) the dye is regenerated by the electron donation from the hole conductor, after electron injection into the conduction bad of the TiO_2. A constructive scheme of a solid-state DSSC is presented in the Figure 5.

Inorganic p-type semiconductors (CuI, CuBr, CuSCN) or organic p-type semiconductors such as poly (3-alkylthiophene), 2, 2', 7, 7'-tetranix(N,

N'-di-p-methoxipheyl-amine) 9, 9'-spirobifluorene (OMETAD), polypyrrole, triphenyldiamine, p-phenylene vinylene copolymers have been infiltrated in the pores of TiO_2 with suitable organic dyes. After improvements, this type of cell gave a maximum efficiency of 2.6% for organic hole-conducting materials and up to 4% for p-type inorganic materials (Lancelle-Beltran, et al., 2006; Schmidt-Mende & Grätzel, 2006).

The main electric parameters proved for DSSCs are presented in the Table 1.

Solar Cells Based on Nanostructured MeO Infiltrated with Polymers

This type of hybrid cells contains an active layer (heterojunction) which consists of a nanostructured metal oxide, as inorganic component, and a p-type semiconducting polymer as organic matrix.

Transparent semiconducting metal oxides like TiO_2 (Lin, et al., 2007), ZnO (Beek, Wienk, & Janssen, 2006), SnO_2 (Kudo, Shimazaki, Ohkita, Ohoka, & Ito, 2007), have been used as the electron accepting materials in combination with p-type conjugated polymers such as poly (3-alkylthiophene) (P3AT) (Beek, et al., 2006) (alkyl = hexyl, octyl, dodecyl), poly (2-methoxy-5-(2'-ethylhexyloxy)-p-phenylenevinylene (MEH-PPV) (Kudo, et al., 2007), poly (2-methoxy-5-(3',7'-dimethyloxtyloxy)-p-phenylenevinylene) (MDMO-PPV) (Beek, et al., 2006), water-soluble polythiophene polymer (McLeskey & Qiao, 2006), poly (3-(2-methylhexan-2-yl)-oxy-carbonyl-dithiophene) (P3MHOCT), etc. (Krebs, et al., 2008).

The hybrid cell based on polymer nanostructured semiconductor metal oxides can take advantages of both materials: solution processability, high-hole mobility, and photosensitivity of conjugated polymers and high mobility of inorganic semiconductors. Because the diffusion length of excitons generated in polymer is shorter than 15-20 nm, the metal oxide must be mixed with polymer at a nanoscale so that the distance between two inorganic nanoparticles does not exceed 15-20 nm. The metal oxide can be nanostructured as a layer composed by interconnected nanoparticles or as an array of nanorods/nanofibers infiltrated with polymer forming a bulk heterojunction.

A cell with the solar-energy conversion improved up to ≈0.9% has been obtained from P3HT and nanocrystalline zinc oxide (nc-ZnO) after the thermal annealing of the inorganic-organic blends (Beek, et al., 2006).

An efficient bulk heterojunction can be made using ZnO nanoparticles and MDMO-PPV polymer (Beek, Wienk, & Janssen, 2004). The blend ZnO-polymer (67% wt.-nc-ZnO) was processed by spin-casting from solution into thin films with a thickness of ca. 80 nm on a glass substrate coated with ITO and poly(3,4-ethylene-dioxythiophene): poly(styrene sulphonate) (PEDOT:PSS). The device structure is presented in Figure 6.

The maximum energy-conversion efficiency provided by this hybrid photovoltaic system is $\eta \approx 1.6\%$ and the authors explain this value by the relative energy levels (HOMO, LUMO, valence, and conduction bands) in polymer and ZnO.

Figure 5. Constitutive scheme of a solid state DSSC

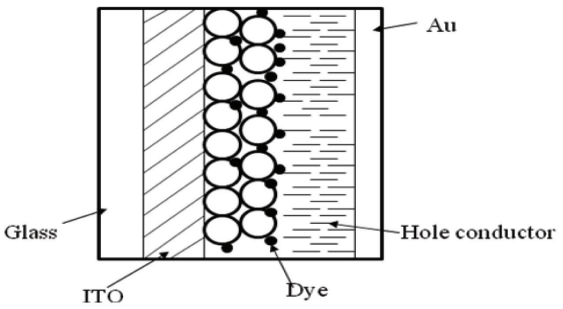

Table 1. The main electric parameters proves for DSSCs

Cell type	Grätzel cell	Solid-state DSSC
Efficiency, %	10-11	≈4
V_{oc}, V	0.7	0.4
J_{sc}, mA/cm^2	20	9.1

Photovoltaic devices based on conjugated polymer, P3HT, deposited into the mesoporous titania films (diameter of the pores≈10 nm) which provides continuous pathways for electrons, have been demonstrated an energy-conversion efficiency of ≈1.5% (Coakley & McGehee, 2003).

Recently, polymer-based solar cells consisting of ZnO vertically aligned nanorods and conducting polymers MEH-PPV (Bi, et al., 2010) have been investigated and the results show a maximum value for power conversion efficiency of 0.34%.

An interesting nanostructured photovoltaic device based on ZnO nanorods/P3HT+TiO_2 nanorods have been obtained by solution processes at low temperature (Lin, et al., 2007). Thicker ZnO nanorods (50 nm diameter, 180 nm length) are grown on the surface of ITO/glass electrode in order to obtain an efficient electron collection. Thinner TiO_2 nanorods (4-5 nm diameter, 20-30 length) are mixed with P3HT to provide increased interfacial area and the mix is the incorporated into nanostructured ZnO. A schematic representation of a photovoltaic device base on the ZnO/P3HT+TiO_2 hybrid material is given in the Figure 7a, and the corresponding energy levels in Figure 7b.

Figure 6. Structure of the photovoltaic device: 80nm thick MDMO-PPV:nc-ZnO blend layer, sandwiched between PEDOT:PSS+ITO and an aluminium electrode

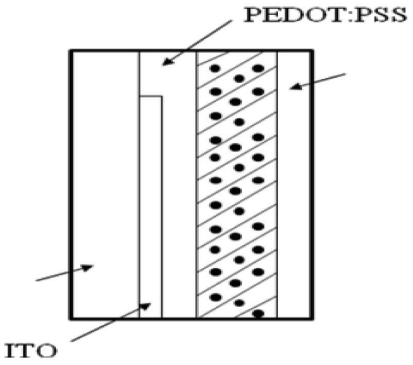

This type of PV device gives for energy conversion efficiency a maximum of 0.59%.

The use of water-soluble and light-harvesting polythiophene, sodium poly (2-(3-thienyl)-ethoxy-4-butylsulfate) (PTEBS) and TiO_2 to fabricate photovoltaic devices was reported by McLeskey (McLeskey & Qiao, 2006). Water as solvent, brings some benefits:

- Controllable solvent evaporation rate
- Non-toxic solvent
- Improved stability for devices under atmospheric conditions

This type of solar cells has been fabricated in two configurations: in a bilayer heterojunction (TiO_2 and polymer PTEBS) and in a bulk heterojunction (TiO_2 nanocrystals blended into the polymer PTEBS). Unfortunately, the maximum value for energy conversion efficiency obtained with this device is 0.15%.

Chemical modification of inorganic semiconductors using organic materials improves the electronic junction at the interface. Kudo et al. (2007) reported that chemical modification of the nanostructured SnO_2 film with fullerene derivate, C_{60}-malonic acid ($C_{60}C(COOH)_2$), activates the electron injection at the interface organic/inorganic. They fabricated a cell with the layer structure: ITO/SnO_2+C_{60}-$C(COOH)_2$/MDMO-PPV/Au and found an improved energy conversion efficiency (≈0.84%) by chemical modification of SnO_2 particles.

Hybrid Solar Cells Based on Inorganic Nanoparticles (Group II-VI, CdS, CdSe, CdTe) and Conjugated Polymers

Hybrid solar cells based on blends of inorganic nanoparticles (CdS, CdSe, CdTe) and conjugated polymers have been extensively studied due to their high intrinsic electron nobilities that exist in inorganic semiconductor, high hole mobility

Figure 7. a) Scheme of the PV device based on ZnO nanorods/P3HT+TiO2 nanorods; b) energy level diagram for the PV device based on ZnO/P3HT+TiO2

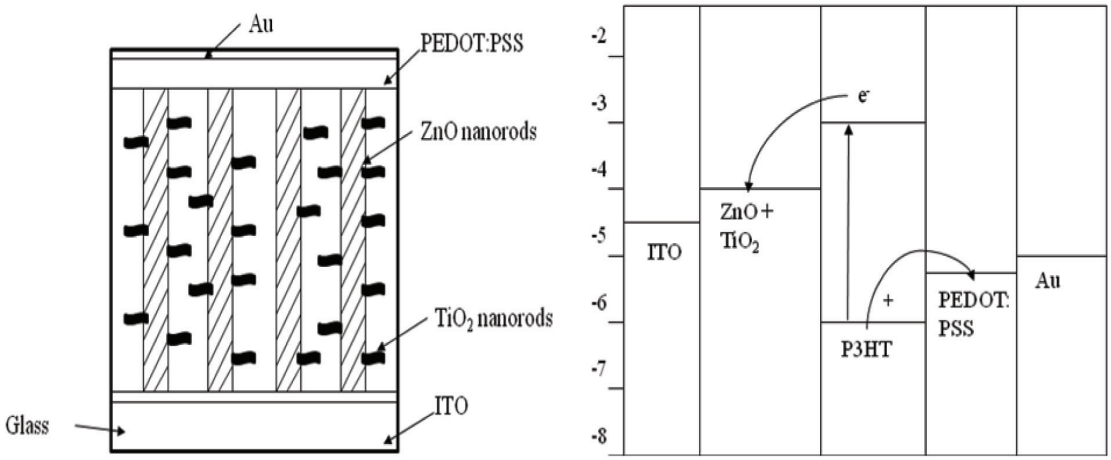

observed in polymers (0.1 $cm^2V^{-1}S^{-1}$), low cost and the use of materials which can be processed from solution (Ginger & Greenham, 1999a; Greenham, Peng, & Alivisatos, 1996; Huynh, et al., 2002; Kang, Park, & Kim, 2005; Wu & Zhang, 2010). The nature of the blend components and the morphology of the nanocomposite photoactive layer strongly dictate the performance of the cell. Polymer domains must be limited in dimension to the exciton diffusion length (typically 5-20 nm), for an efficient charge separation. In addition, both the organic and inorganic phases must form percolation networks to assure an efficient charge circulation.

Ginger and Greenham (1999a) fabricated a cell using a blend of CdSe nanoparticles (diameter ≈ 5 nm) and MEH-PPV (5 weight % polymer) with a layer structure: ITO/CdSe+MEH-PPV/Al and they obtained a power conversion efficiency of 0.25%.

In order to enhance the cell efficiency the spherical CdSe nanocrystal particles have been replaced with elongated ones (nanorods) (Huynh, et al., 2002) and blended in P3HT to create charge transfer junctions with high interfacial area. Different CdSe nanocrystals with aspect ratios ranging from 1 to 10 (diameter/length): spherical particles with diameter of 7 nm and nanorods 7 nm/30 nm, 7 nm/ 60 nm, have been obtained and dispersed in P3HT. By varying the radius of the nanorods, the quantum size effect can be used to control the band gap and enhance the absorption of the light. At the same time, the length of the nanorods can be adjusted to the device thickness required for optimal photovoltaic activity.

Solar cells were fabricated by spin-casting a solution of 90 weight % CdSe nanoparticles (7x7 nm and 7x60 nm) in P3HT onto an ITO glass substrate coated with poly(3,4-ethylenedioxythiophene) doped with polystyrene sulfonic acid (PEDOT:PSS) and aluminium as counter electrode. For this type of cell, the external quantum efficiency (ICPE) increases directly proportional with the length of the nanoparticles from ca. 20% for 7x7 nm up to ca. 55% for 7x60 nm particles (Arici, Saricitci, & Meissener, 2004; Huynh, et al., 2002).

A photovoltaic device with the structure device with the structure: Glass/ITO/PEDOT:PSS/P3HT+CdSe (nanorods 7x60 nm)/Al under Air Mass (AM) 1.g Global solar conditions has a power

conversion efficiency of 1.7%. (Kang, et al., 2005) assume that this performance may be improved if the nanorods are aligned vertically between the two electrods to minimize the carrier transport paths. A PV device based on CdTe (not CdSe) an aligned nanorods/poly (3-octylthiophene) with Ti and Au electrodes, has been fabricated and tested. The obtained value (≈1.06%) for power conversion efficiency is not improved but this fact can be explained by the use of CdTe instead of CdSe nanocrystals. While both CdSe and CdTe semiconductors are considered good photovoltaic materials, CdSe is significantly better than CdTe in hybrid nanocrystal/polymer solar cells (Sun, Snaith, Dhoot, Westenhoff, & Greenham, 2005).

A real improvement in current density and power conversion efficiency has been observed in CdSe nanorods/P3HT hybrid solar cells after chemical reaction with 1, 3-dithiol benzene. The change in the morphology of the blended film is responsible for the performance enhancement (Wu & Zhang, 2010).

Gur, Fromer, Chen, Kanaras, and Alivisatos (2006) proposed the use of hyperbranched CdSe or CdTe nanocrystals integrated into a matrix of P3HT to fabricate an active film for hybrid solar cells. The hyperbranched structure of CdSe nanocrystals affords some advantages for a solar cell:

- Good and controlled dispersion of the inorganic phase in the polymer matrix
- Large surface are for charge separation
- Each hyperbranched particle contains a percolation pathway for transport of electrons through the thickness of the active film

Cells based on hyperbranched particles (150 nm x150 nm x150 nm) of CdSe and P3HT exhibit and immediate rise of V_{oc} to its full value of 0.6 V and an immediate, near linear rise in both I_{sc} and power conversion efficiency with increasing of CdSe concentration in comparison with other types of nanocrystals.

An optimum value of 2.2% power conversion efficiency using this type of solar cell, under AM 1.5 G solar conditions, has been reported (Gur, et al., 2006).

Hybrid Solar Cells Based on Inorganic Semiconductors (Group IV, III-V) and Organics

Inorganic Semiconductors (Flat Surfaces) Polymer Solar Cells

Sailor et al. (1990) fabricated a hybrid solar cell form poly/ $(CH_3)_3$Si-cyclooctatetraene deposited on crystalline silicon (c-Si) surface and reported a power conversion efficiency between 1% and 5%.

The layered polymeric materials have been obtained either by spin-coating of preformed polymers, or by polymerization of the monomers on the silicon surface. After the doping of the polymer with iodine vapors, the film became transparent to solar light so, in this case, the polymer is not involved in excitons generation.

Gowrishankar, Scully, McGehee, Wang, and Branz (2006) studied hybrid solar cells based on hydrogenated amorphous silicon (a-Si) and conjugated polymers such as P3HT and MEHPPV. In comparison with crystalline silicon, amorphous silicon is inexpensive and can be deposited as a thin film over flexible substrates. Based on experimental data, the authors proposed a mechanism for exciton production in the polymer, its dissociation at the interface polymer-silicon, electron injection to inorganic semiconductor and hole injection in the polymer. Unfortunately, this type of hybrid photovoltaics has a very low conversion efficiency, e.g, 0.16% for a-Si/P3HT and 0.01% for a-Si/MEH-PPV devices.

After replacement of a-Si with c-Si in a thin film hybrid solar cell P3HT/silicon, the power conversion efficiency enhanced up to 2.46%. This phenomenon is explained by faster electron mobility, higher absorption spectral range and lower charge recombination in the crystalline

phase as compared with amorphous phase of silicon (Nolasco, Estrada, Matsumoto, Marsal, & Pallares, 2007).

A very efficient hybrid organic-inorganic photovoltaic device has been described by Garnier: n-type GaAs associated with organic p-type device polythiophene derivate (Garnier, 2002). A film of poly(3-methylthiophene) (25 nm thickness) has been electrochemically deposited onto a monocrystalline n-GaAs and then a thin film of Au completed the cell. The power conversion efficiency measured with this device was of 17.5% and compared to those of classical Schottky cell, n-GaAs/metal (14%). It is considered that the enhancement of the conversion efficiency is due to the large increase of the open-circuit voltage.

Hybrid solar cells based on GaAs/ thiophene oligomers (octithiophene) have been studied and revealed the importance of the crystallinity of the organic phase (Ackermann, Videlot, El Kassmi, Guglielmetti, & Fages, 2005). The thiophene polymer was replaced by thermally evaporated rod-like octitiophene (8T) because these rigid oligomers have demonstrated high charge-carrier mobility in thin films, between 10^{-2} and $10^{1}cm^{2}V^{-1}s^{-1}$, values comparable to those of amorphous silicon.

The hybrid cell used has the following structure: GaAs/8T/Au, with the organic film thickness of 20-120 nm having nano-or microscrystalline morphology. In order to reduce the contact resistance at the Au/8T interface and obtain higher energy conversion efficiency, the gold layer was doped with iodine.

Experimental tests demonstrated that microcrystalline 8T films (grain size 1-2 μm) exhibited higher energy conversion efficiency than nanocrystalline 8T films (grain size 0.1 μm). This difference is explained by the existence of a high trap density in nanocrystalline films, mostly at the grain border and by using a semitransparent gold layer (doped with iodine) as the front contact deposited onto the 8T films, energy conversion efficiency up to 4.2 has been obtained.

Inorganic Semiconductors (Flat Surfaces): Small Molecules Solar Cells

A lot of heterojunctions are based on small organic molecules and inorganic semiconductor such as Si and GaAs. The small molecules selected for this purpose have some advantages over polymers:

- Higher degree of crystallinity
- Better environmental stability
- The charge carrier mobility is comparable or exceed the mobility in thiophene based polymers
- High absorption coefficient in the solar spectrum

Among these organic materials are the porphyrins (P) or metal free (H_2Pc) and metal (Zn, Cu, Pb, Fe, Mg) substituted phthalocyanines (MePc) which are considered p-type materials. Pc and P compounds have low solubility in organic solvents and water; this is the reason that film deposition requires vacuum sublimation, an expensive and complex process.

Hybrid solar cells with the structure Au/p-ZnPc/p-Si (El-Nahass, Zeyada, Aziz, & El-Ghamaz, 2005), Ag/p-CuPc/n-GaAs/Ag (Karimov, Ahmed, Moiz, & Fedorov, 2005), p-MgPc/n-Si (Riad, 2000), NiPc/p-Si (El-Nahass, Abd-El-Rahman, Farag, & Darwish, 2005), n-Si/tetraphenyl P (El-Nahass, Zeyada, Aziz, & Makhlouf, 2005), etc. were reported in literature and photovoltaic properties were evaluated. For example, the power conversion efficiency has values for this type of cells in the range of 1-3.5%.

Cooper Phthalocyanine (CuPc) is one of the well-studied organic semiconductor with small molecule because its purification is simple and economical by recrystallization from organic solution at normal temperature. The CuPc films can be deposited on inorganic surfaces by vacuum sublimation and this material has a high absorption coefficient in a wide spectrum of the light.

Karimov et al. (2005) fabricated an organic/inorganic cell with the structure Ag/p-Cu/n-GaAs/Ag and studied its photoelectric properties in the temperature range 23-74°C, using a laser beam illumination.

A thin organic film of CuPc (p-type semiconductor) was deposited by vacuum evaporation on n-type GaAs single-crystal substrate. This device showed that V_{OC} and power conversion efficiency decrease with temperature whereas I_{SC} is constant for the temperature range studied.

NiPc is a potential candidate for photovoltaic devices, because for thin films from this material has been reported a relatively high charge mobility ($\approx 10^{-5}$ $m^2V^{-1}s^{-1}$), when compared with the mobility reported for other phthalocyanine compounds ($7.6x10^{-9}$ $m^2V^{-1}s^{-1}$ for ZnPc, $3x10^{-7}$ $m^2V^{-1}s^{-1}$ for CoPc, 10^{-7} $7.6x10^{-3}$ $m^2V^{-1}s^{-1}$ for CuPc) (El-Nahass, et al., 2005).

A photovoltaic device Au/NiPc/Si/Al was fabricated by deposition of NiPc thin film using thermal evaporation technique onto p-Si single crystal, and tested. The junction exhibits the following photovoltaic characteristics at room temperature and under illumination of 6 $mVcm^{-2}$ white light: V_{OC} of 0.32 V, I_{SC} of 186 μA and power conversion efficiency of 1.11%.

The photovoltaic properties of a Au/Tetraphenylporphyrin (TPP)/n-type silicon (n-Si)/Al heterojunction solar cell have been evaluated and reported by El-Nahass, Zeyada, Aziz, & Makhlouf (2005).

A film of TPP with 67 nm thickness was deposited onto single cystal of n-type silicon wafer. Pure gold and aluminium film were deposited on the faces of TPP/n-Si layer.

From experimental data using the photovoltaic device Au/TPP/n-Si/Al the following cell parameters were deduced: I_{SC}=0.442 mA, V_{OC}=0.478 V and power conversion efficiency 2.45%.

Inorganic Nanostructured Semiconductors-Organics

Hybrid solar cells based on conjugated polymers and inorganic nanostructured semiconductors bring some advantages in comparison with flat heterojunctions. Firstly, the blend with nanostructured morphology has an increased interfacial area and reduced average distance between organic/inorganic components. As the excitons dissociation occurs at the interface, this morphology will enhance the dissociation and, consequently, the intensity of the photocurrent. Additionally, a reduced distance between the blend phases in the range of exciton diffusion length is an important parameter in diminution of the charges recombination.

Secondly, nanostructured inorganic semiconductors (nanoparticles, nanopillars, nanorods, nanowires, hyperbranched nanoparticles) have favorable optoelectronic properties due to the quantum confinement phenomenon. Therefore, they have a tunable band gap, an enhancement of the light absorption and an optimal compatibility between the heterojunction phases.

These nanostructured inorganic semiconductors can be easily fabricated by various techniques such as Chemical Vapor Deposition (CVD), laser ablation; Molecular Beam Epitaxy (MBE), dry wet etching and conjugated polymers are solution processable so that these materials have great potential for inexpensive large-scale solar cell manufacturing.

Silicon, as inorganic semiconductor, is an important candidate for polymer-nanocrystal cells given its abundance, nontoxicity, and strong UV absorption. Liu, Holman, & Kortshagen (2008) fabricated a hybrid solar cell based on blend of silicon nanocrystals (Si-nc) and P3HT polymer where silicon nanocrystals act as electron conducting phase. Three groups of silicon nanocrystals

were synthesized by dissociation of silane: 3-5 nm in diameter, 5-9 nm in diameter and 10-20 nm in diameter. Solar cells were fabricated by spin coating, and Si-nc/P3HT onto Indium Tin Oxide (ITO) coated glass substrate. Finally, 2 mm wide aluminium electrodes (100 nm thick) were evaporated on top of Si-nc/P3HT film.

The photovoltaic properties of this cell were studied as a function of Si-nc size and Si-nc/P3HT ratio. Experimental data showed that the open circuit voltage (V_{OC}) is inversely related to Si-nc size and does not depend on the materials ratio. Short-circuit current I_{SC} also increases with decreasing Si-nc size.

An optimization of Si-ncs size and Si-nc/P3HT ration showed that small Si-ncs size and roughly 35 wt. % Si-nc produced the best solar cells with power conversion efficiency of 1.15%.

Recently, Kno and Gau (2009) fabricated a solar cell based on Silicon Nanowires (SiNWs) arrays covered with P3HT polymer mixed with [6,6] –Phenyl-C_{60}-Butiric acid Methyl ester (PCBM). Silicon nanowires were grown vertically on an indium tin oxide glass substrate by tha vapor-liquid-solid process. The blend polymers/inorganic nanorods or nanowires have the advantages of very large donor-acceptor interface area, continuous and minimized carrier-conducting pathways that explain the increase of the power conversion efficiency of the cell. The authors above mentioned have demonstrated that the cell with structure ITO/SiNW/P3HT+PCBM/Au has better photovoltaic properties (I_{SC}=5.25 mA/cm^2, V_{OC}=0.259 V, power conversion efficiency =0.427%) than the cell without SiNWs (I_{SC}=4.41 mA/cm^2, V_{OC}=0.20 V, power conversion efficiency=0.299%).

Silicon can be replaced with germanium for building of the hybrid inorganic/organic devices. So, Germanium Nanowires (GeNWs) were grown on SiO_2 substrate by the vapor-liquid-solid method catalyzed using 20 nm Au seeds (Pasquier, Mastrogiovanni, Klein, Wang, & Garfunkel, 2007), dispersed in a P3HT solution and spin cast into films. The authors of this study concluded that the GeNWs may act as a very good electron acceptor for hybrid organic/inorganic photovoltaic devices.

Photovoltaic devices which combine inorganic nanostructured semiconductors, such as GaAs, and organic polymers could improve their energy conversion efficiency. Bi and LaPierre (2009) studied hybrid solar cells based on P3HT polymer deposited onto vertically aligned n-type GaAs arrays. The energy levels HOMO and LUMO are -4.76 eV and -2.74eV, respectively, whereas the values for GaAs HOMO= -5.49 eV and LUMO= -4.07 eV. Therefore, GaAs nanowires are suitable as the electron acceptor, and P3HT as the electron donor, in a PV device according to these energy levels.

GaAs nanowires with a maximum length of about 4 μm and average diameter of about 70 nm were obtained by molecular beam epitaxy method, and P3HT polymer was deposited onto nanowire arrays by spin-coating from solution.

The fabrication process for this type of PV device is relatively complicated, and GaAs is an expensive material so that the hybrid cells with an energy conversion efficiency of 1.04% fabricated in the work, are not very economically attractive.

Hybrid Solar Cells Based on Carbon Nanotubes (CNTs)

Since their discovery in 1991, carbon nanotubes have attracted a high interest due to their outstanding mechanical, mechanical and electrical properties (Bokobza, 2007; Coleman, Khan, Blau, & Gun'ko, 2006; Kaneto, Tsuruta, Sakai, Cho, & Ando, 1999). Depending on how the carbon sheet is rolled into a nanotube, the resulting nanotube may have a gap in the electron spectrum. The gap in the nanotube spectrum is determined by its radius, which offers a direct root towards engineering semiconductors with a prescribed band gap, for use in electronic and optoelectronic devices (Odom, Huang, Kim, & Lieber, 1998).

The primary application of CNTs in organic solar cells has been as nanoscale fillers in polymer films (Kymakis & Amaratunga, 2002; Landi, Raffaelle, Castro, & Bailey, 2005). The nanotubes were chosen due to their acceptor properties and also to their large surface area, both elements considered to be favorable for higher exciton dissociation and increased charge carrier transport. However, these configurations remain to have low power conversion efficiency (<1%). CNTs were also employed in solar cell design to serve as a replacement for the transparent conductive oxide layer (TCO, e.g. ITO) (Barnes, et al., 2007; Contreras, et al., 2007; van de Lagemaat, et al., 2006).

Recently MWCNTs, have been used in hybrid solar cells based on a heterojunction with and n-type Si (Jia, et al., 2008; Wei, et al., 2007), MWCNTs having the role of light-harvesting, charge-separation and charge transport. Lin et al. fabricated a hybrid solar cell using a nanocomposite obtained by coating of the MWCNT with Si nanoparticles (Si-NP), this combination responds more sensitively than those from P3HT/Si-NP or P3HT/CNT (Lin, et al., 2010).

SWCNTs-CdS nanocomposites light-harvesting assemblies were also obtained by Robel, Bunker, and Kamat (2005), they obtained both suspensions and films. The Incident Photon-to-Charge Carrier Efficiency (IPCE) was low (<1%) indicating problems associated with charge collection and charge transport in these films.

Functionalized carbon nanotubes (f-CNT) were used to attach ZnO nanoparticles and used in a photochemical solar cell by Vietmeyer et al. (Vietmeyer, Seger, & Kamat, 2007). Although they did not obtain a significant improvement to the ICPE value, the photocurrent response proves the charge transfer interaction between the excited ZnO and f-CNT.

An interesting variety of CNT with superior properties are the Stacked Cup Carbon Nanotubes (SSCNTs), consisting of truncated conical graphene layer providing a hallow tubular morphology. This type of carbon nanotubes poses a superior charge separation efficiency compared to SWCNT and MWCNT. Hasobe, Fukuzumi, and Kamat (2006) have studied the optical properties and fabricated a high photoconversion efficiency solar cell using this type of carbon nanotubes. The SSCNT have been used in combination with SnO_2 and TiO_2. In the case of TiO_2 the photocurrent response was negligibly small, due to the discrepancy in the band energy of the two components. Iodine redox electrolyte was used in the photoelectrochemical solar cell.

Another approach in hybrid solar cell involving CNTs was to use the CNTs in order to improve the efficiency of DSSCs. The CNTs are meant to improve the charge collection and transport of charge carriers. The first step in building a DSSC incorporating SWCNTs is to obtain a CNT scaffold that will allow the dispersion of the TiO_2 nanoparticles, this has been studied by Kongkanand, Martínez Domínguez, and Kamat (2007). Brown, Takechi, and Kamat (2008) further examined this approach fabricating a DSSC and studying the transfer phenomenon. They observed that the SWCNT do not influence significantly the charge injection from the Ru complex to the TiO_2 layer but they play an important part in improving the charge separation by slowing the recombination rate of the back electron transfer between the oxidized Ru complex and the injected electrons. However, this improvement in terms of current generation comes with a cost, the photovoltage being lower due to the fact that the modification of the apparent Fermi level of the TiO_2 and SWCNT composite.

All this approaches in solar cells based on carbon nanotubes show their versatility and positive effects in terms of charge collection and charge carrier transport. This type of cell being able to became the next generation in solar cells.

TECHNOLOGIES FOR HYBRID SOLAR CELLS FABRICATION

The hybrid solar cell "generation" uses a blend of cheaper organic and inorganic materials but the technology used for their fabrication is a very important factor in total manufacturing costs.

In this chapter, we shall describe the technologies for fabrication of the most expensive components of these devices.

Transparent Thin Films

Many photovoltaic devices use transparent thin films as conductors of electrical charge (electrodes). Among these materials are included fluorine-doped tin oxide (SnO_2:F; or FTO), doped zinc oxide (e.g. ZnO:Al), Indium Tin Oxide (ITO), and Fluorine-Indium Tin Oxide (F-ITO). They require very special deposition conditions at high temperature and expensive equipment for high vacuum.

Experimental procedure for preparing of F-ITO (Takeuchi, et al., 2008) consists in the heating the mixture of In_2O_3 (99.99% purity) and SnO_2 (99.99% purity) powders at 1400°C for 2 h. The obtained ITO powder is mixed with HF solution and heated at 80°C and then at 300°C for 2h. The resulting light-green powder was sintered by Spark Plasma Sintering (SPS) process at 1000-1250°C and DC electric current of 1000-6000 A, using a special equipment. Using the F-ITO disks (obtained by SPS process) as sputtering target, thin films were deposited on the glass substrates.

ITO powder without fluorine content was also sintered by the same method SPS, and the films were deposited in the same procedure.

Oxide Films

Nanoporous TiO_2 films, as electrodes for hybrid solar cells, are typically prepared from colloidal suspension containing TiO_2 nanoparticles. The suspension is applied on a substrate (e.g. a Transparent Conductive Oxide, TCO) with doctor blade or spin-coating techniques, and then the resulting film is sintered between 450°C and 550°C. There are many commercially available TiO_2 nanoparticles with different characteristics. TiO_2 nanoparticles with anatase crystalline structure and diameter around 20 nm give the best results in solar cell fabrication (Mori & Yanagida, 2006). Synthesis of TiO_2 nanoparticles can be achieved from titanium (IV) isopropoxide and nitric acid solution under vigorous stirring (Barbé, et al., 1997). The white precipitate is heated to 80°C for destruction of the agglomerates, filtered and heated for 12 h in the temperature range of 200-250°C to obtain particles with diameter of 10-25 nm.

TiO_2 nanoporous films can also be obtained via sol-gel process or by electrodeposition starting from porous Al_2O_3 films (Hoyer & Masuda, 1996).

Nanostructured SnO_2 films were prepared from SnO_2 colloidal suspension containing 4 wt.% polyethylene glycol coated on a substrate. The SnO_2-coated substrates were annealed at 400°C for 1h in an electric furnance to obtain SnO_2 films (Kudo, et al., 2007).

Nanostructured Film from Other Inorganic Materials

Classical photovoltaic materials like CdTe (Mastai & Hodes, 1997), CdS (Behar, Rubinstein, Hodes, Cohen, & Cohen, 1999), $CuInS_2$, $CuInSe_2$ and other semiconductors derived from group 6A of the periodic table (Rajeshwar & de Tacconi, 1997), have also been nanoscale structured onto different substrates using electrochemical deposition method.

This method offers several advantages, such as: it involves relatively simple and inexpensive equipment, films can be fabricated on large scale and irregular surfaces; the deposition occurs closer to equilibrium and the process can be precisely controlled.

Films from Organic/Inorganic Blends

Hybrid solar cells contain a photovoltaic active layer based on the blend of inorganic semiconductors and an organic material, such as polymers or small molecules. Inorganic material is nanostructured (nanoparticles, nanocrystals, nanorods, nanowires, hyperbranched nanocrystals) to increase the solar cell performance.

The active hybrid layer is deposited either from the mixture (solution, suspension) of inorganic and organic phases, by spin-coating/casting, or by coating of the inorganic phase with the organic component.

Huynh et al. (2002) fabricated an efficient inorganic/organic hybrid solar cell by spin-casting a solution/dispersion of P3HT polymer and CdSe nanorods in a mixture of pyridine and chloroform onto an indium tin oxide glass substrate.

Hybrid solar cells based on blends of silicon nanocrystals (Si-ncs) and polymer were obtained by spin-coating a mixture Si-ncs/P3HT from a common solvent (Liu, et al., 2008).

A bulk heterojunction based on a mixture of TiO_2 nanoparticles and a watersoluble polymer, poly [2-(3-thienyl)-ethoxy-4-butylsulfonate], was obtained by drop casting a composite solution TiO_2/polymer on a FTO substrate (McLeskey & Qiao, 2006).

Nanocrystalline-ZnO particles were blended with a conjugated polymer MDMO-PPV without the use of surfactant in a common solvent (chlorobenzene-methanol) and the spin-casting method was used to prepare thin bulk heterojunction films (Beek, et al., 2004).

Frequently, the hybrid active film organic/inorganic is obtained by casting a prefabricated nanostructured inorganic film with a polymer solution.

ZnO nanorod arrays were grown on Au-coated ITO substrate using a pulsed current electrolysis method and then the space between the nanorods was infiltrated with a P3HT solution in chloroform (Lin, et al., 2007).

Hybrid active films were fabricated by spin-coating P3HT as a solution in chlorobenzene, onto vertically aligned n-type GaAs nanowires synthesized by molecular beam epitaxy method (Bi & LaPierre, 2009).

Vertically aligned CdTe nanorods were obtained by electrodeposition on aluminium oxide substrate and the active layer was formed by drop casting or spin-coating of a poly(3-octylthiophene) solution in chloroform on the nanostructured CdTe substrate (Kang, et al., 2005).

(Novotny, Yu, & Yu (2008) reported the synthesis of InP nanowires from trimethylindium and phosphine on the ITO-coated glass substrate. A P3HT solution in 1, 2, 4 trichlorobenzene was drop cast onto the nanowires-ITO-glass layer and the solvent was evaporated by heating at 120°C under high vacuum (10^{-6} torr) to obtain a hybrid active film.

Silicon nanocrystals were synthesized in a non-thermal radio frequency plasma via dissociation of silane, mixed with a P3HT polymer solution and deposited onto ITO coated glass substrate by spin-coating method (Liu, et al., 2008).

Organic (Small Molecules) and Metallic Films

Metal phthalocyanines or other organic dyes used in hybrid solar cells are deposited onto different substrates by thermal sublimation. For example, copper phthalocyanine, one of the well-studied organic photosensitive semiconductors was thermally sublimated on GaAs substrate at 400-450°C and 10^{-4} Pa (Karimov, et al., 2005). The same method of thermal evaporation was used for coating silicon wafers with nickel phthalocyanine (El-Nahass, et al., 2005) or tetraphenylporphyrin thin films (El-Nahass, Zeyada, Aziz, & Makhlouf, 2005).

Other small organic molecules, such as octithiophene (8T) were deposited on monocrystalline n-GaAs wafers under high vacuum ($1\text{-}3\text{x}10^{-6}$ mbar) and 100-140°C (Ackermann, et al., 2005).

Metallic films (Au, Al, Ti) are deposited onto different substrates by thermal evaporation under high vacuum or by sputtering method (Novotny, et al., 2008).

CONCLUSION

Hybrid solar cell combine the advantages of inorganic semiconductors (high electron mobility, long-term stability) with the advantages of organic phase such as light weight, flexibility, low cost, large diversity, and solution processing.

However, this type of cells suffers from low efficiencies as compared to inorganic devices. Their efficiency is limited by the low dissociation probability of excitons at the interface and relatively inefficient charge carrier transport.

It is possible to improve the performance of the hybrid solar cells by acting in the following directions:

- Adding inorganic semiconductors with very high carrier mobility and high electron affinity such as silicon crystals or CdSe, GaAs crystals, nanocrystalline oxides, etc;
- Changing bilayer (planar) heterojunction with bulk (dispersed) heterojunction;
- Using nanostructured inorganic semiconductors, such as nanoparticles, nanorods, nanocrystals, nanopillars, nanowires, hyperbranched nanocrystals, etc;
- Varying the size of the nanoparticles the band gap can be tuned and consequently, the absorption range can be tailored;
- Mixing organic and inorganic phases on a nanometer scale (5-20 nm) comparable with exciton diffusion length;
- Both the organic and inorganic phases must form high-quality percolation network spanning the thickness of the active layer film for an efficient charge transport;
- Enhancing light absorption in the red/NIR part of the spectrum by chemical modification of the organic phase;
- Incorporating electroactive surfactant, which controls physical and electronic interactions between inorganic and organic phases.

Besides the efficiency, an important characteristic of a solar cell is represented by its lifetime, which can make the difference between solar cells with similar outputs. Solar cells presenting even a low efficiency but presenting a high lifetime and low manufacturing cost can represent the solution for solar cells to be implemented at large scale with affordable investment costs. Hybrid solar cells present the possibility for the development of this type of technologies.

In Chapter 8 is analyzed modeling and simulation of hybrid solar cells (DSSC and nanotubes) based on J-V characteristics curves. In this way, new information of improved design and manufacturing of solar cells from this category is obtained.

The recent progress in advanced inorganic nanostructured materials in combination with the new polymers or small organic molecules opens opportunities to overcome the 8% barrier of power conversion efficiency for hybrid solar cells in the near future.

REFERENCES

Ackermann, J., Videlot, C., El Kassmi, A., Guglielmetti, R., & Fages, F. (2005). Highly efficient hybrid solar cells based on an octithiophene–GaAs heterojunction. *Advanced Functional Materials*, *15*(5), 810–817. doi:10.1002/adfm.200305142

Arici, E., & Saricitci, N. S., & Meissener, D. (2004). Hybrid solar cells. *Encyclopedia of Nanoscience and Nanotechnology, 3*, 929-944.

Barbé, C. J., Arendse, F., Comte, P., Jirousek, M., Lenzmann, F., & Shklover, V. (1997). Nanocrystalline titanium oxide electrodes for photovoltaic applications. *Journal of the American Ceramic Society*, *80*(12), 3157–3171. doi:10.1111/j.1151-2916.1997.tb03245.x

Barnes, T. M., Wu, X., Zhou, J., Duda, A., van de Lagemaat, J., & Coutts, T. J. (2007). Single-wall carbon nanotube networks as a transparent back contact in CdTe solar cells. *Applied Physics Letters*, *90*(24), 243503–243503. doi:10.1063/1.2748078

Beek, W. J. E., Wienk, M. M., & Janssen, R. A. J. (2004). Efficient hybrid solar cells from zinc oxide nanoparticles and a conjugated polymer. *Advanced Materials (Deerfield Beach, Fla.)*, *16*(12), 1009–1013. doi:10.1002/adma.200306659

Beek, W. J. E., Wienk, M. M., & Janssen, R. A. J. (2006). Hybrid solar cells from regioregular polythiophene and ZnO nanoparticles. *Advanced Functional Materials*, *16*(8), 1112–1116. doi:10.1002/adfm.200500573

Behar, D., Rubinstein, I., Hodes, G., Cohen, S., & Cohen, H. (1999). Electrodeposition of CdS quantum dots and their optoelectronic characterization by photoelectrochemical and scanning probe spectroscopies. *Superlattices and Microstructures*, *25*(4), 601–613. doi:10.1006/spmi.1999.0696

Bi, D., Wu, F., Yue, W., Guo, Y., Shen, W., & Peng, R. (2010). Device performance correlated with structural properties of vertically aligned nanorod arrays in polymer/ZnO solar cells. *The Journal of Physical Chemistry C*, *114*(32), 13846–13852.

Bi, H., & LaPierre, R. R. (2009). A GaAs nanowire/P3HT hybrid photovoltaic device. *Nanotechnology*, *20*(46), 465205. doi:10.1088/0957-4484/20/46/465205

Bokobza, L. (2007). Multiwall carbon nanotube elastomeric composites: A review. *Polymer*, *48*(17), 4907–4920. doi:10.1016/j.polymer.2007.06.046

Brown, P., Takechi, K., & Kamat, P. V. (2008). Single-walled carbon nanotube scaffolds for dye-sensitized solar cells. *The Journal of Physical Chemistry C*, *112*(12), 4776–4782. doi:10.1021/jp7107472

Cao, F., Oskam, G., & Searson, P. C. (1995). A solid state, dye sensitized photoelectrochemical cell. *Journal of Physical Chemistry*, *99*(47), 17071–17073. doi:10.1021/j100047a003

Coakley, K. M., & McGehee, M. D. (2003). Photovoltaic cells made from conjugated polymers infiltrated into mesoporous titania. *Applied Physics Letters*, *83*(16), 3380–3382. doi:10.1063/1.1616197

Coleman, J. N., Khan, U., Blau, W. J., & Gun'ko, Y. K. (2006). Small but strong: A review of the mechanical properties of carbon nanotube-polymer composites. *Carbon*, *44*(9), 1624–1652. doi:10.1016/j.carbon.2006.02.038

Contreras, M. A., Barnes, T., van de Lagemaat, J., Rumbles, G., Coutts, T. J., & Weeks, C. (2007). Replacement of transparent conductive oxides by single-wall carbon nanotubes in Cu(In,Ga) Se2-based solar cells. *The Journal of Physical Chemistry C*, *111*(38), 14045–14048. doi:10.1021/jp075507b

Diacon, A., Fara, L., Cincu, C., Mitroi, M. R., Zaharia, C., & Rusen, E. (2010). New materials for hybrid dye-sensitized solar cells. *Optical Materials*, *32*(12), 1583–1586. doi:10.1016/j.optmat.2010.06.003

El-Nahass, M. M., Abd-El-Rahman, K. F., Farag, A. A. M., & Darwish, A. A. A. (2005). Photovoltaic properties of NiPc/p-Si (organic/inorganic) heterojunctions. *Organic Electronics*, *6*(3), 129–136. doi:10.1016/j.orgel.2005.03.007

El-Nahass, M. M., Zeyada, H. M., Aziz, M. S., & El-Ghamaz, N. A. (2005). Carrier transport mechanisms and photovoltaic properties of Au/p-ZnPc/p-Si solar cell. *Solid-State Electronics*, *49*(8), 1314–1319. doi:10.1016/j.sse.2005.06.001

El-Nahass, M. M., Zeyada, H. M., Aziz, M. S., & Makhlouf, M. M. (2005). Current transport mechanisms and photovoltaic properties of tetraphenylporphyrin/n-type silicon heterojunction solar cell. *Thin Solid Films*, *492*(1-2), 290–297. doi:10.1016/j.tsf.2005.06.050

Garnier, F. (2002). Hybrid organic-on-inorganic photovoltaic devices. *Journal of Optics. A, Pure and Applied Optics*, *4*(6), S247. doi:10.1088/1464-4258/4/6/361

Ginger, D. S., & Greenham, N. C. (1999a). Charge separation in conjugated-polymer/nanocrystal blends. *Synthetic Metals*, *101*(1-3), 425–428. doi:10.1016/S0379-6779(98)00330-0

Ginger, D. S., & Greenham, N. C. (1999b). Photoinduced electron transfer from conjugated polymers to CdSe nanocrystals. *Physical Review B: Condensed Matter and Materials Physics*, *59*(16), 10622. doi:10.1103/PhysRevB.59.10622

Gledhill, S. E., Scott, B., & Gregg, B. A. (2005). Organic and nano-structured composite photovoltaics: An overview. *Journal of Materials Research*, *20*(12), 3167–3179. doi:10.1557/jmr.2005.0407

Gowrishankar, V., Scully, S. R., McGehee, M. D., Wang, Q., & Branz, H. M. (2006). Exciton splitting and carrier transport across the amorphous-silicon/polymer solar cell interface. *Applied Physics Letters*, *89*(25), 252102–252103. doi:10.1063/1.2408641

Grätzel, M. (2003). Dye-sensitized solar cells. *Journal of Photochemistry and Photobiology C, Photochemistry Reviews*, *4*(2), 145–153. doi:10.1016/S1389-5567(03)00026-1

Grätzel, M. (2004). Conversion of sunlight to electric power by nanocrystalline dye-sensitized solar cells. *Journal of Photochemistry and Photobiology A Chemistry*, *164*(1-3), 3–14. doi:10.1016/j.jphotochem.2004.02.023

Grätzel, M. (2005). Solar Energy Conversion by Dye-Sensitized Photovoltaic Cells. *Inorganic Chemistry*, *44*(20), 6841–6851. doi:10.1021/ic0508371

Greenham, N. C., Peng, X., & Alivisatos, A. P. (1996). Charge separation and transport in conjugated-polymer/semiconductor-nanocrystal composites studied by photoluminescence quenching and photoconductivity. *Physical Review B: Condensed Matter and Materials Physics*, *54*(24), 17628–17637. doi:10.1103/PhysRevB.54.17628

Günes, S., & Sariciftci, N. S. (2008). Hybrid solar cells. *Inorganica Chimica Acta*, *361*(3), 581–588. doi:10.1016/j.ica.2007.06.042

Gur, I., Fromer, N. A., Chen, C.-P., Kanaras, A. G., & Alivisatos, A. P. (2006). Hybrid solar cells with prescribed nanoscale morphologies based on hyperbranched semiconductor nanocrystals. *Nano Letters*, *7*(2), 409–414. doi:10.1021/nl062660t

Halme, H. (2002). *Dye sensitized nanostructured and organic photovoltaics cell*. PhD Thesis. Espoo, Finland: Espoo University.

Hasobe, T., Fukuzumi, S., & Kamat, P. V. (2006). Stacked-cup carbon nanotubes for photoelectrochemical solar cells. *Angewandte Chemie International Edition*, *45*(5), 755–759. doi:10.1002/anie.200502815

Hoyer, P., & Masuda, H. (1996). Electrodeposited nanoporous TiO_2 film by a two-step replication process from anodic porous alumina. *Journal of Materials Science Letters*, *15*(14), 1228–1230. doi:10.1007/BF00274383

Huynh, W. U., Dittmer, J. J., & Alivisatos, A. P. (2002). Hybrid nanorod-polymer solar cells. *Science*, *295*(5564), 2425–2427. doi:10.1126/science.1069156

Jia, Y., Wei, J., Wang, K., Cao, A., Shu, Q., & Gui, X. (2008). Nanotube–silicon heterojunction solar cells. *Advanced Materials (Deerfield Beach, Fla.)*, *20*(23), 4594–4598. doi:10.1002/adma.200801810

Kaneto, K., Tsuruta, M., Sakai, G., Cho, W. Y., & Ando, Y. (1999). Electrical conductivities of multi-wall carbon nano tubes. *Synthetic Metals*, *103*(1-3), 2543–2546. doi:10.1016/S0379-6779(98)00221-5

Kang, Y., Park, N.-G., & Kim, D. (2005). Hybrid solar cells with vertically aligned CdTe nanorods and a conjugated polymer. *Applied Physics Letters*, *86*(11), 113101–113103. doi:10.1063/1.1883319

Karimov, K. S., Ahmed, M. M., Moiz, S. A., & Fedorov, M. I. (2005). Temperature-dependent properties of organic-on-inorganic Ag/p-CuPc/n-GaAs/Ag photoelectric cell. *Solar Energy Materials and Solar Cells*, *87*(1-4), 61–75. doi:10.1016/j.solmat.2004.07.014

Kim, J. Y., Lee, K., Coates, N. E., Moses, D., Nguyen, T.-Q., & Dante, M. (2007). Efficient tandem polymer solar cells fabricated by all-solution processing. *Science*, *317*(5835), 222–225. doi:10.1126/science.1141711

Kongkanand, A., Martínez Domínguez, R., & Kamat, P. V. (2007). Single wall carbon nanotube scaffolds for photoelectrochemical solar cells: Capture and transport of photogenerated electrons. *Nano Letters*, *7*(3), 676–680. doi:10.1021/nl0627238

Krebs, F. C. (2008). A simple nanostructured polymer/ZnO hybrid solar cell—Preparation and operation in air. *Nanotechnology*, *19*(42), 424013. doi:10.1088/0957-4484/19/42/424013

Kr, üger, J., Plass, R., Cevey, L., Piccirelli, M., Gratzel, M., & Bach, U. (2001). High efficiency solid-state photovoltaic device due to inhibition of interface charge recombination. *Applied Physics Letters*, *79*(13), 2085–2087. doi:10.1063/1.1406148

Kubo, W., Murakoshi, K., Kitamura, T., Yoshida, S., Haruki, M., & Hanabusa, K. (2001). Quasi-solid-state dye-sensitized TiO_2 solar cells: Effective charge transport in mesoporous space filled with gel electrolytes containing iodide and iodine. *The Journal of Physical Chemistry B*, *105*(51), 12809–12815. doi:10.1021/jp012026y

Kudo, N., Shimazaki, Y., Ohkita, H., Ohoka, M., & Ito, S. (2007). Organic-inorganic hybrid solar cells based on conducting polymer and SnO2 nanoparticles chemically modified with a fullerene derivative. *Solar Energy Materials and Solar Cells*, *91*(13), 1243–1247. doi:10.1016/j.solmat.2006.11.019

Kuo, C. Y., & Gau, C. (2009). Arrangement of band structure for organic-inorganic photovoltaics embedded with silicon nanowire arrays grown on indium tin oxide glass. *Applied Physics Letters*, *95*(5), 053302. doi:10.1063/1.3189088

Kymakis, E., & Amaratunga, G. A. J. (2002). Single-wall carbon nanotube/conjugated polymer photovoltaic devices. *Applied Physics Letters*, *80*(1), 112–114. doi:10.1063/1.1428416

Lancelle-Beltran, E., Prené, P., Boscher, C., Belleville, P., Buvat, P., & Sanchez, C. (2006). All-solid-state dye-sensitized nanoporous TiO_2 hybrid solar cells with high energy-conversion efficiency. *Advanced Materials (Deerfield Beach, Fla.)*, *18*(19), 2579–2582. doi:10.1002/adma.200502023

Landi, B. J., Raffaelle, R. P., Castro, S. L., & Bailey, S. G. (2005). Single-wall carbon nanotube–polymer solar cells. *Progress in Photovoltaics: Research and Applications*, *13*(2), 165–172. doi:10.1002/pip.604

Li, Z., Kunets, V. P., Saini, V., Xu, Y., Dervishi, E., & Salamo, G. J. (2009). Light-harvesting using high density p-type single wall carbon nanotube/n-type silicon heterojunctions. *ACS Nano*, *3*(6), 1407–1414. doi:10.1021/nn900197h

Lin, C. (2010). Hybrid solar cells based on P3HT and Si MWCNT nanocomposite. *Nanotechnology*, *21*(34), 345201. doi:10.1088/0957-4484/21/34/345201

Lin, Y.-Y., Chen, C.-W., Chu, T.-H., Su, W.-F., Lin, C.-C., & Ku, C.-H. (2007). Nanostructured metal oxide/conjugated polymer hybrid solar cells by low temperature solution processes. *Journal of Materials Chemistry*, *17*(43), 4571–4576. doi:10.1039/b710400f

Liu, C.-Y., Holman, Z. C., & Kortshagen, U. R. (2008). Hybrid Solar cells from P3HT and silicon nanocrystals. *Nano Letters*, *9*(1), 449–452. doi:10.1021/nl8034338

Mao, H., Deng, H., Li, H., Shen, Y., Lu, Z., & Xu, H. (1998). Photosensitization of TiO_2 semiconductor with porphyrin. *Journal of Photochemistry and Photobiology A Chemistry*, *114*(3), 209–212. doi:10.1016/S1010-6030(97)00260-8

Mastai, Y., & Hodes, G. (1997). Size quantization in electrodeposited CdTe nanocrystalline films. *The Journal of Physical Chemistry B*, *101*(14), 2685–2690. doi:10.1021/jp963069v

McGehee, M. D. (2009). Nanostructured organic-inorganic hybrid solar cells. *MRS Bulletin*, *34*(02), 95–100. doi:10.1557/mrs2009.27

McLeskey, J. T. Jr, & Qiao, Q. (2006). Hybrid solar cells from water-soluble polymers. *International Journal of Photoenergy*, (n.d), 2006.

Mori, S., & Yanagida, S. (2006). TiO2-based dye-sensitized solar cell . In Tetsuo, S. (Ed.), *Nanostructured Materials for Solar Energy Conversion* (pp. 193–225). Amsterdam, The Netherlands: Elsevier. doi:10.1016/B978-044452844-5/50008-1

Murai, S., Mikoshiba, S., Sumino, H., & Hayase, S. (2002). Quasi-solid dye-sensitized solar cells containing chemically cross-linked gel: How to make gels with a small amount of gelator. *Journal of Photochemistry and Photobiology A Chemistry*, *148*(1-3), 33–39. doi:10.1016/S1010-6030(02)00046-1

Nazeeruddin, K., Humphry-Baker, M., Gratzel, M., & Murrer, B. (1998). Efficient near IR sensitization of nanocrystalline TiO2 films by ruthenium phthalocyanines. *Chemical Communications*, *6*, 719–720. doi:10.1039/a708834e

Nolasco, J. C., Estrada, M., Matsumoto, Y., Marsal, L. F., & Pallares, J. (2007). Characterization of a P3HT- Si heterojuntion for solar cells applications. *ECS Transactions*, *9*(1), 587–593. doi:10.1149/1.2766933

Novotny, C. J., Yu, E. T., & Yu, P. K. L. (2008). InP nanowire/polymer hybrid photodiode. *Nano Letters*, *8*(3), 775–779. doi:10.1021/nl072372c

O'Regan, B., & Gratzel, M. (1991). A low-cost, high-efficiency solar cell based on dye-sensitized colloidal TiO_2 films. *Nature*, *353*(6346), 737–740. doi:10.1038/353737a0

O'Regan, B. C., López-Duarte, I., Martínez-Díaz, M. V., Forneli, A., Albero, J., & Morandeira, A. (2008). Catalysis of recombination and its limitation on open circuit voltage for dye sensitized photovoltaic cells using phthalocyanine dyes. *Journal of the American Chemical Society*, *130*(10), 2906–2907. doi:10.1021/ja078045o

Odom, T. W., Huang, J.-L., Kim, P., & Lieber, C. M. (1998). Atomic structure and electronic properties of single-walled carbon nanotubes. *Nature*, *391*(6662), 62–64. doi:10.1038/34145

Ong, P. L., Euler, W. B., & Levitsky, I. A. (2010). Hybrid solar cells based on single-walled carbon nanotubes/Si heterojunctions. *Nanotechnology*, *21*(10). doi:10.1088/0957-4484/21/10/105203

Ong, P.-L., & Levitsky, I. (2010). Organic / IV, III-V semiconductor hybrid solar cells. *Energies*, *3*(3), 313–334. doi:10.3390/en3030313

Pasquier, A. D., Mastrogiovanni, D. D. T., Klein, L. A., Wang, T., & Garfunkel, E. (2007). Photoinduced charge transfer between poly(3-hexylthiophene) and germanium nanowires. *Applied Physics Letters*, *91*(18), 183501. doi:10.1063/1.2801554

Polo, A. S., Itokazu, M. K., & Murakami Iha, N. Y. (2004). Metal complex sensitizers in dye-sensitized solar cells. *Coordination Chemistry Reviews*, *248*(13-14), 1343–1361. doi:10.1016/j.ccr.2004.04.013

Prabakar, K., Seo, H., Son, M., & Kim, H. (2009). CdS quantum dots sensitized TiO_2 photoelectrodes. *Materials Chemistry and Physics*, *117*(1), 26–28. doi:10.1016/j.matchemphys.2009.05.056

Rajeshwar, K., & de Tacconi, N. R. (1997). Electrodeposition and characterization of nanocrystalline semiconductor films . In Prashant, V. K., & Dan, M. (Eds.), *Studies in Surface Science and Catalysis* (*Vol. 103*, pp. 321–351). London, UK: Elsevier. doi:10.1016/S0167-2991(97)81109-3

Rehm, J. M., McLendon, G. L., Nagasawa, Y., Yoshihara, K., Moser, J., & Gratzel, M. (1996). Femtosecond electron-transfer dynamics at a sensitizing dye−semiconductor (TiO_2) interface. *Journal of Physical Chemistry*, *100*(23), 9577–9578. doi:10.1021/jp960155m

Riad, S. (2000). Dark and photoelectric conversion properties of p-MgPc/n-Si (organic/inorganic) heterojunction cells. *Thin Solid Films*, *370*(1-2), 253–257. doi:10.1016/S0040-6090(99)00951-7

Robel, I., Bunker, B. A., & Kamat, P. V. (2005). Single-walled carbon nanotube–CdS nanocomposites as light-harvesting assemblies: Photoinduced charge-transfer interactions. *Advanced Materials (Deerfield Beach, Fla.)*, *17*(20), 2458–2463. doi:10.1002/adma.200500418

Sailor, M. J., Ginsburg, E. J., Gorman, C. B., Kumar, A., Grubbs, R. H., & Lewis, N. S. (1990). Thin films of n-Si/poly-$(CH_3)_3$Si-cyclooctatetraene: Conducting-polymer solar cells and layered structures. *Science*, *249*(4973), 1146–1149. doi:10.1126/science.249.4973.1146

Saunders, B. R., & Turner, M. L. (2008). Nanoparticle-polymer photovoltaic cells. *Advances in Colloid and Interface Science*, *138*(1), 1–23. doi:10.1016/j.cis.2007.09.001

Scheblykin, I. G., Yartsev, A., Pullerits, T., Gulbinas, V., & Sundström, V. (2007). Excited state and charge photogeneration dynamics in conjugated polymers. *The Journal of Physical Chemistry B*, *111*(23), 6303–6321. doi:10.1021/jp068864f

Schmidt-Mende, L., & Grätzel, M. (2006). TiO_2 pore-filling and its effect on the efficiency of solid-state dye-sensitized solar cells. *Thin Solid Films*, *500*(1-2), 296–301. doi:10.1016/j.tsf.2005.11.020

Shaw, P. E., Ruseckas, A., & Samuel, I. D. W. (2008). Exciton diffusion measurements in poly(3-hexylthiophene). *Advanced Materials (Deerfield Beach, Fla.)*, *20*(18), 3516–3520. doi:10.1002/adma.200800982

Sun, B., Snaith, H. J., Dhoot, A. S., Westenhoff, S., & Greenham, N. C. (2005). Vertically segregated hybrid blends for photovoltaic devices with improved efficiency. *Journal of Applied Physics*, *97*(1), 014914–014916. doi:10.1063/1.1804613

Takeuchi, T., Kageyama, H., Nakazawa, H., Atsumi, T., Tamura, S., & Kamijo, N. (2008). Preparation of fluorine-containing indium tin oxide sputtering targets using spark plasma sintering process. *Journal of the American Ceramic Society*, *91*(8), 2495–2500. doi:10.1111/j.1551-2916.2008.02503.x

van de Lagemaat, J., Barnes, T. M., Rumbles, G., Shaheen, S. E., Coutts, T. J., & Weeks, C. (2006). Organic solar cells with carbon nanotubes replacing In_2O_3:Sn as the transparent electrode. *Applied Physics Letters*, *88*(23), 233503–233503. doi:10.1063/1.2210081

Vietmeyer, F., Seger, B., & Kamat, P. V. (2007). Anchoring ZnO particles on functionalized single wall carbon nanotubes: Excited state interactions and charge collection. *Advanced Materials (Deerfield Beach, Fla.)*, *19*(19), 2935–2940. doi:10.1002/adma.200602773

Vlachopoulos, N., Liska, P., Augustynski, J., & Graetzel, M. (1988). Very efficient visible light energy harvesting and conversion by spectral sensitization of high surface area polycrystalline titanium dioxide films. *Journal of the American Chemical Society*, *110*(4), 1216–1220. doi:10.1021/ja00212a033

Wei, J., Jia, Y., Shu, Q., Gu, Z., Wang, K., & Zhuang, D. (2007). Double-walled carbon nanotube solar cells. *Nano Letters*, *7*(8), 2317–2321. doi:10.1021/nl070961c

Wu, Y., & Zhang, G. (2010). Performance enhancement of hybrid solar cells through chemical vapor annealing. *Nano Letters*, *10*(5), 1628–1631. doi:10.1021/nl904095n

Chapter 7
Polymer Solar Cells

Catalin Zaharia
Polytechnic University of Bucharest, Romania

ABSTRACT

Currently, the active materials used for the fabrication of solar cells are mainly inorganic. Materials such as silicon (Si), gallium-arsenide (GaAs), cadmium-telluride (CdTe), and cadmium-indium-selenide (CIS). Nevertheless, the large production cost for the silicon solar cells is one of the major drawback in this field. This chapter is dedicated to a critical presentation of another type of photovoltaics, called polymer, or plastic, solar cell technology. Polymer solar cells have attracted significant attention in the past few years due to their potential of providing environmentally safe, lightweight, flexible, and efficient solar cells.

INTRODUCTION

Photovoltaics (PV) is one of the fastest growing of all the renewable energy technologies. Solar cell manufacturing based on the technology of crystalline, silicon devices is growing by approximately 40% per year and this growth rate is increasing nowadays (Jäger-Waldau, 2003). This has been realized mainly by special market implementation programs to encourage a substantial use of the current PV technologies based on silicon. Efforts are now made to diminish the costs of these silicon-based technologies. To ensure a sustainable technology path for PV, efforts to reduce the costs of the current silicon technology need to be balanced with variety in PV technology.

DOI: 10.4018/978-1-4666-1927-2.ch007

Figure 1. Molecular structures of conjugated polymers: polyacetylene (PA), poly(p-phenylene vinylene) (PPV), and poly(2-methoxy-5-(3,7'-dimethyloctyloxy)-1,4-phenylene vinylene) (MDMO-PPV)

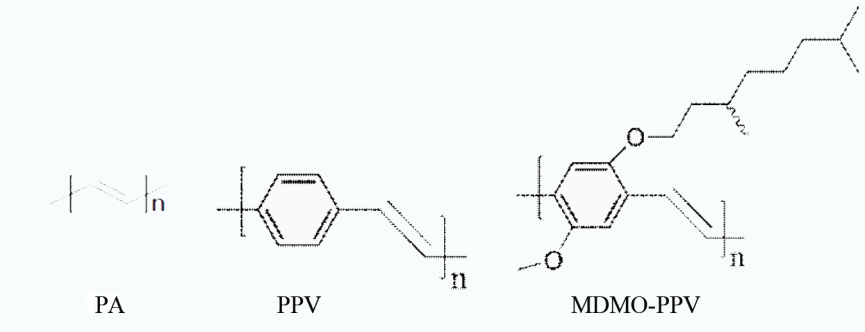

The new approach consists in entirely new materials, namely conjugated polymers and molecules. Polymer solar cells are lightweight, flexible, and cheap to make (Chen, Hong, Li, & Yang, 2009; Roncali, 2009; Tremolet de Villers, Tassone, Tolbert, & Schwartz, 2009). Nevertheless, these devices have been too inefficient to compete with silicon solar cells for most applications. Now researchers from a few institutions claim to have made polymer solar cells with record-breaking efficiencies. These cells still are not good enough to compete with silicon, but polymer efficiencies have been increasing at a rate of about 1 percent a year. If this rate increases, plastic solar cells will be competing with silicon within a few years.

Conjugated materials are organics consisting of alternating single and double bonds. Conjugated polymers and molecules have the immense advantage of facile, chemical tailoring to alter their properties, such as the band gap. Conjugated polymers (Figure 1) combine the electronic properties known from the traditional semiconductors and conductors with the ease of processing and mechanical flexibility of plastics. Therefore, this new class of materials has attracted considerable attention owing to its potential of providing environmentally safe, flexible, lightweight, inexpensive electronics. The field of electronics based on conjugated materials started in 1977 when Heeger, MacDiarmid, and Shirakawa discovered that the conductivity of the conjugated polymer polyacetylene (PA, Figure 1) can be increased by seven orders of magnitude upon oxidation with iodine, for which they were awarded the Nobel Prize in Chemistry in 2000 (Heeger, 2001; MacDiarmid, 2001; Shirakawa, 2001; Shirakawa, McDiarmid, Heeger, 2003) This discovery led, subsequently, to the discovery of electroluminescence in a poly(p-phenylene vinylene) (PPV, Figure 1) by Burroughes et al. (1990). The first light-emitting products based on electroluminescence in conjugated polymers have already been emerged on the consumer market by Philips (The Netherlands) in 2002, and light-emitting products based on conjugated molecules have been introduced by the joint venture of Kodak and Sanyo (Japan).

In organic Photovoltaic Devices (PVDs), the energy conversion efficiency up to 3% under illumination of AM 1.5 has now been reached, in devices based on organic small molecule solar cells and in polymer-based systems such as poly(3-hexylthiophene) (P3HT) and poly (2-methoxy, 5-(3',7'-dimethyl-octyloxy))-p-phenylene vinylene) (MDMO-PPV, Figure 1) combined with a fullerene derivative [6,6]-phenyl-C61-butyric acid methyl ester (PCBM, Figure 2) (Brabec, Sariciftci, & Hummelen, 2001; Chen, et al., 2009; Hoppe, et al., 2006; Offermans, Meskers, & Janssen, 2006; Padinger, Rittberger, & Sariciftci, 2003; Roncali, 2009).

Figure 2. Molecular structures of [6,6]-phenyl-C61-butyric acid methyl ester and phenyl-C_{71}-butyric-acid-methyl ester, $PCBM_{60}$ and $PCBM_{70}$

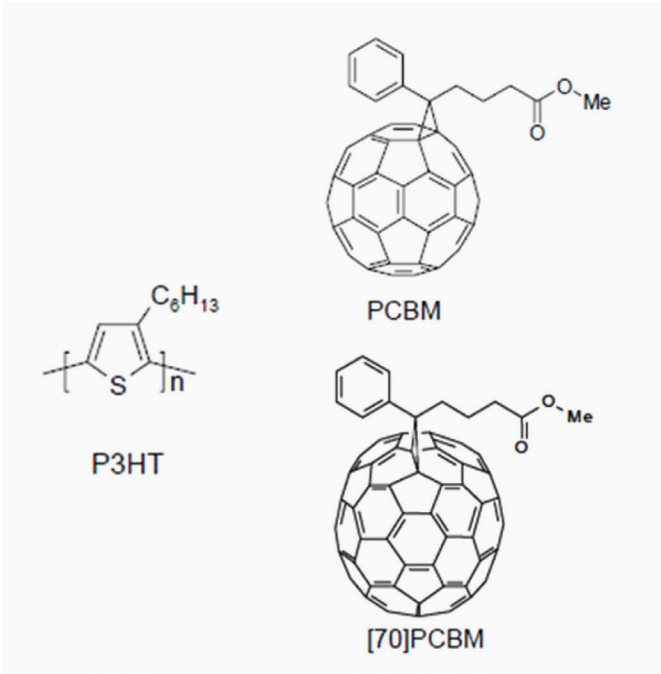

Polymer PVDs are thin film cells with a thickness of only a few hundred nanometers (nm), in which a polymer film deposited by solution processing is the active layer. The film is sandwiched between two electrodes with different work functions, one of which is transparent for incident light. The requirements for electrodes in such devices are that they give solid film with high conductivity and desired work function. Polymers have not been routinely used as electrodes due to their low conductivity compared to their inorganic counterpart ITO. Even though ITO coated on flexible substrates is an option for flexible electrodes, its flexibility is limited. Gustafsson et al. made a fully flexible PLED by using poly(ethylene terephthalate) (PET) as the substrate, soluble polyaniline (PANI) as the hole injection electrode and polymer poly(2-methoxy,5-(2'-ethyl-hexoxy)-1,4-phenylene vinylene) (MEH-PPV) as emitter (Gustafsson, et al., 1993). Their results demonstrated the possibility to use conducting polymer PANI as an electrode for polymer electronics. The optical absorption of polyaniline is found in the visible wavelengths and compromises the transmission to the active layer. The use of a doped conjugated polymer as an injection layer in polymer devices was therefore extended to the polythiophene family of polymers. Previous papers showed that poly(3,4-ethylenedioxythiophene) doped with polystyrene sulphonic acid (PSS) could be obtained by electropolymerization, and used as the anode in nano-LEDs and flexible nano LEDs (Cui, Teixeira, Zhang, & Lee, 2006; Granström, Berggren, & Inganäs, 1995; Inganas, 2010). Another material PEDOT–PSS was also employed, showing a major improvement of performance and stability of LEDs (Kymakis, et al., 2006; Nardes, Kemerink, & Janssen, 2007; Nardes, et al., 2007) Flexible organic small molecular LEDs, using commercial PEDOT–PSS conducting film coated on flexible substrate PET as an anode, were fabricated and reached maxi-

mum illumination 2760 cd/m^2, and maximum External Quantum Efficiency (EQE) of 1.3%, which is close to the performance of similar Organic Light-Emitting Diodes (OLEDs) using ITO as electrode, and with better flexibility.

As a conclusion, we may say that organic PV devices show great promise for decreasing the cost of solar energy to the point where it may become widespread in the decades ahead. While great progress has been made in the last years with respect to understanding the chemistry, physics, and materials science of organic photovoltaics, work remains to be done to further improve their performance. Specifically, novel nanostructures must be optimized to promote charge carrier diffusion; transport must be enhanced through control of order and morphology.

BASIC CONCEPTS IN POLYMER SOLAR CELLS

This chapter will focus on the presentation of the main types of polymer solar cells and their characteristics.

Double Layer Cells

The first approach to obtain organic solar cells was made by sandwiching a single layer of organic material between two dissimilar electrodes. In these cells, the photovoltaic properties strongly depend on the nature of the electrodes. The power conversion efficiencies reached almost 0.3% (Al-Mohamad, 2004; Yu, Gao, Hummelen, Wudl, & Heeger, 1995).

Tang proposed a double-layer structure of a p-n organic semiconductor (Tang, 1986). A 70 nm thick two-layer device was made using copper phthalocyanine as the electron donor, and a perylene tetracarboxylic derivative as the electron acceptor. The photoactive material was placed between two dissimilar electrodes, Indium Tin Oxide (ITO) for collection of the positive charges and silver (Ag) to collect the negative charges. A power conversion efficiency of about 1% was achieved under simulated AM2 illumination. In the double-layer structure the photoexcitations in the photoactive material have to reach the p-n interface where charge transfer can occur, before the excitation energy of the molecule is lost via intrinsic radiative and non-radiative decay processes to the ground state. Because the exciton diffusion length of the organic material is in general limited to 5-10nm, only absorption of light within a very thin layer around the interface contributes to the photovoltaic effect. This limits the performance of double-layer devices, because such thin layer can impossibly absorb all the light (Palmaerts, et al., 2009; Sariciftci, Smilowitz, Heeger, & Wudl, 1992). A strategy to improve the efficiency of the double-layer cell is related to structural organization of the organic material to extend the exciton diffusion length and, therefore, create a thicker photoactive interfacial area.

Bulk Heterojunction Cells

Organic solar cells rely on a heterojunction resulting from the contact of a donor (D) and an acceptor (A) material. Absorption of solar photons creates excitons, which diffuse to the D/A interface, where they are dissociated into free holes and electrons by the electric field. This type of heterojunction can be created with two types of architectures, namely, bilayer heterojunction and bulk heterojunction solar cells. Bulk heterojunction cells combine the advantages of easier fabrication and higher conversion efficiency due to the high D/A interface (Koetse, et al., 2006; Moulé & Meerholz, 2007; Parmer, et al., 2008; Roncali, 2009).

Solar cells based on conjugated polymers gained a lot of attention since the discovery of the bulk heterojunction cell in 1995 (Yu, et al., 1995). Hereby we describe first the principles of the bulk heterojunction process.

If we combine electron donating (*p*-type) and electron accepting (*n*-type) materials in the active

layer of a solar cell, we should be aware of the fact that excitons created in material may diffuse at the interface to enable charge separation. Due to their short lifetime and low mobility, the diffusion length of the excitons in organic semiconductors is limited to about 10 nm only. This means an important limit to efficient charge generation. Anywhere in the active layer, the distance to the interface should be on the order of the exciton diffusion length. Despite their high absorption coefficients a 20 nm double layer of donor and acceptor materials would not be optical dense, allowing most photons to pass freely. The solution to this quite serious problem is relatively simple. By simple mixing the *p* and *n* type materials and relying on the intrinsic tendency of polymer materials to phase separate on a nanometer dimension, junctions throughout the bulk of the material are created that ensure quantitative dissociation of photogenerated excitons. The main operation scheme of such a heterojunction cell is presented in Figure 3.

The bulk heterojunction is presently the most widely used photoactive layer. As a result of the intimate mixing, the interface where charge transfer can occur has increased enormously. The exciton, created after the absorption of light, has to diffuse towards this charge-transfer interface for charge generation to occur. The diffusion length of the exciton in organic materials, however, is typically 10 nm or less. This means that for efficient charge generation after absorption of light, each exciton has to find a donoracceptor interface within a few nanometers; otherwise, it will be lost without charge generation. An intimate bicontinuous network of donor and acceptor materials in the nanometer range should suppress exciton loss prior to charge generation. Control of morphology is not only required for a large charge-generating interface and suppression of exciton loss, but also to ensure percolation pathways for both electron and hole transport to the collecting electrodes.

Figure 3. Schematic representation of bulk heterojunction concept. The photoactive material absorbs light and then the charge transfer occur through nanoscopic mixing of donor and acceptor. Next, the photogenerated charges are transported and collected at the electrodes.

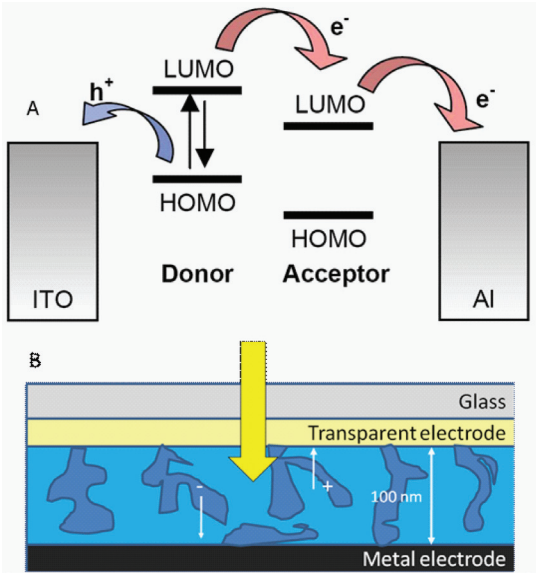

State of the Art in Bulk Heterojunction Cells (BHJ)

Numerous combinations of donor and acceptor materials have been used to set up bulk heterojunction solar cells in which the composite active layer is inserted between two electrodes.

A major breakthrough to truly appealing power conversion efficiencies exceeding 2.5% under simulated AM1.5 illumination was realized for bulk-heterojunction solar cells based on MDMO-PPV as a donor and PCBM as an acceptor (Hoppe, Drees, Schwinger, Schaffler, & Sariciftcia, 2005; Shaheen, et al., 2001). In PCBM, the fullerene cage carries a substituent that prevents extensive crystallization upon mixing with the conjugated polymer and enhances the miscibility. In these 2.5% efficient cells, the photoactive composite layer is sandwiched between two electrodes with different work functions: a transparent front elec-

trode consisting of indium tin oxide covered with a conducting polymer poly(ethylene dioxythiophene):poly(styrenesulfonate) (PEDOT:PSS) for hole collection and a metal back electrode consisting of a very thin (~ 1 nm) layer of lithium flouride covered with Al for electron collection. A brief representation of the architecture of polymer-fullerene bulk heterojunction cell is shown in Figure 4.

In the last years various studies have focused on serious understanding of these MDMO-PPV/ PCBM bulk heterojunctions (Hoppe, et al., 2006; Manca, et al., 2003; Martens, et al., 2003). Investigations into the morphology, electronic structure, and charge transport have provided detailed understanding of the degree and dimensions of the phase separation in the active layer, on the origin of the open-circuit voltage, the influence of electrode materials, and the magnitude of charge carrier mobilities for electrons and holes. These studies revealed that PCBM has high electron mobility compared to many other organic or polymer materials that can be deposited by spin coating.

One of the most extensively investigated and promising material combination in polymer solar cells are that of regioregular poly(3-hexylthiophene) (rr-P3HT) with a fullerene derivative ([6,6]-phenyl-C61 butyric acid methyl ester, PCBM) as the donor and acceptor materials, respectively, in a bulk-heterojunction (Hauch, et al., 2008; Keawprajak, Piyakulawat, Klamchuen, Iamraksa, & Asawapirom, 2010; Li, Shrotriya, Yao, Huang, & Yang, 2007).The bulk-heterojunction PVCs made from a blend of rr-P3HT and PCBM have been shown to have a PCE up to 3–5% and more than 6% for tandem cells (Baek, et al., 2009; Kim, et al., 2006). In order to achieve the high photovoltaic performance, the band gap energy, HOMO/ LUMO levels and carrier mobilities of the heterojunction materials need to be optimized simultaneously. Within a relatively short period, P3HT has become the most important donor for

Figure 4. Schematic architecture of a polymer-fullerene bulk heterojunction cell

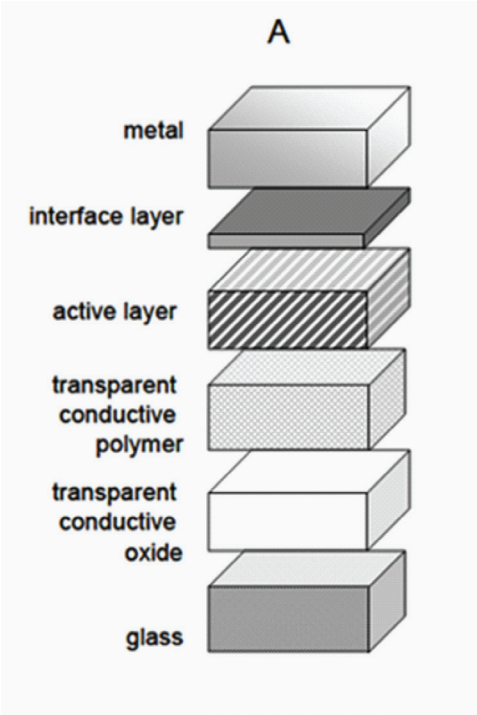

BHJ cells and power conversion efficiencies of about 5% have been recently reported in literature [roncali]. Nevertheless, P3HT has a number of drawbacks related to its synthesis, purification, and intrinsic electronic properties. The synthesis of this regioregular polymer is conducted in harsh conditions (cryogenic). Grignard method simplified the synthesis but terminal bromine atom groups still remained in the polymer. Furthermore, the molecular weight, regioregularity and polydisperisty seriously affect the efficiencies of bulk heterojunction solar cells (Roncali, 2009). P3HT can absorb only a limited fraction of the solar photons (around 30%) due to a law band gap (1.90 eV). A relatively high-lying HOMO level sets the maximum cell voltage to 0.60-0.65 V and represents a potential cause of instability in atmospheric conditions. Post thermal process treatment of the P3HT-PCBM material improves the morphology of the bicontinuous phase and the

Figure 5. Tandem solar cells for different connection types. Parallel and serial connections (right and left side).

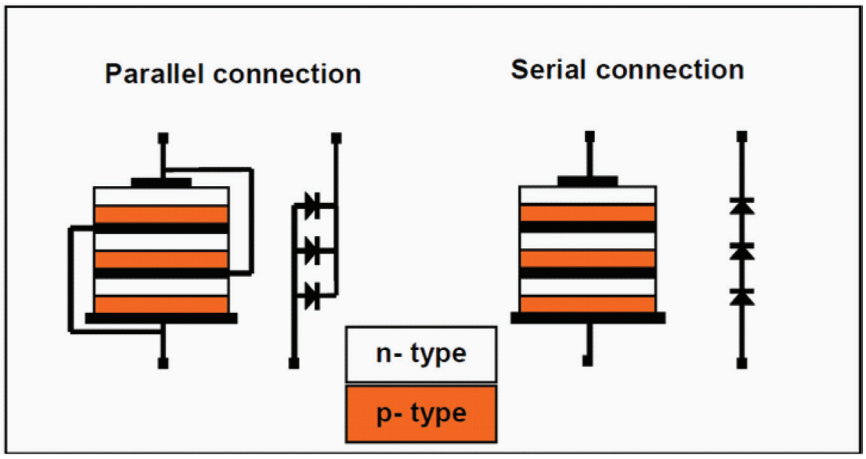

crystallinity of P3HT. Only in this way efficiencies up to 5% could be reached (Roncali, 2009).

An interesting type of polymer cell based on conjugated polymer and fullerene composites is represented by tandem polymer solar cells.

In tandem cells, two or more heterojunction solar cells are deposited on top of each other. Two methods are available to stack these cells: parallel or serial (Figure 5). For parallel connections intermediate electrodes ensure the charge collection for each cell. These electrodes have to be transparent to minimize photon losses and highly conducting to maximize charge carriers collection. An obvious material for such electrode would be Indium Tin Oxide (ITO). However, ITO is usually deposited via reactive sputtering which might severely damage the conjugated polymer. Therefore, such parallel connections could be achieved very easy in the case of organic semiconductor solar cells. Serial connection is much likely to be obtained since it does just require thin, non-continuous, non-absorbing metallic layers to separate the different cells and act as recombination layer.

Polymer-fullerene composites offer special opportunities as renewable energy sources because they can be fabricated to extend over large areas by means of low-cost printing and coating technologies that can simultaneously pattern the active materials on lightweight flexible substrates. Although progress has been made with power conversion efficiencies (η_e) of 5% (Kim, et al., 2007; Reyes-Reyes, Kim, & Carroll, 2005), the limited efficiency has negative impacts on commercialization. The "tandem cell" system, a multilayer structure that is equivalent to two photovoltaic cells in series, offers a number of advantages (Kim, et al., 2007). Because the two cells are in series, the open circuit voltage (Voc) is increased to the sum of the V_{oc} of the individual cells. The use of two semiconductors with different band gaps enables absorption over a broad range of photon energies within the solar emission spectrum. The two cells typically use a wide band-gap semiconductor for the first cell and a smaller band-gap semiconductor for the second cell. Because the electron-hole pairs generated by photons with energies greater than that of the energy gap rapidly relax to the respective band edges, the power-conversion efficiency of the two cells in series is better than that of a single cell made from the smaller band-gap material. Due to the low mobility of the charge carriers in the polymer-fullerene composites, an increase in the

thickness of the active layer increases the internal resistance of the device, which reduces both the V_{oc} and fill factor (FF). The tandem cell can therefore improve the light harvesting in polymer-based photovoltaic cells (Kim, et al., 2007).

Most of the tandem structures have been proposed for small molecules heterojunction and hybrid organic solar cells (Drechsel, et al., 2005; Kim, et al., 2007). However, a lot of recent studies showed polymer-fullerene composite systems in tandem architecture (Kawano, Ito, Nishimori, & Sakai, 2006; Shrotriya, Wu, Li, Yao, & Yang, 2006). These polymer based tandem cells exhibit a high V_{oc}, close to the expected sum of the V_{oc} of the two subcells, but the short-circuit current (J_{sc}) is lower than that of either single cell. When the same polymer was used for the front and back cells, the small J_{sc} was attributed to the absorption spectra being identical, so that the back cell absorbs less incident light and thus limits the photocurrent. Some authors show for the tandem cells the TiO_x intermediate layer was deposited from solution (by means of sol-gel chemistry) with no substantial interlayer mixing (Kim, et al., 2007). The performance of the polymer tandem solar cell is summarized as follows: J_{sc} = 7.8 mA/ cm^2, V_{oc} = 1.24 V, FF = 0.67, and η_e = 6.5% (Kim, et al., 2007).

Another interesting system is composed of Single-Wall Carbon Nanotubes (SWNTs) donor conjugated polymer composites (Kymakis & Amaratunga, 2004; Park, et al., 2008; Song, Lee, & Jo, 2010). We illustrate here an example of hotovoltaic devices based on the dispersed heterojunction concept, containing a blend of SWNTs and soluble poly(3-octylthiophene) (P3OT) (Carroll, Czerw, Harrison2006; Song, et al., 2010; Stefopoulos, et al., 2008).

Here the approach focuses on the the formation of an interpenetrating blend of polymer electron donors and carbon nanotubes electron acceptors. The charge separation is achieved due to a band offset at the interface and collection because of the existence of a bi-continuous network along which electrons and holes can travel through the electron acceptor and the electron donor, respectively, towards their respective contacts. In this way, the blend can be considered as a network of donor and acceptor heterojunctions that allows efficient exciton dissociation and balanced bipolar transport throughout its entire volume.

Poly(3-octylthiophene) (P3OT), acting as the photoexcited electron donor, is blended with SWNTs, which act as the electron acceptor. Efficient exciton dissociation is expected at the polymer–nanotube interface. Charge transfer would then follow by the transport of electrons through the nanotube length to the electron contacting contact (Al), and holes through the polymer to the hole collecting contact (ITO). The polymer P3OT is assumed to behave as a p-type semiconductor, since its hole mobility is much higher than its electron mobility. While the carbon nanotubes are assumed to behave as metals, due to the fact that they are either metallic, or semiconducting with a very small bandgap of 0.1–0.2 eV. When the polymer (p-semiconductor) comes into contact with the nanotube (metal), the difference in the electrochemical potential of the polymer and the contacting phase of the nanotube results in charge equilibration at the heterojunction.

The current-voltage characteristics of these types of devices (ITO/P3OT–SWNTs/Al) under dark and under white light illumination (AM1.5, 100mW/cm^2). Under illumination, the blend device shows short circuit photocurrent density (Jsc) of 0.12 mA/ cm^2 and an open circuit voltage (V_{oc}) of 0.75V while the pristine device shows J_{sc}=0.7 mA/cm^2 and V_{oc}=0.35 V (Kymakis & Amaratunga, 2002).

The power efficiency of the blend device is dramatically increased from $2.5x10^{-5}$ to 0.04% with respect to the pristine one. Thus, a considerable improvement of photovoltaic effect is observed with the P3OT-SWNTs blend structure. The J_{sc} in the blend device is larger than that in the pristine device by about two orders of magnitude. Moreover, the V_{oc} and the fill factor in the blend

device are also significantly larger than those in the pristine diode (Kymakis & Amaratunga, 2002).

Although the efficiencies of the polymer solar cells are significantly increased upon the introduction of nanotubes, they are far from rivaling those of fullerene-based devices. The low photocurrent is caused by the mismatch of the optical absorption of the polymer and the solar spectrum, and the fact that the nanotubes do not contribute to the photogeneration process, as the fullerenes do. Nevertheless, this type of polymer solar cell represents an interesting alternative to organic semiconductors for the manufacture of solar cells with improved performance.

The last approach presented here is targeted on Poly(2,5-bis(3-tetradecyllthiophen-2-yl) thieno[3,2-*b*]thiophene) (pBTTT) which has caused recent excitement in the organic electronics community because of its high reported hole mobility (0.6 $cm^2/V{\cdot}s$) (Parmer, et al., 2008) that was measured in field effect transistors and its ability to form large crystals. The hole mobility of the most efficient pBTTT:PCBM cells as measured by Space Charge Limited Current (SCLC) modeling was found to be $3.8x10^{-4}$ $cm^2/V{\cdot}s$. This value is lower than the typical reported out-of-plane mobility of PCBM. By varying the polymer/fullerene blend ratio, the choice of fullerene, and annealing conditions authors found a maximum efficiency of 2.3% for a 1:4 blend ratio having a short-circuit current density (J_{sc})of 9.37 mA/cm^2, an open circuit voltage (V_{oc}) of 0.525 V, and a Fill Factor (FF) of 0.48 (Parmer, et al., 2008). These initial results show the potential of pBTTT as a light absorbing, hole transporting material for use in high efficiency polymer:PCBM bulk heterojunction solar cells.

TECHNOLOGIES FOR HYBRID SOLAR CELLS FABRICATION

Most improvements in polymer cells have been done through materials such as P3HT and the fullerenes $PCBM_{60}$ and $PCBM_{70}$. In terms of device structure, efforts have been relatively limited for various reasons. There is a considerable drive towards achieving high power conversion efficiency and this implies small devices and a high conductivity of the electrodes. Since the back electrode for cells is typically an evaporated metal electrode the limiting electrode in terms of conductivity is the necessarily transparent front electrode. The best performing transparent electrode material that combines high transparency over a broad range of wavelengths and high electrical conductivity is Indium Tin Oxide (ITO). From the point of view of processing polymer solar cells on a large scale there are several problems connected to the use of ITO but for the purpose of breaking power conversion efficiency records there are few. The reason that nearly all reported devices with any significant power conversion efficiency are prepared on ITO covered glass substrates is understandable. This has severely limited the evolution of both device geometry and processing techniques.

Polymer solar cells typically show a multilayer structure where each layer in the stack may be formed by an individual film-forming technique. This could be regarded as a particular advantage of the technology. First, it is very versatile that one in principle can arrive at the same device geometry through many different routes. Next, it is of some importance from an Intellectual Property Rights (IPR) point of view as this implies that it will be almost impossible to efficiently protect a polymer solar cell product unless it is materials specific. Since both the available device geometries and many materials are prior art there is little hope that one can protect ideas through a particular process sequence and even if possible it would be very easy to circumvent. A further complication lies in the fact that it is not always possible with a printed film at hand to establish how it was made. While some printing methods give rise to characteristics in the printed film that does allow for their identification it can be anticipated to be very difficult for multilayer

films. This should be viewed as strengths of the technology as it increases competition and places focus of the competition on what matters, namely overall performance, and places the judgment in the hand of the consumer, where it should be, rather than Olympic records in scientific articles. Thirdly, this aspect makes it desirable to invent new device structures and electrodes as this would become valuable IPR in the event that a competitive device could be prepared.

There are many explored film-forming techniques for the processing of polymer solar cell (Dang, Wantz, Hirsch, & Parneix, 2009; Kim, et al., 2007; Krebs, Alstrup, Spanggaard, Larsen, & Kold, 2004). The techniques that have been explored are generally suitable for individual processing of small substrates (i.e. spin coating, doctor blading and casting) and this could be a drawback. Nevertheless, there are many techniques specialized for developed for high volume processing of paper, plastic and textile materials where the substrate is in the form of a continuous roll of material. This is often called roll-to-roll coating or reel-to-reel coating and the processing equipment generally comprises: unwinding, coating and rewinding of the material (Krebs, 2009a). Other processes may be involved such as cleaning, pre/post treatments of the fabric, heating, drying, etc. (Krebs, 2009a). The coating techniques are very useful for high-rate coating or printing and they have been developed with the aim of achieving a very low process cost. While this has not been shown repeatedly in the context of polymer solar cells it is generally accepted that R2R processing is cheap and fast.

One of the challenges is to identify the ideal coating techniques for polymer solar cells. Some techniques are suited only for coating an even layer over the entire substrate surface thus giving 0-dimensional control (i.e. no ability to create a pattern), other techniques allow for 1-dimensional control of the pattern and in the context of a substrate passing a coating head this implies that a striped pattern can be created (Krebs, 2009a). Further, some methods allow for full 2-dimensional control of the printed pattern where any shape can be reproduced on the substrates. Finally, some coating methods allow for the formation of multilayer films in the same coating step. Combinations of these techniques can in principle enable pseudo 3-dimensional control during printing (i.e. both pattern and multilayer structure). A second challenge is that with each of these coating techniques there are often a window of operation in terms of processing speed and achievable wet layer thickness that all hinges on the properties of the ink and the interplay between the surface that is to be coated. Viscosity, surface tension, surface energy, volatility are a few of the important ink properties that have to be taken into account when procuring the ink. It should be noted that it is customary in the coating industry to employ additives and adjuvants that are added to the ink to adjust the properties such that printability/coatability of the ink is achieved. This is all very well for traditional coating and printing where the transfer of a pattern is all that is required. In the case of polymer solar cells, the coated pattern has to be functional after the film is formed. It should thus be anticipated that there is limited freedom when choosing additives to aid printing/coating.

Coating and Printing Techniques

We have to establish from the beginning the difference between a coating and a printing technique. Printing is used to describe a method by which a layer of ink is transferred from a stamp to a substrate by a reversing action. By contrast, coating is used to describe a process by which a layer of ink is transferred to the substrate by essentially pouring, painting, spraying, casting, or smearing it over the surface.

Printing techniques include techniques such as screen-printing, pad printing, gravure printing, flexographic printing, and offset printing. Coating techniques include spin-coating, doctor blading, casting, painting, spray coating, slot-

Figure 6. Schematic illustration of the spin coating technique

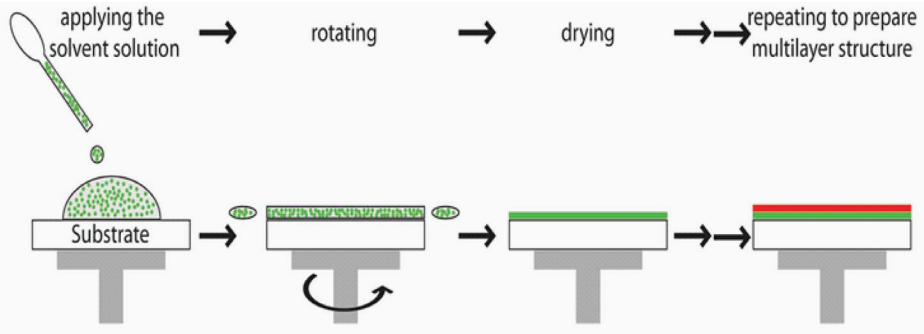

die coating, slide coating, and knife-over-edge coating. Some of them will be briefly discussed within this chapter.

Casting on Single Substrate

Casting on single substrate is the simplest film-forming technique available. The advantage is that only a horizontal work surface is needed. The procedure is to simply cast a solution onto a substrate followed by drying. While it is possible to prepare films of good quality and also thick films the technique suffers from a lack of control over the film thickness and often picture framing effects are observed near the edges of the film or precipitation during drying. In cases where the surface tension of the liquid dominates the drying is inhomogeneous. Also there is a requirement that the material to be coated has a high solubility in the solvent used if crystallisation or precipitation is to be avoided.

Spin-Coating on Single Substrate

The film-forming technique which has been most important for the obtaining of polymer solar cells to this day is spin coating. In spite of the complexity of film formation it allows for the highly reproducible formation of films and has several advantages over other coating techniques during drying which allows for the formation of very homogenous films over a large area (the diameter of the substrate can be as high as 30 cm). The technique is used in the microelectronics industry during application of polymeric photoresists to silicon wafers and is involved in crucial steps during the production of Digital Versatile Discs (DVDs) and Compact Discs (CDs). The typical spin coating operation involves application of a liquid to a substrate followed by acceleration of the substrate to a chosen rotational speed (Figure 6). Alternatively the liquid solution may be applied while the substrate is spinning. The angular velocity of the substrate with the overlying solution results in the ejection of most of the applied liquid where only a thin film is left on the substrate. The thickness, morphology, and surface topography of the final film obtained from a particular material in a given solvent at a given concentration is highly reproducible. Some examples of this are the spin coating of P3HT–PCBM mixtures from 1,2-dichlorobenzene (Krebs, 2009a) while allowing the wet film to dry slowly (either while spinning or by leaving the wet film in an environment saturated with solvent).

Screen Printing on Single Substrate

The first developments of screen printing date back to the beginning of the 20th century. It is a very versatile printing technique that allows for full 2-dimensional patterning of the printed layer.

Its main distinction from all other printing and coating techniques is a large wet film thickness and a requirement for a relatively high viscosity and a low volatility of the coating solution. An interesting process is presented in literature with silk fibre material (Krebs, et al., 2004). The conjugated polymer MEH-PPV with a molecular weight, M_w=100 000 g/mol a polydispersity of 2.0 was commercially available and was issolved in chlorobenzene at a concentration of 14.6 mg/ml. The concentration was found to be critical since the viscosity has a large influence on the silkscreen printing process and has to match the mesh used in the silk screen mask such that the polymer solution will not run through the mask but will be transferred through the mesh upon application of a mechanical pressure. The substrates were ITO covered 200 mm Polyethyleneterephthalate (PET) foil with a surface resistance lower than 70 Ω^{-1}. The electrode pattern was prepared by standard silkscreen printing of an etch resist and subsequent etching as described earlier. Thermosetting silver epoxy contacts were silkscreen printed onto the etched substrates followed by hardening at 150 °C. The substrate with contacts was then ready for printing of the conjugated polymer pattern. The drying of the printed pattern was achieved in approximately 15 s while we observed few problems with drying (and subsequent changes in viscosity) of the polymer solution on the silk screen for the duration of the experiment (30 min) where the printing and drying of a solar cell could be completed in 20 s by manually operating the printing machine. The final polymer films had thicknesses in the 140 150 nm range and absorbencies equal to 3.0. The substrate with the ITO electrode surface and the printed polymer was then transferred to a vacuum chamber and mounted with a shadow mask in front providing the pattern of the second electrode. The best device performance was obtained by sublimation of a thin layer of C_{60} (ca. 225 nm) followed by aluminum (ca. 34 nm). The completed solar cell device was removed from the vacuum chamber and was ready for experiments or for lamination. The lamination was achieved using PET foil in an office laminator at a temperature of ca. 125 °C. The areas of the conjugated polymer film that were not covered by aluminum for the solar cells that were not laminated bleached quickly due to interaction with molecular oxygen from the atmosphere.

The performances of this type pf solar cell are the following: J_{sc}=20 μA/cm^2, V_{oc}= 0.73 V, FF= 0.49 and the efficiency 0.0046% (Krebs, et al., 2004).

Ink Jet Printing

Ink jet printing is a relatively novel process from the point of view of industrial printing and coating and the technology has been driven forward by the typical low-cost ink jet printer for the home office (Krebs, 2009a). Industrial ink jet printers where one has some choice in the type of solvents used have become commercially available recently. The printing head is ceramic or especially resistant towards organic solvents and it is thus possible for the experimentalist to procure an ink formulation based on wide range of solvents. The ink jet printing process has the advantage of quite high resolution, which is easily 300 dpi and up to as a much as 1200 dpi without too great difficulty. In contrast to most other printing techniques relevant to polymer solar cells there is no need for a complex master as the source image to be printed is digital.

It is difficult at the current stage to determine whether ink jet printing will play an important role in the high volume fabrication of polymer solar cells. The advantages offered by the technique and the good literature examples of its use makes it likely that it will become of use for creating complex patterns and perhaps devices with a small outline of the active area.

Figure 7. Schematic representations of roll coating and printing techniques. Notice the dotted line showing the coated material and the thin line showing the web.

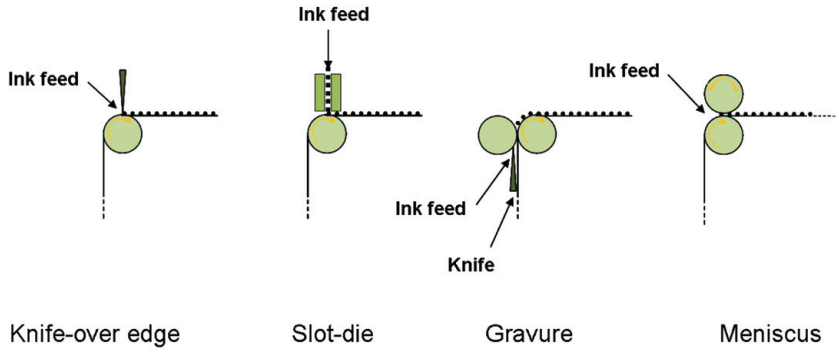

Roll-to-Roll Techniques

These techniques involve substrates as long sheets wound on a roll. A web-type substrate material is used and requires mechanical flexibility. During printing and coating the web material is unwound from the roll and passed through the printing or coating machine and once through the process the material is rewound on a roll. Aside from the printing or coating operation there may be other process steps involved such as heating, drying, UV-curing, etc. Ideally the raw substrate should enter the processing machine at one end and the completed flexible polymer solar cell should emerge in the other end. This is appealing and in the printing and coating industry one strives to process in such an integrated manner as the handling damage is significantly reduced and often throughput can be increased.

Most printing and coating methods only deal with the formation of the wet film and that the dry film that is employed in the solar cell is obtained by a secondary process to the printing and coating operation such as drying or curing.

There are several examples presented in the literature on these roll-to-roll techniques and especially on coating and printing systems (Krebs, 2009a, 2009b). The simplest one is presented in Figure 7.

The printing or coating may take place over unsupported web but is most often carried out over a roller of some sort that guides the web past the coating or printing unit and acts as a solid support. The coating roller may be run by a motor or may simply rotate freely and follow the web. The simplest systems comprise at least one roller (i.e. knife-over-edge, slot-die and curtain coating) but more rollers may be involved as in 2-roller gravure systems where one roller with the pattern to be printed is brought into contact with web supported by the coating roller. More rolls may also be involved where a feed, metering or fountain roller is employed that feeds the roller carrying the motif with ink.

Next we will present some examples of roll-to-techniques based on recent literature data (Krebs, 2009a, 2009b).

Slot Die Coating

This type of coating is suited for multilayer solar cell having materials stripes layered on top of each other. The alignment of the pattern is easy as the coating head is simply translated along the direction perpendicular to the direction of the web movement. The technique belongs to the premetered coating techniques where all the ink supplied to the coating head is coated with no loss.

If we consider ink solution for polymer solar cells (1-20 cP viscosity) the mask thickness should be around 25-50 mm (Krebs, 2009a). The coated pattern could be easily changed if the mask must be changed.

This type pf coating is very popular and intensively studied especially for viscous solutions at high coating speeds (higher than 11 mm/min). There are of range of web speeds in which slot die coating may be applied for a specific ink composition. If we deal with lower or higher speeds this type of coating is no longer possible.

Knife-over-Edge Coating and Meniscus Coating

This technique is not so used in the processing of polymer solar cells but it is an interesting one. In this case the knife is stationary and the web is moving. The knife is suitably used in conjunction with an ink bath positioned in front of the knife. The knife may also be placed over unsupported web.

Knife-over-edge coating is a 0-dimensional coating technique and the coating is applied evenly over the surface of the substrate (Krebs, 2009a, 2009b). While it is not suited for patterning, the barriers of the coating bath may be adjusted so as to limit the coating to a part of the knife width. The edge definition is not sharp and depends on the gap between the knife and the substrate and the web speed. At slow speeds and a short knife-to-web distance, the meniscus of the liquid will draw out along the knife and will extend over the entire length of the knife. This process works well for liquids of low viscosity.

Knife-over-edge coating fills out an uneven surface and if the ink has good levelling properties very smooth films are obtained. Meniscus coating offers the possibility to coat an even layer over the surface just like knife-over-edge coating but the metering of the ink is done by a roller separated by some distance from the coating roller carrying the web. The direction of rotation of the roller may be in the same direction as the web or opposite. The meniscus formed in the gap between the two rollers can be controlled and a variation in the thickness may be obtained by controlling the gap distance and the speed/direction of the roller.

Curtain, Multilayer, Slot, and Slide Coating

This is the most promising technique for polymer solar cells manufacture. Nevertheless, it could become a very expensive and complex technique to be commercially applied for the polymer photovoltaics.

Slide and curtain coating use simultaneous coating of a multilayer film (maximum 18 layers) and they were developed for photographic film industry (Krebs, 2009a, 2009b). For the proper combination of ink solutions all the layers within the solar cell could be printed in a single coating step. The large number of layers that can be coated implies that it would be possible to process tandem and multijunction cells in one coating step. The challenge with these coating techniques is that a very rapid ink flow is required and this implies that a large web speed (4 m/s) is needed for the coating to work properly when thin films are prepared. This procedure requires also large amount of material and substrate.

The potential saving in cost could be so large that it is very likely that some or all of the layers in future low cost polymer solar cells will be coated using slide or curtain coating techniques.

FUTURE DIRECTIONS AND PERSPECTIVES

New materials that are being developed in various laboratories focus on improving the three parameters that determine the energy conversion efficiency of a solar cell, *i.e.* the open-circuit voltage (V_{oc}), the short-circuit current (J_{sc}), and the fill factor (FF) (Platzer-Björkman, Zabierowski, Pettersson, Törndahl, & Edoff, 2010; Wagner, et al., 2010).

The open-circuit voltage of bulk-heterojunction polymer photovoltaic cells is governed by the energy levels of the Highest Occupied Molecular Orbital (HOMO) and the Lowest Unoccupied Molecular Orbital (LUMO) of donor and acceptor, respectively. In most polymer/fullerene solar cells, the positioning of these band levels of donor and acceptor is such that up to ~0.4–0.8 eV is lost in the electron-transfer reaction. By more careful positioning of these levels, it is possible to raise the open-circuit voltage well above 1 V.

One of the crucial parameters for increasing the photocurrent is the absorption of more photons. This may be achieved by increasing the layer thickness and by shifting the absorption spectrum of the active layer to longer wavelengths. When the mobility is too low or the layer too thick, the transit time of photogenerated charges in the device becomes longer than the lifetime, resulting in charge recombination. The use of polymers such as P3HT that are known to have high charge carrier mobilities allows an increase in film thickness from the usual ~100 nm to well above 500 nm, without a loss of current.

A high fill factor is advantageous and indicates that fairly strong photocurrents can be extracted close to the open-circuit voltage. The internal field in the device that assists in charge separation and transport is fairly small. Consequently, a high fill factor can be obtained when the charge mobility of both charges is high. Presently the fill factor is limited to about 60% in the best devices, but values up to 70% have been achieved recently.

CONCLUSION

We like to stress the fact that this field of research of polymer solar cells is just at the beginning. The bulk heterojunction concept is promising for solar energy conversion. Although chemical design and synthesis offers almost unlimited possibility of using new materials and material combinations, the development of efficient bulk heterojunction solar cells requires the optimization of closely interrelated properties at different levels requiring interdisciplinary expertise in various fields of material science.

Recently, there has been an increase in the understanding and performance of polymer-fullerene bulk heterojunction solar cells. Comprehensive insights have been obtained in materials parameters in terms of morphology, energy levels, charge transport, and electrode materials. Power conversion efficiencies close to 3% are routinely obtained and some laboratories have reported power conversion efficiencies of ~4–5% and now aim at increasing the efficiency to 8–10%. By combining synthesis, processing, and materials science with device physics and fabrication there is little doubt that these appealing levels of performance will be achieved in the near future.

REFERENCES

Al-Mohamad, A. (2004). Solar cells based on two organic layers. *Energy Conversion and Management*, *45*(17), 2661–2665. doi:10.1016/j.enconman.2003.12.005

Baek, W.-H., Yang, H., Yoon, T.-S., Kang, C. J., Lee, H. H., & Kim, Y.-S. (2009). Effect of P3HT:PCBM concentration in solvent on performances of organic solar cells. *Solar Energy Materials and Solar Cells*, *93*(8), 1263–1267. doi:10.1016/j.solmat.2009.01.019

Brabec, C. J., Sariciftci, N. S., & Hummelen, J. C. (2001). Plastic solar cells. *Advanced Functional Materials*, *11*(1), 15–26. doi:10.1002/1616-3028(200102)11:1<15::AID-ADFM15>3.0.CO;2-A

Burroughes, J. H., Bradley, D. D. C., Brown, A. R., Marks, R. N., Mackay, K., & Friend, R. H. (1990). Light-emitting diodes based on conjugated polymers. *Nature*, *347*(6293), 539–541. doi:10.1038/347539a0

Carroll, D.L., Czerw, R., & Harrisbon, B. (2006). Carbon nanotubepoly(3-octylthiophene) composite photovoltaic cells. *Journal of Nanoscience and Nanotechnology*, *6*, 2204–2207. doi:10.1166/jnn.2006.373

Chen, L.-M., Hong, Z., Li, G., & Yang, Y. (2009). Recent progress in polymer solar cells: Manipulation of polymer: Fullerene morphology and the formation of efficient inverted polymer solar cells. *Advanced Materials (Deerfield Beach, Fla.)*, *21*(14-15), 1434–1449. doi:10.1002/adma.200802854

Cui, H.-N., Teixeira, V., Zhang, J., & Lee, H. (2006). Size controlled nano meter phase structure in thin films of blend polythiophene derivatives. *Thin Solid Films*, *515*(1), 301–306. doi:10.1016/j.tsf.2005.12.108

Dang, M. T., Wantz, G., Hirsch, L., & Parneix, J. P. (2009). Solution processing of polymer photovoltaic solar cells in air or under inert atmosphere. *ECS Transactions*, *23*(1), 449–454. doi:10.1149/1.3183750

Drechsel, J., Mannig, B., Kozlowski, F., Pfeiffer, M., Leo, K., & Hoppe, H. (2005). Efficient organic solar cells based on a double p-i-n architecture using doped wide-gap transport layers. *Applied Physics Letters*, *86*(24), 244102–244103. doi:10.1063/1.1935771

Granström, M., Berggren, M., & Inganäs, O. (1995). Micrometer- and nanometer-sized polymeric light-emitting diodes. *Science*, *267*(5203), 1479–1481. doi:10.1126/science.267.5203.1479

Gustafsson, G., Treacy, G. M., Cao, Y., Klavetter, F., Colaneri, N., & Heeger, A. J. (1993). The "plastic" led: A flexible light-emitting device using a polyaniline transparent electrode. *Synthetic Metals*, *57*(1), 4123–4127. doi:10.1016/0379-6779(93)90568-H

Hauch, J. A., Schilinsky, P., Choulis, S. A., Childers, R., Biele, M., & Brabec, C. J. (2008). Flexible organic P3HT: PCBM bulk-heterojunction modules with more than 1 year outdoor lifetime. *Solar Energy Materials and Solar Cells*, *92*(7), 727–731. doi:10.1016/j.solmat.2008.01.004

Heeger, A. J. (2001). Semiconducting and metallic polymers: The fourth generation of polymeric materials (nobel lecture). *Angewandte Chemie International Edition*, *40*(14), 2591–2611. doi:10.1002/1521-3773(20010716)40:14<2591::AID-ANIE2591>3.0.CO;2-0

Hoppe, H., Drees, M., Schwinger, W., Schaffler, F., & Sariciftcia, N. S. (2005). Nano-crystalline fullerene phases in polymer/fullerene bulk-heterojunction solar cells: A transmission electron microscopy study. *Synthetic Metals*, *152*(1-3), 117–120. doi:10.1016/j.synthmet.2005.07.217

Hoppe, H., Glatzel, T., Niggemann, M., Schwinger, W., Schaeffler, F., & Hinsch, A. (2006). Efficiency limiting morphological factors of MDMO-PPV: PCBM plastic solar cells. *Thin Solid Films*, *511-512*, 587–592. doi:10.1016/j.tsf.2005.12.071

Inganas, O. (2010). Hybrid electronics and electrochemistry with conjugated polymers. *Chemical Society Reviews*, *39*(7), 2633–2642. doi:10.1039/b918146f

Jäger-Waldau, A. (2003). *PV status report 2003. European Commission, EUR 20850*. Geneva, Switzerland: European Commission.

Kawano, K., Ito, N., Nishimori, T., & Sakai, J. (2006). Open circuit voltage of stacked bulk heterojunction organic solar cells. *Applied Physics Letters*, *88*(7), 073514–073513. doi:10.1063/1.2177633

Keawprajak, A., Piyakulawat, P., Klamchuen, A., Iamraksa, P., & Asawapirom, U. (2010). Influence of crystallizable solvent on the morphology and performance of P3HT: PCBM bulk-heterojunction solar cells. = . *Solar Energy Materials and Solar Cells*, *94*(3), 531–536. doi:10.1016/j.solmat.2009.11.018

Kim, J. Y., Lee, K., Coates, N. E., Moses, D., Nguyen, T.-Q., & Dante, M. (2007). Efficient tandem polymer solar cells fabricated by all-solution processing. *Science*, *317*(5835), 222–225. doi:10.1126/science.1141711

Kim, Y., Cook, S., Tuladhar, S. M., Choulis, S. A., Nelson, J., & Durrant, J. R. (2006). A strong regioregularity effect in self-organizing conjugated polymer films and high-efficiency polythiophene:fullerene solar cells. *Nature Materials*, *5*(3), 197–203. doi:10.1038/nmat1574

Koetse, M. M., Sweelssen, J., Hoekerd, K. T., Schoo, H. F. M., Veenstra, S. C., & Kroon, J. M. (2006). Efficient polymer: Polymer bulk heterojunction solar cells. *Applied Physics Letters*, *88*(8), 083504–083503. doi:10.1063/1.2176863

Krebs, F. C. (2009a). Fabrication and processing of polymer solar cells: A review of printing and coating techniques. *Solar Energy Materials and Solar Cells*, *93*(4), 394–412. doi:10.1016/j.solmat.2008.10.004

Krebs, F. C. (2009b). Polymer solar cell modules prepared using roll-to-roll methods: Knife-over-edge coating, slot-die coating and screen printing. *Solar Energy Materials and Solar Cells*, *93*(4), 465–475. doi:10.1016/j.solmat.2008.12.012

Krebs, F. C., Alstrup, J., Spanggaard, H., Larsen, K., & Kold, E. (2004). Production of large-area polymer solar cells by industrial silk screen printing, lifetime considerations and lamination with polyethyleneterephthalate. *Solar Energy Materials and Solar Cells*, *83*(2-3), 293–300. doi:10.1016/j.solmat.2004.02.031

Kymakis, E., & Amaratunga, G. A. J. (2002). Single-wall carbon nanotube/conjugated polymer photovoltaic devices. *Applied Physics Letters*, *80*(1), 112–114. doi:10.1063/1.1428416

Kymakis, E., & Amaratunga, G. A. J. (2004). Optical properties of polymer-nanotube composites. *Synthetic Metals*, *142*(1-3), 161–167. doi:10.1016/j.synthmet.2003.08.011

Kymakis, E., Klapsis, G., Koudoumas, E., Stratakis, E., Kornilios, N., & Vidakis, N. (2006). Carbon nanotube/PEDOT: PSS electrodes for organic photovoltaics. *The European Physical Journal Applied Physics*, *36*(3), 257–259. doi:10.1051/epjap:2006148

Li, G., Shrotriya, V., Yao, Y., Huang, J., & Yang, Y. (2007). Manipulating regioregular poly(3-hexylthiophene): [6,6]-Phenyl-C61-butyric acid methyl ester blends-route towards high efficiency polymer solar cells. *Journal of Materials Chemistry*, *17*(30), 3126–3140. doi:10.1039/b703075b

MacDiarmid, A. G. (2001). Synthetic metals: A novel role for organic polymers (nobel lecture). *Angewandte Chemie International Edition*, *40*(14), 2581–2590. doi:10.1002/1521-3773(20010716)40:14<2581::AID-ANIE2581>3.0.CO;2-2

Manca, J. V., Munters, T., Martens, T., Beelen, Z., Goris, L., D'Haen, J., et al. (2003). *State-of-the-art MDMO-PPV:PCBM bulk heterojunction organic solar cells: Materials, nanomorphology, and electro-optical properties*. Paper presented at SPIE. Seattle, WA.

Martens, T., D'Haen, J., Munters, T., Beelen, Z., Goris, L., & Manca, J. (2003). Disclosure of the nanostructure of MDMO-PPV: PCBM bulk hetero-junction organic solar cells by a combination of SPM and TEM. *Synthetic Metals*, *138*(1-2), 243–247. doi:10.1016/S0379-6779(02)01311-5

Moulé, A. J., & Meerholz, K. (2007). Minimizing optical losses in bulk heterojunction polymer solar cells. *Applied Physics. B, Lasers and Optics*, *86*(4), 721–727. doi:10.1007/s00340-006-2542-1

Nardes, A. M., Kemerink, M., & Janssen, R. A. J. (2007). Anisotropic hopping conduction in spin-coated PEDOT:PSS thin films. *Physical Review B: Condensed Matter and Materials Physics*, *76*(8), 085208. doi:10.1103/PhysRevB.76.085208

Nardes, A. M., Kemerink, M., Janssen, R. A. J., Bastiaansen, J. A. M., Kiggen, N. M. M., & Langeveld, B. M. W. (2007). Microscopic understanding of the anisotropic conductivity of PEDOT: PSS thin films. *Advanced Materials (Deerfield Beach, Fla.)*, *19*(9), 1196–1200. doi:10.1002/adma.200602575

Offermans, T., Meskers, S. C. J., & Janssen, R. A. J. (2006). Electro-optical studies on MDMO-PPV: PCBM bulk-heterojunction solar cells on the millisecond time scale: Trapped carriers. *Organic Electronics*, *7*(4), 213–221. doi:10.1016/j.orgel.2006.02.001

Padinger, F., Rittberger, R. S., & Sariciftci, N. S. (2003). Effects of postproduction treatment on plastic solar cells. *Advanced Functional Materials*, *13*(1), 85–88. doi:10.1002/adfm.200390011

Palmaerts, A., Lutsen, L., Cleij, T. J., Vanderzande, D., Pivrikas, A., & Neugebauer, H. (2009). Development of novel processable electron accepting conjugated polymers containing fluoranthene units in the main chain. *Polymer*, *50*(21), 5007–5015. doi:10.1016/j.polymer.2009.08.031

Park, H. M., Kim, K. H., Lee, S. H., Park, D. H., Hong, Y. K., & Joo, J. (2008). Electrochemical polymerization of polypyrrole (PPy) and poly(3-hexylthiophene) (P3HT) using functionalized single-wall carbon nanotubes. *Colloids and Surfaces A: Physicochemical and Engineering Aspects*, *313-314*, 72–76. doi:10.1016/j.colsurfa.2007.04.077

Parmer, J. E., Mayer, A. C., Hardin, B. E., Scully, S. R., McGehee, M. D., & Heeney, M. (2008). Organic bulk heterojunction solar cells using poly(2,5-bis(3-tetradecyllthiophen-2-yl) thieno[3,2,-b]thiophene). *Applied Physics Letters*, *92*(11), 113309–113303. doi:10.1063/1.2899996

Platzer-Björkman, C., Zabierowski, P., Pettersson, J., Törndahl, T., & Edoff, M. (2010). Improved fill factor and open circuit voltage by crystalline selenium at the Cu(In,Ga)Se2/buffer layer interface in thin film solar cells. *Progress in Photovoltaics: Research and Applications*, *18*(4), 249–256.

Reyes-Reyes, M., Kim, K., & Carroll, D. L. (2005). High-efficiency photovoltaic devices based on annealed poly(3-hexylthiophene) and 1-(3-methoxycarbonyl)-propyl-1- phenyl-(6,6) C[sub 61] blends. *Applied Physics Letters*, *87*(8), 083506–083503. doi:10.1063/1.2006986

Roncali, J. (2009). Molecular bulk heterojunctions: An emerging approach to organic solar cells. *Accounts of Chemical Research*, *42*(11), 1719–1730. doi:10.1021/ar900041b

Sariciftci, N. S., Smilowitz, L., Heeger, A. J., & Wudl, F. (1992). Photoinduced electron transfer from a conducting polymer to buckminsterfullerene. *Science*, *258*(5087), 1474–1476. doi:10.1126/science.258.5087.1474

Shaheen, S. E., Brabec, C. J., Sariciftci, N. S., Padinger, F., Fromherz, T., & Hummelen, J. C. (2001). 2.5% efficient organic plastic solar cells. *Applied Physics Letters*, *78*(6), 841–843. doi:10.1063/1.1345834

Shirakawa, H. (2001). The discovery of polyacetylene film: The dawning of an era of conducting polymers (nobel lecture). *Angewandte Chemie International Edition*, *40*(14), 2574–2580. doi:10.1002/1521-3773(20010716)40:14<2574::AID-ANIE2574>3.0.CO;2-N

Shirakawa, H., McDiarmid, A., & Heeger, A. (2003). Twenty-five years of conducting polymers. *Chemical Communications*, *1*, 1–4. doi:10.1039/b210718j

Shrotriya, V., Wu, E. H.-E., Li, G., Yao, Y., & Yang, Y. (2006). Efficient light harvesting in multiple-device stacked structure for polymer solar cells. *Applied Physics Letters*, *88*(6), 064104–064103. doi:10.1063/1.2172741

Song, Y. J., Lee, J. U., & Jo, W. H. (2010). Multi-walled carbon nanotubes covalently attached with poly(3-hexylthiophene) for enhancement of field-effect mobility of poly(3-hexylthiophene)/multi-walled carbon nanotube composites. *Carbon*, *48*(2), 389–395. doi:10.1016/j.carbon.2009.09.041

Stefopoulos, A. A., Chochos, C. L., Prato, M., Pistolis, G., Papagelis, K., & Petraki, F. (2008). Novel hybrid materials consisting of regioregular poly(3-octylthiophene)s covalently attached to single-wall carbon nanotubes. *Chemistry (Weinheim an der Bergstrasse, Germany)*, *14*(28), 8715–8724. doi:10.1002/chem.200800683

Tang, C. W. (1986). Two-layer organic photovoltaic cell. *Applied Physics Letters*, *48*(2), 183–185. doi:10.1063/1.96937

Tremolet de Villers, B., Tassone, C. J., Tolbert, S. H., & Schwartz, B. J. (2009). Improving the reproducibility of P3HT: PCBM solar cells by controlling the PCBM/cathode interface. *The Journal of Physical Chemistry C*, *113*(44), 18978–18982. doi:10.1021/jp9082163

Wagner, J., Gruber, M., Hinderhofer, A., Wilke, A., Bröker, B., & Frisch, J. (2010). High fill factor and open circuit voltage in organic photovoltaic cells with diindenoperylene as donor material. *Advanced Functional Materials*, *20*(24), 4295–4303. doi:10.1002/adfm.201001028

Yu, G., Gao, J., Hummelen, J. C., Wudl, F., & Heeger, A. J. (1995). Polymer photovoltaic cells: Enhanced efficiencies via a network of internal donor-acceptor heterojunctions. *Science*, *270*(5243), 1789–1791. doi:10.1126/science.270.5243.1789

Chapter 8
Organic Solar Cells Modeling and Simulation

Mihai Razvan Mitroi
Polytechnic University of Bucharest, Romania

Laurentiu Fara
Polytechnic University of Bucharest, Romania & Academy of Romanian Scientists, Romania

Andrei Galbeaza Moraru
Polytechnic University of Bucharest, Romania

ABSTRACT

Modeling and simulation of organic (polymer, dye sensitized, and nanotube) solar cells is discussed. High J-V theoretical curves, the calculation of key parameters, and also the relative influence of different parameters on the cell operation, are evidenced and analyzed. On this basis, the authors obtain information on the optimization of the solar cell design and manufacturing.

MODELING AND SIMULATION OF ORGANIC CELLS BASED ON POLYMERS

Introduction

The polymer-based photovoltaic devices present some important advantages, such as the low cost and the easy manufacturing from thin films by chemical/physical vapour deposition, screen-printing, or casting. The band gap of the films can be adjusted by chemical synthesis to convenient values and the carrier mobility can reach 10 $cm^2/V{\cdot}s$ (Dimitrakopoulos & Mascaro, 2001; Kwok, 2003). Therefore, the polymer-based photovoltaic cells are competitive with those based on amorphous silicon, so that the interest for both the properties of the polymer materials and the characteristics of the polymer-based cells increases.

The first structure was a Schottky diode type structure, which has a conversion efficiency under 1%. In 1986, Tang (1986) introduced the planar donor-acceptor heterojunction, which has a higher conversion efficiency. Hiramoto, Fujiwara, and Yokoyama (1991) developed this idea. Tang introduced the concept of Bulk Heterojunction—BH. Xue et al. (2005) introduced the concept of Hybrid Heterojunction (HH) with higher efficiency 5%.

DOI: 10.4018/978-1-4666-1927-2.ch008

Solar cells based on organic polymers used photoinduced transfer of electrons from semiconductor polymers, donor / acceptor polymers or acceptor molecules (such as C_{60}). Pairs of layers polymer / fullerene have a poor conversion efficiency of solar cell. Nanomorfological control at nanoscale of the separate regions in an interlaced network (BH) significantly increased the conversion efficiency of solar energy cells made of MDMO-PPV/C_{60}. Typical dimensions of the separate regions must be smaller than the exciton diffusion length. On the other hand, bicontinue percolation paths for the transport of charge carriers at the electrodes must be provided in order to increase the transport of charge carriers in organic and polymeric materials, and for mesoscopic order to improve crystallinity. So, an interlaced network at nanoscale with crystalline order of the both constituents is formed (these ones belong to individual sub-networks). Such a network is a convenient structure for the active layer of polymer PV devices. At the same time, forbidden bands of the photoactive layer materials should be chosen in order to absorb more light in solar radiation spectrum.

Using a mixture of MDMO-PPV soluble fullerene derivative (for example PCBM), it is possible to obtain solar cells with a 2.5% conversion efficiency.

It was shown (Shaheen, et al., 2001) that a conversion efficiency of 2.5% (for AM 1.5) can be obtained using chlorobenzenes as a solvent for the deposition by centrifuging in the mass ratio of 1:4 for the MDMO- PPV: PCBM. Using chlorobenzenes instead of toluene nanomorfology changes were remarked and the efficiency conversion increases 3 times . Such BH solar cells contain 80% PCBM . However, the MDMO-PPV polymer could be the main light absorber from these solar cells, because PCBM does not achieve almost no absorption in the visible and near infrared region. So an increase in volume concentration of MDMO-PPV was necessary for a better absorption of sunlight.

Figure 1. Schematic representation of standard bulk heterojunction solar cell

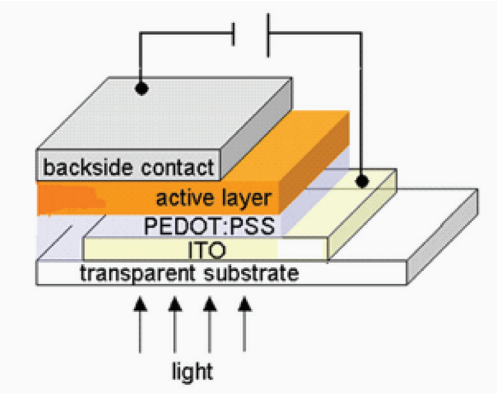

The electron mobility from pure PCBM is proved to be higher $(\sim 10^{-3}\ \mathrm{cm}^2/\mathrm{Vs})$ compared to the holes mobility from the MDMO-PPV $(\sim 10^{-4}\ \mathrm{cm}^2/\mathrm{Vs})$ and the holes mobility in the mixture increases with the increasing of fullerene mass, despite of the fact that the addition of fullerene introduces more defects (which would reduce the mobility).

By replacing in PCBM the C_{60} fullerene with C_{70} one, the HOMO-LUMO transition would be easier and would increase the absorption of light. An improved efficiency of BH solar cells in isomeric mixture of MDMO-PPV and C_{70} derivatives was obtained (Wienk, et al., 2003). Mixtures of this kind are suitable when they are prepared from a solution of o-dichlorobenzene (ODCB) and solar cells have a conversion efficiency of $\eta = 3\ \%$ for PM 1.5.

Operating Principle of Polymer-Based Solar Cell

The process of conversion of light into electricity using a organic solar cell (Figure 1) can be plotted by the following steps: 1) absorption of a photon determining the formation of an excited state, that is, the creation of an exciton (electron-hole pair); 2) exciton diffusion to a region where dissociation occurs; 3) charge transport within the organic semiconductor to the respective electrodes.

The obtained photo-voltage is a direct result of the departure from thermodynamic equilibrium state after the movement of charge carriers, generated by solar radiation under the action of local fields, which in the case of organic semiconductors is due to the change in chemical composition. Because of the large band gap in organic materials, only a small portion of the incident solar light is absorbed. A band gap of 1.1 eV (1100 nm) is able of absorbing 77% of the solar irradiation on Earth (Nunzi, 2002). But, the majority of semiconducting polymers have band gaps higher than 2 eV (620 nm), which limits the possible harvesting of solar photons to about 30% (Nunzi, 2002). On the other hand, because the absorption coefficients of organic materials are higher than 10^5 cm^{-1}, only 100 nm thickness is enough to absorb most of the photons when a reflective back contact is used.

The primary photoexcitations in organic materials do not influence directly the release of charge carriers, but determine to obtain the electron-hole pairs (it is estimated that only 10 % of photoexcitations leads to the free charge carriers in conjugated polymers). For an efficient dissociation of excitons, strong electric fields are necessary.

At an interface, where sudden changes of the potential energy occur, strong local electrical fields are possible ($E = -grad\ U$). Photoinduced charge transfer can occur when the exciton has reached such an interface within its lifetime. Therefore, the exciton diffusion length limits the thicknesses of the double layers. Exciton diffusion length should be the same order of magnitude with the separation distance between donor and acceptor fields. Otherwise, the excitons recombine radiatively or non-radiatively before reaching the interface and their energy no longer contributes to solar energy conversion. Exciton diffusion length in organic polymers is usually around 10÷20 nm.

In the materials obtained by combining conjugated polymers with the acceptor materials, as fullerenes, the efficiency of converting the photogenerated excitons to free charge carriers increases. By the absorption of light in a donor an excited state from which the electron can be transferred to the LUMO unoccupied orbital of the acceptor arises. Following the transfer, the hole that appears remains in the donor material. Measurements showed that the photoinduced charge transfer in such a compound occurs in $45\ fs$, so in a much smaller time than other similar processes (e.g. photoluminescence transition lasts around 1 ns) (Brabec, et al., 2001).

Charge carriers are extracted from the device by two selective contacts. A contact of Indium and Tin Oxide (ITO) with a Fermi level of about 4.8eV matches with the HOMO levels of most conjugated polymers (contact holes), and a contact of aluminum with a Fermi level of roughly 4.3.eV matches with the LUMO of the PCBM acceptor (contact for electrons).

Theoretical Models

A number of models were developed aimed to the modeling and simulation of the organic solar cells based on polymers. Many of these models based on the diode-like equivalent circuit of a solar cell are analysing the $J - V$ characteristics; they can simulate the cell behaviour and/or evaluate their macroscopic parameters (Aernouts, 2006; Marlein & Burgelman, 2007; Marlein, Decock, & Burgelman, 2009; Greulich, et al., 2010; Chuan, et al., 2011).

In the absence of illumination typical current density-voltage characteristics of a solar cell is shown in Figure 2a; in the presence of illumination it is shown in Figure 2b.

In the following a modeling and simulation analyses is presented (Mitroi, Iancu, Fara, & Ciurea, 2010).

To represent a solar cell under illumination, an equivalent electronic circuit can be drawn as shown in Figure 3. It consists basically from a

Figure 2. Current density-voltage characteristic in the absence of illumination

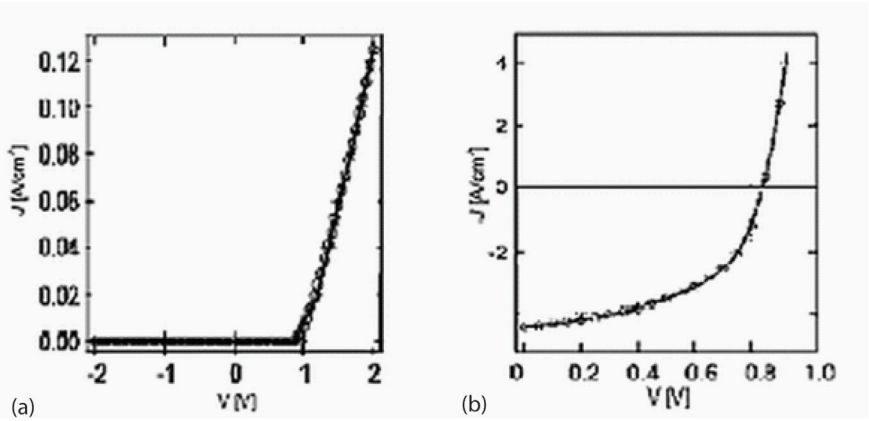

Figure 3. The diode-like equivalent circuit of a solar cell under illumination

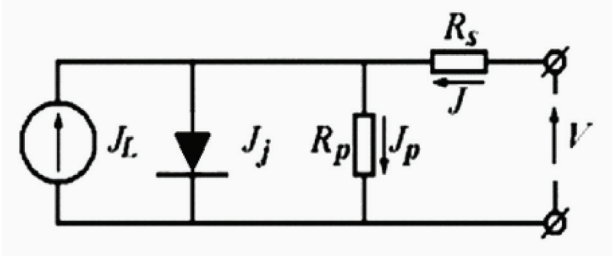

constant current source parallel to a diode. This current source is supposed to be bias independent and represents the current J_L, generated in the device due to the incoming light. Its value might thus vary according to the intensity of the illumination. A series and parallel resistance, R_s and R_p respectively, are additionally included to account for non-ideal behavior.

Under illumination the total current density is:

$$J = J_s\left\{\exp\left[\frac{e\left(V - R_s J\right)}{\gamma\, k_B T}\right] - 1\right\} + \frac{V - R_s J}{R_p} - eG\mu\tau\left(\frac{V_{bi} - V}{L}\right) \cdot\left[1 - \exp\left(\frac{L^2}{\mu\tau\left(V_{bi} - V\right)}\right)\right] \qquad (1)$$

where J_s is the saturation current density, $e > 0$ is the elementary charge, V is the applied voltage, R_s and R_p are the linear series and derivation resistances, γ is the ideality factor, k_B is the Boltzmann constant, and T is the cell temperature, G is the pair generation rate, V_{bi} is the bias voltage, V is the voltage on a external resistance R_{ext}, L is the thickness of the active layer, and the product $\mu\tau$ is given by the relation:

$$\mu\tau = \mu_p\tau_p + \mu_n\tau_n\,, \qquad (2)$$

where μ_p, μ_n, and τ_p, τ_n are the hole and electron mobilities and lifetimes, respectively. This product obviously depends on the recombination and carrier transport processes.

The effect of R_s and R_p on the illuminated J-V characteristics is shown in Figure 4.

Figure 4. Parallel and series resistance influence on the J-V characteristic of the cell

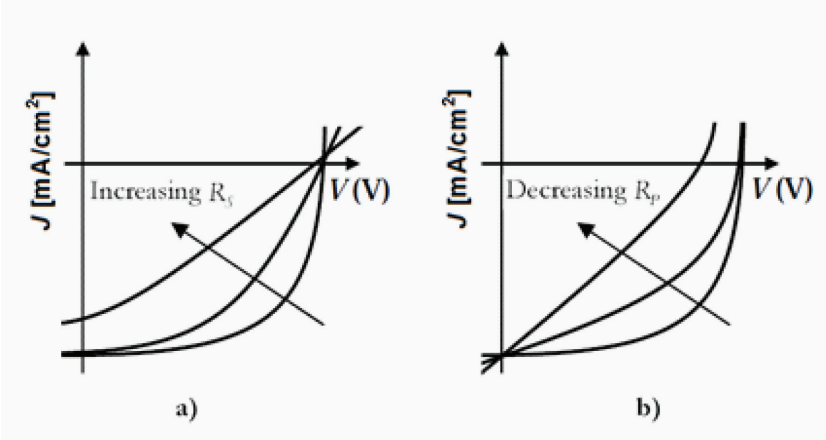

This resistances act to reduce the fill factor, whereas very high values of R_s and very low values of R_p can also reduce J_{sc} and V_{oc}, respectively.

From the Formula (1) the following relationships results:

$$J_{sc} = J_s\left\{\exp\left[\frac{e\left(-R_s J_{sc}\right)}{\gamma\, k_B T}\right]-1\right\} - \frac{R_s J_{sc}}{R_p} - eG\mu\tau\left(\frac{V_{bi}}{L}\right)\cdot\left[1-\exp\left(\frac{L^2}{\mu\tau V_{bi}}\right)\right] \tag{3}$$

and

$$J_s\left\{\exp\left[\frac{eV_{oc}}{\gamma\, k_B T}\right]-1\right\} + \frac{V_{oc}}{R_p} - eG\mu\tau\left(\frac{V_{bi}-V_{oc}}{L}\right) \cdot\left[1-\exp\left(\frac{L^2}{\mu\tau\left(V_{bi}-V_{oc}\right)}\right)\right] = 0 \tag{4}$$

Equations (3) and (4) allow the calculation of the short-circuit current density J_{sc} and the open circuit voltage V_{oc}, respectively. Based on *J-V* theoretical curve, the Fill Factor (*FF*), and the energy conversion efficiency (η) are defined as:

The Fill Factor (FF):

$$FF = \frac{V_M J_M}{V_{oc} J_{sc}} = \frac{P_M}{V_{oc} J_{sc}}, \tag{5}$$

where $P_M = V_M J_M$ is the maximum power density. V_M and J_M are the corresponding voltage and current density and they are determined from the $J-V$ curve.

The power conversion efficiency (η)

$$\eta = \frac{P_M}{P_L}\cdot 100\ \% = \frac{V_M J_M}{P_L}\cdot 100\ \%, \tag{6}$$

where P_L is the incident light flux power density.

Results and Discussion

The analyzed model allows the determination of the main parameters of the cell: the saturation current density J_s, the series and derivation (parallel) linear resistances R_s and R_p, the ideality factor γ, the product $\mu\tau$, the pair generation rate G, the built-in voltage V_{bi}, the short-circuit current

density J_{sc}, the open-circuit voltage V_{oc}, the fill factor *FF* and the power conversion efficiency η. These parameters describe both the physical nature of the active layer and the technological characteristics of the cell.

From the Equation (3), one can see that *J* depends on seven parameters: J_s, R_s, R_p, μ, τ, γ, *G*, and V_{bi}. These parameters can be obtained by fitting the experimental data for the $J-V$ characteristics with this formula. These values were then introduced in the equation (8.1), and theoretical curves can be drawn (see Figure 5). Theoretical curves are obtained using the values of J_M and V_M. Then by solving the system of Equations (3) and (4), J_{sc} and V_{oc} could be obtained, and by using the Equations (5) and (6) *FF* and η could be calculated.

The dependences of the fill factor and the power conversion efficiency on the thickness of the active layer highlights the following results (Mitroi, Iancu, Fara, & Ciurea, 2010): the fill factor has a maximum at $L \approx 120\,\text{nm}$, namely $FF_{max} \approx 44.5\,\%$, while the power conversion efficiency has a maximum of $\cdot_{max} \approx 1.22\,\%$ at $L \approx 230\,\text{nm}$.

Conclusion

This model highlights the properties to be considered for improvement of photovoltaic cells based on organic polymers. Results obtained using this model are consistent with those reported in the literature (Nelson, 2003; Dennler, et al., 2006; Greulich, et al., 2010).

The model allows the determination of all the main parameters of the cell: the saturation current density J_s, the series and derivation (parallel) linear resistances R_s and R_p, the ideality factor γ, the product $\mu\tau$, the pair generation rate *G*, the bias voltage V_{bi}, the short-circuit current density J_{sc}, the open circuit voltage V_{oc}, the fill factor *FF*, and the conversion efficiency η. These parameters describe both the physical nature of the active layer and the technological characteristics of the cell. In addition, this model can determine the influence of various parameters on the total current density, fill factor and, importantly, the conversion efficiency.

The appearance of a maximum of the conversion efficiency leads to the optimization of such solar cells design and manufacturing.

Figure 5. J – V characteristics for the investigated cell

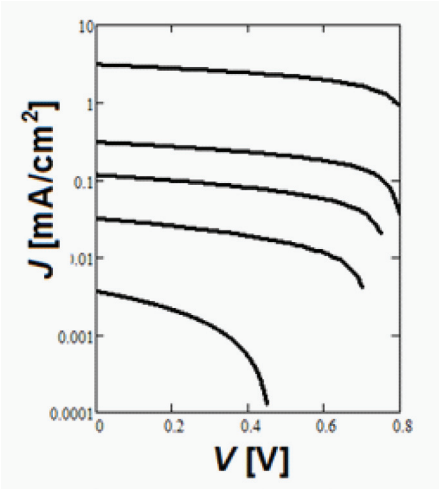

MODELING AND NUMERICAL SIMULATION OF DYE-SENSITIZED SOLAR CELLS

Introduction

Dye-Sensitized Solar Cells (DSSC) are based on sensitized nanostructures or mesoporous metal oxides. DSSC have attracted considerable attention starting from the work of O'Regan and Grätzel (1991; Grätzel, 2003).

Dye Sensitized Solar Cell (DSSC) is the only one that can offer both the flexibility and transparency.

Although, good results were obtained using DSSC both with nanostructures of TiO_2 and

ZnO electrodes, ionic liquid electrolytes, carbon nanotubes, graphene and solid state DSSC (Cheng & Hsieh 2010**;** Nazeeruddin, et al., 2005; Gao, et al., 2008; Giannouli, et al., 2010; Meng, et al., 2003; Zhang & et al., 2004), maximum efficiency of such devices was only 11% (Chiba, et al., 2006), in comparison with other reported results (Zhao, et al., 1998; Contreras, et al., 1999; King, et al., 2007). These cells have potentially reduced fabrication costs in comparison with conventional silicon-based solar cells, due to the low costs of materials and the facility of the fabrication process. An optimization of DSSC requires a better insight into the interrelated processes of transport and accumulation of electrons in the mesoporous oxide phase and recombination of electrons with electron acceptors (Ferber & Luther, 2001; Knodler, et al., 1993; Smestad, Bignozzi, & Argazzi, 1994). Charge generation, transport, and recombination in DSSC are generally described by a continuity equation, in which transport is assumed to be purely diffusive, i.e. driven by concentration gradients only. However, time-dependent characterization techniques have later shown that charge transport through the TiO_2 film is impaired by multiple trapping/detrapping events (Bisquert & Vikhrenko, 2004).

Theoretical Model

The device structure of the DSSC used in our model is presented in Figure 6. Sensitive dye solar cell is formed by a TiO_2 electrode nanopores; the pores are filled with an iodine redox electrolyte / triodura, coated with a dye that provides absorbing and transferring light task.

The two glass electrodes are made of transparent conducting electrode (fluorine-doped tin oxide, FTO). The front electrode is a transparent conductive oxide glass (FTO) coated with nanoporous TiO_2 covered with a monolayer of the Ruthenium-complex dye; the counter electrode is a FTO glass coated with a thin layer of platinum (~5 nm), where it regenerates the oxidized mediator. The gap between the two electrodes is filled by an electrolyte containing an iodide/tri-iodide (I^- / I_3^-) redox couple. Besides two different anions, the electrolyte also consists of cations being introduced by ionic liquid, usually by propylmethyl-imidazolium iodide. The cations provide electro-neutrality of the electrolyte; nevertheless they are not involved in the charge transport process in dye-sensitized solar cells.

Figure 6. Device structure of the dye-sensitized solar cell

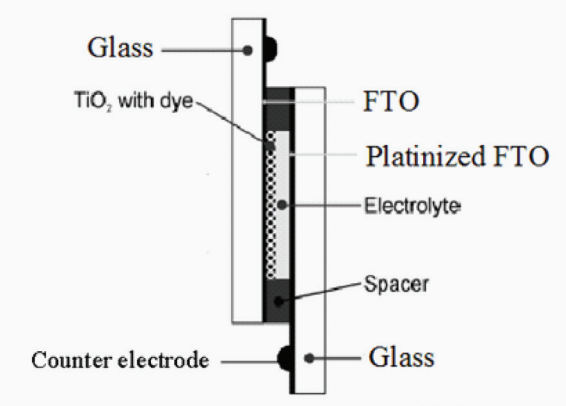

Figure 7 shows the mechanism of a traditional wet-type DSSC containing redox couples in electrolyte. Under illumination, the dye molecules become excited and initial charge separation occurs in a femtosecond time regime by injection of an electron from the dye into the conduction band of the TiO_2. This electron is transported to the external load via the nanostructured TiO_2 and TCO, while the positively charged photo-excited (S^+) dye is restored to its ground state (S) in a nanosecond time regime by receiving an electron from the iodide (I^-) (Wei, D., 2010).

Regeneration of iodide ions, which are oxidized in this reaction to tri-iodide, is achieved at a platinised counter electrode, according to Equations (7), (8), (9), (10), (11), and (12):

$$TiO_2|S + h\nu \rightarrow TiO_2|S^* \quad (7)$$

Figure 7. The energy level scheme and the operating principle of a DSSC

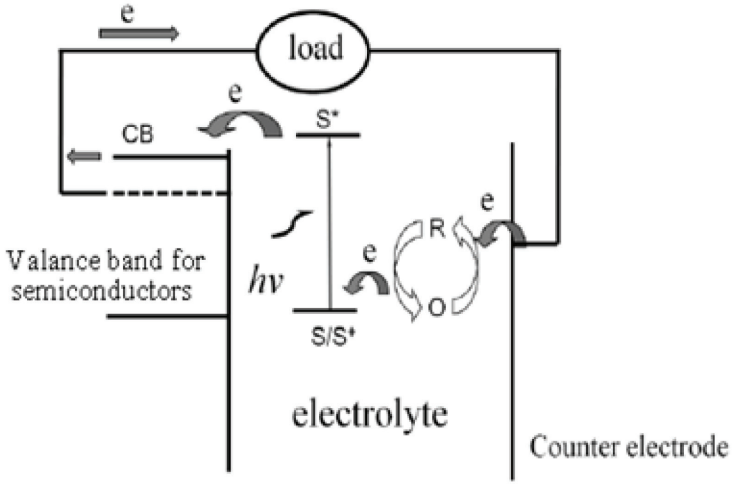

$$TiO_2\left|S^* \rightarrow TiO_2\right|S^+ + e \tag{8}$$

$$TiO_2\left|S^+ + e \rightarrow TiO_2\right|S \tag{9}$$

$$TiO_2\left|S^+ + \frac{3}{2}I^- \rightarrow TiO_2\right|S + \frac{1}{2}I_3^- \tag{10}$$

$$\frac{1}{2}I_3^- + e \rightarrow \frac{3}{2}I^- \tag{11}$$

$$I_3^- + 2e \rightarrow 3I^- \tag{12}$$

In these equations, *S* represents the dye sensitizer.

Iodide is subsequently regenerated by the reduction of tri-iodide (I_3 –) at the counter electrode (Equation 12) to complete the circuit.

The Pt on the counter electrode acts as a catalyst for the reduction of tri-iodide. So far, the highest reported efficiency for a small area (< 0.2 cm^2) DSSC is 11.3%, using acetonitrile electrolytes (Grätzel, 2006) while great effort is still devoted to enhance the recorded efficiency.

Electrical Model

We will present a electric model of dye-sensitized solar cell where the active layer is modelled as a one dimensional pseudo-homogeneous layer. The electro active particles included in the model are generated by free electrons injected in nanoporous TiO_2; iodide and tri-iodide ions and cations are introduced into the cell together with electrolyte. The electrical model is based on continuity, transport, and Poisson's non-linear differential equations and permits the steady-state calculation of the complete *J-V* characteristics, concentration of electro active species and their current densities in dye-sensitized solar cells (Oda, Tanaka, & Hayase, 2006; Ferber, Stangl, & Luther, 1998; Soedergren, Hagfeldt, Olsson, & Lindquist, 1994; Smestad, Bignozzi, & Argazzi, 1994).

The first important equation that connects generations and recombinations of dye-sensitized solar cell is a continuity equation for conduction band electrons:

$$-\frac{1}{e}\frac{dJ}{dx} = G(x) - R(x) \tag{13}$$

Here, *e* is the elementary charge, *x* represents the position inside the TiO_2 film thickness in interval [0, *d*], *G(x)* is the electron injection rate, determined from the optical model, *R(x)* is the recombination rate.

We assume that only electrons from the conduction band can recombine with tri-iodide in the electrolyte and that the recombination rate is linear in $n(x) - \overline{n}$:

$$R(x) = \frac{n(x) - \overline{n}}{\tau} \tag{14}$$

Here, τ is the lifetime of the conduction band electrons and $\overline{n}$ is the electron number density at equilibrium in the dark.

The movement of all four charged species in pseudo-homogeneous medium could be described by transport equations:

$$-\frac{1}{e}\frac{dJ_e(x)}{dx} = D_e \frac{d\,n_e(x)}{dx} + \mu_e\, n_e(x)E(x) \tag{15}$$

$$-\frac{1}{e}\frac{dJ_{I^-}(x)}{dx} = D_{I^-} \frac{d\,n_{I^-}(x)}{dx} + \mu_{I^-}\, n_{I^-}(x)E(x) \tag{16}$$

$$-\frac{1}{e}\frac{dJ_{I_3^-}(x)}{dx} = D_{I_3^-} \frac{d\,n_{I_3^-}(x)}{dx} + \mu_{I_3^-}\, n_{I_3^-}(x)E(x) \tag{17}$$

$$-\frac{1}{e}\frac{dJ_c}{dx} = -D_c \frac{d\,n_e(x)}{dx} + \mu_c\, n_c(x)E(x) \tag{18}$$

where D_e, D_{I^-}, $D_{I_3^-}$, and D_c are the diffusion coefficients, n_e, n_{I^-}, $n_{I_3^-}$, and n_c are electron, iodide, tri-iodide and cations concentrations, μ_e, μ_{I^-}, $\mu_{I_3^-}$, and μ_c are the mobilities of the individual charged spices, while $E(x)$ is the electrical field. Relation between diffusion coefficient and mobility of the same charged species could be described with the Einstein relation:

$$D = \frac{k_B T}{e}\mu \tag{19}$$

where k_B is the Boltzman constant and *T* is thermodynamic temperature.

Optical Model

The optical model is based on the Lambert-Beer law to determine the electron injection rate $G_e(x)$. The rate of incident photons flux is given by:

$$G_\lambda(x) = \int_{\lambda_1}^{\lambda_2} \alpha(\lambda)\,\varphi(\lambda)\exp\left(-\alpha(\lambda)\cdot x\right) d\lambda \tag{20}$$

Where λ is the wavelength of radiation, limits λ_1, λ_2 are imposed by the characteristics of absorptance α (λ) of dye used, φ (λ) is the incident photon flux density, and *x* is the distance from the illuminated surface of the cell to the point found inside the cell.

The incident photon flux density is reduced due to absorptance, reflectance and glass substrates (Smestad, Bignozzi, & Argazzi, 1994), and relation (20) becomes:

$$G_\lambda(x) = \beta \cdot G_\lambda(x) \tag{21}$$

Here β is a factor that shapes the reflectance and absorptance.

The electron injection rate $G_e(x)$ is obtained multiplying the relation (21) with the injection efficiency η_{inj} :

$$G_e(x) = \eta_{inj} \cdot \beta \cdot G_\lambda(x) \tag{22}$$

If the quasi-equilibrium approximation is used (one single quasi-Fermi level for conduction band

and trapped electrons), then, under steady-state conditions, the continuity equation does not include terms due to trapping/detrapping.

Boundary Conditions

Boundary conditions, in the integral form, are necessary to solve a coupled set of non-linear differential equations.

Conditions of preserving the total number of particles for each type of charge are:

$$\int_0^d n_c(x)dx = n_c^0 \cdot d \tag{23}$$

$$\int_0^d \left(\frac{1}{3} n_{I^-}(x) + n_{I_3^-}(x)\right)dx = \left(\frac{1}{3} n_{I^-}^0 + n_{I_3^-}^0\right)\cdot d \tag{24}$$

$$\int_0^d \left(\frac{1}{3} n_{I^-}(x) + \frac{1}{2} n_e(x)\right)dx = \left(\frac{1}{3} n_{I^-}^0 + \frac{1}{2} n_e^0\right)\cdot d \tag{25}$$

The boundary conditions which assure electroneutrality of solar cells are:

$$\int_0^d \left(n_e(x) + n_{I^-}(x) + n_{I_3^-}(x)\right)dx = \left(n_e^0 + n_{I^-}^0 + n_{I_3^-}^0\right)\cdot d \tag{26}$$

$$\int_0^d \left(n_e(x) + n_{I^-}(x) + n_{I_3^-}(x) - n_c(x)\right)dx = 0 \tag{27}$$

The electric field at both boundaries equals zero, i.e.:

$$E(0) = E(d) = 0 \tag{28}$$

The electron current density at the front TCO $(x = 0)$ equals to external current density:

$$J_e(0) = J_{ext} \tag{29}$$

No electron transfer exists at $x = d$ since there is no TiO_2 layer and only a tiny bulk electrolyte layer exists:

$$J_e(d) = 0 \tag{30}$$

The opposite is true for iodide and tri-iodide ions where the iodide and tri-iodide current densities at $x = 0$ equals 0.

The cell's voltage, V, is calculated by the following relation:

$$V = \frac{1}{e}\left(E_F^n(0) - E_R(d)\right) \tag{31}$$

Here, $E_F^n(0)$ is the Fermi level of TiO_2 at the TCO-TiO_2 interface which is determined from the concentration of free electrons at TCO-TiO_2 interface $n_e(0)$:

$$E_F^n(0) = E_{CB} + k_B \cdot T \cdot \ln\left(\frac{n_e(0)}{N_{CB}}\right) \tag{32}$$

where N_{CB} is the effective density:

$$N_{CB} = 2 \cdot \left(\frac{2 \cdot \pi \cdot m_e^* \cdot k_B \cdot T}{h^2}\right)^{\frac{3}{2}} \tag{33}$$

and m_e^* is the effective electron mass, h is Planck's constant, and E_R (d) is the redox potential at counter electrode (the deviation of E_R from equilibrium value due to diffusion limitation is not taken into account).

Results and Discussion

For the numerical simulation, incident photon flux density was calculated using the global dis-

tribution of the solar spectrum type AM1.5, between the limits $\lambda_1 = 300\,nm$ and $\lambda_2 = 800\,nm$, because ruthenium was considered as dye. It was chosen because it is one of the dyes commonly used, and has values of $\alpha(\lambda)$ during the (λ_1, λ_1) range (Ferber, Stangl & Luther, 1998). The model permits the steady-state calculation of the complete *J-V* characteristic, electro active spices densities and their current densities in dye-sensitized solar cell. Such a current-voltage characteristic for illuminated DSSC is shown in Figure 8.

Using the simulated *J-V* characteristics could be determined the following parameters:

The fill factor:

$$FF = \frac{V_M J_M}{V_{oc} J_{sc}} = \frac{P_M}{V_{oc} J_{sc}}, \tag{34}$$

where $P_M = V_M J_M$ is the maximum power density; V_M and J_M are the corresponding voltage and current density and they are determined from the *J-V* curve.

The conversion efficiency:

$$\eta = \frac{P_M}{P_L} \cdot 100\,\% = \frac{V_M J_M}{P_L} \cdot 100\,\%, \tag{35}$$

where P_L is the incident light flux power density.

Conclusion

The method allow simulated *J-V* characteristics of dye-sensitized solar cells and determination of all main parameters characterizing solar cells: the short-circuit current density J_{sc}, the open circuit voltage V_{oc}, the fill factor *FF* and the conversion efficiency η. These parameters describe both the physical nature of the active layer and the technological characteristics of the cell.

- The used method also enable to determine the influence of the different parameters of the cells on the total current density, the fill factor and, the most important, the conversion efficiency.
- Internal electric field has low values, up to 1 mV / cm, confirming that transport tasks are carried out mainly by diffusion.
- The results based on such a model (Wenger, et al., 2009; Berginc, et al., 2009; Wenger, 2010) are consistent with theoretical results reported by different authors (Oda, Tanaka, & Hayase, 2006; Ferber, Stangl, & Luther, 1998; Oda, Tanaka, & Hayase, 2006; Ferber, Stangl, & Luther, 1998; Green, et

Figure 8. The typical simulated J-V characteristics for illuminated DSSC

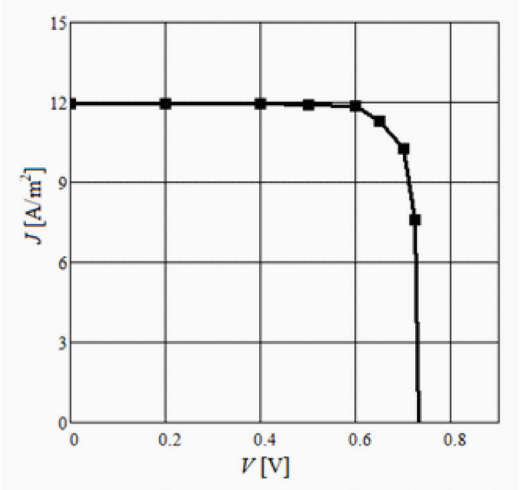

al., 2011; Bowers, et al., 2010; Lai, et al., 2010; Agnaldo, et al., 2009; Hardin, et al., 2009; Deb, 2004; Yong, et al., 2008; Tian, et al., 2011).

NUMERICAL SIMULATION OF HIGH-ORDER TIO$_2$ NANOTUBE DYE-SENSITIZED SOLAR CELLS

Introduction

The electron-collecting layer in a DSSC is typically a 10 mm thick nanoparticle film, with a three-dimensional network of interconnected 15÷20 nm sized nanoparticles (Gratzel, 2004). The slow percolation of electrons (through the three-dimensional network) and low absorption of photons are two major factors which are limiting the conversion efficiency of DSSC cells using nanoparticles (Law, et al., 2005).

By using the nanotubes we could obtain a considerable increase in the photo- conversion of the DSSC. This is due to the improvement of the electrons transport in comparison to the nanoparticles one (Adachi, et al., 2010; Cummings, 2002).

In the last years, two different methods of obtaining Dye Sensitized Solar Cells have been studied (Mor, et al., 2006; Wang, et al., 2010; Flores, et al., 2007; Martinson, et al., 2007; Myahkostupov, et al., 2011), both aiming to develop new structures with improved properties in comparison with TiO_2 nanoparticles.

The arrangement of the highly ordered titania nanotube array perpendicular to the surface permits facile charge transfer along the length of the nanotube from the solution to the conductive substrate and simultaneously reduce the losses incurred by charge hopping across the nanoparticle grain boundaries (Gratzel, 2004; Law, et al., 2005; Tenne & Rao, 2004; Adachi, et al., 2003).

The enhancement in the electronic transport also allows the improved light harvesting as thicker films can be used to increase the optical density, thus improving the absorption of low-energy photons in the red and infrared without losing the additionally harvested charge carriers for recombination (Law, et al., 2005).

A highly-order TiO_2 nanotube dye-sensitized solar cell (Figure 9) consists of a TiO_2 nanotube electrode, coated with a suitable light-absorbing charge-transfer dye and wetted with an iodide/triiodide redox electrolyte. This compound is sandwiched between two Transparent and Conducting Oxide (TCO) glass. Usually fluorine doped SnO_2, exhibiting metallic conductivity, is used as the TCO. The TCO layer on the back glass substrate is covered with sputtered platinum, which acts as a catalyst for the redox reaction.

Theoretical Model

The simulation model (www.paper.edu.cn/index.php/default/feature/downCount/815) having a TiO_2 barrier layer, an electrolyte layer in TiO_2 nanotubes and a bulk electrolyte layer. This model introduces the TiO_2 barrier layer and the distinction between the electron transfer rate in the nanotube and in the nanoporous layer. The electrical model is based on that proposed by Ferber (Ferber, et al., 1998) and Oda (Oda, et al., 2006).

In the developed model (www.paper.edu.cn/index.php/default/feature/downCount/815), the electric field E has been ignored because of the negligible effect on charge carriers in the cell (Ferber, et al., 1998). A system of differential equations is obtained which is solved using the finite difference method (Ferber, et al., 1998). The equation system used in this model is very similar with the presented one. In this model, the ions n_{I^-}, $n_{I_3^-}$, and cations n_c depend on the porosity of TiO_2 nanotube layer. Figure 10 shows the view of nanotube arrays.

The porosity of nanotubes films is given by:

Figure 9. Scheme of a cell structure with nanotube DSSC (Mor, et al., 2006)

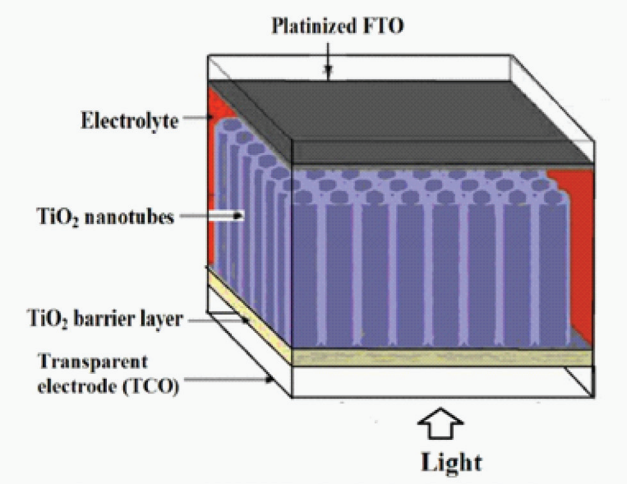

Figure 10. Nanotube array with a corresponding top view

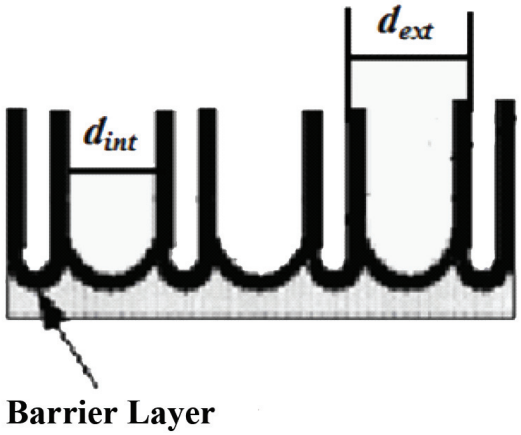

$$\rho_{nanotub} = 1 - \frac{V_e - V_i}{V} = 1 - \frac{\pi\left(r_{ext}^2 - r_{\text{int}}^2\right) l}{3\sqrt{2}\ r_{ext}^2\ l} \tag{36}$$

where

$r_{\text{int}} = \frac{d_{\text{int}}}{2}$, $r_{ext} = \frac{d_{\text{int}}}{2} + t_w$, dint = pore size, t_w = wall thickness, l = TiO_2 nanotube length

The incident photon flux density was calculated using the global distribution of the solar spectrum type AM 1.5 G, and has the value of $1000\ \mathrm{W/m^2}$.

Material parameters are directly related to the performance parameters of the cell. The influence of the most important material parameters, such as electron mean lifetimes and mobilities, on the cell performance was investigated. The model permits the calculation of complete *J-V* curves, from which characteristical parameters of the

solar cell are obtained: the short-circuit current (J_{sc}), the open-circuit voltage (V_{oc}), the fill factor (FF), and the energy conversion efficiency (η). Optimum parameters of Dye Sensitized Solar Cells based on TiO_2 nanotubes can be obtained.

Results and Discussion

The following values were obtained for characteristic parameters: $J_{sc} = 15.3\ \mathrm{mA/cm^2}$, $V_{oc} = 0.82\ \mathrm{V}$, $FF = 0.50$, and $\eta = 5.9\ \%$. These values are close to the experimental ones (Mor, et al., 2006; Wang, et al., 2010). In comparison with the present values obtained for nanocrystalline cells (Oda, et al., 2006): $J_{sc} = 16.1\ \mathrm{mA/cm^2}$, $V_{oc} = 0.81\ \mathrm{V}$, $FF = 0.72$, and $\eta = 9.7\ \%$ the first ones are a little lower.

There are several reasons for the low efficiency of the nanotube DSSC cells:

- The used solar cells had the nanotubes of the negative electrode relatively short (of 6000 nm). This was reflected in a lower absorption than in the case of standard DSSC which have TiO_2 nanoparticles of 10 nm. It suggests the need of increasing the length of the nanotube array on the negative electrode as the amount of the absorbed dye appears to be the limiting factor.
- The low value of the form factor, $FF \sim 0.50$, is caused by the serial resistance barrier introduced by the barrier layer thickness and poor contact between the barrier layer and FTO substrate. The annealing step used to crystallize the nanotube arrays can significantly increase the barrier layer thickness up to approximately 1 ¼m (Varghese, et al., 2003).
- The value of the conversion rate (power conversion efficiency) is influenced by the uniformity of the colorant absorbtion in the pores of the nanotube arrays. The nanotube has an array geometry which can absorb air and that is why the dye is not uniformly distributed.

CONCLUSION

Although the conversion rate of the nanotube solar cells is still low in this moment, a great potential can be foreseen.

REFERENCES

Adachi, M., Murata, Y., Okada, I., & Yoshikawa, S. (2003). Formation of titania nanotubes and applications for dye-sensitized solar cells. *Journal of the Electrochemical Society*, *150*, G488–G493. doi:10.1149/1.1589763

Adachi, M., Okada, I., Ngamsinlapasathian, S., Murata, Y., & Yoshikawa, S. (2002). Dye-sensitized solar cells using semiconductor thin film composed of titania nanotubes. *Electrochemistry*, *70*, 449–452.

Aernouts, T. (2006). *Organic bulk heterojunction solar cells: From single cell towards fully flexible photovoltaic module*. PhD Thesis. Belgium, The Netherlands: Katholieke Universiteit Leuven. Retrieved from https://lirias.kuleuven.be/bitstream/1979/402/5/PhDþThesisþTomþAernoutsþ18-09-06.pdf

Agnaldo, J. S., Cressoni, J. C., & Viswanathan, G. M. (2009). Universal photocurrent-voltage characteristics of dye sensitized nanocrystalline TiO2 photoelectrochemical cells. *Physical Review B: Condensed Matter and Materials Physics*, *79*(3), 035308. doi:10.1103/PhysRevB.79.035308

Berginc, M., Filipic, M., Krašovec, U. O., Nerat, M., Campa, A., & Hocevar, M. … Topic, M. (2009). *Electrical model of dye-sensitized solar cells*. Retrieved from http://www.solamon.eu/eng/Publications/Electrical-Model-of-Dye-Sensitized-Solar-Cells

Bowers, J. W., Upadhyaya, H. M., Nakada, T., & Tiwari, A. N. (2010). Effects of surface treatments on high mobility ITiO coated glass substrates for dye sensitized solar cells and their tandem solar cell applications. *Solar Energy Materials and Solar Cells*, *94*(4), 691–696. doi:10.1016/j.solmat.2009.10.023

Brabec, C., & Zerza, G., Cerullo, et al. (2001). Tracing photoinduced electron transfer process in conjugated polymer/fullerene bulk heterojunctions in real time. *Chemical Physics Letters*, *340*(3-4), 232–236. doi:10.1016/S0009-2614(01)00431-6

Cheng, H. M., & Hsieh, W. F. (2010). High-efficiency metal-free organic-dye-sensitized solar cells with hierarchical ZnO photoelectrode. *Energy and Environmental Science*, *3*(4), 442–447. doi:10.1039/b915725e

Chiba, Y., Islam, A., Watanabe, Y., Komiya, R., Koide, N., & Han, L. (2006). dye-sensitized solar cells with conversion efficiency of 11.1%. *Japanese Journal of Applied Physics*, *45*, L638–640. doi:10.1143/JJAP.45.L638

Chuan, J., Tianze, L., Luan, H., & Xia, Z. (2011). Research on the characteristics of organic solar cells. *Journal of Physics Conference Series*, *276*(1), 012169. doi:10.1088/1742-6596/276/1/012169

Chuan, J., Tianze, L., Luan, H., & Xia, Z. (2011). Research on the characteristics of organic solar cells. *Journal of Physics: Conference Series*, *276*(1).

Contreras, M. A., Egaas, B., Ramanathan, K., Hiltner, J., Swartzlander, A., Hasoon, F., & Noufi, R. (1999). Progress toward 20% efficiency in Cu(In,Ga)Se2 polycrystalline thin-film solar cells. *Progress in Photovoltaics: Research and Applications*, *7*(4), 311–316. doi:10.1002/(SICI)1099-159X(199907/08)7:4<311::AID-PIP274>3.0.CO;2-G

Cummings, F. (2010). *Application of TiO_2 nanotubes in dye-sensitised solar cells for improved charge transport.* Paper presented at the Renewable Energy Photovoltaics, SA Germany Workshop on Photovoltaics. Grahamstown, Germany.

Deb, K. S. (2004). Dye-sensitized TiO_2 thin-film solar cell research at the national renewable energy laboratory (NREL). *Solar Energy Materials and Solar Cells*, *88*(1), 1–10. doi:10.1016/j.solmat.2004.09.007

Dennler, G., Mozer, A. J., Juška, G., Pivrikas, A., Österbacka, R., Fuchsbauer, A., & Sariciftci, N. S. (2006). Charge carrier mobility and lifetime versus composition of conjugated polymer/fullerene bulk-heterojunction solar cells. *Organic Electronics*, *7*, 229–234. doi:10.1016/j.orgel.2006.02.004

Dimitrakopoulos, C. D., & Mascaro, D. J. (2001). Organic thin-film transistors: A review of recent advances. *IBM Journal of Research and Development*, *45*, 11–28. doi:10.1147/rd.451.0011

Ferber, J., & Luther, J. (2001). Modeling of photovoltage and photocurrent in dye-sensitized titanium dioxide solar cells. *The Journal of Physical Chemistry B*, *105*(21), 4895–4903. doi:10.1021/jp002928j

Ferber, J., Stangl, R., & Luther, J. (1998). An electrical model of the dye-sensitized solar cell. *Solar Energy Materials and Solar Cells*, *53*(1-2), 29–54. doi:10.1016/S0927-0248(98)00005-1

Flores, I. C., de Freitas, J. N., Longoa, C., De Paoli, M., Winnischofer, H., & Nogueira, A. F. (2007). Dye-sensitized solar cells based on TiO2 nanotubes and a solid-state electrolyte. *Journal of Photochemistry and Photobiology A Chemistry*, *189*, 153–160. doi:10.1016/j.jphotochem.2007.01.023

Gao, F., Wang, Y., Shi, D., Zhang, J., Wang, M. K., & Jing, X. Y. (2008). Enhance the optical absorptivity of nanocrystalline TiO_2 film with high molar extinction coefficient ruthenium sensitizers for high performance dye-sensitized solar cells. *Journal of the American Chemical Society*, *130*(32), 10720–10728. doi:10.1021/ja801942j

Giannouli, M., Syrrokostas, G., & Yianoulis, P. (2010). Effects of using multi-component electrolytes on the stability and properties of solar cells sensitized with simple organic dyes. *Progress in Photovoltaics: Research and Applications*, *18*(2), 128–136. doi:10.1002/pip.952

Grätzel, M. (2003). Dye-sensitized solar cells. *Journal of Photochemistry and Photobiology C, Photochemistry Reviews*, *4*(2), 145–153. doi:10.1016/S1389-5567(03)00026-1

Gratzel, M. (2004). Conversion of sunlight to electric power by nanocrystalline dye-sensitized solar cells . *Journal of Photochemistry and Photobiology A Chemistry*, *168*(1-3), 235–237. doi:10.1016/j.jphotochem.2004.08.014

Grätzel, M. (2006). The advent of mesoscopic injection solar cells. *Progress in Photovoltaics: Research and Applications*, *14*(5), 429. doi:10.1002/pip.712

Green, M. A., Emery, K., Hishikawa, Y., & Warta, W. (2011). Solar cell efficiency tables (version 37). *Progress in Photovoltaics: Research and Applications*, *19*(1), 84–92. doi:10.1002/pip.1088

Greulich, J., Markus Glatthaar, M., & Rein, S. (2010). Fill factor analysis of solar cells' current–voltage curves. *Progress in Photovoltaics: Research and Applications*, *18*(7), 511–515. doi:10.1002/pip.979

Hardin, B. E., Hoke, E. T., Armstrong, P. B., Yum, J. H., Comte, P., & Torres, T. (2009). Increased light harvesting in dye-sensitized solar cells with energy relay dyes. *Nature Photonics*, *3*(11), 667. doi:10.1038/nphoton.2009.212

Hiramoto, M., Fujiwara, H., & Yokoyama, M. (1991). Three-layered organic solar cell with a photoactive interlayer of codeposited pigments. *Applied Physics Letters*, *58*(10), 1062–1064. doi:10.1063/1.104423

King, R. R., Law, D. C., Edmondson, K. M., Fetzer, C. M., Kinsey, G. S., & Yoon, H. (2007). 40% efficient metamorphic GaInP/GaInAs/Ge multijunction solar cells. *Applied Physics Letters*, *90*(18), 183516–1835111. doi:10.1063/1.2734507

Knodler, R., Sopka, J., Harbach, F., & Grunling, H. W. (1993). Photoelectrochemical cells based on dye sensitized colloidal TiO_2 layers. *Solar Energy Materials and Solar Cells*, *30*(3), 277–281. doi:10.1016/0927-0248(93)90147-U

Kwok, H. L. (2003). Carrier mobility in organic semiconductor thin films. *Reviews on Advanced Materials Science*, *5*, 62–66.

Lai, Y. H., Lin, C. Y., Chen, J. G., Wang, C. C., Huang, K. C., & Liu, K. Y. (2010). Enhancing the performance of dye-sensitized solar cells by incorporating nanomica in gel electrolytes. *Solar Energy Materials and Solar Cells*, *94*(4), 668–674. doi:10.1016/j.solmat.2009.11.027

Law, M., Greene, L. E., Johnson, J. C., Saykally, R., & Yang, P. D. (2005). Nanowire dye-sensitized solar cells. *Nature Materials*, *4*, 455–459. doi:10.1038/nmat1387

Marlein, J., & Burgelman, M. (2007). Electrical properties of CIGS cells. In *Proceedings of the 22nd European Photovoltaic Solar Energy Conference*. Milan, Italy: EU PVTSEC.

Marlein, J., Decock, K., & Burgelman, M. (2009). Analysis of electrical properties of CIGSSe and Cd-free buffer CIGSSe solar cells. *Thin Solid Films*, *517*(7), 2353–2356. doi:10.1016/j.tsf.2008.11.048

Martinson, A. B. F., Elam, J. W., Hupp, J. T., & Pellin, M. J. (2007). ZnO nanotube based dye-sensitized solar cells. *Nano Letters*, *7*(8), 2183–2187. doi:10.1021/nl070160+

Meng, Q.-B., Takahashi, K., Zhang, X.-T., Sutanto, I., Rao, T. N., Sato, O., & Fujishima, A. (2003). Fabrication of an efficient solid-state dye-sensitized solar cell. *Langmuir*, *19*, 3572. doi:10.1021/la026832n

Mitroi, M. R., Iancu, V., Fara, L., & Ciurea, M. L. (2011). Numerical analysis of J–V characteristics of a polymer solar cell. *Progress in Photovoltaics: Research and Applications*, *19*(3), 301–306. doi:10.1002/pip.1026

Mor, G. K., Varghese, O. K., Paulose, M., Shankar, K., & Grimes, C. A. (2006). A review on highly ordered, vertically oriented TiO2 nanotube arrays: Fabrication, material properties, and solar energy applications. *Solar Energy Materials and Solar Cells*, *90*, 2011–2075. doi:10.1016/j.solmat.2006.04.007

Myahkostupov, M., Zamkov, M., & Castellano, F. N. (2011). Dye-sensitized photovoltaic properties of hydrothermally prepared TiO2 nanotubes. *Energy and Environmental Science*, *4*, 998–1010. doi:10.1039/c0ee00533a

Nazeeruddin, M. K., De Angelis, F., Fantacci, S., Selloni, A., Viscardi, G., & Liska, P. (2005). Combined experimental and DFT-TDDFT computational study of photoelectrochemical cell ruthenium sensitizers. *Journal of the American Chemical Society*, *127*(48), 16835–16847. doi:10.1021/ja052467l

Nelson, J. (2003). Diffusion-limited recombination in polymer-fullerene blends and its influence on photocurrent collection. *Physical Review B: Condensed Matter and Materials Physics*, *67*, 155209. doi:10.1103/PhysRevB.67.155209

Nunzi, J. M. (2002). Organic photovoltaic materials and devices. *Comptes Rendus Physique*, *3*(4), 523–542. doi:10.1016/S1631-0705(02)01335-X

O'Regan, B., & Grätzel, M. (1991). A low-cost, high-efficiency solar cell based on dye-sensitized colloidal TiO2 films. *Nature*, *353*, 737–740. doi:10.1038/353737a0

Oda, T., Tanaka, S., & Hayase, S. (2006). Differences in characteristics of dye-sensitized solar cells containing acetonitrile and ionic liquid-based electrolytes studied using a novel model. *Solar Energy Materials and Solar Cells*, *54*(16), 2696–27011. doi:10.1016/j.solmat.2005.11.013

Paper. (2011). *Website.* Retrieved from http://www.paper.edu.cn/index.php/default/feature/downCount/815

Shaheen, S., Brabec, C. J., Sariciftci, N. S., Padinger, F., Fromherz, T., & Hummelen, J. C. (2001). 2.5% efficient organic plastic solar cells. *Applied Physics Letters*, *78*, 841–843. doi:10.1063/1.1345834

Smestad, G., Bignozzi, C., & Argazzi, R. (1994). Testing of dye sensitized TiO2 solar cells I: Experimental photocurrent output and conversion efficiencies. *Solar Energy Materials and Solar Cells*, *32*(3), 259–272. doi:10.1016/0927-0248(94)90263-1

Soedergren, S., Hagfeldt, A., Olsson, J., & Lindquist, S. E. (1994). Theoretical models for the action spectrum and the current-voltage characteristics of microporous semiconductor films in photoelectrochemical cells. *Journal of Physical Chemistry*, *98*(21), 5552–5556. doi:10.1021/j100072a023

Tang, C. W. (1986). Two-layer organic photovoltaic cell. *Applied Physics Letters*, *48*(2), 183–185. doi:10.1063/1.96937

Tenne, R., Rao, C. N. R. (2004). Inorganic nanotubes. *Philosophical Transactions of the Royal Society A, 362*(1823), 2099-2125.

Tian, H., Zhang, J., & Yangjing, Yu. T., & Zou, Z. (2011). Analysis on dye-sensitized solar cell's efficiency improvement. *Journal of Physics: Conference Series, 276*, 012188.

Varghese, O. K., Gong, D., Paulose, M., Ong, K. G., Dickey, E. C., & Grimes, C. A. (2003). Extreme changes in the electrical: Resistance of titania nanotubes with hydrogen exposure. *Advanced Materials (Deerfield Beach, Fla.)*, *15*, 624–627. doi:10.1002/adma.200304586

Wang, Y., Yang, H., Liu, Y., Wang, H., Shen, H., Yan, J., & Xu, H. (2010). The use of Ti meshes with self-organized TiO_2 nanotubes as photoanodes of all-Ti dye-sensitized solar cells. *Progress in Photovoltaics: Research and Applications*, *18*, 285–290.

Wei, D. (2010). Dye sensitized solar cells. *International Journal of Molecular Sciences*, *11*, 1103–1113. doi:10.3390/ijms11031103

Wenger, S. (2010). *Strategies to optimizing dye-sensitized solar cells: Organic sensitizers, tandem device structures, and numerical device modeling*. Retrieved from http://library.epfl.ch/en/theses/?nr=4805

Wenger, S., Schmid, M., Rothenberger, G., Grätzel, M., & Schumacher, J. O. (2009). *Model-based optical and electrical* characterization of dye-sensitized solar cells. Retrieved from http://www.juergenschumacher.de/html/material/veroeffentlichungen/DSC-EUPVSEC-Hamburg.pdf

Wienk, M., Kroon, J. M., Verhees, W. J. H., Krol, J., Hummelen, J. C., Van Haal, P., & Janssen, R. A. J. (2003). Efficient methano[70] fullerene/MDMO-PPV bulk heterojunction photovoltaic cells. *Angewandt Chemie International Edition, 42*(29), 3371-3375.

Xue, J., Rand, B. P., Uchida, S., & Forrest, S. R. (2005). A hybrid planar-mixed molecular heterojunction photovoltaic cell. *Advanced Materials (Deerfield Beach, Fla.)*, *17*(1), 66–71. doi:10.1002/adma.200400617

Yong, V., Ho, S. T., & Chang, R. P. H. (2008). Modeling and simulation for dye-sensitized solar cells. *Applied Physics Letters*, *92*(14), 143506. doi:10.1063/1.2908204

Zhang, X.-T., Liu, H.-W., Taguchi, T., Meng, Q. B., Sato, O., & Fujishima, A. (2004). Slow interfacial charge recombination in solid-state dye-sensitized solar cell using Al_2O_3-coated nanoporous TiO_2 films. *Solar Energy Materials and Solar Cells*, *81*(2), 197–203. doi:10.1016/j.solmat.2003.11.005

Zhao, J., Wang, A., Green, M. A., & Ferrazza, F. (1998). 11.8% efficient "honeycomb" textured multicrystalline and 24.4% monocrystalline silicon solar cells. *Applied Physics Letters*, *73*(14), 1991–1993. doi:10.1063/1.122345

Section 4

High Efficiency Solar Cells

Chapter 9
Super High Efficiency Multi-Junction Solar Cells and Concentrator Solar Cells

Masafumi Yamaguchi
Toyota Technological Institute (TTI), Japan

ABSTRACT

While single-junction solar cells may be capable of attaining AM1.5 efficiencies of up to 29%, Multi-Junction (MJ, Tandem) III-V compound solar cells appear capable of realistic efficiencies of up to 50% and are promising for space and terrestrial applications. In fact, the InGaP/GaAs/Ge triple-junction solar cells have been widely used in space since 1997. In addition, industrialization of concentrator solar cell modules using III-V compound MJ solar cells have been announced by some companies. This chapter presents principles and key issues for realizing high-efficiency MJ solar cells, issues relating to development and manufacturing, and applications for space and terrestrial uses.

INTRODUCTION

Multi-Junction (MJ, Tandem) solar cells are composed of multi-layers with different bandgap energies are shown in Figure 1 and have the potential for achieving high conversion efficiencies of over 50% and are promising for space and terrestrial applications due to wide photo response. Figure 2 shows theoretical conversion efficiencies of single-junction and Multi-Junction (MJ) solar cells in comparison with experimentally realized efficiencies.

DOI: 10.4018/978-1-4666-1927-2.ch009

Tandem solar cells were proposed by Jackson (1955) and Wolf (1960). Table 1 shows progress of the III-V compound multi-junction solar cell technologies. MIT group (Fan, Tsaur, & Palm, 1982) encouraged R&D of tandem cells based on their computer analysis. Although AlGaAs/GaAs tandem cells, including tunnel junctions and metal interconnectors, were developed in the early years, a high efficiency close to 20% was not obtained (Hutchby, Markunas, & Bedair, 1985). This is because of difficulties in making high performance and stable tunnel junctions, and the defects related to the oxygen in the AlGaAs

Figure 1. A schematic structure of a multi-layer solar cell

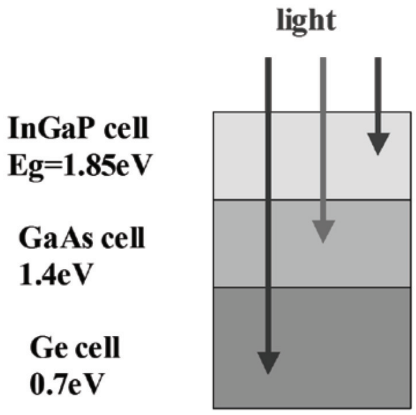

Figure 2. Theoretical conversion efficiencies of single-junction and multi-junction solar cells in comparison with experimentally realized efficiencies

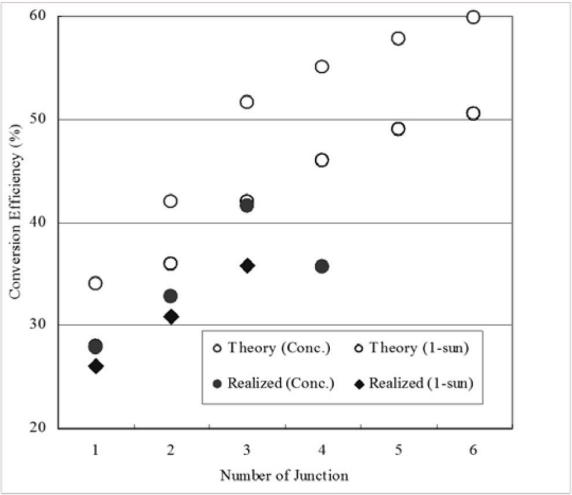

materials (Ando, Amano, Sugiura, et al., 1987). A Double Hetero (DH) structure tunnel junction was found to be useful for preventing diffusion from the tunnel junction and improving the tunnel junction performance by the authors (Sugiura, Amano, Yamamoto, & Yamaguchi, 1988). The authors demonstrated 20.2% efficiency AlGaAs/GaAs 2-junction cells (Amano, Sugiura, Yamamoto, & Yamaguchi, 1987). An InGaP material for the top cell was proposed by NREL group (Olson, Kurtz, & Kibbler, 1990). As a result of performance improvements in tunnel junction and top cell, over 30% efficiency has been obtained with InGaP/GaAs 2-junction cells by the authors (Takamoto, Ikeda, Kurita, et al., 1997).

InGaP/GaAs-based MJ solar cells have drawn increased attention for space applications because superior radiation-resistance of InGaP top cells and materials have been discovered by the authors (Yamaguchi, Okuda, Taylor, et al., 1997). and those have the possibility of high conversion efficiency of over 30%. In fact, the commercial

Table 1. Progress of the III-V compound multi-junction solar cell technologies

1955 1960	Proposal of multi-junction solar cell	Jackson Wolf
1982	Efficiency calculation of tandem cells	MIT
1982	15.1% AlGaAs/GaAs 2-junction (2-J) cell	RTI
1987	Proposal of double-hetero structure tunnel junction for multi-junction interconnection	NTT
1987	20.2% AlGaAs/GaAs 2-J cell	NTT
1989	32.6% GaAs//GaSb concentrator 2-J cell (mechanical-stacked, 100-suns concentration)	Boeing
1990	Proposal of InGaP as top a cell material	NREL
1990	27.3% InGaP/GaAs 2-J cell	NREL
1996	30.3% InGaP/GaAs 2-J cell	Jpn. Energy
1997	Discovery of radiation-resistance of InGaP top cell	Toyota Tech. Inst.
1997	33.3% InGaP/GaAs//InGaAs 3-J cell (mechanical-stacked)	Jpn. Energy, Sumitomo & Toyota Tech. Inst.
1997	Commercial satellite with 2-J cells	Hughes
2000	31.7% InGaP/InGaAs/Ge 3-J cell	Jpn. Energy
2003	37.4% InGaP/InGaAs/Ge 3-J cell (200-suns concentration)	Sharp
2004	38.9% InGaP/InGaAs/Ge 3-J cell (489-suns concentration)	Sharp & Toyota TI
2006	31.5% large-area (5,445cm^2) InGaP/InGaAs/Ge 3-J cell module (outdoor)	Daido Steel, Daido Metal, Sharp &Toyota T.I.
2006	40.7% InGaP/GaAs/Ge 3-J cell (236-suns concentration)	Spectrolab
2009	41.1% InGaP/InGaAs/Ge 3-J cell (454-suns concentration)	Fraunhofer ISE
2009	41.6% InGaP/InGaAs/Ge 3-J cell (364-suns concentration)	Spectrolab
2009	35.8% InGaP/GaAs/InGaAs 3-J cell (1-sun)	Sharp

satellite (HS 601HP) with 2-junction GaInP/GaAs-on Ge solar arrays was launched in 1997 (Brown, Goldhammer, Goodelle, et al., 1997).

More recently, InGaP/GaAs-based MJ solar cells have drawn increased attention for terrestrial applications because concentrator operation of MJ cells have great potential of providing high performance and low-cost solar cell modules. For concentrator applications, grid structure has been designed in order to reduce the energy loss due to series resistance, and 38.9% (AM1.5G, 489-suns) efficiency has been demonstrated by Sharp (Takamoto, Kaneiwa, Imaizumi, & Yamaguchi, 2005). Most recently, 41.6% efficiency has been reported with InGaP/GaAs/Ge 3-junction concentrator cells by Spectrolab (King, Boca, Hong, et al., 2009). In addition, the authors have realized high-efficiency and large-area (5,445cm^2) concentrator InGaP/InGaAs/Ge 3-junction solar cell modules of an outdoor efficiency of 31.5% (Araki, Uozumi, Egami, et al., 2005). as a result of developing high-efficiency InGaP/InGaAs/Ge 3-junction cells, low optical loss Fresnel lens and homogenisers, and designing low thermal conductivity modules. Some companies including Sharp (Tomita, 2006) have announced to commercialise InGaP/GaAs/Ge 3-junction concentrator cell modules for terrestrial use.

KEY ISSUES FOR REALIZING HIGH-EFFICIENCY MJ SOLAR CELLS

Key issues for realizing high-efficiency MJ tandem cells are discussed based on our results.

Selection of Cell Materials and Improving the Quality

MJ cells with different band gaps are stacked in tandem so that the cells cover wide wavelength region from 300 nm to 1800 nm. Cell materials are selected by considering band gap energies close to the optimal band gap energy combination based on theoretical efficiency calculation, and by considering lattice matching to substrates and less impurity problems. Figure 3 shows minority-carrier diffusion length dependence of GaAs single-junction solar cell efficiency. It is clear that the higher minority-carrier diffusion length L (minority-carrier lifetime $\tau = L^2 / D$, where D is minority-carrier diffusion coefficient) is substantially necessary to realize the higher efficiency solar cells. Figure 4 shows carrier concentration dependence of minority-carrier lifetime in p-type and n-type GaAs (Ahrenkiel, Keyes, Durbin, & Gray, 1993). Minority-carrier lifetime τ is dependent on carrier concentration N of solar cell layers as expressed by:

$$\tau = 1 / BN \quad (1)$$

where, B is radiative recombination coefficient. Therefore, carrier concentration of cell layers must be optimised by considering minority-carrier lifetime, build-in potential, and series resistance of p-n junction diodes.

Selection of cell materials, especially selection of top cell materials is also important for high-efficiency tandem cells. It has been found by the authors (Hutchby, Markunas, &. Bedair, 1985) that oxygen-related defect in the AlGaAs top cell materials acts as the recombination centre. As a top cell material latticed matched to GaAs or Ge substrates, InGaP has some advantages (Olson, Kurtz, & Kibbler, 1990) such as lower interface recombination velocity, less oxygen problem and good window layer material compared to AlGaAs. The top cell characteristics depend on the minority carrier lifetime in the top cell layers. Figure 5 shows changes in Photoluminescence (PL) intensity of the solar cell active layer as a function of the minority carrier lifetime τ of the p-InGaP base layer grown by MOCVD (metal-organic

Figure 3. Minority-carrier diffusion length dependence of GaAs single-junction solar cell efficiency

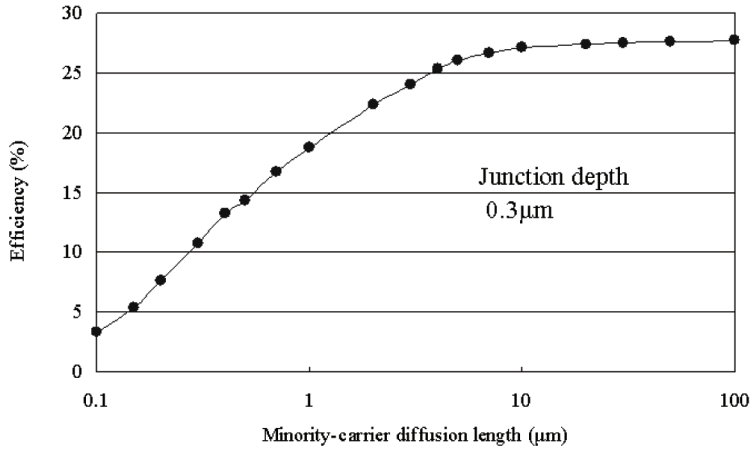

Figure 4. Carrier concentration dependence of minority-carrier lifetime in p-type and n-type GaAs (Ahrenkiel, Keyes, Durbin, & Gray, 1993)

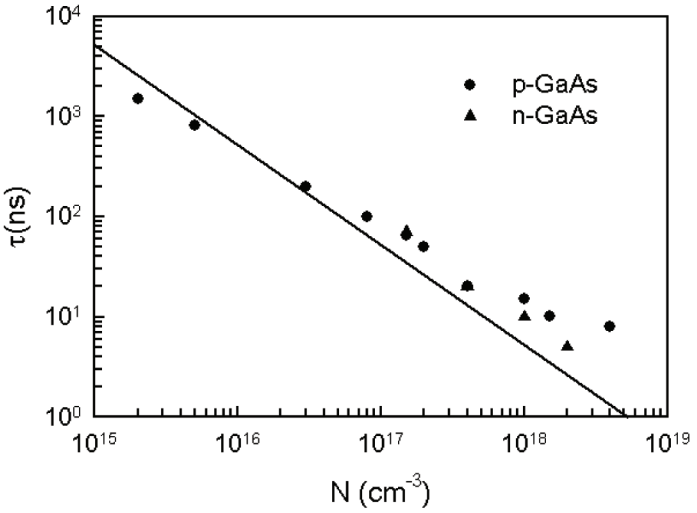

chemical vapour deposition) and surface recombination velocity (S). The lowest S was obtained by introducing the AlInP window layer and the highestτwas obtained by introducing buffer layer and optimising the growth temperature. The best conversion efficiency of the InGaP single-junction cell was 18.5% (Yang, Yamaguchi, Takamoto, et al., 1997).

Lattice Matching between Cell Materials and Substrates

Lattice mismatching of cell materials to substrates should be decreased because miss-fit dislocations must be generated in the upper cell layers and deteriorate cell efficiency. Figure 6 shows calculated and experimental dislocation density dependence of minority-carrier lifetime in GaAs (Yamaguchi & Amano, 1985). Dislocation density N_d dependence of minority-carrier lifetime τ is expressed by the following equation (Yamaguchi & Amano, 1985):

$$1/\tau = 1/\tau_r + 1/\tau_0 + \pi^3 D N_d / 4 \qquad (2)$$

where τ_r is radiative recombination lifetime and τ_0 is minority-carrier lifetime associated with recombination at other unknown defects.

Application of InGaAs middle cell (Yamaguchi & Amano, 1985) lattice-matching to Ge substrates has demonstrated to increase open-circuit voltage (V_{oc}) due to lattice-matching and short-circuit current density (J_{sc}) due to decrease in bandgap energy of middle cell.

Effectiveness of Wide Bandgap Back Surface Field (BSF) Layer

Figure 7 shows surface recombination effect on short-circuit current density J_{sc} of $In_{0.14}Ga_{0.86}As$ homo-junction solar cells as a function of junction depth. Therefore, in order to improve efficiency drop attributed from front and rear surface recombination as shown in Figure 8, formation of heteroface or double-hetero structure is necessary.

Figure 5. Changes in photoluminescence (PL) intensity of the solar cell active layer as a function of the minority carrier lifetime in GaAs, grown by MOCVD and surface recombination velocity (S)

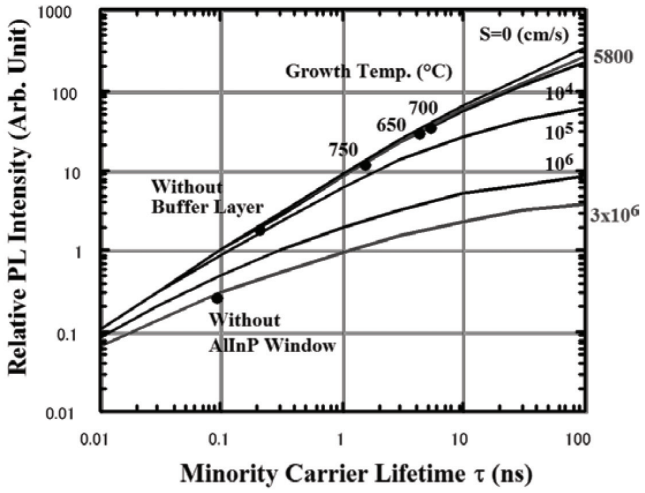

Figure 6. Calculated and experimental dislocation density dependence of minority-carrier lifetime in GaAs, InP, and InGa

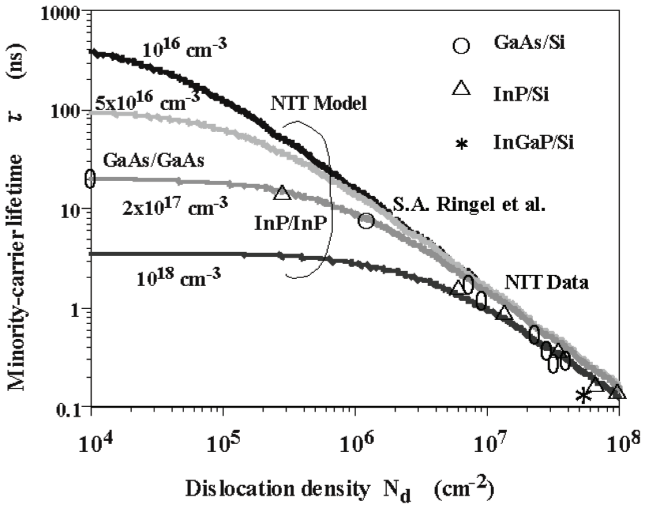

Figure 8 shows changes in V_{oc} and J_{sc} of InGaP single-junction cells as a function of potential barrier ΔE. Wide bandgap Back-Surface Field (BSF) layer (Yamaguchi & Amano, 1985) is found to more effective for confinement of minority carriers compared to highly doped BSF layers.

Low Loss Tunnel Junction for Intercell Connection and Preventing Impurity Diffusion from Tunnel Junction

Another important issue for realizing high-efficiency monolithic-cascade type tandem cells is the achievement of optically and electrically low-loss interconnection of two or more cells. A degenerately doped tunnel junction is attractive because it only involves one extra step in the growth process. To minimize optical absorption, formation of thin and wide-bandgap tunnel junctions is necessary as shown in Figure 9. However, the formation of a wide-bandgap tunnel junction is very difficult because the tunnelling current decreases exponentially with increase in bandgap energy.

In addition, impurity diffusion from a highly doped tunnel junction during overgrowth of the top cell increases the resistivity of the tunnel junction. As shown in Figure 10, a Double Hetero (DH) structure was found to be useful for preventing diffusion by the authors (Sugiura, Amano, Yamamoto, & Yamaguchi, 1988). An InGaP tunnel junction has been for the first time tried for an InGaP/GaAs tandem cell in our work (Takamoto, Ikeda, Kurita, et al., 1997). As p-type and n-type dopants, Zn and Si were used, respectively. Peak tunnelling current of the InGaP tunnel junction is found to increase from 5mA/cm^2 up to 2A/cm^2 by making a DH structure with AlInP barriers. Therefore, the InGaP tunnel junction has been observed to be very effective for obtaining high tunnelling current, and DH structure has also been confirmed to be useful for preventing diffusion.

DH structure effect on suppression of impurity diffusion from the tunnel junction has been examined. Effective suppression of the Zn diffusion from tunnel junction by the InGaP tunnel junction with the AlInP-DH structure is thought to be attributed to the lower diffusion coefficient

Figure 7. Surface recombination effect on short-circuit current density Jsc of $In_{0.14}Ga_{0.86}As$ homo-junction solar cells as a function of junction depth

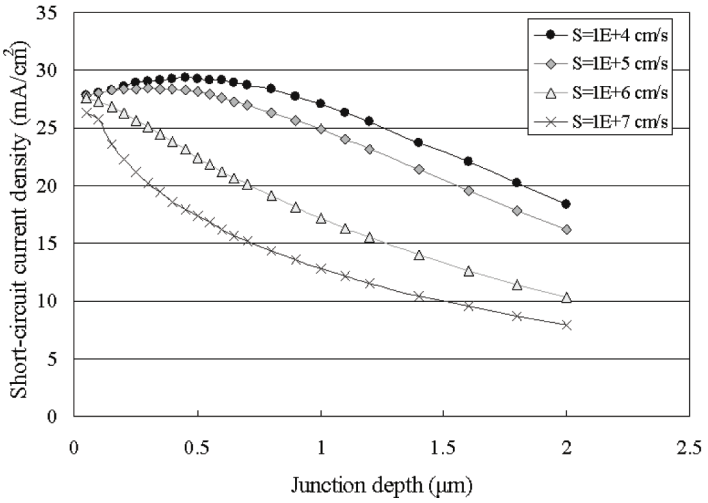

Figure 8. Changes in Voc and Jsc of InGaP single-junction cells as a function of potential barrier ΔE

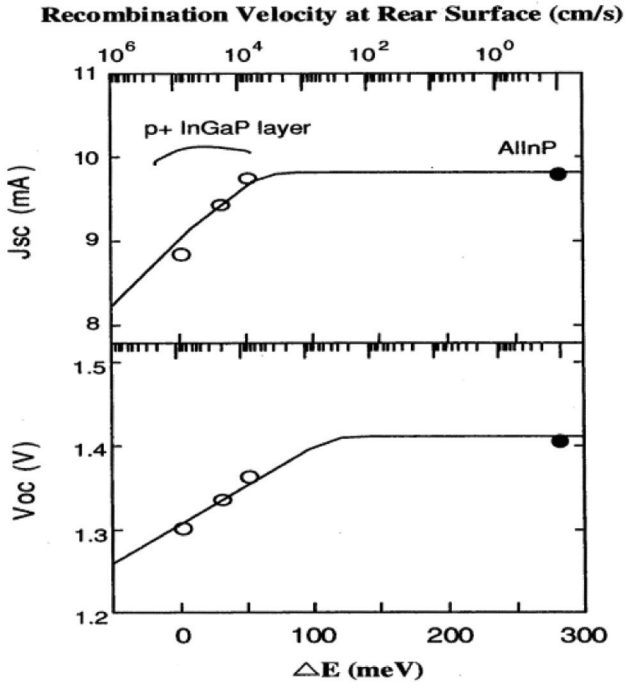

Figure 9. Calculated tunnel peak current density and short-circuit current density Jsc of GaAs bottom cell as a function of bandgap energy of tunnel junction

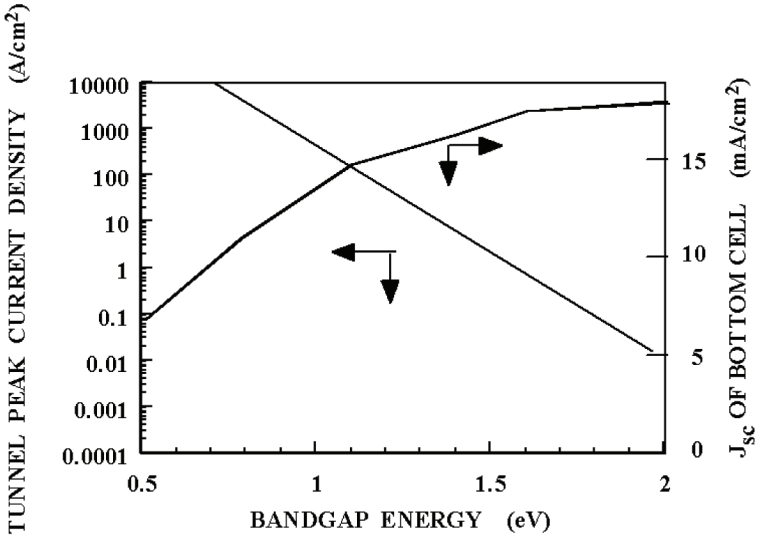

Figure 10. Annealing temperature dependence of tunnel peak current densities for double hetero structure tunnel diodes. X is the Al mole fraction in AlxGa1-xAs barrier layers.

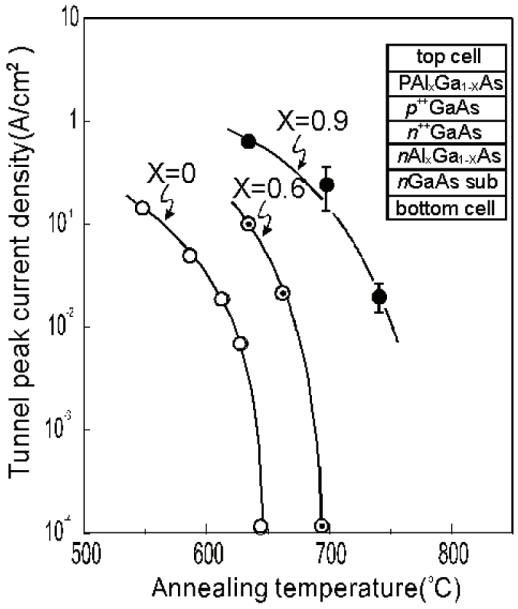

(Takamoto, Yamaguchi, Ikeda, et al., 1999) for Zn in the wider bandgap energy materials such as the AlInP barrier layer and InGaP tunnel junction layer.

Table 2 summarizes key issues of realizing super-high-efficiency MJ solar cells

HIGH-EFFICIENCY INGAP/GAAS/GE 3-JUNCTION SOLAR CELLS AND THEIR SPACE APPLICATIONS

Development of High-Efficiency InGaP/GaAs/Ge 3-Junction Solar Cells

As one of the Sunshine Program in Japan, an R&D project for super high-efficiency MJ solar cells was started in 1990. Conversion efficiency of InGaP/GaAs based multijunction solar cells has been improved by the following technologies. A schematic illustration of the InGaP/(In)GaAs/Ge triple junction solar cell and key technologies for improving conversion efficiency are shown in Figure 11.

Wide Band-Gap Tunnel Junction

A wide band-gap tunnel junction which consists of double-hetero structure p-Al(Ga)InP/p-AlGaAs/n-(Al)InGaP/n-Al(Ga)InP increases incident light into the (In)GaAs middle cell and produces effective potential barriers for both minority-carriers generated in the top and middle cells. Both Voc and Isc of the cells are improved by the wide band-gap tunnel junction without absorption and recombination losses (Takamoto, Ikeda, Kurita, et al., 1997). It is difficult to obtain high tunnelling peak current with wide gap tunnel junction, so thinning depletion layer width by formation of highly doped junction is quite necessary. Since impurity diffusion is occurred during growth of

Table 2. Key issues for realizing super high-efficiency multi-junction solar cells

Key Issue	Past	Present	Future
Top cell materials	AlGaAs	InGaP	AlInGaP
3rd layer materials	None	Ge	InGaAsN etc.
Substrate	GaAs	Ge	Si
Tunnel junction	DH-structure GaAs Tunnel Junction (TJ)	DH-structure InGaP TJ.	DH-structure InGaP or GaAs TJ
Lattice matching	GaAs middle cell	InGaAs middle cell	(In)GaAs middle cell
Carrier confinement	InGaP-BSF	AlInP-BSF	Widegap-BSF Quantum Dots (QDs)
Photon confinement	None	None	Bragg reflector, QDs, etc.
others	None	Inverted Epi.	Inverted Epi. Epitaxial Lift Off

Figure 11. Schematic illustration of a triple-junction cell and approaches for improving efficiency of the cell

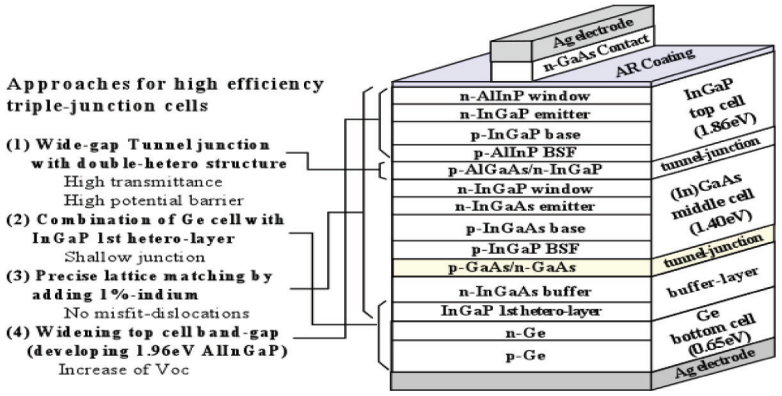

the top cell (Sugiura, Amano, Yamamoto, & Yamaguchi, 1988), carbon and silicon which have low diffusion coefficient are used for p-type AlGaAs and n-type (Al)InGaP, respectively. Furthermore, the double-hetero structure supposes to suppress impurity diffusion from the highly doped tunnel junction (Takamoto, et al., 1999). The second tunnel junction between middle and bottom cells consists of p-InGaP/p-(In)GaAs/ n-(In)GaAs/n-InGaP which have wider band-gap than middle cell materials.

Heteroface Structure Ge Bottom Cell

InGaP/GaAs cell layers are grown on a p-type Ge substrate. PN junction is formed automatically during MOCVD growth by diffusion of V-group atom from the first layer grown on the Ge substrate. So, the material of the first hetero layer is important for the performance of Ge bottom cell. An InGaP layer is thought to be suitable material for the first hetero layer, because phosphor has lower diffusion coefficient in Ge than arsenic and

Figure 12. Change in the spectral response due to modification of the 1st hetero-layer from GaAs to InGaP (without anti-reflection coating)

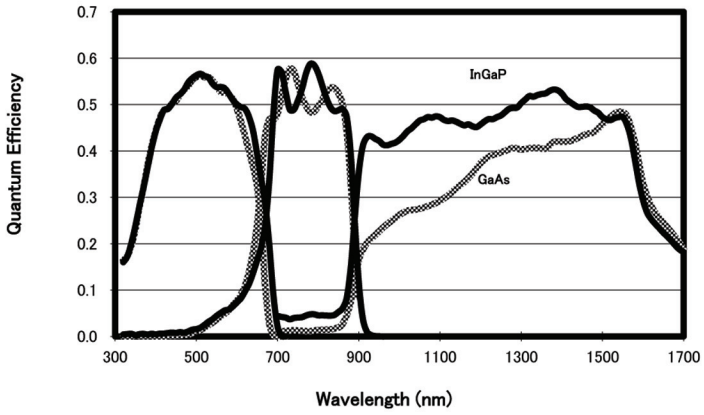

indium has lower solubility in Ge than gallium. Figure 12 shows the change in spectral response of the triple-junction cell by changing the first hetero growth layer on Ge from GaAs to InGaP. Quantum efficiency of the Ge bottom cell was improved by the InGaP hetero-growth layer. In the case of GaAs hetero-growth layer, junction depth was measured to be around 1μm. On the other hand, thickness of n-type layer produced by phosphor from the InGaP layer was 0.1μm. An increase in Ge quantum efficiency was confirmed to be due to a reduction in junction depth.

Precise Lattice-Matching to Ge Substrate

Although 0.08% lattice-mismatch between GaAs and Ge was thought to be negligibly small, misfit-dislocations were generated in thick GaAs layers and deteriorated cell performance. By adding about 1% indium into the InGaP/GaAs cell layers, all cell layers are lattice-matched precisely to the Ge substrate. As a result, crosshatch pattern caused by misfit-dislocations due to lattice-mismatch was disappeared in the surface morphology of the cell with 1% indium, as shown in Figure 13. The misfit-dislocations were found to influence not to Isc but to Voc of the cell. Voc was improved by eliminating misfit-dislocations for the cell with 1% indium. In addition, wavelength of the absorption edge became longer and Isc of both top and middle cells increased, by adding 1% indium.

As one of the Sunshine Program in Japan, an R&D project for super high-efficiency MJ solar cells was started based on our results in 1990. Conversion efficiency of InGaP-based 3-junction

Figure 13. Surface morphology of InGaAs with various indium compositions grown on Ge

solar cells has been improved by the following technologies:

1. Selection and high quality growth of InGaP as a top cell material
2. Proposal of double-hetero structure and wide-band gap tunnel junction for cell interconnection.
3. Precise lattice matching of InGaP top cell and InGaAs middle cell with Ge substrate
4. Proposal of AlInP as a back surface field layer for the InGaP top cell
5. Proposal of InGaP-Ge heteroface structure bottom cell

As a result of the above proposals and performance improvements, we have demonstrated a world-record efficiency (33.3% at 1-sun AM1.5G) InGaP/GaAs/InGaAs 3-junction solar cell in 1997 (Takamoto, Ikeda, Agui, et al., 1997). The conversion efficiency of InGaP/(In)GaAs/Ge 3-junction solar cells has been improved to 31.7% (AM1.5G) (Takamoto, et al., 2000).

Radiation-Resistance of InGaP-Based MJ Solar Cells

Figure 14 shows effectiveness of radiation-resistance and high conversion efficiency of space cells from the point view of power density. Since radiation in space is severe, particularly in the Van Allen radiation belt, lattice defects are induced in semiconductors due to high-energy electron and proton irradiations, and the defects cause a decrease in the output power of solar cells. Further improvements in conversion efficiency and radiation-resistance of space cells are necessary for widespread applications of space missions. Recently, InGaP/GaAs-based MJ solar cells have drawn increased attention because of the possibility of high conversion efficiency of over 40% and radiation-resistance. An AM0 efficiency of 29.2% has been demonstrated for an InGaP/InGaAs/Ge 3-junction cell (4cm^2) (Takamoto, et al., 1997).

Figure 15 shows the maximum power recovery due to light illumination of 100 mW/cm^2 at various temperatures for 1-MeV electron-irradiated InGaP/GaAs tandem cells (Yamaguchi, et al., 1997). The ratios of maximum power after

Figure 14. Effectiveness of radiation-resistance and high conversion efficiency of space cells from the point view of power density

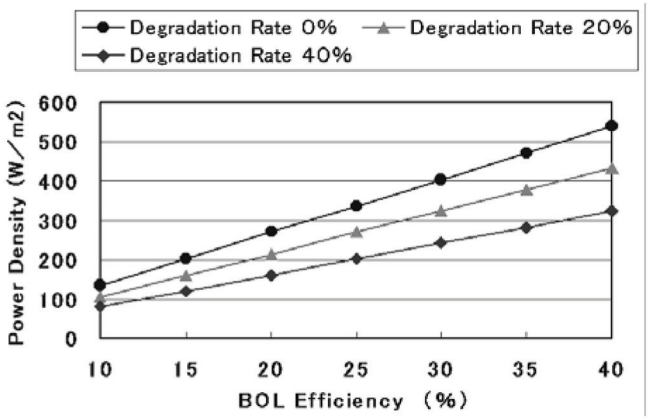

Figure 15. The maximum power recovery of the InGaP/GaAs tandem cell due to light illumination at various temperatures

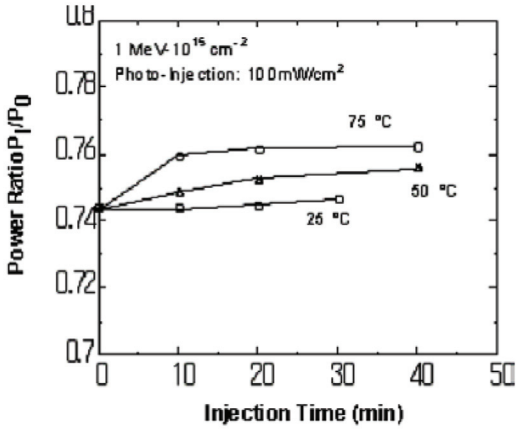

injection, P_I, to maximum power before irradiation, P_0, are shown as a function of injection time. Even at room temperature, photo injection-enhanced annealing of radiation damage to InGaP/GaAs tandem cells was observed. The recovery ratio increases with an increase in ambient temperature within the operating range for space use. Such a recovery is found to be attributed from damage recovery in InGaP top cell layer (Yamaguchi, et al., 1997). Therefore, the results show that InGaP/GaAs tandem cells under device operation conditions have superior radiation-resistant properties.

Figure 16 shows DLTS (Deep Level Transient Spectroscopy) spectrum of Trap H2 (Ev+0.55eV) for various injection times at 25^0C with an AM1.5 light intensity of 100mA/cm^2. It is also found (Kahn et al., 2000) by DLTS measurements that a major defect level H2 (Ev+0.55eV) recovers by forward bias or light illumination. Moreover, the H2 center is confirmed to act as a recombination center by using the double carrier pulse DLTS method. The enhancement of defect annealing in InGaP top cell layer under minority-carrier injection conditions is thought to occur as a result of the nonradiative electron-hole recombination process (Lang & Leung, 1976) whose energy E_R enhances the defect motion. The thermal activation energy E_A (1.1eV) of the defect is reduced to E_I (0.48~0.54eV) by an amount E_R (0.56~0.62eV). Thus electronic energy from a recombination event can be channeled into the lattice vibration mode which drives the defect motion: $E_I = E_A - E_R$.

Space Applications of InGaP/GaAs/Ge 3-Junction Solar Cells

Advanced technologies for high efficiency cells and discovery of superior radiation-resistance of InGaP based materials are thought to contribute to industrialization of InGaP-based multijunction space solar cells in Japan. Figure 17 shows Sharp space solar cell conversion efficiency heritage. Since 2002, InGaP/GaAs/Ge 3-junction solar cells have been commercialized for space use in Japan.

LOW COST POTENTIAL OF CONCENTRATOR MJ SOLAR CELL MODULES AND HIGH EFFICIENCY CONCENTRATOR INGAP/GAAS/GE 3-JUNCTION SOLAR CELL MODULES AND TERRESTRIAL APPLICATIONS

Concentrator operation is very effective for cost reduction of solar cell modules and thus that of PV systems. Figure 18 shows configuration of PV system composed of solar cell, optics and tracker. Concentrator operation of the MJ cells is essential for their terrestrial applications. Since the concentrator PV systems using MJ solar cells have great potential of cost reduction as shown in Figure 19 (Yamaguchi, et al., 2003), R&D on concentrator technologies including MJ cells is started in Japan.

In order to apply a high efficiency MJ cell developed for 1 sun condition to a concentrator cell operating under ~500suns condition, reduction in energy loss due to series resistance is the most

Figure 16. DLTS spectrum of trap H2 (Ev+0.55eV) for various injection timesat 25^{0}C with an injection density of 100mA/cm^2

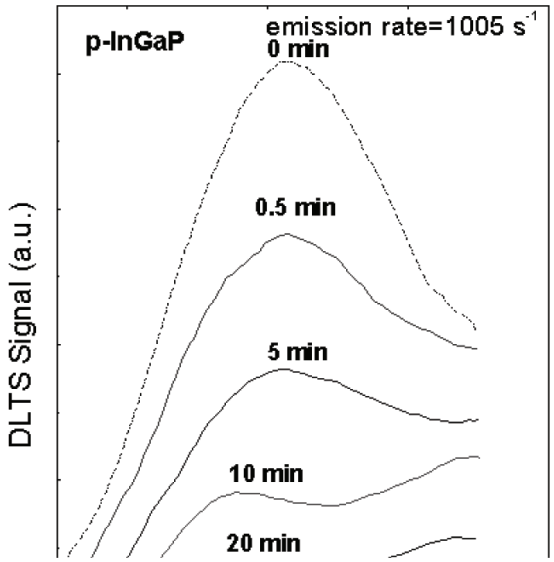

Figure 17. Sharp space solar cell conversion efficiency heritage

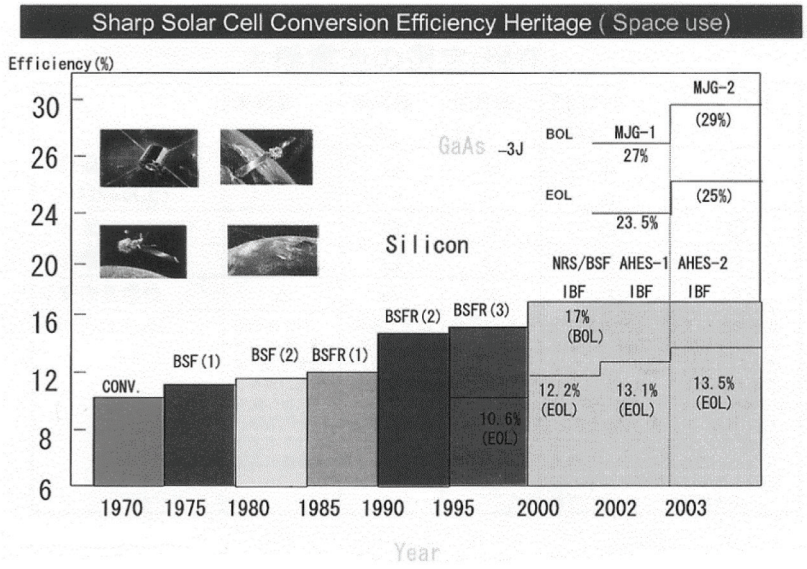

important issue. Cell size was determined to be 7mm x 7mm with considering total current flow. Grid electrode pitching, height and width were designed in order to reduce series resistance. Figure 20 shows fill factor (FF) of the cell with various grid pitching under 250 suns. Grid electrode with 5μm height and 5μm width was made of Ag. Grid pitching influences lateral resistance

Figure 18. Configuration of PV system composed of solar cell, optics, and tracker

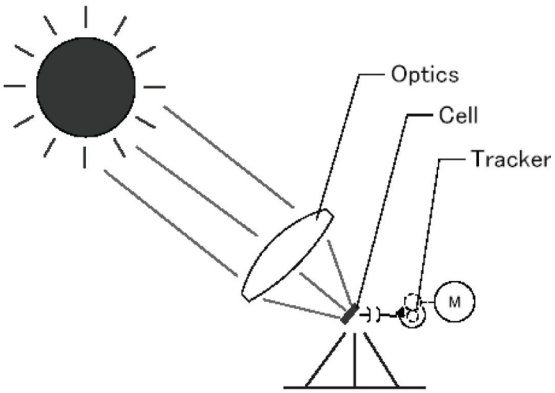

Figure 19. Summary of estimated cost for the concentrator PV systems vs. concentration ratio (Yamaguchi, et al., 2003)

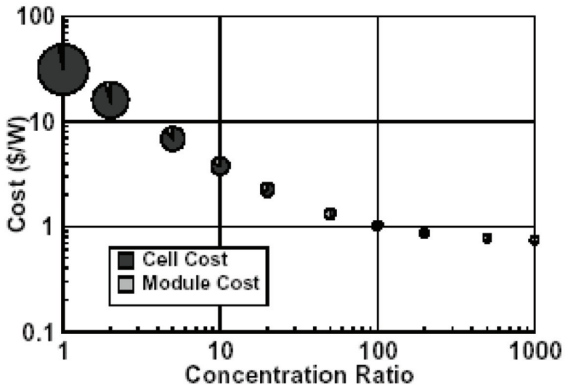

between two grids (RL) and total electrodes resistance (RE). Series resistance of the cell (RS), RE and RL are also shown in Figure 20. RE was measured directly after removing electrode from the cell by chemical etching. RL was calculated by using sheet resistance of window and emitter layers. Based on the data in Figure 20, the grid pitching is determined to be 0.12 mm at this time. In order to reduce series resistance down to 0.01Ω and obtain high FF under 500 suns, grid height should be increased to be twice. High efficiency under <500 suns is thought to be obtained by the optimal grid design without modification of the cell layer.

For concentrator applications, the grid structure has been designed in order to reduce the energy loss due to series resistance as shown in Figure 20. The authors have successfully fabricated high efficiency concentrator InGaP/InGaAs/Ge 3-junction solar cells designed for 500-sun application. The efficiencies by in-house measurement are 39.2% at 200-suns and 38.9% at 489-suns as

Figure 20. FF of the concentrator cells with various grids pitching under 250-suns light. Series resistance (Rs), lateral resistance (RL) and total electrodes resistance (RE) are also shown.

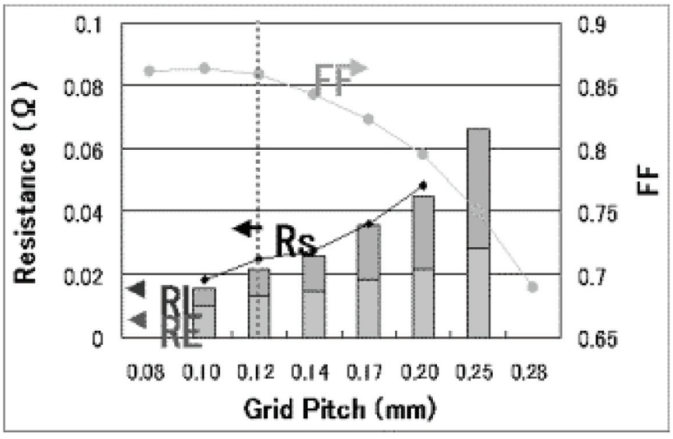

shown in Figure 21 (Takamoto, et al., 1997). The solar simulator was equipped with both Xe lamp and halogen lamp and adjusted AM1.5G spectrum. Most recently, 41.6% efficiency has been reported with InGaP/GaAs/Ge 3-junction concentrator cells by Spectrolab (King, et al., 2009).

Concentrator InGaP/GaAs/Ge 3-junction solar cell modules have also been developed for terrestrial use (Araki, et al., 2005). A new concentrator optics is introduced, consist of a non-imaging dome-shaped Fresnel lens, and a kaleidoscope homogenizer. The non-imaging Fresnel lens allows wide acceptance half angle with keeping the same optical efficiency with minimum chromatic aberration. The homogenizer reshapes the concentrated into square solar cell aperture, mixed rays to uniform flux. Injection molding is capable of manufacturing thousands of lenses in a single day and by a single machine. The drawback of this method is difficulty of creating precise prism angles and flat facets. The maximum efficiency was a little above 80% and overall efficiency was 73%. After improvement of the process conditions, the averaged efficiency raised to 85.4%.

A new packaging structure for III-V concentrator solar cells is developed, applicable mainly to Fresnel lens concentrator modules but may also be used in dish concentrator systems. The solar cell used in the new receiver package is III-V 3-junction concentrator solar cell developed. It is grown on a fragile Ge substrate with thickness of only 150 um. The overall size was 7 mm X 9 mm with 7 mm square aperture area.

In addition, the following technologies have been developed:

1. Super-high pressure and vacuum-free lamination of the solar cell that suppresses the temperature rise to 20 degrees under 550 X geometrical concentration illumination of sunbeam.
2. Direct and voids-free soldering technologies of the fat metal ribbon to the solar cell, suppressing hot-spots and reducing the resistance, thereby allowing a current 400 times higher than normal non-concentration operation to be passed with negligible voltage loss.
3. A new encapsulating polymer that survives exposure to high concentration UV and heat cycles.
4. Beam-shaping technologies that illuminate the square aperture of the solar cell, from a round concentration spot.

Figure 21. Efficiency of a high-efficiency InGaP/InGaAs/Ge 3-junction cell vs. number of suns

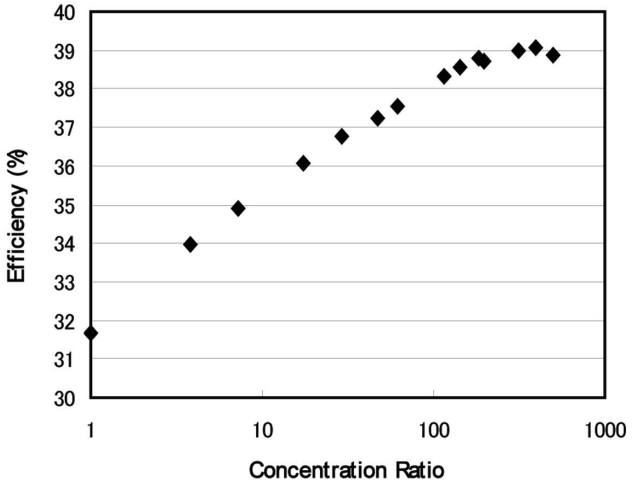

5. Homogeniser technologies that give a uniform flux and prevent the conversion losses that stem from chromatic aberration and flux intensity distribution.

The concentrator module is designed with ease of assembly in mind. All the technologically complex components are packaged into a receiver so that a series of receivers and lenses can be assembled with standard tools, using local materials and workforce. The concept is similar to the computer and automobile assembly industries, where key components are imported but the product assembled locally. It is anticipated that this approach will reduce the manufacturing cost of the module as shown in Figure 22.

The peak uncorrected efficiency for the 7,056 cm^2 400 X module with 36 solar cells connected in series was 26.6%, measured in house. The peak uncorrected efficiencies for the same type of module with 6 solar cells connected in series and 1,176 cm^2 area measured by Fraunhofer ISE and NREL were 27.4% and 24.9%. The 5,445 cm^2 550 X modules have also demonstrated 27-28.9%, measured in house. Table 3 summarizes the measured efficiency in three different sites.

A new 400X and 550X (geometrical concentration ratio) are developed and show the highest efficiency in any types of PV as well as more than 20 years of accelerated lifetime. This achievement is blessed with new innovative concentrator technologies. The new concentrator system is expected to open a door to a new age of high efficiency PV.

MOST RECENT RESULTS OF MJ CELLS

Recently, more than 40% efficiency cells were reported by Fraunhofer ISE (Bett, et al., 2009) and Spectrolab (King, et al., 2009). Concentrator 4-junction or 5-junction solar cells have great potential for realizing super high efficiency of over 50%. We have been studying concentrator multi-junction solar cells under Japanese Innovative Photovoltaic R&D program started since FY2008 (King, et al., 2009). Figure 23 shows overview of NEDO's PV R&D Program. Japanese Innovative Photovoltaics R&D Program has been started from fiscal year 2008 and the target in this program is to develop high efficiency solar cells with conversion

Figure 22. Inside of the 400 X concentrator module with 36 receivers connected in series

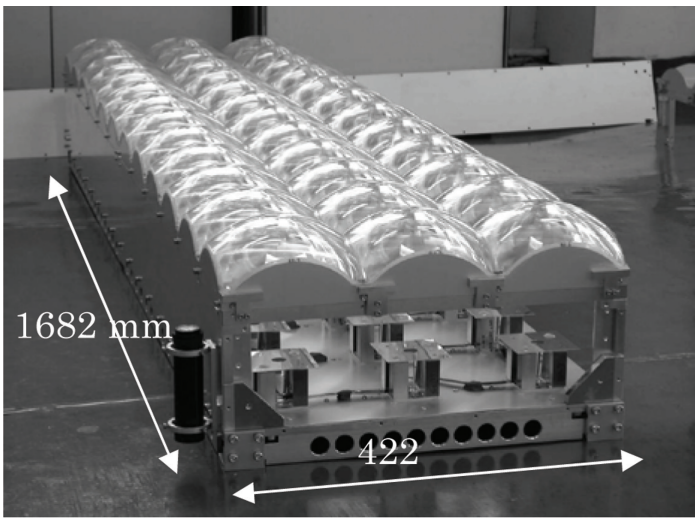

Table 3. Uncorrected peak efficiency measurement

Concentration	Area cm²	Site	Ambient	Uncorrected Efficiency	DNI W/m²
400 X	7,056	Inuyama, Japan Manufacturer	29 C	27.6%	810
400 X	7,056	Toyohashi, Japan Independent	7 C	25.9%	645
400 X	1,176	Fraunhofer ISE, Germany Independent	19 C	27.4%	839
400 X	1,176	NREL, USA Independent	29 C	24.9%	940
550 X	5,445	Inuyama, Japan Manufacturer	33 C	28.9%	741
550 X	5,445	Toyohashi, Japan Independent	28 C	27%	777

Figure 23. Overview of NEDO's PV R&D program

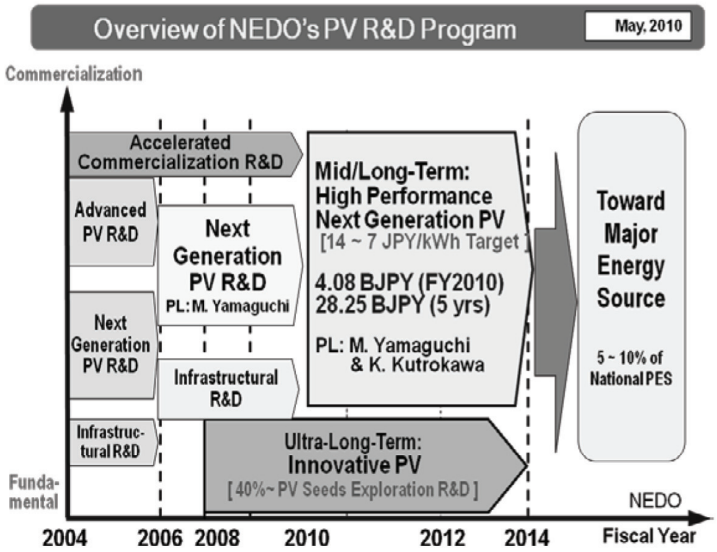

efficiency of more than 40% and low electricity cost of less than 7 JPY/kWh until 2050.

Most recently, world-record efficiency (36.9%) at 1-sunAM1.5G has been realized with inverted epitaxial grown InGaP/GaAs/InGaAs 3-junction cells by Sharp (Takamoto, et al., 2010). Figure 24 fabrication process of InGaP/GaAs/InGaAs 3-J solar cell inverted epitaxial grown. Figure 24 shows I-V curve of world-record efficiency InGaP/GaAs/InGaAs solar cell. Figure 25 shows chronological improvements in conversion efficiencies of III-V compound MJ solar cells under 1-sun and concentrator conditions (see Figure 26).

Most recently, 42.1% efficiency under 230-suns has been obtained with InGaP/GaAs/InGaAs cell as shown in Figure 27 (Takamoto, et al., 2010).

Figure 24. Fabrication process of InGaP/GaAs/InGaAs 3-J solar cell inverted epitaxial grown

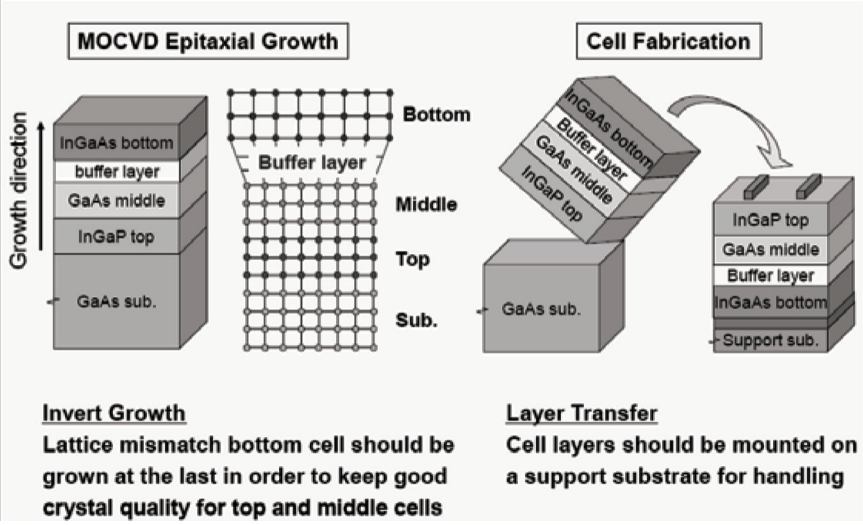

Figure 25. Current(I)–voltage(V) curve of world-record efficiency InGaP/GaAs/InGaAs measured by the AIST

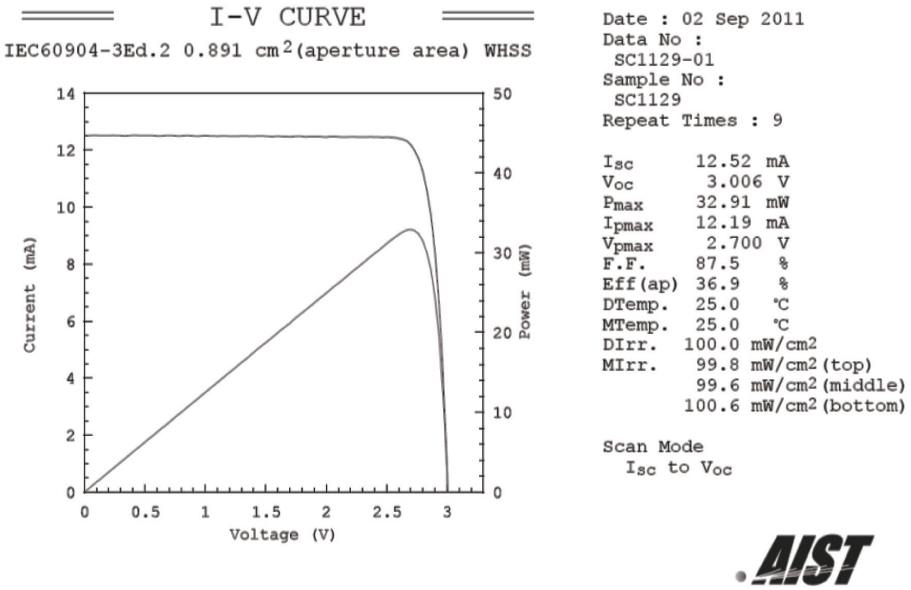

FUTURE DIRECTION

Multi-junction solar cells will be widely used in space because of their high conversion efficiency and better radiation-resistance. In order to apply super high-efficiency cells widely, it is necessary to improve their conversion efficiency and reduce their cost. The new Concentrator PV system with two times more annual power generation than the conventional crystalline silicon flat-plate system will open a new market for apartment or building rooftop applications. Another interesting appli-

Figure 26. Chronological improvements in conversion efficiencies of III-V compound multi-junction solar cells under 1-sun and concentrator conditions

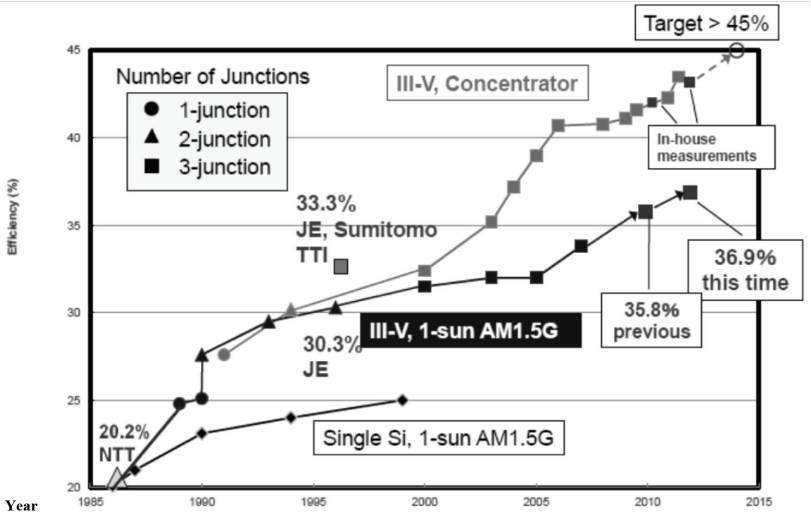

cation is what we call the tree planting PV and large-scale PV power plant applications

Now, we are approaching 40% efficiency by developing concentrator MJ solar cells as shown in Figure 28. Concentrator 4-junction or 5-junction solar cells have great potential for realizing super high-efficiency of over 50% [29,30]. Therefore, concentrator 3-junction and 4-junction solar cells have great potential for realizing super high-efficiency of over 40%. As a 3-junction combination, InGaP/InGaAs/Ge cell on a Ge substrate will be widely used because this system has already been developed. The 4-junction combination of an Eg=2.0eV top cell, a GaAs second-layer cell, a material third-layer cell with an Eg of 1.05eV, and a Ge bottom cell is lattice-matched to Ge substrates and has a theoretical efficiency of about 42% under 1-sun AM0. This system has a potential efficiency of over 47% under 500-suns AM1.5 condition.

The new Concentrator PV (CPV) system with two times more annual power generation than the conventional crystalline silicon flat-plate system will open a new market for apartment or building rooftop applications. Another interesting application is what we call the tree planting PV and large-scale PV power plant applications. Since concentrator MJ and crystalline Si solar cells are expected to contribute to electricity cost reduction for widespread PV applications as shown in Figure 29, we would like to contribute to commercialization of CPV technologies as the 3rd PV technologies in addition to the first crystalline Si PV and the 2nd thin-film PV technologies. The

Figure 27. Concentration ration dependence of efficiency of a high-efficiency InGaP/GaAs/InGaAs 3-junction cell

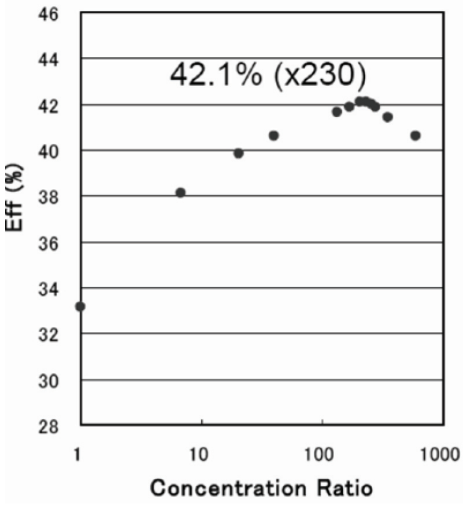

Figure 28. Future predictions of solar cell efficiencies

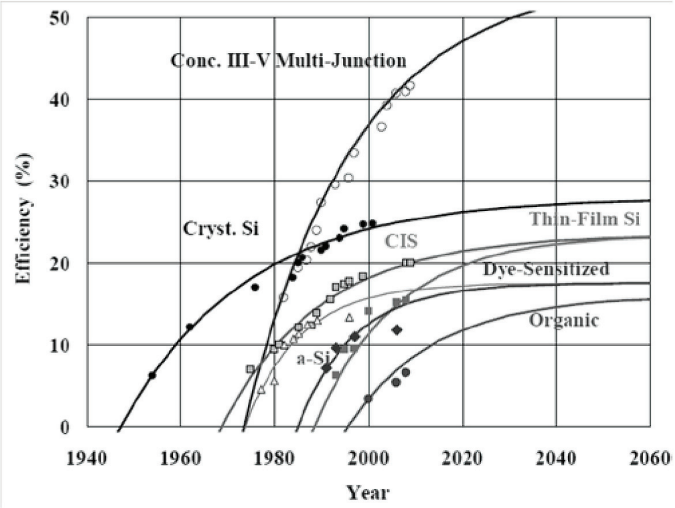

Figure 29. Scenario of electricity cost reduction by developing concentrator solar cells

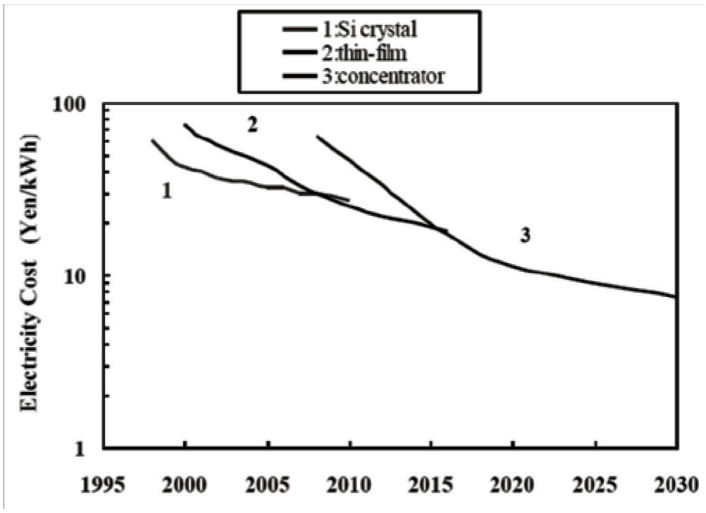

scale of the CPV industry lags that of flat-plate PV by about one or two decades. It is expected, however, to make up this delay to the point where, in, 2013 the cumulative installed capacity will lie in the region of several hundred MWp. R&D work has to be undertaken particularly in the area of large-scale production, i.e. high-throughput, to realise this ambition. Material consumption must also be reduced. A projection for future turnkey CPV system prices extrapolated from current prices are shown in Figure 30. Figure 30 shows the expected yearly production of Concentrator PV (CPV) systems (red) and the price of turn-key installed CPV systems in Euro/W_p (black) (EC, 2007).

The most important R&D in CPV manufacturing will aim at (EC, 2007):

1. Improving the efficiency of mass-produced cells to the levels currently seen in the labora-

Figure 30. The expected yearly production of concentrator PV (CPV) systems (red) and the price of turn-key installed CPV systems in euro/W_p (black)

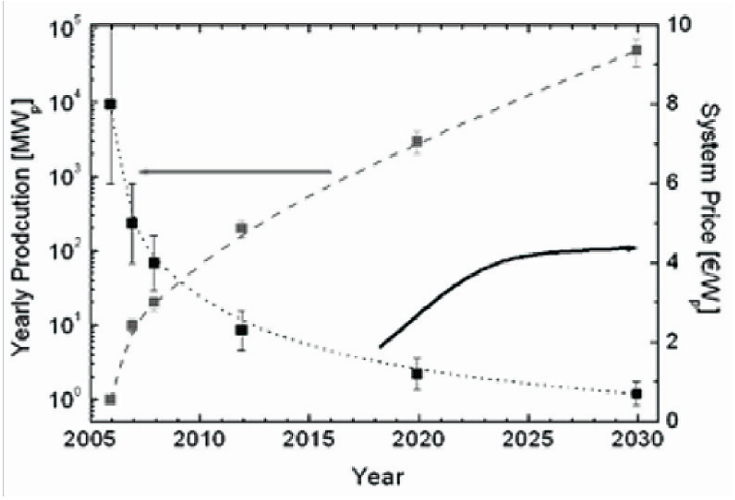

Figure 31. World energy vision 2100 recommended by the German council on global change

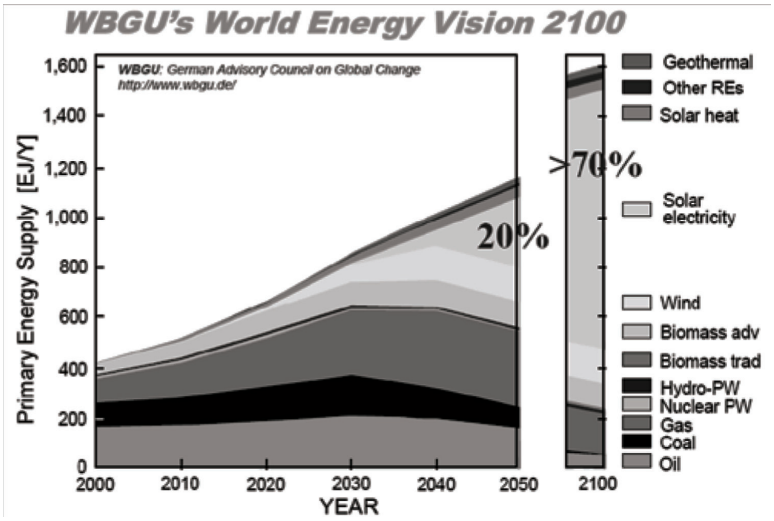

tory (over 26%) and to 35 to 45% efficiency in the longer term

2. Improving optical elements (optical efficiency, lifetime and product engineering)
3. Automated industrial module assembly (adjustment of elements, packaging and sealing), high-throughput manufacturing with high yield, resulting in products with long lifetimes
4. Construction of light, robust, and precise trackers for all outdoor climate conditions
5. Set-up and monitoring of demonstration systems and large plants, in the range several hundred kWp (short term) to multi-MWp (medium term)
6. Techniques for guaranteeing the quality of products with intended lifetimes of over 20 years, development of standards, in-line testing, and recycling methods for the modules.

Figure 31 shows World Energy Vision 2100 recommended by the German Council on Global Change (WBGU, 2003). As a result of further development of higher efficiency, lower cost and highly reliable solar cells, larger contribution to world energy by PV is expected.

ACKNOWLEDGMENT

This work was supported by New Energy and Industrial Technology Development Organization (NEDO) under METI (Ministry of Economy, Trade, and Industry). The author thanks members of Toyota Tech. Inst., Sharp, Daido Steel, JAXA, JAEA, Univ. Tokyo, Meijo Univ., Kyushu Univ., and Miyazaki Univ. for their collaboration and cooperation.

REFERENCES

Ahrenkiel, R. K., Keyes, B. M., Durbin, S. M., & Gray, J. L. (1993). Paper. In *Proceedings of the 23rd IEEE Photovoltaic Specialists Conference,* (p. 42). New York, NY: IEEE Press.

Amano, C., Sugiura, H., Yamamoto, A., & Yamaguchi, M. (1987). Paper. Applied Physics Letters, (n.d), 51.

Ando, K., Amano, C., Sugiura, H., Yamaguchi, M., & Salates, A. (1987). Nonradiative e-h recombination characteristics of mid-gap electron trap in $Al_xGa_{1-x}As$ (x=0.4) grown by molecular beam epitaxy. *Japanese Journal of Applied Physics*, *26*, L266.

Araki, K., Uozumi, H., Egami, T., Hiramatsu, M., Miyazaki, Y., & Kemmoku, Y. (2005). Development of concentrator modules with dome-shaped fresnel lenses and triplejunction concentrator cells. *Progress in Photovoltaics: Research and Applications*, *13*, 513.

Bett, A. W., et al. (2000). Paper. In *Proceedings of the 24th European Photovoltaic Solar Energy Conference*, (p. 1). WIP.

Brown, M. R., Goldhammer, L. J., Goodelle, G. S., Lortz, C. U., Perron, J. N., & Powe, J. S. … Krut, D. D. (1997). Paper. In *Proceedings of the 26th IEEE Photovoltaic Specialists Conference,* (p. 805). New York, NY: IEEE Press.

EU. (2007). *A strategic research agenda for photovoltaic solar energy technology PV technology platform*. Retrieved from http://www.eupvplatform.org/fileadmin/Documents/PVPT_SRA_Complete_070604.pdf

Fan, J. C. C., Tsaur, B.-Y., & Palm, B. J. (1982). Paper. In *Proceedings of the 16th IEEE Ptotovoltaic Specialists Conference*, (p. 692). New York, NY: IEEE Press.

Goetzberger, J., Luther, & Willeke, G. (2002). Solar cells: Past, present, future. *Solar Energy Materials and Solar Cells*, *74*, 1. doi:10.1016/S0927-0248(02)00042-9

Hutchby, J. A., Markunas, R. J., & Bedair, S. M. (1985). Paper. In *Proceedings of the SPIE, Photovoltaics*, (Vol. 543), (p. 543). SPIE.

Jackson, E. D. (1955). *Transactions of the conference on the use of solar energy 5*. Tucson, AZ: Tucson University of Arizona Press.

Khan, A., Yamaguchi, M., Bourgoin, J. C., & Takamoto, T. (2000). Room-temperature minority-carrier injection-enhanced recovery of radiation-induced defects in p-InGaP and solar cells. *Applied Physics Letters*, *76*, 2559. doi:10.1063/1.126407

King, R. R., Boca, A., Hong, W., Liu, X.-Q., Bhusari, D., & Larrabee, D. … Karam, N. H. (2009). Paper. In *Proceedings of the 24th European Photovoltaic Solar Energy Conference*, (p. 55). Munich, Germany: WIP.

Lang, D. V., Kimerling, L. C., & Leung, S. Y. (1976). Recombination-enhanced annealing of the $E1$ and $E2$ defect levels in 1-MeV-electron–irradiated n-GaAs. *Journal of Applied Physics*, *47*, 3587. doi:10.1063/1.323161

Olson, J., Kurtz, S., & Kibbler, K. (1990). A 27.3% efficient $Ga_{0.5}In_{0.5}P$/GaAs tandem solar cell. *Applied Physics Letters*, *56*, 623. doi:10.1063/1.102717

Osaka, Japan: WCPEC. Takamoto, T., Yamaguchi, M., Ikeda, E., Agui, T., Kurita, H., & Al-Jassim, M. (1999). Mechanism of Zn and Si diffusion from a highly doped tunnel junction for InGaP/GaAs tandem solar cells. Journal of Applied Physics, 85, 1481.

Sugiura, H., Amano, C., Yamamoto, A., & Yamaguchi, M. (1988). Double heterostructure GaAs tunnel junction for a AlGaAs/GaAs tandem solar cell. *Japanese Journal of Applied Physics*, *27*, 269.

Takamoto, T., Agui, T., Ikeda, T., & Kurita, E. (2000). Paper. In *Proceedings of the 28th IEEE Photovoltaic Specialists Conference*, (p. 976). New York, NY: IEEE Press.

Takamoto, T., Agui, T., Kamimura, K., Kaneiwa, M., Imaizumi, M., Matsuda, S., & Yamaguchi, M. (2003). Paper. In *Proceedings of the 3rd World Conference on Photovoltaic Energy Conversion, WCPEC-3*, (p. 581).

Takamoto, T., Agui, T., Yoshida, A., Nakaido, K., Juso, H., & Sasaki, K. … Takahashi, M. (2010). Paper. In *Proceeding of 35th IEEE Photovoltaic Specialists Conference*, (p. 412). New York, NY: IEEE Press.

Takamoto, T., Ikeda, E., Agui, T., Kurita, E., Tanabe, T., & Tanaka, S. … Yamaguchi, M. (1997). Paper. In *Proceedings of the 26th IEEE Photovoltaic Specialists Conference*, (p. 1031). New York, NY: IEEE Press.

Takamoto, T., Ikeda, E., Kurita, H., Ohmori, M., & Yamaguchi, M. (1997). Two-terminal monolithic *$In_{0.5}Ga_{0.5}P$/GaAs* tandem solar cells with a high conversion efficiency of over 30%. *Japanese Journal of Applied Physics*, *36*, 6215. doi:10.1143/JJAP.36.6215

Takamoto, T., Kaneiwa, M., Imaizumi, M., & Yamaguchi, M. (2005). InGaP/GaAs-based multijunction solar cells. *Progress in Photovoltaics: Research and Applications*, *13*, 495. doi:10.1002/pip.642

Tomita, T. (2006). Paper. In *Proceedings of the 4th World Conference on Photovoltaic Energy Conversion*, (p. 2450). New York, NY: IEEE Press.

WBGU. (2003). *World in transition – Towards sustainable energy systems*. Retrieved from http://www.wbgu.de/

Wolf, M. (1960). Detailed balance limit of efficient p-n junction solar cells. In *Proceedings of IRE 48*, (pp. 1246). IRE.

Yamaguchi, M. (2003). III–V compound multi-junction solar cells: Present and future. *Solar Energy Materials and Solar Cells*, *75*, 261. doi:10.1016/S0927-0248(02)00168-X

Yamaguchi, M. (2004). Paper. In *Proceedings of the 19th European Photovoltaic Solar Energy Conference*. Munich, Germany: WIP.

Yamaguchi, M., & Amano, C. (1985). Numerical analysis for high-efficiency GaAs solar cells fabricated on Si substrates. *Journal of Applied Physics*, *58*, 3601.

Yamaguchi, M., Okuda, T., Taylor, S. J., Takamoto, T., Ikeda, W., & Kurita, H. (1997). Superior radiation-resistant properties of InGaP/GaAs tandem solar cells. *Applied Physics Letters*, *70*, 1566. doi:10.1063/1.118618

Yang, M.-J., Yamaguchi, M., Takamoto, T., Ikeda, E., Kurita, H., & Ohmori, M. (1997). III–V compound multi-junction solar cells: Present and future. *Solar Energy Materials and Solar Cells*, *45*, 331. doi:10.1016/S0927-0248(96)00079-7

Chapter 10
Quantum Dot Solar Cells

Yoshitaka Okada
The University of Tokyo, Japan

Katsuhisa Yoshida
The University of Tokyo, Japan

Yasushi Shoji
University of Tsukuba, Japan

ABSTRACT

Advanced concepts for high efficiency solar cells such as hot carrier effects, Multi-Exciton Generation (MEG), and Intermediate-Band (IB) absorption in low-dimensional nanostructures are under focused research topics in recent years. Among various potential approaches, this chapter is devoted to the device physics and development of the state-of-the-art technologies for quantum dot-based IB solar cells.

INTRODUCTION

By avoiding all the nonradiative recombination processes within the solar cell, the theoretical maximum efficiency to a thermodynamic upper limit becomes ~ 85% for a fully concentrated black-body radiation of 5,800K (Green, 2003; Würfel, 2009). On the other, the maximum efficiency of a single-junction solar cell is limited to the Shockley-Queisser (1961) limit of ~ 31% for AM1.5 spectrum. The main physical processes that limit the efficiency of a solar cell are the losses by thermal dissipation or thermalization, and non-absorption of low-energy below-bandgap photons.

Thus improving the efficiency means developing the methods to reduce these losses. One of the concepts is to split the solar spectrum among multiple bandgap absorbers or sub-cells, e.g. tandem or multijunction cells. The others employ more advanced techniques such as hot carrier effects, Multi-Exciton Generation (MEG), and Intermediate-Band (IB) absorption in low-dimensional nanostructures such as semiconductor quantum dots (Nozik, 2002, 2008; Green, 2003; Luque, 1997). Among various approaches available, this Chapter is devoted to the device physics and development of the state-of-the-art technologies for quantum dot-based IB solar cells.

DOI: 10.4018/978-1-4666-1927-2.ch010

Quantum Dot (QD) superlattice incorporated in the active region of a *p-i-n* single-junction solar cell has attracted significant interest as a potential means of utilizing the sub-bandgap infra-red photons to generate additional photocurrents, through absorption *via* superlattice miniband states, beyond that corresponding to the valence-to-conduction band transitions (Luque, 1997). The QDs also offer the possibility for reducing thermal dissipation loss. If such a nanostructure solar cell were realized, the conversion efficiency could not only exceed the Shockley-Queisser (1961) limit of a conventional single-junction solar cell, which is ~ 31% for AM1.5 spectrum, but further provides a pathway to increase the efficiency up to the thermodynamic limit of > ~ 60% under full concentration.

In a QD solar cell, QDs are required to be homogeneous and small in size, and are regularly and tightly placed in all three dimensions. This configuration then leads to formation of an Intermediate-Band (IB) or a superlattice miniband that is well separated in energy from the higher-order states (Tomić, 2008). Secondly, IB states should ideally be half-filled with electrons in order to ensure an efficient pumping of electrons by providing both the empty states to receive electrons being photo-excited from the Valence Band (VB), and filled states to promote electrons to the Conduction Band (CB) via absorption of second sub-bandgap photons (Martí, 2001). This implies that its own quasi-Fermi level is defined within IB, as schematically shown in Figure 1.

Proposed implementation of QD-IB solar cells must accompany two-step carrier generation *via* IB states and it has been difficult to clearly verify this concept at room temperature. The demonstration of QD-IB solar cells is presently undergoing two research stages. The first is to develop the technologies to realize a high-density QD array or superlattice of low defect density, which is placed in the central active region of the cell. The fabrication of QD arrays is most commonly achieved by taking advantage of spontaneous self-assembly of coherent three-dimensional (3D) islands in lattice-mismatched epitaxy long known as Stranski-Krastanov (S-K) growth in Molecular Beam Epitaxy (MBE). However, the number of QDs is severely limited by the lattice strain accumulation in the crystalline material as the number of stacked QD layers is increased. In S-K growth of InAs/(Al)GaAs system, misfit disloca-

Figure 1. Schematic energy band diagram of QD-IB solar cell shown with possible photo-absorption processes involved. The energy bandgap of host material and quasi-Fermi level of IB are given by E_g and E_{IF}, respectively.

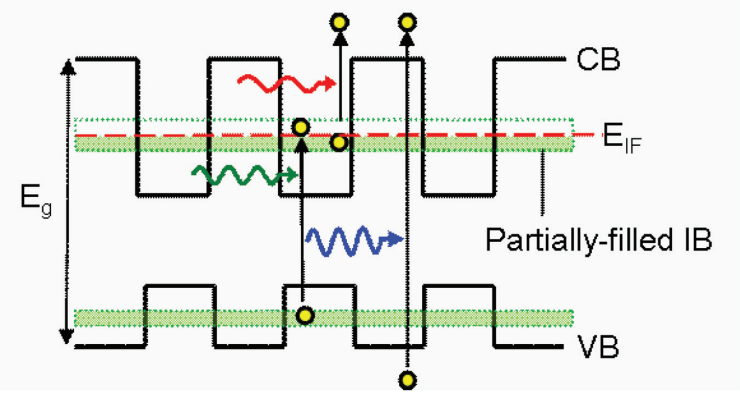

tions are generated after typically 10 ~ 15 layers of stacking (Solomon, 1996; Blokhin, 2009). Recently, it has been proven that strain-compensated or strain-balanced growth techniques can significantly improve the QD quality and characteristics of QD solar cells even after stacking of 50 ~ 100 QD layers by S-K growth. To date, InAs QDs in AlGaInAs matrix on InP substrate (Okada, 2005), InAs QDs in GaAsP (Popescu, 2008), and in GaP (Hubbard, 2008) matrix on GaAs substrate, and InAs QDs in GaNAs on GaAs (001) (Oshima, 2008; Okada, 2009; Takata, 2010), and on (311)B substrates (Shoji, 2010a) of high material quality have been reported.

The second stage is to realize ideal half-filled IB states to maximize the photocurrent generation by two-step photon absorption, which is the central operation principle of IB solar cells. Martí *et al.* (2006) has used a modulation doping technique to fabricate QD-IB solar cell, in which GaAs barrier is delta-doped with Si impurities with a sheet density equaling the InAs QD areal density. Due to spin degeneration, this condition equals half the density of electronic states in IB. On the other, Strandberg *et al*. (2009) showed that IB must be partially filled by means of doping within reasonable optical lengths in order to achieve high efficiencies, if QD-IB solar cells were to be operated under 1 sun condition. However, it becomes possible to sustain a reasonable population of photo-generated electrons even in non-doped QD-IB solar cells if operated under concentrated sunlight, typically 100 ~ 1000 suns. Yoshida (2010a) has also recently reported similar calculated results based on a self-consistent device simulation.

The sub-bandgap photons can *optically* pump the electrons both from VB to IB states and from IB to CB states. However the rate of *thermal* escape of electrons from IB to CB continuum states as well as recombination loss from CB to IB transitions will increase significantly at room temperature. If all the carriers in IB states are not in electrochemical equilibrium, then a clear detection of photo-excitation of electrons from IB to CB giving rise to an increase in the photocurrent at room temperature more difficult. A photocurrent production as a result of two-step photon absorption has been successfully detected at cryogenic temperatures by Martí *et al.* (2006), and more recently at room temperature by Okada *et al.* (2010), though the efficiencies are still small and require improvements.

In this chapter, we will first review the theoretical analysis for various cell designs where QD technology could be implemented to configure a high-efficiency intermediate-band solar cell. Then the self-organized growth of QDs, growth mechanisms and control of size and density of QDs, and direct doping of QDs will be reviewed. We will summarize with specific experimental behavior for proof of operation with two-step photon absorption from current state-of-the-art IB solar cells implementing QD superlattice.

DEVICE PHYSICS AND TECHNOLOGIES OF QUANTUM DOT SOLAR CELLS

Device Physics and Efficiency Analysis of QD Intermediate-Band Solar Cells

Multi-stacked or three dimensional superlattice Quantum Dot Solar Cells (QDSCs) can operate as the intermediate band solar cells. To fabricate QDSC, not only high crystalline quality but also structural optimization is very important. Thus, device domain simulations for IBSCs would play important roles. In this section, we introduce 1 dimensional device domain simulation for IBSCs by using drift-diffusion method (Selberherr, 1984) and show its calculation results and future topics. Device domain simulations also have been shown in some papers (Lin, 2009; Strandberg, 2009; Yoshida, 2010a, 2010b, 2010c; Tobias, 2010).

Device Simulation for QD Intermediate Band Solar Cells

Drift diffusion method (Selberherr, 1984) can provide powerful solutions for semiconductor devices analysis. Basic equations for semiconductor devices are the Poisson equation, carrier continuity equations. These equations must be solved self-consistently. The Poisson equation gives electrostatic potentials. Carrier continuity equations provide carrier densities related their mobility and life times. For IBSCs, the electrons in intermediate band state also affect to the electrostatic potentials and also carrier generation and recombination rates. Therefore, we have to solve the basic equations with carrier continuity equation for electrons in intermediate band. In present stage of QDSCs, coupling effects of each QD are not clear. Therefore, we assume that electron transport in intermediate band can be negligible and the IB is treated as a locally fixed level.

According to our assumption, electron densities in each local position in real space are determined by the electron transition rates between from valence band to intermediate band and from intermediate band to conduction band. These transition rates must be balanced in the steady state. For equilibrium condition, there is no net recombination rate in each position. In non-equilibrium condition, by using local equilibrium approximation, quasi-Fermi levels can be defined for each carrier because of the difference of "life times." The image of local balance treatment is similar to Shockley-Read-Hall type recombination except for allowing optical transition both from VB to IB and from IB to CB.

In the Poisson equation, net charge density is determined by electrons in CB and IB, holes, ionized accepter and donor densities (see Equation 1).

Where q is elementary charge, ε^* is the relative permittivity, ε_0 is the vacuum permittivity, $p(x)$ is the hole density, $n_C(x)$ is electron density in CB, $n_I(x)$ is electron density in IB, $N^+_D(x)$ is the ionized donor density, and $N^-_A(x)$ is the ionized accepter density. The relations between carrier densities and their quasi Fermi levels (or Fermi level in thermal equilibrium) are approximately described by:

$$n_C(x) = N_C \exp\left(\frac{\mu_C(x) - E_C(x)}{k_B T}\right) \tag{2}$$

$$p(x) = N_V \exp\left(\frac{E_V(x) - \mu_V(x)}{k_B T}\right) \tag{3}$$

$$n_I(x) = N_I f_I(x) \tag{4}$$

$$f_I(x) = \frac{1}{\exp\left(\frac{E_I(x) - \mu_I(x)}{k_B T}\right) + 1} \tag{5}$$

where k_B is Boltzmann constant, T is the temperature of the system, N_C and N_V are the effective density of states for CB and VB, N_I is the effective density of state for IB which is assumed as twice the density of QDs, μ_C, μ_V and μ_I are quasi Fermi levels for CB, VB and IB, and f_I is occupation rate of IB, respectively. In the steady state, these carriers satisfy carrier continuity equations. Quasi-

Equation 1.

$$\frac{d\psi(x)}{dx^2} = -\frac{q}{\epsilon^* \epsilon_0}\left[n_C(x) - p(x) + n_I(x) - N_D^+(x) - N_A^+(x)\right] \tag{1}$$

Fermi level of IB can be distinguished from other quasi-Fermi levels, especially for QD-IBSC case and would be defined in the same temperature of the system. This quasi-Fermi level splitting is important for IBSC operation.

The carrier continuity equation for electrons in CB is expressed as:

$$G_{CV}(x) - U_{CV} + G_{CI}(x) - U_{CI}(x) + \frac{1}{q}\frac{dJ_C(x)}{dx} = 0 \quad (6)$$

The continuity equation of holes is:

$$G_{CV}(x) - U_{CV} + G_{IV}(x) - U_{IV}(x) - \frac{1}{q}\frac{dJ_V(x)}{dx} = 0 \quad (7)$$

In Equation (6) and(7), G_{ij} is the optical generation rate, U_{ij} is the recombination rate where subscript *ij=CI, IV, CV* expresses CB-IB, IB-VB and CB-VB transition respectively, J_C is the electron current density in CB and J_V is the hole current density. For electrons in IB, under present assumptions:

$$G_{CI}(x) - U_{CI}(x) = G_{IV}(x) - U_{IV}(x)$$

This is local IB balance equation. This equation determines the electron density in IB. J_C and J_V are given by drift-diffusion equations.

$$J_C = -q\mu_e n_C \frac{d\psi}{dx} + qD_e \frac{dn_C}{dx} \quad (8)$$

$$J_V = -q\mu_h p \frac{d\psi}{dx} - qD_h \frac{dp}{dx} \quad (9)$$

where μ_e and μ_h are the carrier mobility of electrons in CB and holes, D_e and D_h are the diffusion coefficients, respectively.

The optical generation rate for CV can be described by:

$$G_{CV}(x) = \int_0^\infty \alpha^*_{CV}(E,x)\alpha_{CV}(E)F_{sun}(E)e^{-F_D(x)} \quad (10)$$

where α^*_{CV} is absorption factor of CV, α_{CV} is the absorption coefficient of CV, F_{sun} is AM0 solar spectrum, $F_D(E)$ is decay factor of incident photons which has an energy, E. Incident photon spectrum can be expressed as the black body radiation:

$$F_{sun}(E) = Xf_s \frac{2\pi}{h^3c^2}\frac{E^2}{\exp(E/k_BT_S) - 1} \quad (11)$$

where X is the amplitude of concentration, f_S expresses the angular rage of the Sun, h is Planck's constant, c is the speed of light, and T_S is temperature of the sun. The optical generation rates usually are assumed that occupation rates of electrons in CB and holes in VB are negligible because their rates are small compared to their effective density of states. On the other hand, the occupation rate of IB affects the generation rate *via* IB. Thus, these generation rates are expressed by Equations (12) and (13) where α^*_{CI} and α^*_{IV} are the absorption factors and α_{CI} and α_{IV} are the absorption coefficients of CI and IV transitions. These absorption factors and the decay factor

Equation 12.

$$G_{CI}(x) = \int_0^\infty \alpha^*_{CI}(E,x)\alpha_{CI}(E)f_I(x)F_{sun}(E)e^{-F_D(E,x)} \quad (12)$$

Equation 13.

$$G_{IV}(x) = \int_0^\infty \alpha^*_{IV}(E,x)\alpha_{IV}\{1 - f_I(x)\}F_{sun}(E)e^{-F_D(E,x)} \tag{13}$$

Equation 14.

$$\alpha^*_{CV}(E,x) = \frac{\alpha_{CV}(E)}{\alpha_{CI}(E)f_I(x) + \alpha_{IV}(E)\{1 - f_I(x)\} + \alpha_{CV}(E)} \tag{14}$$

Equation 15.

$$\alpha^*_{CI}(E,x) = \frac{\alpha_{CI}(E)f_I(x)}{\alpha_{CI}(E)f_I(x) + \alpha_{IV}(E)\{1 - f_I(x)\} + \alpha_{CV}(E)} \tag{15}$$

Equation 16.

$$\alpha^*_{IV}(E,x) = \frac{\alpha_{IV}(E)\{1 - f_I(x)\}}{\alpha_{CI}(E)f_I(x) + \alpha_{IV}(E)\{1 - f_I(x)\} + \alpha_{CV}(E)} \tag{16}$$

depend on the relation of absorption coefficients, the IB occupation rates and the position from the solar cell surface. The absorption factors mean distributions of incident photon fluxes weighted by each absorption rate. Thus, α^*_{CV}, α^*_{CI} and α^*_{IV} are expressed in Equations (14), (15), and (16). The outside of the IB region, there is no IB state. Therefore, α^*_{CV} is 1. The decay factor changes in the front-, in- and back-side of IB region, respectively. For the front-side:

$$F_D(E,x) = \alpha_{CV}(E)x \tag{17}$$

For the inside:

$$\begin{aligned} F_D(E,x) = {} & \alpha_{CI}(E)\int_{x_0}^{x} f_I(x')dx' \\ & + \alpha_{IV}(E)\int_{x_0}^{x}\{1 - f_I(x')\}dx' \\ & + \alpha_{CV}(E)x \end{aligned} \tag{18}$$

where x_0 is the starting point of IB region. For the back-side:

$$\begin{aligned} F_D(E,x) = {} & \alpha_{CI}(E)\int_{x_0}^{x_I} f_I(x')dx' \\ & + \alpha_{IV}(E)\int_{x_0}^{x_I}\{1 - f_I(x')\}dx' \\ & + \alpha_{CV}(E)x \end{aligned} \tag{19}$$

where x_I is the end of IB region. In the device simulation, recombination rates, U_{ij}, in Equation (6), Equation (7), and Equation (8) usually include recombination and thermally generation processes. This point is different from the detailed balance method. The detail description of the recombination process is omitted here, (please refer to some papers). The treatment of the boundary conditions for Equation (1), Equation (6), and Equation (7) are described in Selberherr (1984).

Simplified Examples of Calculation Results

We present simplified results by using above-mentioned models with non-overlapping absorption coefficients, radiative recombination process, fixed boundary conditions and GaAs material parameters except for the absorption coefficients. About more detail description, please refer to Yoshida (2010b).

Calculated band diagrams in an equilibrium condition and a short-circuit condition under 1sun illumination are presented in Figure 2. Electrons in IB can act as fixed negative charge in each position. Thus, the contact between IB region and n-type base layer makes "*p-n* junction" like profile in Figure 2a. In Figure 2b, the band diagram is drastically changed by photofilling effects of IB state (Strandberg, 2010). Therefore, the fixed potential modeling is not suitable and the self-consistent treatment is very important for IBSC device simulations. In Figure 3, the band diagrams with *n*-type doping to IB region are presented. The doping density is set a half of IB effective density of states (or same density of QDs) to satisfied pre-filled or half-filled conditions. In the middle of IB region, the electrostatic potential is almost flat because of existence of the ionized donors (Figure 3a). Under the short-circuit condition, the diagram, Figure 3b is similar to Figure 3a by ionized dopant in IB region. In Figure 4, optical generation rates *via* IB states are presented in both Figure 2 and Figure 3 cases. The difference of $G_{CI}(x)$ and $G_{IV}(x)$ diminishes by the recombination rates according to the requirement of Equation (8). Effects of the doping in IB region can decrease the difference and help the net optical carrier generation *via* IB state.

In Figure 5, current density-voltage characteristics are presented in both cases and the without IB state case. Contrasting to the without IB state case, short circuit current densities are enhanced by two-step photon absorption *via* IB. While, the open circuit voltages of IBSC are slightly reduced because of the existence of IB states. This reduction is an intrinsic behavior of IBSC operation.

Figure 6a and 6b are energetic position dependence of conversion efficiencies of Figure 2 and Figure 3 cases, respectively. Under 1 sun illumination, the undoped IB region case has the maximum efficiency around 1.3eV. This peak is created by the relation of quasi-Fermi levels both CB and IB and recombination process works as thermal carrier generation. Under lager concentrations, this peak is diminished and occupation rates of IB states are increased by photofilling effects. On the other hand, in the doped IB region case, there is a single peak for each concentration and the peak is fixed around 0.95eV. This energy position halves the incident photon fluxes absorbed by G_{CI} and G_{IV}. In this case, the occupation rates do not strongly depend on incident light concentration ratio and pre-filling effects dominate.

In the simplified example, the doping to IB region is very important to realize the high efficiency IBSC operation and optimal IB energetic position is determined by the relation of absorption spectra *via* IB. The doping effects can suppress Shockley-Read-Hall type recombination in this region (Tobías, 2011). To investigate the optimal design of IBSCs, the spectrum and values of absorption coefficients must be treated carefully. If absorption coefficients related IB state are very small, the short circuit current enhancement decreases and the open circuit voltage increases—thus just working as the single junction solar cells (Yoshida, 2010c). For QD-IBSCs, low or non-

Figure 2. The calculated band diagrams in equilibrium (a) and in short circuit (b) condition by using the self-consistent treatment. The intermediate band region is undoped. (Reprinted from Yoshida, Okada, & Sano, 2010. Copyright 2010, IEEE.)

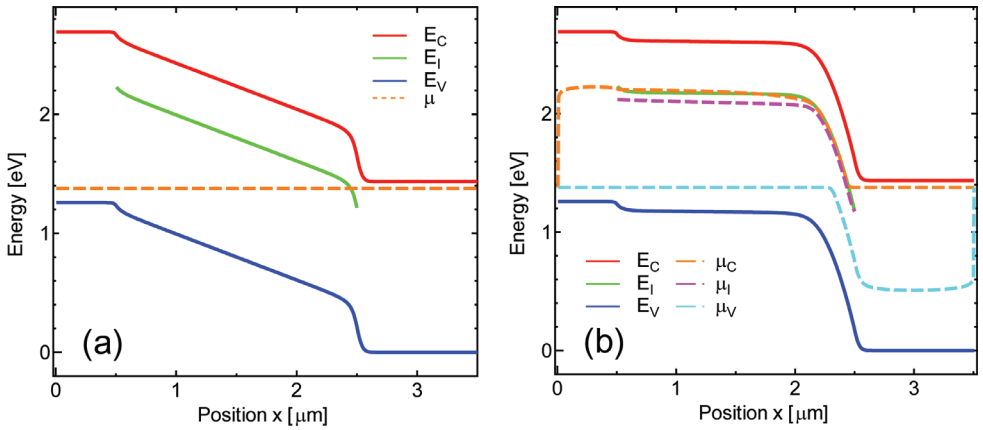

Figure 3. The calculated band diagrams in equilibrium (a) and in short circuit (b) condition by using the self-consistent treatment. The intermediate band region is doped. (Reprinted from Yoshida, Okada, & Sano, 2010. Copyright 2010, IEEE.)

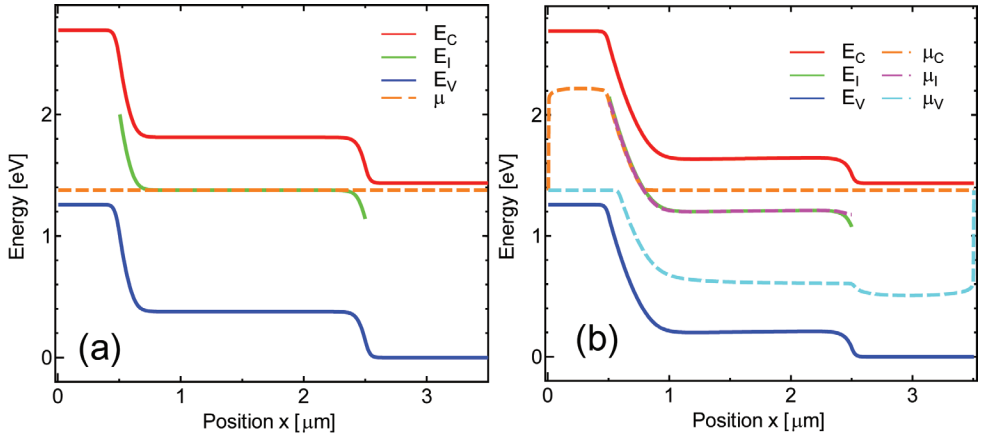

enhancement of short circuit current and non-degraded open circuit voltage just are realized too small QD density under low concentrations. Under high concentrations, the open circuit voltage of the IBSC increases and approaches single junction solar cells as net carrier generation increase.

GROWTH TECHNOLOGY OF SELF-ORGANIZED QD SUPERLATTICE SOLAR CELLS

In QD solar-cells, the QDs must ideally be uniform in size and closely and periodically positioned in all three dimensions in order to formation of

Figure 4. Optical generation rates in doped and undoped IB region cases with 1 sun illumination on the short circuit condition. The structure and the parameters are the same as Figure 2 and Figure 3.

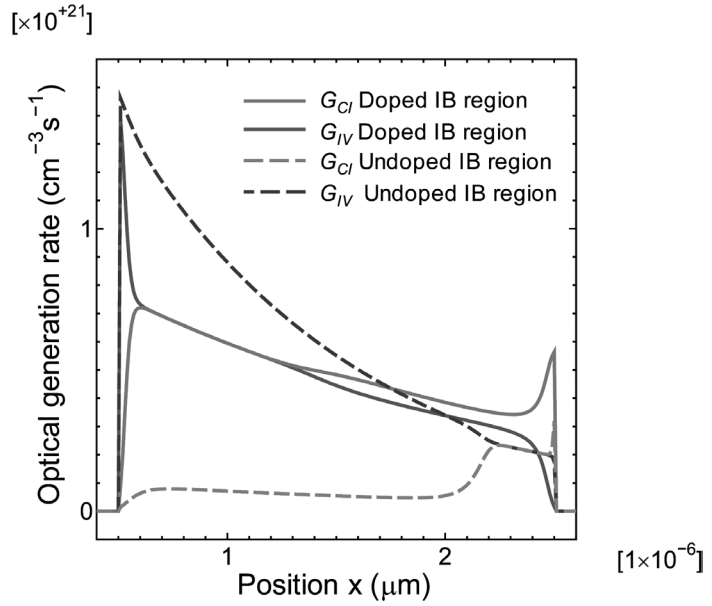

an IB or a superlattice miniband. Therefore, the advanced crystal growth technologies are required.

The most popular fabrication technique of QDs is to take advantage of spontaneous self-assembly or self-organization of coherent three-dimensional islands in lattice-mismatched heteroepitaxy known as S-K growth mode in MBE or Metal Organic Chemical Vapor Deposition (MOCVD). The heteroepitaxy of InAs grown on GaAs (001) substrate is one of the most intense studies of QDs formed by S-K mode. The lattice mismatch between InAs bulk and GaAs bulk is about 7.2%. The InAs 2D layer called wetting layer is grown in the initially growth step, and then the 3D coherent island are self-organized with increase in the InAs supply due to the increased strain energy. Figure 7a shows the Atomic Force Microscope (AFM) image for a 2.0 monolayers (MLs) of InAs QDs grown on GaAs (001) substrate. The mean diameter, height, and sheet density are 28.7 nm, 4.8 nm, and 6.1 × 10^{10} cm^{-2}, respectively. Although small size and good uniformity can be achieved for InAs self-assembled QDs grown on GaAs (001) substrate, QD structures grown on high index (311)B substrate exhibit a particular property. Figure 7b shows the AFM image for a 8.8 MLs of $In_{0.4}Ga_{0.6}As$ QDs grown on GaAs (311)B substrate. On GaAs (311)B, an in-plane ordered QDs structure with a six-fold symmetry caused by the large elastic anisotropy of surface is obtained (Akahane, 2001). When the supply increases over a critical thickness, the closely InAs QDs grown on GaAs (001) substrate often coalesce into large one and the strain energy is relaxed as dislocations are incorporated in the QDs. However, $In_{0.4}Ga_{0.6}As$ QDs grown on GaAs (311)B do not merge to form larger one beyond the thickness as shown in Figure 7b.

Figure 8 shows the AFM images for $In_{0.4}Ga_{0.6}As$ QDs on GaAs (311)B substrate grown at (a) 520 °C, (b) 500 °C, (c) 480 °C and (d) 460 °C, respectively. The QD size and density are controlled by changing the growth temperature with maintaining an ordered structure. The surface coverage of QDs is almost 100% for samples grown below 480 °C. An ordered QDs structure with a seat

Figure 5. Current-voltage characteristics of undope (case 1), doped (case 2) IB region and without IB state cases (Reprinted from Yoshida, Okada, & Sano, 2010. Copyright 2010, IEEE.)

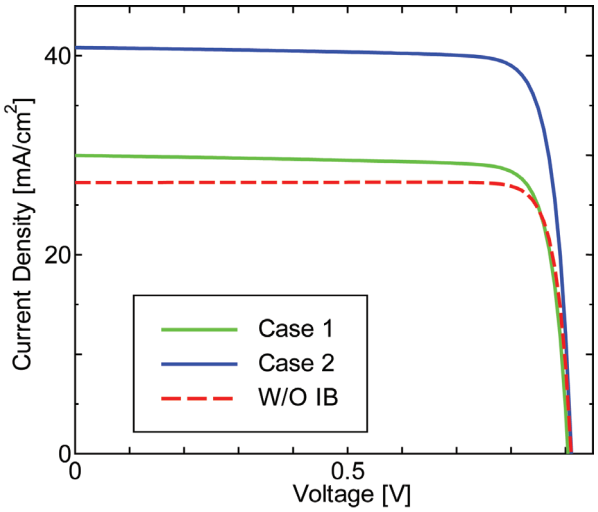

Figure 6. Conversion efficiency dependences on energetic position of IB state, E_I, in undoped (a) and doped (b) IB region cases. E_I changes form middle of host material band gap to the conduction band edge. (Reprinted from Yoshida, Okada, & Sano, 2010. Copyright 2010, IEEE.)

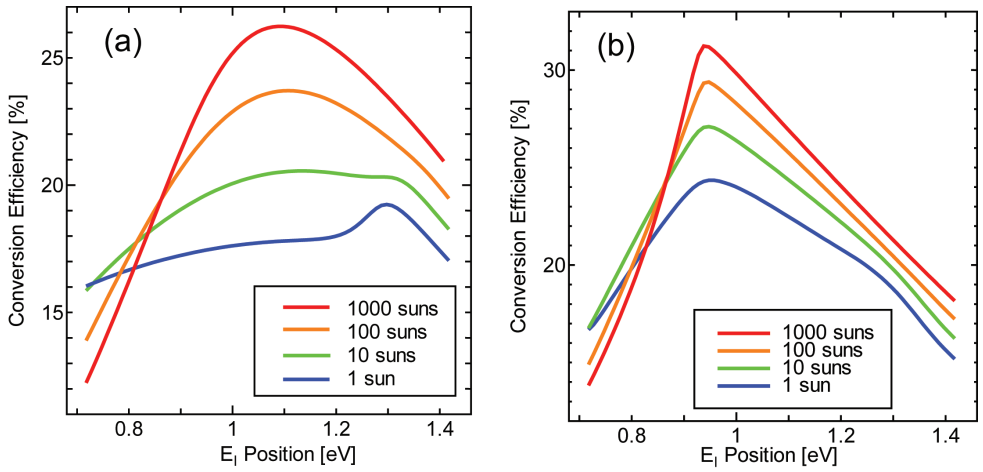

density of 1.4×10^{11} cm^{-2} has been achieved grown at 460°C. As another means to fabricate the high-density QDs, the growth on AlAs matrix layer (Park, 2004), a high growth rate method (Chia, 2007), and InAs QDs using surface modification effects by Sb atoms (Inaji, 2010) have been reported.

As explained above, high-quality single layer QDs is obtained by S-K growth mode. However, S-K growth in In(Ga)As/GaAs system usually results in a degradation of stacked QD structure and generation of misfit dislocations, typically after 10 layers of stacking, as a result of accumulation of internal strain beyond the critical thickness (Solomon, 1996; Wasilewski, 1999). For this

Figure 7. AFM image of self-assembled QDs grown by S-K growth mode. (a) InAs QDs grown on GaAs (001), (b) InGaAs QDs grown on GaAs (311)B, respectively. The scan size is 1μm × 1μm.

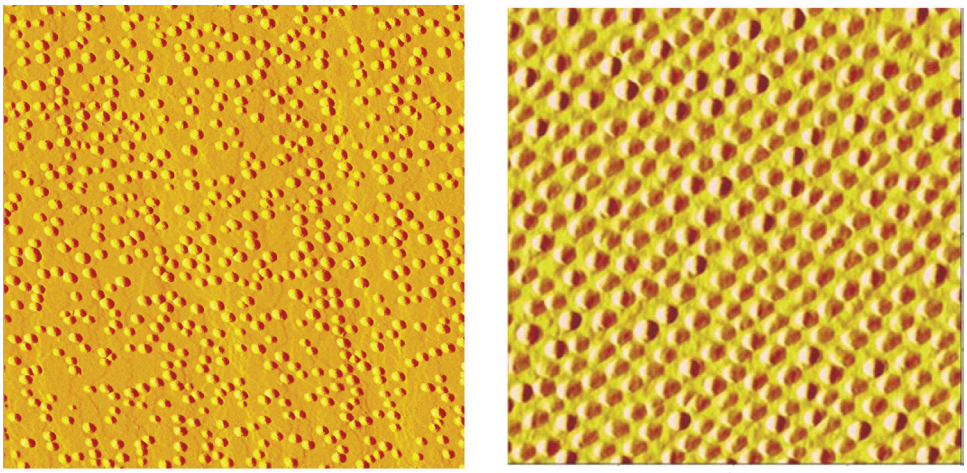

reason, tensile-strained barriers have been studied to balance out or compensate for the compressive strain induced in QD active regions as shown in Figure 9. This growth method is called the strain-compensation technique or strain-balanced technique, which has been reported in PbSe/PbEuTe grown on BaF_2 substrate (Springholz, 1998), InAs/AlGaInAs grown on InP substrate (Okada, 2005), InAs QDs in GaAsP on GaAs substrate (Popescu, 2008), and InAs/GaAsP grown on GaAs substrate (Hubbard, 2008),

Oshima *et al*. (2008) studied the strain-compensation technique for InAs/GaNAs system grown on GaAs (001) substrate. Figure 10 show a high resolution X-Ray Diffraction (XRD) spectra for samples with 20 stacked layers of InAs QDs embedded in (a) GaNAs Strain-Compensation Layer (SCL) and (b) GaAs spacer layer (SL). The satellite peaks originating from the periodic superlattice structure can be clearly observed in each sample, and hence abrupt hetero-interfaces are maintained. For InAs/GaNAs system, the zeroth-order satellite peak S(0) indicated by an arrow in the figure shows a near lattice match with GaAs substrate as shown in Figure 10a. Therefore, the net average compressive strain induced by InAs QDs layers is approximately compensated by GaNAs SCLs though not precisely balanced out in all three dimensions of QDs.

Figure 11 shows the cross-sectional Scanning Transmission Electron Microscope (STEM) image measured for 20 stacked InAs/GaNAs QD layers with 20 nm-thick SCL. An alignment of lens-shaped QDs along the growth direction is maintained from one QD layer to the next without degrading the structure and size homogeneity. In addition, there are no strain-induced defects or dislocations, which would otherwise be generated if the buildup of lattice strain exceeds the critical layer thickness during the stacking. These results indicate that the high quality stacked QDs structure is formed by the strain-compensation technique. Until now, Takata *et al*. (2010) demonstrate a high quality growth of up to 100 layer stacked InAs/GaNAs QD superlattice on GaAs (001) substrate. Furthermore, Akahane *et al*. (2010) succeeded in stacking 300 QDs layers for InAs/AlInGaAs system on InP substrate.

Figure 12a–d shows the effect of strain-compensation on the Internal Quantum Efficiencies (IQEs) of multi-stacked QD solar cells. The

Figure 8. AFM images for $In_{0.4}Ga_{0.6}As$ QDs on GaAs (311)B substrate grown at (a) 520 °C, (b) 500 °C, (c) 480 °C and (d) 460 °C, respectively. The scan size is 1μm × 1μm. (Reprinted from Akahane, et al., 1998. Copyright 1998, American Institute of Physics.)

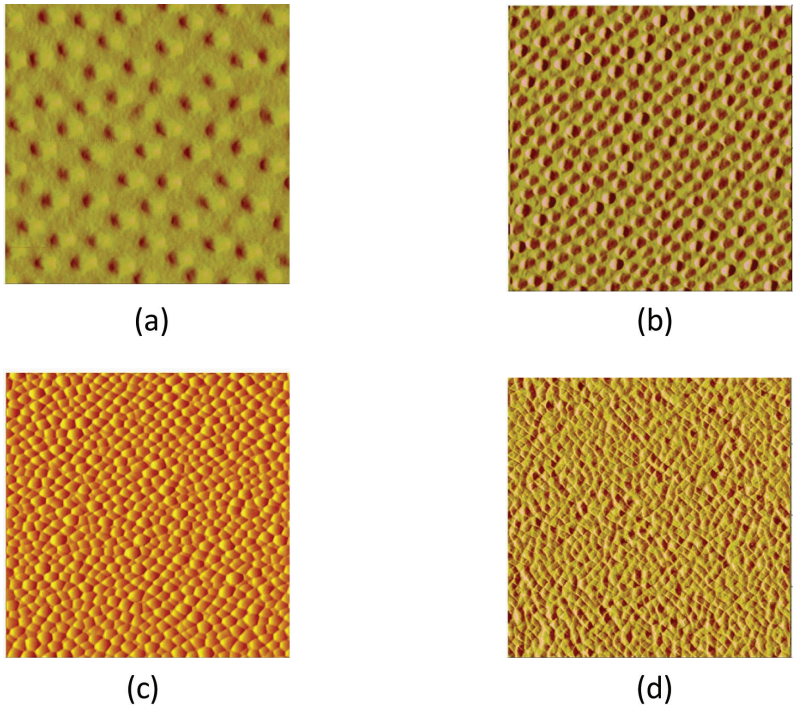

Figure 9. Schematic image of strain-compensation technique

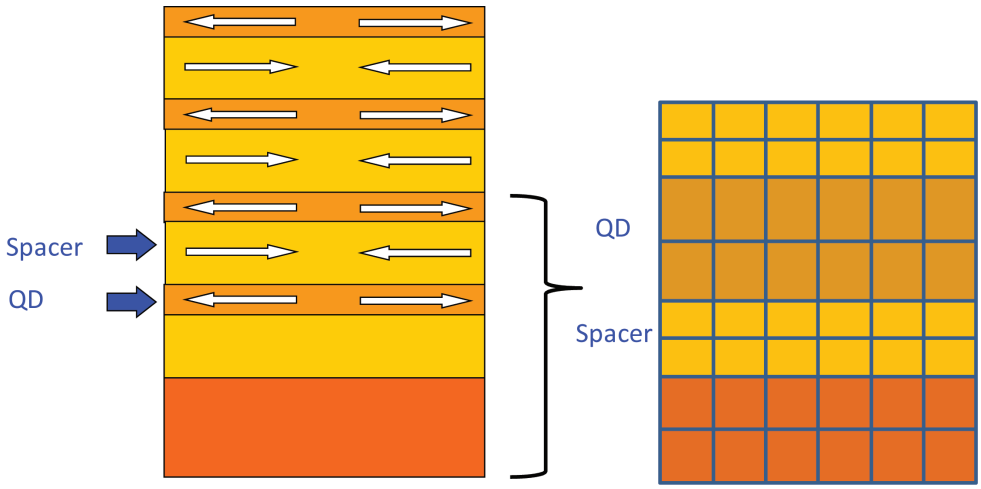

four samples were identical in the structure except for the *i*-layer region. The samples (a) and (b) were grown with 10 and 20 stacked pairs of an InAs QD layer with 2.0 MLs thicknesses and a 20 nm-thick GaNAs SCL, respectively. The sample (c) comprised of 20 pairs of 2.0 MLs InAs QDs and 20 nm-thick GaAs spacer layers, and hence the QD structure was strained. Last, the sample (d) was a GaAs control cell with a 400 nm-thick *i*-GaAs layer used as a reference. The IQE was determined from a direct measurement of the external QE under a constant photon irradiation of 10^{16} /cm^2, then discounting for the shadowing loss and residual reflection loss arising from ARC. Additionally, Figure 12e shows the Photoluminescence (PL) spectrum for 20 stacked pairs of an InAs QDs layer and GaNAs SCL which is used to identify the photo-absorption edge for each layer. First, a single PL emission peak from the ground state of InAs QDs is observed at around 1170 nm. In addition, a shoulder peak originating from both GaNAs spacer layer and InAs wetting layer is seen at around 980 nm for (a) and (b), and 880 nm for (c), respectively. Second, the absorption edge redshifts from 1150 nm for (c) up to 1200 nm for (b), and this is because the quantum confinement is lower at the conduction band interface when GaNAs is used as the barrier instead of GaAs. The filtered short-circuit current density (I_{sc}) of sample (a) beyond the GaAs bandedge of (880 nm), which gives the contribution from QD layer, was determined to be 2.47 mA/cm^2 by taking the product of IQE and solar spectrum (AM1.5). This value was twice that of (a) and four times larger than that of (c), respectively. Though the obtained value is notably higher than the reported values for QDSCs, the maximum IQE from the QD layers even for (b) is still limited to 5%, and thus a larger stack of QD layers is required to obtain higher photo-absorption. Furthermore, the fact that the degradation of QEs in the shorter wavelength is not observed after increasing the QD layer from 10 to 20 stacks suggests that the crystalline quality is maintained in our strain-compensated QDSCs as the contribution to the photocurrent generated by the *p*-GaAs emitter is not affect. The I_{sc} improved to 21.1 mA/cm^2 for (a) compared to 19.0 mA/cm^2 for (b) and

Figure 10. Symmetric (004) XRD patterns for 20 stacked layers of InAs QDs structure embedded in (a) GaNAs SCL and (b) GaAs SL, respectively. S(± x) means x th-order satellite peak. (Reprinted from Oshima, Takata, & Okada, 2008. Copyright 2008, American Institute of Physics.)

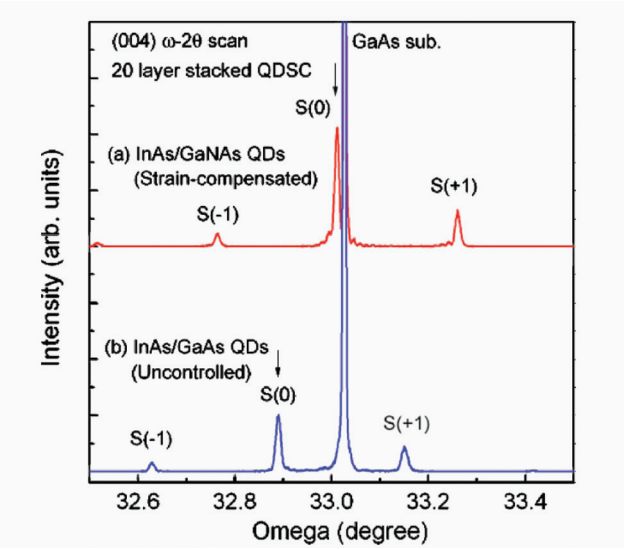

Figure 11. Cross-sectional STEM image of 20 stacked layers of InAs QDs embedded in 20 nm-thick GaNAs SCL (Reprinted from Oshima, Takata, & Okada, 2008. Copyright 2008, American Institute of Physics.)

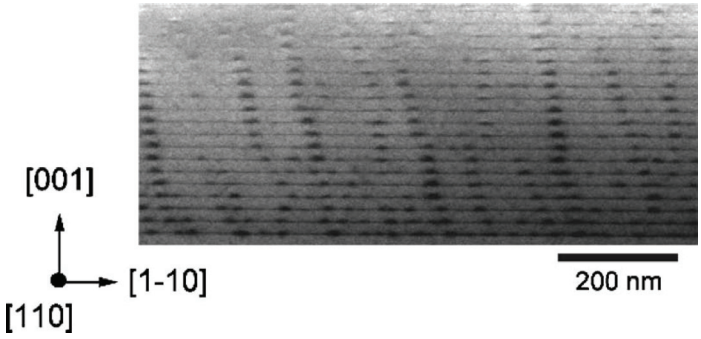

19.6 mA/cm^2 for (c), respectively, and I_{sc} = 19.7 mA/cm^2 for the control cell (d) with 400 nm-thick *i*-GaAs layer as a reference. The projected conversion efficiency is 8.5% and 5.7% for strain-compensated (a) and (b) QDSC, respectively.

For InGaAs/GaNAs QDs grown on GaAs (311) B, the multi-staked structure have an interesting future. Figure 13a shows the high-angle annular dark-field STEM image for the portion of embedded QD structure with 40 nm-thick SCL viewed along [01-1] and Figure 13b, c, and d show STEM images for the embedded QD structure with (b) 40 nm-thick, (c) 30 nm-thick and (d) 20 nm-thick SCL viewed along [-233], respectively. QDs are vertically aligned in the growth direction when viewed along [01-1] as in (a), because symmetrical lens shaped QDs are observed resulting in the generation of isotropic strain field along [01-1] direction. On the other hand, the QD alignment is inclined at an angle of 22° with respect to the growth direction when viewed along [-233] as shown in (b). Because their shape is asymmetric with two dominant facets along [-233], the local strain around QD extends further outward from the lower angle facet (Shoji, 2010b). Further, the inclination angle of vertical alignment QDs becomes smaller from 22° to 2° with decreasing SCL thickness from 40 nm to 20 nm. These results suggest that the strain field extends asymmetrically resulting in vertically tilted alignment of QDs for sample with thick SCLs, while the propagated local strain field is strong enough to generate the nucleation site of QD formation just above lower QD in the sample with thinner SCLs.

Figure 14 shows the projected AM1.5 current-voltage curves measured for 10-layer stacked InGaAs/GaNAs QDSC grown on GaAs (311)B substrate. A higher I_{sc} of 24.26 mA/cm^2 is achieved compared to the GaAs *p-i-n* reference cells. This result due to the high density QDs grown on GaAs (311)B substrate. The Fill Factor (*FF*) and open-circuit voltage (V_{oc}) are determined *FF* = 0.791 and V_{oc} = 0.840 V, respectively. Further, the measured efficiency for 10 stacked InGaAs/GaNAs QDSC grown on GaAs (311)B substrate amounts to 16.1% under AM 1.5 irradiation.

EFFECT OF SPACER LAYER THICKNESS

In QD-IB solar cells, QDs are required to be homogeneous and small in size, and are regularly and tightly placed in all three dimensions. This configuration then leads to formation of a superlattice miniband that is well separated in energy from the higher-order states. For this, separation thickness between QD layers becomes a factor that needs to be controlled.

Okada *et al*. (2009) investigated the effect of spacer layer thickness on the performance of multi-stacked QD solar cells. Each sample grown by MBE, consists of 10 multi-stacked pairs of an InAs QD layer with 2.0 MLs thickness and a strain-compensating GaN_xAs_{1-x} spacer layer with varying thickness d nm and nitrogen composition x, (a) d = 15 nm and x = 1.5%, (b) d = 20 nm and x = 1.0%, (c) d = 30 nm and x = 0.7%, and (d) d = 40 nm and x = 0.5%, respectively, grown on GaAs (100) substrate. The net biaxial compressive strain induced by InAs QD layer has been compensated by the given GaN_xAs_{1-x} spacer layer. Changing the nitrogen composition has two effects; one is the change in the lattice constant and hence the amount of tensile strain that is used to compensate for the compressive strain by InAs QDs. The other is the change in the conduction band offset or bandgap energy of GaN_xAs_{1-x} spacer layer and hence the position of the quantized energy states in InAs QDs. Due to a large bowing parameter of GaN_xAs_{1-x} alloy, a small change in nitrogen composition results in a large change in the bandgap (Wu, 2002).

Figure 15 shows the projected AM1.5 current-voltage curves measured for InAs/GaN_xAs_{1-x} QD solar cells with varying thickness and nitrogen composition of strain-compensating spacer layer. The short-current density steadily increases from I_{sc} = 23.7 to 24.5, 24.8, and 24.9 mA/cm^2 as the thickness of spacer layer is reduced from d = 40 to 30, 20, and 15 nm, respectively. The filtered I_{sc} above the GaAs bandedge of 880 nm for QD solar cell with d = 20 nm and x = 1.0% is 1.2 mA/cm^2

Figure 12. (a)-(d) show IQE spectra for (a) strain-compensated InAs/GaNAs QDSC with 10 stacks, (b) strain-compensated InAs/GaNAs QDSC with 20 stacks, (c) strained InAs/GaAs QDSC with 20 stacks, (d) GaAs p-i-n control cell, and (e) shows the PL spectrum at room temperature for strain-compensated InAs/GaNAs QDSC with 20 stacks, respectively. (Reprinted from Oshima, Takata, & Okada, 2008. Copyright 2008, American Institute of Physics.)

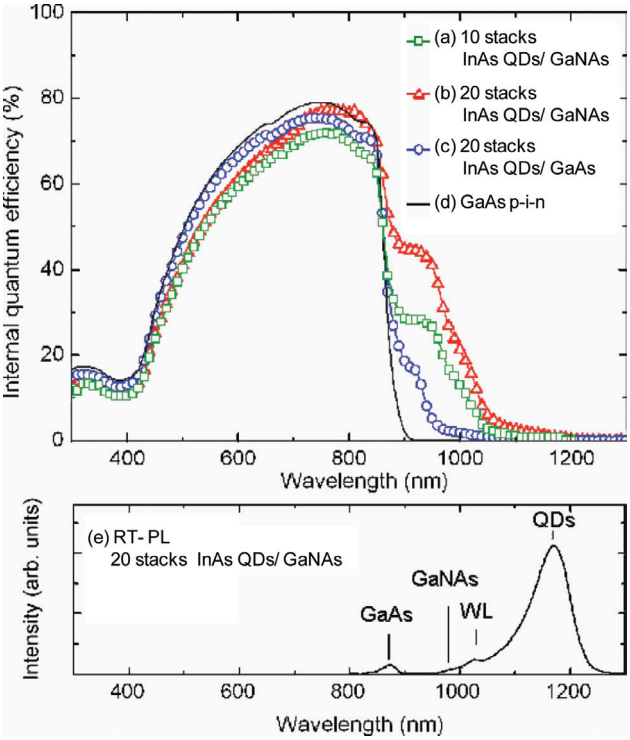

Figure 13. (a) Cross-sectional STEM image for the embedded QD structure with 40 nm-thick SCL viewed along [01-1]. (b), (c) and (d) show images for the embedded QD structure with (b) 40 nm-thick, (c) 30 nm-thick, and (d) 20 nm-thick SCL viewed along [-233], respectively. (Reprinted from Shoji, Oshima, Takata, & Okada, 2010. Copyright 2010, Elsevier B.V.).

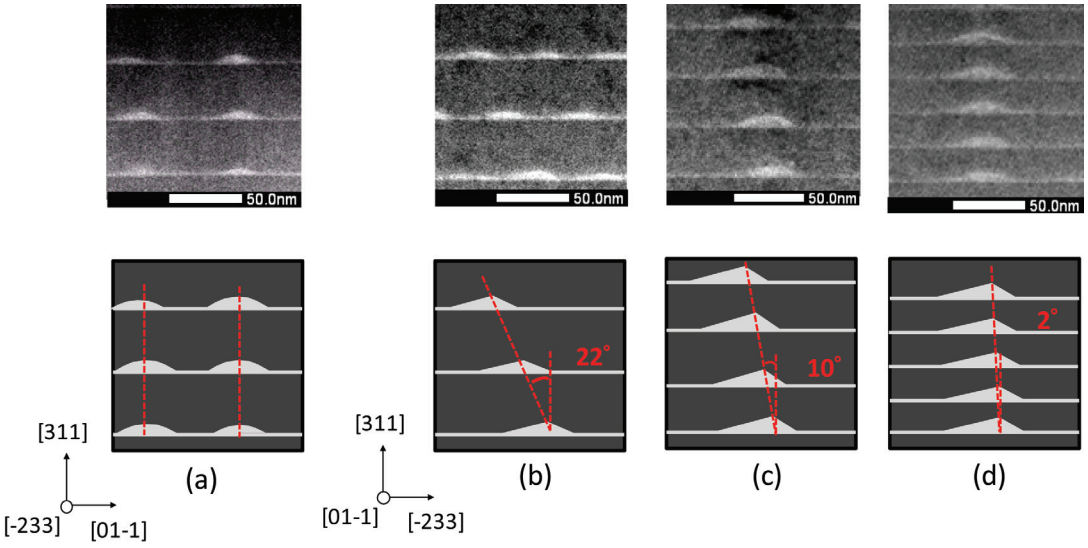

and the maximum QE from the QD layers is about 5% at a wavelength of ~ 1100 nm. On the other, the open-circuit voltage shows a decreasing trend with reducing spacer layer thickness from V_{oc} = 0.805 to 0.729, 0.654, and 0.634 V, respectively. The conversion efficiency is 15.7% for QD solar cell with d = 40 nm and x = 0.5%, which steadily decreases to 12.5% for the cell with d = 15 nm and x = 1.5%, respectively. The fact that the series resistance does not, in principle, affect V_{oc} of solar cell and the measured shunt resistance is practically identical in all four samples could lead to conclusions that (1) the strain-compensation growth provides good junction quality in all samples with a fill-factor of 0.79 ~ 0.82, and (2) the drop in V_{oc} is due to an increase in the conduction-band offset ΔE_c at the GaAs/GaN_xAs_{1-x} heterointerface, which in turn increases the recombination loss within QDs, thereby leading to an increased dark current.

Figure 16 shows a clear correlation between the drop in V_{oc} and the increase in ΔE_c at the GaAs/GaN_xAs_{1-x} heterointerface as a function of nitrogen composition x in GaN_xAs_{1-x}. For GaAs/GaN_xAs_{1-x} heterointerface, the most portion of the band offset is known to appear in the conduction band (Wu, 2002). One further point to note is $\Delta V_{oc} < \Delta E_c/q$ has been observed. The results suggest that the predominant operation for these multi-stacked QD solar cells is by the carriers generated in QDs to escape out of the potential well by thermal excitation thereby contributing to additional current output, but not by absorption of 2 photons with sub-bandgap energies of GaAs barrier material to be harvested in generating additional one electron-hole pair which is the required mechanism in high-efficiency IBSCs. Similar observations have been reported in most reports to date (Martí, 2001, 2006; Okada, 2005, 2009; Oshima, 2008; Popescu, 2008; Hubbard, 2008; Blokhin, 2009; Shoji 2010).

Therefore, there is a large mismatch between the rates of photo-excitation of carriers from the VB to the quantized states in QD or miniband and from QD states into CB in most of the QD-IB solar cells reported to date. However, $\Delta V_{oc} < \Delta E_c/q$ has been often observed and the recombination

Figure 14. Projected AM1.5 current-voltage curves measured for (a) 10-layer stacked InGaAs/GaNAs QDSC grown on GaAs (311)B substrate, (b) GaAs p-i-n reference SC grown on GaAs(001) substrate

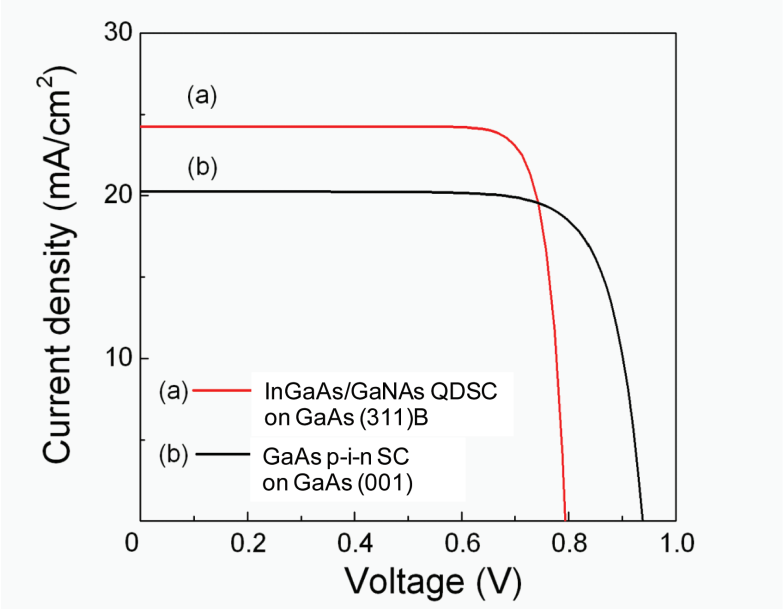

Figure 15. Projected AM1.5 current-voltage curves measured for InAs/GaN$_x$As$_{1-x}$ QD solar cells with varying thickness d and nitrogen composition x of strain-compensating spacer layer, (a) d = 15nm and x = 1.5%, (b) d = 20nm and x = 1.0%, (c) d = 30nm and x = 0.7%, and (d) d = 40nm and x = 0.5%, respectively. The net strain-balanced condition has been was achieved in all samples (Reprinted from Okada, Oshima, & Takata, 2009. Copyright 2009, American Institute of Physics.).

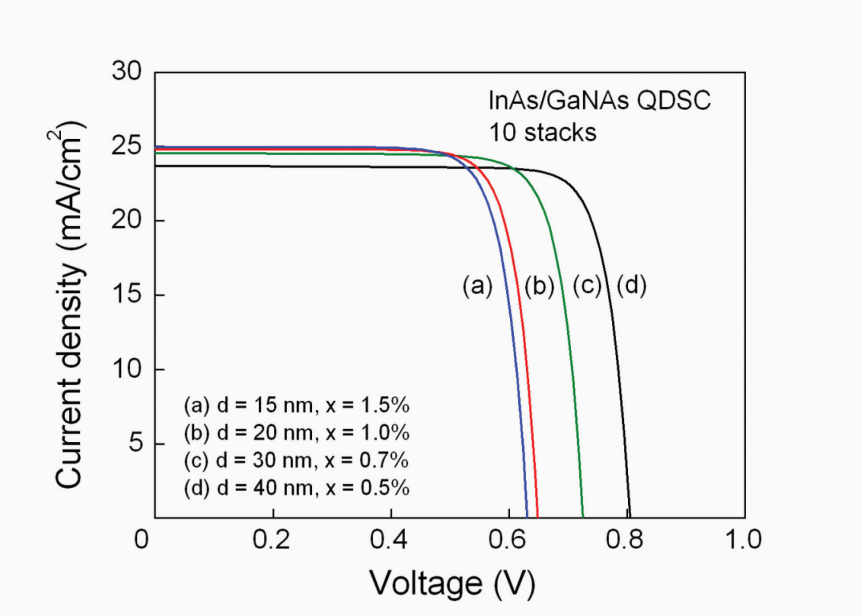

Figure 16. Dependence of decrease in the open-circuit voltage ΔV_{oc} (solid circle) and increase in the conduction-band offset ΔE_c at the GaAs/GaN_xAs_{1-x} heterointerface (solid line) as a function of nitrogen composition x in GaN_xAs_{1-x}

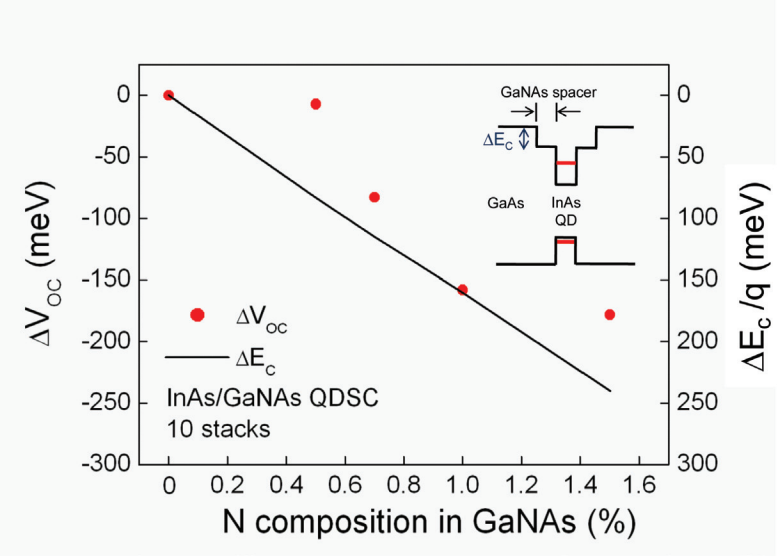

loss within QDs is the key factor degrading V_{oc} even for the sample with the smallest spacer layer thickness of d = 15 nm as from Figure 16. The wave function delocalization *via* coupling of QDs forming an IB (Tomić, 2008) as well as increased radiative recombination lifetime (Kojima, 2008) should become possible if the thickness d is further reduced to form a more ideal superlattice structure.

EFFECT OF DOPING

In QD-IB solar cells, IB states should ideally be half-filled with electrons in order to ensure an efficient pumping of electrons by providing both the empty states to receive electrons being photo-excited from the Valence Band (VB), and filled states to promote electrons to the Conduction Band (CB) *via* absorption of second sub-bandgap photons.

One method of providing carriers into QDs is by modulation doping technique. Martí *et al.* (2006) has fabricated InAs/GaAs QD-IB cell, for which each GaAs barrier layer is delta-doped with Si with a sheet density equaling the InAs QD areal density. Due to spin degeneration, this condition equals half the density of electronic states in IB. Morioka *et al.* (2010) have developed a technique by MBE to fabricate Quantum Dot (QD) solar cells with direct Si-doping of InAs QDs in GaNAs strain-compensating matrix in order to control the quasi-Fermi level of intermediate QD states as schematically shown in Figure 17. The structure consisted of 25 pairs of a 2.0 MLs of InAs QD layer and a 20 nm-thick $GaN_{0.01}As_{0.99}$ strain-compensating spacer layer in the *i*-layer whereby keeping the net average lattice strain to a minimum. The Si atoms can be evenly incorporated into QDs during the assembling stage of growth (Kudo, 2008; Inoue, 2010) such that a uniform partially-filled QD array has been obtained. The sheet density of Si doping has been set to be 5.0×10^{10} cm^{-2} per QD layer in order to dope approximately one Si atom per QD. The growth rate of QD layer is 0.09 μm/h, and growth temperature is 480°C. The mean QD diameter, height, size uniformity in diameter, and areal density reported for this structure are 24.6 nm, 4.7 nm, 11.1%, and 5.0×10^{10} cm^{-2}, respectively.

Figure 17. Schematic layer structure of QD solar cell grown on GaAs(001) substrate with 25 multi-stacks of InAs QDs, either direct Si-doped or non-doped, embedded by 20 nm-thick $GaN_{0.01}As_{0.99}$ strain-compensating spacer layers (SCLs)

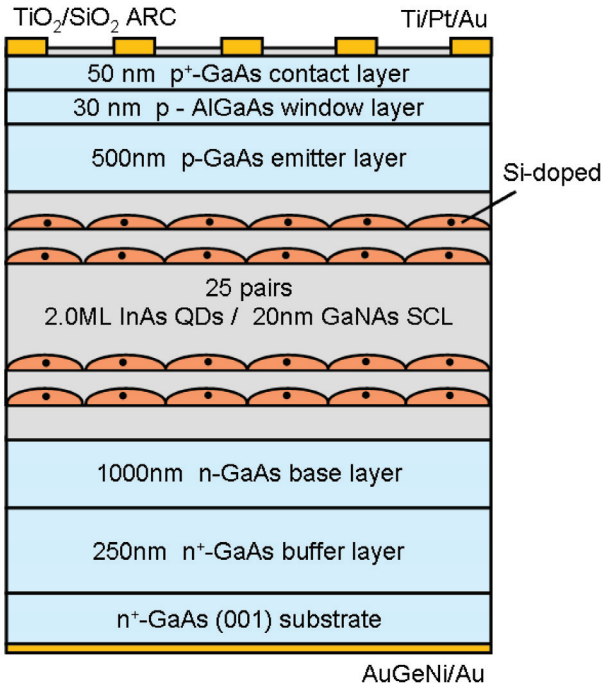

One further important effect of Si-doping not to be taken lightly is the passivation of non-radiative recombination centers in GaAs and heterointerfaces (Phillips, 1997; Attaluni, 2006).

Figure 18 show the measured Quantum Efficiency (QE) spectra measured for QD solar cells with (a) direct Si-doped, and (b) non-doped QDs, respectively (Okada, 2011). The QE response for $\lambda < 880$ nm is mainly the contribution from the top *p*-GaAs emitter layer, while the peak observed around 970 nm is from GaNAs spacer layers. Then QE response for $\lambda > 1000$ nm is reported to be solely due to contribution from InAs QDs. The external QE of direct Si-doped InAs QDs is 6% at the wavelength of ~ 1050 nm, which is notably higher than the reported values. It is further noted that Figure 16a shows a higher QE response than for (b) in the wavelength range of $\lambda < 880$ nm. This suggests that the electrons are transported across the direct Si-doped QD region more efficiently compared to non-doped QD region. In fact, the dark current measured for direct Si-doped QDSC is roughly halved compared to non-doped QDSC. The results agree well with PL results and we can firmly conclude that relaxation of electrons by non-radiative process in the QD region is effectively reduced by Si doping. Consequently, the short-circuit current density I_{sc} of QD solar cell increases from $I_{sc} = 24.1$ (non-doped) to 30.6 mA/cm^2 (direct Si-doped QDs) under AM1.5 irradiation.

Figure 19 plots the difference between the QE curves ΔQE, measured at room temperature, with (QE_{IRon}) and without (QE_{IRoff}) IR light illumination, whose energies would only be able to pump the electrons from IB to CB. Okada *et al*. (2011) observed a clear increase in the photocurrent, given by $\Delta QE = QE_{IRon} - QE_{IRoff}$ for a direct Si-

Figure 18. External QE spectra taken at the short-circuit condition for 25 layer-stacked InAs/GaNAs strain-compensated QDSCs with (a) direct Si-doped, and (b) non-doped QDs, respectively (Reprinted from Okada, Morioka, Yoshida, OshimaShoji, Inoue, & Kita, 2011. Copyright 2011, American Institute of Physics.)

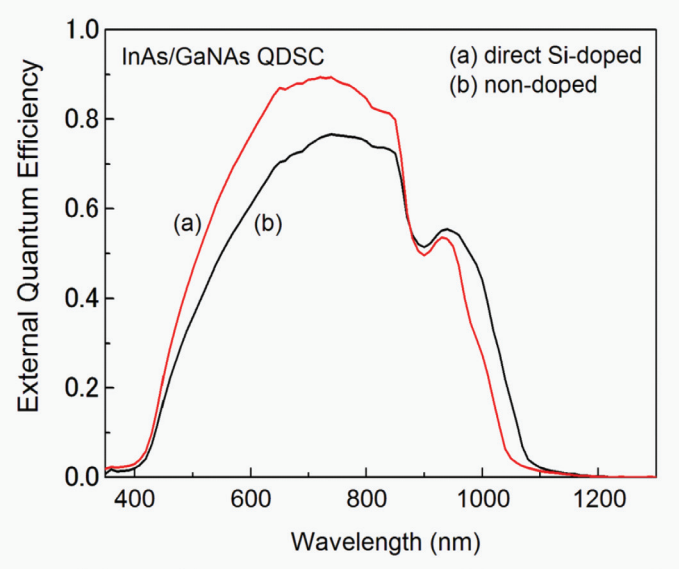

Figure 19. Difference in QE values ΔQE with (QE_{IRon}) and without (QE_{IRoff}) IR light illumination, whose energies would only be able to pump the electrons from IB to CB. A clear increase of photocurrent, given by $\Delta QE = QE_{IRon} - QE_{IRoff}$ has been detected for direct Si-doped QDSC at room temperature (Reprinted from Okada, Morioka, Yoshida, Oshima, Shoji, Inoue, & Kita, 2011. Copyright 2011, American Institute of Physics.).

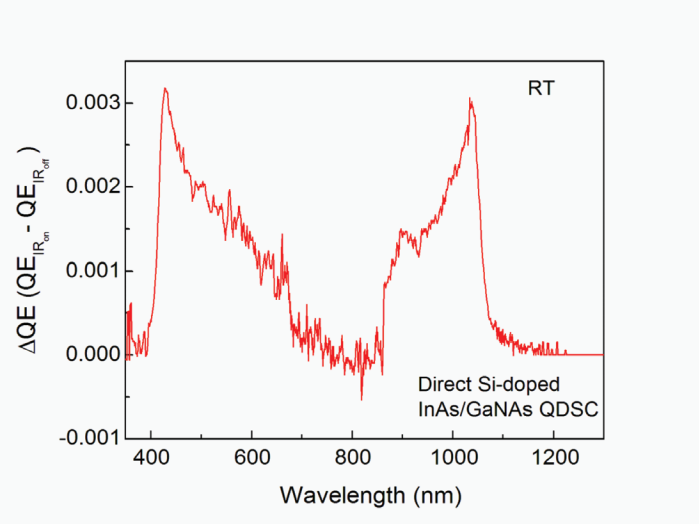

doped QD solar cell. A sharp peak feature seen at λ ~ 1050nm matches with the condition that the electrons are pumped from VB to IB, and a consequent increase in the population in IB in turn increases optical transitions from IB to CB. The increase of QE at λ ~ 1050 nm is ~ 0.3%. The external QE of direct Si-doped InAs QDs is ~ 6% as from Figure 18, which thus implies that the ratio of optical transition rate from IB to CB with respect to thermal escape is estimated to be ~ 1: 20. Further, the photo-response is increased over the whole wavelength range, which can be qualitatively explained that; (1) non-radiative recombination loss from CB to VB for the carriers that have been pumped to high energy states is reduced by the effect of Si doping such that those captured into direct Si-doped QDs (IB) after thermalization can absorb IR photons and make direct optical transitions from IB to CB, and contributes to an increase in the photocurrent (λ = 450 ~ 850 nm), and (2) the electrons pumped from VB to CB in GaNAs spacer layers undergo similar steps (λ = 900 ~ 1000 nm), respectively. The results evidence the fundamental operation principle of QD-IB solar cells.

CONCLUSION AND FUTURE RESEARCH

We have attempted to review the theoretical analysis and the QD technologies that could be implemented to realize a high-efficiency intermediate-band solar cell.

By using the self-consistent drift-diffusion method for IBSC, doping in the IB region can help the carrier generation *via* IB state, especially for lower concentrations. However, the optimal doping density must be carefully estimated not to degrade the cell performance. Under higher concentration conditions, photofilling effects can control the occupation rates of IB and the estimation condition will relaxed. To evaluate the potential of QD-IBSCs, the relations of absorption coefficients for each band-to-band transition should be clarified. Tomić (2010) provided the details of these relations.

Then the self-organized growth of QDs, growth mechanisms and control of size and density of QDs, and direct doping of QDs will be reviewed. We will summarize with specific experimental behavior for proof of operation with two-step photon absorption from current state-of-the-art IB solar cells implementing QD superlattice.

Compensating for or balancing out the lattice strain induced by self-assembled QDs with a spacer layer which exerts an opposite biaxial strain works remarkably well to achieve improved size uniformity and to avoid generation of defects and dislocations in multiple stacked QD superlattice structure. Up to 100 layers of multi-stacking of InAs/GaNAs QDs are reproducibly achieved with the present technology (Takata, 2010). The junction quality is good and the fundamentals of solar cell performance can be studied and analyzed clearly without the need to be concerned about the crystalline quality.

However, if the IB is not partially filled with carriers, one can expect to observe a large mismatch between the rates of excitation of carriers from VB into miniband or IB in QD superlattice, and from QD-IB into CB in III-V based QD material system. Of the two absorption processes, the absorption rate from QD-IB to CB is the limiting factor in maximizing the photocurrent generation by two-step photon absorption and hence the recombination loss in QDs is the dominant factor limiting V_{oc} in most of the QD solar cells reported to date.

Modulation doping technique has been applied to fabricate QD-IB solar cell (Martí, 2006), in which the barrier is delta-doped with a sheet density equaling the QD areal density. Photofilling is another approach to achieve partial filling of QD-IB states (Strandberg, 2009). It is expected that a reasonable population of photo-generated

electrons is sustained even in non-doped QD-IB solar cells if operated under concentrated sunlight, typically 100 ~ 1000 suns. A direct doping method is a new evolving technology in order to control the quasi-Fermi level of QD-IB states in solar cell. In direct Si-doping of InAs QDs in GaNAs strain-compensating matrix, it has been shown that Si atoms are evenly incorporated into QDs during the assembling stage of growth and a uniform array of partially filled QDs has been obtained. A clear photocurrent increase due to two-step photon absorption has recently been detected at room temperature for the first time in IB solar cells with doped QDs (Okada, 2011). This evidences the proof of concept of QD-IB solar cells and it could open up a pathway for fast development of high-efficiency IB solar cells with efficiencies exceeding the Shockley-Queisser limit.

ACKNOWLEDGMENT

We would like to gratefully acknowledge Profs. A. Luque and A. Martí of Universidad Politécnica de Madrid, K. Barnham and N. Ekins-Daukes of Imperial College London, N. Sano of University of Tsukuba, T. Kita of Kobe University for their valuable comments and discussion. The New Energy and Industrial Technology Development Organization (NEDO), Ministry of Economy, Trade and Industry (METI), Japan, and the Strategic International Cooperative Program by Japan Science and technology Agency (JST) are also acknowledged.

REFERENCES

Akahane, K., Xu, H., Okada, Y., & Kawabe, M. (2001). Formation of lateral-two-dimensional ordering in self-assembled InGaAs quantum dot on high index substrates. *Physica E, Low-Dimensional Systems and Nanostructures*, *11*, 94. doi:10.1016/S1386-9477(01)00182-5

Akahane, K., Yamamoto, N., & Kawanishi, T. (2010). Fabrication of ultra-high-density InAs quantum dots using the strain-compensation technique. *Physica Status Solidi. A, Applications and Materials Science*, *208*, 425. doi:10.1002/pssa.201000432

Akahane, K., Yamamoto, N., & Tsuchiya, M. (2008). Highly stacked quantum-dot laser fabricated using a strain compensation technique. *Applied Physics Letters*, *93*, 041121. doi:10.1063/1.2968211

Attaluni, R. S., Annamalai, S., Posani, K. T., Stintz, A., & Krishna, S. (2006). Influence of Si doping on the performance of quantum dots-in-well photodetectors. *Journal of Vacuum Science & Technology B Microelectronics and Nanometer Structures*, *24*, 1553. doi:10.1116/1.2190676

Blokhin, S. A., Sakharov, A. V., Nadtochy, A. M., Pauysov, A. S., Maximov, M. V., & Ledentsov, N. N. (2009). AlGaAs/GaAs photovoltaic cells with an array of InGaAs QDs. *Semiconductors*, *43*, 514. doi:10.1134/S1063782609040204

Chia, C. K., Zhang, Y. W., Wong, S. S., Yong, A. M., Chow, S. Y., & Chua, S. J., &d Guo, J. (2007). Saturated dot density of InAs/GaAs self-assembled quantum dots grown at high growth rate. *Applied Physics Letters*, *93*, 161906. doi:10.1063/1.2724776

Green, M. A. (2003). *Third generation photovoltaics*. Berlin, Germany: Springer-Verlag.

Hubbard, S. M., Cress, C. D., Bailey, C. G., Raffaelle, R. P., Bailey, S. G., & Wilt, D. M. (2008). Effect of strain compensation on quantum dot enhanced GaAs solar cells. *Applied Physics Letters*, *92*, 123512. doi:10.1063/1.2903699

Inaji, T., Ohta, J., & Yamaguchi, K. (2010). Stacking growth of in-plane InAs quantum-dot superlattices on GaAsSb/GaAs(001) for solar cell applications. In *Proceedings of the 35th IEEE Photovoltaic Specialists Conference*, (p. 1885). Honolulu, HI: IEEE Press.

Inoue, T., Kido, S., Sasayama, K., Kita, T., & Wada, O. (2010). Impurity doping in self-assembled InAs/GaAs quantum dots by selection of growth steps. *Journal of Applied Physics*, *108*, 063524. doi:10.1063/1.3483252

Kojima, O., Nakatani, H., Kita, T., Wada, O., Akahane, K., & Tsuchiya, M. (2008). Photoluminescence characteristics of quantum dots with electronic states interconnected along growth direction. *Journal of Applied Physics*, *103*, 113504. doi:10.1063/1.2936320

Kudo, T., Inoue, T., Kita, T., & Wada, O. (2008). Real time analysis of self-assembled InAs/GaAs quantum dot growth by probing reflection high-energy electron diffraction chevron image. *Journal of Applied Physics*, *104*, 074305. doi:10.1063/1.2987469

Lin, A. S., & Phillips, J. D. (2009). Drift-diffusion modeling for impurity photovoltaic devices. *IEEE Transactions on Electron Devices*, *56*, 3168. doi:10.1109/TED.2009.2032741

Luque, A., & Martí, A. (1997). Increasing the efficiency of ideal solar cells by photon induced transitions at intermediate levels. *Physical Review Letters*, *78*, 5014. doi:10.1103/PhysRevLett.78.5014

Martí, A., Antolín, E., Stanley, C. R., Farmer, C. D., López, N., & Días, P. (2006). Production of photocurrent due to intermediate-to-conduction-band transitions: A demonstration of a key operating principle of the intermediate-band solar cell. *Physical Review Letters*, *97*, 247701. doi:10.1103/PhysRevLett.97.247701

Martí, A., Cuadra, L., & Luque, A. (2001). Partial filling of a quantum dot intermediate band for solar cells. *IEEE Transactions on Electron Devices*, *48*, 2394. doi:10.1109/16.954482

Morioka, T., Oshima, R., Takata, A., Shoji, Y., Inoue, T., Kita, T., & Okada, Y. (2010). Multi-stacked InAs/GaNAs quantum dots with direct Si doping for use in intermediate band solar cell. In *Proceedings of the 35th IEEE Photovoltaic Specialists Conference*, (p. 1834). Honolulu, HI: IEEE Press.

Nozik, A. J. (2002). Quantum dot solar cells. *Physica E, Low-Dimensional Systems and Nanostructures*, *14*, 115. doi:10.1016/S1386-9477(02)00374-0

Nozik, A. J. (2008). Multiple exciton generation in semiconductor quantum dots. *Chemical Physics Letters*, *457*, 3. doi:10.1016/j.cplett.2008.03.094

Okada, Y., Morioka, T., Yoshida, K., Oshima, R., Shoji, Y., Inoue, T., & Kita, T. (2011). Increase of photocurrent by optical transitions via intermediate quantum states in direct-doped InAs/GaNAs strain-compensated quantum dot solar cell. *Journal of Applied Physics*, *109*, 024301. doi:10.1063/1.3533423

Okada, Y., Oshima, R., & Takata, A. (2009). Characteristics of InAs/GaNAs strain-compensated quantum dot solar cell. *Journal of Applied Physics*, *106*, 024306. doi:10.1063/1.3176903

Okada, Y., Shiotsuka, N., Komiyama, H., Akahane, K., & Ohtani, N. (2005). Multi-stacking of highly uniform self-organized quantum dots for solar cell applications. In *Proceedings of the 20th European Photovoltaic Solar Energy Conference*, (p. 51). Barcelona, Spain: WIP.

Oshima, R., Okada, Y., Takata, A., Yagi, S., Akahane, K., Tamaki, R., & Miyano, K. (2011). High-density quantum dot superlattice for application to high-efficiency solar cells. *Physica Status Solidi. C, Current Topics in Solid State Physics*, *8*, 619. doi:10.1002/pssc.201000461

Oshima, R., Takata, A., & Okada, Y. (2008). Strain compensated InAs/GaNAs quantum dots for use in high-efficiency solar cells. *Applied Physics Letters*, *93*, 083111. doi:10.1063/1.2973398

Park, S., Tatebayashi, J., & Arakawa, Y. (2004). Formation of ultrahigh-density InAs/AlAs quantum dots by metalorganic chemical vapor deposition. *Applied Physics Letters*, *84*, 1877. doi:10.1063/1.1687465

Phillips, J., Kamath, K., Zhou, X., Chervela, N., & Bhattacharya, P. (1997). Photoluminescence and far-infrared absorption in Si-doped self-organized InAs quantum dots. *Applied Physics Letters*, *71*, 2079. doi:10.1063/1.119347

Popescu, V., Bester, G., Hanna, M. C., Norman, A. G., & Zunger, A. (2008). Theoretical and experimental examination of the intermediate-band concept for strain-balanced (In,Ga)As/Ga(As,P) quantum dot solar cells. *Physical Review B: Condensed Matter and Materials Physics*, *78*, 205321. doi:10.1103/PhysRevB.78.205321

Selberherr, S. (1984). *Analysis and simulation of semiconductor device simulation*. New York, NY: Springer-Verlag. doi:10.1007/978-3-7091-8752-4

Shockley, W., & Queisser, H. (1961). Detailed balance limit of efficiency of p-n junction solar cells. *Journal of Applied Physics*, *32*, 510. doi:10.1063/1.1736034

Shoji, Y., Oshima, R., Takata, A., Morioka, T., & Okada, Y. (2010a). Multi-stacked InGaAs/GaNAs quantum dot solar cell fabricated on GaAs (311) B substrate. In *Proceedings of the 35th IEEE Photovoltaic Specialists Conference*, (p. 1859). Honolulu, HI: IEEE Press.

Shoji, Y., Oshima, R., Takata, A., & Okada, Y. (2010b). Structural properties of multi-stacked self-organized InGaAs quantum dots grown on GaAs (311)B substrate. *Journal of Crystal Growth*, *312*, 226. doi:10.1016/j.jcrysgro.2009.10.053

Solomon, G. S., Trezza, J. A., Marshall, A. F., & Harris, J. S. Jr. (1996). Vertically aligned and electronically coupled growth induced InAs islands in GaAs. *Physical Review Letters*, *76*, 952. doi:10.1103/PhysRevLett.76.952

Springholz, G., Holy, V., Pnczolits, M., & Bauer, G. (1998). Self-organized growth of three-dimensional quantum-dot crystals with fcc-like stacking and tunable lattice constant. *Science*, *282*, 734. doi:10.1126/science.282.5389.734

Strandberg, R., & Reenaas, T. W. (2009). Photofilling of intermediate bands. *Journal of Applied Physics*, *105*, 124512. doi:10.1063/1.3153141

Strandberg, R., & Reenaas, T. W. (2011). Drift-diffusion model for intermediate band solar cells including photofilling effects. *Progress in Photovoltaics: Research and Applications*, *19*, 21. doi:10.1002/pip.983

Takata, A., Oshima, R., Shoji, Y., Akahane, K., & Okada, Y. (2010). Paper. In *Proceedings of the 35th IEEE Photovoltaic Specialists Conference*, (p. 1877). Honolulu, HI: IEEE Press.

Tobías, I., Luque, A., & Martí, A. (2011). Numerical modeling of intermediate band solar cells. *Semiconductor Science and Technology*, *26*, 014031. doi:10.1088/0268-1242/26/1/014031

Tomić, S. (2010). Intermediate-band solar cells: Influence of band formation on dynamical processes in InAs/GaAs quantum dot arrays. *Physical Review B: Condensed Matter and Materials Physics*, *82*, 195321. doi:10.1103/PhysRevB.82.195321

Tomić, S., Jones, T. S., & Harrison, N. M. (2008). Absorption characteristics of a quantum dot array induced intermediate band: Implications for solar cell design. *Applied Physics Letters*, *93*, 263105. doi:10.1063/1.3058716

Wasilewski, R. Z., Fafard, S., & McCaffrey, P. J. (1999). Size and shape engineering of vertically stacked self-assembled quantum dots. *Journal of Crystal Growth*, *20-202*, 1131. doi:10.1016/S0022-0248(98)01539-5

Wu, J., Walukiewicz, W., & Haller, E. E. (2002). Band structure of highly mismatched semiconductor alloys: Coherent potential approximation. *Physical Review B: Condensed Matter and Materials Physics*, *65*, 233210. doi:10.1103/PhysRevB.65.233210

Würfel, P. (2009). *Physics of solar cells: From basic principles to advanced concepts*. New York, NY: Wiley.

Yoshida, K., Okada, Y., & Sano, N. (2010a). Self-consistent simulation of intermediate band solar cells: Effect of occupation rates on device characteristics. *Applied Physics Letters*, *97*, 133503. doi:10.1063/1.3488815

Yoshida, K., Okada, Y., & Sano, N. (2010b). Self-consistent drift-diffusion approach for analysis intermediate band solar cells with multi-stacked quantum dots. In *Proceedings of 25th European Photovoltaic Solar Energy Conference and Exhibition / 5th World Conference on Photovoltaic Energy Conversion*, (p. 545). Valencia, Spain: WIP.

Yoshida, K., Okada, Y., & Sano, N. (2010c). Self-consistent drift-diffusion analysis of intermediate band solar cell (IBSC): Effect of energetic position of IB on conversion efficiency. In *Proceedings of 35th IEEE Photovoltaic Specialists Conference*, (p. 71). Honolulu, HI: IEEE Press.

Chapter 11
Intermediate Band Solar Cells: Modeling and Simulation

Pablo García-Linares
Universidad Politécnica de Madrid, Spain

Elisa Antolín
Universidad Politécnica de Madrid, Spain

Antonio Martí
Universidad Politécnica de Madrid, Spain

Antonio Luque
Universidad Politécnica de Madrid, Spain

ABSTRACT

The Intermediate Band Solar Cell (IBSC) is a novel photovoltaic device with the potential of surpassing the efficiency limit of conventional solar cells. It is based on a new class of materials characterized by the insertion of a collection of energy levels within the material bandgap. These levels act as the so-called Intermediate Band (IB) and cause a larger portion of the solar spectrum to be useful for photovoltaic conversion. Sub-bandgap photons can ideally be collected via two-step absorption mechanisms through the IB and thus enhance the photogenerated current without a significant voltage degradation. In this chapter, the authors show the state of the art of the modeling and simulation within the IBSC research field.

1. INTRODUCTION

The solar energy utilization is inherently and fundamentally inefficient because it is very diluted compared to other sources of energy. This causes the exploitation of the Sun as a direct source of energy for cheap electricity production to be very challenging.

There are two ways of reducing the cost of Photovoltaics (PV): 1) reducing the solar cell manufacturing cost and/or 2) boosting the solar cell efficiency, which implies PV concepts with a high efficiency ceiling. Both strategies cannot be compared under the same standards, since the cost associated to the PV module is expected to be approximately half of the price of the whole PV power plant (the Balance-of-System account-

DOI: 10.4018/978-1-4666-1927-2.ch011

ing for the other half) and the solar cell cost (in current flat panels) approximately accounts, in average, for the 60% of the PV module cost (del Cañizo, del Coso, & Sinke, 2009). This implies that any PV technology cost reduction only affects approximately 30% of the overall cost; while the efficiency enhancement strategy affects the entire cost of the investment. Furthermore, the marginal cost of operation and maintenance can be neglected in PV and therefore, the generation cost of solar electricity ultimately depends on the electricity produced and thus, on the efficiency.

One of the paths leading to a possible PV breakthrough is the Intermediate Band Solar Cell (IBSC) concept, for which a limiting efficiency as high as 63.2% (Luque & Martí, 1997) has been calculated, to be compared to the 40.7% of a conventional solar cell (Araujo & Martí, 1994; Shockley & Queisser, 1961). The IBSC is based on the so-called Intermediate Band (IB) materials, which can be regarded as a new type of materials engineered so that an energy band or a collection of energy levels are inserted within the semiconductor bandgap. These materials are capable of absorbing sub-bandgap photons, which otherwise would be useless for PV conversion. These sub-bandgap photons are collected via two-step electronic transitions through the IB, thus enabling the pumping of an extra electron flux from the Valence Band (VB) to the Conduction Band (CB). This mechanism is sketched in Figure 1. The first step, or sub-bandgap transition, g_{IV}, represents the pumping from the VB to the IB, through the bandgap E_H. The second step is denoted as g_{CI} and represents the electron pumping from the IB to the CB (through the bandgap defined as E_L). The conventional transition from the VB to the CB is denoted as g_{CV} in the figure (and occurs through E_G). The choice of the location of the IB closer to the CB and therefore in the upper half of the host material bandgap has been arbitrarily made in this example. In this respect, the IB concept is symmetric from a theoretical point of view (E_L can be above E_H and vice versa). In many practical cases however (particularly in the implementation with QDs), as it will be seen later, the IB will be located in the upper half.

Figure 1. Simplified band diagram of an IBSC where the QFLs associated to each of the bands (VB, IB, and CB) are represented together with their corresponding transitions and bandgap distribution

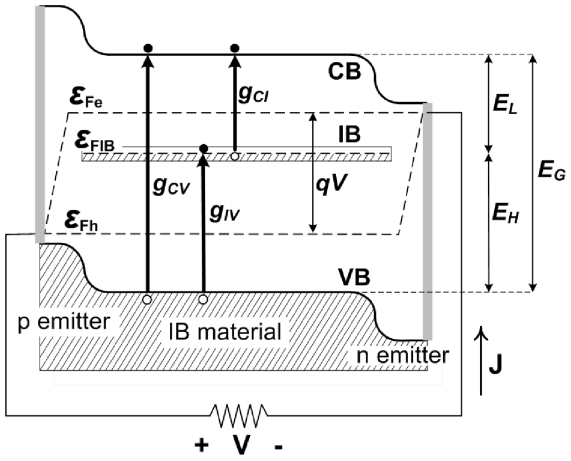

The overall effect of this double absorption causes a larger portion of the solar spectrum to become useful for the extraction of carriers. At the same time, these photogenerated carriers must preserve their electrochemical potential. As a result, the IBSC has the potential to achieve a short circuit current (I_{SC}) enhancement without a significant degradation of the open circuit voltage (V_{OC}). The latter occurs under the assumption that three electron gases coexist, each of them associated to each of the three bands: VB, IB and CB. Out of the equilibrium, these electron gases are defined by their own Quasi-Fermi Level (QFL) and they are respectively denoted as ε_{Fh}, ε_{FIB} and ε_{Fe}, in Figure 1. The existence of three well defined and separated electronic populations associated to each band is on the basis of a V_{OC} not limited by any of the sub-bandgaps (E_L or E_H, in this case), but only limited by the host or barrier material bandgap, E_G.

Another important condition is the need for electric isolation of the IB from the contacts so that the electron and hole QFL split does not collapse at these contacts (Luque & Martí, 2001; Luque, Martí, & Cuadra, 2000). This isolation is achieved by inserting two conventional semiconductors, called emitters, on both sides of the IB material. When this configuration is not implemented, no QFL separation can be achieved between ε_{FIB} and ε_{Fe} or ε_{Fh} and as a consequence, the voltage cannot be preserved limiting the efficiency ceiling to that of a single gap solar cell.

The rest of the features concerning the operation of the IBSC will be extensively reviewed in the following sections, firstly attending to the general IBSC case and then to the specific case of each particular implementation.

So far, none of the existing semiconductors have shown to be endowed with the singular features required for a proper operation of an IBSC. This implies that a new generation of IB materials has to be engineered. For this reason, an extensive research has recently begun on the identification of appropriate IB candidate materials. So far, most part of the research has been focused on two different families: the Quantum Dot (QD) IB approach and the bulk approach, which will be reviewed in the following sections. Nevertheless, other interesting configurations have been proposed, as for example the molecular approach (Ekins-Daukes & Schmidt, 2008) which are out of the scope of this work.

At the beginning of the IB research, the detailed balance model was used to calculate the optimum bandgap distribution of an IBSC. Under maximum concentration (46050 suns for the Earth's surface) and the irradiance distribution of a black-body at 6000 K, the following values attain the theoretical 63.2%: E_H=1.24 eV, E_L=0.71 eV and E_G=1.95 eV (Luque & Martí, 1997).

During the first years after the concept was released, more IB features were modeled, either to analyze the suitability of the different IB materials or the impact of non-idealizations regarding the practical implementation of the IBSC. In an initial stage, the concept fundamentals had to be verified, for which some evidences concerning the operating principles of the IBSC were to be tested. The latter required the implementation of dedicated experimental set-ups in order to measure these verification effects, i.e. the production of sub-bandgap photocurrent, the preservation of the voltage and the suppression of the non-radiative recombination.

2. BACKGROUND

We will review in this section the different approaches for the implementation of the IBSC, stressing some of their specific features in each case.

2.1. The Quantum Dot Intermediate Band Solar Cell (QD-IBSC)

Quantum dots are also known as 'artificial atoms or molecules' because their electronic properties are in same aspects similar to those of the single atoms and can be tuned so that they behave in a desired manner. A QD system consists of a collection of small semiconductor crystals of nanometric dimension (QD material) embedded in another crystal of different nature (barrier material). The barrier (or host) material is characterized, in most cases, by the largest bandgap, so that a confining potential is created inside the dots. QDs can be treated in an ideal way as spherical, although most of them resemble a concave lens in practice (Sugawara, 1999). Anyhow, they are restricted to the nanometric range in the three spatial directions. This causes the appearance of discrete confined energy levels (electron, holes or both). Their Density Of States (DOS) is therefore characterized by a delta-like function (Figure 2d).

Quantum dots can be used to implement the intermediate band solar cell concept (Martí,

Figure 2. Schematics of DOS functions: (a) the crystal in bulk has a continuous DOS; (b) a QW is characterized by a stair-like DOS function; (c) a QWR allows only one degree of freedom; (d) a QD presents a delta-function like DOS

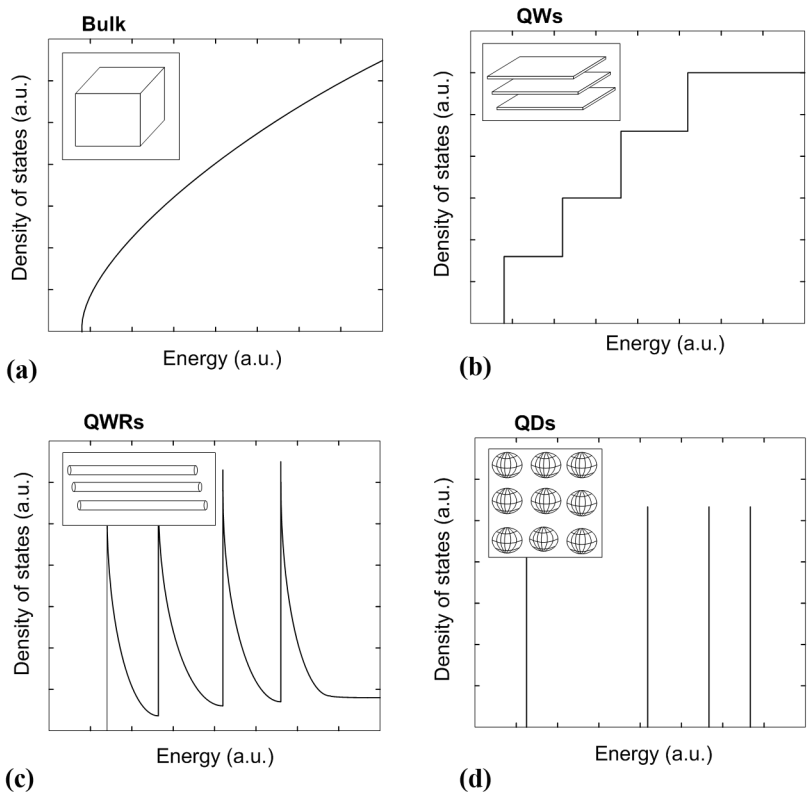

Cuadra, & Luque, 2000). Under this approach, the fundamental confined state is meant to act as the IB and it requires to be well separated from the CB so that carrier escape from this confined state to the CB does not become too large or otherwise the QFL split between IB and CB will not take place. When the confined states are separated by an energy greater than that of the optical phonons, the carrier thermalization through the emission of a single phonon is inhibited. This Non-Radiative Recombination (NRR) blockade, peculiar to zero-dimensional nanostructures, is also known as *phonon-bottle-neck-effect* (Bockelmann & Bastard, 1990).

Not every kind of nanostructure is satisfactory for the implementation of an IBSC. Any nanotechnology approach with a lower degree of confinement, i.e. Quantum Wires (QWRs) or Quantum Wells (QWs), respectively characterized by one or two degrees of freedom in real space, allow carriers to move freely throughout the crystal lattice in, at least, one direction. Thus, these other approaches present in fact a continuum in the DOS function, starting from the fundamental confined state towards higher energies. This has been represented in Figure 2b and Figure 2c, where the DOS function for QWs and QWRs are schematically shown. This continuum in the DOS function prevents the existence of an IB isolated from both the VB and the CB and thereby prevents the IB to CB QFL split.

As mentioned, the IB concept is theoretically symmetric with respect to the position of the IB within the host bandgap. However, when

implemented with QDs, the high hole effective mass leads to a hole energy level distribution where the confined levels are separated from their adjacent by a small energy gap. If we could think of a QD-IBSC produced by hole confinement, a strong carrier escape from the IB to the VB would dominate the g_{IV} transition. A very little QFL separation would then be achieved, implying that the voltage preservation condition is not fulfilled. As a result of this reasoning, the IBSC concept, when engineered with QDs, can only be likely implemented through electron confinement and not through hole confinement.

A few important issues related to the practical implementation of QD systems can be regarded as frequent topics for modeling and simulation of IBSCs; among them, the ones that are worth mentioning are: impact of the shape, size, and aspect ratio on the QD absorption, accumulation of strain and impact of the wetting layer. All of them will be discussed in Section 3.

Attending to the previous considerations, it will be useful to define the 'effective bandgap' of a QD-IBSC with a significant Valence Band Offset (VBO), which is a usual case in most of the favorable QD/barrier III-V material combinations (graphically shown in Figure 3 for the InAs/GaAs QD system). For that we will take into account that in real QDs, most part of the VBO can be considered full of energy levels. Therefore, the effective bandgap, marked as $E_{G.eff}$, $E_{H.eff}$ or $E_{L,eff}$ in Figure 3, accounts for the energy reduction (with respect to the conventional values of E_G, E_H and E_L) caused by both the Wetting Layer (WL) continuum of states and the quasi-continuum of confined hole energy levels. This concept is important for a correct understanding of the QD solar cell in terms of the interpretation of electrical and optical measurements, as well as the modeling and simulation of its electronic performance.

The IB region of a QD-IBSC is constituted by the QD layers, separated by the barrier material spacers. As any other IBSC, it requires to be sandwiched between a p-emitter and an n-emitter, so the IB is not connected to the metal contacts. A simple solar cell configuration of this type is detailed in Ref. (Martí, et al., 2000). The "n doping" appearing next to each QD is meant to produce the partial filling of the IB by modulated doping, which is discussed in Section 3.3.

2.2. The Bulk-Based IBSC

The other big group of IB materials besides QDs is the one based on bulk semiconductors. Several lines have been proposed in this direction, which

Figure 3. Band diagram of the InAs/GaAs QD system illustrating the effective bandgaps. The confined electron wavefunction is sketched together with the electrons populating the IB and coming from the QD modulated doping.

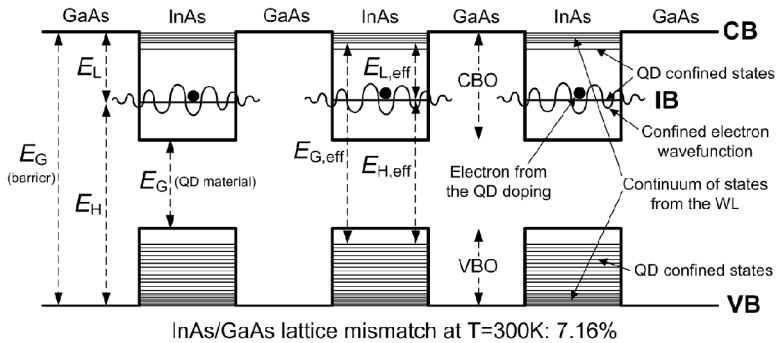

are, in most cases, based on the introduction of suitable impurity atoms. Different material systems have been theoretically investigated containing impurities of the appropriate nature, placed in the adequate locations within the periodic lattice and being in sufficient concentration as to fulfill the IBSC requirements.

Deep-Level (DL) impurities (atomic species that introduce an energy level inside the host material bandgap far from the band edges) could be thought as the precursor of the IB. However, they have been traditionally called traps (recombination centers) and therefore, considered as 'lifetime killers' in semiconductors. Therefore, their use in high efficiency solar cells requires further justification.

The answer to why impurities in high concentration inside the crystal might not increase the Shockley-Read-Hall (SRH) recombination (Luque, Martí, Antolín, & Tablero, 2006) as it has been traditionally stated in conventional semiconductor physics is related to the so-called lattice relaxation multiple phonon emission (Lang & Henry, 1975). The latter is believed to be the main responsible for the SRH recombination, since the simultaneous emission of several phonons is considered highly improbable in bulk semiconductors. The electron is de-excited from the CB to a DL trap, which implies a transition from a delocalized state to a localized one, causing an important swift movement of the charge, because it was initially distributed throughout the whole band and it is afterwards highly packed next to the impurity atom. In this case, the atom vibrates violently (in real space) in a mode other than the usual lattice phonons, the so-called breathing mode. This violent vibration is then attenuated through the successive emission of phonons produced by conventional electron-phonon interaction. Thereby, if the impurities giving rise to the IB are present within the bulk material in a sufficiently high concentration as to produce the overlapping of their wavefunctions, the recombination through intermediate states takes place between delocalized states, thus inhibiting the production of breathing modes and the lattice relaxation multiple phonon emission. As a result, the SRH recombination is also inhibited.

The idea of using DLs to study the possibility of sub-bandgap photon absorption is not modern. Actually, Wolf introduced the concept of *multitransition solar cell* in 1960 with the purpose of improving the solar cell performance (Wolf, 1960) and a year later, based on Wolf proposals, Grimmeiss manufactured and tested a DL impurity-based solar cell with negative results (Grimmeiss & Koelmans, 1961). This is not surprising because both the theoretical proposal and the experimental implementation paid no attention, for example, to the need for selective contacts, i.e. they did not identified the need for non-DL-doped portions of semiconductor separating the doped material and the metal contact. Also, in the proposals by Wolf, there was no explicit mention to the need for a high enough impurity concentration as to enable the formation of a band with the aforementioned NRR blockade. Thanks to the IBSC theory, we now know that because the previous considerations were not taken into account, the voltage of the DL solar cell proposed by Wolf and implemented by Grimmeiss was fundamentally limited. The efficiency ceiling of such configuration was in the best case the one of a low bandgap conventional solar cell.

DLs introduced by impurities of any kind can be considered as an option for bulk IB materials if they are located at an appropriate energy and they can be half filled with electrons at room temperature. Actually, even DLs associated to a vacant or an interstitial atom might also lead to adequate configurations.

The first stage after the IBSC concept was first presented in 1997 dealt with theoretical analysis of possible IB candidate materials. In this respect, some bulk materials doped with transition metal impurities were proposed, as for

example, Ti-substituted GaAs or GaP (Wahnón & Tablero, 2002), as well as other substituting impurities such as Sc, V or Cr. An experimental research line has been proposed using an MBE reactor for the insertion of a high impurity concentration of Ti inside a GaAs matrix (Martí, et al., 2009).

Another bulk-based IB candidate material is a well-known semiconductor for PV applications: silicon. Although in the IBSC theory it is far from the optimum in terms of efficiency (because of its small bandgap), it seems to be a good material to test some of the principles of the IBSC theory. Hence, a high dose of Ti has been already implanted thanks to ion-implantation techniques together with pulsed laser melting in order to recover the crystallinity of the implanted sample (Antolín, et al., 2009; González-Díaz, et al., 2009; Olea, Toledano-Luque, Pastor, González-Díaz, & Mártil, 2008). Some important conclusions concerning the operation fundamentals of the IBSC have been extracted from this work. They will be presented in Section 4.

IB solar cells based on thin-film-based materials, such as $CuInS_2$, $CuGaSe_2$ and $CuGaS_2$, which can also be doped with transition metals, such as Ti, V, Cr or Mn (Martí, Fuertes Marrón, & Luque, 2008; Palacios, Sánchez, Conesa, Fernández, & Wahnón, 2007; Tablero & Fuertes Marrón, 2010) have also been proposed. This research line seems to be very encouraging since chalcopyrite structures can constitute an easy and versatile way to produce IB materials, i.e. the insertion of certain transition metal species seems realizable (in a sufficient concentration) from a thermodynamic point of view. An experimental line has also begun in this topic (Martí, et al., 2009).

Another research line also based on the thin-film technology is being developed at the University of Michigan for the ZnTe material doped with oxygen (Weiming, Albert, & Jamie, 2009). So far, it has rendered excellent results, including a substantial efficiency enhancement with respect to the ZnTe reference cell.

In-thiospinels such as In_2S_3 have also been proposed with a high V concentration. This last work allowed the recent implementation of the IB material by solvo-thermal synthesis, in which sub-bandgap absorption was measured (Lucena, Aguilera, Palacios, Wahnón, & Conesa, 2008).

Recent works on bulk IB materials are based on the so-called highly mismatched materials (Yu, et al., 2006), e.g. the GaNAsP alloy, which has also shown IB properties through photoreflectance measurements. This kind of nitrogen dilute alloys is believed to experience the splitting of the CB because of the interaction between the nitrogen level and the CB of the non-nitrogen-doped host matrix (in this case, the GaAsP). In some cases, a real bandgap is created between the two splitted CBs as a result of this interaction and the lower splitted CB is then regarded as the IB. The mechanism leading to this effect is known as band anticrossing (Shan, et al., 1999).

InGaN-based alloys have also been presented as practically feasible candidates (Martí, et al., 2008), since they present exceptionally high solubility ranges for some metal transition impurities (e.g. Mn) and they cover a high range of energy bandgaps.

3. MODELING AND SIMULATION OF THE IBSC

Modeling and simulation on new IB material candidates, as well as on IB practical features are cornerstones for a fast development of the IBSC. In this section, we will summarize some of the master lines related to the modeling and simulation tools available for the IBSC, emphasizing the results derived from their use.

3.1. Detailed Balance Modeling

The detailed balance theory (Shockley & Queisser, 1961) is especially useful for computing the limiting efficiency of new IB candidate materials. The basis of the theory is the account for the minimal losses of the device, i.e. only radiative recombination, disregarding any NRR mechanism. Detailed balance calculations allow the determination of the optimal bandgap distribution of an IBSC with respect to the efficiency limit.

Figure 4a shows four different current density-voltage (*J-V*) characteristics calculated from detailed balance arguments under the irradiance of a black-body at 6000K and maximum concentration. The black solid curve corresponds to the ideal IBSC case and the other three correspond to different single gap cases for comparison: the blue and the red solid curves represent single gap solar cells with a bandgap E_G that equals one of the sub-bandgaps of the optimum IBSC, E_H or E_L respectively. The dashed black curve represents the optimum single gap solar cell (1.11 eV). From this plot it is clear how the IBSC benefits from both high current and high voltage and renders a maximized efficiency compared to any single gap solar cell: it preserves the voltage of the high bandgap solar cell at the time it increases its photogenerated current approaching that of the optimum single gap solar cell.

Figure 4b (Luque & Martí, 1997) shows the detailed balance efficiency limit calculation of an IBSC and a double junction tandem solar cell as a function of the lowest of the bandgaps involved in each structure and maximum light concentration. The limiting efficiency of a single gap solar cell is also shown for comparison. This plot illustrates the higher potential of the IBSC concept and as well as the bandgap distribution that optimizes the efficiency in each case. Strandberg and Reenas (Strandberg & Reenaas, 2010) have recalculated the IBSC limiting efficiency considering the possibility of using selective energy reflector filters and found that this efficiency increases with respect to the original calculation without filters for the case of low concentrations.

Nevertheless, some IBSC configurations have the potential for exceeding the previous 63.2% limit (Antolín, Martí, & Luque, 2006). For example, a tandem of two IBSCs has a detailed balance limit efficiency of 73.2% when the cells are independently connected. When the cells are connected in series, the system exhibits a slightly lower efficiency limit of 72.7% (Antolín, 2010). Regarding the number of bandgaps involved in the structure, each of the aforementioned IBSC tandem configurations is equivalent to a Multiple-Junction Solar Cell (MJSC) with six junctions, which respectively achieve 74.4% and 73.3% for the independently and series connected cases. When comparing both the tandem IBSC and the MJSC for the two-terminal case (monolithically grown), the obvious benefit involving the IB concept is the need for only one tunnel junction, instead of the five tunnel junctions required for a MJSC with six junctions.

The problem would still be the difficulty for engineering IBSCs endowed with such optimal configurations. In this respect, other works have identified the possibility of combining a single gap solar cell and an IBSC (either as the top or the bottom cell) in a tandem configuration as a more realistic device with a sufficiently high efficiency threshold as to remain attractive compared to its equivalent 4-junction single gap solar cell (Antolín, Martí, Linares, Ramiro, Hernández, & Luque, 2010). The calculated limiting efficiency of such concept is represented in Figure 4c, where a tandem made of a single gap solar cell and an IBSC are shown (the IBSC configured as either the bottom or the top cell). The plots also illustrate the constrained (sub-cells under series interconnection) and the unconstrained (independently interconnected) cases. The specific configuration based on a GaAs IBSC is

Figure 4. Detailed balance calculations of the IBSC. (a) Ideal J-V curves, where X is the concentration ratio, in this case 46050. Reprinted with permission from (Antolín, 2010). (b) Efficiency limit with respect to ε_l, which corresponds to the lowest bandgap in each structure. Reprinted figure with permission from (Luque & Martí, 1997). Copyright 1997 by the American Physical Society. (c) Efficiency of the tandem constituted by a single gap solar cell and an IBSC plotted for the cases in which the IBSC is the top (grey) and bottom (thin black) cell and also for the series connected (solid) or independently connected (dashed) cases. The single IBSC with optimal configuration (thick black) is added for comparison. Reprinted with permission from (Antolín, Martí, Linares, Ramiro, Hernández, & Luque, 2010).

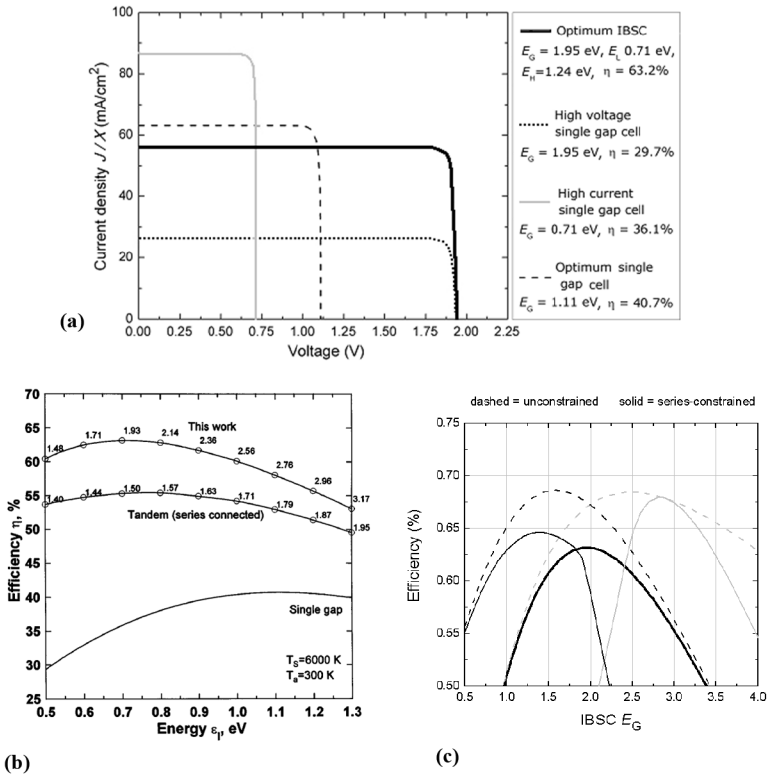

identified as a feasible implementation capable of achieving a high efficiency threshold (above 64%) when monolithically grown in a tandem configuration together with a single gap AlGaAs-based top cell with a low Al content (<20%). The latter is regarded as a specifically feasible configuration because: 1) the IBSC may be more easily achievable for the case of the well-known GaAs technology; 2) the AlGaAs single gap solar cell seems to be a feasible technology when implemented with a low Al content; and 3) both cells are lattice-matched.

In Cuadra, Martí, and Luque (2000) the maximum bandwidth of the IB is calculated for the case in which stimulated emission does not take place. A wide IB may appear, for example, if the impurity concentration (or density of confined states) giving rise to the IB is large. As a result, any of the IBSC sub-bandgaps, for example E_L, can get reduced (because it is defined from the CB to the upper edge of the IB) to an extent

where it is even smaller than the ε_{Fe}-ε_{FIB} QFL separation, which causes stimulated emission processes, thus degrading the solar cell performance. Therefore, the maximum IB bandwidth is limited by the maximum QFL separation at a given sunlight concentration. The modeling of this constrain sets an upper limit for the IB width of about 700meV for a 1 sun illumination and about 700meV for maximum concentration (for the optimum E_G value of 1.95 eV).

3.2. Photon Selectivity and Photon Recycling

The absorption coefficient determines the probability of an optical transition to occur as a function of the photon energy. In an IBSC, three of them are identified for each transition: α_{CV}, α_{IV} and α_{CI} (respectively corresponding to g_{CV}, g_{IV}, and g_{CI} in Figure 1).

In the general case of an IBSC, a photon of the appropriate energy could be absorbed producing an electronic transition between any of the three bands. However, as stated in the original reference (Luque & Martí, 1997), the absorption coefficient profiles have to be spectrally selective in any of the transitions for an optimized IBSC performance. In other words, no energy overlap is permitted between them, what implies that for maximum performance, an incident photon should exclusively pump an electron in one of the transitions, but not in the others.

The reason why this photon selectivity renders the maximum possible efficiency can intuitively be understood from Figure 5, where different cases of high-energy photons being absorbed in low energy transitions are displayed. Figure 5a sketches a qualitative absorption coefficient diagram where the different absorption functions overlap, i.e. their value is not zero in some of the energy ranges where the other functions are also defined. Figure 5b exemplifies one of the cases in which the absorption of a high energy photon ($E_{photon}>E_H$) in a low energy transition (of only E_L eV) is associated with an energy loss mechanism. The excess of energy is wasted via the thermalization of the electron within the CB. Figure 5c exemplifies another analogous case in which the loss mechanism occurs for $E_{photon}>E_G$ and the production of a transition through E_H (and the subsequent thermalization of a hole in the VB). An IBSC efficiency degradation effect equivalent to those of the previous examples is shown in Figure 5d, where the overlap between absorption coefficients causes the energy loss throughout the photon recycling process.

Several works have modeled the performance of the IBSC taking into account the impact from the possible overlapping between the absorption coefficient profiles. In order to quantify the influence of non-ideal absorption coefficients, a model was developed by Cuadra, Martí, and Luque (2004) accounting certain degree of overlapping between them. The corresponding simulations showed a degradation of the IBSC performance which is traduced into an efficiency loss that increases as the overlapping increases. For reference, we will recall that, the first efficiency simulation presented in this context (the one in Figure 4b) assumed an ideal situation: full light absorption (sufficiently thick solar cell) and non-overlapping of the absorption coefficients.

When taking into account the possibility of absorption coefficient overlap, one has to realize that the cell thickness (W) becomes a parameter to be optimized, even within the detailed balance realm. The reason for this dependence of the efficiency on the thickness is related to the loss mechanisms shown in Figure 5d. These losses are produced during the photon recycling processes and they are caused by the reabsorption of photons in a transition with an energy threshold lower than that in which it was created. Even though these recombination processes are of radiative nature, entropy is created, thus degrading the cell efficiency. The optimum thickness of the cell will be the result of the trade-off between

Figure 5. Different situations implying the absorption of high-energy photons in low energy transitions. The absorption does not always promote electrons in the highest possible transitions but in lower ones. Therefore, the energy in excess above the bandgap is wasted. (a) Example of non-idealized absorption coefficients; (b) a photon of $E_{photon}>E_H$ produces a g_{CI} transition; (c) a photon of $E_{photon}> E_G$ produces a g_{IV} transition; and (d) example of process involving photon recycling and generating entropy.

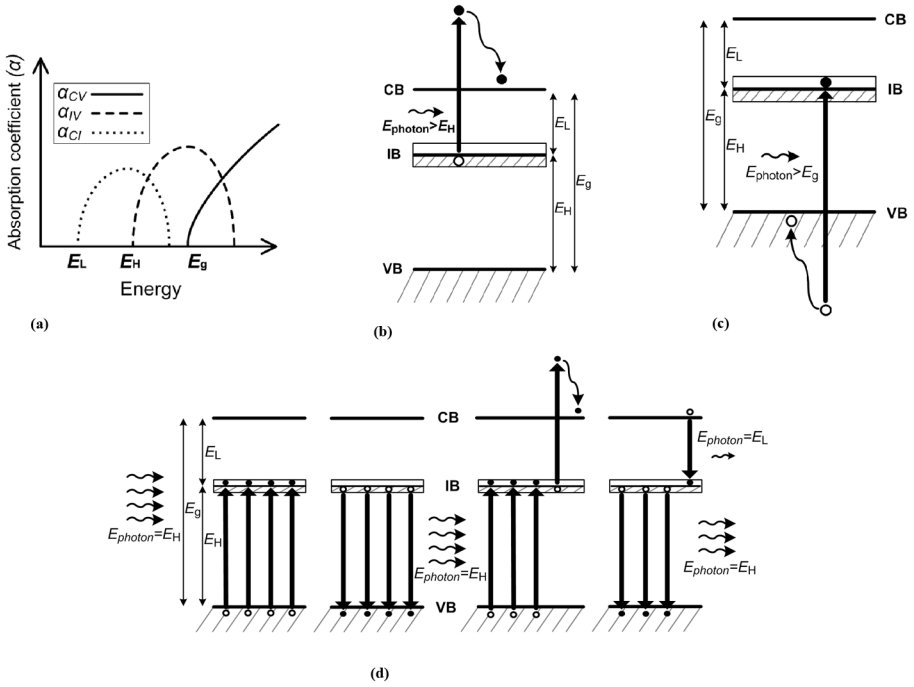

the absorptivity (a), typically given when a plain back reflector exists by (Cuadra, et al., 2004):

$$a(E) \sim 1 - \exp[-(\alpha_{CV} + \alpha_{IV} + \alpha_{CI})\, 2W] \qquad (1)$$

which increases as W increases, and the recombination, which depends on the bulk semiconductor volume (and therefore, also on W) and is caused by the inefficient photon recycling; therefore, it also increases when W increases.

The photon recycling mechanism is important in radiatively dominated single gap solar cells as well as in IBSCs. The latter can be deduced from Figure 6, where the efficiency of an IBSC of optimum bandgap is calculated for maximum concentration (46050 suns), constant and non-overlapping absorption coefficients and the Sun modeled as a blackbody at 6000K (Martí, Antolín, Cánovas, Linares, & Luque, 2008). The simulation is carried out for the two cases of an IBSC operating at the radiative limit and also for an IBSC in which no photon recycling takes place; both as a function of the cell thickness. In this analysis, it is patent how the efficiency of an IBSC in the radiative limit (accounting the photon recycling processes) increases towards the 63.2% maximum efficiency as the thickness increases, that is reached once all the photons are absorbed ($\alpha W>>1$) and remains essentially constant regardless of any further thickness increase. However, when photon recycling is not accounted in the model (lower curve in Figure 6), the efficiency initially improves as the thickness increases (due to a higher absorption of photons) reaching a maximum at 56.1%. Once the optimum thickness corresponding to this maximum has

Figure 6. Efficiency versus cell thickness for two IBSC scenarios: with and without photon recycling. The model assumes an IBSC with optimum bandgaps, maximum concentration, and 6000K blackbody irradiance. Constant and non-overlapping absorption coefficients are considered in both cases. Reprinted with permission from Martí et al. (2008).

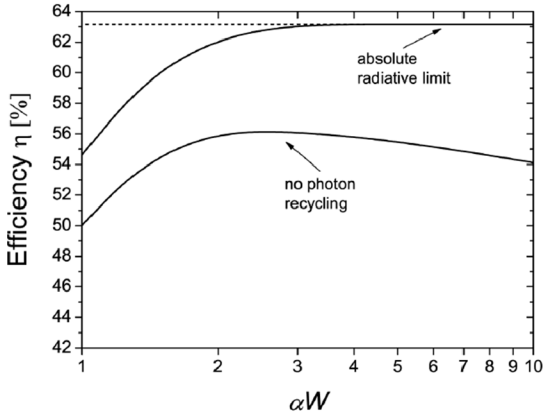

been reached, the efficiency decreases due to the increased radiative recombination without, however, recycling of photons.

As explained in Cuadra et al. (2004), when more than one absorption coefficient are non-zero in the same energy range, a drop in the limit efficiency occurs even in a purely radiative case; at 1000 suns, for example, the efficiency drops from 57% to 32%, when considering $\alpha_{CV}=\alpha_{IV}=\alpha_{CI}=4\ 10^4\ cm^{-1}$ (which is a value that is in the range of the GaAs absorption coefficient). But this harmful effect can be mitigated if the IBSC is engineered so that a large difference between each of the values of the absorption coefficients exists, i.e. $\alpha_{CV}>>\alpha_{IV}$ as well as $\alpha_{IV}>>\alpha_{CI}$. For the sake of simplicity, we represent this difference by a fix proportionality factor denoted as γ so that:

$$\gamma = \alpha_{IV}/\alpha_{CV} = \alpha_{CI}/\alpha_{IV} \quad (2)$$

This situation, which has been sketched in Figure 7a, causes one absorption coefficient to dominate in each of the three energy ranges ($E_L<E<E_H$, $E_H<E<E_G$ and $E>E_G$), approaching the non-overlapping condition.

A problem derived from such scenario is associated to the weakness of the absorption related to the lowest absorption coefficient, which in turn implies a reduced g_{CI}. A possible solution relies on the use of light trapping techniques, such as the texturing of the IBSC or the use of a cavity (Luque, et al., 1991), which increases the optical path length inside the cell. Other light management techniques can be implemented through the use of Metal Nanoparticles (MNPs) that, within the near-field approximation, provide encouraging results for amplification of the absorption of the IR light. This amplification is produced by the MNP plasmonic resonance and depends on the MNP material and shape (Luque, Martí, Mendes, & Tobías, 2008). On the other hand, micrometric patterned diffraction grids have also been postulated for their calculation under the far-field approximation as another possible strategy for light trapping applied to the IR range (Mellor, Tobías, Martí, Mendes, & Luque, 2010; Tobías, Luque, & Martí, 2008).

In Figure 7b a simulation from Cuadra et al. (2004) is shown where the results from considering γ=1 and γ=10 are compared considering the case of an IBSC with optimum bandgaps at 1000 suns (i.e. E_H=1.32 eV and E_L=0.77 eV). For this model, a constant numerical value of $\alpha_{CV}=4\ 10^4\ cm^{-1}$ has been also used. The use of light confinement through the insertion of the cell inside an ideal cavity is represented by dashed lines in the figure. When considering this last condition, the cell efficiency is enhanced and the optimum cell thickness can be dramatically reduced. The thickness of the IBSC, represented also on the curves in Figure 7b, has been optimized for each case.

Other published works (Navruz & Saritas, 2008) also study the impact of the overlap of the absorption coefficients, for different values of γ,

Figure 7. (a) Sketch of the absorption coefficients minimizing the detrimental effect of overlapping. (b) IBSC efficiency for a concentration of 1000 suns and optimum bandgaps in accordance with the degree of overlapping. The γ parameter is either 1 or 10 in the model. Light confinement case is represented by dashed curves. The optimum thicknesses are expressed in micrometers on the curves. Reprinted with permission from Cuadra et al. (2004) © 2004 IEEE.

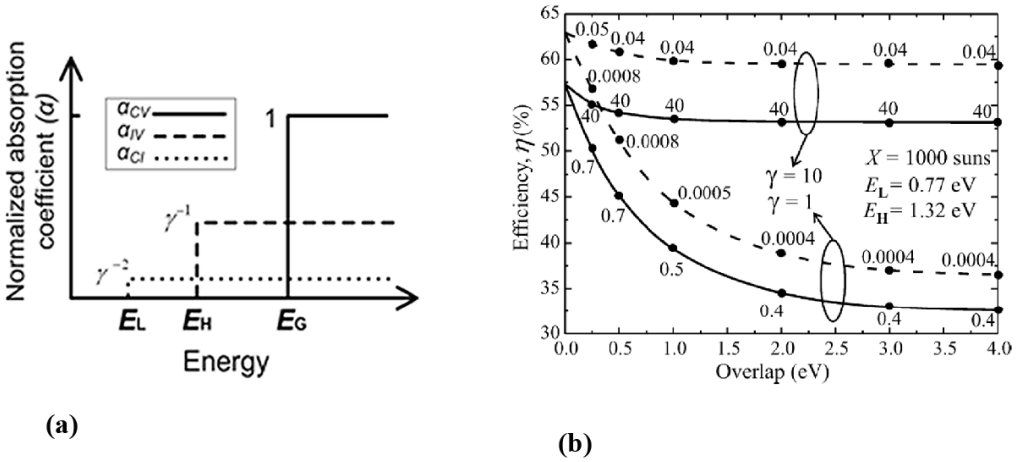

on the efficiency, the optimum IB position, the IB material width or base width, the *I–V* curves, the bandgap and the combined effect with NRR.

3.3. Partial Filling of the IB

It must be noticed that an electron pumped from the VB to the IB does not necessary have to be the same one that is promoted to the CB by the absorption of the second low-energy photon that pumps an electron from the IB to the CB. If the same electron were the only available carrier for the second sub-bandgap absorption step (g_{CI}), the associated probability of the process would be that of a three-particle collision (involving two photons and one electron), which is more unlikely than a process involving a two-particle collision. In contrast, a steady state carrier population is required in the IB in order to assist the second sub-bandgap transition. For the g_{IV} transition to occur, the IB states cannot be completely occupied with electrons, otherwise there would not be room for any other electron to be pumped from the VB and the associated probability would be null. For the fulfillment of both IB population constrains, the IB has to be partially filled.

There are several ways to achieve such partial occupation condition. The IBSC may be engineered so that the IB is naturally partially filled at room temperature. However, if empty or completely filled it may be 'artificially' doped with impurities that are ionized at the temperature of operation as to tune the desired IB filling level (in QD-IBSCs, this can be attained by modulation doping in the barrier as explained in Martí, Cuadra, and Luque (2001). Also, in steady state conditions, it may be photofilled with the electrons from the first transition (Strandberg & Reenaas, 2009).

Figure 8 shows the efficiency of an IBSC with different densities of IB states (N_{ib}) in accordance with the solar concentration level and considering the effect of photofilling according to the work by Strandberg and Reenaas (2009). Their simulation reveals that high efficiencies can be attained without prefilling the IB only when

Figure 8. Efficiency as a function of the concentration level for IBSCs with different number of IB states. Reprinted with permission from Strandberg and Reenaas (2009). Copyright 2009, American Institute of Physics.

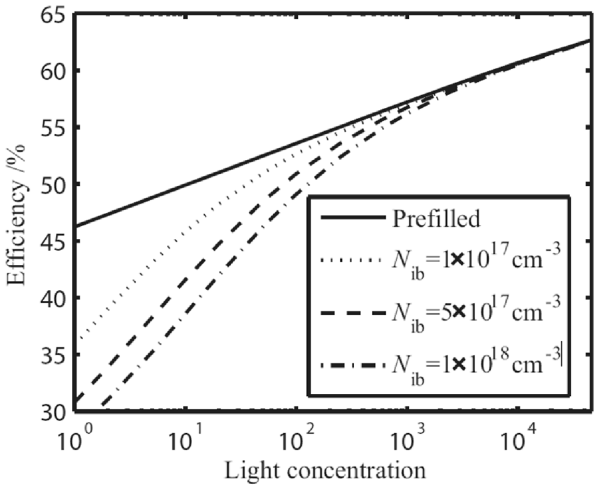

the cell operates at sufficiently high sunlight concentrations.

There is a QFL associated to the carrier population at the IB (ε_{FIB}) and, ideally, it has to remain clamped at its equilibrium position. The latter depends on the IB density of states. When the IB exhibits a high capture cross section for electrons in the CB (i.e. the IB is connected to the CB through recombination), a low filling factor seems to improve the IBSC Quantum Efficiency (QE) profile and consequently, the extracted photocurrent. However, the voltage and thus the efficiency will then be fundamentally limited by the IB→CB transition. The latter is simulated using the Generalized Shockley Read Hall model applied to the IBSC (Luque, et al., 2006) in the study on the influence of the filling factor (Luque & Martí, 2010), where the effect of a pre-filled IB is discussed for different cases of QD-IBSCs.

All the calculations presented are analytical and may be improved in the future through the use of numerical-based models that solve the semiconductor equations that also account for the specific IB material physics.

3.4. Impact Ionization

Auger recombination can cause de-excitation of electrons, thus reducing the cell efficiency. The complementary mechanism of the Auger recombination is the Auger generation, through which the electrons can be transferred to a higher energy band. It is more likely to occur in bands with a high density of electrons. Besides, this kind of process is also more likely if the energy required for the impact ionization-assisted transition is small.

Impact ionization may also be particularly useful to exploit the IBSC concept when any of the involved transition is limited or even forbidden for a certain polarization of the light. For example, if the transition through E_L can only be produced by impact ionization from the IB→VB electron de-excitation, as depicted in Figure 9a. This has been studied within the IBSC context in Luque, Martí, and Cuadra (2003), where it was assumed that selection rules imposed a zero matrix element associated to g_{CI}. As a consequence, according to detailed balance arguments (Shockley & Queisser, 1961), no luminescence

Figure 9. (a) Simplified sketch of a two-step VB→CB transition in an impact-ionization-assisted IBSC. Two photons are absorbed in the E_H transition and the de-excitation of one of the electrons in the IB promotes an electron transition through E_L by the impact ionization mechanism. (b) Efficiency limit of an impact-ionization-assisted IBSC, together a double junction tandem cell and a purely radiative photon IBSC. Reprinted with permission from Luque et al. (2003) © 2003 IEEE.

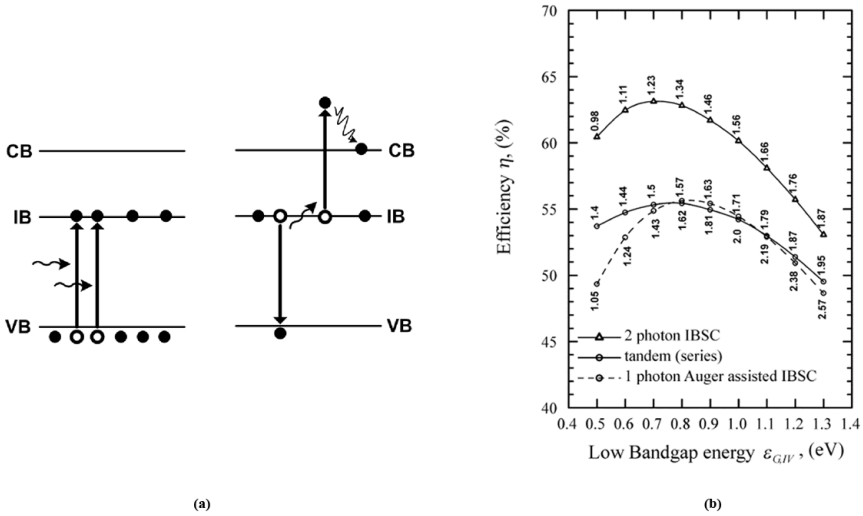

is assumed in this transition. In this model, flat QFLs are also assumed, implying infinite mobility of the carriers. In Figure 9b, the simulation of the impact-ionization-assisted IBSC is compared to a double junction tandem solar cell and a purely radiative IBSC with the same lower bandgap. The plot of the efficiencies reveals that, although lower than the purely radiative IBSC, the maximum efficiency achievable by the impact ionization-assisted IBSC is comparable to that of the double junction tandem cell.

Other simulation exercises have been carried out (Navruz & Saritas, 2009) including the simulation of IBSCs in which impact ionization mechanisms are not substitute but complementary to the IB→CB photon absorption. This study compares the IBSC with and without the additional impact ionization component for the case of overlapping and not overlapping of the absorption coefficients and under different multiplication probabilities.

3.5. QD-IBSC Modeling

There are several features defining QD structures, which are worth discussing from the perspective of their impact on the operation of the IBSC. We will particularize them in the framework of the InAs/GaAs QD system, which is the best-known material system. These features are:

- **Dot Shape and Aspect Ratio:** The aspect ratio is defined as the QD's base width divided by its height. Actual InAs/GaAs QDs are often characterized by a rather high aspect ratio of about 4 or 5. Moreover, the QDs that have been grown so far account a convex lens or a truncated pyramid shape with a large base (Sugawara, 1999). The aspect ratio influences the confined states distribution. In this respect, QDs with squat shapes host a collection of confined states which are separated by a small energy (approaching the QW case).

- **Minimum Size:** The QD systems used in crystalline solar cells are commonly grown by means of a Molecular Beam Epitaxy (MBE) reactor. The Stranski-Krastanov (Sugawara, 1999) growth mode consists on the 2-D to 3-D nucleation of the dots as a way to release the strain of the InAs layer after a critical amount of material has been deposited on top of the GaAs. Because of the specific nature of the nucleation, the dots do not achieve the desired small size that allows the appearance of only one energy state in the CBO. Depending on the MBE growth conditions this size can be tuned, although very small QDs in the range of 3 or 4 nanometers are required, as shown in Linares, Martí, Antolín, and Luque (2010). So far, several levels seem to be confined within the CBO (Luque, et al., 2010).
- **Absorption and Dot Density:** A strong IR absorption of the dots is required for the electron pumping through the IB. Both sub-bandgap transitions are weak in QDs, although the IB→CB transition is believed to be weaker. The IR absorption depends on the QD density, which has to be maximized. The use of high index GaAs substrates, such as the 311B (Akahane, et al., 1998) is intended to increase both the density and ordering of the QDs. At a sufficiently high density, the IB electron wavefunctions could ultimately overlap and delocalize, forming a miniband and strengthening transitions from IB states to the barrier CB continuum due to increased wavefunction overlap (Martí, et al., 2006). On the contrary, the selection rules do not permit transitions from localized to delocalized states (Luque, Marti, Antolin, & Linares, 2010).
- **Accumulation of Strain:** The previous arguments lead to the necessity of stacking several QD layers in order to increase the cell absorptivity. The difference in lattice constant between the QD and the barrier material causes a hydrostatic strain that is indeed at the origin of the QD nucleation. The formation of the islands (QDs) relaxes part of this strain; however, a significant part of it is not relaxed but vertically transmitted towards the next QD layer, which will then add more strain to the system. After several periods, the strain can relax inelastically, producing threading dislocations and damaging the material quality (Martí, et al., 2007). There are two strategies to solve this problem: 1) the introduction of strain compensating layers, i.e. portions of material with a lattice constant producing a strain field of opposite sign so that the overall strain is cancelled (Oshima, Takata, & Okada, 2008; Popescu, Bester, Hanna, Norman, & Zunger, 2008); and 2) growing thick spacers between successive QD layers, thus causing the strain to dilute before the new QD layer is grown (Antolín, 2010). The accumulation of strain can be modeled so that the thickness and the composition of the strain compensating layer as well as the strain release spacer layer are optimized, so that the total volume of the active region is optimally reduced.
- **Wetting Layer:** QD growth techniques such as the Stranski-Krastanov cause a thin layer of QD material to remain unaltered under the dots (Sugawara, 1999), i.e. not all the QD material is employed in the formation of the dots. This is a WL, which is a QW that worsens the performance of the IBSC because of the introduction of a continuum of states close to the CB (as depicted in Figure 3).

In order to better understand the nanostructure non-idealities applied to the QD-IBSC, a model including several IB levels has been proposed (Luque, et al., 2010). The equivalent circuital

model increases the complexity beyond the one of the conventional IBSC, which only accounts for a generator/diode set for each of the three transitions (Figure 10b). In this analysis, up to four intermediate levels were identified through photoreflectance and quantum efficiency techniques, which corresponding equivalent circuit is the one shown in Figure 10c. The circuit is aimed to evaluate the impact of each of the recombination processes associated to the diodes present in the multiple-level IBSC model. This is carried out through the fitting of the photogenerated current density (J_L)-V_{OC} curve (dashed and hollow circles curves in Figure 10d), which is measured for a wide range of concentrations, up to 1000 suns. Two different cases are considered together with their respective mathematical expressions for the fitting of the J_L-V_{OC} curve: the connection or disconnection of the IB→CB transition through recombination mechanisms. In the case of the IBSC analyzed in this work, a connected-based model best fitted the experimental behavior. At the end of this analysis, the model sets a fitting parameter to each of the involved transitions, giving an idea of the recombination taking place through it, although the parameter may also account for the combined effect of a low absorption.

Another theoretical work devoted to the simulation of the QD-IBSC intraband absorption (Luque, et al., 2010) is based on the quantum-mechanic analysis of a parallelepiped potential well for which the matrix elements are calculated. It verified that the absorption strength of the IB→CB transition (provided the IB is the fundamental confined state and the CB is the first confined state above the barrier CB) is very weak, which supports what is experimentally observed.

3.6. New IB Material Search

After the IBSC fundamentals have been verified in QD-IBSCs, the search for new IB candidate

Figure 10. Simplified circuital models of: (a) a conventional solar cell; (b) a single level IBSC; and (c) a 4 level IBSC. (d) Measured J_L-V_{OC} of a GaAs reference and an IBSC with its corresponding '4 connected level' fitting. Reprinted with permission from Luque et al. (2010). Copyright 2010, American Institute of Physics.

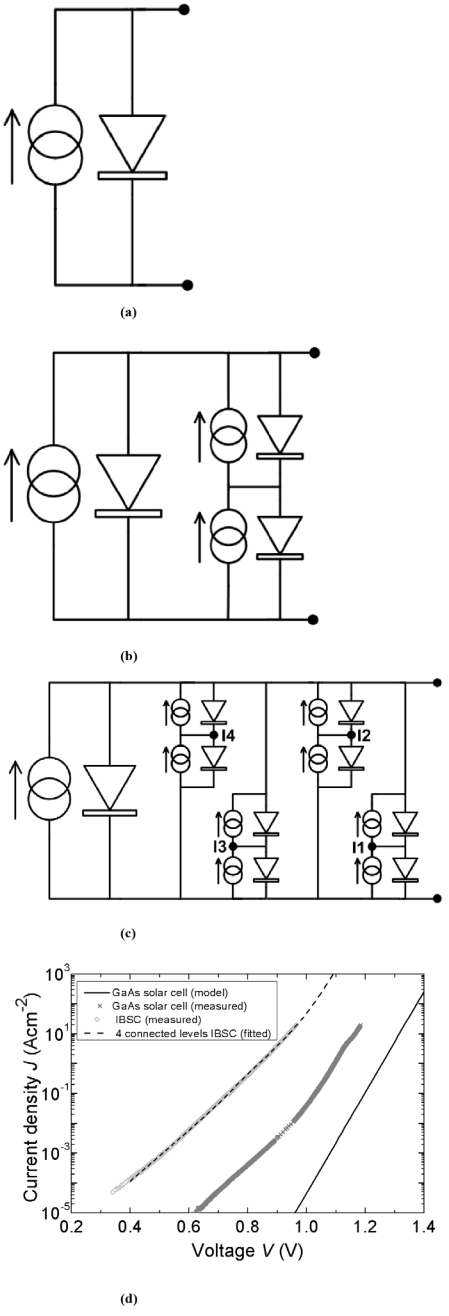

Figure 11. Simulation of the Ga_4P_3Ti (a) band diagram in some directions of the Brillouin zone; and (b) absorption coefficient for the most relevant IBSC transitions. Reprinted from Tablero (2006). Copyright 2006, with permission from Elsevier.

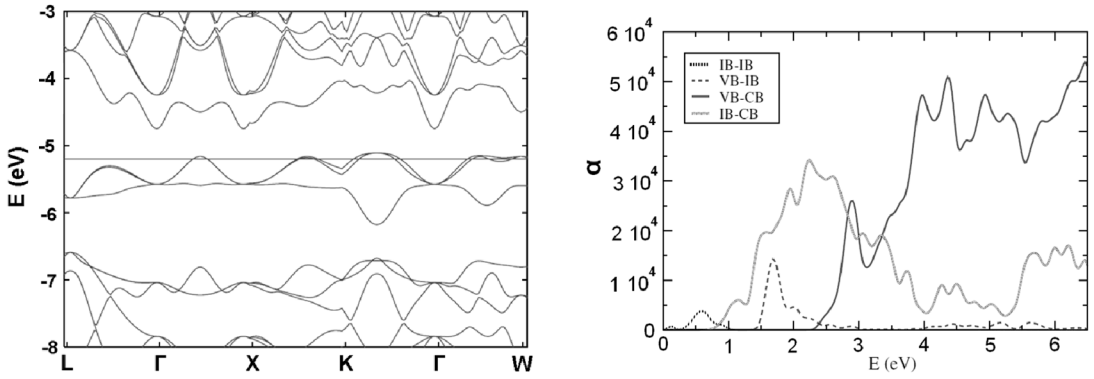

materials with the potential of achieving high conversion efficiency is still very important.

In Sections 2.1 and 2.2 several research lines have been introduced including a wide variety of structures fulfilling the IBSC constrains. The detailed study of them all is out of the scope of this chapter and therefore only one example of bulk-based and QD-based IBSC involving quantum mechanical calculations will be presented as an example.

The simulation of one of the first proposed bulk materials, the Ga_4P_3Ti, from first principle calculations (Tablero, 2006), was based on the Density Functional Theory (DFT) and the Local-Density Approximation (LDA), leading to the energy band diagrams shown in (Figure 11a). A clear isolated band between VB and CB becomes apparent when the Ti atoms are included in the ordinary semiconductor structure. The momentum matrix elements are calculated and together with the band, energies and the occupation numbers are used to calculate the main optical properties, such as the absorption coefficient, which can be appreciated in Figure 11b.

An exhaustive search for new QD/barrier material combinations has also been undertaken in order to identify an optimized candidate with a high efficiency threshold (not only from fundamental point of view, but also assuming constrains that account for their practical implementation). One of the crucial problems of the currently fabricated In(Ga)As/GaAs QD-IBSCs is the short-circuiting of the g_{CI} transition because of the large number of levels confined into a relatively small CBO, favoring quick carrier relaxation from the CB to the IB.

Several constrains have to be defined for the selection of the QD material combination. Levy, Honsberg, Martí, and Luque (2005) proposed materials with zero or negligible VBO in order to avoid the thermalization of holes giving rise to a reduction of the effective bandgap and the consequent efficiency loss. Recent calculations also considered the following constrains: a CBO greater than 0.4 eV and a barrier material bandgap of at least 1.2 eV. Two QD material combinations were identified: $Al_{0.57}In_{0.43}As/InP_{0.87}Sb_{0.13}$ grown on lattice matched metamorphic buffer layer and

$Al_{0.5}In_{0.5}As/InAs_{0.41}P_{0.59}$ grown on pseudomorphic buffer layer, denoted as "fully strained" (Dahal, Bremner, & Honsberg, 2010). Their respective limiting efficiencies are 58% and 53% calculated under the detailed balance realm and an AM1.5D spectrum at 1000 suns.

Such modeling eludes the analysis of the actual position of the electron (and hole) confined states inside the nanostructure and supposes a best case scenario for the energy of the fundamental confined level (IB), which will in turn define the energy of the sub-bandgaps. The existence of extra confined levels within the CBO is also disregarded. However, the analysis of the precise number and position of the confined levels is crucial for the calculation of the limiting efficiency. Otherwise, the assumption of having a single confined level located at an optimized energy within the CBO, may result unrealistic or even physically unsound, for example, for the case when this confined level is located at the lower edge of the CBO, because it accounts for an impossible situation, even for an ideal QD.

In Linares et al. (2010), a first analysis of the band alignment is carried out taking the lattice strain into account. The constrain for large host material bandgap and CBO is imposed (above 1.6 eV and 1 eV respectively). On the other hand, a negligible VBO is not indispensable in this model, since it will help to define the effective bandgap as it was described in Section 2.1 (considering this VBO as short-circuited from the fundamental confined hole state). After the band diagram at the QD is calculated, both the energy of the CBO (or VBO) and the estimated effective mass values inside and outside the dots are used as the data input for the computation of the confined levels, for both electrons in the CBO (or holes in the VBO), as a function of the QD radius (under the assumption of spherical dots, for simplicity). The choice of the optimum radius is conditional to the existence of only one confined electron state. The last step consists on the computation of the potential efficiency of each III-V candidate QD system, which is essential to provide feedback for the survey. Such efficiency is calculated for a black body at 6000K and maximum concentration for an appropriate comparison with respect to previous analysis. Efficiencies over 61.5% are obtained with this method for InAsN/AlAsSb and InAsN/AlGaInP QD systems with optimized QD radii in the range of 3nm. The InAs/AlGaAs is also identified as a promising QD material for its manufacturing feasibility (the barrier is lattice matched to GaAs) combined with a high potential efficiency (over 56%).

4. FUTURE RESEARCH DIRECTIONS

The IBSC is regarded as a promising technology for developing high efficiency devices capable of surpassing the Shockley-Queisser single gap efficiency limit. As it has been exposed throughout this chapter, the modeling of new IB material implementations as well as the simulation of the IBSC specific features regarding the performance of real devices have been of inestimable help for the improvement of the IBSC technology. However, the future of the research will require dealing with more experimental work and their interpretation will require further modeling.

Some of the concept fundamentals have been already verified through experimental analysis and modeling of the results. Both bulk and QD-based IBSC prototypes have been manufactured and tested. The best results in this sense are: 1) the verification of photocurrent production due to the absorption of sub-bandgap photons; 2) the verification of the voltage preservation; 3) the demonstration of the increase of the minority carrier lifetime in highly doped bulk IB materials. These results are summarized hereafter.

The capability of the IBSC for the production of photocurrent due to the absorption of low energy photons through both sub-bandgap transitions, g_{IV} and g_{CI}, has been measured under

Figure 12. (a) Comparison between V_{OC} and the barrier material absorption threshold of a QD-IBSC (QD ground sate transition). Reprinted with permission from Antolín et al. (2010) © 2010 IEEE. (b) Wafer effective carrier lifetime vs carrier injection level in samples implanted with Ti doses of 10^{15}, 5 10^{15}, and 10^{16} cm^{-2}. Reprinted with permission from Antolín et al. (2009). Copyright 2010, American Institute of Physics.

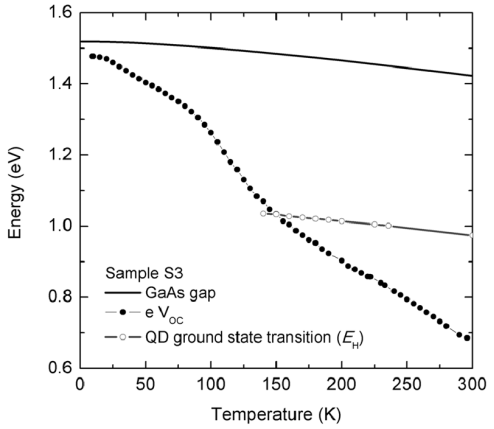

(a)

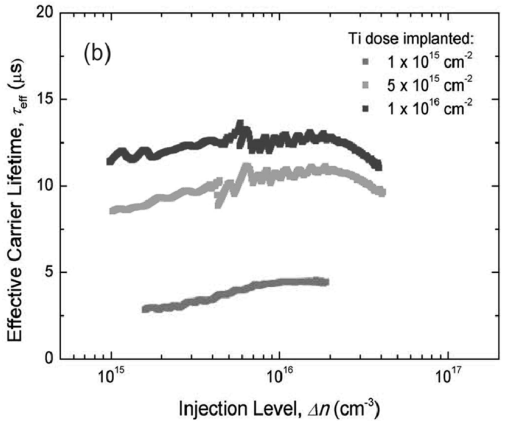

(b)

cryogenic temperatures in Martí et al. (2006). The success of this so-called *two-photon experiment* was achieved for a QD-IBSC sample using lock-in techniques that confirmed that the sub-bandgap photocurrent signature appeared and disappeared when the infrared source was respectively turned on and off.

The first empirical demonstration of the IBSC voltage preservation was first obtained also with a QD-IBSC sample and presented in Antolín et al. (2010). It consists on the verification of a V_{OC} not limited by neither E_L nor E_H sub-bandgaps. In Figure 12a, a plot of the measured V_{OC} is represented with black filled circles as a function of the temperature; the QD ground state transition (VB→IB), obtained from the peaks in the QE signature is represented with grey hollow circles; and the GaAs gap (barrier material of the QD-IBSC in this case) is represented with a black solid line, them all as a function of the temperature. The IBSC V_{OC} almost reaches the absorption threshold of the GaAs, which is a clear confirmation of the voltage not being fundamentally limited by any of the IBSC sub-bandgaps. The extinction of the ground state transition signature from 150K towards lower temperatures implies that no carrier escape is being produced in this sample, firstly because of the suppression of the thermal component at low temperatures and secondly, because the tunneling component has also been prevented through the introduction of thicker spacers.

The last proof-of-concept concerns the bulk IBSC lifetime recovery. In Figure 12b a lifetime measurement from Antolín et al. (2009) is presented for different Ti-implanted doses in a Si wafer developed . The model for highly-doped impurity semiconductors presented in Luque et al. (2006) predicts the suppression of non-radiative recombination thanks to the delocalization of the impurity wavefunctions, which occurs when a sufficiently high impurity concentration is reached (in the range of 6 10^{19} cm^{-3}). This is a very important result, contrary to the classic

intuition for which DLs are considered as lifetime killers at any density.

The future success of this IB-based novel concept in PV relies on the manufacturing of new devices implemented with novel IB materials and also on the capability of modeling their experimental behavior so an appropriate feedback is provided and they can be improved so that an optimized IBSC is finally achieved.

5. CONCLUSION

According to the predictive model presented in Ref. (Luque, 2001), a breakthrough in PV can modify the relatively slow growth of PV, so that the associated learning curve promotes a sufficiently fast development.

In this chapter, the IBSC concept has been reviewed as one of the technologies in the research for novel PV concepts. Development of modeling and simulation tools for this concept are of crucial importance, since, as it has been shown throughout Section 3, the concept can be implemented by means of many different approaches and the impact of their properties and features still requires further understanding.

The simulation of the electronic and optical properties of new IB candidate materials by means of first principle analysis is still a relevant research field. Quantum mechanical calculation including the confined energy levels inside nanostructured materials, such as QDs is a very fruitful tool for the understanding of this new research field. Optimized QD systems are required accounting both a high efficiency threshold and a feasible manufacturing process. Finally, the modeling of relevant IBSC features, such as the ones presented in Section 3, accounting more realistic premises are also important for the appropriate evaluation of the measured prototypes.

REFERENCES

Akahane, K., Kawamura, T., Okino, K., Koyama, H., Lan, S., & Okada, Y. (1998). Highly packed InGaAs quantum dots on GaAs(311)B. *Applied Physics Letters*, *73*(23), 3411–3413. doi:10.1063/1.122781

Antolín, E. (2010). *Development of experimental techniques for the demonstration of the operation principles of the intermediate band solar cell*. Madrid, Spain: Universidad Politécnica de Madrid.

Antolín, E., Martí, A., Linares, P. G., Ramiro, I., Hernández, E., Farmer, C. D., et al. (2010). *Advances in quantum dot intermediate band solar cells.* Paper presented at the 35th IEEE Photovoltaic Specialists Conference. Hawaii, HI.

Antolín, E., Martí, A., Linares, P. G., Ramiro, I., Hernández, E., & Luque, A. (2010). *Raising the efficiency limit of the GaAs-based intermediate band solar cell through the implementation of a monolithic tandem with an AlGaAs top cell.* Paper presented at the 25th European Photovoltaic Solar Energy Conference. Valencia, Spain.

Antolín, E., Martí, A., & Luque, A. (2006). *Energy conversion efficiency limit of series connected intermediate band solar cells.* Paper presented at the 21st European Photovoltaic Solar Energy Conference. Dresden, Germany.

Antolín, E., Martí, A., Olea, J., Pastor, D., González-Díaz, G., & Mártil, I. (2009). Lifetime recovery in ultrahighly titanium-doped silicon for the implementation of an intermediate band material. *Applied Physics Letters*, *94*(4), 1–3. doi:10.1063/1.3077202

Araujo, G. L., & Martí, A. (1994). Absolute limiting efficiencies for photovoltaic energy conversion. *Solar Energy Materials and Solar Cells*, *33*(2), 213–240. doi:10.1016/0927-0248(94)90209-7

Bockelmann, U., & Bastard, G. (1990). Phonon scattering and energy relaxation in two-, one- and zero-dimensional electron gasses. *Physical Review B: Condensed Matter and Materials Physics*, *42*(14), 8947–8951. doi:10.1103/PhysRevB.42.8947

Cuadra, L., Martí, A., & Luque, A. (2000). *Modeling of the absorption coefficients of the intermediate band solar cell.* Paper presented at the 16th European Photovoltaic Solar Energy Conference. Glasgow, UK.

Cuadra, L., Martí, A., & Luque, A. (2004). Influence of the overlap between the absorption coefficients on the efficiency of the intermediate band solar cell. *IEEE Transactions on Electron Devices*, *51*(6), 1002–1007. doi:10.1109/TED.2004.828161

Dahal, S. N., Bremner, S. P., & Honsberg, C. B. (2010). Identification of candidate material systems for quantum dot solar cells including the effect of strain. *Progress in Photovoltaics: Research and Applications*, *18*(4), 233–239.

del Cañizo, C., del Coso, G., & Sinke, W. C. (2009). Crystalline silicon solar module technology: Towards the 1Eur per watt-peak goal. *Progress in Photovoltaics: Research and Applications*, *17*, 199–209. doi:10.1002/pip.878

Ekins-Daukes, N. J., & Schmidt, T. W. (2008). A molecular approach to the intermediate band solar cell: The symmetric case. *Applied Physics Letters*, *93*(6), 063507. doi:10.1063/1.2970157

González-Díaz, G., Olea, J., Mártil, I., Pastor, D., Martí, A., & Antolín, E. (2009). Intermediate band mobility in heavily titanium-doped silicon layers. *Solar Energy Materials and Solar Cells*, *93*(9), 1668–1673. doi:10.1016/j.solmat.2009.05.014

Grimmeiss, H. G., & Koelmans, H. (1961). Analysis of p-n luminescence in Zn-doped GaP. *Physical Review*, *123*(6), 1939. doi:10.1103/PhysRev.123.1939

Lang, D. V., & Henry, C. H. (1975). Nonradiative recombination at deep levels in GaAs and GaP by lattice-relaxation multiple phonon emission. *Physical Review Letters*, *35*(32).

Levy, M. Y., Honsberg, C., Martí, A., & Luque, A. (2005). Quantum dot intermediate band solar cell material systems with negligible valence band offsets. In *Proceedings of the 31st IEEE Photovoltaics Specialists Conference*, (pp. 90–93). IEEE Press.

Linares, P. G., Martí, A., Antolín, E., & Luque, A. (2010). III-V compound semiconductor screening for implementing quantum dot intermediate band solar cells. *Journal of Applied Physics*, *109*(1).

Lucena, R., Aguilera, I., Palacios, P., Wahnón, P., & Conesa, J. C. (2008). Synthesis and spectral properties of nanocrystalline V-substituted In2S3, a novel material for more efficient use of solar radiation. *Chemistry of Materials*, *20*(16), 5125–5127. doi:10.1021/cm801128b

Luque, A. (2001). Photovoltaic markets and costs forecast based on a demand elasticity model. *Progress in Photovoltaics: Research and Applications*, *9*, 303–312. doi:10.1002/pip.371

Luque, A., Linares, P. G., Antolin, E., Canovas, E., Farmer, C. D., & Stanley, C. R. (2010). Multiple levels in intermediate band solar cells. *Applied Physics Letters*, *96*(1), 013501–013503. doi:10.1063/1.3280387

Luque, A., & Martí, A. (1997). Increasing the efficiency of ideal solar cells by photon induced transitions at intermediate levels. *Physical Review Letters*, *78*(26), 5014–5017. doi:10.1103/PhysRevLett.78.5014

Luque, A., & Martí, A. (2001). A metallic intermediate band high efficiency solar cell. *Progress in Photovoltaics: Research and Applications*, *9*(2), 73–86. doi:10.1002/pip.354

Luque, A., & Martí, A. (2010). On the partial filling of the intermediate band (IB) in IB solar cells. *IEEE Transactions on Electron Devices*, *57*(6), 1201–1207. doi:10.1109/TED.2010.2045681

Luque, A., Marti, A., Antolin, E., & Linares, P. G. (2010). Intraband absorption for normal illumination in quantum dot intermediate band solar cells. *Solar Energy Materials and Solar Cells*, *94*(12), 2032–2035. doi:10.1016/j.solmat.2010.06.008

Luque, A., Martí, A., Antolín, E., & Tablero, C. (2006). Intermediate band versus levels in non-radiative recombination. *Physica B, Condensed Matter*, *382*, 320–327. doi:10.1016/j.physb.2006.03.006

Luque, A., Martí, A., & Cuadra, L. (2000). *High efficiency solar cell with metallic intermediate band*. Paper presented at the 16th European Photovoltaic Solar Energy Conference. London, UK.

Luque, A., Martí, A., & Cuadra, L. (2003). Impact-ionization-assisted intermediate band solar cell. *IEEE Transactions on Electron Devices*, *50*(2), 447–454. doi:10.1109/TED.2003.809024

Luque, A., Martí, A., López, N., Antolín, E., Cánovas, E., & Stanley, C. R. (2006). Operation of the intermediate band solar cell under nonideal space charge region conditions and half filling of the intermediate band. *Journal of Applied Physics*, *99*(1), 094503. doi:10.1063/1.2193063

Luque, A., Martí, A., Mendes, M. J., & Tobías, I. (2008). Light absorption in the near field around surface plasmon polaritons. *Journal of Applied Physics*, *104*(11), 1–8. doi:10.1063/1.3014035

Luque, A., Miñano, J. C., Davies, P., Terrón, M. J., Tobías, I., Sala, G., et al. (1991). *Angle-limited cavities for silicon solar cells*. Paper presented at the Photovoltaic Specialists Conference, 1991. New York, NY.

Martí, A., Antolín, E., Cánovas, E., Linares, P. G., & Luque, A. (2008). Light management issues in intermediate band solar cells. In *Proceedings of the MRS, Spring Meeting,* (vol 1101E), (pp. KK06-02). San Francisco, CA: MRS.

Martí, A., Antolín, E., Cánovas, E., López, N., Luque, A., Stanley, C., et al. (2006). *Progress in quantum-dot intermediate band solar cell research.* Paper presented at the 21st European Photovoltaic Solar Energy Conference. Munich, Germany.

Martí, A., Antolín, E., Linares, P. G., Cánovas, E., Marrón, D. F., Tablero, C., et al. (2009). *IB-POWER: Intermediate band materials and solar cells for photovoltaics with high efficiency and reduced cost.* Paper presented at the Photovoltaic Specialists Conference (PVSC). New York, NY.

Martí, A., Antolín, E., Stanley, C. R., Farmer, C. D., López, N., & Díaz, P. (2006). Production of photocurrent due to intermediate-to-conduction-band transitions: A demonstration of a key operating principle of the intermediate-band solar cell. *Physical Review Letters*, *97*(24), 247701. doi:10.1103/PhysRevLett.97.247701

Martí, A., Cuadra, L., & Luque, A. (2000). *Quantum dot intermediate band solar cell.* Paper presented at the Photovoltaic Specialists Conference, 2000. New York, NY.

Martí, A., Cuadra, L., & Luque, A. (2001). Partial filling of a quantum dot intermediate band for solar cells. *IEEE Transactions on Electron Devices*, *48*(10), 2394–2399. doi:10.1109/16.954482

Martí, A., Fuertes Marrón, A., & Luque, A. (2008). Evaluation of the efficiency potential of intermediate band solar cells based on thin-film chalcopyrite materials. *Journal of Applied Physics*, *103*(7), 1–6. doi:10.1063/1.2901213

Martí, A., López, N., Antolín, E., Cánovas, E., Luque, A., & Stanley, C. R. (2007). Emitter degradation in quantum dot intermediate band solar cells. *Applied Physics Letters*, *90*, 233510. doi:10.1063/1.2747195

Martí, A., Tablero, C., Antolín, E., Luque, A., Campion, R. P., & Novikov, S. V. (2008). Potential of Mn doped In1-xGaxN for implementing intermediate band solar cells. *Solar Energy Materials and Solar Cells*, *93*, 641–644. doi:10.1016/j.solmat.2008.12.031

Mellor, A., Tobías, I., Martí, A., Mendes, M. J., & Luque, A. (2010). *Upper limits to absorption enhancement in thick solar cells using difraction grids*. Unpublished.

Navruz, T. S., & Saritas, M. (2008). Efficiency variation of the intermediate band solar cell due to the overlap between absorption coefficients. *Solar Energy Materials and Solar Cells*, *92*(3), 273–282. doi:10.1016/j.solmat.2007.08.012

Navruz, T. S., & Saritas, M. (2009). The detailed analysis of auger effect on the efficiency of intermediate band solar cells. *Solar Energy Materials and Solar Cells*, *93*, 1913–1922. doi:10.1016/j.solmat.2009.06.024

Olea, J., Toledano-Luque, M., Pastor, D., González-Díaz, G., & Mártil, I. (2008). Titanium doped silicon layers with very high concentration. *Journal of Applied Physics*, *104*(1), 016105–016103. doi:10.1063/1.2949258

Oshima, R., Takata, A., & Okada, Y. (2008). Strain-compensated InAs/GaNAs quantum dots for use in high-efficiency solar cells. *Applied Physics Letters*, *93*, 083111. doi:10.1063/1.2973398

Palacios, P., Sánchez, K., Conesa, J. C., Fernández, J. J., & Wahnón, P. (2007). Theoretical modeling of intermediate band solar cell materials based on metal-doped chalcopyrite compounds. *Thin Solid Films*, *515*(15), 6280–6284. doi:10.1016/j.tsf.2006.12.170

Popescu, V., Bester, G. L., Hanna, M. C., Norman, A. G., & Zunger, A. (2008). Theoretical and experimental examination of the intermediate-band concept for strain-balanced (In,Ga)As/Ga(As,P) quantum dot solar cells. *Physical Review B: Condensed Matter and Materials Physics*, *78*(20), 205321. doi:10.1103/PhysRevB.78.205321

Shan, W., Walukiewicz, W., Ager, J. W., Haller, E. E., Geisz, J. F., & Friedman, D. J. (1999). Band anticrossing in GaInNAs alloys. *Physical Review Letters*, *82*(6), 1221. doi:10.1103/PhysRevLett.82.1221

Shockley, W., & Queisser, H. J. (1961). Detailed balance limit of efficiency of p-n junction solar cells. *Journal of Applied Physics*, *32*(3), 510–519. doi:10.1063/1.1736034

Strandberg, R., & Reenaas, T. W. (2009). Photofilling of intermediate bands. *Journal of Applied Physics*, *105*(12), 124512. doi:10.1063/1.3153141

Strandberg, R., & Reenaas, T. W. (2010). Limiting efficiency of intermediate band solar cells with spectrally selective reflectors. *Applied Physics Letters*, *97*(3), 031910. doi:10.1063/1.3466269

Sugawara, M. (1999). *Self-assembled InGaAs/GaAs quantum dots*. San Diego, CA: Academic Press.

Tablero, C. (2006). Analysis of the optical properties for Ga4P3Ti compound with a metallic intermediate band. *Computational Materials Science*, *36*(3), 263–267. doi:10.1016/j.commatsci.2005.04.005

Tablero, C., & Fuertes Marrón, D. (2010). Analysis of the electronic structure of modified CuGaS2 with selected substitutional impurities: Prospects for intermediate-band thin-film solar cells based on cu-containing chalcopyrites. *The Journal of Physical Chemistry C*, *114*(6), 2756–2763. doi:10.1021/jp909895q

Tobías, I., Luque, A., & Martí, A. (2008). Light intensity enhancement by diffracting structures in solar cells. *Journal of Applied Physics*, *104*(3), 034502–034509. doi:10.1063/1.2960586

Wahnón, P., & Tablero, C. (2002). Ab initio electronic structure calculations for metallic intermediate band formation in photovoltaic materials. *Physical Review B: Condensed Matter and Materials Physics*, *65*(16), 1–10. doi:10.1103/PhysRevB.65.165115

Weiming, W., Albert, S. L., & Jamie, D. P. (2009). Intermediate-band photovoltaic solar cell based on ZnTe:O. *Applied Physics Letters*, *95*(1), 011103. doi:10.1063/1.3166863

Wolf, M. (1960). Limitations and possibilities for improvements of photovoltaic solar energy converters: Part I: Considerations for earth's surface operation. *Proceedings of the IRE*, *48*(7), 1246–1263. doi:10.1109/JRPROC.1960.287647

Yu, K. M., Walukiewicz, J. W. A., Bour, D., Farshchi, R., & Dubon, O. D. (2006). Multiband GaNAsP quaternary alloys. *Applied Physics Letters*, *88*(9), 092110. doi:10.1063/1.2181627

ADDITIONAL READING

Antolín, E., Martí, A., & Luque, A. (2010). High efficiency intermediate band solar cells implemented with quantum dots . In Lee, E.-H., Eldada, L., Razeghi, M., & Jagadish, C. (Eds.), *VLSI Micro- and Nanophotonics: Science, Technology, and Applications*. Boca Raton, FL: CRC Press. doi:10.1201/b10371-30

Balenzategui, J. L. (2004). *Influencia del reciclaje de fotones en el funcionamiento y el diseño de las células solares de arseniuro de galio*. Madrid, Spain: Universidad Politécnica de Madrid.

Brown, G. F., & Wu, J. (2009). Third generation photovoltaics. *Laser & Photonics Reviews*, *3*(4), 394–405. doi:10.1002/lpor.200810039

Cánovas, E. (2009). *Desarrollo de técnicas de caracterización para materiales de banda intermedia*. Madrid, Spain: Universidad Politécnica de Madrid.

Cánovas, E., Martí, A., López, N., Antolín, E., Linares, P. G., & Farmer, C. D. (2008). Application of the photoreflectance technique to the characterization of quantum dot intermediate band materials for solar cells. *Thin Solid Films*, *516*(20), 6943–6947. doi:10.1016/j.tsf.2007.12.038

CIEMAT (Ed.). (2004). *Fundamentos, dimensionado y aplicaciones de la energía solar fotovoltaica* (*Vol. 1*). Madrid, Spain: CIEMAT.

Cuadra, L. (2004). *Development of intermediate band solar cells*. Madrid, Spain: Universidad Politécnica de Madrid.

Datta, S. (1989). *Quantum phenomena* (*Vol. 8*). Reading, MA: Addison-Wesley.

Datta, S. (2005). *Quantum transport: Atom to transistor*. Cambridge, UK: Cambridge University Press.

Green, M. A. (1986). *Solar cells: Operating principles, technology and system applications*. Kensington, UK: University of New South Wales.

Green, M. A. (2001). Third generation photovoltaics: Ultra-high conversion efficiency at low cost. *Progress in Photovoltaics: Research and Applications*, *9*(2), 123–135. doi:10.1002/pip.360

Harrison, P. (2000). *Quantum wells wires and dots*. New York, NY: John Wiley and Sons.

Hovel, H. J. (1975). *Solar cells* (*Vol. 11*). New York, NY: Academic Press.

Levy, M. Y. (2008). *Design, experiment, and analysis of a photovoltaic absorbing medium with intermediate levels*. Atlanta, GA: Georgia Institute of Technology.

López, N. (2007). *Caracterización experimental de células solares de banda intermedia con puntos cuánticos*. Madrid, Spain: Universidad Politécnica de Madrid.

Luque, A., & Hegedus, S. (Eds.). (2003). *Handbook of photovoltaic science and engineering*. Chichester, UK: John Wiley & Sons. doi:10.1002/0470014008

Luque, A., & Martí, A. (2010). The intermediate band solar cell: Progress toward the realization of an attractive concept. *Advanced Materials (Deerfield Beach, Fla.)*, *22*(2), 160–174. doi:10.1002/adma.200902388

Markvart, T., & Castañer, L. (Eds.). (2003). *Practical handbook of photovoltaics: Fundamentals and applications*. Oxford, UK: Elsevier.

Martí, A., Cuadra, L., & Luque, A. (2001). Quantum dot analysis of the space charge region of intermediate band solar cell. In *Proceedings of the 199th Electrochemical Society Meeting,* (pp. 46-60). Pennington, UK: The Electrochemical Society.

Martí, A., & Luque, A. (Eds.). (2003). *Next generation photovoltaics: High efficiency through full spectrum utilization*. Bristol, UK: Institute of Physics Publishing.

Martí, A., Stanley, C. R., & Luque, A. (2006). Intermediate band solar cell using nanotechnology . In Soga, T. (Ed.), *Nanostructured Materials for Solar Energy Conversion* (pp. 539–566). Amsterdam, The Netherlands: Elsevier. doi:10.1016/B978-044452844-5/50018-4

Neudeck, G. W. (1983). *The pn junction diode* (*Vol. 2*). Reading, MA: Addison-Wesley Publishing Company.

Olea, J. (2009). *Procesos de implantación iónica para semiconductores de banda intermedia*. Madrid, Spain: Facultad de Ciencias Físicas de la Universidad Complutense de Madrid.

Pierret, R. F. (1989). *Semiconductor fundamentals* (*Vol. 1*). Reading, MA: Addison-Wesley Publishing Company.

Strandberg, R. (2010). *Theoretical studies of the intermediate band solar cell*. Trondheim, Norway: Norwegian University of Science and Technology.

Sze, S. M. (2001). *Semiconductor devices: Physics and technology*. New York, NY: John Wiley & Sons.

Wei, G. D., & Forrest, S. R. (2007). Intermediate-band solar cells employing quantum dots embedded in an energy fence barrier. *Nano Letters*, *7*(1), 218–222. doi:10.1021/nl062564s

Wei, G. D., Shiu, K. T., Giebink, N. C., & Forrest, S. R. (2007). Thermodynamic limits of quantum photovoltaic cell efficiency. *Applied Physics Letters*, *91*(22). doi:10.1063/1.2817753

Würfel, P. (2005). *Physics of solar cells: From principles to new concepts*. Weinheim, Germany: Wiley.

Chapter 12
Phononic Engineering for Hot Carrier Solar Cells

Sana Laribi
Institute of Research and Development on Photovoltaic Energy (IRDEP), France

Arthur Le Bris
Institute of Research and Development on Photovoltaic Energy (IRDEP), France

Lun Mei Huang
Institute of Research and Development on Photovoltaic Energy (IRDEP), France

Par Olsson
Institute of Research and Development on Photovoltaic Energy (IRDEP), France

Jean Francois Guillemoles
Institute of Research and Development on Photovoltaic Energy (IRDEP), France

ABSTRACT

The concept underlying the hot carrier solar cell is to slow the rate of photo-excited carrier cooling to allow time for the carriers to be collected while they are still at elevated energies ("hot"), and thus allowing higher voltages to be achieved from the cell. Significant reduction in carrier cooling has been observed in Quantum Well (QW) nano-structures at very high illumination intensities due to a "phonon bottleneck" mechanism. With the phononic gaps in nano-structures, the optical phonon lifetime can be prolonged by blocking the main phonon decay from optical branches to acoustical branches (such as the Klemens or Ridley decay channels). Si-based hot carrier cell is a very active topic and Si-Ge nano-structures are especially interesting for the application, as their fabrication process is well developed.

In this chapter, the authors first analyse the operation of a hot carrier solar cell and lay down the general principles. They then discuss the opportunity of phonon engineering to improve the phonon bottleneck. Finally, they present how these can be modeled in nanostuctures comprising several thousand atoms, where true 3D phonon dispersion relations for Si-Ge nano-structures are obtained using first principles methods. The effects of the nano-structure size and geometry on the phonon dispersion relations are investigated. The possible phonon decay processes in the nano-structures are discussed and compared with the bulk crystal materials. The performance of calculated nano-structures on the hot carrier solar cell is evaluated with the acquired knowledge of phonon modes.

DOI: 10.4018/978-1-4666-1927-2.ch012

1. THE HOT CARRIER SOLAR CELL CONCEPT

1.1. Principles of the Hot Carrier Solar Cell

The concept of hot carrier solar cell was first introduced by Ross and Nozik (1982). In standard devices, the photon energy in excess of the threshold absorption energy is given to the photogenerated carrier population, and then to the lattice as heat, with only the band gap energy being converted as electrical energy. If the carrier thermalization (thermal equilibration of carriers with the lattice) is suppressed, then the conversion of the total available energy into potential energy is possible and leads to higher conversion efficiency.

The energy distribution of the photogenerated carriers is, immediately after absorption, a non-equilibrium distribution that depends on the energy distribution of the incident photons, and on the electron and hole effective masses and density of states. After absorption, the fate of the carrier distribution can be:

- **Hot Non-Equilibration:** The carriers are not even equilibrated among themselves, the carrier temperature cannot be defined.
- **Hot Equilibration:** The carriers equilibrate among themselves but not with the lattice, resulting in a hot carrier population at $T_H > T_C$, where T_C is the temperature of the lattice.
- **Full Thermalization:** The common situation where carriers are at thermal equilibrium with the environment at ambient temperature.

The comparison between the thermalization rate (due to interactions with phonons, see section 1.3), the carrier-carrier scattering rate, and the carrier extraction rate (the rate at which carriers are removed from the system through contacts or by radiative recombination) will determine which one of the above cases applies.

Table 1. Typical time constants of various carrier interaction mechanisms in semiconductors, from Othonos (1998)

Type of interaction	Characteristic time (s)
Carrier-Carrier scattering	$10^{-15} – 10^{-12}$
Carrier - Optical phonon interaction	$\geq 10^{-12}$
Optical phonon - Acoustic phonon interaction	$\sim 10^{-11}$
Auger recombination	$\sim 10^{-10}$
Radiative recombination	$\geq 10^{-9}$

Typical time constants for these different mechanisms in III-V materials are given in Table 1, from Othonos (1998).

The carrier-carrier scattering time constant is usually below the picosecond, and decreases with an increasing carrier density, while the time constant for the carrier-phonon interaction is of the order of the picosecond. Considering these time constants and without carrier extraction, the dynamics of the carrier after a pulsed monochromatic excitation is described in Figure 1 from Green (2003). Immediately after absorption at t = 0, carriers are generated in a narrow energy range (2). Carrier-carrier scattering then occurs and carriers are redistributed in a hot thermal distribution (3)-(4), within a picosecond. This distribution is then cooled towards the lattice temperature because of interaction with phonons (5). Finally, carriers recombine with a sub-microsecond time constant (7).

If the excitation rate is higher than the thermalization rate, and lower than the carrier-carrier scattering rate, a steady state hot distribution can be established, and the carrier kinetic energy, which is usually lost as heat, can be used and contributes to the conversion efficiency.

Assuming such steady state hot carrier population is achieved, a specific care is required regarding carrier extraction. If the photogenerated

Figure 1. Time evolution of electron and hole population after a laser excitation from Green (2003)

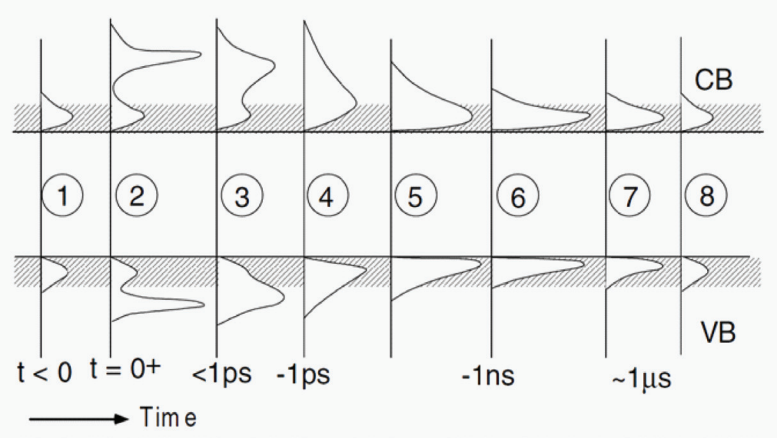

electrons and holes are withdrawn towards metallic electrodes, where interactions with the lattice cannot be avoided before they produce work in the external circuit, thermalization of excited carriers to the lattice temperature will occur, and with it, the carrier kinetic energy will be lost.

A specific cooling of the carriers with minimum heat losses (adiabatic cooling) is necessary to cool down the carriers to the lattice temperature with production of chemical energy that appears as quasi-Fermi level splitting. In other words, the carrier's kinetic energy has to be converted into potential energy, or voltage. This can be achieved with energy selective contacts (Würfel, 1997) that are described in Section 1.4.

In Figure 2, a schematic of the principle of a hot carrier solar cell is presented. Photons are absorbed in the absorber having a band gap E_g, where carriers are in thermal and chemical disequilibrium with the lattice at temperature T_C, characterized by a temperature $T_H > T_C$ and a quasi Fermi level splitting $\Delta\mu_H = \mu^e - \mu^h \neq 0$. Carriers are extracted through selective contacts with a transmission energy range δE, electrons at energy E^e_{ext}, and holes at energy E^h_{ext}, towards electrodes with an applied voltage $V = (\mu^n - \mu^p) / q$. The extraction energy E_{ext} is defined as the difference $E^e_{ext} - E^h_{ext}$. E_{ext} can be higher than the band gap.

1.2. Detailed Balance Models and Limit of Efficiency

In order to evaluate the potential of the hot carrier solar cell concept, models have been developed to evaluate its maximal achievable efficiency. These models are based on a detailed balance approach that defines the electrical power output of a device as the difference between the power absorbed and the different types of losses.

The first non-empirical method to determine a solar cell efficiency limit was proposed by Trivich and Flinn (1995). In their analysis, they assumed that all photons above the band gap are absorbed, and that all electron-hole pairs photogenerated are collected with the energy of the band gap. In these conditions, the electrical power produced is the number of photons with energy higher than the band gap that are incident on the cell times the band gap energy and the efficiency is defined as:

$$\eta = E_G \frac{\int_{E_G}^{\infty} n(\hbar\omega)d\hbar\omega}{\int_{0}^{\infty} \hbar\omega n(\hbar\omega)d\hbar\omega} \quad (1)$$

Figure 2. Schematic of a hot carrier solar cell

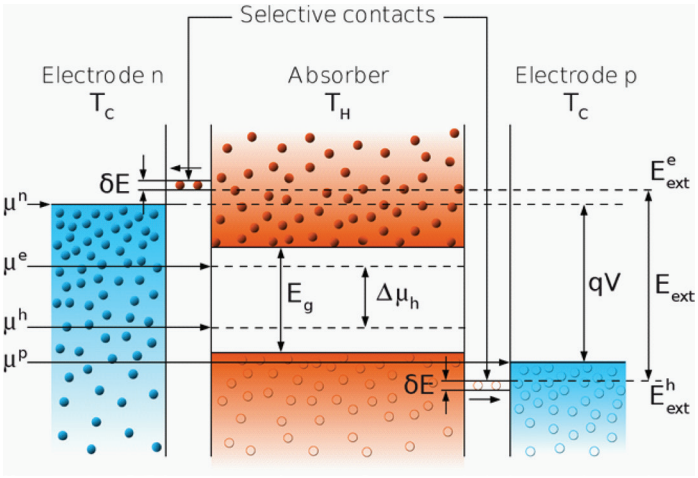

where $n(\hbar\omega)$ is the photon current density and E_G is the absorber band gap energy.

This model predicts an optimal efficiency of 44% for a non-concentrated black body spectrum at 6000 K and with a 1.1 eV band gap absorber. However, it does not account for any recombination process, and for that reason is not a true indicator of the efficiency limit of a solar cell.

In 1961, a model was proposed by Shockley and Queisser (1961) where the current is not only determined by photon absorption, but is equal to the difference between absorption and radiative recombination.

$$J = q(\dot{N}_{abs} - \dot{N}_{em}(V)) \tag{2}$$

where J is the electric current density in A/m^2, N_{abs} is the absorbed photon current density in $m^{-2}.s^{-1}$, N_{em} is the emitted photon current density in $m^{-2}.s^{-1}$ depending on the terminal voltage V of the device, and q is the charge of an electron.

Assuming the sun emits a black body spectrum at their respective temperature T_S, the photon flux incident on the cell per unit area, per unit solid angle and per photon energy is seen in Equation (3).

Where E is the photon energy, θ is the inclination angle, and ϕ is the azimuthal angle.

Integrating over directions and energies, the absorbed photon current density is then given by Planck's law:

$$\dot{N}_{abs} = \frac{1}{4\pi^2\hbar^3c^2}\int_{E_G}^{\infty}\frac{E^2dE}{\exp(\frac{E}{k_BT_S})-1} \tag{4}$$

where f is a geometrical factor that accounts for the solid angle for photoabsorption. If incident photons comes from a cone with half angle θ_{max},

Equation 3.

$$dN_{ph} = \frac{1}{4\pi^3\hbar^3c^2}\frac{E^2}{\exp(\frac{E}{k_BT_S})-1}\cos\theta\,\sin\theta\,d\theta\,\phi\,dE \tag{3}$$

Equation 7.

$$J = \frac{1}{4\pi^2\hbar^3c^2}\int_{E_G}^{\infty}\left[\frac{f\,E^2}{\exp(\frac{E}{k_BT_S})-1} - \frac{\exp(\frac{qV}{k_BT_C})}{\rho(E)}\frac{E^2}{\exp(\frac{E}{k_BT_C})-1}\right]dE \quad (7)$$

f is given by: $f = 2\pi\int\cos\theta\sin\theta d\theta = \pi\sin^2\theta_{\max}$. It is 1 for maximally concentrated radiation ($\theta_{\max} = \pi/2$) and $6.7\text{x}10^{-4}$ for non-concentrated light (the sun is viewed from a solid angle $\Omega = 6.8\text{x}10^{-5}$). The absorptivity is assumed to be one above the band gap energy, and zero below.

The photon current density emitted by the cell with applied voltage V and at the cell temperature T_C is defined as:

$$\dot{N}_{em}(V) = \frac{np}{n_i^2}\dot{N}_0 = \exp(\frac{qV}{k_BT_c})\dot{N}_0 \quad (5)$$

where n and p are the electron and hole densities in the cell, and n_i is the equilibrium carrier density. $\dot{N}_0$ is the equilibrium black body emission at temperature T_C, and is defined, for emission in a 2π solid angle, by:

$$\dot{N}_0 = \frac{1}{4\pi^2\hbar^3c^2}\int_{E_G}^{\infty}\frac{E^2dE}{\exp(\frac{E}{k_BT_C})-1} \quad (6)$$

For a cell temperature $T_C = 0$ K, radiative recombinations become negligible and the open-circuit voltage is equal to the band gap. This model gives the same results as the Trivich-Finn model (Shockley & Queisser, 1961). However, for higher cell temperatures, radiative recombinations lead to reduced current and open-cricuit voltage and a lower efficiency. At 300 K, the efficiency limit given by the Shockley-Queisser model under unconcentrated sun light is 31% for a band gap $E_G = 1.4$ eV. The efficiency limit for fully concentrated sun light ($\Omega = \pi$) is 41% with a 1.1 eV band gap.

If non-radiative recombination occurs, the current-voltage characteristic is given in Equation (7).

Where ρ is the fraction of the total recombination that is radiative, $\rho(E) \leq 1$ ($\rho(E) = 1$ in the Scockley-Queisser approach.

The next major development in the detailed balance theory was brought by Würfel (1982). He provided a more detailed argument regarding the expression of the radiation emitted by the cell. By analyzing the balance between absorption, spontaneous emission and stimulated emission, he was able to relate the emitted photon current to the internal electron-hole gas chemical potential (or quasi-Fermi level splitting), and therefore to the ouput voltage. The following expression was obtained for the emitted photon current density:

$$\dot{N}_{em} = \frac{1}{4\pi^2\hbar^3c^2}\int_{E_G}^{\infty}\frac{E^2dE}{\exp(\frac{E-qV}{k_BT_C})-1} \quad (8)$$

In all the above models, the carriers were supposed to be at thermal equilibrium with the lattice. In 1982, Ross and Nozik (1982) suggested a device where the carriers thermally equilibrate among themselves, but are thermally insulated from the lattice, and are therefore characterized by a temperature $T_H > T_C$. Equation (2) becomes Equation (9).

Equation 9.

$$J = \frac{q}{4\pi^2\hbar^3c^2}\int_{E_G}^{\infty}\left[\frac{f\,E^2}{\exp(\frac{E}{k_BT_S})-1} - \frac{E^2}{\exp(\frac{E-\Delta\mu_H}{k_BT_C})-1}\right]dE \quad (9)$$

Equation 11.

$$J\cdot E_{ext} = \frac{q}{4\pi^2\hbar^3c^2}\int_{E_G}^{\infty}E\left[\frac{f\,E^2}{\exp(\frac{E}{k_BT_S})-1} - \frac{E^2}{\exp(\frac{E-\Delta\mu_H}{k_BT_C})-1}\right]dE \quad (11)$$

Here, electrons in the conduction band and holes in the valence band are assumed to be thermally equilibrated at T_H and have a chemical potential μ^e and μ^h respectively. $\Delta\mu_H = \mu^e - \mu^h$ is the chemical potential difference between electron and hole gases. A pathway is introduced for carrier extraction, where electrons and holes are extracted at specific energy levels E^e and E^h, and the energy extracted per electron-hole pair is $E_{ext} = E^e - E^h$. Such an extraction pathway provides a limited interaction between the outside world and the hot system that continues to be thermally insulated. In those conditions, a relation between the internal chemical potential $\Delta\mu_H$ and the output voltage V is related to the quasi-Fermi level splitting in the absorber $\Delta\mu_H$ according to the Ross and Nozik (1982) model:

$$qV = E_{ext}\left(1-\frac{T_C}{T_H}\right) + \Delta\mu_H\,\frac{T_C}{T_H} \quad (10)$$

where T_C is the lattice temperature and T_H is the carrier temperature.

Equation (9) is not sufficient to determine the current voltage characteristic because of the two unknowns $\Delta\mu_H$ and T_H. An additional equation describing the energy balance in the system is required. The absorbed and emitted energy current are simply obtained from the photon current expressions by multiplying the integrand by the energy E of the photons. The energy current extracted through the utilization pathway is the charge current J multiplied by the extracted energy per electron-hole pair E_{ext} (see Equation 11).

Combining Equations (9) and (11), the current is determined for a given value of E_G, E_{ext} and f. The voltage is then obtained from Equation (10). The current-voltage characteristic and the cell efficiency are obtained, with a predicted optimal limit of 66% under AM1.5 illumination and a band gap approaching zero.

In this model, particle conservation was assumed, which means that only radiative recombinations are considered, but also that Auger recombination and impact ionization are neglected. In 1997, Würfel (Würfel, 1997) proposed another approach where impact ionization is assumed to be dominant over all other recombination processes and faster than carrier extraction. In these conditions, the electrons and holes are at chemical equilibrium ($\Delta\mu_H$) and are described by a Fermi-Dirac distribution at a temperature $T_H > T_C$. The limit of efficiency in that case is 53% under non

Table 2. Comparison of limits of efficiency (η_{max}), optimal band gap ($E_{G\,opt}$), and carrier temperature in optimal operating conditions (T_H) for conventional single junction and different hot carrier models under unconcentrated ($\Omega_S = 6.8 \times 10^{-5}$) and fully concentrated ($\Omega_S = 2\pi$) 6000 K black body spectrum

Model	Ω_S	η_{max}	$E_{G\,opt}$	T_H
Conventional single junction	6.8×10^{-5} 2π	31% 41%	1.4 eV 1.1 eV	300 K 300 K
Particle conservation	6.8×10^{-5} 2π	66% 86%	0 eV 0 eV	3600 K 4200 K
Impact ionization	6.8×10^{-5} 2π	53%	0.9 eV	348 K
		85%	0 eV	2470 K

concentrated 6000 K black body illumination, and 85% under full concentration.

1.3. The Mechanisms of Carrier Thermalization

In the above determination of achievable efficiencies, it was stated that the electron-hole plasma was thermally insulated from the environment, which is not the case in practical conditions. The carriers thermalize with the environment mainly because of interactions with the lattice vibration modes. This process usually occurs in few picoseconds, which is much faster than the carrier extraction time in conventional cells. In order to allow a hot carrier population regime, the carriers have to be extracted before they thermalize, which means that the thermalization rate has to be controlled and reduced, but also that the extraction time should be shorter than the thermalization time (Neges, et al., 2006) (see Table 2).

1.3.1. Carrier-Carrier Scattering

Immediately after absorption, the photogenerated electron-hole plasma distribution is not an equilibrium Fermi-Dirac distribution. In the case of a laser exciting the carriers, for instance, electrons and holes are generated in a very narrow region in the energy-momentum space. This population, in chemical and thermal disequilibrium with the environment, is subject to different scattering processes that brings it to equilibrium.

1.3.1.1. Intraband Scattering

The intraband scattering comes from Coulomb elastic interaction between free carriers (Yu & Cardona, 2001; Ridley, 1999). Electron-electron, electron-hole, and hole-hole scattering occur with exchange of energy and momentum to more uniformly distribute the excess kinetic energy amongst carriers. Here the carriers stay in their respective energy band (no recombination), and this interaction is called intraband scattering.

The intraband scattering is a very fast two-particle process that depends quadratically on the carrier density. Its typical time scale is in the femtosecond range.

Considering this process, the free carrier population naturally evolves towards a Fermi-Dirac distribution defined by a temperature that is common to electrons and holes (thermal equilibrium), that can be much higher than the environment temperature, since no interaction with the lattice has occured. In the case of different time constant for electron-hole interaction and electron-electron or hole-hole interaction, different temperatures for electrons and holes can be obtained (Shah, et al., 1985).

1.3.1.2. Interband Scattering

The collisions between carriers can also result in electron-hole pair generation or recombination in non-radiative processes. Two cases are possible (see Figure 3)

- Auger Recombination: An electron and a hole recombine, and give their energy to a third free carrier (electron or hole).
- Impact Ionization: A high-energy free electron (or hole) gives a part of its energy to give rise to an exciton.

Here again the free carrier plasma total energy is conserved, but the number of particles is not. It is a three particle process, and therefore less probable than intraband scattering. A typical time constant is 100 *ps,* given in Table 1. It also depends on the band gap, and can become a very efficient process in small band gap materials. The exchange between electrons and holes results in an equilibration of electron and hole chemical potentials. In the limit of very fast Auger recombination and impact ionization, electrons and holes can be considered in chemical equilibrium with quasi Fermi level splitting approaching zero (Würfel, 1997, 2005).

1.3.2. Electron-Hole Plasma Dynamics

An insight into the dynamics of an electron-hole plasma after photoexcitation and subsequent relaxation in a semiconductor is obtained by considering the case of a semiconductor illuminated by a short, high intensity pulse of light with a narrow spectral range such that from a laser (Green, 2003).

The photogenerated plasma is subject to a succession of scattering event that brings the initial distribution in chemical and thermal disequilibrium to a fully equilibrated Fermi-Dirac population (see Figure 1). In the first femtoseconds following light absorption, a thermal Fermi-Dirac distribution is established thanks to carrier-carrier intraband scattering. This distribution is however still at thermal and chemical disequilibrium with the lattice. Then, interaction with the lattice occurs in a picosecond time scale resulting in the cooling of the carriers to reach thermal equilibrium with the environment. Finally, interaction with photons through radiative recombination occurs in a nanosecond time scale, with reduction of the quasi Fermi level splitting, until the initial equilibrated distribution is reached.

The carrier-cooling rate has been investigated using time resolved photoluminescence (Ulbrich, 1973; Tanaka, et al., 1980; Rosenwaks, et al., 1993; Ryan, et al., 1984). It was observed that the electron energy loss rate was reduced with an increase of the carrier density in the material, when the injection level was varied. Two explanations were proposed for such an effect:

- A screening of the photogenerated-electron-induced electric field by free carriers that weakens the electron-LO-phonons interaction (described in the next section) and reduces the phonon emission rate
- The formation of a "hot" LO phonon population that is thermally equilibrated with the electrons and not with the lattice. The absorption of phonon becomes as probable as the emission, and the energy loss process is blocked.

Only the second possibility was proven to be in quantitative agreement with experiments.

1.3.3. Electron/Hole-Phonon Interaction

1.3.3.1. General Case

The electron-hole plasma that is photogenerated is initially hot (electron/hole with energy far above/below the conduction/valence band edge) immediately after absorption. This excess kinetic energy is lost mainly by phonon emission that comes from interaction between the charge carriers and the ions of the lattice. This process brings the excited carrier population to thermal equilibrium with the lattice within a few picoseconds and can be detected by time resolved photoluminescence spectroscopy experiments (Ulbrich, 1973; Tanaka, et al., 1980; Rosenwaks, et al., 1993; Ryan, et al., 1984).

Figure 3. Schematic of Auger recombination (a) and impact ionization (b). In Auger recombination, the three carriers at initial time (1) end up in one carrier at final time (2) having all the energy. Impact ionization is the opposite process with one initial energetic electron generating an additional electron-hole pair.

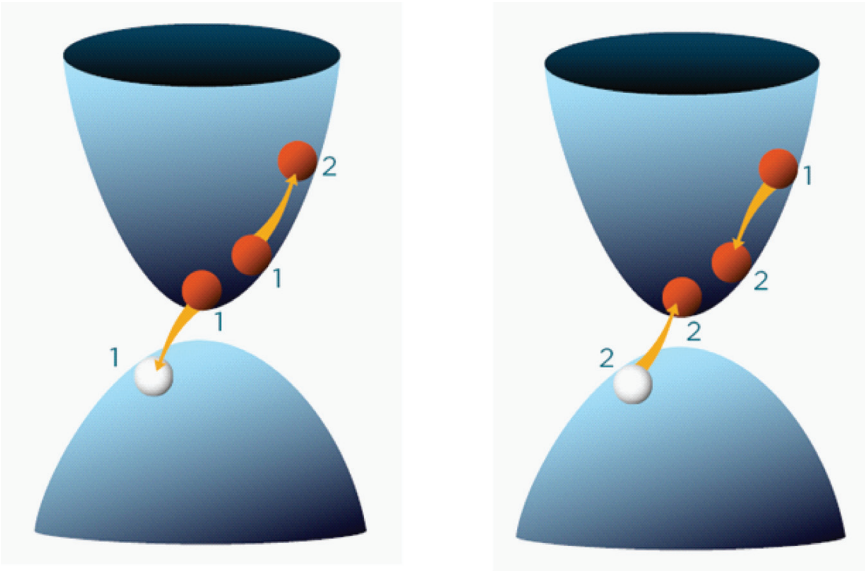

(a) Auger recombination (b) Impact ionization

The momentum conservation condition in a scattering event implies that carriers are coupled primarily to long wavelength (small wave vector) phonons. There are four types of zone center phonons in diamond- and zinc-blende-type semiconductors: Transverse Acoustic (TA), Longitudinal Acoustic (LA), Transverse Optical (TO), and Longitudinal Optical (LO) phonons, involving different types of interactions (Yu & Cardona, 2001; Ridley, 1999).

- **Deformation Potential Interaction:** In the case of a long wavelength acoustic phonon, the atomic displacement corresponds to a deformation of the crystal that changes the electronic energy levels. This change in electronic energies induced by static distortion of the lattice is described by a parameter called the deformation potential. Such lattice deformation affects all energy bands, so electrons and holes are coupled in the same way. It is independent of the phonon wavevector and is therefore a short-range interaction.
- **Piezoelectric Interaction:** An acoustic phonon is associated with an oscillating strain that can induce a macroscopic electric polarization field in noncentrosymmetric crystals. This phenomenon is known as the piezoelectric effect. The electron-acoustic-phonon interaction that results from this effect is a long wavelength interaction, thus a long-range interaction.
- **Electron-Optical-Phonon Deformation Potential Interaction:** A long wavelength optical phonon involves relative displacement of atoms that can be seen as microscopic distortion within the primitive unit cell. In non-polar semiconductor, such distortion affects the energy levels by changing bond length and bond angles. It is the

analog to the deformation potential interaction of acoustic phonons.

- **Fröhilch Interaction:** In a polar semiconductor, a longitudinal optical mode involves a uniform displacement of the charged atoms in the primitive cell, that creates an electromagnetic field that interacts wih the charge carriers. It is analog to the piezoelectric effect with acoustic phonons. It is a long range interaction, specific to polar semiconductors such as III-V compounds.

Interactions with small wavelength (zone edge) phonons are also possible through intervalley electron-phonon interaction. A zone edge phonon can scatter an electron from a band minimum at the zone center to a band minimum at a zone edge. For indirect semiconductors, such as silicon, this can play an important role in optical absorption. In addition, the high energy electrons in a hot carrier distribution can be scattered to band minima at zone edges even in direct semiconductors. It can be avoided with a well chosen material with X and L band minima high enough to prevent such intervalley scattering.

1.3.3.2. The Case of III-V Compounds

In the case of GaAs, which is an emblematic case of a polar semiconductor that has been widely studied, the intensities of the different interactions depend on the phonon occupation, and therefore on the lattice temperature. At low temperature (<40 K), electrons are not sufficiently energetic to excite LO phonons. Only acoustic phonons can be generated and carrier-phonon interactions are dominated by piezoelectric interaction and acoustic deformation potential (Pugnet, et al., 1981). For temperature exceeding ~40 K, the Fröhlich interaction becomes dominant and other types of interaction become negligible.

This means that at ambient temperature, the electron-hole plasma loses its energy mainly through emission of LO phonons. The coupled modes have a small wave vector because of the wave vector dependent Frölich matrix element. Thus, the carrier cooling process results in generation of a large number of zone center LO phonons, which can result in an unequilibrated LO phonon population (Shah, et al., 1985; Pötz & Kocevar, 1983).

The caracteristic time of this Fröhlich interaction is typically the picosecond. Experimental studies reported a time constant for electron-LO-phonon interaction of a few *ps* in GaAs (4 *ps* in [1], ≥1 *ps* in Green, 2003). A value of close to 1 *ps* (depending on the carrier temperature) was theoretically determined in Luque and Marti (2010) in GaAs at 300 K. The calculated value is slightly higher in GaSb (~2 *ps*).

1.4. Energy Selective Contacts for Carrier Extraction

In the paper by Ross and Nozik (1998) that first introduced the concept of hot carrier solar cells, the extraction of carriers was not treated in details. An extraction pathway was assumed that removes carriers at an energy U and returns them at another energy L where $U - L = E_{ext}$ is the energy extracted from the system per electron-hole pair. It was simply stipulated that the hot carrier system had to interact with the outside world in a very limited way to ensure its thermal insulation. Specific features of such extraction mechanisms, and its technological feasibility were not discussed.

The withdrawal of electron-hole pairs was first treated by Würfel (1997). Considering that the carrier thermalization in the electrodes could not be avoided, a cooling mechanism is necessary when extracting excited carriers towards the contacts, to bring them to the lattice temperature without entropy losses and prevent heat dissipation. He proposed a system of membranes allowing carrier transport in a narrow energy range $\delta E << kT$, that allows such isentropic cooling. In these membranes, all carriers have the same energy,

and no energy loss process can occur at constant carrier concentration. This leads to an isentropic cooling of electrons to the lattice temperature with production of chemical potential. The carrier kinetic energy (temperature) is converted into potential energy (chemical potential).

Extraction of electrons would then occur through a n-type membrane, and extraction of holes through a p-type membrane, the energy difference between extracted electrons and holes being the extracted energy E_{ext} mentionned in Ross and Nozik paper (see Figure 2). In the limit of discrete energy levels and infinite carrier mobility in the membrane, this system enables optimal energy extraction with minimal entropy losses. The output voltage V is then related to the quasi-Fermi level splitting $\Delta\mu_H$ in the absorber through (Würfel, 2005)

$$qV = E_{ext}\left(1 - \frac{T}{T_H}\right) + \Delta\mu_H \frac{T}{T_H} \qquad (12)$$

where T is the lattice temperature and T_H is the carrier temperature.

2. PHONONS ENGINEERING FOR HOT CARRIER SOLAR CELLS

The energy loss rate of a carrier - also known as the thermalization rate of the carrier - is determined by both the rate at which the carrier's energy is lost by optical-phonon emission and the rate at which the carrier gains energy from optical-phonon absorption. This latter rate can be significant in low dimensional quantum structures since the phonon emitted by energetic carriers can accumulate in these structures due to the phonon spatial confinement. The phonon densities in confined semiconductor are typically well above those of the equilibrium (called hot), phonons will be reabsorbed by the carriers. This phenomenon of reabsorption of hot phonons is referred to as the 'hot-phonon-bottleneck effect,' which is an important effect for many low dimensional semiconductor electronics performances (Othonos, 1998; Pötz & Kocevar, 1983; Van Driel, 1979). Moreover, according to the anharmonicity of crystals, the emitted LO phonons in semiconductors have lifetimes of typically a few picoseconds to about 10 *ps*. Afterwards, LO phonons decay to two or several lower energy phonons based on energy and momentum conservation. These decayed LO phonons are no longer available for absorption by carriers, in this case clearly, the lifetimes of the optical phonons are very important in determining the total energy loss rate for carriers (Campos, et al., 1992; Das Sarma, et al., 1992). It has been recognized that the Klemens (1966) channel, where one optical phonon decays into two Longitudinal Acoustic (LA) phonons, is the dominant mechanism for many semiconductors. However for some materials, like GaN and InN, where the large gaps in phonons dispersion inhibit the Klemens channel, Ridley (1999) proposed that the decay channel where LO phonon decays to a Transversal Optical (TO) phonon and an LA phonon will dominate.

In conventional electronics, faster carrier thermalization rate provides faster device performances. While for the new concept of the hot carrier photovoltaics, if we could collect hot carriers with high kinetic energy before their thermalization, thus the work per one absorbed photon (Ross, et al., 1982) could be significantly increased. Theoretical simulation on hot carrier solar cells show optimal efficiency of 86%, close to the maximum theoretical performance (Würfel, 1997, 2005; Nozik, et al., 1990). Experimentally, it has been found that the hot carrier cooling rate can be much slower in GaAs quantum wells compared (at the same photo-generated carrier density) to bulk GaAs at very high illumination intensities (Rosenwaks, 1993). Experimental and theoretical studies to achieve efficient hot carrier solar cell absorbers with slowed carrier cooling rate up to the nanosecond range and without applying high

illumination intensities are still under way. The phononic engineering by using low dimensional confined structures and mass difference effect have been used to design phononic structures as good hot carrier absorbers (Conibeer, et al., 2005, 2006, 2008; Guillemoles, et al., 2005). However even though the accurate description on the phonon dispersion and phonon lifetimes in bulk IV and III-V semiconductors have already been achieved by ab-initio density-functional perturbation theory calculations (Debernardi, 1998), the full theoretical description of the alloys and other quantum microstructures is still a challenge with most available calculation resources. In this case, calculations based on the empirical models, such as the shell model, bond-charge model, or elastic continuum model (Srivastava, 1990, 2008) have been widely used for more complex structures (Fu, et al., 1999; Ren, et al., 2004).

2.1 Phonons Modeling: Theoretical Method

Ab-initio DFT force constant method combined with mass approximation has been used to calculate the phonon modes in the nanostructures and will be presented in Section 2.2. The accuracy of this method is mainly dependent on the limitation of the mass approximation. For the low dimensional structures, the mass approximation, i.e., neglecting the dependence of the force constants upon composition, was used. The accuracy of such approximation has been tested (Giannozzi, et al., 1991) and found to be good for substitutional intermixing structures in binary semiconductors and elemental semiconductors. In the case of the Si-Ge system, the mass approximation is applicable because of their very similar crystal structures and lattice parameters, as it is shown in the following calculations results. Therefore, using this method, the phonon dispersion and phonon confinement in respectively 1, 2, or 3 dimensions in superlattices, Multiple Quantum Wires (MQWR), and Multiple Quantum Dots (MQD) are theoretically calculated.

2.1.1. Phonon Frequencies and Eigenstates: Bulk and Nanostructures

If the crystal is near its minimum energy, the potential energy function U_{harm} can be written as the sum of equilibrium total energy E_{equil} that depends on the equilibrium atomic positions, *R(lm)* and a quadratic term of the atomic displacements *u(lm)* (see Equation 13).

Here *u(lm)* or *u(jk)* denotes the displacement of atom *l* or *j* in the unit cell *m* or *k*, α and β are cartesian components, and $\varphi_{\alpha\beta}(lm, jk)$ is the force constant matrix, given by the double derivative $\partial^2 U / \partial u_\alpha(lm)\,\partial u_\beta(jk)$. The derivative of Equation (13) on displacement $u_\beta(jk)$ allows to get the forces $F_\alpha(jk)$

$$F_\alpha(jk) = \sum_{lm,\beta} \varphi_{\alpha\beta}(lm, jk)\, u_\beta(jk) \tag{14}$$

In order to calculate the full phonon dispersion curves, the dynamic matrix is built as Equation (15).

Here, M_l and M_j is the atomic mass of atom *l* or *j*. $\boldsymbol{q}$ is the wavevector in the first Brillouin zone. The dispersion curve can be obtained by solving the secular equation:

Equation 13.

$$U_{harm} = E_{equil} + 1/2 \sum_{lm,jk} \varphi_{\alpha\beta}(lm, jk)\, u_\alpha(lm)\, u_\beta(jk) \tag{13}$$

Equation 15.

$$D_{\alpha\beta}(lj,q)=\frac{1}{(M_l M_j)^{1/2}}\sum_m \varphi_{\alpha\beta}(lm,jk)\,u_\alpha(lm)\,e^{iq(R_{lm}-R_{jk})} \tag{15}$$

$$\left|D_{\alpha\beta}(lj,q)-\omega^2(j,q)\delta_{lj}\delta_{\alpha\beta}\right|=0 \tag{16}$$

The vibration amplitudes $u(jk)$ correspond to the eigen vectors $A_\alpha(j,q)$ of Equation (16):

$$u_\alpha(lj,q)=\frac{1}{M_j^{1/2}}A_\alpha(j,q)e^{iqRlj} \tag{17}$$

In this study, all the nanostructures are repeated periodically to form a 3D superlattice, so that periodic boundary conditions can be used. In equations 13 to 17, the unit cell is the supercell containing the repeated nanostructure motif.

The full force field derived from the supercell atoms displacements can be accurately calculated from *ab-initio* DFT method. Here, the so-called PHON code (Alfe, 1998) and full electron DFT calculations VASP code (Blöchl, 1994; Kresse, et al., 1993, 1996; Perdew, et al., 1992) have been used to get the full force constant matrix. By including all the calculated long-range force constants, the full phonon dispersion for the crystal can be reproduced very accurately, when compared with experimental values. Figure 4 shows the calculated force constant matrix for bulk Si and Ge versus the distance between two atoms. First, the forces between atoms dramatically decrease with distance. The interactions are dominated by the first neighbor atoms. The interactions between an atom with its second nearest neighbors are already very small. Therefore, a cut-off radius of 9.5 Å has been used for the force constant matrix elements calculations. Second, Si and Ge have the same crystal structure and a very close equilibrium crystal parameters: 5.43 Å and 5.65

Figure 4. First principle calculated force constants versus the interatomic distance in bulk Si and Ge

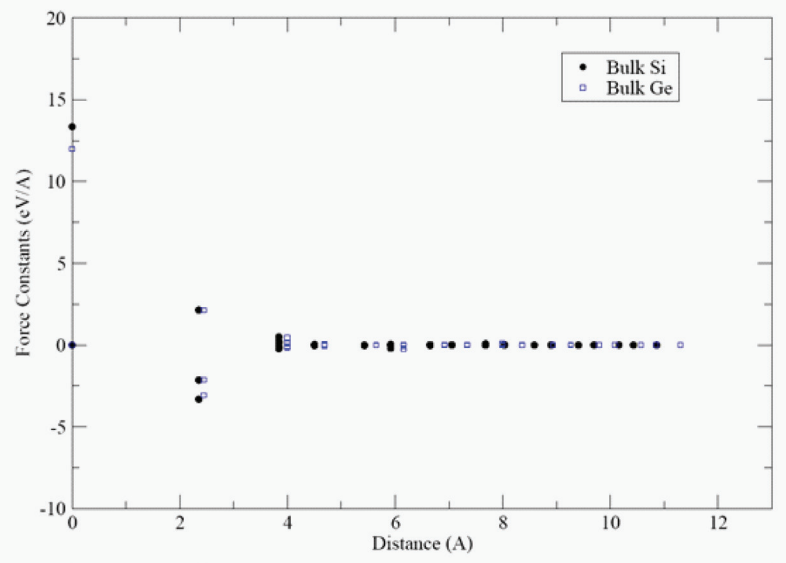

Å, respectively. The force constants show similar behavior in Si and Ge. In this case, for the low dimensional structures, a mass approximation has been used.

2.1.2. Methods for Analyzing the Eigenmodes

In the case of nanostructures with two different materials, there are several thousands of phonon eigenmodes in the reduced first Brillouin zone. Therefore, it is important to find an efficient way to distinguish and analyze their characters, in order to achieve phonon confinement. For this purpose, the confined phonon modes in each material, the common modes which propagate through the whole structure and the interface modes should all be identified and distinguished. For each phonon mode, the phonon energy distribution in space is described by a physical quantity known as the Vibration-Amplitude-Squared (VAS) (Ren, et al., 2004), which is related to the vibration amplitudes of the atoms in the lattice $A_\alpha(j,q) / M_j^{1/2}$ and proportional to the local vibrational energy that is used to investigate the microscopic details of these modes.

For each single mode, the sum of the VAS of all the atoms is normalized with the total number of atoms N per supercell:

$$\sum_j \left(A_\alpha(j,q) / M_j^{1/2} \right)^2 = N \qquad (18)$$

Note absolute values of VAS here have no physical meaning due to this simple normalization of vibrational amplitudes, only the relative values between atoms within one mode is meaningful.

Three kinds of calculated quantities derived from VAS are used in criteria to analyze the confined modes, common modes, and interface modes. First, the Average of VAS (AVAS) for each material in nanostructures is calculated. For each mode, the value of the difference between the two AVAS for the two materials reflects the intensity of the phonon confinement. Second, the Maximum Value of VAS (MVAS) for each material reflects the localization of the modes. If the MVAS is significantly higher than AVAS for a single mode, then this mode is highly localized, since it indicates that only certain atoms vibrate very stronger than most other atoms. Third, the maximum value of VAS at the interface (IMVAS) between two materials indicates whether the localized phonon mode is at the interface. If the peak of IMVAS and MVAS occur for the same mode, this indicates that this mode is a confined phonon mode at the interface. Here, the interface is defined as the atoms having at least one neighbor bonded with a different type of atom. Further, the quotient of the two AVAS quantities for the two materials is used to characterize each phonon mode. If divide of AVAS of material A over material B is higher than 0.5, then this mode is assigned to material B, while if it is lower than 2, the mode is assigned to material A. If it is between 0.5 to 2, the mode is assigned to common modes, which can propagate through both materials. Using this definition, the so-called Partial Phonon Density Of States (PPDOS) can be obtained.

Further, to describe the phonon propagating properties, the dependence of phonon group velocity (v_g) on phonon energy is investigated, for different configurations. The group velocity of phonons in the nanostructure is tightly related to the phonon space confinement. If the phonons are totally confined in a certain space, as it is expected for phonon modes in quantum dots or interface modes, then the group velocity will be zero. While for phonons propagating in the whole structure, the phonon velocity will be greatly influenced by the used nanostructures.

2.2. Phonon Modes and Phonon Confinement in Si,Ge Based Structures

Here, Si,Ge based nanostructures have been considered as a test system as the Si-Ge system

have been well studied and experimental data are available, allowing a comparison to the calculated properties. Besides, the mass approximation is applicable because of the very similar crystal structures and lattice parameters of Si and Ge, as it is shown in the following calculations results.

2.2.1. Phonons in Bulk Si, Ge, and SiGe Zinc Blend Structures

Phonon dispersion have been calculated for pure bulk Si and bulk Ge systems and Si-Ge zinc blend structure alloys within the mass approximation. Figure 5 shows the calculated phonon dispersion curves for bulk Si, Si-Ge zinc blend structure and bulk Ge, compared to experimental Si and Ge bulk material results. The ab-initio calculated Si phonon dispersion shows very good agreement with experimental values (Dolling, et al., 1963). The Ge and SiGe phonon dispersion are calculated using mass approximation from the ab initio computed Si force constants. The Ge phonon dispersion is also consistent with the experimental results (Nilsson, et al., 1971; Nelin, et al., 1972) only a slight deviation is found for a small range of high energy acoustic modes. The optical phonon frequencies for Si-Ge modes in the Si-Ge zinc blend structure

Figure 5. (a) Ab-initio calculated phonon dispersion of Si. (b) Phonon dispersion of Si-Ge alloys calculated with mass approximation. (c) Phonon dispersion of Ge calculated within the mass approximation. The dots in curve (a) and (c) are experimental results for Si (Dolling, et al., 1963), and Ge (Nilsson et al, 1971), respectively.

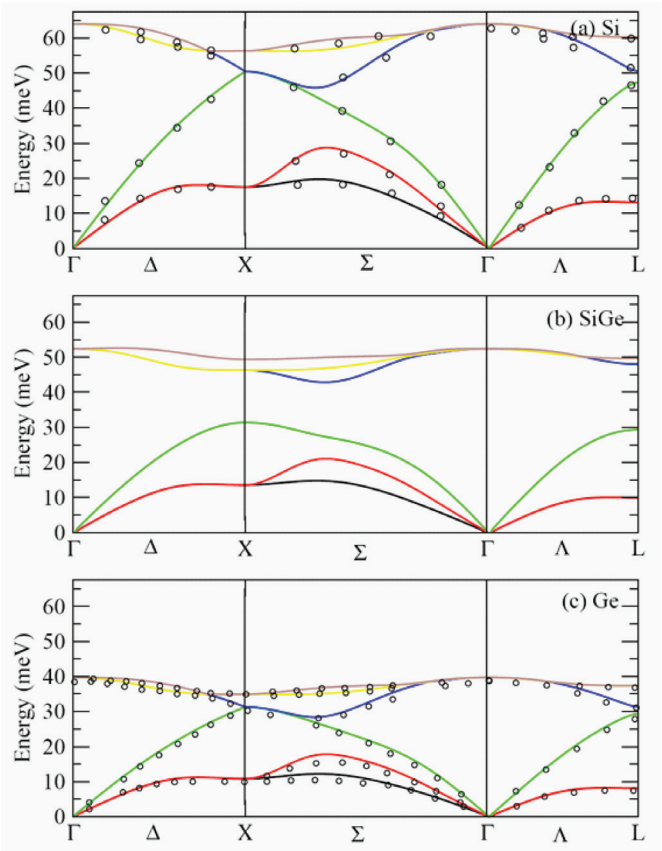

Figure 6. Phonon density of states for (a) SiGe zinc blend structure, (b) pure Ge, and (c) pure Si

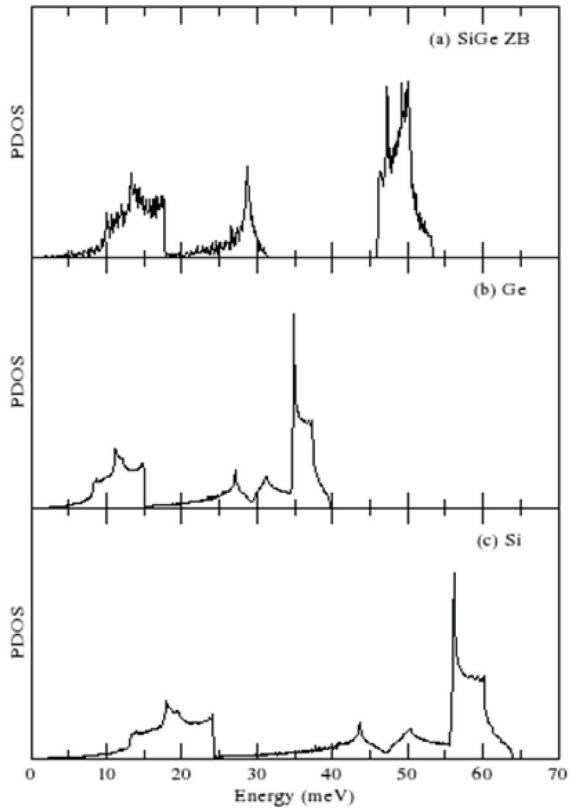

are also shown in the figure and are in agreement with the experimental data (Alonso, et al., 1989).

For nanostructures composed of two materials, phonons should be identified as bulk-like or interface-like modes, so it is very useful to calculate the phonon modes for bulk Si and Ge and SiGe alloys first, then in the next sections, a comparison will be made to phonon modes obtained in the Si,Ge based nanostructures. In Figure 6, the Phonon Density Of States (PDOS) is plotted for Si, Ge and zinc blend structure SiGe. As expected, because of the mass difference between Si and Ge, the acoustic and optical phonon density of states for SiGe shows obvious gap between 30-45 meV, also visible in the SiGe phonon dispersion curve in Figure 5.

Figure 7 shows the Average Vibration-Amplitude-Squared (AVAS) for Si-Ge zinc blend structure. If the number of AVAS is close to 1, this means both Si and Ge vibrate. While if the number of AVAS is equal to 0, this means the atoms do not vibrate for this mode. While when AVAS equals 2, this means that mainly this kind of atoms contributes in all the phonon vibration.

For bulk Si and bulk Ge, because the two atoms in primitive unit cell have the same mass and symmetry, they have the same vibration amplitude for all modes, the AVAS will always be 1 in both cases. Therefore, the AVAS for bulk Si and Ge are not shown here.

In the case of bulk SiGe, for low energy acoustic phonons, both Si and Ge atoms vibrate significantly, while for high-energy acoustic modes, vibrations of the heavy element Ge are more active than those of the light element Si. As for the optical phonons, the vibrations of Ge

Figure 7. Average vibration-amplitude-squared (AVAS) versus phonon energy for SiGe zinc-blend structure

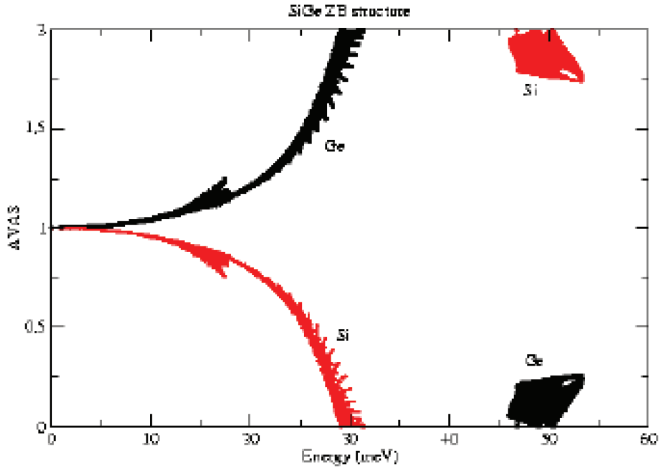

Figure 8. Calculated group velocity versus phonon energy for Si, SiGe zinc-blend structure and Ge along the Γ-X direction

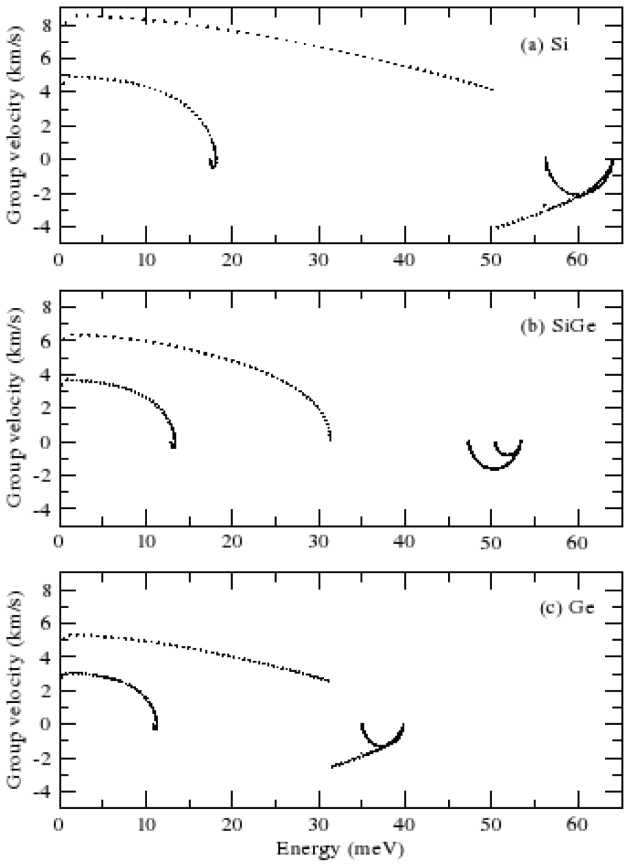

atoms seem to be damped; the main vibration energy comes from the Si atoms. This is confirmed also by the v_g calculation shown in Figure 8, for SiGe (b) where the group velocity for Ge modes equals 0 for energies higher than 40 meV (which corresponds to the higher Ge LO phonon mode energy), whereas for Si phonon modes, the group velocity increases in absolute value, meaning that Si atoms vibrate.

2.2.2. Phonon Modes and Phonon Confinement in SiGe Superlattices

First, we studied the SiGe superlattice structures using the same layer thickness for Si and Ge. In superlattice structures, it is expected that the spatial confinement along the z direction would induce phononic Bragg reflections, while in the plane of layers, the phonons can propagate freely. Therefore, the total PDOS including the three dimensions DOS did not show any gaps for all calculated structures. In Figure 9, the phonon density of states integrated only in the z direction is shown for different superlattice thicknesses. Gaps arising from the Bragg reflections at the mini-zone boundaries are clearly observed in the z direction PDOS. Furthermore, the phonon modes, especially the high energy optical phonons, show significant discrete energy level when the size of the superlattice is small enough (lower than around 8 nm in the case of Si:Ge superlattices).

The width of the minigaps arising from the phonon confinement along the confined *z* direction depends linearly on the size of the folded Brillouin zone, as shown in Figure 10.

To analyze the different types of atoms contribution, the Partial Phonon Densities Of States (PPDOS) along the z direction for a SiGe superlattice (with layer thicknesses of 13.6 nm) are plotted in Figure 11. The main phonon peaks for SiGe superlattice structures are identified from bulk Si and Ge modes. The common PDOS shows clearly that in the energy range of (0-10 meV), the acoustic phonons propagate through the Si and Ge layers, while in the range of (10-40 meV), fewer phonon modes are shared between both Si and Ge layers. For higher energy Si modes

Figure 9. Phonon density of states (PDOS) in the confined z direction for different thicknesses of SiGe superlattices

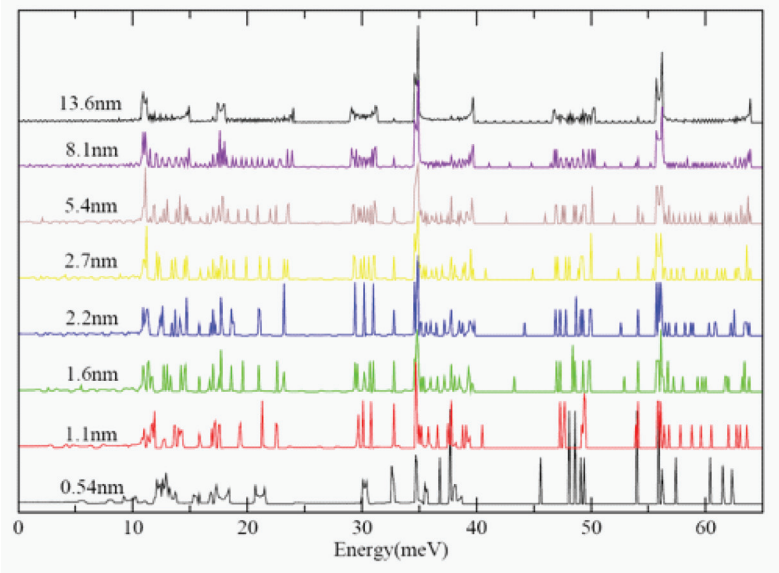

Figure 10. Minigaps in confined z-direction, the width of gaps depends linearly on the folded BZ edge

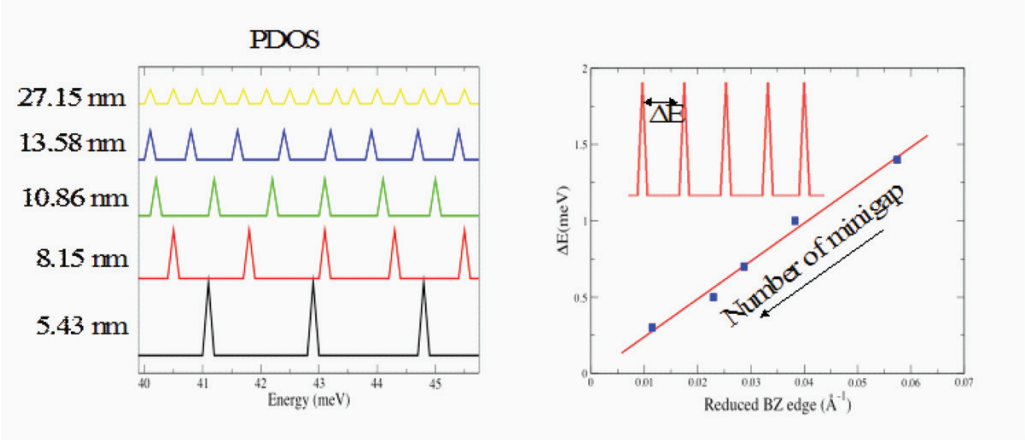

Figure 11. Calculated partial phonon density of states (PDOS) in Si layers or Ge layers, and common phonon density of states propagating in both Si and Ge layers for a 13.6nm Si:Ge superlattice. PDOS is only integrated in the confined z direction.

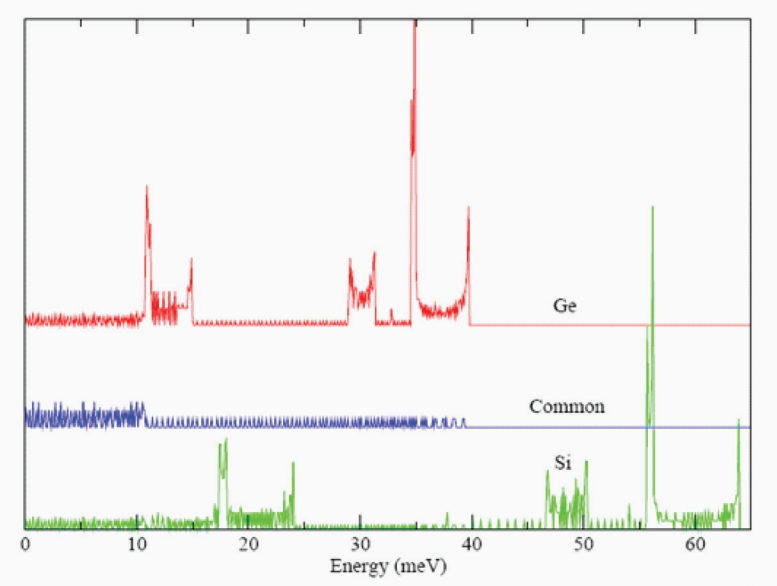

(larger than the maximum Ge phonon energy: 40 meV) are totally confined in the Si layers.

Next, as discussed in Section 2.1.2, different phonons derived quantities are calculated in order to analyze the phonon confinement. Figure 12a depicts the Average of Displacement Amplitude-Squared (AVAS) versus phonon energy within Si and Ge atoms. Clearly, for the low energy acoustic phonons (lower than 10 *meV*), both Si atoms and Ge atoms show significant amplitude of vibrations (AVAS = 1), which means that the phonon modes are not confined neither in Si or Ge lattice, and should be able to propagate freely through the lattice. The latter point is confirmed by the group velocities calculations shown in Figure 12b. In fact, the propagating acoustic modes are related to the nearly linear dispersion relations of acoustic phonons with k vector around Γ point, which usually prevent phonon confinement: for any system of two given materials, there are propagating acoustic modes in both materials within the range of frequencies from zero to the maximum phonon frequency of the elastically softer of the two of them (Yu & Cardona, 2001; Rytov, 1956). For higher phonon energies, we observe phonon modes with AVAS close to 2 or 0. This indicates that phonons in this range of frequencies are confined on either Si or Ge layers, which means there are Si-like modes for which the Ge layers act as barriers, and Ge-like modes, for which the Si layers act as barriers. However, for energies up to 40 meV (the highest energy for the bulk Ge optical modes), there are still phonon modes that could propagate through both Si and Ge layers. For energies higher than 40 meV and up to 64 meV (the highest energy for the bulk Si optical modes), all the phonon vibrations are constrained within the Si atoms.

This is consolidated by the calculations of the average amplitude of atoms vibrations, within a 13.6nm Si:Ge superlattice (Figure 13), for a selection of modes. These modes are either pure Ge modes, pure Si modes or common modes.

Figure 12. (a) Average vibration-amplitude-squared (AVAS) calculated for 8.1nm Si:Ge superlattices. The red solid dots represent AVAS within Si atoms, the black open dots represent AVAS within Ge atoms. (b) Phonon group velocity versus phonon energy with k vector of phonon modes along Γ -X directions.

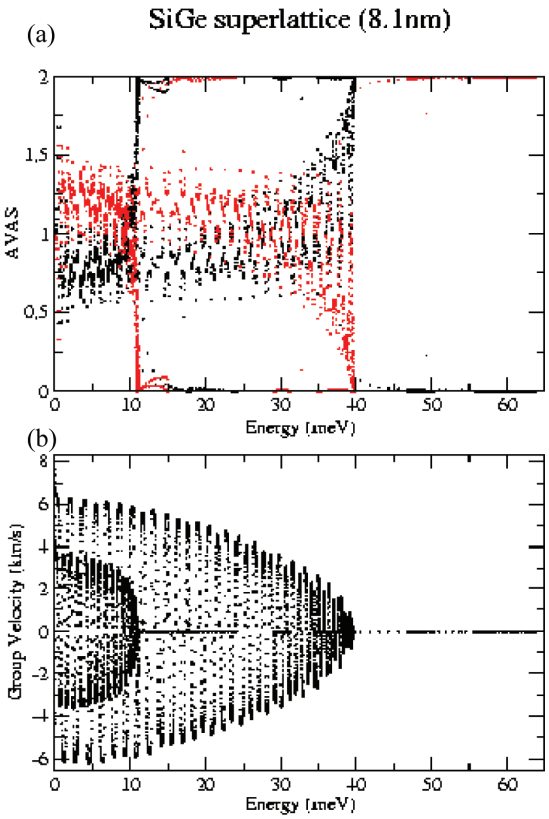

The central curve shown in Figure 13 is the Phonon Density Of States (PDOS), which is also the superposition of the PPDOS show in Figure 11. The six surrounding curves are the average amplitude vibrations of Si and Ge atoms along the z axis, for six different modes. The green line indicates the Si and Ge layers boundary (at z = 13.6 nm). Starting from top left to bottom right, the first curve, calculated for a 38.45meV mode which is a common mode for Si and Ge, shows that both Si and Ge atoms vibrate at this fre-

Figure 13. Typical PDOS of a 13.6 nm SiGe superlattice (central curve) and the plots of the average amplitude of vibration ofSi and Ge atoms along the z axis for a selection of modes with a periodicity of 27.2 nm. The green line indicates the Si and Ge layers boundary (at z=13.6 nm).

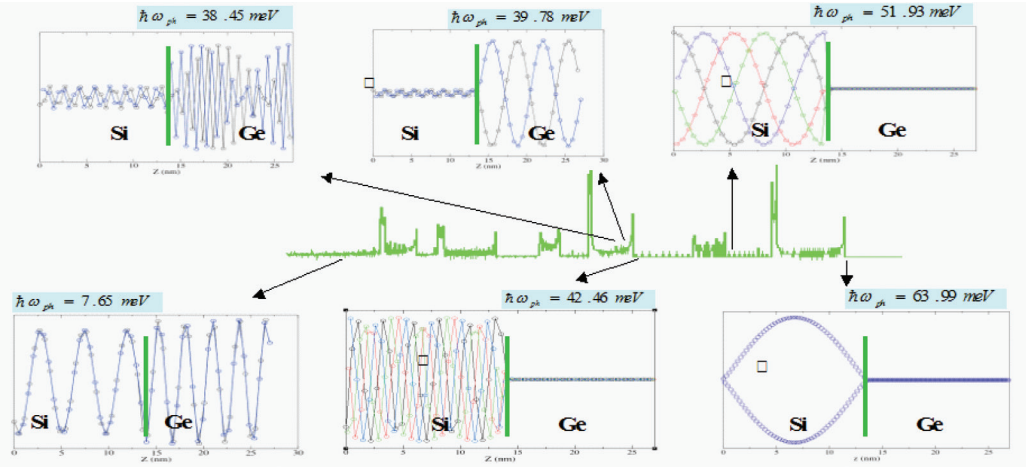

quency with a higher contribution of Ge atoms, according to the PPDOS plot (Figure 11). A similar behavior is obtained in the 4th curve at 7.65 meV, but with a more equilibrated contribution from Si and Ge atoms, in agreement with an equilibrated distribution of common modes, as shown in the PPDOS plot. The second one, at 39.78 meV, which corresponds to the Ge LO mode frequency, shows only vibrations from Ge atoms and a very limited average vibrations from Si atoms arising from the slight contribution of common modes in this range of frequency. In the third one obtained at 51.93 meV, one can see vibrations only arising from the Si atoms, common modes with Ge are limited to the Ge LO mode frequency. This is also obtained in the fifth curve at 42.46 meV, and in the sixth curve at 63.99 meV, corresponding to the Si LO mode frequency. In the latter case, the Si vibrations are more coherent, due to the only contribution of LO modes.

To investigate the phonon interface modes, the Maximum VAS (MVAS) and Interface Maximum VAS (IMVAS) are calculated for SiGe superlattice with layer thicknesses of 13.6 nm, and shown in Figure 14. As mentioned in Section 2.1.2, first, the peaks of MVAS correspond to the localized phonon modes. Second, the coincidence of the peaks of IMVAS with MVAS indicates that the localized phonon mode is confined at the interface between Si and Ge layers. From Figure 14, we obtain that the interface Si-Ge modes are present in a large range of energies and that for energies lower than around 40 meV (which is the maximum phonon energy for bulk Ge), both Si and Ge vibrations contribute to the energy of the interface modes. However for higher energies, the interface modes between Si and Ge layers are constrained mainly on the Si atoms.

Clearly, the high energy phonon modes in Si:Ge superlattice are confined and energy segregated in the confined z direction. In the next section, similar calculations on Si:Ge quantum wires superlattices are discussed. This is bound to be extremely important when analyzing the phonon-phonon interactions in such superlattices, as phonons overlap is factored in interactions ratios (Ridley, 1999).

2.2.3. Phonon Confinements in Si:Ge Multiple Quantum Wires

From the electronic point of view, the electronic gap in Si is larger than in Ge, so it would have been suitable to use Ge as the nanostructure

Figure 14. Calculated maximum VAS (MVAS) and maximum interface VAS (IMVAS) along the confined z direction for SiGe superlattice with layer thicknesses of 13.6 nm. The red solid dots are related to the Si modes, the black open dots are related to the Ge modes.

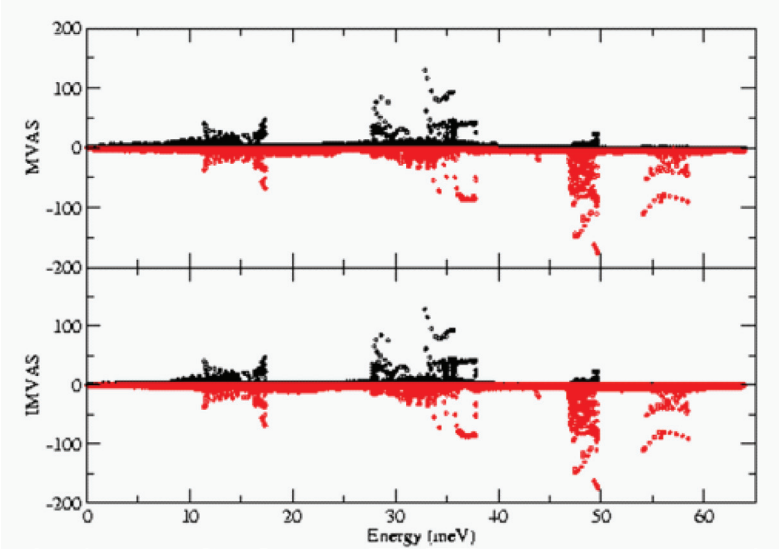

(wire or dot) material and Si as the matrix one. However as mentioned in the previous study, the heavy element of Ge behaves as a barrier to the Si phonon modes, whereas the Si cannot completely prohibit the Ge phonon modes propagation. Therefore, nanostructures of Si in Ge matrix are addressed here. In this section, simulation results of Si multiple quantum wires in Ge matrix (Si:Ge MQWR) are presented.

The Phonon Density Of States (PDOS) along the confined direction is presented in Figure 15 for a range of Si wire size from 3.51nm to 0.87nm, with a fixed Ge matrix size. The discrete energy levels in the density of states are visible for wire sizes lower than ~2nm, fir the Si modes > 40meV, as expected according to the mass contrast between the two elements.

Figure 16 shows the calculated AVAS (a), MVAS (b), and IMVAS (c) for Si:Ge MQWR. The phonon confinement in this structure are similar to that in SiGe superlattices. The acoustic phonons can propagate though the whole lattice, while optical phonon of both Si and Ge phonons show strong confinement in their own lattices. However, compared to the SiGe superlattice, the energy levels for interface modes in Si:Ge quantum wires are mostly located around 49 meV.

2.2.4. Phonon Confinement in Si:Ge Quantum Dots Superlattices

Here, we expect that the phonons will undergo three-dimension confinement in Quantum Dots (QD) structures. The full phonon gaps using quantum structures are expected to occur for the quantum dot material.

Figure 17 shows our calculated phonon density of states for ~2 nm Si quantum dots in Ge matrix. In fact, except when the size of quantum dots is small enough (less than 1 nm), the full density of states for Si:Ge quantum dots is quite similar to the one obtained with a mixture of PDOS of bulk Si and bulk Ge. There is no absolute gaps that are detected in the whole energy range. However, the optical phonon energy in QD shows very discrete nature due to the Bragg reflections at the mini-Brillouin zone in 3D (see Figure 18).

Figure 15. Phonon modes in Si-Ge quantum wires as a function of wire sizes

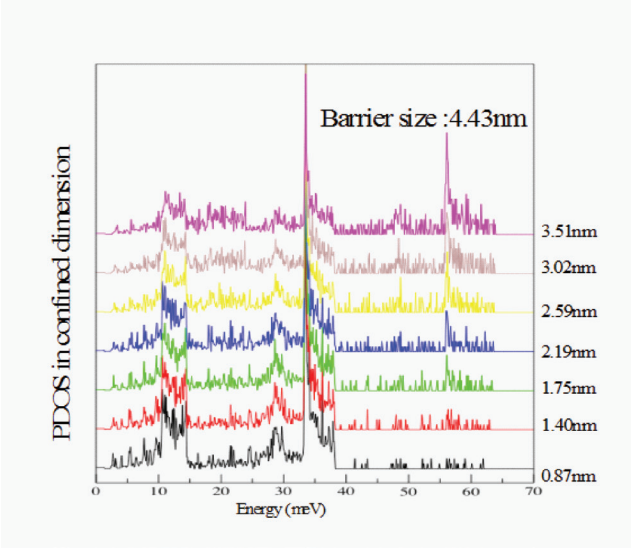

Figure 16. Calculated AVAS, MVAS, and IMVAS for Si:Ge MQWR. The red solid dots are related to the Si modes, the black open dots are related to the Ge modes.

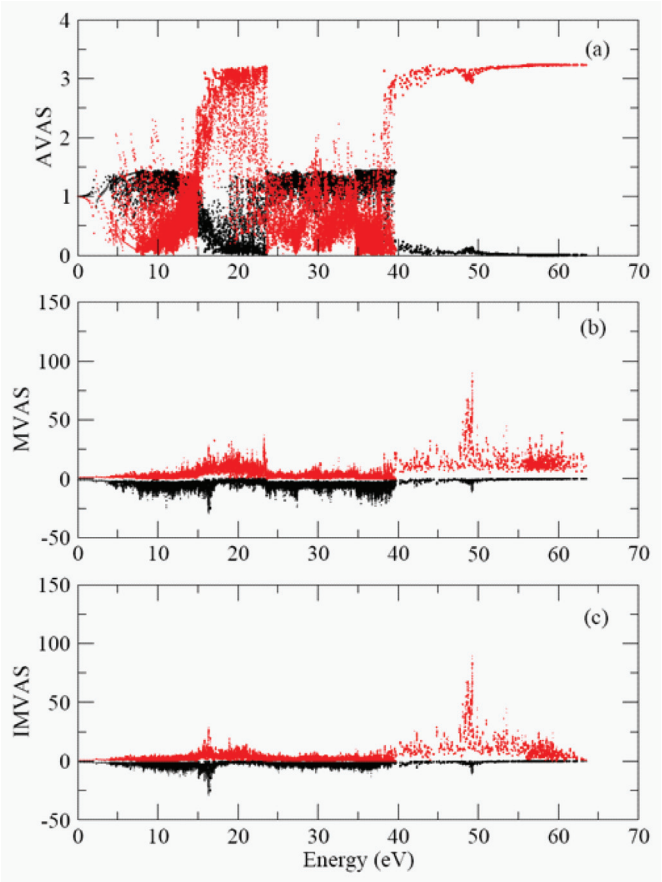

Figure 17. Calculated phonon density of states (PDOS) and partial PDOS (PPDOS) for a Si quantum dot in Ge matrix with a 2nm diameter

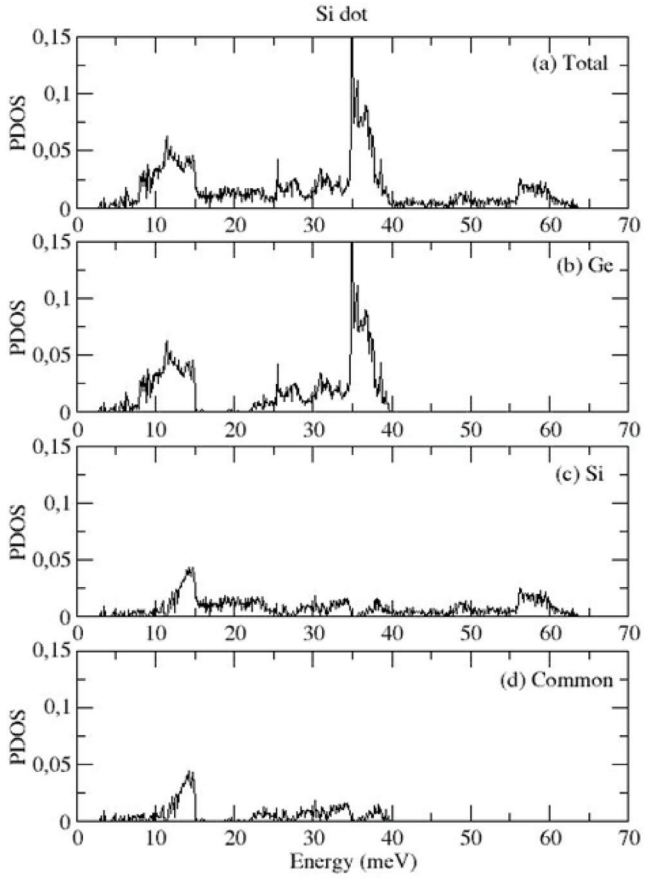

However, this minigaps contribution to the phonon decay and electron-phonon interaction has to be studied further. The characters of phonon confinements, and interface modes for Si:Ge MQD are very similar to the ones obtained with the Si:Ge MQWR (see Figure 19).

2.3. Discussion and Conclusion

Thermal processes, linked to the phonon dynamics, need a good microscopic description in order to be understood. This is required to understand processes in semiconductors for photovoltaics or for applications in thermoelectricity for instance. In both cases, phonon propagation and electron phonon coupling are of relevance.

The need for an accurate description is especially true in nanostructured materials where our conventional view in reciprocal space can be challenged. Phonon propagation and phonon interaction (e.g. with electrons) are altered by the important change in the symmetry properties of the material. In ordinary materials, having a relatively small number of atoms per unit cell, dispersion curves in reciprocal space hold much of the information about the phonon dynamics.

Figure 18. Calculated phonon density of states (PDOS) for a Si dot in Ge matrix (matrix size=4.3nm), for two different dot sizes(1.3 and 2.1nm). Minigaps near the Si LO mode energy are visible in the insets are more significant in the case of the 1.3nm diameter dot.

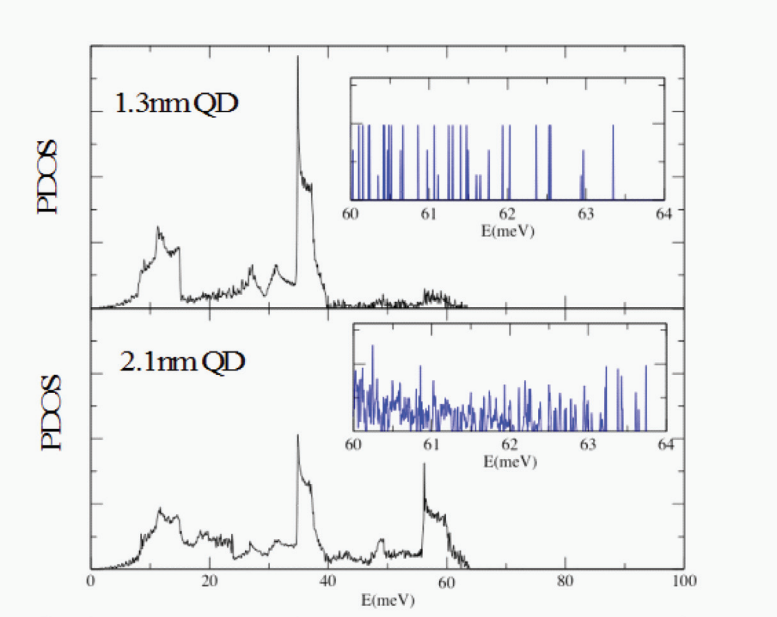

In nanostructures, Brillouin zones are small; therefore, quasi impulsion is not an appropriate quantum number. One has to resort to different tools: here we have used ab initio methods in order to get a precise description of the phonon modes in nanostructures.

First, our first-principle phonon calculation methods showed a good accuracy to treat the phonon spectra of dimension-confined nanostructures. The propagating folded acoustic phonons and highly confined discrete optical phonons in nanostructures were described well, as in other models. However, with our model a good description was obtained for all modes over the full Brillouin zone. The interface modes constrained in the interface between two materials were also accurately calculated and identified. In this study, Si/Ge superlattices, multiple quantum wires, multiple quantum dots were calculated. The methods described here showed how the dispersion curves are altered at the Brillouin zone edges, leading to phonon gaps, and how these phonon gaps depend on the size of nanostructuration. These methods can be applied to other well studied quantum structures, like GaAs/AlAs nanostructures.

Nevertheless, this study could describe the discrete nature of phonon energy levels in confined directions, with minigaps found in 1 to 3 dimensions in quantum superlattices, quantum wires, and quantum dots respectively.

Moreover, the mass contrast is indeed a key factor to determine the phonon confinement in quantum structures, the phonons of light elements with frequencies higher than the maximum frequency (LO) of heavy elements being confined in their matrix. However, the low frequency acoustic phonons can propagate through the quantum structure, as expected from acoustic macroscopic models.

The improved description of the phonon dynamics in nanostructures is instrumental in answering questions on hot carrier cells such as the mass contrast effect on the phonon confinement in quantum structures; the minigaps effect

Figure 19. Calculated AVAS, MVAS, and IMVAS for Si:Ge MQD. The red solid dots are related to the Si modes, the black open dots are related to the Ge modes.

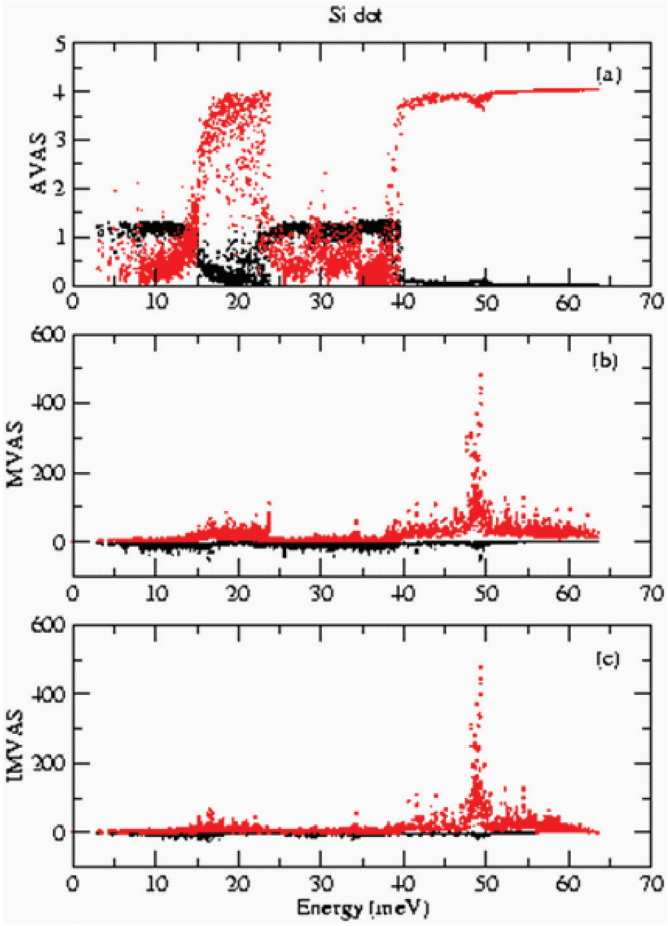

on the phonon decay dynamics and the phonon lifetimes in nanostructures, compared to their bulk parentage; the possibility to increase significantly the number of LO phonons close to the Brillouin zone center and to favor LO phonons reabsorption by electrons in order to slow down the electrons cooling.

Applications to thermoelectric devices also follow directly from above simulation as phonon propagation can be readily obtained from group velocities. As concerned to the application on the hot-carrier solar cells, accurate phonon dispersion in confined structures have been obtained. We observed obvious phononic gaps for optical phonon branches, however the size (small than a few meV) and position of gaps are sensitively related to folded Bloch k wavevectors, it seems hard to control and manipulate the gaps to block the Klemens channels. However the optical phonon confinement and discrete nature of phonon energy levels effect on the phonon-electron interaction and phonon-phonon scattering are not clearly understood yet. The models including full phonon dispersion and confinements in quantum structures are needed to fully understand hot carrier relaxation processes in the confined structures.

REFERENCES

Alfè, D. (1998). *Chianti.* Retrieved from http://chianti.geol.ucl.ac.uk/ dario

Alonso, M. I., & Winer, K. (1989). Raman spectra of *c*-$Si_{1-x}Ge_x$ alloys. *Physical Review B: Condensed Matter and Materials Physics*, *39*, 10056–10062. doi:10.1103/PhysRevB.39.10056

Blöchl, P. E. (1994). Projector augmented-wave method. *Physical Review B: Condensed Matter and Materials Physics*, *50*, 17953. doi:10.1103/PhysRevB.50.17953

Campos, V. B., Das, S. S., & Stroscio, M. A. (1992). Phonon-confinement effect on electron energy loss in one-dimensional quantum wires. *Physical Review B: Condensed Matter and Materials Physics*, *46*, 3849. doi:10.1103/PhysRevB.46.3849

Conibeer, G. J., et al. (2006). Paper. In *Proceedings of 21st Euro PV SEC*. Dresden, Germany, (p. 47). PV SEC.

Conibeer, G. J., Ekins-Daukes, N., Guillemoles, J. G., & Green, M. A. (2005). Paper. In *Proceedings of the 20th European PV Conference*, (p. 35). Barcelona, Spain: EU PV.

Conibeer, G. J., König, D., Green, M. A., & Cuillemoles, J. F. (2008). Slowing of carrier cooling in hot carrier solar cells. *Thin Solid Films*, *516*, 6948. doi:10.1016/j.tsf.2007.12.102

Debernardi, A. (1998). Phonon linewidth in III-V semiconductors from density-functional perturbation theory. *Physical Review B: Condensed Matter and Materials Physics*, *57*(12), 847.

Dolling, G. (1963). Paper. In *Proceedings of the Symposium on Inelastic Scattering Neutrons in Solids and Liquids*, (vol 2), (p. 37). Vienna, Austria: IAEA.

Fu, H. X., Ozolins, V., & Zunger, A. (1999). Phonons in GaP quantum dots. *Physical Review B: Condensed Matter and Materials Physics*, *59*, 2881. doi:10.1103/PhysRevB.59.2881

Giannozzi, P., De Gironcoli, S., Pavone, P., & Baroni, S. (1991). Ab initio calculation of phonon dispersions in semiconductors. *Physical Review B: Condensed Matter and Materials Physics*, *43*, 7231. doi:10.1103/PhysRevB.43.7231

Green, M. A. (2003). *Third generation photovoltaics - Advanced solar energy conversion*. London, UK: Springer.

Guillemoles, J. F., Conibeer, G. J., & Green, M. (2005). Paper. In *Proceedings of the 15th PV SEC*. (p. 375). Shanghai, China: PV SEC.

Klemens, P. G. (1966). Anharmonic decay of optical phonons. *Physical Review*, *148*, 845. doi:10.1103/PhysRev.148.845

Kresse, G., & Furthmüller, J. (1996). Efficient iterative schemes for ab initio total-energy calculations using a plane-wave basis set. *Physical Review B: Condensed Matter and Materials Physics*, *54*, 11169. doi:10.1103/PhysRevB.54.11169

Kresse, G., & Hafner, J. (1993). Ab initio molecular dynamics for liquid metals. *Physical Review B: Condensed Matter and Materials Physics*, *47*, 558. doi:10.1103/PhysRevB.47.558

Luque, A., & Martí, A. (2010). Electron-phonon energy transfer in hot-carrier solar cells. *Solar Energy Materials and Solar Cells*, *94*, 287–296. doi:10.1016/j.solmat.2009.10.001

Neges, M., Schwarzburg, K., & Willig, F. (2006). Monte Carlo simulation of energy loss and collection of hot charge carriers, first step towards a more realistic hot-carrier solar energy converter. *Solar Energy Materials and Solar Cells*, *90*(14), 2107–2128. doi:10.1016/j.solmat.2006.02.008

Nelin, G., & Nilsson, G. (1972). Weak absorption tails in amorphous semiconductors. *Physical Review B: Condensed Matter and Materials Physics*, *5*, 3151. doi:10.1103/PhysRevB.5.3151

Nilsson, G., & Nelin, G. (1971). Paper. *Physical Review B: Condensed Matter and Materials Physics*, *3*, 364. doi:10.1103/PhysRevB.3.364

Nozik, A. J., Parsons, C. A., Dunlary, D. J., Keyes, B. M., & Ahrenhiel, R. K. (1990). Dependence of hot carrier luminescence on barrier thickness in GaAs/AlGaAs superlattices and multiple quantum wells. *Solid State Communications*, *75*, 247. doi:10.1016/0038-1098(90)90900-V

Othonos, A. (1998). Probing ultrafast carrier and phonon dynamics in semiconductors. *Applied Physics Reviews*, *83*, 1789. doi:10.1063/1.367411

Perdew, J. P., & Wang, Y. (1992). Accurate and simple analytic representation of the electron-gas correlation energy. *Physical Review B: Condensed Matter and Materials Physics*, *45*, 13244. doi:10.1103/PhysRevB.45.13244

Pötz, W., & Kocevar, P. (1983). Electronic power transfer in pulsed laser excitation of polar semiconductors. *Physical Review B: Condensed Matter and Materials Physics*, *28*, 7040. doi:10.1103/PhysRevB.28.7040

Pugnet, M., Collet, J., & Cornet, A. (1981). Cooling of hot electron-hole plasmas in the presence of screened electron-phonon interactions. *Solid State Communications*, *38*, 531–536. doi:10.1016/0038-1098(81)90431-2

Ren, S. F., Cheng, W., & Yu, P. Y. (2004). Microscopic investigation of phonon modes in SiGe alloy nanocrystals. *Physical Review B: Condensed Matter and Materials Physics*, *69*, 235327. doi:10.1103/PhysRevB.69.235327

Ridley, B. K. (1999). *Quantum processes in semiconductors*. Oxford, UK: Oxford University Press.

Rosenwaks, Y., Hanna, M. C., Levi, D. H., Szmyd, D. M., Ahrenkiel, R. K., & Nozik, A. J. (1993). Hot-carrier cooling in GaAs: Quantum wells vs bulk. *Physical Review B: Condensed Matter and Materials Physics*, *48*, 14675. doi:10.1103/PhysRevB.48.14675

Ross, R. T., & Nozik, A. J. (1982). Efficiency of hot-carrier solar energy converters. *Journal of Applied Physics*, *53*, 3813. doi:10.1063/1.331124

Ryan, J. F., Taylor, R. A., Tuberfield, A. J., Maciel, A., Worlock, J. M., Gossard, A. C., & Wiegmann, W. (1984). Time-resolved photoluminescence of two-dimensional hot carriers in GaAs-AlGaAs heterostructures. *Physical Review Letters*, *53*(19), 1841–1844. doi:10.1103/PhysRevLett.53.1841

Rytov, S. M. (1956). Acoustical properties of a thinly laminated medium. *Soviet Physics: Acoustics*, *2*, 69.

Sarma, S., Das, S. M. A., & Kim, K. W. (1992). Paper. *Semiconductor Science and Technology*, *60*(7).

Shah, J., Pinczuk, P., Gossard, A. C., & Wiegmann, W. (1985). Energy-loss rates for hot electron and holes in GaAs quantum wells. *Physical Review Letters*, *18*, 2045. doi:10.1103/PhysRevLett.54.2045

Shockley, W., & Queisser, H. J. (1961). Detailed balance limit of efficiency of p-n junction solar cells. *Journal of Applied Physics*, *32*, 510. doi:10.1063/1.1736034

Srivastava, G. P. (1990). *The physics of phonons*. Bristol, UK: Adam Hilger.

Srivastava, G. P. (2008). Paper. *Physical Review B: Condensed Matter and Materials Physics*, *77*, 155–205.

Tanaka, S., Kobayashi, H., Saito, H., & Shionoya, S. (1980). Luminescence of high density electron-hole plasma in GaAs. *Journal of the Physical Society of Japan*, *49*, 1051. doi:10.1143/JPSJ.49.1051

Trivich, D., & Flinn, P. A. (1955). Maximum efficiency of solar energy conversion by quantum process. *Solar Energy Research*, 143-147.

Ulbrich, R. (1973). Energy relaxation of photoexcited hot electrons in GaAs. *Physical Review B: Condensed Matter and Materials Physics*, *8*, 5719. doi:10.1103/PhysRevB.8.5719

Van Driel, H. M. (1979). Influence of hot phonons on energy relaxation of high-density carriers in germanium. *Physical Review B: Condensed Matter and Materials Physics*, *19*, 5928. doi:10.1103/PhysRevB.19.5928

Würfel, P. (1982). The chemical potential of radiation. *Journal of Physics. C. Solid State Physics*, *15*, 3967–3985. doi:10.1088/0022-3719/15/18/012

Würfel, P. (1997). Solar energy conversion with hot electrons from impact ionization. *Solar Energy Materials and Solar Cells*, *46*, 43. doi:10.1016/S0927-0248(96)00092-X

Würfel, P., Brown, A. S., Humphrey, T. E., & Green, M. A. (2005). Particle conservation in the hot-carrier solar cell. *Progress in Photovoltaics: Research and Applications*, *13*, 277. doi:10.1002/pip.584

Yu, P. Y., & Cardona, M. (2001). *Fundamentals of semiconductors*. Berlin, Germany: Springer-Verlag.

Section 5

Luminescent Solar Concentrators:

Prospects and Strategies for Advanced Solar Cells

Chapter 13
The Luminescent Solar Concentrator:
Advances, Optimization, and Outlook

Rahul Bose
Imperial College London, UK

Keith W. J. Barnham
Imperial College London, UK

Amanda J. Chatten
Imperial College London, UK

ABSTRACT

Luminescent Solar Concentrators (LSCs) offer a way of making Photovoltaic (PV) systems more attractive through reduced energy costs, the possibility of application in cloudy regions, and improved building integration. LSCs collect light over a large area and concentrate it, both spatially and spectrally, onto solar cells at the edges of the device, such that the total cell area required to generate a specific power is reduced. Since the solar cells constitute the more expensive component in the system, this leads to cost reductions. Unlike conventional geometric concentrators, LSCs do not require solar tracking and can collect diffuse as well as direct sunlight. The current research challenges lie in increasing the efficiency of the LSC and extending it to larger areas to make it commercially viable. In this chapter, the authors outline the mode of operation of the LSC, with particular regard to cost considerations and device geometry. They then review recent approaches aiming to increase device efficiency and, finally, introduce their versatile raytrace approach to modeling the LSC. The model is utilised here to investigate tapered LSC designs and rationalise the optimal geometry and configuration for planar LSCs.

DOI: 10.4018/978-1-4666-1927-2.ch013

1. INTRODUCTION

In light of the world's ever-growing energy demands (OECD, 2009) and the urge to reduce greenhouse gases, the development of sustainable energy is a pressing task for science. As a renewable energy technology Photovoltaics (PV) is likely to play a key role in our future energy mix (MacKay, 2009). Indeed currently about a quarter of the world's population still lives without electricity (World Bank, 2008). Climate change and energy independence aside, renewable energy seems the only long term, sustainable solution to the world's growing energy need and diminishing resources.

The point at which electricity from renewable sources is cost-competitive with conventional electricity from the grid is called grid-parity. Grid-parity has not yet been achieved for PV, but, since solar irradiation does not vary notably from year to year, technological development and economies of scale continuously drive the efficiency of PV up and the cost down. Given that two thirds of conventional electricity is globally generated by fossil fuels (IEA, 2009) with obviously finite supplies we can expect a rise in the cost of conventional electricity that will ultimately favour renewable sources. The aim of the Luminescent Solar Concentrator (LSC) is to accelerate the process of making PV more cost-effective, by boosting the power conversion of solar cells with the use of a relatively inexpensive, versatile concentrator. It is a planar low-concentration device employing luminescent centres such as dyes or nanocrystals and is particularly well suited to Building Integrated Photovoltaics (BIPV).

The LSC can collect direct as well as indirect diffuse light and, unlike geometrical concentrators, does not require tracking. Costing more than the solar cells, tracking is the highest single expenditure in conventional concentrator PV systems (Extance, 2010). The non-tracking approach of LSCs alleviates space, cost, and maintenance requirements, allowing for a different range of applications. The LSC outputs a narrow, red-shifted spectrum, which can be matched to the PV cell absorption. This way the light coupled into the cell is converted more efficiently. Because thermalisation happens in the LSC, unwanted heating of the cell can be avoided. The LSC is versatile in that they can be designed semi-transparent or coloured and also flexible. By reducing the amount of solar cells required, the LSC could help make photovoltaic energy generation more viable.

In the next section, the operation of the LSC is explained in terms of its light-capture and waveguiding properties. Efficiency limits and cost considerations are detailed and alternative geometries are reviewed.

2. PRINCIPLES OF THE LSC

There are two main principles that govern the luminescent solar concentrator: light capture and waveguiding. A typical LSC as depicted in Figure 1 consists of a transparent plate doped with luminescent centres. Incident light is absorbed by these centres and re-radiated. Due to the difference in refractive index between the plate and the surrounding air a large fraction of the luminescent radiation is trapped within the plate by Total Internal Reflection (TIR). The trapped luminescence is wave-guided to the plate edges where it is converted by PV cells. Ideally, the output is in a narrow spectrum that is matched to the cells. The geometric ratio between the top surface and the edges leads to the concentration.

2.1. Light Capture

Light impinging on the surface of an LSC is either reflected or transmitted into the LSC. The LSC is a dielectric waveguide and as such has a refractive index n that is higher than that of its surrounding, i.e. higher than 1 in the case of air. Light is therefore refracted into the LSC at an angle closer to the surface normal according to Snell's

Figure 1. A schematic representation of the luminescent solar concentrator (LSC). Incident light from the top is absorbed by a luminescent centre and re-emitted. An escaping ray, a ray emitted toward an edge and a ray trapped by total internal reflection (TIR) are depicted. Solar cells on the edges collect the emission.

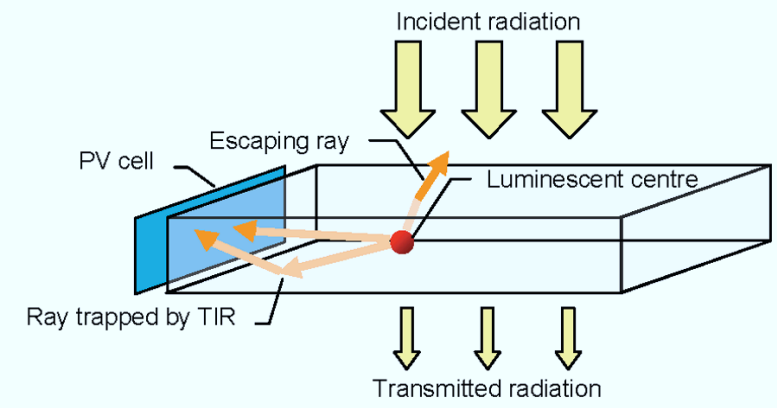

law. The refractive index change at the interface to the LSC also gives rise to Fresnel reflection described by the Fresnel equations. Variations of the refractive index with wavelength can generally be disregarded in the case of the LSC. For practical application of the LSC it is also safe to assume that the incident light is unpolarised, in which case the average of the two reflection coefficients for *s* and *p* polarised light is taken (see Figure 2). A typical LSC made of glass or poly(methyl methacrylate) (PMMA) has a refractive index of:1.5, which yields an average coefficient of reflection of:4% for light at normal incidence.

The light capture efficiency η_{capture} is defined as the ratio of photons absorbed (by luminescent centres) to incident photons. Figure 2 shows that reflection is only dominant at large angles above:60°, which indicates that reflection has a small effect on the light capture efficiency.

Neglecting scattering losses due to surface roughness, absorption in the host material and multiple Fresnel reflections from the back and front interfaces, the capture efficiency can be written in terms of the internal spectral absorptance, $A_{\lambda,\text{internal}} = 1 - e^{-\alpha(\lambda)z(\theta)}$ (where α is the absorption coefficient and z the thickness of material, itself dependent on the angle of incidence, θ), the spectral reflectance for reflection from the front surface, R_λ, and the spectral photon flux Φ_λ (see Equation 1).

The capture efficiency is sensitive to the spectrum of the incident irradiation, which, in terms of the LSC, is an external quantity.

2.2. Waveguiding

In contrast to the light capture, the waveguiding is a purely internal property of the LSC. The waveguiding efficiency $\eta_{\text{waveguide}}$ is defined as

Equation 1.

$$\eta_{\text{optical}} = \frac{\int_\theta \int_\lambda \Phi_\lambda(\lambda,\theta)\, A_{\lambda,\text{internal}}(\lambda,\theta)\left[1 - R_\lambda(\theta)\right] d\lambda d\theta}{\int_\lambda \Phi_\lambda(\lambda,\theta)\, d\lambda} \qquad (1)$$

Figure 2. The Fresnel reflection coefficients for unpolarised light incident from air onto media with refractive indices of 1.5 and 2.0

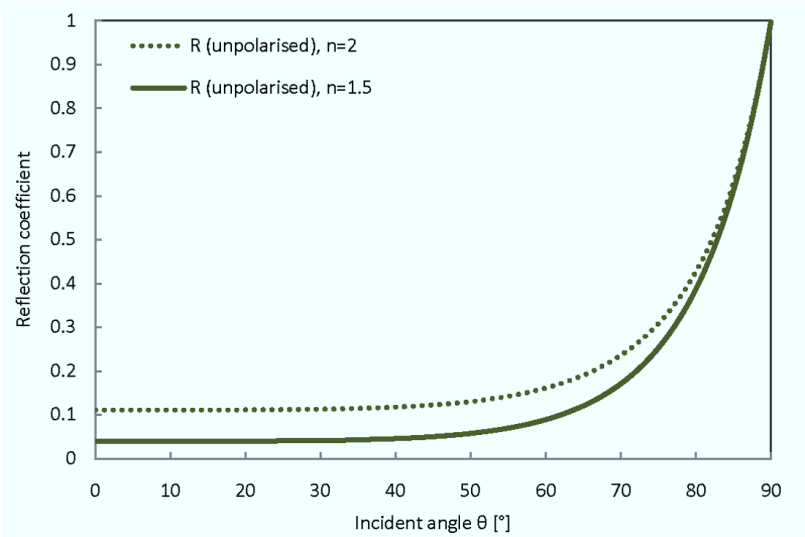

the ratio of photons guided to the LSC edges to photons absorbed. In order to trap light in a waveguide, a change in its direction is required since light that enters a planar waveguide will also leave it due to the symmetry of light paths. The LSC achieves this change in direction through absorption and subsequent emission of light by luminescent centres from within the waveguide. In the case of isotropic luminescence, the fraction of light lost in a single emission step through escape cones (at angles less than the critical angle for TIR, $\theta_c = \arcsin(n_1/n_2)$ for a ray travelling from a medium of refractive n_2 to n_1, with $n_2 > n_1$), η_{escape}, is twice the ratio of the solid angle of the escape cone Ω_{escape} to the solid angle of the sphere (4π) in order to account for losses from both the top and bottom surfaces. Consequently, the single emission trapping efficiency is $\eta_{trap} = 1 - \eta_{escape} = \cos\theta_c$ which may be rewritten as:

$$\eta_{trap} = \sqrt{1 - \sin^2 \theta_c} = \sqrt{1 - \frac{n_1^2}{n_2^2}}. \qquad (2)$$

Even though in real systems TIR is never perfect, reflectances of 99.99% are not uncommon, and thus for all practical purposes TIR in the LSC can be treated as being perfect. The assumption of isotropic luminescence is also a simplification since the electronic transition dipole of a luminescent centre dictates the angular dependence of both absorption and emission. Therefore the emission from an ensemble of isotropically oriented dyes will be directional to a degree dependent on the angle (or angular distribution) of the incident light. However, this is a second order effect and the simplifying assumption of isotropic emission is generally considered to be sufficient.

Based on the typical refractive indices of n_1 = 1 (air) and n_2 = 1.5 (LSC), 75% of the initial luminescence is trapped within the LSC according to Equation 13.2. However, light can be re-absorbed and re-emitted along its path. Assuming no other losses due to the luminescence quantum yield or absorption in the host material, the overall trapped fraction can be computed with respect to the number of (re-)emissions. Figure 3 shows the

dramatic loss of trapped light with multiple re-emissions. While it is evident from Equation 13.2 that a higher refractive index results in smaller escape cones and better trapping, Figure 3 shows that a higher index also leads to more surface reflection and worse light capture. In theory, this trade-off would have to be optimised individually for every LSC. In practice, the range of refractive indices of materials with high transparency in the visible is fairly limited: 1.5 - 1.9 for optical glass and 1.3 - 1.8 for polymers. Besides trapping light, a good waveguide also needs to transmit it well. The host materials used for LSCs typically have absorption coefficients below $1m^{-1}$ in the visible spectrum, and for high quality glass or PMMA they can be as low as $0.3m^{-1}$.

The waveguiding efficiency is not straightforward to analyse. It clearly depends on the trapping efficiency to some degree. Other factors that play a role are the luminescence Quantum Yield (QY) and the self-absorption of the luminescent centres. Self-absorption leads to QY losses and escape cone losses. QYs above 90% are routinely obtained with organic dyes. The trapping efficiency, i.e. the probability of light trapping upon a single emission, of a waveguide with a typical refractive index of 1.5 is only 75%. Even with a refractive index of 2.0, which is unrealistically high for an LSC waveguide, the trapping efficiency is 87%, still lower than the typical QY. This means that the bottleneck in the waveguiding efficiency is the escape cone losses.

2.3. Luminescent Centres

Not taking into account photon multiplication, an ideal luminescent centre for the LSC would have a QY of 1 and a strong absorption across a large part of the solar spectrum. It would also have a relatively narrow emission spectrum that is matched to the solar cells attached to the LSC and be photo-stable for the lifetime of the LSC. Moreover, it is important to minimise self-absorption, which can be achieved with a small overlap between the absorption and emission spectra. Organic dyes have been the conventional choice of luminescent material in LSCs. Today, there are alternatives (discussed in detail in Section 3) with the potential to overcome some of the drawbacks of organic dyes, notably poor spectral coverage, significant self-absorption and poor stability.

Figure 3. The fraction of light trapped by total internal reflection (TIR) decreases exponentially with the number of re-emissions, as shown for waveguides with refractive indices of 1.5 and of 2.0

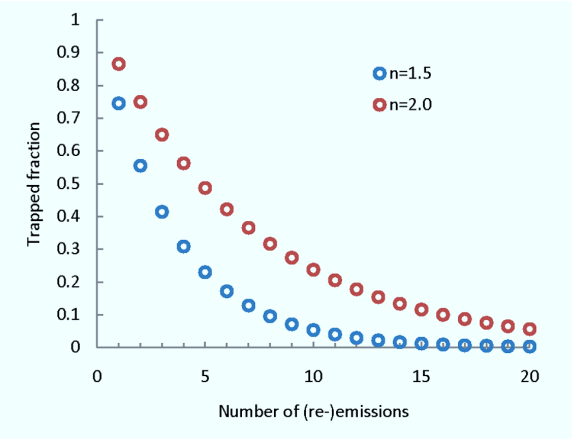

2.4. Concentration and Efficiency

The optical efficiency of the luminescent solar concentrator is the ratio of photons guided to the edges (or coupled into solar cells) to photons incident over the top surface. It is the product of the capture efficiency and the waveguiding efficiency, $\eta_{optical} = \eta_{capture}\eta_{waveguide}$. The optical efficiency is fundamentally less than one, due to several loss mechanisms. The losses can be split into external ones, pertaining to incident light that is not absorbed, and internal ones, pertaining to absorbed light that is lost to non-radiative processes in the luminescent centres or the host or to radiative emission out of escape cones. External losses are reflected in $\eta_{capture}$ and internal ones in $\eta_{waveguide}$. Internal losses are amplified by

re-absorptions, rendering escape cone losses in particular a predominant loss mechanism. The optical concentration (or photon concentration) C, defined as the ratio of the photon flux out of the edges to photon flux incident on the top surface, is the product of the geometric gain G and the optical efficiency, $C = G\eta_{\text{optical}}$ where G is the ratio of the LSC collection surface area to solar cell area. For a square top surface concentrator of length and width l and depth d with solar cells attached to all four edges the geometric gain is given by $G = l/4d$.

Based on an approach by Ross (1967), Yablonovitch (1980) derived the LSC concentration limit from thermodynamics by considering the entropy change associated with the absorption and emission by the LSC. The maximum concentration under terrestrial conditions is approximated as:

$$C \leq \left(\frac{v_1}{v_2}\right)^2 e^{\frac{v_1 - v_2}{kT}} \tag{3}$$

where h is Planck's constant, k the Boltzmann constant, T the temperature (in Kelvin), v_1 the frequency of the incident light and v_2 the frequency of the emitted light. Hence, $v_1 - v_2$ is the Stokes shift of the luminescence. Figure 4 shows the maximum concentration as a function of Stokes shift. The dependency of the concentration limit on the incident wavelength is exemplified by three different wavelengths. Realistic concentrations are substantially smaller than the thermodynamic limit. Nevertheless, Equation 3 emphasises how light concentration via the LSC is fundamentally linked to the luminescent down-shift.

An LSC with solar cells attached to it is called an LSC module. The system efficiency of such a module is defined as electrical power out over incident radiative power and depends on the solar cell efficiency as well as the optical efficiency of the LSC. The bandgap of the cell limits the absorption range of the LSC. While a large Stokes shift increases the concentration limit (see Equation 3) it also represents a loss of energy, and this trade-off needs to be taken into account for the efficiency considerations. By matching the luminescence to the cell spectral response, the cell can convert the concentrated light more efficiently than the broad solar spectrum.

The optical efficiency of the LSC decreases with the size of the top surface area, while the geometric gain increases linearly with the top surface. As long as the rate of decrease of η_{optical} is lower than the rate of increase of G, the concentration increases. Since the power incident on the LSC is proportional to the top surface area, the reduction in optical efficiency leads to a decrease of the system efficiency with top surface area and hence with geometric gain. The optimal LSC configuration balances concentration and system efficiency to maximise the power-to-cost ratio of the module, assuming no constraints on space.

2.5. Cost per Watt

In order to make the LSC competitive with other PV technologies, the efficiency, i.e. the power generated over a given area, will need to meet certain minimum requirements. However, the priority is to minimise the cost-to-power ratio (or cost per Watt). The cost per Watt depends on the cost of the components and the energy conversion efficiency. The power out of a solar cell of area A with a conversion efficiency η_{PV} under an irradiance I_γ is $P = I_\gamma A \eta_{\text{PV}}$. The cost per unit power, symbolised here by \$/P, in the case of a PV cell is given by:

$$\left(\frac{\$}{P}\right)_{\text{PV}} = \left(\frac{\$}{A}\right)_{\text{PV}} \frac{1}{I_\gamma A \eta_{\text{PV}}} \tag{4}$$

It is clear that this ratio becomes more favourable under higher irradiance. However, within the scope of solar cell design, the only factors that can be optimised are efficiency and areal cost \$/A. A module consisting of LSC and PV cell collects

Figure 4. The thermodynamic limit for photon concentration via the LSC. According to Equation 3, the upper limit for concentration depends on the Stokes shift. It is represented here in units of wavelength for three different incident wavelengths.

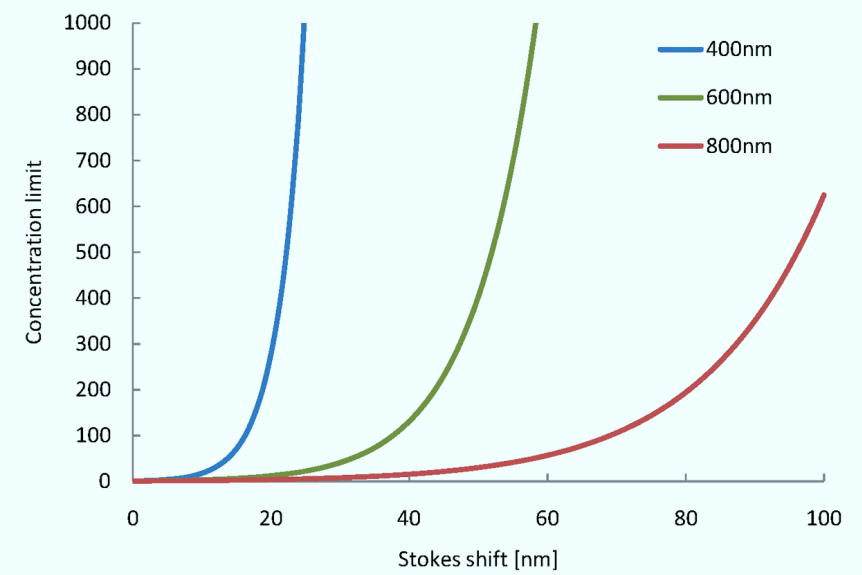

light over a larger area. It has a combined efficiency $\eta_{\mathrm{LSC+PV}}$ and can have reduced areal costs. The cost per unit power in this case is:

$$\left(\frac{\$}{P}\right)_{\mathrm{LSC+PV}} = \left(\frac{\$}{A}\right)_{\mathrm{LSC+PV}} \frac{1}{I_{\gamma} A \eta_{\mathrm{LSC+PV}}} \tag{5}$$

The areal cost ratio of LSC to PV can be defined by γ.

$$\gamma = \left(\frac{\$}{A}\right)_{\mathrm{LSC}} \left(\frac{\$}{A}\right)_{PV}^{-1}. \tag{6}$$

Clearly, γ needs to be considerably less than 1. Using the expression for γ, the combined areal cost in terms of the geometric gain is:

$$\left(\frac{\$}{A}\right)_{\mathrm{LSC+PV}} = \left(\gamma + G^{-1}\right)\left(\frac{\$}{A}\right)_{\mathrm{PV}}. \tag{7}$$

The combined efficiency is defined as the output power divided by the incident power over the LSC collection area (as opposed to the PV cell area alone). Although it depends on various factors, such as the spectral match between the LSC and the cell or the output intensity, the system efficiency may be approximated by $\eta_{\mathrm{LSC+PV}} \approx \eta_{\mathrm{optical}}\, \eta_{\mathrm{PV}}$. This yields:

$$\left(\frac{\$}{P}\right)_{\mathrm{LSC+PV}} = \left(\frac{\$}{P}\right)_{\mathrm{PV}} \frac{\gamma + G^{-1}}{\eta_{\mathrm{optical}}} \tag{8}$$

which allows us to calculate the cost advantage of the LSC module over the solar cells alone for given γ, G and η_{optical}. Assuming that the LSC design does not influence γ substantially, it is concluded that reducing the cost-to-power ratio means optimising both G and η_{optical}, bearing in mind that these two factors are linked.

2.6. Geometries

The LSC geometry mainly affects the geometric gain G, but it can also affect the light capture efficiency through reduced reflection of incident light and the transport of light to the cells, which depends on the waveguiding efficiency and the average pathlength to the cells. The conventional LSC is flat, since a thin shape produces a high geometric gain. Recently, a theoretical study by McIntosh *et al.* (2007) has shown that under certain conditions, when the emission occurs close to the concentrator surface, a cylindrical geometry can produce an optical concentration that is almost twice that of a square planar LSC of the same collection area and volume. This is mainly due to the greater geometric gain of the cylinder with solar cells on the two ends. In addition, a design comprising multiple cylinders aligned next to each other can achieve a further increase of the concentration by several percent as a result of improved light capture from multiple reflections between neighbouring cylinders.

Increasing the LSC performance cannot be achieved simply by increasing the geometric gain, for example by increasing the collection area while keeping the thickness constant. As the dimensions of the waveguide increase, the optical efficiency inevitably decreases since photons have longer paths on average before being collected. A longer path leads to increased self-absorption and host absorption losses, so the rate of the decrease in optical efficiency depends on the transparency of the waveguide and the extent of the self-absorption. The relationship between G and $\eta_{optical}$ means that the increase of the optical concentration C (see Equation 3) with growing G eventually flattens off. For a given set of parameters, including the cost ratio γ, there are optimal dimensions that minimise the cost-to-power ratio. G is scale invariant, but $\eta_{optical}$ is not, due to the constant absorption coefficient of the host material. This means that compared to a large LSC with identical shape and absorbance a small LSC would have a smaller fraction of host absorption losses. In practice, this effect is not expected to affect the scaling of the LSC noticeably since host absorption losses are small and outweighed by more substantial loss mechanisms.

Within the scope of planar concentrators, it is straightforward to calculate gains. Let us assume a thickness d and solar cells around the entire perimeter p of the shape. In most practical applications the LSC will probably be required to tessellate. The only polygons that fulfil this criterion are the triangle, the square and the hexagon with geometric gains compared to that of a square, G/G_{square}, of 0.88, 1, and 1.07 respectively. The circular geometry produces the highest gain for a given area with G/G_{square} of 1.13. Consequently, the best tessellating shape is the hexagon, since it comes closest to the circle, and the worst is the triangle. However, the additional geometric gain the hexagon provides compared to the square is only 7%. Raytrace simulations carried out by Kennedy (2007), comparing the optical concentrations for these same four geometries, produced results that support the findings presented in this section. Moreover, the results are also in agreement with experimental measurements by Roncali and Garnier (1984). Kennedy *et al.* draw the conclusion that despite the slightly higher concentration achieved with the hexagonal design, cost considerations would favour the square geometry. A further theoretical study by Loh and Scalapino (1986) reinforces that variations in the planar geometry have little effect on the performance of the LSC. It should be noted, that Goetzberger *et al.* (Goetzberger, 1978; Goetzberger & Wittwer, 1981) suggest a triangular concentrator with mirrors on some of its edges as the optimal configuration. This geometry is not prioritised due to the findings regarding the use of edge mirrors, as discussed in Section 8.

The next two sections of this chapter discuss the luminescent materials that have been considered for the LSC and additional structures that when utilised in conjunction with the LSC may provide a boost in output.

3. REVIEW OF LUMINESCENT MATERIALS

While organic dyes were the conventional choice of luminescent centres, various other materials are being used in LSCs today. This section presents the main types of luminescent materials along with their strengths and weaknesses.

3.1. Organic Dyes

During the early years of LSC research, the laser dyes employed, typically rhodamine or coumarin compounds, had lifetimes in the order of days or shorter (Batchelder, et al., 1981; Wittwer, et al., 1984). Since then, the photo-stability of dyes has improved significantly, and recent developments in the encapsulation of organic molecules in the OLED industry make lifetimes of up to 30 years appear viable (Currie, et al., 2008).

In a degradation study by Sloof *et al.* (2007) a BASF Lumogen F Red 305 dye incorporated in a homogeneous LSC made of the commercial polymer matrix Plexit 55 was examined. The LSC was illuminated continuously with a 1/3 sun white light source without UV component for a period of 250 days. The dye was found to degrade initially over a period of approximately 50 days, leading to a loss in the LSC short-circuit currentof 20%, but it then remained stable for the subsequent 200 days. An outdoor study of BASF dyes in PMMA by Mansour (Wilson & Richards, 2008) showed that the BASF 241 dye degraded by only 6.2% in terms of its absorbance after a year of exposure to daylight. Further degradation studies by Wilson and Richards (2008) on five Lumogen F series dyes in PMMA showed a degradation of only 5 to 15% in the absorption coefficient of four of the dyes after a 5 week exposure to light, humidity and temperature in a QUV exposure machine. The Violet 570 dye degraded by 60% as it was the most susceptible to the UV light. Red 305 was found to be most suitable in terms of stability and absorption properties, whilst also having a high QY.

Dyes are particularly attractive due to their high QYs, typically > 90%, and availability in large quantities at low costs. However, most dyes have relatively narrow absorption spectra with respect to the solar spectrum available for photovoltaic energy conversion.

3.2. Nanocrystals

Inorganic nanocrystals such as Quantum Dots (QDs) have been proposed as an alternative to dyes (Barnham, et al., 2000), since competitive QYs are attainable (Alivisatos, 1998). Commercial QDs are reported to have QYs ranging from 20% to 90% (Evident Technologies, 2002) depending on their bandgap. Some advantages of nanocrystals are their broad absorption spectrum, extending into the blue and UV, and the tunability of their absorption edge via control of their size (Barnham, et al., 2000; Murray, et al., 1993). One of the current drawbacks of nanocrystals is that they are a relatively expensive luminescent material.

Mostly, the nanocrystals are prepared through colloidal synthesis. In this scalable technique, the nanocrystals are grown under thermal control via nucleation processes in a solution containing precursor compounds. The nanocrystals generally consist of group II-VI compounds such as PbS, PbSe, CdS, CdSe, ZnSe, and ZnS. PbSe and PbS absorb in the NIR, the others in the visible. Figure 5 shows the broad absorption spectrum of a QD compared to a dye with similar absorption edge. A challenge that remains is the development of NIR absorbing nanocrystals with high QYs. Shcherbatyuk *et al.* (2010) have reported a liquid LSC with dimensions of 45mm ×12mm ×3mm that employed commercial PbS QDs from Evident Technologies with QYs of 50% and below. These QDs absorbed in the visible as well as the NIR spectrum. This particular LSC was designed with a spectral match to silicon solar cells in mind and achieved an optical efficiency of 12.6%.

The QDs used in recent LSC development have typical dimensions of several nanometres, containing hundreds to thousands of atoms. These structures cannot be considered 0-dimensional; in fact, they have an approximately 3D density of states. The QD absorption spectrum is related to the bandgap of the bulk material, but quantum confinement alters the energy states, providing a degree of freedom in tuning the absorption spectrum: a smaller QD size leads to a higher bandgap energy and vice versa. For example, the bandgap of CdS can be varied from 2.5 eV to 4 eV via quantum confinement (Alivisatos, 1996). Moreover, the spread in the QD sizes determines the Stokes shift in accordance with the generalised Planck equation (Barnham, et al., 2000).

As in a bulk semiconductor, the absorption cross-section of a QD increases with increasing photon energy (or decreasing wavelength), which leads to a broad absorption band (see Figure 5). Photo-generated electron-hole pairs tend to form excitons, bound states, which can move within the QD. If they reach the surface of the QD before spontaneous photon emission takes place, non-radiative recombination is very likely since the surface contains defect and recombination sites. Due to the large ratio of surface area to volume, QDs suffer significant losses from surface recombination. This loss mechanism is reduced by passivating the surface, for example with organic ligands, but the resulting luminescence quantum yields are generally still below 10% (Murray, et al., 1993). A significant improvement is achieved by adding a QD shell made of a higher bandgap semiconductor. This creates either a type I QD, in which the electron and hole are in the same material in their lowest excited state, or a type II QD, in which they are in separate regions (Kim, et al., 2003). Surface recombination can be suppressed by confining the excitons to the core. It is possible to achieve this by confining the hole alone to the core while the electron is delocalised in the entire QD (Peng, et al., 1997). The core-shell approach leads to QYs above 50% (Alivisatos, 1998; Dabbousi, et al., 1997) and even close to 100% in some cases (Peng, et al., 1997). Multiple shells can improve the passivation further and also alter the spectral properties of the QD (Bleuse,

Figure 5. The spectra of quantum dots from Nanoco (SD396) are shown in comparison to the absorbance of a Lumogen F orange dye from BASF. The broader absorption spectrum of the QDs is apparent. An exciton feature is observed around 510nm in the absorbance of the QDs.

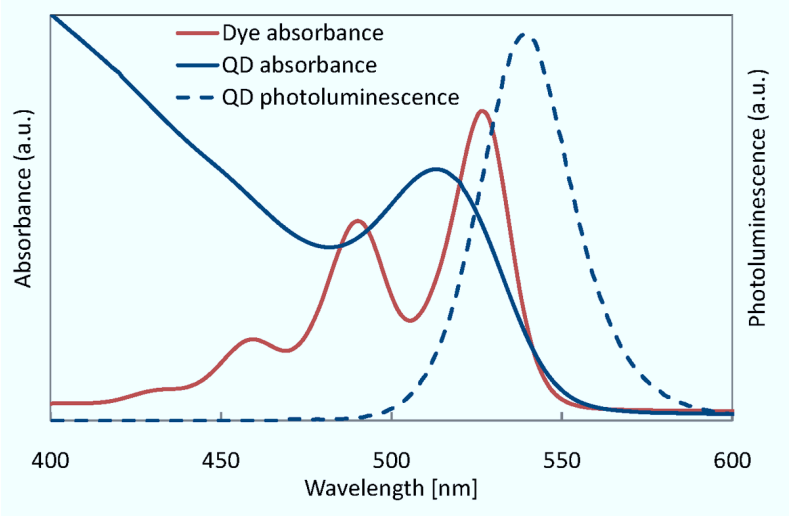

2004). In fact, the indirect exciton induced in a type II QD leads to a strong Stokes shift because the energy of the emission depends on the band offsets of the core and the shell materials, which can be smaller than the bandgap of either material (Kim, et al., 2003).

It has been found that besides the size, the shape of a nanocrystal also affects its optical properties (Debije, et al., 2010). Nanocrystals can be grown with a high level of control in an elongated core-shell structure comprising a spherical (0-D) core (e.g. CdSe) and a rodlike (1-D) shell (e.g. CdS) (Chatten, et al., 2007). Such a structure, referred to as a nanorod, can offer a large absorption cross-section like a quantum dot and QYs of:80% (Wilson, 1987). Efficient energy transfer from the shell to the core leads to a large, length dependent Stokes shift. We have shown that the resultant reduction in self-absorption losses can double the output of an LSC compared to one containing comparable QDs (Bose, et al., 2008).

Since they consist of semiconductor material, nanocrystals are expected to be potentially more stable than organic luminescent materials. However, simple nanocrystals tend to degrade in the presence of oxygen. To prevent this, core-shell structures are usually used since the shell not only enhances the luminescence quantum yield, but also improves the stability (Peng, et al., 1997). A degradation study carried out on five nanocrystal LSCs indicated a reasonably good photo-stability (Quilitz). Homogeneous polymer LSCs with surface areas of 10-25 cm^2 and a thickness of 4mm were prepared using CdSe/CdS/CdZnS/ZnS core-multishell QDs. The stability tests were carried out by recording the short-circuit current from an a-Si PV cell attached to one LSC edge at regular intervals while the samples were under continuous irradiation. The light source was a 1000W sulphur lamp with a good spectral match to the solar irradiation, in particular in the UV region, which is assumed to have the greatest contribution to degradation. The test was carried out for 280 hours, which is comparable to three months of outdoor exposure. After this duration, four of the samples degraded by less than 5%.

Peng *et al.* (1997) carried out a degradation study on CdSe/CdS core-shell QDs over 4 months in air under room lighting. The change in the absorption spectrum was minimal, while the QY decreased from 90±10% to 75±10% over this period. Zhou *et al.* (2005) showed that encapsulation of quantum dots in silica can also dramatically enhance the stability as well as the quantum yield. They demonstrated how a CdSe QD that due to photo-oxidation degraded in its absorbance to approximately 1/3 of the original value within 6 days in an air could be stabilised through silica coating such that it produced no noticeable (< 2%) degradation over the same period. In a less realistic setting in the absence of oxygen, a comparison of CdSe/ZnS quantum dots with a Lumogen F Red 300 dye was reported in which the QD photo-degraded five times slower than the dye and fully recovered after a prolonged dark cycle (Hyldahl & Wittmershaus, 2009).

3.3. Materials with Minimal Self-Absorption

Minimal self-absorption, i.e. a small overlap between the absorption and emission spectra can reduce escape cone losses and ideally limit them to the initial loss of:25%. Since the Stokes shift in typical dyes appears to be insufficient, a range of alternative luminescent materials and approaches has been considered, which generally rely on the same principle: the relaxation of the absorbed photon energy to a energetically lower state at a rate much faster than the rate of spontaneous emission. The absorbing component needs to have a significantly higher absorptance than the emitting component.

Non-radiative energy transfer has been proposed in the early years of LSC research as a method to minimise self-absorption (Olson, et al., 1981). Fluorescence (or Förster) Resonance Energy Transfer (FRET) is such a mechanism, in

which light is absorbed by a large concentration of donor molecules and transferred to a small concentration of acceptor molecules, which emit photons that are significantly red-shifted. The efficiency of FRET depends crucially (to the sixth power) on the separation *r* between the donor and acceptor molecules (Förster, 1948). The small separations (in the order of nanometres) required for efficient FRET can be attained using a thin-film configuration. For example, Bailey *et al.* (2007) reported nearly 100% efficient FRET in a 3-dye LSC. Moreover, FRET has been achieved from organic luminescent centres to quantum dots (Anni, et al., 2004) as well as the other way around (Clapp, et al., 2004) with FRET efficiencies of the order of 65%. The latter seems attractive for the LSC as the broad absorption of inorganic nanocrystals could be combined with the near unity QY of organic dyes. More interesting research in the field of resonance energy transfer between organic and inorganic luminescent materials is being carried out by G. Calzaferri's group (see for example Calzaferri, 2001; Minkowski & Calzaferri, 2005).

Another approach, utilised for example by Currie *et al.* (2008), is intersystem crossing in organic molecules. Incident photons are absorbed by the electron pairs that form the chemical bonds between the atoms of the molecule. Each electron has a spin of $\pm\hbar/2$. A singlet state describes an electron pair with an overall spin of 0. In this case, the two electrons are correlated, and the Pauli exclusion principle dictates opposing spins. In a triplet state, one of the electrons is excited, and the spins of the two electrons are aligned, so that the overall spin magnitude is $\hbar$. This gives rise to 3 quantum numbers (-1, 0 and 1), which explains the name of the triplet state. Excitation from a singlet ground state to a singlet excited state is more probable than to a triplet state since the latter involves a forbidden spin transition. Intersystem crossing occurs when the excited singlet state transitions non-radiatively to a triplet state, which can subsequently relax radiatively to the ground state in a process called the phosphorescence. A red-shifted emission is attained due to the lower energy of the triplet state compared to the excited singlet.

In rare-earth lanthanide complexes such as neodymium (Nd3+) or ytterbium (Yb3+) studied in Refs. (Rowan, et al., 2008; Rowan, et al., 2009; Wilson, et al., 2010; Reisfeld, 1984; Reisfeld, 1987), forbidden or weakly allowed transitions lead to a very large separation between the absorption and emission spectra and a narrow emission peak. A further consequence is a very weak absorption cross-section, but sensitising the complexes with organic ligands is proposed as a solution. This involves intersystem crossing from the singlet to the triplet state in the ligand and non-radiative energy transfer to the lanthanide complex, which acts as the emitter. The efficiency of this energy transfer depends also on the energy gap between the sensitiser and the emitter. If the energy gap is too large, then the efficiency of the energy transfer is compromised. However, if the gap is too small, then thermally activated back-energy transfer can occur from the emitter to the sensitiser, which of course degrades the luminescence quantum yield. With lanthanide complexes, the elimination of self-absorption at quantum yields of:86% is possible (Wilson, et al., 2010), but a narrow absorption spectrum remains an issue.

Saraidarov *et al.* (2010) have investigated a compound, diheptyl-bipyridyl-diol, that has virtually no self-absorption due to a phenomenon termed the anomalous Stokes shift. However, low quantum yields (< 30%) appear to pose a challenge for this compound. We have also investigated two further luminescent centres that could deliver low self-absorption; the nanorods discussed above in Section 3.2. (see Bose, et al., 2008 for further details) and bio-derived phycobilisomes (Bose, et al., 2010), extracted from algae, in which a protein complex provides for efficient FRET leading to a

large Stokes shift and high QY of 95% (Mulder, et al., 2009).

3.4. Multiple Luminescent Species

Many luminescent materials such as dyes have the drawback that their absorption spectrum is relatively narrow. In this section, the use of multiple luminescent species is considered with the aim to broaden the absorption spectrum of the LSC.

The first group to propose multiple luminescent dyes in the LSC were Swartz *et al.* (Wilson & Richards, 2008). In this concept, the incident radiant energy is absorbed by one out of several dyes that collectively span a wide spectrum. The energy is cascaded down to the lowest energy dye for final emission. The emission spectrum of each dye needs to be matched to the absorption spectrum of the next lower energy one. The absorption spectrum of the collective would be the combined spectrum of each individual dye, while the emission spectrum would be that of the lowest energy dye alone, assuming ideal energy transfer. There are two competing energy transfer processes: radiative and non-radiative in form of FRET. The advantage of FRET over radiative energy transfer is that escape cone losses can be bypassed. The efficiency of FRET is very sensitive to the intermolecular separation. Swartz *et al.* fabricated LSCs with two dyes, Coumarin 6 (C6) and Rhodamine (Rh6G). Because their LSCs were homogeneously doped, the concentrations of the dyes were too small by an order of magnitude to facilitate efficient FRET.

The high dopant concentrations required for FRET can be achieved with the thin-film configuration, which has been chosen in several recent approaches using multiple dyes (Bailey, et al., 2007; Richards, 2006; Burgers, 2006; Richards, 2004). As mentioned above Bailey *et al.* (2007) reported a 3 dye LSC with highly efficient FRET close to 100%. The dyes used in their research were derivatives of a molecule designed by a collaborative partner. The multiple dye LSC showed an increase in output of 45-170% compared to single dye LSCs comprising the individual dyes. Richards (2006) modelled LSCs containing up to seven dyes from the BASF Lumogen series, including Near-Infrared (NIR) absorbing dyes. They found that the highest system efficiency of 4.4% was obtained with five dyes, while adding further dyes with lower quantum yields lowered the system efficiency.

An alternative approach to the ones described above, suggested by Farrell (2008), comprises multiple luminescent species without spectral overlap, so that the emission spectrum has separate peaks. By coupling the output to a multijunction solar cell one could achieve similar results as with an LSC stack in terms of optimising the output voltage, but without the need for several layers.

3.5. Directional Emission

Escape cone losses can be avoided in an LSC with preferential emission in the plane of the waveguide. This approach requires the alignment of anisotropic, directionally emitting luminescent centres. Batchelder *et al.* (1979) predicted that this could potentially reduce the probability of emission into escape cones from 26% to 9% for an LSC with refractive index of 1.49. Debije's group (Debije, et al., 2008; Verbunt, et al., 2009) was the first to carry out research on dye alignment in liquid crystal layers, recently followed by Baldo's group (Mulder, et al., 2010; Mulder, et al., 2010) and Schmidt's group (MacQueen, et al., 2010). These approaches are based on the thin-film LSC.

The main alignments of interest are the planar one (with the molecules aligned in the plane of the waveguide) and the homeotropic one (perpendicular to the plane of the waveguide). Both the absorption and emission of a luminescent centre is governed by its transition dipole moment. Homeotropic alignment maximises the coupling of

incident light into waveguide modes and thereby enhances the waveguiding efficiency, but the dipole orientation also weakens the absorption strength and hence the capture efficiency. The opposite applies to planar alignment. Debije *et al.* (2007) demonstrated the concept by showing an improved waveguiding efficiency, but an enhancement of the optical efficiency was not achieved due to the losses in the light capture. A tilted alignment was suggested as a compromise between the homeotropic and the planar. Further studies (Verbunt, et al., 2009) revealed another potential drawback of directional emission: in the homeotropic alignment, the absorption and emission dipoles are arranged in a way that amplifies self-absorption. Even if escape cone losses are reduced, the LSC remains susceptible to QY losses, which increase in the presence of self-absorption.

Mulder *et al.* (2010) modelled luminescent molecules as Hertzian dipoles and predicted that the trapping efficiency of a waveguide with a refractive index of 1.5 would increase from 71% to 91% under homeotropic alignment and decrease to 66% under planar alignment. Using a homeotropically aligned Coumarin 6 dye and a refractive index of 1.7 they reported an experimentally measured increase of η_{trap} from 66% to 81%. With a diffuser on top of the LSC to compensate for the weakened absorption a 16% relative increase in the optical efficiency was achieved compared to the isotropic case.

Another way to make use of directional emission is to emit preferentially towards two of the four LSC edges, thereby reducing the solar cell area required (Verbunt, et al., 2009). It was found that a planar dye layer produced a 60% higher emission out of the edges parallel to the alignment direction than out of the edges perpendicular, as well as a 30% higher maximum emission than a isotropic layer.

The research described in this subsection has so far been focussed on dyes, but anisotropic nanocrystals in the form of nanorods could also lend themselves to directional emission. Indeed dipolar emission has been observed (Krahne, et al., 2011) and alignment of nanorods has already been demonstrated on a micrometre scale (Carbone, et al., 2007).

4. ADDITIONAL STRUCTURES

The main losses in the LSC are due to insufficient absorption of incident light and emission out of escape cones. Mirrors mainly aid the absorption of incident light, as do plasmonic layers. Selective reflectors address the escape cone losses.

4.1. Mirrors

Mirrors or reflectors can improve LSC efficiencies, however at the cost of any partial transparency that may be desirable for certain applications. A metallic surface produces a specular reflection, meaning that the reflected angle is equal to the incident angle. A specular reflector on the back of the LSC effectively doubles the thickness of the LSC and hence the path of incident light, without increasing the solar cell area. A bottom mirror cannot remove the escape cone losses out of the bottom since reflected light within the bottom escape cone would simply escape out of the top. The advantage of the bottom mirror is that the longer pathlength aids the absorption of incident light and gives light within the bottom escape cone a greater chance of being re-absorbed and redirected before escaping. The absorption probability could also be increased by raising the concentration of luminescent centres, but this would simultaneously amplify unwanted self-absorption. To a small degree, a mirror can also reflect light at high angles of incidence close to the LSC edges directly towards the PV cells. This effect is only significant along the perimeter of the LSC. The thickness of the LSC determines the required vicinity of the incident light to the edge. At a fixed thickness, the contribution of reflected light to the overall optical efficiency

would decrease with increasing top surface area and hence with increasing geometric gain. At practical LSC dimensions, the effect of reflected light is considered to be insignificant. Since the reflectance of a metal reflector cannot compete with TIR it is advantageous to leave an air gap between the reflector and the LSC so that TIR is preserved.

A sheet of white paper or any other matt white solid produces diffuse reflection. Diffuse reflection is the result of multiple scattering of light under the surface of a material or from a rough surface (see for example Hanrahan & Krueger, 1993). Light impinging on a diffuse reflector such as white paint enters the top layers and is randomly scattered internally until is exits out of the surface. The light scattered from the surface has a direction that is independent of the angle of incidence. The intensity profile of reflection from a flat, diffuse reflector is described by Lambert's cosine law.

By attaching a diffuse reflector to the back surface without an air gap, incident light could be partially directed towards the edges at angles that undergo TIR at the top surface. However, without TIR at the bottom surface, light travelling within the waveguide could be reflected out again by the diffuse reflector. The net effect is that no concentration above the n^2 limiting factor can be achieved with a non-luminescent concentrator that relies only on a diffuse back reflector. This has been verified with raytrace simulations. A non-luminescent concentrator has been proposed in Ref. 68, based on their raytrace simulations, but these simulations assumed isotropic reflection from the back surface, which, in practice is impractical since according to Grabowski (1914), no flat, reflecting surface can create an isotropic reflection that is independent of the angle of incidence.

Simulations of back reflectors are presented in Section 9. Replacing some of the cells on the LSC edges by mirrors has been proposed as a way of further reducing the cell area, but the study presented in Section 8. suggests that this configuration does not yield any advantages.

4.2. Selective Reflectors

A wavelength (or energy) selective reflector placed on the top surface of the LSC can confine the escape cone emission, as shown in Figure 6.

Figure 6. Schematic of a selectively refractive layer that transmits higher energy light within the absorption spectrum of the luminescent centres and reflects lower energy light within the emission spectrum

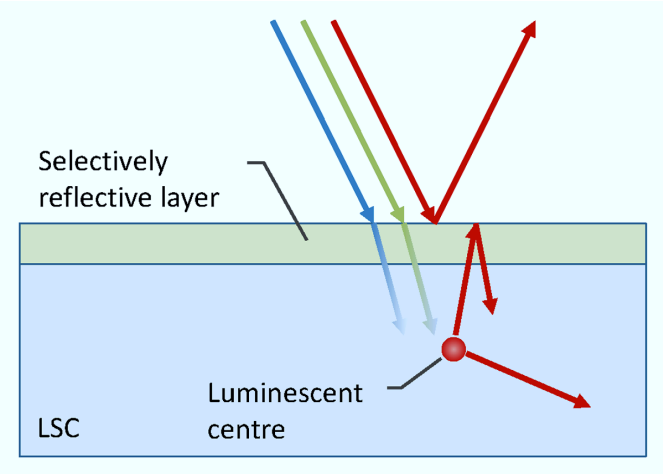

Combined with a back reflector, this approach affords trapping beyond the limitations of TIR. The desired properties of a selective reflector are a high spectral transmittance over the LSC absorption range and a high reflectance over the emission range. Using this method, the light capture efficiency can be maintained for the most part whilst the waveguiding efficiency is boosted. The approach relies on the Stokes shift between the absorption and emission spectra, but since most luminescent materials have a finite overlap between the absorption and emission despite a Stokes shift, even an ideal selective reflector cannot eliminate escape cone losses entirely without paying a penalty in terms of the capture efficiency.

Richards and Corkish (2004) first proposed the use of a selective reflector for the LSC in form a Distributed Bragg Reflector (DBR), also referred to as a hot-mirror or dichroic filter. A DBR consists of a sequence of dielectric layers with alternating refractive indices. Fresnel reflection at the interfaces between the layers leads to interference, which governs the reflective properties of the DBR. The optical thickness (the product of refractive index and geometric thickness) of the layers is generally a quarter or a half of the peak wavelength the DBR is designed to reflect. The same principle of interference also applies to anti-reflective coatings, where either the optical thickness or the arrangement of the layers is changed to produce the opposite effect of DBRs. For a sharp onset of the reflectance, a large number of layers is required. A variant of the DBR is the Rugate filter, in which the alternating refractive indices are sinusoidally modulated to produce a better spectral reflectance profile. Goldschmidt *et al.* (2009) have fabricated LSCs with Rugate filters and achieved relative enhancements in the system efficiency of 20%.

A drawback of the DBR is its angular dependence: since the optical path governing the interference depends on the angle of incidence, the spectral reflectance profile is shifted when light is not normally incident, making it difficult to optimise the DBR response for the LSC. Though it has been suggested to utilise the angular dependence in the design of an LSC with an angularly selective filter (Peterst, et al., 2008), it is the authors' opinion that such a device would forfeit one of the main selling points of the LSC as it would be limited to only small acceptance angles for incident light. The drawback of DBRs can be addressed with 3-dimensional photonic structures. Photonic structures are designed on the light wavelength scale and exploit the analogy between electron waves in a periodic atomic lattice and electromagnetic waves in a photonic crystal (Yablonovitch, 1993). In a similar fashion to the electronic bandgap in a semiconductor, a photonic bandgap in a photonic structure prohibits the propagation of light that is energetically within the bandgap. A DBR is essentially a 1-dimensional photonic structure. 3-dimensional photonic structures eliminate the angular sensitivity and are therefore attractive as a selective reflector. A naturally occurring 3-dimensional photonic structure is the opal. However, photonic crystals with reflectance profiles tailored to the LSC need to be made artificially.

Selective reflection can also be achieved with cholesteric coatings made from liquid crystals. Liquid crystals are organic molecules that can be in a liquid phase whilst still maintaining a crystal structure. In the cholesteric phase, also referred to as the chiral nematic phase, the liquid crystals are aligned within individual layers, with a twisting of the directionality between adjacent layers resulting in a helical structure. This structure requires chiral dopants, i.e. molecules with no inversion symmetry, which also leads to a chirality (or handedness) of the cholesteric phase. A cholesteric coating reflects only circularly polarised light of matching handedness within a narrow wavelength band (:75 nm). The position of the reflection band can be tuned via the amount of chiral dopant. Since the emission from the LSC is unpolarised, a combination of two cholesterics with opposite handedness would be required to

create a practical selective reflector. The use of cholesteric coatings on LSCs has been pioneered by Debije *et al.* (Debije et al., 2006) and shown to recover more than 30% of the waveguiding losses in 50mm×50mm×3mm samples [77, 78]. Much like the DBRs, cholesteric coatings suffer from a strong angular dependence of the reflectivity profile (Chatten, et al., 2007). An advantage of the cholesteric coatings over inorganic reflectors is that they can be deposited from solution, enabling large area roll-to-roll processing.

4.3. Plasmonic Layers

A further development of the LSC is the use of plasmonic layers to enhance the fluorescence from dyes (Wilson, 1987; Wilson, 1988; Reisfeld, 2010). A plasmon is a quantum of plasma oscillations (collective oscillations of the free electron gas), which can couple with electromagnetic radiation to create a quasi-particle called a plasmon polariton (Maier & Atwater, 2005). A plasmonic layer on top of the LSC can also scatter light and couple it into waveguide modes. Although this also enables the reverse path (the coupling out of light within waveguide modes) the longer pathlengths of scattered light can aid absorption. A plasmonic layer usually consists of microscopic metal islands. The geometry and size of the structures determines the optical properties of the plasmons. Since the interactions with light are based on the wave optics, low areal densities of the metal islands around 5% can be sufficient to have strong plasmonic effects. Another property of surface plasmons that could be interesting for LSC research is their effect on the emission from luminescent centres. Zhang *et al.* (2007) reported an enhancement of the fluorescence of perylene dyes in close proximity to silver island films. In recent PV research, plasmons have been successfully used to enhance solar cells performances (Pryce, et al., 2010; Ferry, et al., 2008).

5. RECORD EFFICIENCIES

In recent years, LSC module efficiencies around 7% have been reported based on different approaches: Marc Baldo's group received much media attention for a publication by Currie *et al.* presenting a series of LSCs and LSC stacks that achieved efficiencies up to 6.8% (Currie, et al., 2008) using organic luminescent materials exhibiting FRET or phosphorescence. Goldschmidt *et al.* (Goldschmidt, et al., 2009) measured a maximum efficiency of 6.7% using a stack of dye doped LSCs including a photonic structure as selective reflector. An efficiency of 7.1% from a single LSC module was reported by Sloof *et al.* (2008). It should be noted, however, that the efficiency alone is not a sufficient measure of LSC performance. The aforementioned LSC modules had geometric gains of 3, 2.1, and 2.5, respectively. In fact, one may argue that in some of these cases there is actually no concentration and the cells alone would generate more power under direct illumination than in combination with the LSC. However, at larger LSC sizes with large geometric gains, this can change, provided that the optical efficiency does not decrease too fast with G. In conclusion, scalability is very important. It turns out that the high efficiency published by Sloof *et al.* is partly due to contributions of incident light coupling directly into the solar cells due to a spread of incident angles. This effect does not scale with G and would diminish at larger LSC sizes. Meanwhile, the design by Currie *et al.* (2008) exhibits very little self-absorption and can therefore maintain relatively high efficiencies of up to 6.1% even at a geometric gain of 45. This constitutes a relative loss of only:10% at a 15-fold increase in geometric ratio. The highest concentration factor reported by Currie *et al.* is 11, but according to their projections, concentrations up to 50 should be feasible. Such a concentration could be achieved with a geometric gain of 250

(e.g. dimensions of 1m by 1m by 1mm with cells on all edges) and an optical efficiency of 20%.

The remainder of this chapter describes our versatile Raytrace Model for the LSC and a selection of studies based on raytrace simulations. The first study examines the angular response of the LSC and is complemented by experimental measurements. As an extension of this study, the LSC outputs under direct and diffuse sunlight are compared. The second study examines whether mirrors on the edges produce any practical advantage. The subsequent section investigates the efficacy of specular and diffuse back surface reflectors and is followed by simulations of tapered geometries, which aim to improve the internal light guiding properties of the LSC. Self-absorption is the dominant loss mechanism in the LSC and the final study focuses on modeling this phenomenon.

6. RAYTRACE MODEL

The Raytrace Model of the luminescent solar concentrator is a Monte Carlo model: it generates random numbers to determine the outcome of physical processes based on statistical distributions. It treats light as rays as opposed to waves, since the processes governing the LSC can generally be described by geometrical optics alone.

The model can be applied to a variety of concentrator configurations, including LSC stacks, thin-film LSCs and LSCs with reflectors on surfaces or with multiple luminescent species. The concentrator dimensions can be modified arbitrarily, but the geometry is essentially limited to planar shapes and cylinders. These limitations are not considered major drawbacks since the square planar geometry appears to be the most practical one. Since it is based on geometric optics, the model cannot describe anti-reflective coatings or Distributed Bragg Reflectors (DBRs) from fundamental principles, since these rely on interference effects governed by wave optics. However, phenomenological spectral and angular reflectance or transmittance data can be input to emulate these optical structures. Solar cells on the edges can also be simulated to produce short-circuit currents, based on their quantum efficiency. Due to its statistical nature, the model requires a large number of rays to obtain reliable results. A million rays, enough to produce reasonably accurate results for a typical concentrator, can be traced in a matter of minutes on a standard desktop PC.

The Raytrace Model can shed light on the internal processes of the LSC via comparison with experimental observations, it can be used as a quick and efficient tool for the optimisation of parameters, such as absorber concentration or concentrator dimensions, by step-by-step variation of one parameter at a time, and it can be used to make performance projections on the basis of realistic input data. Photons are described in the model as rays with position and direction vectors in 3-dimensional space and a wavelength. The concentrator is described by its bounding surfaces and material properties, such as refractive index and background absorption. The concentrator can consist of several host materials, which, in turn, can be doped with one or several types of luminescent centres. Most experiment-specific parameters are defined in a setup file. The setup information also specifies the type of light source and luminescent species to be modelled. The incident spectrum as well as the absorption and emission spectra and the luminescence QYs of the luminescent centres are read from their respective data files. This data can be acquired from experimental measurements or computer generated. The concentration and quantum yield of luminescent centres can be easily manipulated for the purposes of optimisation or performance projection. There are no restrictions on the spectra used. The Raytrace Model has been tested against Thermodynamic Model developed by Chatten (Rowan, et al., 2008; Reisfeld, 1984; Reisfeld, 1987; Saraidarov, et al., 2010; Burgers, et al., 2006) and a raytrace model from the Energy

research Centre of the Netherlands (ECN) (Richards & Corkish, 2004). A small rectangular LSC doped with a red dye under AM1.5g illumination was modelled. The fraction of the incident light output from the different LSC surfaces varied by less than 1% for all three models and the excellent agreement validates the Raytrace Model utilised in this work.

The good match between the results from the Raytrace Model and the Thermodynamic Model is remarkable, considering the fundamentally different approaches taken by the two models: while the Raytrace Model is rooted in a microscopic description of the concentrator, the Thermodynamic Model is based on the principle of detailed balance. The Thermodynamic Model assumes thermodynamic equilibrium between the radiation field and the luminescent absorbers and employs radiative transfer methods to compute the detailed balance equation.

7. ANGULAR RESPONSE OF THE LSC

Averaged over the year, 60% of the sunlight received in central Europe is diffuse (Goetzberger, 1978). The main claim differentiating the luminescent concentrator from geometric ones is its effectiveness in a non-tracking setup and under diffuse irradiation. Using the LSC as a static concentrator means that the angle of the direct component of solar irradiation approximation is that it is incident over an entire hemisphere. Thus, quantifying the angular response of the LSC is important for practical applications. This study was carried out experimentally and with the aid of the Raytrace Model.

7.1. Experimental Details

The experimental setup is illustrated in Figure 7. The sample was a square LSC (10.6 cm×10.6 cm×5 mm), doped homogeneously with a Fluorescent Red dye from Bayer with a QY of 95%. The host material was PMMA with a refractive index of 1.49 and an absorption coefficient in the visible of:$2m^{-1}$. A 5mW blue laser with a wavelength of 404nm was used as the light source since a narrow, collimated beam was required. The laser beam had a cross-section of:$2mm^2$ and was incident on the centre of the LSC top surface. The short-circuit current developed in a calibrated solar cell positioned against the LSC edge was measured while the LSC was rotated through a range of incident angles. The relatively large dimensions of the LSC ensured that spatial variations in the illumination spot with changing angle did not significantly affect the distance between the illuminated area and the detection edge. Due to a relatively weak signal arriving at the edge a lock-in amplifier was used for the measurement. Changing the angle of incidence from the normal reduces the incident photon flux by the cosine of the angle. However, since the LSC was illuminated over a small spot and not uniformly over its entire surface, the change in the photon flux with the angle of incidence did not affect the overall rate of photons incident on the LSC. It is important to note that in a practical application one would assume uniform illumination, which would lead to a reduction of incident photon rate with shallower angle of incidence.

A sufficiently large separation between the illumination spot and the PV cell ensured that incident light could not reach the cell directly.

Figure 7. Setup for the measurement of incident angle dependence

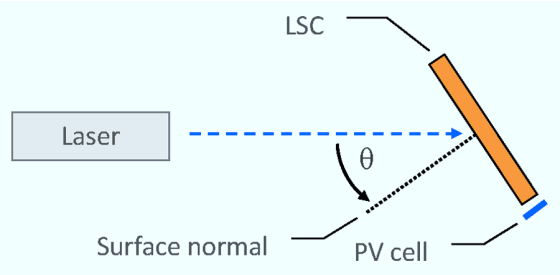

Moreover, due to the reversibility of light paths, it is clear that incident light cannot couple into a waveguide mode via refraction through the top surface or reflection from the back surface. Due to the planar symmetry of the waveguide, light entering through the top surface inevitably exits out of the back, unless it is absorbed, scattered or subjected to Fresnel reflection off the back surface. It is therefore safe to assume that the signal detected by the PV cell originated almost exclusively from luminescent light. Given that the spatial variations of the illumination spot were negligible and that the luminescence was isotropic, it is safe to assume that the incident angle dependence measurement is symmetric about the normal angle.

7.2. Results and Discussion

The experimental results for the incident angle dependence are presented in Figure 8. For comparison, the experiment was also simulated with the Raytrace Model. The short circuit current density measured by a reference PV cell at the LSC edge was used as the performance indicator. The values are plotted on an arbitrary scale since only the relative variation of the output with angle of incidence was under examination. The cosine factor in the photon flux arising from the angle of incidence has been excluded in this visualisation, so that purely the response of the LSC as a function of angle of incidence can be examined.

Surprisingly, the edge output was found to increase with increasing angle of incidence up to:70°, after which it dropped off sharply. This observation was confirmed by the Raytrace Model. The explanation for this behaviour is that the LSC used in this experiment was relatively lightly doped, which meant that the absorbance was low at the laser wavelength. In such a case, a large fraction of normally incident light simply passes through the LSC. Though a larger angle

Figure 8. Angular response of the LSC from experimental measurements and from raytrace simulations. The relative short-circuit current density generated by a solar cell attached to an edge of the LSC is plotted against the angle of incident light. Since the illumination spot was small compared to the LSC surface, the reduction of the incident photon flux by the cosine of the angle of incidence did not affect the results. Therefore, the graph purely shows the LSC response as a function of incident angle.

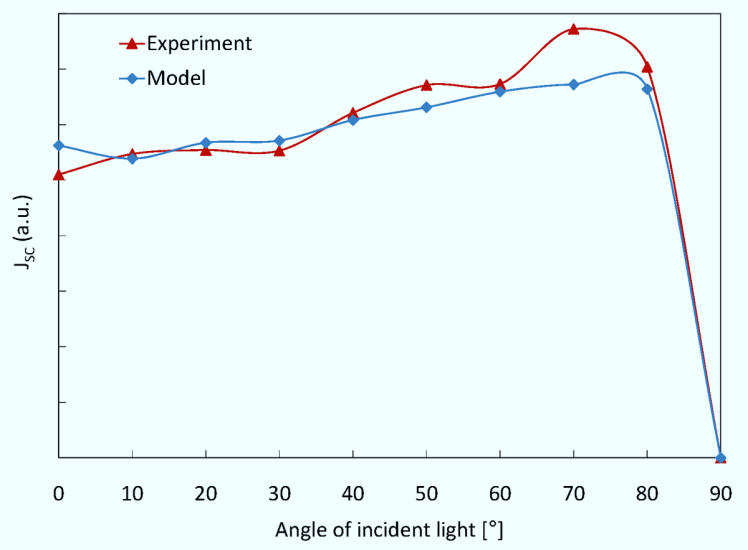

Figure 9. Angular response of the LSC simulated with the raytrace model for an optically dense LSC. The transmittance of incident light through the top surface is shown for comparison.

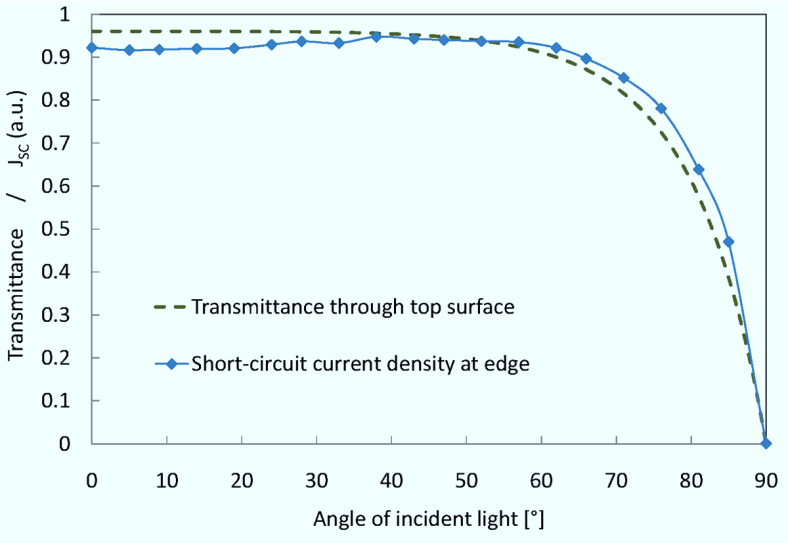

of incidence increases the reflection off the top surface, it also increases the pathlength of the light in the material and hence the absorbance. In a lightly doped LSC, the gain from the additional absorbance can outweigh the loss from the reflectance up to large angles.

While the initial results show a very optimistic incident angle dependence of the LSC, they are not considered to be representative since the reference sample was not optimally doped. Therefore, a further raytrace study was carried out on an optically dense LSC. The results in Figure 9 show a slight increase of the output up to:60°. The transmittance of incident light through the top surface, calculated by subtracting the Fresnel reflectance from unity, is plotted for comparison. As expected, there is a strong correlation between the transmittance and the edge output, but the positive effect of increased pathlengths with increasing angle is noticeable. This effect exists not only in lightly doped LSCs, but also in optimally doped ones, since a longer pathlength of incident light improves the absorption without the drawbacks of a higher concentration of luminescent centres, which would escalate re-absorption losses. For comparison the angular response of the LSC from Figure 9 is plotted next to the response of typical encapsulated silicon PV cells in Figure 10. Two curves are shown for the Si cell, one using our experimental measurements of the cell and one from the literature (Balenzategui & Chenlo, 2005). . The latter was a multi-crystalline silicon substrate cell processed with Edge-Defined Film-Fed Growth (EFG) technology and encapsulated in a cerium doped low-iron front glass followed by an Ethylene Vinyl Acetate (EVA) layer and float glass. Interestingly, this comparison indicates that the reflectance of the encapsulated silicon cell, which contains several layers spanning a range of refractive indices (from that of glass to that of silicon), can be comparable with the reflectance of the LSC, i.e. the reflectance of glass or PMMA with a refractive index of 1.49.

In conclusion, it has been established that the LSC is reasonably insensitive to a change in angle of incidence up to approximately 70° from the normal. Yet the angular response of the LSC is not notably better than that of standard encapsulated silicon cells. However, compared to geo-

Figure 10. Comparison of the angular response of an optically dense LSC (modelled) with a typical encapsulated silicon PV cell (from experimental measurement and from literature [Balenzategui & Chenlo, 2005]). One can see that the responses are very similar.

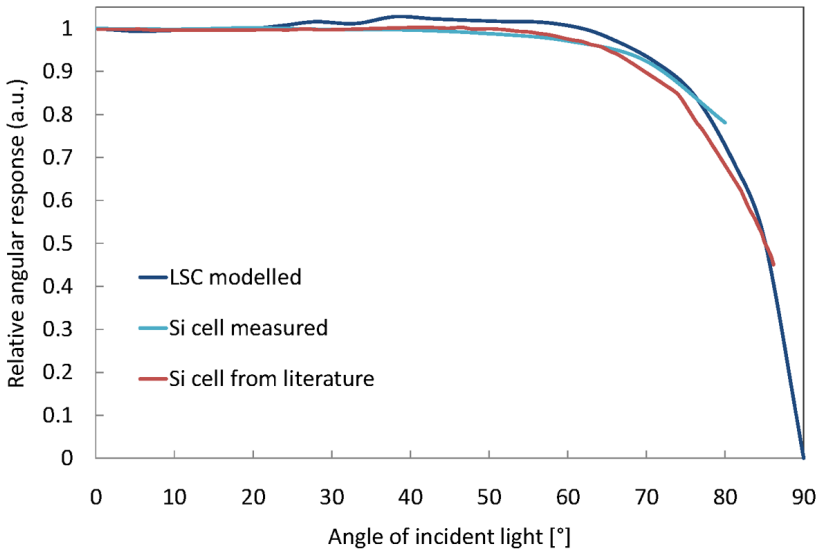

metric concentrators, the LSC has a clear advantage in terms of angular response.

7.3. Capture of Direct vs. Diffuse Light

The solar irradiance has a diffuse component that can be higher than the direct component in regions like the UK. Figure 11 shows the direct and the diffuse components of the AM1.5 spectrum, where the diffuse is defined as the difference between the global spectrum (AM1.5g) and the direct (AM1.5d). The diffuse spectrum is blue rich, since blue light is more effectively scattered in the atmosphere. The performance of the LSC under diffuse irradiation is clearly linked to the incident angle dependence. A large (1m×1m×5mm) LSC was modelled with the same properties (apart from the dimensions) as the one in the previous section, i.e. a PMMA host doped with the Fluorescent Red dye as active material. Simulations were carried out under a direct AM1.5 spectrum incident at a normal angle and compared with a diffuse AM1.5 spectrum incident over a hemisphere. Of course, a normal angle of incidence over the course of a day is not obtainable without solar tracking, but this simplification is justified by the low angular sensitivity of the LSC established in the previous section. An equal ratio between the direct and diffuse components was assumed.

The final distribution of photons shown in Figure 12 provides an insight into the differences in LSC performance under direct and diffuse irradiation. It should be noted that only the spectrum up to the silicon band gap of approximately 1100nm was modelled, and thus the percentages shown in Figure 12 are relative to only a part of the AM1.5 spectrum. Diffuse light incident close to an LSC edge can reach the PV cell directly. However, due to the large geometric gain of LSC that was modelled, the contribution of incident light coupling into cells was found to be negligible compared to the contribution from luminescent light.

The optical efficiency, the escape cone losses and the internal losses are similar under both types

Figure 11. The AM1.5 direct and diffuse spectra. The intensity ratio chosen here is arbitrary as it varies with geographical location. According to Ref. 12 central Europe receives more diffuse than direct irradiation.

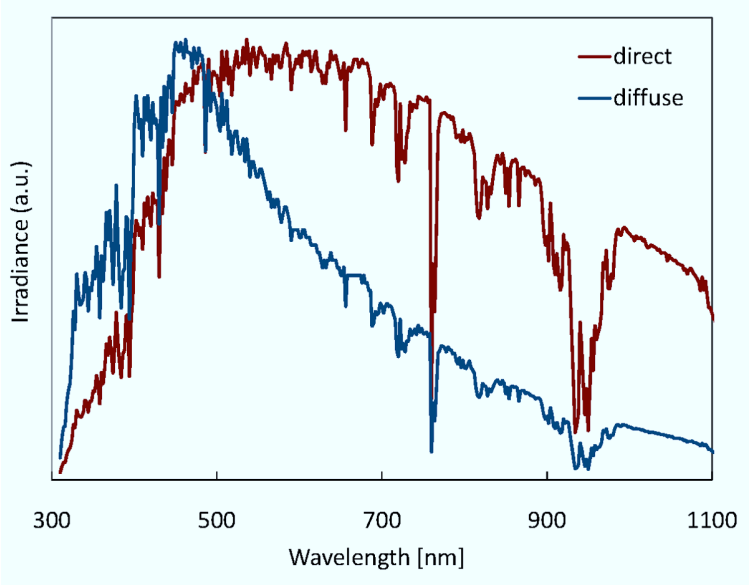

Figure 12. Raytrace simulations comparing the LSC performance under direct and diffuse AM1.5 irradiation. It should be noted that the absorption of incident light leads to either the emission out of one of the surfaces or an internal loss. Therefore, the absorption of incident light needs to be ignored in the final balance, which of course adds up to 100%.

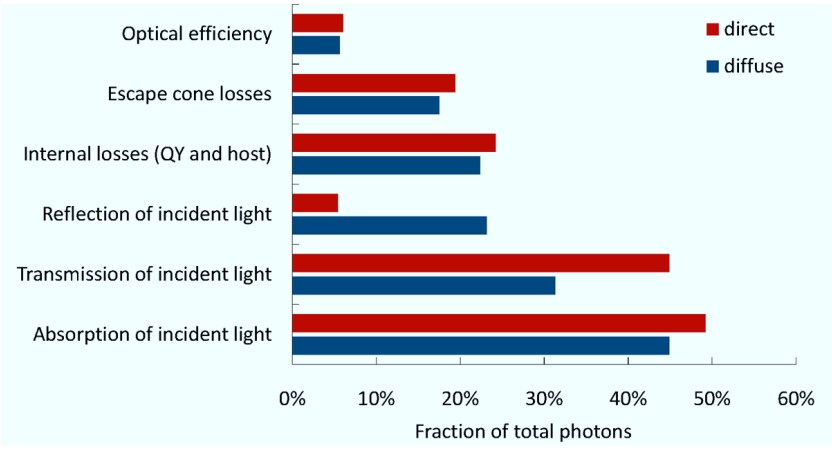

of irradiation, but slightly higher under direct light. The difference is proportional to the greater absorption of direct light. As expected, in the diffuse case there is more reflection from the top surface and consequently less absorption of light and less transmission through the bottom compared to the direct case. However, despite significantly less diffuse light being transmitted into the LSC the absorbed fraction of diffuse light is only slightly smaller than that of direct light. This is a result of the longer pathlengths of diffuse light in the LSC. This simulation shows that the contribution from diffuse irradiation to the LSC output is comparable to the contribution from a simplified calculation of direct irradiation.

8. MIRRORS ON EDGES

Mirrors are often used to replace solar cells on some of the LSC edges (see for example Slooff, et al., 2008). The advantage of such a configuration for characterisation purposes is obvious: mirrors are usually easier to attach to the LSC than solar cells because they do not require electrical connections. Whether edge mirrors bring an advantage to the practical application of LSCs is investigated in this section, using a graphical, an analytical, and a computational approach.

Goetzberger (1978) proposes mirrors on edges as they increase the effective area of the solar cells, as illustrated in Figure 13. The motivation to use edge mirrors is that the cost of mirrors is significantly lower than that of solar cells. If the power output can be preserved, mirrors could reduce the cost-to-power ratio by essentially providing a higher geometric gain.

Having demonstrated in Section 2.6 that a square geometry is convenient, this investigation can be limited to mirrored geometries that are equivalent to square shapes without mirrors. This is the case for modules (b) and (c) depicted in Figure 13. It has previously been shown with a raytracing approach that a square configuration with perfect mirrors on three edges does not have any advantage over an configuration with cells on all four edges (Kennedy, 2007). In this section, a square LSC with mirrors on two adjacent edges was compared to one without mirrors. Due to the equivalent transformations shown in Figure 13, the conclusions drawn from this comparison are also valid for the right-angled isosceles triangle shown in Figure 13.

It has previously been established that the optical efficiency decreases with increasing concentrator size, because of the longer average path length resulting in more self-absorption and background absorption. Since a mirror effectively increases the area, it also reduces the optical efficiency. Edge mirrors would only be favourable if the cost savings from the smaller solar cell area outweighed this loss in optical efficiency.

8.1. Graphical Reasoning

The mirrors in module (b) (see Figure 13) effectively double the length along each dimension and quadruple the concentrator surface area, making it equivalent to module (a).

Based on the current state of development it is asserted that the dimensions of an efficient mirrored module are smaller than the overall area to be covered for a practical application. This means, that several mirrored modules (b) would need to be arranged next to each other. By choosing the arrangement shown in configuration (d) in Figure 14 one can see that modules (a) and (d) are effectively indistinguishable: the pathlength of a photon from the point of emission to the PV cell is identical in both cases (a) and (d), independent of the initial position or direction of the photon. Consequently, under the assumption of perfect mirrors, both modules (a) and (d) have the same optical efficiency and generate the same power. The only difference in the cost-to-power ratio is that module (d) includes additional mirror costs. This suggests that it is favourable to omit the mirrors.

Figure 13. Mirrors on some of the LSC edges can increase the effective area covered by solar cells. The large square without mirrors (a) is equivalent to the small square (b) with two adjacent mirrors, which in turn is equivalent to the triangle (c) with two mirrors. It should be noted that these transformations only express the ratio of collection area to cell area, i.e. the geometric gain. The absolute collection area does not transform by using mirrors. The area of module (a) is 4 times that of module (b) and 8 times that of module (c).

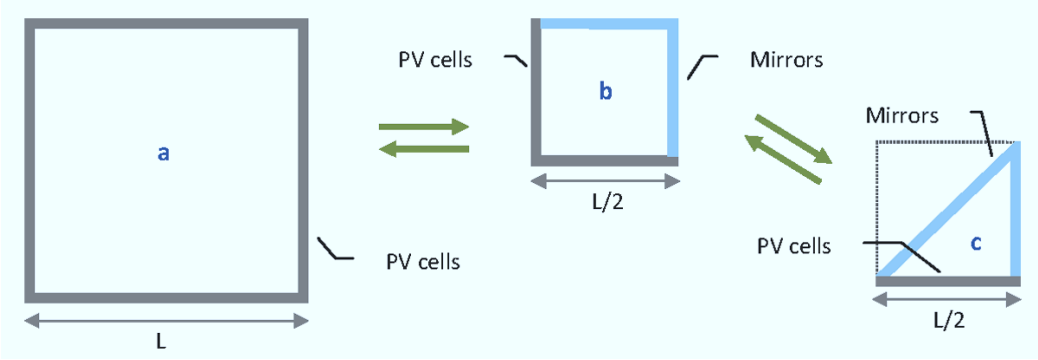

Figure 14. Comparison of a module without mirrors (a) and a module with mirrors (d), consisting of 4 units of module (b) as depicted in Figure 13. One can see that the photon pathlength before reaching a solar cell is the same in both cases.

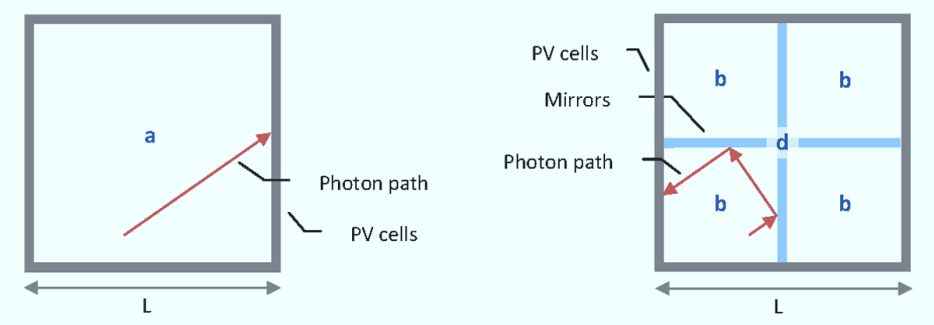

The power output of the LSC module is approximated by:

$$P = I_{\gamma} A \eta_{\text{optical}} \eta_{\text{PV}}. \tag{9}$$

Since P scales with LSC surface area A, the power generated by module (a) is 4 times as large as the power generated by module (b), given that their optical efficiencies are equal. Module (a) also has 4 times as many solar cells as (b). The cost-to-power ratio is calculated as follows:

$$\begin{aligned}\left(\frac{\$}{P}\right)_{\text{b}} &= \frac{\$_{\text{PV(b)}} + \$_{\text{LSC(b)}} + \$_{\text{mirrors}}}{P_{\text{b}}} \\ &= \frac{\frac{1}{4}\$_{\text{PV(a)}} + \frac{1}{4}\$_{\text{LSC(a)}} + \$_{\text{mirrors}}}{\frac{1}{4}P_{a}} \\ &= \left(\frac{\$}{P}\right)_{\text{a}} + \frac{\$_{\text{mirrors}}}{P_{\text{b}}}.\end{aligned} \tag{10}$$

The cost-to-power ratio of module (b) is higher due to the additional mirror costs. This means that for any given module of type (b) one could select

a corresponding module (a) which offers a lower cost per unit power. The mirrored configuration would only be preferable if the availability of area restricted the choice to a small LSC.

8.2. Raytrace Simulation

The Raytrace Model was applied to compare the two types of configurations at different sizes. Typical LSC characteristics were input (a thickness of:3mm, a refractive index of 1.49, a background absorption coefficient of $2m^{-1}$ and a Lumogen Violet dye with a QY of 95% and a peak absorption coefficient of:$2150m^{-1}$), and perfect mirrors were modelled. The resulting optical efficiencies are shown in Figure 15. A decrease in optical efficiency with collection area is observed, which can be attributed mainly to increased self-absorption as well as host background absorption. It is also evident that the optical efficiency of the 50 cm×50 cm module without mirrors is identical, within errors, to that of the 25 cm×25 cm module with mirrors. The same applies to the other pair (no mirrors 100 cm×100 cm and 2 mirrors 50 cm×50 cm). The simulation supports the claim that the efficiency of a module with mirrors is equal to that of a four times as large module without mirrors. It also confirms that at equal sizes the module without mirrors performs better, as seen by comparing the two 50 cm×50 cm configurations.

8.3. Discussion

The effect of mirrors on LSC edges was investigated. While mirrors increase the effective area of the solar cells and produce a greater geometric gain, they also lead to a lower optical efficiency since self-absorption and background absorption are increased. It was found that a given area covered with several mirrored LSC modules produces the same power as a large individual module with cells on all edges. The additional cost of the mirrors gives the mirrored configuration an unfavourable

Figure 15. A raytrace comparison between LSCs with no mirrors and with mirrors on two adjacent edges. The optical efficiency is plotted for different surface areas. The decrease of the optical efficiency with size due to increased self-absorption and background absorption is evident. Moreover, the optical efficiency of a module with mirrors is identical (within errors) to that of a four times as large module without mirrors.

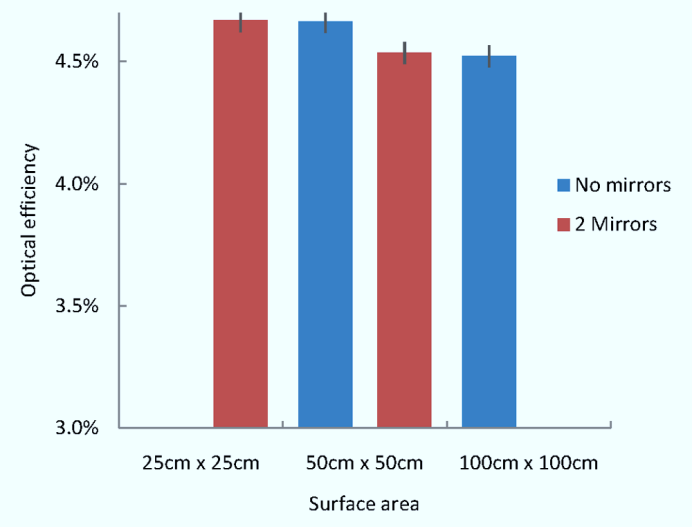

Figure 16. Schematic of LSCs with specular (a) and diffuse (b) back reflector. The air gap between the waveguide and the plate is required to preserve total internal reflection.

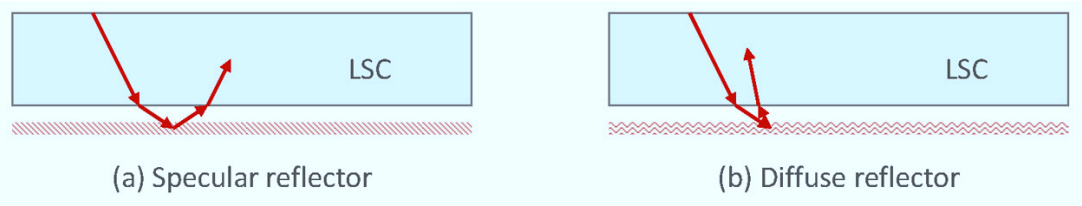

cost-to-power ratio, even under the assumption of 100% reflecting mirrors. With real mirrors, this ratio would be even worse. The only situation in which mirrors on the edges would be preferable is when the available area restricts the size of the LSC to one that is smaller than the optimum. Since this is unrealistic in most practical applications, given the fact that efficient LSCs are currently expected to be smaller than $1m^2$ in area, it is concluded that the use of mirrors on the edges of an LSC module is disadvantageous in general.

9. BACK SURFACE REFLECTORS

In this section, the model was applied to quantify the improvement in light capture with the use of reflectors on the back surface. The two types of reflectors examined were the specular and the diffuse. In both cases, an air gap was left between the LSC and the reflector in order to retain Total Internal Reflection (TIR) (see Figure 16). It should be noted that with an air gap, any light reflected off a mirror at the back will be within an escape cone, since that is the only way it can enter the LSC. Consequently, the reflected light will leave the LSC out of the front unless it is absorbed or subject to Fresnel reflection. The dimensions of the modelled LSC were $1m \times 1m \times 3$ mm, the refractive index was constant at 1.49, the background absorption coefficient was $2m^{-1}$ and the luminescent material was a hypothetical quantum dot (see Figure 17) with a QY of 90%. A constant reflectance of 96% was input, which is considered the upper limit for realistic reflectors in the visible.

9.1. Simulation Results and Discussion

The Raytrace Model was used to compare photon distributions for a plain LSC without a back reflector, one with a specular reflector and one with a diffuse reflector under direct and diffuse light, separately. A monochromatic reflectance of 96% was assumed for both types of reflectors. Under direct light (see Figure 18) it was found that both reflectors yield a:25% relative improvement in optical efficiency compared to the case without mirrors. The diffuse reflector can, on average, produce longer pathlengths on the secondpass for normally incident light. This results in a slight advantage in optical efficiency of:0.5% absolute. There is also a small contribution of incident light directly reflected out of the edges by the diffuse reflector, but at:0.1% this contribution is too small to show up in Figure 18. The sub-unity reflectance leads to a small transmission of incident light through the bottom, despite the reflectors. In reality, this fraction is more likely to be absorbed in the reflector material. As expected, the reflectors produce a large amount of light reflected out of the top, compared to the plain LSC. The simulation also quantifies the enhanced absorption with the aid of the reflectors, which is between 23% and 27% relative to the plain LSC at the given absorbance. As a result of the higher absorption,

Figure 17. The absorption and emission spectra of a hypothetical QD with a quantum yield of 90%, labelled QD400, on which the simulations of the LSCs with back surface reflectors were based

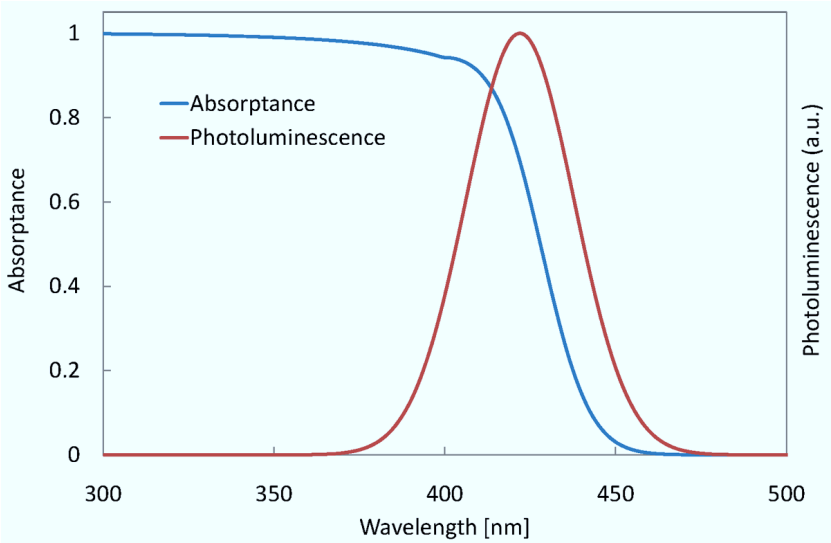

the overall internal losses are also higher with reflectors, but not as high as the gain.

Under diffuse light (see Figure 19) the optical efficiency enhancement from the reflectors is around 20%, smaller than under direct light. This is analogous to the smaller increase in the absorption of incident light of 18% compared to the plain LSC. The reason for this is that the pathlength of diffuse light entering the LSC is already relatively large, and the relative increase in absorbance with the aid of reflectors therefore smaller. With both reflectors there is an insignificant contribution of incident light directly reflected out of the edges (less than 0.2% in optical efficiency). It is evident that under diffuse irradiation the effects of both types of reflectors are virtually identical.

Our results also quantify the effect of light being directly reflected towards the edges and into the PV cells. In the case of the large concentrator modelled in this study, the contribution was found to be than 0.2%. This is in agreement with an investigation by Pravettoni *et al.* (2009). that showed that this direct reflection of light into the cells originates almost exclusively from locations close to the cells. It was found that a small coverage by a diffuse back reflector in form of a thin frame drawing out the perimeter of the LSC produced virtually the same increase as a full back surface coverage. This confirms that the contribution of direct coupling into the cells scales approximately with the inverse of the geometric gain.

10. TAPERED GEOMETRY

Two types of tapering with the aim to improve the LSC performance have been considered in the past. Goetzberger and Schirmer (1979) proposed a taper along the LSC edge consisting of a higher refractive index material than the bulk of the LSC. This concept, depicted in Figure 20, received further attention from other groups (Barnham, et al., 2000; Hermann, 1982) due to its potential to boost the concentration ratio by reducing the required area of solar cell material.

Kennedy (2007) carried out raytrace simulations on a variant that had a PV cell only on one LSC edge and was tapered towards that PV cell edge (see Figure 21), with the motivation to reduce

Figure 18. The effect of back reflectors under direct irradiation, simulated with the raytrace model. A constant reflectance of 96% and an air gap between reflector and LSC were modelled. The reflection profile of the diffuse reflector was assumed to be lambertian.

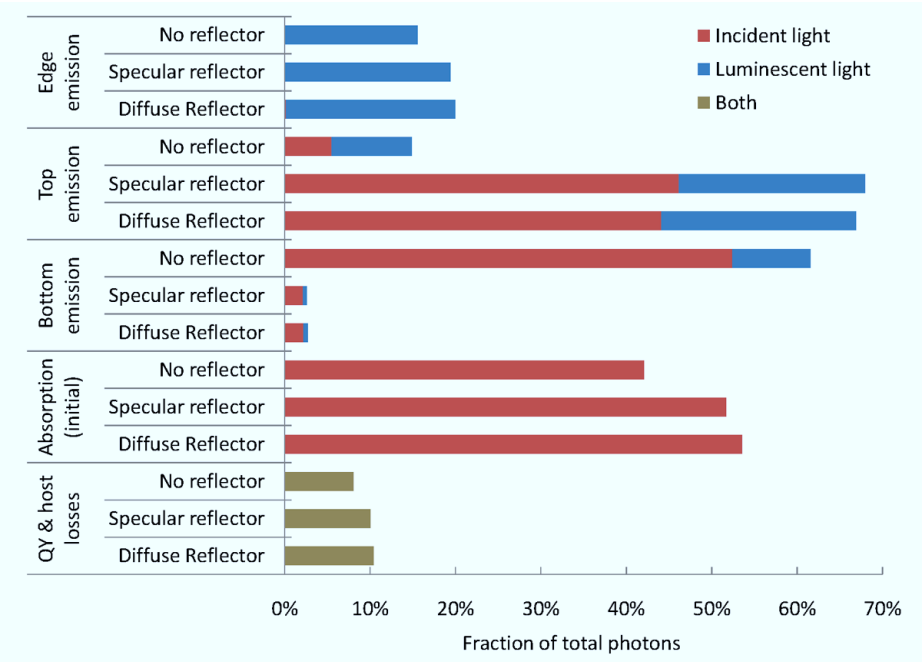

Figure 19. The effect of back reflectors under diffuse irradiation, simulated with the raytrace model. The diffuse light was assumed to be incident over a hemisphere.

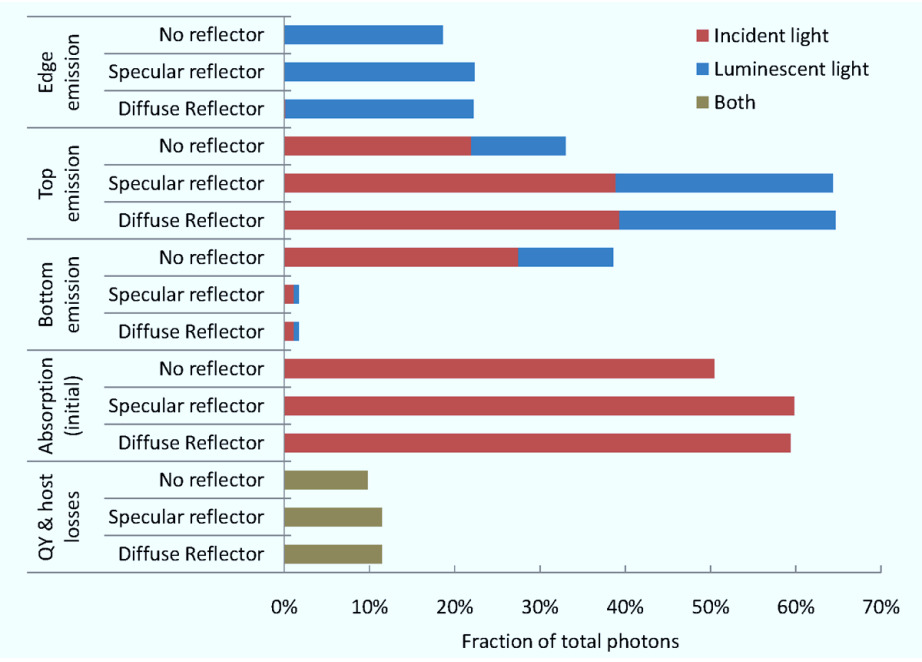

the PV cell area and improve the cost per unit power. However, it was found that in this case light originally trapped by TIR can escape while travelling towards the cell as the angled bottom surface gradually changes the internal angle upon reflection. The overall outcome was that tapering towards the edge with the PV cell always leads to a loss in optical concentration and hence in the cost per unit power.

A different type of tapered geometry is examined in this section, one that also has only one PV cell edge, but is tapered towards the edge opposing the PV cell, as shown schematically in Figure 22. In contrast to the previous two concepts, where the tapering had the purpose of reducing the cell area and thereby increasing the geometric gain and hence the optical concentration, in this concept, the tapering is intended to improve the light guiding properties. The idea behind this is similar to the principle of the wedge-shaped concentrator proposed by Maruyama (1999): the angle of the bottom surface can impart a preferential direction upon reflection that facilitates the light transport towards the PV cell edge. This design could be modified to allow for PV cell coverage on all four LSC edges, for example by tapering the LSC radially towards the centre. However, the simplified case with only once PV cell edge should suffice for the purpose of determining the benefit of the tapered design.

Raytrace simulations were carried out on an LSC with 50×50 cm^2 top surface area where the thickness of the PV cell edge was held constant and the thickness of the opposing edge was varied, as illustrated in Figure 22. A refractive index of 1.49 and constant background absorption of $2m^{-1}$ were input, and the QD400 (see Figure 17) with a QY of 90% was modelled as the luminescent species. The photon flux into the PV cell relative to the case without tapering was recorded. This relative photon flux is proportional to the optical concentration since the dimensions of the PV cell and the LSC top surface area were kept constant. Clearly, the average thickness of the LSC decreases as the tapering becomes more pronounced, so a decrease in the overall absorption of incident light is expected with increasing tapering.

Initial simulations based on an LSC with a 10 cm thick PV cell edge showed improvements in the photon flux into the PV cell of 30-40% with tapering (see Figure 23). Figure 23 also shows a decrease in the relative photon flux when the thickness of the tapered edge is less than:10% the thickness of the PV cell edge. This loss is attributed to a weakened overall absorption due to the smaller average LSC thickness.

Since an LSC thickness of 10 cm is considered impractical, the simulations were repeated using a more realistic thickness of 3mm. As can be seen from the results in Figure 24, the improvements with tapering are small (approximately 10%) in this case.

In conclusion, the tapered geometry presented in this section can improve the light guiding within the LSC. However, to allow for PV cell coverage on all LSC edges, a more complicated design would be required with a constant edge thickness and a tapered centre. Moreover, structural integrity arguments would limit the extent of the tapering in a real application. Given the complications and the marginal advantages, the tapered design is unlikely to be pursued further.

11. RAYTRACE STUDY OF SELF-ABSORPTION

Self-absorption (or re-absorption) is a major loss mechanism as it amplifies luminescence quantum yield losses and escape cone losses, thereby attenuating the waveguiding efficiency of the LSC. Several theoretical models have been proposed in the past that describe self-absorption losses. In this section the Raytrace Model is applied to illuminate the nature of self-absorption further. In particular, this section examines the re-absorption probability for each generation of re-emission in order to determine why the well-known and ap-

Figure 20. Schematic of a LSC with a tapered edge, enabling a reduction of the required solar cell material. The taper needs to have a higher refractive index than the rest of the LSC in order to boost the concentration.

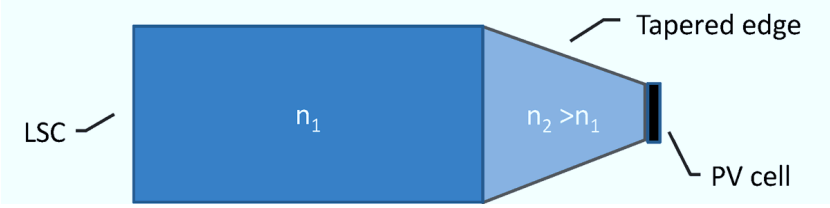

Figure 21. Schematic of a tapered LSC that gets thinner towards the PV cell edge, as discussed by Kennedy (2007)

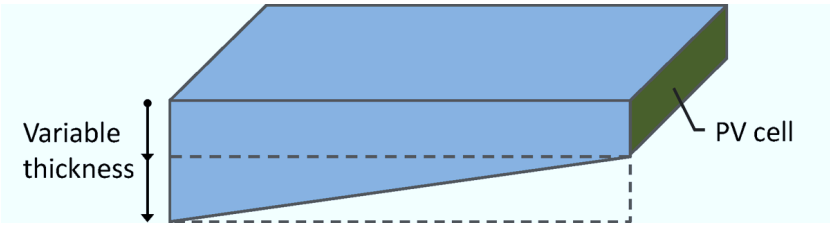

Figure 22. Schematic of a tapered LSC that gets thinner away from the PV cell edge

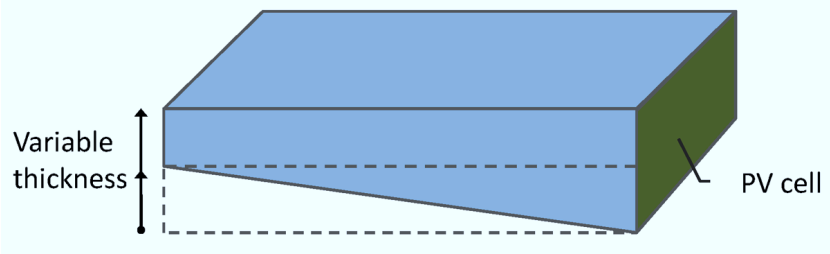

parently sound analytical model by Batchelder *et al.* (1979) is found to break down when the self-absorption is significant.

11.1. Review of Theoretical Models

In the first proposal of the LSC by Weber and Lambe (1976) an analytical model of the LSC was presented that equated the optical efficiency to the product of the absorption efficiency, the luminescence quantum yield and the collection efficiency, defined as the ratio of collected flux (at the edges) to luminescent flux. This model made the approximation that re-absorbed photons were considered to be lost.

Batchelder *et al.* (1979) extended the analytical model of Weber and Lambe by taking multiple re-absorptions into account via a geometric series. Based on the re-absorption probability, the trapping efficiency η_{trap} (see Equation 2) and the QY of the luminescent centre they derived an expression for the waveguiding efficiency:

Figure 23. Modeling of a thick tapered LSC with a surface area of 50×50 cm² and a PV cell edge thickness of 10 cm. The thickness of the edge opposite to the PV cell was varied. The resulting photon flux into the PV cell is shown relative to the case without tapering. The relative photon flux is proportional to the optical concentration. The results show that the tapering can indeed improve the LSC performance, by up to:40% in this example. When the tapered edge goes below 10% of the thickness of the PV cell edge, there is a decrease in the photon flux, which is probably the result of weakened absorptance due to an insufficient LSC thickness.

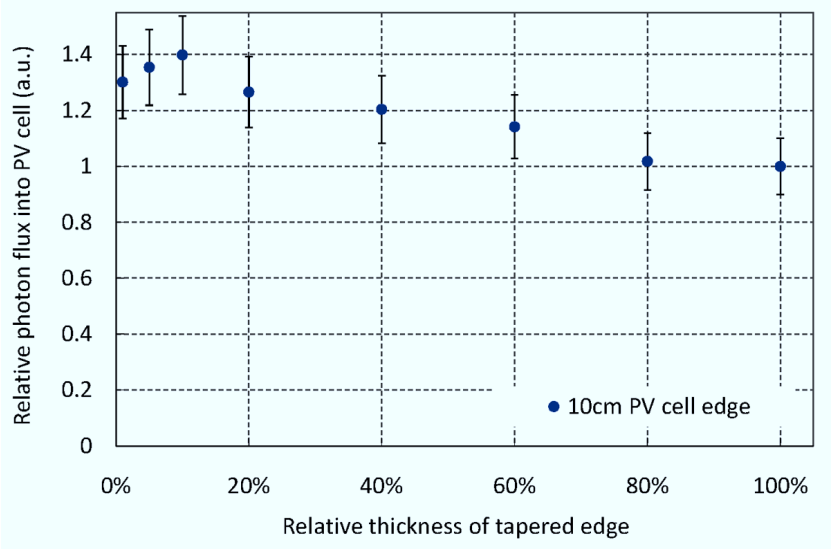

Figure 24. Modeling of a thin tapered LSC with a surface area of 50×50 cm² and a PV cell edge thickness of 3 mm. The thickness of the edge opposite to the PV cell was varied. The resulting photon flux into the PV cell is shown relative to the case without tapering. In this thin case, the advantage of the tapering is significantly smaller than in the thick case. The fluctuations in the trend are attributed to the modeling uncertainty.

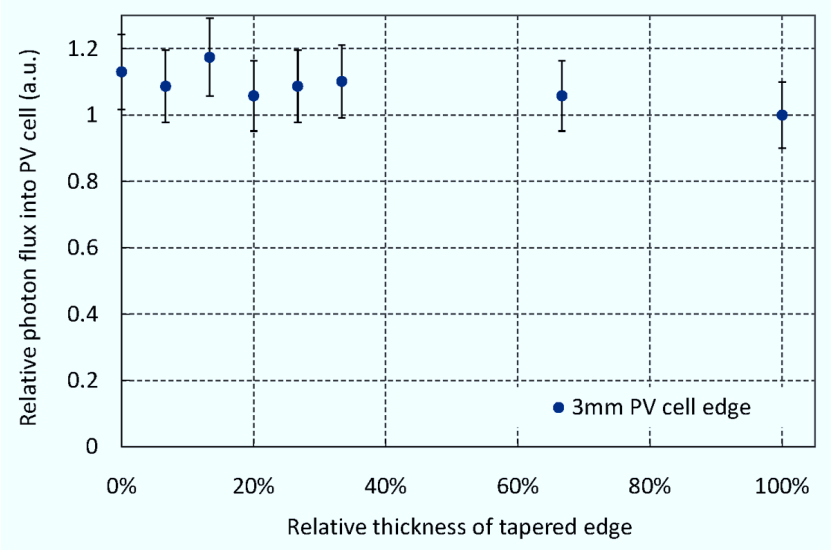

$$\eta_{\text{waveguide}} = \frac{(1-r)\eta_{\text{trap}} QY}{1 - QY\left[\bar{r}\left(1-\eta_{\text{trap}}\right) + r\eta_{\text{trap}}\right]} \tag{11}$$

where r is the probability of re-absorption of light trapped in a waveguide mode and $\bar{r}$ is the probability of re-absorption of light emitted into an escape cone. Equation 3 shows that in the limit of no re-absorption, i.e. $r = 0$ and $\bar{r} = 0$, the waveguiding efficiency equals $\eta_{\text{trap}}\, QY$. Conversely, as r approaches 1 the waveguiding efficiency vanishes.

Kittidachachan *et al.* (2007) derived the model of Batchelder *et al.* (1979) from a two photon flux model based on the detailed balance method. Moreover, through comparison with raytrace simulations they verified the re-absorption probability for first generation emission predicted by the Weber and Lambe model.

Another model was proposed by Roncali and Garnier (1984), who made the same approximation as Weber and Lambe by taking only the first generation of emitted photons into account, thereby neglecting re-emissions. This model accounted for imperfect internal reflection and host matrix absorption. A key parameter in this model is the mean optical pathlength, which is used to calculate the efficiency of internal reflections as well as the probability of self-absorption.

Earp *et al.* (Swift, et al., 2003; Earp, 2004) presented a theoretical model with the aim to predict the luminous efficiency of the LSC since their research was related to daylighting applications. Their model accounts for re-absorption and matrix losses. A key variable in the model is the LSC half-length, defined as the distance over which the light intensity drops by 50%. This quantity is practical for comparison with experimental measurements.

Currie *et al.* (2008) adopted a simplified version of the model by Batchelder *et al.* shown in Equation 11 by assuming that the contribution from re-absorbed escape cone light is negligible compared to the contribution from re-absorbed trapped light, i.e.:

$$\bar{r}\left(1-\eta_{\text{trap}}\right) << r\eta_{\text{trap}}. \tag{12}$$

This assumption is justified because the probability of re-absorption depends on the photon pathlength, and in a typical LSC the pathlength of escaping light is significantly shorter than that of trapped light. The resulting expression for the waveguiding efficiency is:

$$\eta_{\text{waveguide}} = \frac{(1-r)\eta_{\text{trap}} QY}{1 - r\eta_{\text{trap}} QY}. \tag{13}$$

The waveguiding efficiency for an LSC with a trapping efficiency of 74% and a QY of 63%, calculated using the simplified Equation 13, is plotted in Figure 25.

Solving Equation 13 for the re-absorption probability r yields:

Figure 25. The analytical relation between the waveguiding efficiency and the re-absorption probability r, plotted for a QY of 63% and a trapping efficiency of 74%

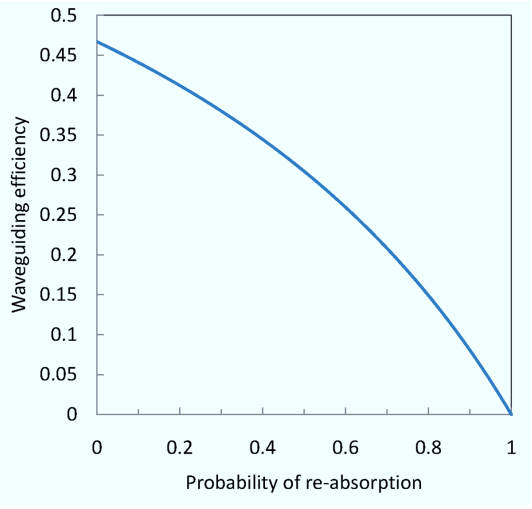

$$r = \frac{\eta_{\text{trap}} QY - \eta_{\text{waveguide}}}{\eta_{\text{trap}} QY \left(1 - \eta_{\text{waveguide}}\right)}. \qquad (14)$$

This expression for the re-absorption probability is examined with the aid of the Raytrace Model. Wilson *et al.* (2010) also presented a raytrace study of re-absorption. They carried out an experimental determination of the re-absorption probability by comparing the edge spectrum with the spectrum in the absence of re-absorptions and using the red-shift to deduce the degree of re-absorptions. They studied the probability of photons from initial emission reaching the edge as a function of the optical density of luminescent centres and supported their data points with raytrace simulations. The study presented in this section differs from previous ones in that it focuses on the probability of re-absorption as a function of previous re-absorptions.

11.2. Raytrace Simulations and Discussion

The waveguiding efficiency and the probability of re-absorption were calculated using the Raytrace Model for a range of LSC sizes. The LSCs were based on the sample discussed in Bose *et al.* (2008) with a refractive index of 1.49, hence a trapping efficiency of 74% and doped with nanorods with a QY of 63%. A monochromatic illumination at a wavelength of 404nm was used in the simulation. By substituting the waveguiding efficiency from the model into Equation 6, the analytical re-absorption probability is obtained. Figure 26 shows a comparison of the analytically and computationally derived re-absorption probabilities for a quantum yield of 63% (1) and of 100% (2). A large discrepancy is evident between the analytical value for *r* and the value obtained from the Raytrace Model, even in the limit of a QY of 100%. Since the Raytrace Model has been proven to make reliable predictions, it is concluded that the analytical model is flawed.

Figure 26. Comparison of the total re-absorption probability r as a function of LSC size, derived from the analytical expression (Equation 6) and computed with the raytrace model. The modelled LSC was based on the sample discussed in Bose et al. (2008), which has a QY of 63%. Monochromatic illumination at 404nm was simulated. In both cases (QY of 63% and 100%) the analytical model is found to deviate strongly from the raytrace model.

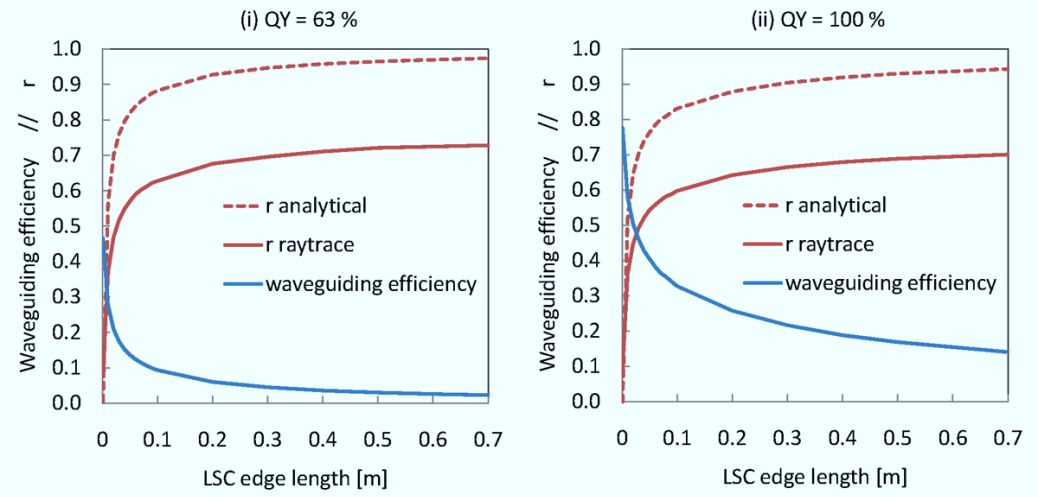

The flaw of the analytical model is found to lie in the assumption of a constant re-absorption probability *r*. Each re-emission produces a red-shift in the emission spectrum, which changes the overlap of the emission with the absorption spectrum and hence the probability of re-absorption. The variation of *r* with the number of re-absorptions in the case of a 25 cm×25 cm LSC based on the properties of the sample discussed in (Bose et al., 2008) is plotted in Figure 27. It is evident that the assumption of a constant *r* is invalid in this case. The shape of the curve for *r* is thought to resemble the spectral absorptance to a degree. It is important to note that the constant *r* assumption would be valid for luminescent materials with a very small overlap between absorption and emission. This explains the good agreement between experimental results and the analytical model reported by Currie *et al.* (2008).

12. CONCLUSION AND OUTLOOK

This chapter describes the principles of the Luminescent Solar Concentrator (LSC) which offers the unique advantage that it concentrates diffuse as well as direct sunlight. The energetic downshift of collected light is the key to concentration via the LSC. An LSC module with solar cells attached to the edges is not expected to outperform the cells alone in terms of power per area, but theoretical considerations show that high system efficiencies could be attainable, while maintaining a lower overall cost.

The cost-to-power ratio was defined for LSC modules, and its dependency on the geometric gain *G*, the optical efficiency $\eta_{optical}$ and the cost ratio of LSC to PV cell γ was established. Assuming that γ is relatively insensitive to the LSC configuration, the focus should be on improving *G* and $\eta_{optical}$, bearing in mind that these two quantities are linked: $\eta_{optical}$ inevitably decreases with increasing *G*. It has been established that the circular geometry produces the highest geometric gain amongst the planar LSC geometries. The best tessellating structure is the hexagon, followed by the square and then the triangle. However, in the authors' opinion, the differences are marginal and do not create a compelling reason to favour a specific geometry based on the gain.

Besides dyes there are a range of luminescent materials being employed in LSCs today, such as semiconductor nanocrystals, material systems utilising resonance energy transfer or rare-earth lanthanide complexes. The main aims are to broaden the absorption, to maintain a high luminescence quantum yield and to enhance the Stokes shift. While shortcomings in the stability of the luminescent centres had posed a problem during the early days of LSC research, recent degradation studies on dyes as well as quantum dots indicate that the desired lifetimes of approximately 20 years could be feasible.

The main losses of the LSC are due to unabsorbed incident light and luminescence lost out of escape cones. Different approaches to improving the LSC have been reviewed in this chapter. These include the use of luminescent materials with little self-absorption, directional emission, back-reflectors and photonic structures on top of the LSC.

The effectiveness of the LSC under indirect light has been demonstrated, validating the claim of its usefulness in regions with high diffuse irradiation and in a static, non-tracking installation. It was shown that the angular response of the LSC is comparable to that of standard encapsulated silicon cells. Having established that the coupling in of incident radiation into the LSC is very efficient, it is the authors' opinion that further reductions of the reflection off the top surface should have a low priority. Anti-reflective coatings are important for solar cells since their refractive indices and hence the reflectances are considerably higher (:4×) than that of the LSC. In the case of the LSC it is questionable whether the efficiency enhancement from an AR coat, which typically comprises sev-

Figure 27. The variation of the re-absorption probability with the number of re-absorptions was modelled for a 25 cm×25 cm LSC based on the properties of the sample discussed in Bose et al. (2008). The plot shows how the probability of re-absorption of a luminescent photon drops with the number of previous re-absorptions.

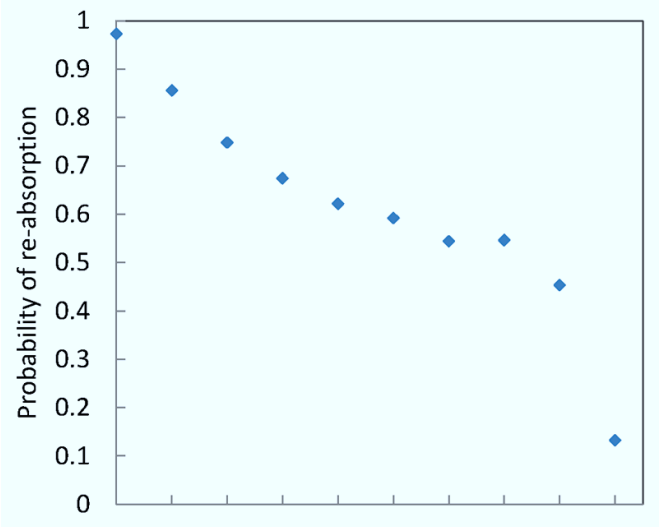

eral layers of varying refractive indices, justifies the additional cost.

The use of mirrors on some of the LSC edges as a method to enhance the geometric gain has been examined. While mirrors increase the effective area of the solar cells and produce a greater geometric gain, they also lead to a lower optical efficiency. Using a graphical reasoning, an analytical approach and raytrace simulations, it has been established that even perfect mirrors on the edges do not benefit the cost-to-power ratio in general. Realistic mirrors with sub-unity reflectance would perform even worse. Edge mirrors could only be of advantage in the case where the available deployment area restricts the size of the LSC. Given that the anticipated optimal sizes of LSCs are considerably smaller than realistic deployment areas, it is concluded that for the purposes of practical application, edge mirrors should be omitted, and PV cells (preferably bifacial) should be placed on all edges of the LSC.

It was found that both specular and diffuse reflectors perform about equally well in improving the optical efficiency of the LSC by increasing the pathlength of incident light. The choice of reflector should be made depending on cost and reflectance considerations. It should be noted that a back reflector would not allow for a semi-transparent LSC, so the advantage in optical efficiency may need to be weighed up against aesthetic requirements.

The concept of a specific tapered geometry has been considered, and although it was found to improve the light guiding properties of the LSC it is not likely to be pursued any further due to impracticalities in the design and rather insignificant advantages. Based on considerations such as the ease of fabrication and attaching of solar cells to the edges, the square planar geometry is considered preferential.

It was shown with the Raytrace Model how the probability of re-absorption decreases with every re-emission due to the progressive red-shift.

This explains why the theoretical models that assume a constant re-absorption probability fail to accurately predict the performance of LSCs with significant self-absorption.

The LSC is essentially a low-concentration device: based on current developments concentration factors up to 20 can be considered a feasible target. Although high-efficiency cells have been considered for the LSC in the past (Heidler, 1986), it is the author's opinion that the choice of solar cells for the LSC is currently limited to relatively inexpensive silicon or thin-film cells. Given the anticipated low cost of the LSC, even a small concentration can lead to cost advantages. For example, to generate the same power as a given solar cell under direct illumination, an LSC module with a concentration of 5 (a conservative example given that Currie *et al.* have already reported a concentration factor of 11 [Currie, et al., 2008]) would require only 1/5 of the solar cell material. In fact, with the right choice of luminescent species the LSC output spectrum can be matched to the cell quantum efficiency so that the cell works more efficiently than under AM1.5, and even less cell material would be required. A cost benefit would remain as long as the cost of the LSC makes up less than 4/5 of the cell. It should be noted, however, that in a practical application the efficiency plays a role as well, since space also comes at a price. In the authors' opinion, a commercially viable opaque LSC would require an efficiency of at least 5%, given that thin-film solar cells with 10% efficiencies could be considered a competitor to such an LSC. However, LSCs can target different markets, as they can be designed in different colours and even semi-transparent and can be integrated into building facades. Moreover, combining the advantages of recent developments suggests LSC efficiencies of over 10% could be achieved for practical module sizes ($> 30 \times 30$ cm^2) in the near future. A combination of approaches is likely to provide the improvement required for the LSC to be commercialised and substantially improve the cost-effectiveness of photovoltaic energy.

REFERENCES

Alivisatos, A. P. (1996). Perspectives on the physical chemistry of semiconductor nanocrystals. *Journal of Physical Chemistry*, *100*, 13226–13239. doi:10.1021/jp9535506

Alivisatos, A. P. (1998). Electrical studies of semiconductor-nanocrystal colloids. *MRS Bulletin*, *23*(2).

Anni, M., Manna, L., Cingolani, R., Valerini, D., Creti, A., & Lomascolo, M. (2004). Förster energy transfer from blue-emitting polymers to colloidal CdSeZnS core shell quantum dots. *Applied Physics Letters*, *85*(18), 4169. doi:10.1063/1.1814795

Bailey, S. T., Lokey, G. E., Hanes, M. S., Shearer, J. D. M., McLafferty, J. B., & Beaumont, G. T. (2007). Optimized excitation energy transfer in a three-dye luminescent solar concentrator. *Solar Energy Materials and Solar Cells*, *91*(1), 67–75. doi:10.1016/j.solmat.2006.07.011

Balenzategui, J., & Chenlo, F. (2005). Measurement and analysis of angular response of bare and encapsulated silicon solar cells. *Solar Energy Materials and Solar Cells*, *86*, 53–83. doi:10.1016/j.solmat.2004.06.007

Barnham, K. W. J., Marques, J. L., Hassard, J., & O'Brien, P. (2000). Quantum-dot concentrator and thermodynamic model for the global redshift. *Applied Physics Letters*, *76*(9), 1197. doi:10.1063/1.125981

Batchelder, J. S., Zewail, A. H., & Cole, T. (1979). Luminescent solar concentrators 1: Theory of operation and techniques for performance evaluation. *Applied Optics*, *18*, 3090–3110. doi:10.1364/AO.18.003090

Batchelder, J. S., Zewail, A. H., & Cole, T. (1981). Luminescent solar concentrators 2: Experimental and theoretical analysis of their possible efficiencies. *Applied Optics*, *20*, 3733. doi:10.1364/AO.20.003733

Bleuse, J. (2004). Optical properties of core/multishell CdSe/Zn(S,Se) nanocrystals. *Physica E, Low-Dimensional Systems and Nanostructures*, *21*(2-4), 331–335. doi:10.1016/j.physe.2003.11.044

Bose, R., Farrell, D. J., Chatten, A. J., Pravettoni, M., Buchtemann, A., & Quilitz, J. … Barnham, K. W. J. (2008). Luminescent solar concentrators: Nanorods and raytrace modeling. In Proceedings of the 33rd IEEE Photovolatic Specialists Conference, (pp. 24-28). San Diego, CA: IEEE Press.

Bose, R., Gonzalez, M., Jenkins, P., Walters, R., Morseman, J., & Moss, M. … Barnham, K. W. J. (2010). Resonance energy transfer in luminescent solar concentrators. In *Proceedings of the 35th IEEE Photovoltaic Specialists Conference*. Honolulu, HI: IEEE Press.

Burgers, A., Slooff, L. H., Buchtemann, A., & van Roosmalen, J. A. M. (2006). Performance of single layer luminescent concentrators with multiple dyes. In *Proceedings of the 4th World Conference on Photovoltaic Energy Conversion*, (pp. 198-200). Hawaii, HI: IEEE Press.

Calzaferri, G. (2001). Organic inorganic composites as photonic antenna. *Chimia*, *55*(12), 1009–1013.

Carbone, L., Nobile, C., De Giorgi, M., Sala, F., Morello, G., & Pompa, P.,…. Manna, L. (2007). Synthesis and micrometer-scale assembly of colloidal CdSe/CdS nanorods prepared by a seeded growth approach. *Nano Letters*, *7*, 2942–2950. doi:10.1021/nl0717661

Chatten, A. J., Farrell, D. J., Bose, R., Debije, M. G., Buchtemann, A., & Barnham, K. W. J. (2007). Thermodynamic modeling of luminescent solar concentrators with reduced top surface losses. In *Proceedings of the 22nd European Photovoltaic Solar Energy Conference*. Milan, Italy: EU PVSEC.

Clapp, A. R., Medintz, I. L., Mauro, J. M., Fisher, B. R., Bawendi, M. G., & Mattoussi, H. (2004). Fluorescence resonance energy transfer between quantum dot donors and dye-labeled protein acceptors. *Journal of the American Chemical Society*, *126*(1), 301–310. doi:10.1021/ja037088b

Currie, M. J., Mapel, J. K., Heidel, T. D., Goffri, S., & Baldo, M. A. (2008). Supporting online material for high-efficiency organic solar concentrators for photovoltaics. *Science*, *321*, 226–228. doi:10.1126/science.1158342

Dabbousi, B. O., Rodriguez-Viejo, J., & Mikulec, F. V. (1997). (CdSe) ZnS core shell quantum dots: Synthesis and characterization of a size series of highly luminescent nanocrystallites. *Journal of Physical Chemistry*, *101*, 9463–9475. doi:10.1021/jp971091y

Debije, M. G., Broer, D. J., & Bastiaansen, C. W. M. (2007). Effect of dye alignment on the output of a luminescent solar concentrator. In *Proceedings of the 22nd European Photovoltaic Solar Energy Conference*, (pp. 87–89). EU PVSEC.

Debije, M. G., Van, M. P., Verbunt, P. P., Kastelijn, M. J., van Der Blom, R. H. L., Broer, D. J., & Bastiaansen, C. W. M. (2010). Effect on the output of a luminescent solar concentrator on application of organic wavelength-selective mirrors. *Applied Optics*, *49*(4), 745–751. doi:10.1364/AO.49.000745

Debije, M. G., Van, M. P., Verbunt, P. P. C., Broer, D. J., & Bastiaansen, C. W. M. (2009). The effect of an organic selectively-reflecting mirror on the performance of a luminescent solar concentrator. In *Proceedings of the 24th European Photovoltaic Solar Energy Conference*. Hamburg, Germany: UE PVSEC.

Debije, M. G., van Der Blom, R. H. L., Broer, D. J., & Bastiaansen, C. W. M. (2006). Using selectively reflecting organic mirrors to improve light output from a luminescent solar concentrator. In *Proceedings of the World Renewable Energy Congress IX*. Florence, Italy: IEEE.

Earp, A., Smith, G. B., Swift, P. D., & Franklin, J. (2004). Maximising the light output of a luminescent solar concentrator. *Solar Energy*, *76*(6), 655–667. doi:10.1016/j.solener.2004.02.001

Earp, A. A., Smith, G. B., Franklin, J., & Swift, P. D. (2004). Optimisation of a three-colour luminescent solar concentrator daylighting system. *Solar Energy Materials*, *84*, 411–426. doi:10.1016/j.solmat.2004.02.046

Efros, A. L., & Rodina, A. V. (1993). Band-edge absorption and luminescence of nonspherical nanometersize crystals. *Physical Review B: Condensed Matter and Materials Physics*, *47*(15), 10005–10007. doi:10.1103/PhysRevB.47.10005

Evident Technologies. (2002). *Core shell EviDots: High yield, narrow emission, photostable fluorescent labels*. Evident Technologies.

Extance, A. (2010). *The concentrated photovoltaics industry report 2010*. CVP Today.

Farrell, D. J. (2008). *Characterising the performance of luminescent solar concentrators.* PhD Thesis. London, UK: Imperial College London.

Ferry, V. E., Sweatlock, L. A., Pacifici, D., & Atwater, H. A. (2008). Plasmonic nanostructure design for efficient light coupling into solar cells. *Nano Letters*, *8*, 4391–4397. doi:10.1021/nl8022548

Förster, T. (1948). Zwischenmolekulare energiewanderung un fluoreszenz. *Annalen der Physik*, *437*(1-2), 55–75. doi:10.1002/andp.19484370105

Goetzberger, A. (1978). Fluorescent solar energy collectors: Operating conditions with diffuse light. *Applied Physics (Berlin)*, *16*, 399–404. doi:10.1007/BF00885865

Goetzberger, A., & Schirmer, O. (1979). Second stage concentration with tapers for fluorescent solar collectors. *Applied Physics (Berlin)*, *42*, 712–758.

Goetzberger, A., & Wittwer, V. (1981). Fluorescent planar collector-concentrators: A review. *Solar Cells*, *4*(1), 3–23. doi:10.1016/0379-6787(81)90033-8

Goldschmidt, J. C., Peters, M., Bosch, A., Helmers, H., Dimroth, F., Glunz, S., & Willeke, G. (2009). Increasing the efficiency of fluorescent concentrator systems. *Solar Energy Materials and Solar Cells*, *93*, 176–182. doi:10.1016/j.solmat.2008.09.048

Goldschmidt, J. C., Peters, M., Dimroth, F., Bett, A. W., Steidl, L., & Zentel, R. … Willeke, G. (2009). Developing large and efficient fluorescent concentrator systems. In *Proceedings of the 24th European Photovoltaic Solar Energy Conference*. Hamburg, Germany: EU PVSEC.

Goldschmidt, J. C., Peters, M., Dimroth, F., Glunz, S. W., & Willeke, G. (2008). Efficiency enhancement of fluorescent concentrators with photonic structures and material combinations. In *Proceedings of the 23rd European Photovoltaic Solar Energy Conference*. Valencia, Spain: EU PVSEC.

Goldschmidt, J. C., Peters, M., Pronneke, L., Steidl, L., Zentel, R., & Blasi, B. (2008). Theoretical and experimental analysis of photonic structures for fluorescent concentrators with increased efficiencies. *Physica Status Solidi. A, Applications and Materials Science*, *205*, 2811–2821. doi:10.1002/pssa.200880456

Grabowski, L. (1914). On the theoretical photometry of diffuse reflection. *The Astrophysical Journal*, *39*, 299. doi:10.1086/142086

Hanrahan, P., & Krueger, W. (1993). Reflection from layered surfaces due to subsurface scattering. In *Proceedings of the 20th Annual Conference on Computer Graphics and Interactive Techniques – SIGGRAPH 1993*, (pp. 165–174). SIGGRAPH.

Heidler, K. (1986). Design considerations for the fluorescent planar concentrator / III-V solar cell system. In *Proceedings of the 7th EC Photovoltaic Solar Energy Conference*. Sevilla, Spain: PVSC.

Hermann, A. M. (1982). Luminescent solar concentrators - A review. *Solar Energy*, *29*(4), 323–329. doi:10.1016/0038-092X(82)90247-X

Hyldahl, M. G., Bailey, S. T., & Wittmershaus, B. P. (2009). Photo-stability and performance of CdSe/ZnS quantum dots in luminescent solar concentrators. *Solar Energy*, *83*(4), 566–573. doi:10.1016/j.solener.2008.10.001

IEA. (2009). *Key world energy statistics*. IEA.

Kennedy, M., Mccormack, S. J., Doran, J., & Norton, B. (2007). Modeling the effect of device geometry on concentration ratios of quantum dot solar concentrators. In *Proceedings of the ISES World Solar Congress*, (pp. 1484-1487). Beijing, China: ISES.

Kim, S., Fisher, B., Eisler, H.-J., & Bawendi, M. (2003). Type-II quantum dots: CdTe/CdSe(core/shell) and CdSe/ZnTe(core/shell) heterostructures. *Journal of the American Chemical Society*, *125*, 11466–11467. doi:10.1021/ja0361749

Kittidachachan, P., Danos, L., Meyer, T. J. J., Alderman, N., & Markvart, T. (2007). Photon collection efficiency of fluorescent solar collectors. *CHIMIA International Journal for Chemistry*, *61*, 780–786. doi:10.2533/chimia.2007.780

Krahne, R., Morello, G., Figuerola, A., George, C., Deka, S., & Manna, L. (2011). Physical properties of elongated inorganic nanoparticles. *Physics Reports*, *501*(3–5), 75–221. doi:10.1016/j.physrep.2011.01.001

Loh, E. Jr, & Scalapino, D. J. (1986). Luminescent solar concentrators: Effects of shape on efficiency. *Applied Optics*, *25*(12), 1901–1907. doi:10.1364/AO.25.001901

MacKay, D. (2009). *Sustainable energy without the hot air*. Cambridge, UK: UIT Cambridge Ltd.

MacQueen, R. W., Cheng, Y. Y., Clady, R. G. C. R., & Schmidt, T. W. (2010). Towards an aligned luminophore solar concentrator. *Optics Express*, *18*, A161–A166. doi:10.1364/OE.18.00A161

Maier, S. A., & Atwater, H. A. (2005). Plasmonics: Localization and guiding of electromagnetic energy in metal/dielectric structures. *Journal of Applied Physics*, *98*(1), 011101. doi:10.1063/1.1951057

Mansour, A. F. (1998). Optical efficiency and optical properties of luminescent solar concentrators. *Polymer Testing*, *17*, 333–343. doi:10.1016/S0142-9418(97)00061-5

Maruyama, T. (1999). Wedge-shaped light concentrator using total internal reflection. *Solar Energy Materials and Solar Cells*, *57*, 75–83. doi:10.1016/S0927-0248(98)00173-1

McIntosh, K. R., Yamada, N., & Richards, B. S. (2007). Theoretical comparison of cylindrical and square-planar luminescent solar concentrators. *Applied Physics. B, Lasers and Optics*, *88*(2), 285–290. doi:10.1007/s00340-007-2705-8

Minkowski, C., & Calzaferri, G. (2005). Forster-type energy transfer along a specified axis. *Angewandte Chemie*, *117*, 5325–5329. doi:10.1002/ange.200500431

Mulder, C. L., Reusswig, P. D., Beyler, A. P., Kim, H., Rotschild, C., & Baldo, M. A. (2010). Dye alignment in luminescent solar concentrators: II: Horizontal alignment for energy harvesting in linear polarizers. *Optics Express*, *18*, 91–99. doi:10.1364/OE.18.000A91

Mulder, C. L., Reusswig, P. D., Vel'azquez, A. M., Kim, H., Rotschild, C., & Baldo, M. A. (2010). Dye alignment in luminescent solar concentrators: I: Vertical alignment for improved waveguide coupling. *Optics Express*, *18*, A79. doi:10.1364/OE.18.000A79

Mulder, C. L., Theogarajan, L., Currie, M. J., Mapel, J. K., Baldo, M. A., & Vaughn, M. (2009). Luminescent solar concentrators employing phycobilisomes. *Advanced Materials (Deerfield Beach, Fla.)*, *21*(31), 3181–3185. doi:10.1002/adma.200900148

Murray, C. B., Norris, D. J., & Bawendi, M. G. (1993). Synthesis and characterization of nearly monodisperse CdE (E = sulfur, selenium, tellurium) semiconductor nanocrystallites. *Journal of the American Chemical Society*, *115*, 8706–8715. doi:10.1021/ja00072a025

OECD. (2009). *World energy outlook 2009*. OECD.

Olson, R. W., Loring, R. F., & Fayer, M. D. (1981). Luminescent solar concentrators and the reabsorption problem. *Applied Optics*, *20*, 2934–2940. doi:10.1364/AO.20.002934

Peng, X., Schlamp, M. C., Kadavanich, A. V., & Alivisatos, A. P. (1997). Epitaxial growth of highly luminescent CdSe/CdS core/shell nanocrystals with photostability and electronic accessibility. *Journal of the American Chemical Society*, *119*, 7019–7029. doi:10.1021/ja970754m

Peters, M., Goldschmidt, J. C., Loeper, P., Blasi, B., & Willeke, G. (2008). Light trapping with angular selective filters. In *Proceedings of the 23rd European Photovoltaic Solar Energy Conference*. Valencia, Spain: EU PVSEC.

Pravettoni, M., Farrell, D. J., Chatten, A. J., Bose, R., Kenny, R. P., & Barnham, K. W. J. (2009). External quantum efficiency measurements of luminescent solar concentrators: A study of the impact of backside reflector size and shape. In *Proceedings of the 24th European Photovoltaic Solar Energy Conference*. Hamburg, Germany: EU PVSEC.

Pryce, I. M., Koleske, D. D., Fischer, A. J., & Atwater, H. A. (2010). Plasmonic nanoparticle enhanced photocurrent in GaN/InGaN/GaN quantum well solar cells. *Applied Physics Letters*, *96*(15), 153501. doi:10.1063/1.3377900

Quilitz, J., Koole, R., Slooff, L. H., Chatten, A. J., Bose, R., & Farrell, D. J. (in press). Fabrication and full characterisation of state-of-the-art CdSe quantum dot luminescent solar concentrators. *Solar Energy Materials and Solar Cells*.

Reisfeld, R. (1984). Spectroscopy and nonradiative phenomena of rare earths in glasses: Future applications. *Inorganica Chimica Acta*, *95*, 69–74. doi:10.1016/S0020-1693(00)87369-7

Reisfeld, R. (1987). Industrial applications of rare earths in fiber optics, luminescent solar concentrators and lasers. *Inorganica Chimica Acta*, *140*, 345–350. doi:10.1016/S0020-1693(00)81119-6

Reisfeld, R. (2010). New developments in luminescence for solar energy utilization. *Optical Materials*, *32*, 1–7. doi:10.1016/j.optmat.2010.04.034

Richards, B. S. (2006). Ray-tracing simulations of luminescent solar concentrators containing multiple luminescent species. In *Proceedings of the 21st European Photovoltaic Solar Energy Conference*. Dresden, Germany: EU PVSEC.

Richards, B. S., Shalav, A., & Corkish, R. P. (2004). A low escape-cone-loss luminescent solar concentrator. In *Proceedings of the 19th European Photovoltaic Solar Energy Conference.* EU PVSEC.

Roncali, J., & Garnier, F. (1984). Photon-transport properties of luminescent solar concentrators: Analysis and optimization. *Applied Optics*, *23*, 2809. doi:10.1364/AO.23.002809

Ross, R. T. (1967). Some thermodynamics of photochemical systems. *The Journal of Chemical Physics*, *46*(12), 4590. doi:10.1063/1.1840606

Rowan, B. C., Richards, B. S., Bcrowanhwacuk, E., Robertson, N., Jones, A. C., Richardson, P., & Moudam, O. (2008). Near-infrared emitting lanthanide complexes for luminescent solar concentrators. In *Proceedings of the 23rd European Photovoltaic Solar Energy Conference*. Valencia, Spain: EU PVSEC.

Rowan, B. C., Wilson, L. R., & Richards, B. S. (2009). Visible and near-infrared emitting lanthanide complexes for luminescent solar concentrators. In *Proceedings of the 24th European Photovoltaic Solar Energy Conference*. Hamburg, Germany: EU PVSEC.

Saraidarov, T., Levchenko, V., Grabowska, A., Borowicz, P., & Reisfeld, R. (2010). Non-self-absorbing materials for luminescent solar concentrators (LSC). *Chemical Physics Letters*, *492*, 60–62. doi:10.1016/j.cplett.2010.03.087

Shcherbatyuk, G. V., Inman, R. H., Wang, C., Winston, R., & Ghosh, S. (2010). Viability of using near infrared PbS quantum dots as active materials in luminescent solar concentrators. *Applied Physics Letters*, *96*(19), 191901. doi:10.1063/1.3422485

Slooff, L. H., Bende, E. E., & Budel, T. (2009). The non-fluorescent flat plate concentrator. In *Proceedings of the 24th European Photovoltaic Solar Energy Conference*. Hamburg, Germany: EU PVSEC.

Slooff, L. H., Bende, E. E., Burgers, A. R., Budel, T., Pravettoni, M., & Kenny, R. P. (2008). A luminescent solar concentrator with 7.1% power conversion efficiency. *Physica Status Solidi*, *2*(6), 257–259. doi:10.1002/pssr.200802186

Slooff, L. H., Bende, E. E., Burgers, A. R., Budel, T., Pravettoni, M., & Kenny, R. P. (2008). Supporting information for a luminescent solar concentrator with 7.1% power conversion efficiency. *Physica Status Solidi*, *2*(6).

Slooff, L. H., Budel, T., Burgers, A. R., Bakker, N. J., Danz, R., Meyer, T., & Meyer, A. (2007). The luminescent concentrator: Stability issues. In *Proceedings of the 22nd European Photovoltaic Solar Energy Conference*. EU PVSEC.

Swartz, B. A., Cole, T., & Zewail, A. H. (1977). Photon trapping and energy transfer in multiple-dye plastic matrices: An efficient solar-energy concentrator. *Optics Letters*, *1*, 73–75. doi:10.1364/OL.1.000073

Swift, P. D., & Smith, G. B. (2003). Color considerations in fluorescent solar concentrator stacks. *Applied Optics*, *42*, 5112–5117. doi:10.1364/AO.42.005112

Swift, P. D., Smith, G. B., & Franklin, J. B. (1999). Light-to-light efficiencies in luminescent solar concentrators. In *Proceedings of the SPIE Conference*, (pp. 21-28). SPIE.

Talapin, D. V., Koeppe, R., Gotzinger, S., Kornowski, A., Lupton, J. M., & Rogach, A. L. (2003). Highly emissive colloidal CdSe/CdS heterostructures of mixed dimensionality. *Nano Letters*, *3*(12), 1677–1681. doi:10.1021/nl034815s

Talapin, D. V., Nelson, J. H., Shevchenko, E. V., Aloni, S., Sadtler, B., & Alivisatos, A. P. (2007). Seeded growth of highly luminescent CdSe/CdS nanoheterostructures with rod and tetrapod morphologies. *Nano Letters*, *7*(10), 2951–2959. doi:10.1021/nl072003g

Verbunt, P. P. C., Bastiaansen, C. W. M., Broer, D. J., & Debije, M. G. (2009). The effect of dyes aligned by liquid crystals on luminescent solar concentrator performance. In *Proceedings of the 24th European Photovoltaic Solar Energy Conference*. Hamburg, Germany: EU PVSEC.

Verbunt, P. P. C., Kaiser, A., Hermans, K., Bastiaansen, C. W. M., Broer, D. J., & Debije, M. G. (2009). Controlling light emission in luminescent solar concentrators through use of dye molecules aligned in a planar manner by liquid crystals. *Advanced Functional Materials*, *19*, 2714–2719. doi:10.1002/adfm.200900542

Weber, W. H., & Lambe, J. (1976). Luminescent greenhouse collector for solar radiation. *Applied Optics*, *15*, 2299. doi:10.1364/AO.15.002299

Wilson, H. R. (1987). Fluorescent dyes interacting with small silver particles: A system extending the spectral range of fluorescent solar concentrators. *Solar Energy Materials*, *16*, 223–234. doi:10.1016/0165-1633(87)90022-0

Wilson, H. R. (1988). Fluorescent quantum yields and long-term stability of silver island/polymer/dye systems, with applications to longer wavelength fluorescent solar concentrators. In *Proceedings of SPIE Conference*. Hamburg, Germany: SPIE.

Wilson, L. R., & Richards, B. S. (2008). High-efficiency dyes for luminescent solar concentrators - Photostability and modeling. In *Proceedings of the 23rd European Photovoltaic Solar Energy Conference*. Valencia, Spain: EU PVSEC.

Wilson, L. R., Rowan, B. C., Robertson, N., Moudam, O., Jones, A. C., & Richards, B. S. (2010). Characterization and reduction of reabsorption losses in luminescent solar concentrators. *Applied Optics*, *49*, 1651. doi:10.1364/AO.49.001651

Wittwer, V., Stahl, W., & Goetzberger, A. (1984). Fluorescent planar concentrators. *Solar Energy Materials*, *11*, 187–197. doi:10.1016/0165-1633(84)90070-4

World Bank. (2008). *World development indicators 2008*. Washington, DC: World Bank.

Yablonovitch, E. (1980). Thermodynamics of the fluorescent planar concentrator. *Journal of the Optical Society of America*, *70*(11), 1362–1363. doi:10.1364/JOSA.70.001362

Yablonovitch, E. (1993). Photonic band-gap structures. *Journal of the Optical Society of America. B, Optical Physics*, *10*, 283. doi:10.1364/JOSAB.10.000283

Zhang, Y., Aslan, K., Previte, M. J. R., & Geddes, C. D. (2007). Metal-enhanced fluorescence: Surface plasmons can radiate a fluorophores structured emission. *Applied Physics Letters*, *90*(5), 053107. doi:10.1063/1.2435661

Zhou, X., Kobayashi, Y., Romanyuk, V., Ochuchi, N., Takeda, M., Tsunekawa, S., & Kasuya, A. (2005). Preparation of silica encapsulated CdSe quantum dots in aqueous solution with the improved optical properties. *Applied Surface Science*, *242*(3-4), 281–286. doi:10.1016/j.apsusc.2004.08.022

Chapter 14
Prospects and Strategy of Development for Advanced Solar Cells

Laurentiu Fara
Polytechnic University of Bucharest, Romania & Academy of Romanian Scientists, Romania

Masafumi Yamaguchi
Toyota Technological Institute (TTI), Japan

ABSTRACT

This chapter presents the necessity for developing high performance, low-cost, and highly reliable solar cells in order to further deployment of photovoltaics, as well as the prospects and strategies for developing advanced solar cells.

1. IMPORTANCE OF SOLAR PHOTOVOLTAICS

As described in chapter 1, solar energy, including solar Photovoltaics (PV), is the only renewable energy resource that has enough terrestrial energy potential to satisfy a 20 TW or more carbon-free supply, because from the $1.2x10^5$ TW (the solar constant is $1.76x10^5$ TW) of solar energy that strikes the Earth's surface, a practical sitting-constrained terrestrial global solar power potential value is about 600 TW, and thus, for a 10% efficient solar farm, at least 60 TW of power could be supplied from terrestrial solar energy resources (Lewis, 2005). According to the World Energy Vision 2100 recommended by WBGU (German Advisory Council on Global Change) (WBGU, 2003), as shown in Figure 1, solar electricity, including PV, is expected to become a major energy source with about 20% of the market in 2050 and about 70% in 2100. That means PV will play an important role to contributing to solving global environmental problems.

On March 11, 2011, heavy earthquakes and a tsunami struck the northeast region of Japan, damaging the Fukushima nuclear power plant No. 1, which now emits higher levels of radiation.

DOI: 10.4018/978-1-4666-1927-2.ch014

Figure 2 shows changes in radiation levels in the northeast and Tokyo areas via distance from the Fukushima nuclear power plant reactor. Figure 3 shows changes in radiation levels in northeast of Japan and Tokyo areas via time (days) since March 15, 2011.

From Figures 2 and 3 we see that people must to live 30 km away from the center of the nuclear power plant in order to be safe from severe radiation exposure. Currently in Japan, 54 nuclear power plants are in operation and an additional 14 plants are planned. However, if almost all the nuclear power generating plants in Japan are heavily damaged in a similar way, it is presumed that possible living areas in Japan are reduced into 1/2 – 2/3 of the country, as shown in Figure 4.

Therefore, further installation of nuclear power plants in Japan will be quite difficult, and further deployment of clean renewable energies, such as solar photovoltaics, will be necessary in order to create a low carbon society.

In order to overcome clean energy supply problems due to possible nuclear power plant crises, further deployment of PV power generating systems as well as further development in science and technology of PV are very important. Very large scale installation of PV power generating systems and further improvements in conversion efficiencies and reliability and lowering the cost of solar cells and modules are necessary.

This chapter presents prospects and strategies for developing advanced solar cells that are highly efficient, lower cost, and highly reliable.

2. FURTHER COST REDUCTION OF SOLAR CELLS, MODULES, AND SYSTEMS

Cost reduction of solar cell modules is very important for large-scale penetration of PV as a primary energy source. Figure 5 shows a comparison of the projected module price with an extension of the historical experience curve (Swanson, 2006). According to the historical experience curve, a price of $1.40/W will be obtained in 2012. A module price of $1.40/W, coupled with a system price of twice ($2.80/W) should result in a cost-effective grid-connected market in many locations. That means that crystalline Si is expected to still be the dominant technology in 10 years.

Since low cost mass production technologies of CdTe solar cell modules with cost of $0.87/W have already been developed, there are several thin-film technologies that are rapidly gaining market share. Figure 6 shows a comparison of the projected system price for crystalline Si PV, thin film PV, and wind systems with an extension of the historical experience curve (Kondo, 2009).

In addition, concentrator PV is also expected to contribute to large-scale power generation systems. Figure 7 shows a comparison of the projected module price for crystalline Si solar cell modules and III-V compound Concentrator PV (III-V CPV) with an extension of the historical experience curve (Luther, Bett, Burger, & Dimroth, 2006). Dye-sensitized, organic, and new types of solar cells may also present great potential for further lowering cost.

These suggest cost reduction of solar cells, modules, and systems by new technology as well as their mass production.

3. FURTHER DEVELOPMENT OF HIGHER EFFICIENCY SOLAR CELLS

A rapid growth in PV system installation creates a need for the development of higher efficiency and lower cost solar cell modules. Table 1 shows an efficiency table of crystalline Si, thin film Si, CIGS, CdTe, III-V compounds, and concentrator, dye-sensitized, and organic solar cells reported in Green, Emery, Hishikawa, and Warta (2011). Although crystalline Si solar cells are mainly used for terrestrial power applications, various types of solar cells are studied and developed,

Figure 1. Transforming the global energy mix: primary energy supply until 2050/2010 (WBGU, 2003)

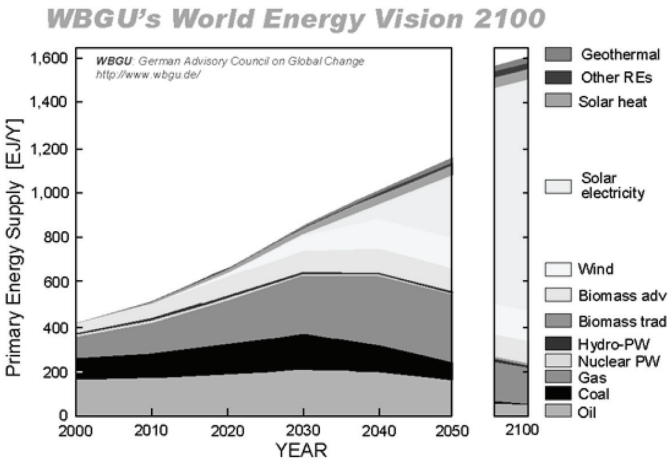

Figure 2. Changes in radiation levels in northeast and Tokyo areas via distance from the Fukushima nuclear power plant reactor

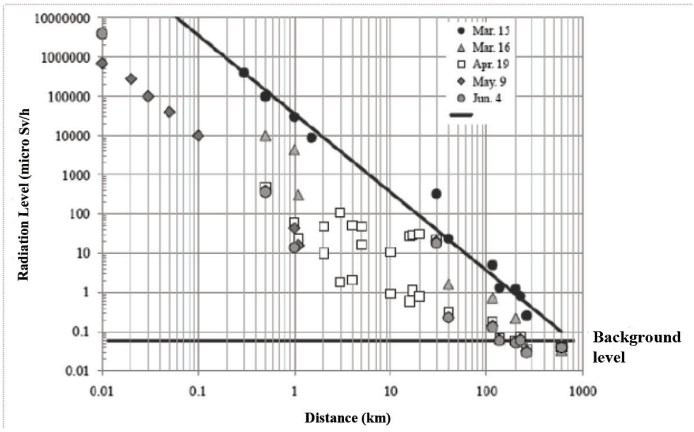

Figure 3. Changes in radiation levels in northeast areas via time (days) since March 15, 2011.

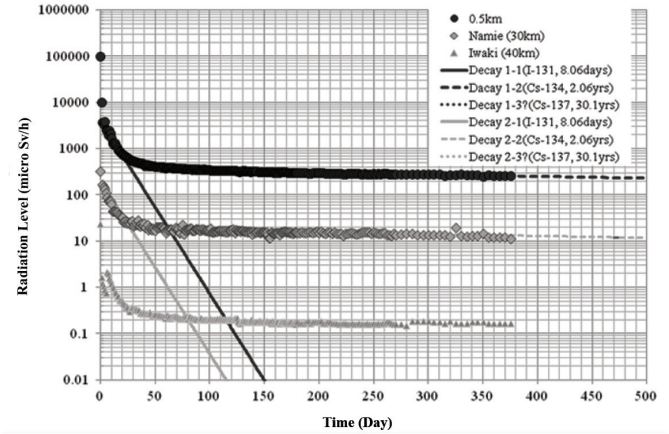

Figure 4. Dark circles show areas with projected severe radiation levels; white circles show planned nuclear power plants

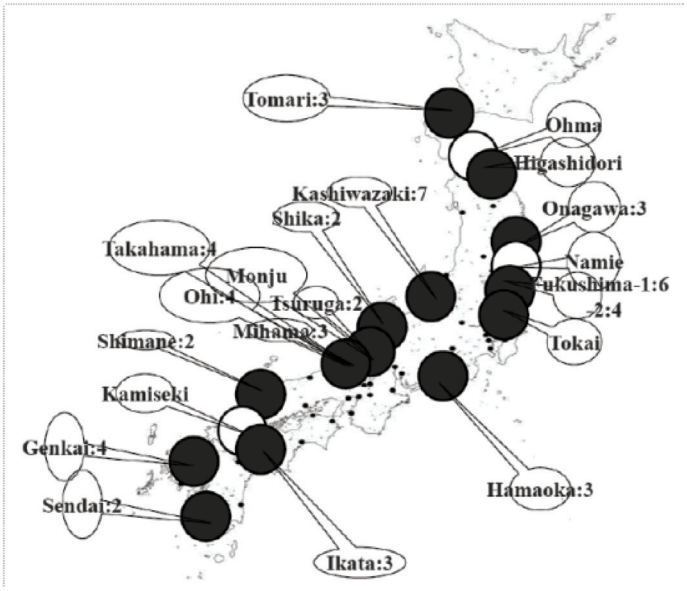

Figure 5. Comparison of the projected module price with an extension of the historical experience curve

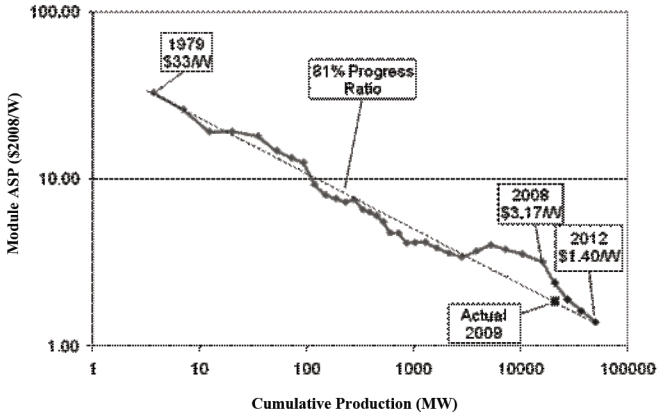

especially III-V compound Multi-Junction (MJ) and concentrator solar cells. 41.6% efficiency at 364-suns has been reported with InGaP/GaAs/Ge 3-junction concentrator cells by Spectrolab (King, et al., 2009). 35.8% efficiency at 1-sun AM1.5G has also been reported with inverted epitaxially grown InGaP/GaAs/InGaAs 3-junction solar cells by Sharp (Takamoto, et al., (2010).

Increasing conversion efficiencies of solar cells has huge positive impacts throughout the entire value chain and means less material, less glass and other module materials, and less installation cost. Although much R&D for various types of solar cells has been carried out and improvements in their conversion efficiencies have been achieved, conversion efficiencies of almost all

the solar cells are expected to have limitations. Figure 8 shows future efficiency predictions of various solar cells (original idea by Goetzberger, Luther, and Willeke [2001] and modified by Yamaguchi [2004]). According to efficiency predictions shown in Figure 8, limiting efficiencies are predicted to be 28.9%, 23.5%, 23.5%, 17.5%, and 16% for crystalline Si, thin-film Si, CIGS as well as CdTe, dye-sensitized, and organic solar cells, respectively. On the other hand, because 41.6% efficiency has been realized with concentrator InGaP/InGaAs/Ge 3-junction solar cells, concentrator 4-junction or 5-junction solar cells have great potential for realizing an efficiency of over 50%. In addition, developing new types of solar cells based on new materials and new concepts is also very important to overcome conversion efficiency limitations.

Figure 6. Comparison of the projected system price for crystalline Si PV, thin film PV, and wind systems with an extension of the historical experience curve

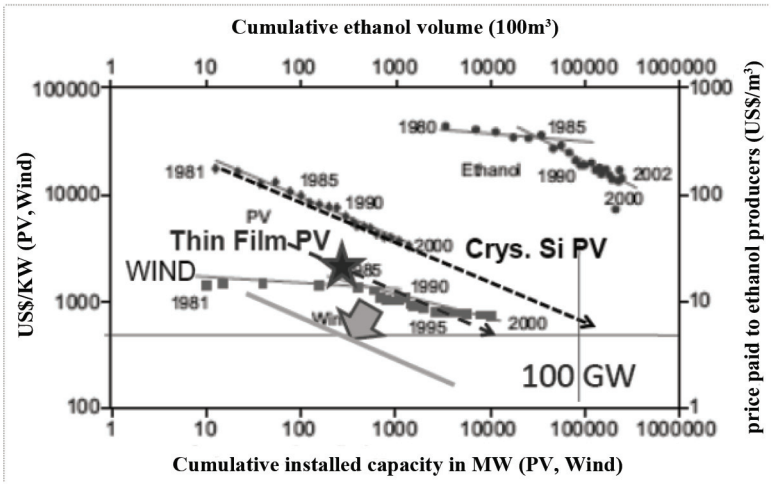

Figure 7. Comparison of the projected module price for crystalline Si solar cell modules and III-V compound Concentrator PV (III-V CPV) with an extension of the historical experience curve

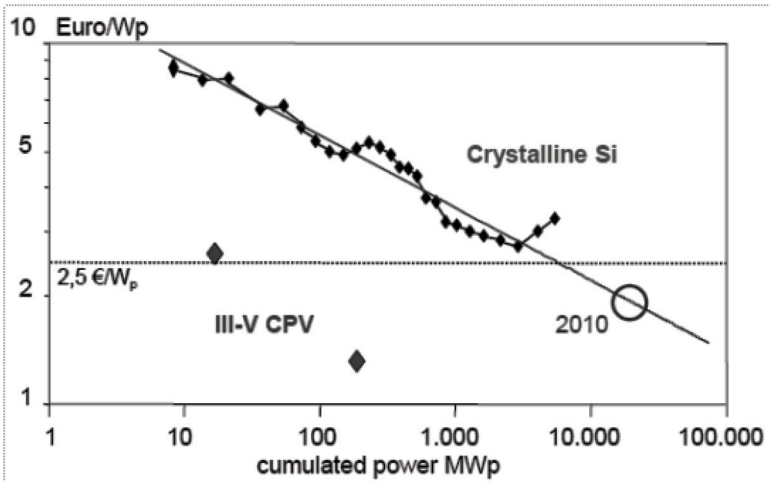

Table 1. Efficiency table of crystalline Si, thin film Si, CIGS, CdTe, dye-sensitized and organic solar cells (Green, Emery, Hishikawa, & Warta, 2011)

Classification	Effic. (%)	Area (cm^2)	Voc (V)	Jsc (mA/cm^2)	FF (%)	Test Centre (date)	Description
Si (single crystal)	25.0±0.5	4.00(da)	0.706	42.7	82.8	Sandia(3/99)	UNSW
Si (multicrystal)	20.4±0.5	1.002(ap)	0.664	38.0	80.9	NREL(5/04)	FhG-ISE
a-Si	9.6±0.3	1.070(ap)	0.859	17.6	63.0	NREL(4/03)	U.Neuchatel
a-Si/nc-Si /nc-Si(tandem)	12.5±0.7	0.27(da)	2.011	9.11	68.4	NREL(3/09)	United Solar stabilized
a-Si/mc-Si (tandem)	11.9±0.8	1.227	1.346	12.92	68.5	NREL(8/10)	Oerlikon
a-Si/mc-Si (tandem)	11.7±0.4	14.23(ap)	5.462	2.99	71.3	AIST(9/04)	Kaneka
CIGS	20.3±0.6	0.5015(ap)	0.740	35.4	77.5	FhG-ISE(6/10)	ZSW
CdTe	16.7±0.5	1.032(ap)	0.845	26.1	75.5	NREL(9/01)	NREL
GaAs	27.6±0.8	0.9989(ap)	1.107	29.6	84.1	NREL(11/10)	Alta Devices
InP	22.1±0.7	4.02(t)	0.878	29.5	85.4	NREL(4/90)	Spire
GaInP/GaInAs /Ge 3-J (concentration)	41.6±2.5 364-suns	0.3174(da)	3.192	1.696A	88.74	NREL(8/09)	Spectrolab
InGaP/GaAs /InGaAs 3-J (1-sun)	35.8±1.5	0.880(ap)	3.012	13.9	86.3	AIST(9/09)	Sharp
Dye-sensitized	11.2±0.3	0.219(ap)	0.736	21	72.2	AIST(3/06)	Sharp
Organic polymer	8.3±0.3	1.031(ap)	0.816	14.46	70.2	NREL(11/10)	Konarka

(da)=designated illumination area, (ap)=aperture area, (t)=total area.

3.1. Most Realistic Approaches

One of the most realistic approaches to overcoming the Shockley-Queisser conversion efficiency limit (Shockley & Queisser, 1961) of 31% at 1-sun and 41% under concentration for single bandgap solar cells is the III-V compound MJ and concentrator solar cells. III-V compound Multi-Junction (MJ) and concentrator solar cells have great potential of more than 50%, as shown in Figure 8, because 41.6% efficiency at 364-suns with InGaP/GaAs/Ge 3-junction concentrator cells by Spectrolab and 35.8% efficiency at 1-sun AM1.5G with inverted epitaxially grown InGaP/GaAs/InGaAs 3-junction solar cells by Sharp have already been achieved. Table 2 shows theoretical conversion efficiencies of MJ solar cells at 1-sun and under concentration in an ideal case. As shown in Table 2, III-V compound Multi-Junction (MJ) and concentrator solar cells have a potential of more than 50%.

Figure 9 shows concepts for increasing conversion efficiency of III-V compound multi-junction solar cells in the future (Luther, Bett, Burger, & Dimroth, 2006).

3.2 New Concepts

Third generation solar cells proposed by Green (2003) are solar cells that are potentially able to overcome the Shockley-Queisser conversion efficiency limit (Shockley & Queisser, 1961). In addition to multi-layer multi-junction (tandem) so-

Figure 8. Future efficiency predictions of various solar cells

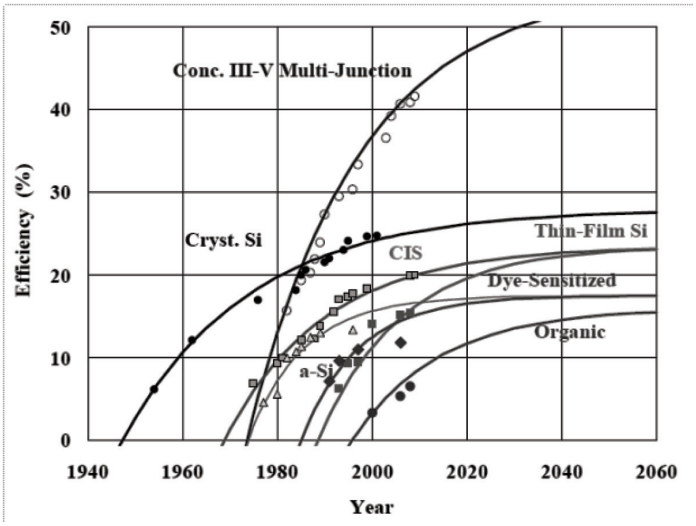

Figure 9. Concepts for increasing conversion efficiency of III-V compound multi-junction solar cells in the future (Luther, Bett, Burger, & Dimroth, 2006)

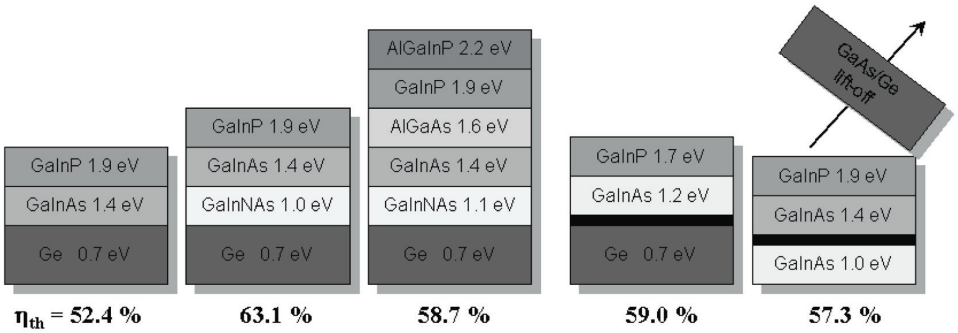

lar cells described in section 3.1, third-generation systems include intermediate bands, hot-carrier effects, and other multiple-carrier ejection.

As shown in Table 3, several ideas (Martí & Luque, 2003) have been proposed to overcome the Shockley-Queisser conversion efficiency limit. Although conversion efficiencies predicted in ideal cases are 85-87% for multiple excitation, hot carrier, intermediate band concepts, realistic conversion efficiencies to be obtained for solar cells by using the above concepts may be less than 55% by considering possible efficiency based on the realistic multi-junction (tandem) concept. However, further fundamental researches for solar cells and materials based on new concepts and fundamental understanding for new concepts is necessary for realizing higher efficiency.

4. SUMMARY

Photovoltaic (PV) power generation technology is one of the most promising renewable energy technologies because of its possibility of solving

Table 2. Theoretical efficiencies of multi-junction solar cells in ideal case

Number of junction	Conversion efficiency under 1-sun	Conversion efficiency under concentrator
1	30.8%	40.8%
2	42.9%	55.7%
3	49.3%	63.8%
4	68.2%	86.8%

Table 3. Efficiency potential (ideal case) of 3rd generation PV technologies

Concept	Year proposed	Conversion efficiency in ideal case
Multi-junction (tandem)	1955	86.8%
Multiple excitation	1972	85.4%
Hot carrier	1981	86.2%
Multi band (intermediate band)	1997	86.8%
Quantum well	1990	60%
Impurity band PV	1960	63%

environmental problems and limited sources for energy. In order to realize widespread deployment of solar photovoltaics and contribute to further development in civilization, further development in science and technology of PV is very important. That is, further improvements in conversion efficiencies and reliability, and lowering cost of solar cells and modules are necessary. Regarding conversion efficiencies of solar cells, because there is the Shockley-Queisser conversion efficiency limit of 31% at 1-sun and 41% under concentration for single bandgap solar cells, several approaches to overcome the Shockley-Queisser limit should be made.

Although much R&D for various types of solar cells has been carried out and improvements in conversion efficiencies have been achieved, conversion efficiencies of almost all the solar cells are expected to have limitations. Limiting efficiencies are expected to be 28.9%, 23.5%, 23.5%, 17.5%, and 16% for crystalline Si, thin-film Si, CIGS, as well as CdTe, dye-sensitized, and organic solar cells, respectively. On the other hand, because 41.6% efficiency has been realized with concentrator InGaP/InGaAs/Ge 3-junction solar cells, concentrator 4-junction or 5-junction solar cells have great potential for realizing efficiency of over 50%. In addition, developing new types of solar cells based on new materials and new concepts is also very important to overcoming the conversion efficiency limitations. In addition to multi-layer multi-junction (tandem) solar cells, third-generation PV systems include intermediate bands, hot-carrier effects, and other multiple-carrier ejection. Although conversion efficiencies in ideal cases are 85%-87% for multiple excitation, hot carrier, intermediate band concepts, realistic conversion efficiencies to be obtained for solar cells by using the above concepts may be less than 55% when considering the possible efficiency based on the realistic multi-junction (tandem) concept. However, further R&D for new materials and new concepts is necessary to overcome the Shockley-Queisser limit.

Figure 10 shows efficiency/cost per unit area regimes for current crystalline Si, thin film PV, and short, midterm, and long-term targets. Since cost studies of any thin-film to date have shown large volume costs below US$100/m^2, this would seem a reasonable prospect for short, mid-, and long-term targets.

Figure 11 shows the PV market forecast made by the IEA (International Energy Agency) PV Power System Experts Task 8 Group (Kurokawa, 2009). As a result of further development for science and technology of advanced solar cells and modules, higher efficiency, lower costs, and highly reliable solar cells will be developed, and thus, a very large PV market is forecasted to be realized (as shown in Figure 11).

Figure 10. Efficiency/cost per unit area regimes for current crystalline Si, thin film PV, and short, mid-term, and long-term targets

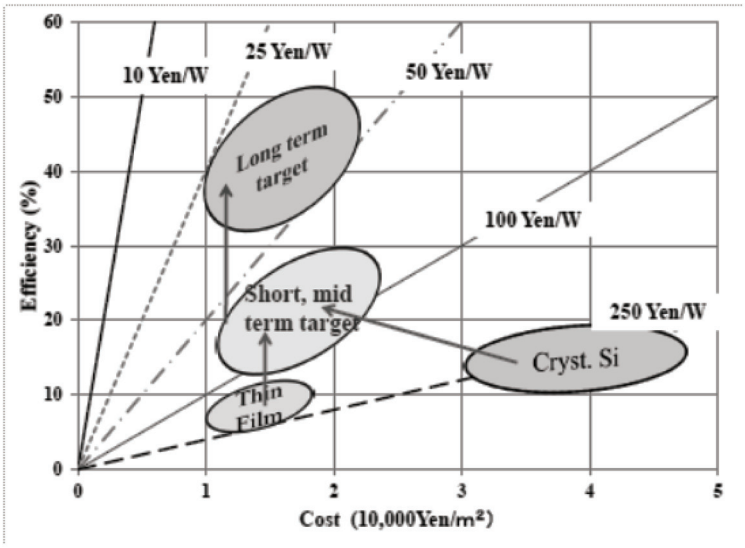

Figure 11. PV market forecast made by the IEA PV power system experts task 8 group (Kurokawa, 2009)

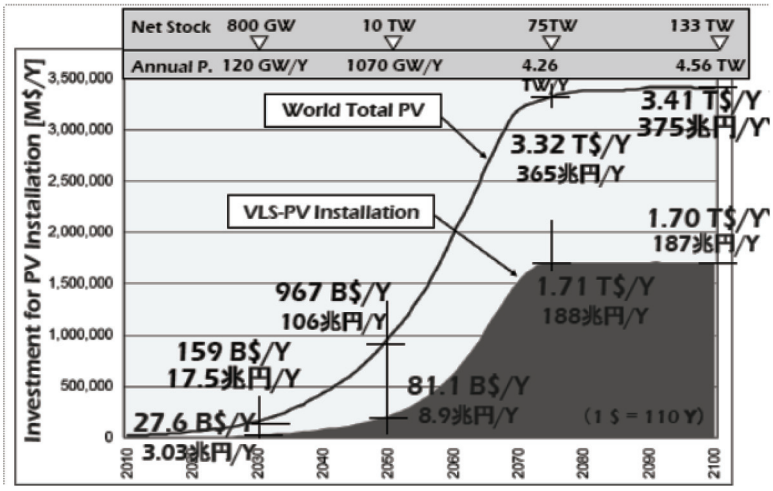

REFERENCES

Goetzberger, A., Luther, J., & Willeke, G. (2001). Paper. In *Proceedings of the 12th International Photovoltaic Science and Engineering Conference,* (p. 5). Taejon, Korea: KIER.

Green, M. (2003). *Third generation photovoltaics: Advanced solar energy conversion*. Berlin, Germany: Springer.

Green, M. A., Emery, K., Hishikawa, Y., & Warta, W. (2011). Solar cell efficiency tables. *Progress in Photovoltaics: Research and Applications*, *19*, 84.

King, R. R., Boca, A., Hong, W., Liu, X.-Q., Bhusari, D., & Larrabee, D. … Karam, N. H. (2009). Paper. In *Proceedings of the 24th European Photovoltaic Solar Energy Conference*, (p. 55). Munich, Germany: WIP.

Kondo, M. (2009). *Paper.* Paper presented at the 19th International Photovoltaic Science and Engineering Conference. Jeju, Korea.

Kurokawa, K. (2009). Paper. *Paper presented at the 34th IEEE Photovoltaic Specialists Conference.* Philadelphia, PA.

Lewis, N. S. (2005). *Radial pn junction nanorod solar cells: device physics principles and routes to fabrication in silicon.* Paper presented at the 31st IEEE Photovoltaic Specialists Conference. Miami, FL.

Luther, J., Bett, A. W., Burger, B., & Dimroth, F. (2006). Paper. In *Proceedings of the 21st European Photovoltaic Solar Energy Conference,* (p. 2054). Munich, Germany: WIP.

Martí, A., & Luque, A. (Eds.). (2003). *Next generation photovoltaics: High efficiency through full spectrum utilization*. Bristol, UK: Institute of Physics Publishing.

Shockley, W., & Queisser, H. J. (1961). Detailed balance limit of efficiency of *p-n* junction solar cells. *Journal of Applied Physics*, *32*, 510. doi:10.1063/1.1736034

Swanson, R. M. (2006). A vision for crystalline silicon photovoltaics. *Progress in Photovoltaics: Research and Applications*, *14*, 443.

Takamoto, T., Agui, T., Yoshida, A., Nakaido, K., Juso, H., & Sasaki, K. … Takahashi, M. (2010). Paper. In *Proceedings of the 35th IEEE Photovoltaic Specialists Conference* (p. 412). New York, NY: IEEE Press.

WBGU. (2003). *World in transition – Towards sustainable energy systems*. London, UK: Earthsan.

Yamaguchi, M. (2004). Paper. In *Proceedings of the 19th European Photovoltaic Solar Energy Conference* (p. xl). Munich, Germany: WIP.

Compilation of References

Abbott, P. (2003). *Characterisation of quantum well solar cells for low temperature thermophotovoltaic applications*. Ph.D. Thesis. London, UK: University of London.

Ackermann, J., Videlot, C., El Kassmi, A., Guglielmetti, R., & Fages, F. (2005). Highly efficient hybrid solar cells based on an octithiophene–GaAs heterojunction. *Advanced Functional Materials*, *15*(5), 810–817. doi:10.1002/adfm.200305142

Adachi, S. (1994). *GaAs and related materials: Bulk semiconducting and superlattice properties*. Singapore: World Scienti□c.

Adachi, M., Murata, Y., Okada, I., & Yoshikawa, S. (2003). Formation of titania nanotubes and applications for dye-sensitized solar cells. *Journal of the Electrochemical Society*, *150*, G488–G493. doi:10.1149/1.1589763

Adachi, M., Okada, I., Ngamsinlapasathian, S., Murata, Y., & Yoshikawa, S. (2002). Dye-sensitized solar cells using semiconductor thin film composed of titania nanotubes. *Electrochemistry*, *70*, 449–452.

Adachi, S. (1992). *Physical properties of III – V semiconductor compounds: InP, InAs, GaAs, GaP, InGaAs, and InGaAsP*. New York, NY: Wiley. doi:10.1002/352760281X

Adams, J. G. J., Elder, W., Hill, G., Roberts, J. S., Barnham, K. W. J., & Ekins-Daukes, N. J. (2010). Higher limiting efficiencies for nanostructured solar cells. In B. Witzigmann, F. Henneberger, Y. Arakawa, & M. Osinski (Eds.), *Proceedings of the SPIE Photonics West 2010 Conference*, (Vol 7597), (pp. 759705-759705-9). Bellingham, WA: SPIE.

Adams, J. G. J., Browne, B. C., Ballard, I. M., Connolly, J. P., & Chan, N. L. A., Ioannides, … Ekins-Daukes, N. J. (2011). Recent results for single-junction and tandem quantum well solar cells. *Progress in Photovoltaics: Research and Applications*, *19*(7), 865–877. doi:10.1002/pip.1069

Aeberhard, U., & Morf, R. H. (2008). Microscopic nonequilibrium theory of quantum well solar cells. *Physical Review B: Condensed Matter and Materials Physics*, *77*(12), 125–343. doi:10.1103/PhysRevB.77.125343

Aernouts, T. (2006). *Organic bulk heterojunction solar cells: From single cell towards fully flexible photovoltaic module*. PhD Thesis. Belgium, The Netherlands: Katholieke Universiteit Leuven. Retrieved from https://lirias.kuleuven.be/bitstream/1979/402/5/PhDþThesisþTomþAernoutsþ18-09-06.pdf

Agachi, S. (1985). GaAs, AlAs, and $Al_xGa_{1-x}As$@B: Material parameters for use in research and device applications. *Journal of Applied Physics*, *58*(3).

Agnaldo, J. S., Cressoni, J. C., & Viswanathan, G. M. (2009). Universal photocurrent-voltage characteristics of dye sensitized nanocrystalline TiO2 photoelectrochemical cells. *Physical Review B: Condensed Matter and Materials Physics*, *79*(3), 035308. doi:10.1103/PhysRevB.79.035308

Ahrenkiel, R. K., Keyes, B. M., Durbin, S. M., & Gray, J. L. (1993). Paper. In *Proceedings of the 23rd IEEE Photovoltaic Specialists Conference,* (p. 42). New York, NY: IEEE Press.

Akahane, K., Kawamura, T., Okino, K., Koyama, H., Lan, S., & Okada, Y. (1998). Highly packed InGaAs quantum dots on GaAs(311)B. *Applied Physics Letters*, *73*(23), 3411–3413. doi:10.1063/1.122781

Akahane, K., Xu, H., Okada, Y., & Kawabe, M. (2001). Formation of lateral-two-dimensional ordering in self-assembled InGaAs quantum dot on high index substrates. *Physica E, Low-Dimensional Systems and Nanostructures*, *11*, 94. doi:10.1016/S1386-9477(01)00182-5

Akahane, K., Yamamoto, N., & Kawanishi, T. (2010). Fabrication of ultra-high-density InAs quantum dots using the strain-compensation technique. *Physica Status Solidi. A, Applications and Materials Science*, *208*, 425. doi:10.1002/pssa.201000432

Akahane, K., Yamamoto, N., & Tsuchiya, M. (2008). Highly stacked quantum-dot laser fabricated using a strain compensation technique. *Applied Physics Letters*, *93*, 041121. doi:10.1063/1.2968211

Alemu, A., Coaquira, J. A. H., & Freundlich, A. (2006). Dependence of device performance on carrier escape sequence in multi-quantum-well p-i-n solar cells. *Journal of Applied Physics*, *99*(8), 84–506. doi:10.1063/1.2191433

Alfè, D. (1998). *Chianti.* Retrieved from http://chianti.geol.ucl.ac.uk/ dario

Alivisatos, A. P. (1996). Perspectives on the physical chemistry of semiconductor nanocrystals. *Journal of Physical Chemistry*, *100*, 13226–13239. doi:10.1021/jp9535506

Alivisatos, A. P. (1998). Electrical studies of semiconductor-nanocrystal colloids. *MRS Bulletin*, *23*(2).

Al-Mohamad, A. (2004). Solar cells based on two organic layers. *Energy Conversion and Management*, *45*(17), 2661–2665. doi:10.1016/j.enconman.2003.12.005

Alonso, M. I., & Winer, K. (1989). Raman spectra of c-$Si_{1-x}Ge_x$ alloys. *Physical Review B: Condensed Matter and Materials Physics*, *39*, 10056–10062. doi:10.1103/PhysRevB.39.10056

Amano, C., Sugiura, H., Yamamoto, A., & Yamaguchi, M. (1987). Paper. Applied Physics Letters, (n.d), 51.

Anderson, N. G. (1995). Ideal theory of quantum well solar cells. *Journal of Applied Physics*, *78*(3), 1850–1861. doi:10.1063/1.360219

Anderson, N. G. (2002). On quantum well solar cell efficiencies. *Physica E, Low-Dimensional Systems and Nanostructures*, *14*(1-2), 126–131. doi:10.1016/S1386-9477(02)00376-4

Ando, K., Amano, C., Sugiura, H., Yamaguchi, M., & Salates, A. (1987). Nonradiative e-h recombination characteristics of mid-gap electron trap in $Al_xGa_{1-x}As$ (x=0.4) grown by molecular beam epitaxy. *Japanese Journal of Applied Physics*, *26*, L266.

Anni, M., Manna, L., Cingolani, R., Valerini, D., Creti, A., & Lomascolo, M. (2004). Förster energy transfer from blue-emitting polymers to colloidal CdSeZnS core shell quantum dots. *Applied Physics Letters*, *85*(18), 4169. doi:10.1063/1.1814795

Antolín, E., Martí, A., & Luque, A. (2006). *Energy conversion efficiency limit of series connected intermediate band solar cells.* Paper presented at the 21st European Photovoltaic Solar Energy Conference. Dresden, Germany.

Antolín, E., Martí, A., Linares, P. G., Ramiro, I., Hernández, E., & Luque, A. (2010). *Raising the efficiency limit of the GaAs-based intermediate band solar cell through the implementation of a monolithic tandem with an AlGaAs top cell.* Paper presented at the 25th European Photovoltaic Solar Energy Conference. Valencia, Spain.

Antolín, E., Martí, A., Linares, P. G., Ramiro, I., Hernández, E., Farmer, C. D., et al. (2010). *Advances in quantum dot intermediate band solar cells.* Paper presented at the 35th IEEE Photovoltaic Specialists Conference. Hawaii, HI.

Antolín, E. (2010). *Development of experimental techniques for the demonstration of the operation principles of the intermediate band solar cell*. Madrid, Spain: Universidad Politécnica de Madrid.

Antolín, E., Martí, A., Olea, J., Pastor, D., González-Díaz, G., & Mártil, I. (2009). Lifetime recovery in ultrahighly titanium-doped silicon for the implementation of an intermediate band material. *Applied Physics Letters*, *94*(4), 1–3. doi:10.1063/1.3077202

Araki, K., Uozumi, H., Egami, T., Hiramatsu, M., Miyazaki, Y., & Kemmoku, Y. (2005). Development of concentrator modules with dome-shaped fresnel lenses and triplejunction concentrator cells. *Progress in Photovoltaics: Research and Applications*, *13*, 513.

Araujo, G. L., & Martí, A. (1994). Absolute limiting efficiencies for photovoltaic energy conversion. *Solar Energy Materials and Solar Cells*, *33*(2), 213–240. doi:10.1016/0927-0248(94)90209-7

Arici, E., & Saricitci, N. S., & Meissener, D. (2004). Hybrid solar cells. *Encyclopedia of Nanoscience and Nanotechnology, 3*, 929-944.

Attaluni, R. S., Annamalai, S., Posani, K. T., Stintz, A., & Krishna, S. (2006). Influence of Si doping on the performance of quantum dots-in-well photodetectors. *Journal of Vacuum Science & Technology B Microelectronics and Nanometer Structures*, *24*, 1553. doi:10.1116/1.2190676

Baek, W.-H., Yang, H., Yoon, T.-S., Kang, C. J., Lee, H. H., & Kim, Y.-S. (2009). Effect of P3HT:PCBM concentration in solvent on performances of organic solar cells. *Solar Energy Materials and Solar Cells*, *93*(8), 1263–1267. doi:10.1016/j.solmat.2009.01.019

Bailey, S. T., Lokey, G. E., Hanes, M. S., Shearer, J. D. M., McLafferty, J. B., & Beaumont, G. T. (2007). Optimized excitation energy transfer in a three-dye luminescent solar concentrator. *Solar Energy Materials and Solar Cells*, *91*(1), 67–75. doi:10.1016/j.solmat.2006.07.011

Balenzategui, J., & Chenlo, F. (2005). Measurement and analysis of angular response of bare and encapsulated silicon solar cells. *Solar Energy Materials and Solar Cells*, *86*, 53–83. doi:10.1016/j.solmat.2004.06.007

Barbé, C. J., Arendse, F., Comte, P., Jirousek, M., Lenzmann, F., & Shklover, V. (1997). Nanocrystalline titanium oxide electrodes for photovoltaic applications. *Journal of the American Ceramic Society*, *80*(12), 3157–3171. doi:10.1111/j.1151-2916.1997.tb03245.x

Bardeen, J., Blatt, F. J., & Hall, L. H. (1956). Paper. In *Proceedings of Atlantic City Photoconductivity Conference*. Atlantic City, NJ: John Wiley and Chapman and Hall.

Barnes, T. M., Wu, X., Zhou, J., Duda, A., van de Lagemaat, J., & Coutts, T. J. (2007). Single-wall carbon nanotube networks as a transparent back contact in CdTe solar cells. *Applied Physics Letters*, *90*(24), 243503–243503. doi:10.1063/1.2748078

Barnham, K. W. J., Ballard, I. M., Browne, B. C., Connolly, J. P., Ekins-Daukes, N. J., & Fuhrer, M.…. Rohr, C. (2010). Recent progress in quantum well solar cells. In L. Tsakalakos (Ed.), *Nanotechnology for Photovoltaics,* (pp. 187-210). New York, NY: CRC Press.

Barnham, K. W. J., Ballard, I., Bessiere, A., Barnham, K. W. J., Ballard, I., & Bessiere, A. … Malik, M. A. (2006). Quantum well solar cells and quantum dot concentrators. In T. Soga (Ed.), *Nanostructured Materials for Solar Energy Conversion*, (pp. 517 – 538). London, UK: Elsevier.

Barnham, K. W. J., Ballard, I., Bessière, A., Chatten, A. J., Connolly, J. P., & Ekins-Daukes, N. J. … Malik, M. A. (2006). Quantum well solar cells and quantum dot concentrator. In T. Soga (Ed.), *Nanostructured Materials for Solar Energy Conversion,* (pp. 517-537). Amsterdam, The Netherlands: Elsevier.

Barnham, K. W. J., Ballard, I., & Connolly, J. P. (2002). Quantum well solar cells. *Physica E, Low-Dimensional Systems and Nanostructures*, *14*(1-2), 27–36. doi:10.1016/S1386-9477(02)00356-9

Barnham, K. W. J., Braun, B., Nelson, J., & Paxman, M. (1991). Short-circuit current and energy efficiency enhancement in a low-dimensional structure photovoltaic device. *Applied Physics Letters*, *59*, 135–137. doi:10.1063/1.105553

Barnham, K. W. J., & Duggan, G. (1990). A new approach to high-efficiency multi-band-gap solar cells. *Journal of Applied Physics*, *67*, 3490–3493. doi:10.1063/1.345339

Barnham, K. W. J., & Duggan, G. (1990). Ideal theory of quantum solar cells. *Journal of Applied Physics*, *67*, 3490. doi:10.1063/1.345339

Barnham, K. W. J., Marques, J. L., Hassard, J., & O'Brien, P. (2000). Quantum-dot concentrator and thermodynamic model for the global redshift. *Applied Physics Letters*, *76*(9), 1197. doi:10.1063/1.125981

Bastard, G. (1988). *Wave mechanics applied to semiconductor heterostructures*. Paris, France: Editions de Physique.

Batchelder, J. S., Zewail, A. H., & Cole, T. (1979). Luminescent solar concentrators 1: Theory of operation and techniques for performance evaluation. *Applied Optics*, *18*, 3090–3110. doi:10.1364/AO.18.003090

Batchelder, J. S., Zewail, A. H., & Cole, T. (1981). Luminescent solar concentrators 2: Experimental and theoretical analysis of their possible efficiencies. *Applied Optics*, *20*, 3733. doi:10.1364/AO.20.003733

Beek, W. J. E., Wienk, M. M., & Janssen, R. A. J. (2004). Efficient hybrid solar cells from zinc oxide nanoparticles and a conjugated polymer. *Advanced Materials (Deerfield Beach, Fla.)*, *16*(12), 1009–1013. doi:10.1002/adma.200306659

Beek, W. J. E., Wienk, M. M., & Janssen, R. A. J. (2006). Hybrid solar cells from regioregular polythiophene and ZnO nanoparticles. *Advanced Functional Materials*, *16*(8), 1112–1116. doi:10.1002/adfm.200500573

Behar, D., Rubinstein, I., Hodes, G., Cohen, S., & Cohen, H. (1999). Electrodeposition of CdS quantum dots and their optoelectronic characterization by photoelectrochemical and scanning probe spectroscopies. *Superlattices and Microstructures*, *25*(4), 601–613. doi:10.1006/spmi.1999.0696

Berghoff, B., Suckow, S., Rölver, R., Spangenberg, B., Kurz, H., Sologubenko, A., & Mayer, J. (2010). Quantum wells based on Si/SiO_x stacks for nanostructured absorbers. *Solar Energy Materials and Solar Cells*, *94*(11), 1893–1896. doi:10.1016/j.solmat.2010.06.033

Berginc, M., Filipic, M., Krašovec, U. O., Nerat, M., Campa, A., & Hocevar, M. … Topic, M. (2009). *Electrical model of dye-sensitized solar cells*. Retrieved from http://www.solamon.eu/eng/Publications/Electrical-Model-of-Dye-Sensitized-Solar-Cells

Bett, A. W., et al. (2000). Paper. In *Proceedings of the 24th European Photovoltaic Solar Energy Conference*, (p. 1). WIP.

Bi, D., Wu, F., Yue, W., Guo, Y., Shen, W., & Peng, R. (2010). Device performance correlated with structural properties of vertically aligned nanorod arrays in polymer/ZnO solar cells. *The Journal of Physical Chemistry C*, *114*(32), 13846–13852.

Bi, H., & LaPierre, R. R. (2009). A GaAs nanowire/P3HT hybrid photovoltaic device. *Nanotechnology*, *20*(46), 465205. doi:10.1088/0957-4484/20/46/465205

Bleuse, J. (2004). Optical properties of core/multishell CdSe/Zn(S,Se) nanocrystals. *Physica E, Low-Dimensional Systems and Nanostructures*, *21*(2-4), 331–335. doi:10.1016/j.physe.2003.11.044

Blöchl, P. E. (1994). Projector augmented-wave method. *Physical Review B: Condensed Matter and Materials Physics*, *50*, 17953. doi:10.1103/PhysRevB.50.17953

Blokhin, S. A., Sakharov, A. V., Nadtochy, A. M., Pauysov, A. S., Maximov, M. V., & Ledentsov, N. N. (2009). AlGaAs/GaAs photovoltaic cells with an array of InGaAs QDs. *Semiconductors*, *43*, 514. doi:10.1134/S1063782609040204

Bockelmann, U., & Bastard, G. (1990). Phonon scattering and energy relaxation in two-, one- and zero-dimensional electron gasses. *Physical Review B: Condensed Matter and Materials Physics*, *42*(14), 8947–8951. doi:10.1103/PhysRevB.42.8947

Bokobza, L. (2007). Multiwall carbon nanotube elastomeric composites: A review. *Polymer*, *48*(17), 4907–4920. doi:10.1016/j.polymer.2007.06.046

Bose, R., Farrell, D. J., Chatten, A. J., Pravettoni, M., Buchtemann, A., & Quilitz, J. … Barnham, K. W. J. (2008). Luminescent solar concentrators: Nanorods and raytrace modeling. In Proceedings of the 33rd IEEE Photovolatic Specialists Conference, (pp. 24-28). San Diego, CA: IEEE Press.

Bose, R., Gonzalez, M., Jenkins, P., Walters, R., Morseman, J., & Moss, M. … Barnham, K. W. J. (2010). Resonance energy transfer in luminescent solar concentrators. In *Proceedings of the 35th IEEE Photovoltaic Specialists Conference*. Honolulu, HI: IEEE Press.

Bowers, J. W., Upadhyaya, H. M., Nakada, T., & Tiwari, A. N. (2010). Effects of surface treatments on high mobility ITiO coated glass substrates for dye sensitized solar cells and their tandem solar cell applications. *Solar Energy Materials and Solar Cells*, *94*(4), 691–696. doi:10.1016/j.solmat.2009.10.023

Brabec, C. J., Sariciftci, N. S., & Hummelen, J. C. (2001). Plastic solar cells. *Advanced Functional Materials*, *11*(1), 15–26. doi:10.1002/1616-3028(200102)11:1<15::AID-ADFM15>3.0.CO;2-A

Brabec, C., & Zerza, G., Cerullo, et al. (2001). Tracing photoinduced electron transfer process in conjugated polymer/fullerene bulk heterojunctions in real time. *Chemical Physics Letters*, *340*(3-4), 232–236. doi:10.1016/S0009-2614(01)00431-6

Brown, M. R., Goldhammer, L. J., Goodelle, G. S., Lortz, C. U., Perron, J. N., & Powe, J. S. … Krut, D. D. (1997). Paper. In *Proceedings of the 26th IEEE Photovoltaic Specialists Conference,* (p. 805). New York, NY: IEEE Press.

Brown, P., Takechi, K., & Kamat, P. V. (2008). Single-walled carbon nanotube scaffolds for dye-sensitized solar cells. *The Journal of Physical Chemistry C*, *112*(12), 4776–4782. doi:10.1021/jp7107472

Bube, R. H. (1992). *Photoelectronic properties of semiconductors*. Cambridge, UK: Cambridge University Press.

Burgers, A., Slooff, L. H., Buchtemann, A., & van Roosmalen, J. A. M. (2006). Performance of single layer luminescent concentrators with multiple dyes. In *Proceedings of the 4th World Conference on Photovoltaic Energy Conversion*, (pp. 198-200). Hawaii, HI: IEEE Press.

Burroughes, J. H., Bradley, D. D. C., Brown, A. R., Marks, R. N., Mackay, K., & Friend, R. H. (1990). Light-emitting diodes based on conjugated polymers. *Nature*, *347*(6293), 539–541. doi:10.1038/347539a0

Bushnell, D. B., Tibbits, T. N. D., Barnham, K. W. J., Connolly, J. P., Mazzer, M., & Ekins-Daukes, N. J. (2005). Effect of well number on the performance of quantum-well solar cells. *Journal of Applied Physics*, *97*(12), 124–908. doi:10.1063/1.1946908

Calzaferri, G. (2001). Organic inorganic composites as photonic antenna. *Chimia*, *55*(12), 1009–1013.

Campos, V. B., Das, S. S., & Stroscio, M. A. (1992). Phonon-confinement effect on electron energy loss in one-dimensional quantum wires. *Physical Review B: Condensed Matter and Materials Physics*, *46*, 3849. doi:10.1103/PhysRevB.46.3849

Cao, F., Oskam, G., & Searson, P. C. (1995). A solid state, dye sensitized photoelectrochemical cell. *Journal of Physical Chemistry*, *99*(47), 17071–17073. doi:10.1021/j100047a003

Carbone, L., Nobile, C., De Giorgi, M., Sala, F., Morello, G., & Pompa, P.,…. Manna, L. (2007). Synthesis and micrometer-scale assembly of colloidal CdSe/CdS nanorods prepared by a seeded growth approach. *Nano Letters*, *7*, 2942–2950. doi:10.1021/nl0717661

Carlson, D. E., & Wronski, C. R. (1976). Amorphous silicon solar cell. *Applied Physics Letters*, *28*, 671. doi:10.1063/1.88617

Carroll, D.L., Czerw, R., & Harrisbon, B. (2006). Carbon nanotubepoly(3-octylthiophene) composite photovoltaic cells. *Journal of Nanoscience and Nanotechnology*, *6*, 2204–2207. doi:10.1166/jnn.2006.373

Catchpole, K. R., & Polman, A. (2008). Plasmonic solar cells. *Optics Express*, *16*(26), 21793–21800. doi:10.1364/OE.16.021793

Chatten, A. J., Farrell, D. J., Bose, R., Debije, M. G., Buchtemann, A., & Barnham, K. W. J. (2007). Thermodynamic modelling of luminescent solar concentrators with reduced top surface losses. In *Proceedings of the 22nd European Photovoltaic Solar Energy Conference*. Milan, Italy: EU PVSEC.

Cheng, H. M., & Hsieh, W. F. (2010). High-efficiency metal-free organic-dye-sensitized solar cells with hierarchical ZnO photoelectrode. *Energy and Environmental Science*, *3*(4), 442–447. doi:10.1039/b915725e

Chen, L.-M., Hong, Z., Li, G., & Yang, Y. (2009). Recent progress in polymer solar cells: Manipulation of polymer: Fullerene morphology and the formation of efficient inverted polymer solar cells. *Advanced Materials (Deerfield Beach, Fla.)*, *21*(14-15), 1434–1449. doi:10.1002/adma.200802854

Chia, C. K., Zhang, Y. W., Wong, S. S., Yong, A. M., Chow, S. Y., & Chua, S. J., &d Guo, J. (2007). Saturated dot density of InAs/GaAs self-assembled quantum dots grown at high growth rate. *Applied Physics Letters*, *93*, 161906. doi:10.1063/1.2724776

Chiba, Y., Islam, A., Watanabe, Y., Komiya, R., Koide, N., & Han, L. (2006). dye-sensitized solar cells with conversion efficiency of 11.1%. *Japanese Journal of Applied Physics*, *45*, L638–640. doi:10.1143/JJAP.45.L638

Chitre, S. R. (1978). A high volume cost efficient production macrostructuring process. In *Proceedings of the 14th IEEE 25th IEEE Photovoltaic Specialists Conference*, (pp. 152-154). Washington, DC: IEEE Press.

Chuan, J., Tianze, L., Luan, H., & Xia, Z. (2011). Research on the characteristics of organic solar cells. *Journal of Physics Conference Series*, *276*(1), 012169. doi:10.1088/1742-6596/276/1/012169

Ciurea, M. L., & Iancu, V. (2007). Why the energy levels observed in electrical transport, phototransport and photoluminescence are different? In *Proceedings of CAS 2007: International Semiconductor Conference,* (pp. 41-44). New York, NY: IEEE Press.

Ciurea, M. L. (2008). Trapping phenomena in nanocrystalline semiconductors. In Korkin, A., & Rosei, F. (Eds.), *Nanoelectronics and Photonics* (pp. 191–222). New York, NY: Springer. doi:10.1007/978-0-387-76499-3_8

Ciurea, M. L., Baltog, I., Lazar, M., Iancu, V., Lazanu, S., & Pentia, E. (1998). Electrical behaviour of fresh and stored porous silicon films. *Thin Solid Films*, *325*(1-2), 271–277. doi:10.1016/S0040-6090(98)00429-5

Ciurea, M. L., & Iancu, V. (2010). Quantum confinement in nanometric structures. In Baleanu, D., Guvenc, Z. B., & Machado, J. A. T. (Eds.), *New Trends in Nanotechnology and Fractional Calculus Applications* (pp. 57–67). Berlin, Germany: Springer. doi:10.1007/978-90-481-3293-5_5

Ciurea, M. L., Iancu, V., & Mitroi, M. R. (2007). Trapping phenomena in silicon-based nanocrystalline semiconductors. *Solid-State Electronics*, *51*(10), 1328–1337. doi:10.1016/j.sse.2007.07.002

Ciurea, M. L., Iancu, V., & Stavarache, I. (2006). Quantum confinement modeling of electrical and optical processes in nanocrystalline silicon. *Journal of Optoelectronics and Advanced Materials*, *8*(6), 2156–2160.

Ciurea, M. L., Lazanu, S., Stavarache, I., Lepadatu, A.-M., Iancu, V., & Mitroi, M. R. (2011). Stress-induced traps in multilayered structures. *Journal of Applied Physics*, *109*(1), 13–717. doi:10.1063/1.3525582

Ciurea, M. L., Teodorescu, V. S., Iancu, V., & Balberg, I. (2006). Electronic transport in Si-SiO_2 nanocomposite films. *Chemical Physics Letters*, *423*(1-3), 225–228. doi:10.1016/j.cplett.2006.03.070

Clapp, A. R., Medintz, I. L., Mauro, J. M., Fisher, B. R., Bawendi, M. G., & Mattoussi, H. (2004). Fluorescence resonance energy transfer between quantum dot donors and dye-labeled protein acceptors. *Journal of the American Chemical Society*, *126*(1), 301–310. doi:10.1021/ja037088b

Coakley, K. M., & McGehee, M. D. (2003). Photovoltaic cells made from conjugated polymers infiltrated into mesoporous titania. *Applied Physics Letters*, *83*(16), 3380–3382. doi:10.1063/1.1616197

Coleman, J. N., Khan, U., Blau, W. J., & Gun'ko, Y. K. (2006). Small but strong: A review of the mechanical properties of carbon nanotube-polymer composites. *Carbon*, *44*(9), 1624–1652. doi:10.1016/j.carbon.2006.02.038

Conibeer, G. J., Ekins-Daukes, N., Guillemoles, J. G., & Green, M. A. (2005). Paper. In *Proceedings of the 20th European PV Conference*, (p. 35). Barcelona, Spain: EU PV.

Conibeer, G. J., et al. (2006). Paper. In *Proceedings of 21st Euro PV SEC*. Dresden, Germany, (p. 47). PV SEC.

Conibeer, G. J., König, D., Green, M. A., & Cuillemoles, J. F. (2008). Slowing of carrier cooling in hot carrier solar cells. *Thin Solid Films*, *516*, 6948. doi:10.1016/j.tsf.2007.12.102

Connolly, J. P. (1997). *Modelling and optimising GaAs/$Al_xGa_{1-x}As$ multiple quantum well solar cells*. Ph.D. Thesis. London, UK: University of London.

Connolly, J. P., Ballard, I. M., Barnham, K. W. J., Bushnell, D. B., Tibbits, T. N. D., & Roberts, J. S. (2004). Efficiency limits of quantum well solar cells. In *Proceedings of the 19th European Photovoltaic Solar Energy Conference*, (pp. 355-359). Paris, France: EU PVSEC.

Connolly, J. P., Johnson, D. C., Ballard, I. M., Barnham, K. W. J., Mazzer, M., & Tibbits, T. N. D.... Calder, C. (2007). Mirrored strain-balanced quantum well concentrator cells in the radiative limit. In *Proceedings of the ICSC-4*, (pp. 21-24). ICSC.

Connolly, J. P., Nelson, J., Barnham, K. W. J., Ballard, I., Roberts, C., Roberts, J. S., & Foxon, C. T. (2000). Simulating multiple quantum well solar cells. In *Proceedings of the 28th IEEE Photovoltaic Specialists Conference*, (pp. 1304-1307). Anchorage, AK: IEEE Press.

Contreras, M. A., Barnes, T., van de Lagemaat, J., Rumbles, G., Coutts, T. J., & Weeks, C. (2007). Replacement of transparent conductive oxides by single-wall carbon nanotubes in Cu(In,Ga)Se2-based solar cells. *The Journal of Physical Chemistry C*, *111*(38), 14045–14048. doi:10.1021/jp075507b

Contreras, M. A., Egaas, B., Ramanathan, K., Hiltner, J., Swartzlander, A., Hasoon, F., & Noufi, R. (1999). Progress toward 20% efficiency in Cu(In,Ga)Se2 polycrystalline thin-film solar cells. *Progress in Photovoltaics: Research and Applications*, *7*(4), 311–316. doi:10.1002/(SICI)1099-159X(199907/08)7:4<311::AID-PIP274>3.0.CO;2-G

Crandall, R. S. (1983). Physics of amorphous silicon alloy p-i-n solar cells. *Journal of Applied Physics*, *54*, 7176. doi:10.1063/1.331955

Cuadra, L., Martí, A., & Luque, A. (2000). *Modeling of the absorption coefficients of the intermediate band solar cell.* Paper presented at the 16th European Photovoltaic Solar Energy Conference. Glasgow, UK.

Cuadra, L., Martí, A., & Luque, A. (2004). Influence of the overlap between the absorption coefficients on the efficiency of the intermediate band solar cell. *IEEE Transactions on Electron Devices*, *51*(6), 1002–1007. doi:10.1109/TED.2004.828161

Cui, H.-N., Teixeira, V., Zhang, J., & Lee, H. (2006). Size controlled nano meter phase structure in thin films of blend polythiophene derivatives. *Thin Solid Films*, *515*(1), 301–306. doi:10.1016/j.tsf.2005.12.108

Cummings, F. (2010). *Application of TiO_2 nanotubes in dye-sensitised solar cells for improved charge transport.* Paper presented at the Renewable Energy Photovoltaics, SA Germany Workshop on Photovoltaics. Grahamstown, Germany.

Currie, M. J., Mapel, J. K., Heidel, T. D., Goffri, S., & Baldo, M. A. (2008). Supporting online material for high-efficiency organic solar concentrators for photovoltaics. *Science*, *321*, 226–228. doi:10.1126/science.1158342

Dabbousi, B. O., Rodriguez-Viejo, J., & Mikulec, F. V. (1997). (CdSe) ZnS core shell quantum dots: Synthesis and characterization of a size series of highly luminescent nanocrystallites. *Journal of Physical Chemistry*, *101*, 9463–9475. doi:10.1021/jp971091y

Dahal, S. N., Bremner, S. P., & Honsberg, C. (2010). Identification of candidate material systems for quantum dot solar cells including the effect of strain. *Progress in Photovoltaics: Research and Applications*, *18*(4), 233–239.

Dahal, S. N., Bremner, S. P., & Honsberg, C. B. (2010). Identification of candidate material systems for quantum dot solar cells including the effect of strain. *Progress in Photovoltaics: Research and Applications*, *18*(4), 233–239.

Dang, M. T., Wantz, G., Hirsch, L., & Parneix, J. P. (2009). Solution processing of polymer photovoltaic solar cells in air or under inert atmosphere. *ECS Transactions*, *23*(1), 449–454. doi:10.1149/1.3183750

de Vos, A. (1992). *Endoreversible thermodynamics of solar energy conversion*. Oxford, UK: Oxford University Press.

Debernardi, A. (1998). Phonon linewidth in III-V semiconductors from density-functional perturbation theory. *Physical Review B: Condensed Matter and Materials Physics*, *57*(12), 847.

Debije, M. G., Broer, D. J., & Bastiaansen, C. W. M. (2007). Effect of dye alignment on the output of a luminescent solar concentrator. In *Proceedings of the 22nd European Photovoltaic Solar Energy Conference*, (pp. 87–89). EU PVSEC.

Debije, M. G., van Der Blom, R. H. L., Broer, D. J., & Bastiaansen, C. W. M. (2006). Using selectively reflecting organic mirrors to improve light output from a luminescent solar concentrator. In *Proceedings of the World Renewable Energy Congress IX*. Florence, Italy: IEEE.

Debije, M. G., Van, M. P., Verbunt, P. P. C., Broer, D. J., & Bastiaansen, C. W. M. (2009). The effect of an organic selectively-reflecting mirror on the performance of a luminescent solar concentrator. In *Proceedings of the 24th European Photovoltaic Solar Energy Conference*. Hamburg, Germany: UE PVSEC.

Debije, M. G., Van, M. P., Verbunt, P. P., Kastelijn, M. J., van Der Blom, R. H. L., Broer, D. J., & Bastiaansen, C. W. M. (2010). Effect on the output of a luminescent solar concentrator on application of organic wavelength-selective mirrors. *Applied Optics*, *49*(4), 745–751. doi:10.1364/AO.49.000745

Deb, K. S. (2004). Dye-sensitized TiO_2 thin-film solar cell research at the national renewable energy laboratory (NREL). *Solar Energy Materials and Solar Cells*, *88*(1), 1–10. doi:10.1016/j.solmat.2004.09.007

del Cañizo, C., del Coso, G., & Sinke, W. C. (2009). Crystalline silicon solar module technology: Towards the 1Eur per watt-peak goal. *Progress in Photovoltaics: Research and Applications*, *17*, 199–209. doi:10.1002/pip.878

Dennler, G., Mozer, A. J., Juška, G., Pivrikas, A., Österbacka, R., Fuchsbauer, A., & Sariciftci, N. S. (2006). Charge carrier mobility and lifetime versus composition of conjugated polymer/fullerene bulk-heterojunction solar cells. *Organic Electronics*, *7*, 229–234. doi:10.1016/j.orgel.2006.02.004

Derkacs, D., Chen, W. V., Matheu, P. M., Lim, S. H., Yu, P. K. L., & Yu, E. T. (2008). Nanoparticle-induced light scattering for improved performance of quantum-well solar cells. *Applied Physics Letters*, *93*(9), 91–107. doi:10.1063/1.2973988

Diacon, A., Fara, L., Cincu, C., Mitroi, M. R., Zaharia, C., & Rusen, E. (2010). New materials for hybrid dye-sensitized solar cells. *Optical Materials*, *32*(12), 1583–1586. doi:10.1016/j.optmat.2010.06.003

Dimitrakopoulos, C. D., & Mascaro, D. J. (2001). Organic thin-film transistors: A review of recent advances. *IBM Journal of Research and Development*, *45*, 11–28. doi:10.1147/rd.451.0011

Dolling, G. (1963). Paper. In *Proceedings of the Symposium on Inelastic Scattering Neutrons in Solids and Liquids*, (vol 2), (p. 37). Vienna, Austria: IAEA.

Drechsel, J., Mannig, B., Kozlowski, F., Pfeiffer, M., Leo, K., & Hoppe, H. (2005). Efficient organic solar cells based on a double p-i-n architecture using doped wide-gap transport layers. *Applied Physics Letters*, *86*(24), 244102–244103. doi:10.1063/1.1935771

Earp, A. A., Smith, G. B., Franklin, J., & Swift, P. D. (2004). Optimisation of a three-colour luminescent solar concentrator daylighting system. *Solar Energy Materials*, *84*, 411–426. doi:10.1016/j.solmat.2004.02.046

Earp, A., Smith, G. B., Swift, P. D., & Franklin, J. (2004). Maximising the light output of a luminescent solar concentrator. *Solar Energy*, *76*(6), 655–667. doi:10.1016/j.solener.2004.02.001

Efros, A. L., & Rodina, A. V. (1993). Band-edge absorption and luminescence of nonspherical nanometersize crystals. *Physical Review B: Condensed Matter and Materials Physics*, *47*(15), 10005–10007. doi:10.1103/PhysRevB.47.10005

Ekins-Daukes, N. J., Barnham, K. W. J., Connolly, J. P., Roberts, J. S., Clark, J. C., Hill, G., & Mazzer, M. (1999). Strain-balanced GaAsP/InGaAs quantum well solar cells. *Applied Physics Letters*, *75*(26), 4195–4197. doi:10.1063/1.125580

Ekins-Daukes, N. J., & Schmidt, T. W. (2008). A molecular approach to the intermediate band solar cell: The symmetric case. *Applied Physics Letters*, *93*(6), 063507. doi:10.1063/1.2970157

El-Nahass, M. M., Abd-El-Rahman, K. F., Farag, A. A. M., & Darwish, A. A. A. (2005). Photovoltaic properties of NiPc/p-Si (organic/inorganic) heterojunctions. *Organic Electronics*, *6*(3), 129–136. doi:10.1016/j.orgel.2005.03.007

El-Nahass, M. M., Zeyada, H. M., Aziz, M. S., & El-Ghamaz, N. A. (2005). Carrier transport mechanisms and photovoltaic properties of Au/p-ZnPc/p-Si solar cell. *Solid-State Electronics*, *49*(8), 1314–1319. doi:10.1016/j.sse.2005.06.001

Emery, K., Burdik, J., Cayem, Y., Dunlavy, D., Field, H., Koposki, B., & Moriarty, T. (1996). Paper. In *Proceedings of the 25th IEEE Photovoltaic Specialists Conference,* (pp. 1275-1278). New York, NY: IEEE Press.

EU. (2007). *A strategic research agenda for photovoltaic solar energy technology PV technology platform*. Retrieved from http://www.eupvplatform.org/fileadmin/Documents/PVPT_SRA_Complete_070604.pdf

Evident Technologies. (2002). *Core shell EviDots: High yield, narrow emission, photostable fluorescent labels*. Evident Technologies.

Extance, A. (2010). *The concentrated photovoltaics industry report 2010*. CVP Today.

Fahrenbrunch, A. L., & Bube, R. H. (1983). *Fundamentals of solar cells*. New York, NY: Academic Press.

Fan, J. C. C., Tsaur, B.-Y., & Palm, B. J. (1982). Paper. In *Proceedings of the 16th IEEE Ptotovoltaic Specialists Conference*, (p. 692). New York, NY: IEEE Press.

Fara, L., Mitroi, M. R., Cincu, C., Iancu, V., Zaharia, C., & Fara, S.…. Iancu, M. (2009). *Physics and technology of solar cells and PV systems.* Bucharest, Romania: Romanian Scientists Academy Publishing House.

Fara, L., Iancu, V., Mitroi, M. R., & Nistor, E. (2007). *Physical bases of the nanotechnologies, applications and perspectives*. Bucharest, Romania: Punct.

Fara, L., Mitroi, M. R., Iancu, V., Milescu, G., & Noaje, G. (2008). *Modeling and numerical simulation of nanostructured solar cells*. Bucharest, Romania: Punct Publishing House.

Farrell, D. J. (2008). *Characterising the performance of luminescent solar concentrators.* PhD Thesis. London, UK: Imperial College London.

Ferber, J., & Luther, J. (2001). Modeling of photovoltage and photocurrent in dye-sensitized titanium dioxide solar cells. *The Journal of Physical Chemistry B*, *105*(21), 4895–4903. doi:10.1021/jp002928j

Ferber, J., Stangl, R., & Luther, J. (1998). An electrical model of the dye-sensitized solar cell. *Solar Energy Materials and Solar Cells*, *53*(1-2), 29–54. doi:10.1016/S0927-0248(98)00005-1

Ferry, V. E., Sweatlock, L. A., Pacifici, D., & Atwater, H. A. (2008). Plasmonic nanostructure design for efficient light coupling into solar cells. *Nano Letters*, *8*, 4391–4397. doi:10.1021/nl8022548

Flores, I. C., de Freitas, J. N., Longoa, C., De Paoli, M., Winnischofer, H., & Nogueira, A. F. (2007). Dye-sensitized solar cells based on TiO2 nanotubes and a solid-state electrolyte. *Journal of Photochemistry and Photobiology A Chemistry*, *189*, 153–160. doi:10.1016/j.jphotochem.2007.01.023

Förster, T. (1948). Zwischenmolekulare energiewanderung un fluoreszenz. *Annalen der Physik*, *437*(1-2), 55–75. doi:10.1002/andp.19484370105

Freundlich, A., Fotkatzikis, A., Bhusal, L., Williams, L., Alemu, A., & Zhu, W. (2007). 3-5 dilute nitride-based multi-quantum well solar cell. *Journal of Crystal Growth*, *301-302*, 993–996. doi:10.1016/j.jcrysgro.2006.11.256

Fu, H. X., Ozolins, V., & Zunger, A. (1999). Phonons in GaP quantum dots. *Physical Review B: Condensed Matter and Materials Physics*, *59*, 2881. doi:10.1103/PhysRevB.59.2881

Gao, F., Wang, Y., Shi, D., Zhang, J., Wang, M. K., & Jing, X. Y. (2008). Enhance the optical absorptivity of nanocrystalline TiO_2 film with high molar extinction coefficient ruthenium sensitizers for high performance dye-sensitized solar cells. *Journal of the American Chemical Society*, *130*(32), 10720–10728. doi:10.1021/ja801942j

Garnier, F. (2002). Hybrid organic-on-inorganic photovoltaic devices. *Journal of Optics. A, Pure and Applied Optics*, *4*(6), S247. doi:10.1088/1464-4258/4/6/361

Giannouli, M., Syrrokostas, G., & Yianoulis, P. (2010). Effects of using multi-component electrolytes on the stability and properties of solar cells sensitized with simple organic dyes. *Progress in Photovoltaics: Research and Applications*, *18*(2), 128–136. doi:10.1002/pip.952

Giannozzi, P., De Gironcoli, S., Pavone, P., & Baroni, S. (1991). Ab initio calculation of phonon dispersions in semiconductors. *Physical Review B: Condensed Matter and Materials Physics*, *43*, 7231. doi:10.1103/PhysRevB.43.7231

Ginger, D. S., & Greenham, N. C. (1999a). Charge separation in conjugated-polymer/nanocrystal blends. *Synthetic Metals*, *101*(1-3), 425–428. doi:10.1016/S0379-6779(98)00330-0

Ginger, D. S., & Greenham, N. C. (1999b). Photoinduced electron transfer from conjugated polymers to CdSe nanocrystals. *Physical Review B: Condensed Matter and Materials Physics*, *59*(16), 10622. doi:10.1103/PhysRevB.59.10622

Gledhill, S. E., Scott, B., & Gregg, B. A. (2005). Organic and nano-structured composite photovoltaics: An overview. *Journal of Materials Research*, *20*(12), 3167–3179. doi:10.1557/jmr.2005.0407

Goetzberger, A., Luther, J., & Willeke, G. (2001). Technical digest. In *Proceedings of the 12th International Photovoltaic Science and Engineering Conference*. Taejon, Japan: KIER.

Goetzberger, A. (1978). Fluorescent solar energy collectors: Operating conditions with diffuse light. *Applied Physics (Berlin)*, *16*, 399–404. doi:10.1007/BF00885865

Goetzberger, A., & Schirmer, O. (1979). Second stage concentration with tapers for fluorescent solar collectors. *Applied Physics (Berlin)*, *42*, 712–758.

Goetzberger, A., & Wittwer, V. (1981). Fluorescent planar collector-concentrators: A review. *Solar Cells*, *4*(1), 3–23. doi:10.1016/0379-6787(81)90033-8

Goetzberger, J., Luther, & Willeke, G. (2002). Solar cells: Past, present, future. *Solar Energy Materials and Solar Cells*, *74*, 1. doi:10.1016/S0927-0248(02)00042-9

Goldschmidt, J. C., Peters, M., Dimroth, F., Bett, A. W., Steidl, L., & Zentel, R. … Willeke, G. (2009). Developing large and efficient fluorescent concentrator systems. In *Proceedings of the 24th European Photovoltaic Solar Energy Conference*. Hamburg, Germany: EU PVSEC.

Goldschmidt, J. C., Peters, M., Dimroth, F., Glunz, S. W., & Willeke, G. (2008). Efficiency enhancement of fluorescent concentrators with photonic structures and material combinations. In *Proceedings of the 23rd European Photovoltaic Solar Energy Conference*. Valencia, Spain: EU PVSEC.

Goldschmidt, J. C., Peters, M., Bosch, A., Helmers, H., Dimroth, F., Glunz, S., & Willeke, G. (2009). Increasing the efficiency of fluorescent concentrator systems. *Solar Energy Materials and Solar Cells*, *93*, 176–182. doi:10.1016/j.solmat.2008.09.048

Goldschmidt, J. C., Peters, M., Pronneke, L., Steidl, L., Zentel, R., & Blasi, B. (2008). Theoretical and experimental analysis of photonic structures for fluorescent concentrators with increased efficiencies. *Physica Status Solidi. A, Applications and Materials Science*, *205*, 2811–2821. doi:10.1002/pssa.200880456

González-Díaz, G., Olea, J., Mártil, I., Pastor, D., Martí, A., & Antolín, E. (2009). Intermediate band mobility in heavily titanium-doped silicon layers. *Solar Energy Materials and Solar Cells*, *93*(9), 1668–1673. doi:10.1016/j.solmat.2009.05.014

Gowrishankar, V., Scully, S. R., McGehee, M. D., Wang, Q., & Branz, H. M. (2006). Exciton splitting and carrier transport across the amorphous-silicon/polymer solar cell interface. *Applied Physics Letters*, *89*(25), 252102–252103. doi:10.1063/1.2408641

Grabowski, L. (1914). On the theoretical photometry of diffuse reflection. *The Astrophysical Journal*, *39*, 299. doi:10.1086/142086

Granström, M., Berggren, M., & Inganäs, O. (1995). Micrometer- and nanometer-sized polymeric light-emitting diodes. *Science*, *267*(5203), 1479–1481. doi:10.1126/science.267.5203.1479

Grätzel, M. (2003). Dye-sensitized solar cells. *Journal of Photochemistry and Photobiology C, Photochemistry Reviews*, *4*(2), 145–153. doi:10.1016/S1389-5567(03)00026-1

Gratzel, M. (2004). Conversion of sunlight to electric power by nanocrystalline dye-sensitized solar cells. *Journal of Photochemistry and Photobiology A Chemistry*, *168*(1-3), 235–237. doi:10.1016/j.jphotochem.2004.08.014

Grätzel, M. (2005). Solar Energy Conversion by Dye-Sensitized Photovoltaic Cells. *Inorganic Chemistry*, *44*(20), 6841–6851. doi:10.1021/ic0508371

Grätzel, M. (2006). The advent of mesoscopic injection solar cells. *Progress in Photovoltaics: Research and Applications*, *14*(5), 429. doi:10.1002/pip.712

Greenham, N. C., Peng, X., & Alivisatos, A. P. (1996). Charge separation and transport in conjugated-polymer/semiconductor-nanocrystal composites studied by photoluminescence quenching and photoconductivity. *Physical Review B: Condensed Matter and Materials Physics*, *54*(24), 17628–17637. doi:10.1103/PhysRevB.54.17628

Green, M. (2003). *Third generation photovoltaics: Advanced solar energy conversion*. Berlin, Germany: Springer Science Business Media.

Green, M. A. (1986). *Solar cells: Operating principles, technology and system applications*. Kensington, Australia: University of NSW.

Green, M. A. (1992). *Solar cells: Operating principles, technology and system applications*. Kensington, Australia: University of NSW.

Green, M. A. (2000). Prospects for photovoltaic efficiency enhancement using low-dimensional structures. *Nanotechnology*, *11*, 401–405. doi:10.1088/0957-4484/11/4/342

Green, M. A. (2003). *Third generation photovoltaics - Advanced solar energy conversion*. London, UK: Springer.

Green, M. A., Emery, K., Hishikawa, Y., & Warta, W. (2011). Solar cell efficiency tables (version 37). *Progress in Photovoltaics: Research and Applications*, *19*(1), 84–92. doi:10.1002/pip.1088

Greulich, J., Markus Glatthaar, M., & Rein, S. (2010). Fill factor analysis of solar cells' current–voltage curves. *Progress in Photovoltaics: Research and Applications*, *18*(7), 511–515. doi:10.1002/pip.979

Grimmeiss, H. G., & Koelmans, H. (1961). Analysis of p-n luminescence in Zn-doped GaP. *Physical Review*, *123*(6), 1939. doi:10.1103/PhysRev.123.1939

Guillemoles, J. F., Conibeer, G. J., & Green, M. (2005). Paper. In *Proceedings of the 15th PV SEC*. (p. 375). Shanghai, China: PV SEC.

Günes, S., & Sariciftci, N. S. (2008). Hybrid solar cells. *Inorganica Chimica Acta*, *361*(3), 581–588. doi:10.1016/j.ica.2007.06.042

Gur, I., Fromer, N. A., Chen, C.-P., Kanaras, A. G., & Alivisatos, A. P. (2006). Hybrid solar cells with prescribed nanoscale morphologies based on hyperbranched semiconductor nanocrystals. *Nano Letters*, *7*(2), 409–414. doi:10.1021/nl062660t

Gustafsson, G., Treacy, G. M., Cao, Y., Klavetter, F., Colaneri, N., & Heeger, A. J. (1993). The "plastic" led: A flexible light-emitting device using a polyaniline transparent electrode. *Synthetic Metals*, *57*(1), 4123–4127. doi:10.1016/0379-6779(93)90568-H

Halme, H. (2002). *Dye sensitized nanostructured and organic photovoltaics cell*. PhD Thesis. Espoo, Finland: Espoo University.

Hanrahan, P., & Krueger, W. (1993). Reflection from layered surfaces due to subsurface scattering. In *Proceedings of the 20th Annual Conference on Computer Graphics and Interactive Techniques – SIGGRAPH 1993*, (pp. 165–174). SIGGRAPH.

Hardin, B. E., Hoke, E. T., Armstrong, P. B., Yum, J. H., Comte, P., & Torres, T. (2009). Increased light harvesting in dye-sensitized solar cells with energy relay dyes. *Nature Photonics*, *3*(11), 667. doi:10.1038/nphoton.2009.212

Harrison, P. (2005). *Quantum wells, wires, and dots: Theoretical and computational physics of semiconductor nanostructures*. Chichester, UK: John Wiley & Sons. doi:10.1002/0470010827

Hasobe, T., Fukuzumi, S., & Kamat, P. V. (2006). Stacked-cup carbon nanotubes for photoelectrochemical solar cells. *Angewandte Chemie International Edition*, *45*(5), 755–759. doi:10.1002/anie.200502815

Hauch, J. A., Schilinsky, P., Choulis, S. A., Childers, R., Biele, M., & Brabec, C. J. (2008). Flexible organic P3HT: PCBM bulk-heterojunction modules with more than 1 year outdoor lifetime. *Solar Energy Materials and Solar Cells*, *92*(7), 727–731. doi:10.1016/j.solmat.2008.01.004

Heeger, A. J. (2001). Semiconducting and metallic polymers: The fourth generation of polymeric materials (nobel lecture). *Angewandte Chemie International Edition*, *40*(14), 2591–2611. doi:10.1002/1521-3773(20010716)40:14<2591::AID-ANIE2591>3.0.CO;2-0

Heidler, K. (1986). Design considerations for the fluorescent planar concentrator / III-V solar cell system. In *Proceedings of the 7th EC Photovoltaic Solar Energy Conference*. Sevilla, Spain: PVSC.

Heitmann, J., Müller, F., & Yi, L. X. (2004). Excitons in Si nanocrystals: Confinement and migration effects. *Physical Review B: Condensed Matter and Materials Physics*, *69*, 195–309. doi:10.1103/PhysRevB.69.195309

Heitmann, J., Müller, F., Yi, L. X., Zacharias, M., Kovalev, D., & Eichhorn, F. (2004). Excitons in Si nanocrystals: Confinement and migration effects. *Physical Review B: Condensed Matter and Materials Physics*, *69*(19), 195–309. doi:10.1103/PhysRevB.69.195309

Hermann, A. M. (1982). Luminescent solar concentrators - A review. *Solar Energy*, *29*(4), 323–329. doi:10.1016/0038-092X(82)90247-X

Hiramoto, M., Fujiwara, H., & Yokoyama, M. (1991). Three-layered organic solar cell with a photoactive interlayer of codeposited pigments. *Applied Physics Letters*, *58*(10), 1062–1064. doi:10.1063/1.104423

Hong, Z. R., Maennig, B., & Lessmann, R. (2007). Improved efficiency of zinc phthalocyanine/C60 based photovoltaic cells via nanoscale interface modification. *Applied Physics Letters*, *90*, 230–505. doi:10.1063/1.2739364

Hoppe, H., Drees, M., Schwinger, W., Schaffler, F., & Sariciftcia, N. S. (2005). Nano-crystalline fullerene phases in polymer/fullerene bulk-heterojunction solar cells: A transmission electron microscopy study. *Synthetic Metals*, *152*(1-3), 117–120. doi:10.1016/j.synthmet.2005.07.217

Hoppe, H., Glatzel, T., Niggemann, M., Schwinger, W., Schaeffler, F., & Hinsch, A. (2006). Efficiency limiting morphological factors of MDMO-PPV: PCBM plastic solar cells. *Thin Solid Films*, *511-512*, 587–592. doi:10.1016/j.tsf.2005.12.071

Hovel, H. J. (1975). *Semiconductors and semimetals*. New York, NY: Academic Press.

Hoyer, P., & Masuda, H. (1996). Electrodeposited nanoporous TiO_2 film by a two-step replication process from anodic porous alumina. *Journal of Materials Science Letters*, *15*(14), 1228–1230. doi:10.1007/BF00274383

Hubbard, S. M., Cress, C. D., Bailey, C. G., Raffaelle, R. P., Bailey, S. G., & Wilt, D. M. (2008). Effect of strain compensation on quantum dot enhanced GaAs solar cells. *Applied Physics Letters*, *92*, 123512. doi:10.1063/1.2903699

Hubin, J., & Shah, A. V. (1995). Effect of the recombination function on the collection in a p-i-n solar cell. *Philosophical Magazine B*, *72*, 589. doi:10.1080/01418639508240314

Hu, C., & White, R. M. (1983). *Solar cells: From basic to advanced systems*. New York, NY: McGraw-Hill.

Hutchby, J. A., Markunas, R. J., & Bedair, S. M. (1985). Paper. In *Proceedings of the SPIE, Photovoltaics*, (Vol. 543), (p. 543). SPIE.

Huynh, W. U., Dittmer, J. J., & Alivisatos, A. P. (2002). Hybrid nanorod-polymer solar cells. *Science*, *295*(5564), 2425–2427. doi:10.1126/science.1069156

Hyldahl, M. G., Bailey, S. T., & Wittmershaus, B. P. (2009). Photo-stability and performance of CdSe/ZnS quantum dots in luminescent solar concentrators. *Solar Energy*, *83*(4), 566–573. doi:10.1016/j.solener.2008.10.001

Iancu, V., & Ciurea, M. L. (1998). Quantum confinement model for electric transport phenomena in fresh and stored photoluminescent porous silicon films. *Solid-State Electronics*, *42*(1), 1893–1896. doi:10.1016/S0038-1101(98)00160-9

Iancu, V., Ciurea, M. L., & Stavarache, I. (2006). Quantum confinement modeling of electrical and optical processes in nanocrystalline silicon. *Journal of Optoelectronics and Advanced Materials*, *8*(6), 2156–2160.

Iancu, V., Fara, L., & Mitroi, M. R. (2009). Modeling of multi-layered quantum well photovoltaic cells. *Scientific Bulletin, Series A. Applied Mathematics and Physics*, *71*(4), 53–62.

Iancu, V., Mitroi, M. R., Lepadatu, A.-M., Stavarache, I., & Ciurea, M. L. (2011). Calculation of the quantum efficiency for the absorption on confinement levels in quantum dots. *Journal of Nanoparticle Research*, *13*(4), 1605–1612. doi:10.1007/s11051-010-9913-6

IEA. (2009). *Key world energy statistics*. IEA.

Inaji, T., Ohta, J., & Yamaguchi, K. (2010). Stacking growth of in-plane InAs quantum-dot superlattices on GaAsSb/GaAs(001) for solar cell applications. In *Proceedings of the 35th IEEE Photovoltaic Specialists Conference*, (p. 1885). Honolulu, HI: IEEE Press.

Inganas, O. (2010). Hybrid electronics and electrochemistry with conjugated polymers. *Chemical Society Reviews*, *39*(7), 2633–2642. doi:10.1039/b918146f

Inoue, T., Kido, S., Sasayama, K., Kita, T., & Wada, O. (2010). Impurity doping in self-assembled InAs/GaAs quantum dots by selection of growth steps. *Journal of Applied Physics*, *108*, 063524. doi:10.1063/1.3483252

INSPEC. (1990). *Properties of gallium arsenide* (2nd ed.). New York, NY: John Wiley.

INSPEC. (1991). *Properties of indium phosphide*. New York, NY: John Wiley.

Jackson, E. D. (1955). *Transactions of the conference on the use of solar energy 5*. Tucson, AZ: Tucson University of Arizona Press.

Jäger-Waldau, A. (2003). *PV status report 2003. European Commission, EUR 20850*. Geneva, Switzerland: European Commission.

Jani, O., Honsberg, C., Asghar, A., et al. (2005). Characterization and analysis of InGaN photovoltaic devices. In *Proceedings of the 31st IEEE Photovoltaic Specialists Conference.* Orlando, FL: IEEE Press.

Jia, Y., Wei, J., Wang, K., Cao, A., Shu, Q., & Gui, X. (2008). Nanotube–silicon heterojunction solar cells. *Advanced Materials (Deerfield Beach, Fla.)*, *20*(23), 4594–4598. doi:10.1002/adma.200801810

Johnson, D. C., Ballard, I. M., Barnham, K. W. J., Connolly, J. P., Mazzer, M., & Bessière, A. (2007). Observa. tion of photon recycling in strain-balanced quantum well solar cells. *Applied Physics Letters*, *90*, 213–505. doi:10.1063/1.2742334

Kaneto, K., Tsuruta, M., Sakai, G., Cho, W. Y., & Ando, Y. (1999). Electrical conductivities of multi-wall carbon nano tubes. *Synthetic Metals*, *103*(1-3), 2543–2546. doi:10.1016/S0379-6779(98)00221-5

Kang, Y., Park, N.-G., & Kim, D. (2005). Hybrid solar cells with vertically aligned CdTe nanorods and a conjugated polymer. *Applied Physics Letters*, *86*(11), 113101–113103. doi:10.1063/1.1883319

Karimov, K. S., Ahmed, M. M., Moiz, S. A., & Fedorov, M. I. (2005). Temperature-dependent properties of organic-on-inorganic Ag/p-CuPc/n-GaAs/Ag photoelectric cell. *Solar Energy Materials and Solar Cells*, *87*(1-4), 61–75. doi:10.1016/j.solmat.2004.07.014

Kawano, K., Ito, N., Nishimori, T., & Sakai, J. (2006). Open circuit voltage of stacked bulk heterojunction organic solar cells. *Applied Physics Letters*, *88*(7), 073514–073513. doi:10.1063/1.2177633

Kazmerski, L. (2009). *Best research-cell efficiencies*. NREL.

Keawprajak, A., Piyakulawat, P., Klamchuen, A., Iamraksa, P., & Asawapirom, U. (2010). Influence of crystallizable solvent on the morphology and performance of P3HT: PCBM bulk-heterojunction solar cells. =. *Solar Energy Materials and Solar Cells*, *94*(3), 531–536. doi:10.1016/j.solmat.2009.11.018

Kennedy, M., Mccormack, S. J., Doran, J., & Norton, B. (2007). Modelling the effect of device geometry on concentration ratios of quantum dot solar concentrators. In *Proceedings of the ISES World Solar Congress*, (pp. 1484-1487). Beijing, China: ISES.

Khan, A., Yamaguchi, M., Bourgoin, J. C., & Takamoto, T. (2000). Room-temperature minority-carrier injection-enhanced recovery of radiation-induced defects in p-InGaP and solar cells. *Applied Physics Letters*, *76*, 2559. doi:10.1063/1.126407

Kim, J. Y., Lee, K., Coates, N. E., Moses, D., Nguyen, T.-Q., & Dante, M. (2007). Efficient tandem polymer solar cells fabricated by all-solution processing. *Science*, *317*(5835), 222–225. doi:10.1126/science.1141711

Kim, S., Fisher, B., Eisler, H.-J., & Bawendi, M. (2003). Type-II quantum dots: CdTe/CdSe(core/shell) and CdSe/ZnTe(core/shell) heterostructures. *Journal of the American Chemical Society*, *125*, 11466–11467. doi:10.1021/ja0361749

Kim, Y., Cook, S., Tuladhar, S. M., Choulis, S. A., Nelson, J., & Durrant, J. R. (2006). A strong regioregularity effect in self-organizing conjugated polymer films and high-efficiency polythiophene:fullerene solar cells. *Nature Materials*, *5*(3), 197–203. doi:10.1038/nmat1574

King, D. L., Kratochvil, J. A., & Boyson, W. E. (1997). Paper. In *Proceedings of the 26th IEEE Photovoltaic Specialists Conference*, (pp. 1183-1186). Anaheim, CA: IEEE Press.

King, R. R., Boca, A., Hong, W., Liu, X.-Q., Bhusari, D., & Larrabee, D. … Karam, N. H. (2009). A photovoltaic system with three solar cells and a band-stop optical filter. In *Proceedings of the 24th European Photovoltaic Solar Energy Conference*. Munich, Germany: WIP.

King, R. R., Fetzer, C. M., Colter, P. C., Edmondson, K. M., Law, D. C., & Stavrides, A. P. … Karam, N. H. (2003). Lattice-matched and metamorphic GaInP/GaInAs/Ge concentrator solar cells. In *Proceedings of 3rd World Conference on Photovoltaic Energy Conversion*, (Vols A-C), (pp. 622-625).Tokyo, Japan: WCPEC-3.

King, R. R., Law, D. C., Edmondson, K. M., Fetzer, C. M., Kinsey, G. S., & Yoon, H. (2007). 40% efficient metamorphic GaInP/GaInAs/Ge multijunction solar cells. *Applied Physics Letters*, *90*(18), 183516–1835111. doi:10.1063/1.2734507

Kirchartz, T., Seino, K., Wagner, J.-M., Rau, U., & Bechstedt, F. (2009). Efficiency limits of Si/SiO_2 quantum well solar cells from first-principles calculations. *Journal of Applied Physics*, *105*(10), 104–511. doi:10.1063/1.3132093

Kireev, P. S. (1975). *Semiconductor physics*. Moscow, Russia: Mir.

Kittidachachan, P., Danos, L., Meyer, T. J. J., Alderman, N., & Markvart, T. (2007). Photon collection efficiency of fluorescent solar collectors. *CHIMIA International Journal for Chemistry*, *61*, 780–786. doi:10.2533/chimia.2007.780

Klemens, P. G. (1966). Anharmonic decay of optical phonons. *Physical Review*, *148*, 845. doi:10.1103/PhysRev.148.845

Knodler, R., Sopka, J., Harbach, F., & Grunling, H. W. (1993). Photoelectrochemical cells based on dye sensitized colloidal TiO_2 layers. *Solar Energy Materials and Solar Cells*, *30*(3), 277–281. doi:10.1016/0927-0248(93)90147-U

Koetse, M. M., Sweelssen, J., Hoekerd, K. T., Schoo, H. F. M., Veenstra, S. C., & Kroon, J. M. (2006). Efficient polymer: Polymer bulk heterojunction solar cells. *Applied Physics Letters*, *88*(8), 083504–083503. doi:10.1063/1.2176863

Kojima, O., Nakatani, H., Kita, T., Wada, O., Akahane, K., & Tsuchiya, M. (2008). Photoluminescence characteristics of quantum dots with electronic states interconnected along growth direction. *Journal of Applied Physics*, *103*, 113504. doi:10.1063/1.2936320

Kondo, M. (2009). *Paper*. Paper presented at the 19th International Photovoltaic Science and Engineering Conference. Jeju, Korea.

Kongkanand, A., Martínez Domínguez, R., & Kamat, P. V. (2007). Single wall carbon nanotube scaffolds for photoelectrochemical solar cells: Capture and transport of photogenerated electrons. *Nano Letters*, *7*(3), 676–680. doi:10.1021/nl0627238

Krahne, R., Morello, G., Figuerola, A., George, C., Deka, S., & Manna, L. (2011). Physical properties of elongated inorganic nanoparticles. *Physics Reports*, *501*(3–5), 75–221. doi:10.1016/j.physrep.2011.01.001

Krebs, F. C. (2008). A simple nanostructured polymer/ZnO hybrid solar cell—Preparation and operation in air. *Nanotechnology*, *19*(42), 424013. doi:10.1088/0957-4484/19/42/424013

Krebs, F. C. (2009a). Fabrication and processing of polymer solar cells: A review of printing and coating techniques. *Solar Energy Materials and Solar Cells*, *93*(4), 394–412. doi:10.1016/j.solmat.2008.10.004

Krebs, F. C. (2009b). Polymer solar cell modules prepared using roll-to-roll methods: Knife-over-edge coating, slot-die coating and screen printing. *Solar Energy Materials and Solar Cells*, *93*(4), 465–475. doi:10.1016/j.solmat.2008.12.012

Krebs, F. C., Alstrup, J., Spanggaard, H., Larsen, K., & Kold, E. (2004). Production of large-area polymer solar cells by industrial silk screen printing, lifetime considerations and lamination with polyethyleneterephthalate. *Solar Energy Materials and Solar Cells*, *83*(2-3), 293–300. doi:10.1016/j.solmat.2004.02.031

Kresse, G., & Furthmüller, J. (1996). Efficient iterative schemes for ab initio total-energy calculations using a plane-wave basis set. *Physical Review B: Condensed Matter and Materials Physics*, *54*, 11169. doi:10.1103/PhysRevB.54.11169

Kresse, G., & Hafner, J. (1993). Ab initio molecular dynamics for liquid metals. *Physical Review B: Condensed Matter and Materials Physics*, *47*, 558. doi:10.1103/PhysRevB.47.558

Kr, üger, J., Plass, R., Cevey, L., Piccirelli, M., Gratzel, M., & Bach, U. (2001). High efficiency solid-state photovoltaic device due to inhibition of interface charge recombination. *Applied Physics Letters*, *79*(13), 2085–2087. doi:10.1063/1.1406148

Kubo, W., Murakoshi, K., Kitamura, T., Yoshida, S., Haruki, M., & Hanabusa, K. (2001). Quasi-solid-state dye-sensitized TiO_2 solar cells: Effective charge transport in mesoporous space filled with gel electrolytes containing iodide and iodine. *The Journal of Physical Chemistry B*, *105*(51), 12809–12815. doi:10.1021/jp012026y

Kudo, N., Shimazaki, Y., Ohkita, H., Ohoka, M., & Ito, S. (2007). Organic-inorganic hybrid solar cells based on conducting polymer and SnO2 nanoparticles chemically modified with a fullerene derivative. *Solar Energy Materials and Solar Cells*, *91*(13), 1243–1247. doi:10.1016/j.solmat.2006.11.019

Kudo, T., Inoue, T., Kita, T., & Wada, O. (2008). Real time analysis of self-assembled InAs/GaAs quantum dot growth by probing reflection high-energy electron diffraction chevron image. *Journal of Applied Physics*, *104*, 074305. doi:10.1063/1.2987469

Kuo, C. Y., & Gau, C. (2009). Arrangement of band structure for organic-inorganic photovoltaics embedded with silicon nanowire arrays grown on indium tin oxide glass. *Applied Physics Letters*, *95*(5), 053302. doi:10.1063/1.3189088

Kurokawa, K. (2009). Paper. *Paper presented at the 34th IEEE Photovoltaic Specialists Conference.* Philadelphia, PA.

Kurtz, S. R., Johnston, S. W., Geisz, J. F., Friedman, D. J., & Ptak, A. J. (2005). Paper. In *Proceedings of the 31st IEEE Photovoltaic Specialists Conference*. New York, NY: IEEE.

Kurtz, S. R., Myers, D., & Olson, J. M. (1997). Paper. In *Proceedings of the 26th IEEE Photovoltaic Specialists Conference*. New York, NY: IEEE.

Kwok, H. L. (2003). Carrier mobility in organic semiconductor thin films. *Reviews on Advanced Materials Science*, *5*, 62–66.

Kymakis, E., & Amaratunga, G. A. J. (2002). Single-wall carbon nanotube/conjugated polymer photovoltaic devices. *Applied Physics Letters*, *80*(1), 112–114. doi:10.1063/1.1428416

Kymakis, E., & Amaratunga, G. A. J. (2004). Optical properties of polymer-nanotube composites. *Synthetic Metals*, *142*(1-3), 161–167. doi:10.1016/j.synthmet.2003.08.011

Kymakis, E., Klapsis, G., Koudoumas, E., Stratakis, E., Kornilios, N., & Vidakis, N. (2006). Carbon nanotube/PEDOT: PSS electrodes for organic photovoltaics. *The European Physical Journal Applied Physics*, *36*(3), 257–259. doi:10.1051/epjap:2006148

Lai, Y. H., Lin, C. Y., Chen, J. G., Wang, C. C., Huang, K. C., & Liu, K. Y. (2010). Enhancing the performance of dye-sensitized solar cells by incorporating nanomica in gel electrolytes. *Solar Energy Materials and Solar Cells*, *94*(4), 668–674. doi:10.1016/j.solmat.2009.11.027

Lancelle-Beltran, E., Prené, P., Boscher, C., Belleville, P., Buvat, P., & Sanchez, C. (2006). All-solid-state dye-sensitized nanoporous TiO_2 hybrid solar cells with high energy-conversion efficiency. *Advanced Materials (Deerfield Beach, Fla.)*, *18*(19), 2579–2582. doi:10.1002/adma.200502023

Landi, B. J., Raffaelle, R. P., Castro, S. L., & Bailey, S. G. (2005). Single-wall carbon nanotube–polymer solar cells. *Progress in Photovoltaics: Research and Applications*, *13*(2), 165–172. doi:10.1002/pip.604

Landsberg, P. T., & Badescu, V. (1998). Solar energy conversion: List of efficiencies and some theoretical considerations, part 1: Theoretical considerations. *Progress in Quantum Electronics*, *22*(4), 211–240. doi:10.1016/S0079-6727(98)00012-3

Lang, D. V., & Henry, C. H. (1975). Nonradiative recombination at deep levels in GaAs and GaP by lattice-relaxation multiple phonon emission. *Physical Review Letters*, *35*(32).

Lang, D. V., Kimerling, L. C., & Leung, S. Y. (1976). Recombination-enhanced annealing of the *E*1 and *E*2 defect levels in 1-MeV-electron–irradiated *n*-GaAs. *Journal of Applied Physics*, *47*, 3587. doi:10.1063/1.323161

Law, M., Greene, L. E., Johnson, J. C., Saykally, R., & Yang, P. D. (2005). Nanowire dye-sensitized solar cells. *Nature Materials*, *4*, 455–459. doi:10.1038/nmat1387

Lepadatu, A.-M., Stavarache, I., Ciurea, M. L., & Iancu, V. (2010). The influence of shape and potential barrier on confinement energy levels in quantum dots. *Journal of Applied Physics*, *107*(3), 33–721. doi:10.1063/1.3284083

Levy, M. Y., Honsberg, C., Martí, A., & Luque, A. (2005). Quantum dot intermediate band solar cell material systems with negligible valence band offsets. In *Proceedings of the 31st IEEE Photovoltaics Specialists Conference*, (pp. 90–93). IEEE Press.

Lewis, N. S. (2005). *Characterization and analysis of InGan photovailic devices*. Paper presented at the 31st IEEE Photovoltaic Specialists Conference. Miami, FL.

Lewis, N. S. (2005). *Radial pn junction nanorod solar cells: device physics principles and routes to fabrication in silicon.* Paper presented at the 31st IEEE Photovoltaic Specialists Conference. Miami, FL.

Li, G., Shrotriya, V., Yao, Y., Huang, J., & Yang, Y. (2007). Manipulating regioregular poly(3-hexylthiophene): [6,6]-Phenyl-C61-butyric acid methyl ester blends-route towards high efficiency polymer solar cells. *Journal of Materials Chemistry*, *17*(30), 3126–3140. doi:10.1039/b703075b

Lin, A. S., & Phillips, J. D. (2009). Drift-diffusion modeling for impurity photovoltaic devices. *IEEE Transactions on Electron Devices*, *56*, 3168. doi:10.1109/TED.2009.2032741

Linares, P. G., Martí, A., Antolín, E., & Luque, A. (2010). III-V compound semiconductor screening for implementing quantum dot intermediate band solar cells. *Journal of Applied Physics*, *109*(1).

Lin, C. (2010). Hybrid solar cells based on P3HT and Si MWCNT nanocomposite. *Nanotechnology*, *21*(34), 345201. doi:10.1088/0957-4484/21/34/345201

Lin, Y.-Y., Chen, C.-W., Chu, T.-H., Su, W.-F., Lin, C.-C., & Ku, C.-H. (2007). Nanostructured metal oxide/conjugated polymer hybrid solar cells by low temperature solution processes. *Journal of Materials Chemistry*, *17*(43), 4571–4576. doi:10.1039/b710400f

Liu, C.-Y., Holman, Z. C., & Kortshagen, U. R. (2008). Hybrid Solar cells from P3HT and silicon nanocrystals. *Nano Letters*, *9*(1), 449–452. doi:10.1021/nl8034338

Li, Z., Kunets, V. P., Saini, V., Xu, Y., Dervishi, E., & Salamo, G. J. (2009). Light-harvesting using high density p-type single wall carbon nanotube/n-type silicon heterojunctions. *ACS Nano*, *3*(6), 1407–1414. doi:10.1021/nn900197h

Loh, E. Jr, & Scalapino, D. J. (1986). Luminescent solar concentrators: Effects of shape on efficiency. *Applied Optics*, *25*(12), 1901–1907. doi:10.1364/AO.25.001901

Lucena, R., Aguilera, I., Palacios, P., Wahnón, P., & Conesa, J. C. (2008). Synthesis and spectral properties of nanocrystalline V-substituted In2S3, a novel material for more efficient use of solar radiation. *Chemistry of Materials*, *20*(16), 5125–5127. doi:10.1021/cm801128b

Luque, A., Martí, A., & Cuadra, L. (2000). *High efficiency solar cell with metallic intermediate band*. Paper presented at the 16th European Photovoltaic Solar Energy Conference. London, UK.

Luque, A., Miñano, J. C., Davies, P., Terrón, M. J., Tobías, I., Sala, G., et al. (1991). *Angle-limited cavities for silicon solar cells*. Paper presented at the Photovoltaic Specialists Conference, 1991. New York, NY.

Luque, A. (2001). Photovoltaic markets and costs forecast based on a demand elasticity model. *Progress in Photovoltaics: Research and Applications*, *9*, 303–312. doi:10.1002/pip.371

Luque, A., Linares, P. G., Antolin, E., Canovas, E., Farmer, C. D., & Stanley, C. R. (2010). Multiple levels in intermediate band solar cells. *Applied Physics Letters*, *96*(1), 013501–013503. doi:10.1063/1.3280387

Luque, A., & Martí, A. (1997). Increasing the efficiency of ideal solar cells by photon induced transitions at intermediate levels. *Physical Review Letters*, *78*(26), 5014–5017. doi:10.1103/PhysRevLett.78.5014

Luque, A., & Martí, A. (2001). A metallic intermediate band high efficiency solar cell. *Progress in Photovoltaics: Research and Applications*, *9*(2), 73–86. doi:10.1002/pip.354

Luque, A., & Martí, A. (2010). Electron-phonon energy transfer in hot-carrier solar cells. *Solar Energy Materials and Solar Cells*, *94*, 287–296. doi:10.1016/j.solmat.2009.10.001

Luque, A., & Martí, A. (2010). On the partial filling of the intermediate band (IB) in IB solar cells. *IEEE Transactions on Electron Devices*, *57*(6), 1201–1207. doi:10.1109/TED.2010.2045681

Luque, A., Marti, A., Antolin, E., & Linares, P. G. (2010). Intraband absorption for normal illumination in quantum dot intermediate band solar cells. *Solar Energy Materials and Solar Cells*, *94*(12), 2032–2035. doi:10.1016/j.solmat.2010.06.008

Luque, A., Martí, A., Antolín, E., & Tablero, C. (2006). Intermediate band versus levels in non-radiative recombination. *Physica B, Condensed Matter*, *382*, 320–327. doi:10.1016/j.physb.2006.03.006

Luque, A., Martí, A., & Cuadra, L. (2003). Impact-ionization-assisted intermediate band solar cell. *IEEE Transactions on Electron Devices*, *50*(2), 447–454. doi:10.1109/TED.2003.809024

Luque, A., Martí, A., López, N., Antolín, E., Cánovas, E., & Stanley, C. R. (2006). Operation of the intermediate band solar cell under nonideal space charge region conditions and half filling of the intermediate band. *Journal of Applied Physics*, *99*(1), 094503. doi:10.1063/1.2193063

Luque, A., Martí, A., Mendes, M. J., & Tobías, I. (2008). Light absorption in the near field around surface plasmon polaritons. *Journal of Applied Physics*, *104*(11), 1–8. doi:10.1063/1.3014035

Luther, J., Bett, A. W., Burger, B., & Dimroth, F. (2006). Paper. In *Proceedings of the 21st European Photovoltaic Solar Energy Conference,* (p. 2054). Munich, Germany: WIP.

Lynch, M. C., Ballard, I. M., Bessiere, A., Johnson, D. C., Stavrinou, P. N., & Barnham, K. W. J. … Calder, C. (2006). Modelling the con□ned carrier states in multi quantum well solar cells. In *Proceedings of the 4th World Conference on Photovoltaic Energy Conversion*, (pp. 67-70). Hawaii, HI: IEEE.

Lynch, M. C., Ballard, I. M., Bushnell, D. B., Connolly, J. P., Johnson, D. C., & Tibbits, T. N. D. (2005). Spectral response and I-V characteristics of large well number multi quantum well solar cells. *Journal of Materials Science*, *40*(6), 1445–1449. doi:10.1007/s10853-005-0580-4

MacDiarmid, A. G. (2001). Synthetic metals: A novel role for organic polymers (nobel lecture). *Angewandte Chemie International Edition*, *40*(14), 2581–2590. doi:10.1002/1521-3773(20010716)40:14<2581::AID-ANIE2581>3.0.CO;2-2

MacKay, D. (2009). *Sustainable energy without the hot air*. Cambridge, UK: UIT Cambridge Ltd.

MacQueen, R. W., Cheng, Y. Y., Clady, R. G. C. R., & Schmidt, T. W. (2010). Towards an aligned luminophore solar concentrator. *Optics Express*, *18*, A161–A166. doi:10.1364/OE.18.00A161

Madelung, O. (Ed.). (1996). *Semiconductors - Basic data*. Berlin, Germany: Springer Verlag. doi:10.1007/978-3-642-97675-9

Maier, S. A., & Atwater, H. A. (2005). Plasmonics: Localization and guiding of electromagnetic energy in metal/dielectric structures. *Journal of Applied Physics*, *98*(1), 011101. doi:10.1063/1.1951057

Manca, J. V., Munters, T., Martens, T., Beelen, Z., Goris, L., D'Haen, J., et al. (2003). *State-of-the-art MDMO-PPV:PCBM bulk heterojunction organic solar cells: Materials, nanomorphology, and electro-optical properties*. Paper presented at SPIE. Seattle, WA.

Mansour, A. F. (1998). Optical efficiency and optical properties of luminescent solar concentrators. *Polymer Testing*, *17*, 333–343. doi:10.1016/S0142-9418(97)00061-5

Mao, H., Deng, H., Li, H., Shen, Y., Lu, Z., & Xu, H. (1998). Photosensitization of TiO_2 semiconductor with porphyrin. *Journal of Photochemistry and Photobiology A Chemistry*, *114*(3), 209–212. doi:10.1016/S1010-6030(97)00260-8

Markvart, T., & Casta, ñer, L. (Eds.). (2003). *Practical handbook of photovoltaics – Fundamentals and applications*. Oxford, UK: Elsevier.

Marlein, J., & Burgelman, M. (2007). Electrical properties of CIGS cells. In *Proceedings of the 22nd European Photovoltaic Solar Energy Conference*. Milan, Italy: EU PVTSEC.

Marlein, J., Decock, K., & Burgelman, M. (2009). Analysis of electrical properties of CIGSSe and Cd-free buffer CIGSSe solar cells. *Thin Solid Films*, *517*(7), 2353–2356. doi:10.1016/j.tsf.2008.11.048

Martens, T., D'Haen, J., Munters, T., Beelen, Z., Goris, L., & Manca, J. (2003). Disclosure of the nanostructure of MDMO-PPV: PCBM bulk hetero-junction organic solar cells by a combination of SPM and TEM. *Synthetic Metals*, *138*(1-2), 243–247. doi:10.1016/S0379-6779(02)01311-5

Martí, A., Antolín, E., Cánovas, E., Linares, P. G., & Luque, A. (2008). Light management issues in intermediate band solar cells. In *Proceedings of the MRS, Spring Meeting,* (vol 1101E), (pp. KK06-02). San Francisco, CA: MRS.

Martí, A., Antolín, E., Cánovas, E., López, N., Luque, A., Stanley, C., et al. (2006). *Progress in quantum-dot intermediate band solar cell research.* Paper presented at the 21st European Photovoltaic Solar Energy Conference. Munich, Germany.

Martí, A., Antolín, E., Linares, P. G., Cánovas, E., Marrón, D. F., Tablero, C., et al. (2009). *IBPOWER: Intermediate band materials and solar cells for photovoltaics with high efficiency and reduced cost.* Paper presented at the Photovoltaic Specialists Conference (PVSC). New York, NY.

Martí, A., Cuadra, L., & Luque, A. (2000). *Quantum dot intermediate band solar cell.* Paper presented at the Photovoltaic Specialists Conference, 2000. New York, NY.

Martí, A., Antolín, E., Stanley, C. R., Farmer, C. D., López, N., & Días, P. (2006). Production of photocurrent due to intermediate-to-conduction-band transitions: A demonstration of a key operating principle of the intermediate-band solar cell. *Physical Review Letters*, *97*, 247701. doi:10.1103/PhysRevLett.97.247701

Martí, A., Cuadra, L., & Luque, A. (2001). Partial filling of a quantum dot intermediate band for solar cells. *IEEE Transactions on Electron Devices*, *48*(10), 2394–2399. doi:10.1109/16.954482

Martí, A., Fuertes Marrón, A., & Luque, A. (2008). Evaluation of the efficiency potential of intermediate band solar cells based on thin-film chalcopyrite materials. *Journal of Applied Physics*, *103*(7), 1–6. doi:10.1063/1.2901213

Martí, A., López, N., Antolín, E., Cánovas, E., Luque, A., & Stanley, C. R. (2007). Emitter degradation in quantum dot intermediate band solar cells. *Applied Physics Letters*, *90*, 233510. doi:10.1063/1.2747195

Martí, A., & Luque, A. (Eds.). (2003). *Next generation photovoltaics: High efficiency through full spectrum utilization*. Bristol, UK: Institute of Physics Publishing.

Martí, A., Tablero, C., Antolín, E., Luque, A., Campion, R. P., & Novikov, S. V. (2008). Potential of Mn doped In1-xGaxN for implementing intermediate band solar cells. *Solar Energy Materials and Solar Cells*, *93*, 641–644. doi:10.1016/j.solmat.2008.12.031

Martinson, A. B. F., Elam, J. W., Hupp, J. T., & Pellin, M. J. (2007). ZnO nanotube based dye-sensitized solar cells. *Nano Letters*, *7*(8), 2183–2187. doi:10.1021/nl070160+

Maruyama, T. (1999). Wedge-shaped light concentrator using total internal reflection. *Solar Energy Materials and Solar Cells*, *57*, 75–83. doi:10.1016/S0927-0248(98)00173-1

Mastai, Y., & Hodes, G. (1997). Size quantization in electrodeposited CdTe nanocrystalline films. *The Journal of Physical Chemistry B*, *101*(14), 2685–2690. doi:10.1021/jp963069v

Mazzer, M., Barnham, K. W. J., & Ballard, I. M. (2006). Progress in quantum well solar cells. *Thin Solid Films*, *511-512*, 76–83. doi:10.1016/j.tsf.2005.12.120

Mazzer, M., Barnham, K. W. J., Ballard, I. M., Bessiere, A., Ioannides, A., & Johnson, D. C. (2006). Progress in quantum well solar cells. *Thin Solid Films*, *511*, 76–83. doi:10.1016/j.tsf.2005.12.120

McGehee, M. D. (2009). Nanostructured organic-inorganic hybrid solar cells. *MRS Bulletin*, *34*(02), 95–100. doi:10.1557/mrs2009.27

McIntosh, K. R., Yamada, N., & Richards, B. S. (2007). Theoretical comparison of cylindrical and square-planar luminescent solar concentrators. *Applied Physics. B, Lasers and Optics*, *88*(2), 285–290. doi:10.1007/s00340-007-2705-8

McLeskey, J. T. Jr, & Qiao, Q. (2006). Hybrid solar cells from water-soluble polymers. *International Journal of Photoenergy*, (n.d), 2006.

Mellor, A., Tobías, I., Martí, A., Mendes, M. J., & Luque, A. (2010). *Upper limits to absorption enhancement in thick solar cells using difraction grids*. Unpublished.

Meng, Q.-B., Takahashi, K., Zhang, X.-T., Sutanto, I., Rao, T. N., Sato, O., & Fujishima, A. (2003). Fabrication of an efficient solid-state dye-sensitized solar cell. *Langmuir*, *19*, 3572. doi:10.1021/la026832n

Minkowski, C., & Calzaferri, G. (2005). Forster-type energy transfer along a specified axis. *Angewandte Chemie*, *117*, 5325–5329. doi:10.1002/ange.200500431

Mitroi, M. R., Iancu, V., Fara, L., & Ciurea, M. L. (2011). Numerical analysis of J–V characteristics of a polymer solar cell. *Progress in Photovoltaics: Research and Applications*, *19*(3), 301–306. doi:10.1002/pip.1026

Miyashita, N., Shimizu, Y., Kobayashi, N., Okada, Y., & Yamaguchi, M. (2006). Paper. In *Proceedings of the 4th World Conference on Photovoltaic Energy Conversion.* New York, NY: IEEE.

Möller, H. J. (1993). *Semiconductors for solar cells*. Boston, MA: Artech House.

Mor, G. K., Varghese, O. K., Paulose, M., Shankar, K., & Grimes, C. A. (2006). A review on highly ordered, vertically oriented TiO2 nanotube arrays: Fabrication, material properties, and solar energy applications. *Solar Energy Materials and Solar Cells*, *90*, 2011–2075. doi:10.1016/j.solmat.2006.04.007

Morioka, T., Oshima, R., Takata, A., Shoji, Y., Inoue, T., Kita, T., & Okada, Y. (2010). Multi-stacked InAs/GaNAs quantum dots with direct Si doping for use in intermediate band solar cell. In *Proceedings of the 35th IEEE Photovoltaic Specialists Conference*, (p. 1834). Honolulu, HI: IEEE Press.

Mori, S., & Yanagida, S. (2006). TiO2-based dye-sensitized solar cell. In Tetsuo, S. (Ed.), *Nanostructured Materials for Solar Energy Conversion* (pp. 193–225). Amsterdam, The Netherlands: Elsevier. doi:10.1016/B978-044452844-5/50008-1

Moulé, A. J., & Meerholz, K. (2007). Minimizing optical losses in bulk heterojunction polymer solar cells. *Applied Physics. B, Lasers and Optics*, *86*(4), 721–727. doi:10.1007/s00340-006-2542-1

Mulder, C. L., Reusswig, P. D., Beyler, A. P., Kim, H., Rotschild, C., & Baldo, M. A. (2010). Dye alignment in luminescent solar concentrators: II: Horizontal alignment for energy harvesting in linear polarizers. *Optics Express*, *18*, 91–99. doi:10.1364/OE.18.000A91

Mulder, C. L., Theogarajan, L., Currie, M. J., Mapel, J. K., Baldo, M. A., & Vaughn, M. (2009). Luminescent solar concentrators employing phycobilisomes. *Advanced Materials (Deerfield Beach, Fla.)*, *21*(31), 3181–3185. doi:10.1002/adma.200900148

Munteanu, D., & Autran, J. L. (2011). Modeling of energy bands in ultra-thin layer quantum nanostructures for solar cell applications. *Journal of Non-Crystalline Solids*, *357*(8-9), 1884–1887. doi:10.1016/j.jnoncrysol.2010.11.112

Munteanu, I. (2003). *Solid state physics*. Bucharest, Romania: Bucharest University Publishing House.

Murai, S., Mikoshiba, S., Sumino, H., & Hayase, S. (2002). Quasi-solid dye-sensitized solar cells containing chemically cross-linked gel: How to make gels with a small amount of gelator. *Journal of Photochemistry and Photobiology A Chemistry*, *148*(1-3), 33–39. doi:10.1016/S1010-6030(02)00046-1

Murray, C. B., Norris, D. J., & Bawendi, M. G. (1993). Synthesis and characterization of nearly monodisperse CdE (E = sulfur, selenium, tellurium) semiconductor nanocrystallites. *Journal of the American Chemical Society*, *115*, 8706–8715. doi:10.1021/ja00072a025

Myahkostupov, M., Zamkov, M., & Castellano, F. N. (2011). Dye-sensitized photovoltaic properties of hydrothermally prepared TiO2 nanotubes. *Energy and Environmental Science*, *4*, 998–1010. doi:10.1039/c0ee00533a

Myong, S. Y. (2007). Recent progress in inorganic solar cells using quantum structures. *Recent Patents on Nanotechnology*, *1*(1), 67–73. doi:10.2174/187221007779814763

Nardes, A. M., Kemerink, M., & Janssen, R. A. J. (2007). Anisotropic hopping conduction in spin-coated PEDOT:PSS thin films. *Physical Review B: Condensed Matter and Materials Physics*, *76*(8), 085208. doi:10.1103/PhysRevB.76.085208

Nardes, A. M., Kemerink, M., Janssen, R. A. J., Bastiaansen, J. A. M., Kiggen, N. M. M., & Langeveld, B. M. W. (2007). Microscopic understanding of the anisotropic conductivity of PEDOT: PSS thin films. *Advanced Materials (Deerfield Beach, Fla.)*, *19*(9), 1196–1200. doi:10.1002/adma.200602575

Navruz, T. S., & Saritas, M. (2008). Efficiency variation of the intermediate band solar cell due to the overlap between absorption coefficients. *Solar Energy Materials and Solar Cells*, *92*(3), 273–282. doi:10.1016/j.solmat.2007.08.012

Navruz, T. S., & Saritas, M. (2009). The detailed analysis of auger effect on the efficiency of intermediate band solar cells. *Solar Energy Materials and Solar Cells*, *93*, 1913–1922. doi:10.1016/j.solmat.2009.06.024

Nazeeruddin, K., Humphry-Baker, M., Gratzel, M., & Murrer, B. (1998). Efficient near IR sensitization of nanocrystalline TiO2 films by ruthenium phthalocyanines. *Chemical Communications*, *6*, 719–720. doi:10.1039/a708834e

Nazeeruddin, M. K., De Angelis, F., Fantacci, S., Selloni, A., Viscardi, G., & Liska, P. (2005). Combined experimental and DFT-TDDFT computational study of photoelectrochemical cell ruthenium sensitizers. *Journal of the American Chemical Society*, *127*(48), 16835–16847. doi:10.1021/ja052467l

Neges, M., Schwarzburg, K., & Willig, F. (2006). Monte Carlo simulation of energy loss and collection of hot charge carriers, first step towards a more realistic hot-carrier solar energy converter. *Solar Energy Materials and Solar Cells*, *90*(14), 2107–2128. doi:10.1016/j.solmat.2006.02.008

Nelin, G., & Nilsson, G. (1972). Weak absorption tails in amorphous semiconductors. *Physical Review B: Condensed Matter and Materials Physics*, *5*, 3151. doi:10.1103/PhysRevB.5.3151

Nell, M. E., & Barnett, A. M. (1987). The spectral p-n junction model for tandem solar-cell design. *IEEE Transactions on Electronic Devices, 34*(2).

Nelson, J. (2003). Diffusion-limited recombination in polymer-fullerene blends and its influence on photocurrent collection. *Physical Review B: Condensed Matter and Materials Physics*, *67*, 155209. doi:10.1103/PhysRevB.67.155209

Nelson, J. (2003). *The physics of solar cells*. London, UK: Imperial College Press.

Nelson, J., Ballard, I., Barnham, K., Connolly, J. P., Roberts, J. S., & Pate, M. (1999). Effect of quantum well location on single quantum well p–i–n photodiode dark currents. *Journal of Applied Physics*, *86*(10). doi:10.1063/1.371609

Nelson, J., Paxman, M., Barnham, K. W. J., & Roberts, J. S., & Button. (1993). Steady-state carrier escape from single quantum wells, C. *IEEE Journal of Quantum Electronics*, *29*(6), 1460–1468. doi:10.1109/3.234396

Nilsson, G., & Nelin, G. (1971). Paper. *Physical Review B: Condensed Matter and Materials Physics*, *3*, 364. doi:10.1103/PhysRevB.3.364

Nishida, M. (2005). Electronic structure of silicon quantum dots: Calculations of energy-gap redshifts due to oxidation. *Journal of Applied Physics*, *98*(2), 23–705. doi:10.1063/1.1985978

Nolasco, J. C., Estrada, M., Matsumoto, Y., Marsal, L. F., & Pallares, J. (2007). Characterization of a P3HT- Si heterojuntion for solar cells applications. *ECS Transactions*, *9*(1), 587–593. doi:10.1149/1.2766933

Norman, A. G., Hanna, M. C., Dippo, P., et al. (2005). InGaAs/GaAs QD superlattices: MOVPE growth, structural and optical characterization and application in intermediate-band solar cells. In *Proceedings of the 31st IEEE Photovoltaic Specialists Conference.* Orlando, FL: IEEE Press.

Novotny, C. J., Yu, E. T., & Yu, P. K. L. (2008). InP nanowire/polymer hybrid photodiode. *Nano Letters*, *8*(3), 775–779. doi:10.1021/nl072372c

Nozik, A. J. (2002). Quantum dot solar cells. *Physica E, Low-Dimensional Systems and Nanostructures*, *14*, 115. doi:10.1016/S1386-9477(02)00374-0

Nozik, A. J. (2008). Multiple exciton generation in semiconductor quantum dots. *Chemical Physics Letters*, *457*, 3. doi:10.1016/j.cplett.2008.03.094

Nozik, A. J., Parsons, C. A., Dunlary, D. J., Keyes, B. M., & Ahrenhiel, R. K. (1990). Dependence of hot carrier luminescence on barrier thickness in GaAs/AlGaAs superlattices and multiple quantum wells. *Solid State Communications*, *75*, 247. doi:10.1016/0038-1098(90)90900-V

Nunzi, J. M. (2002). Organic photovoltaic materials and devices. *Comptes Rendus Physique*, *3*(4), 523–542. doi:10.1016/S1631-0705(02)01335-X

Oda, T., Tanaka, S., & Hayase, S. (2006). Differences in characteristics of dye-sensitized solar cells containing acetonitrile and ionic liquid-based electrolytes studied using a novel model. *Solar Energy Materials and Solar Cells*, *54*(16), 2696–27011. doi:10.1016/j.solmat.2005.11.013

Odom, T. W., Huang, J.-L., Kim, P., & Lieber, C. M. (1998). Atomic structure and electronic properties of single-walled carbon nanotubes. *Nature*, *391*(6662), 62–64. doi:10.1038/34145

OECD. (2009). *World energy outlook 2009*. OECD.

Offermans, T., Meskers, S. C. J., & Janssen, R. A. J. (2006). Electro-optical studies on MDMO-PPV: PCBM bulk-heterojunction solar cells on the millisecond time scale: Trapped carriers. *Organic Electronics*, *7*(4), 213–221. doi:10.1016/j.orgel.2006.02.001

Okada, Y., & Shiotsuka, N. (2005). Paper. In *Proceedings of the 31st IEEE Photovoltaic Specialists Conference*. New York, NY: IEEE.

Okada, Y., Shiotsuka, N., Komiyama, H., Akahane, K., & Ohtani, M. (2005). Paper. In *Proceedings of the 20th European Photovoltaic Solar Energy Conference*. Munich, Germany: WIP.

Okada, Y., Shiotsuka, N., Komiyama, H., Akahane, K., & Ohtani, N. (2005). Multi-stacking of highly uniform self-organized quantum dots for solar cell applications. In *Proceedings of the 20th European Photovoltaic Solar Energy Conference*, (p. 51). Barcelona, Spain: WIP.

Okada, Y., Morioka, T., Yoshida, K., Oshima, R., Shoji, Y., Inoue, T., & Kita, T. (2011). Increase of photocurrent by optical transitions via intermediate quantum states in direct-doped InAs/GaNAs strain-compensated quantum dot solar cell. *Journal of Applied Physics*, *109*, 024301. doi:10.1063/1.3533423

Okada, Y., Oshima, R., & Takata, A. (2009). Characteristics of InAs/GaNAs strain-compensated quantum dot solar cell. *Journal of Applied Physics*, *106*, 024306. doi:10.1063/1.3176903

Okada, Y., Shiotsuka, N., & Takeda, T. (2005). Potentially modulated multi-quantum wells for high-efficiency solar cell applications. *Solar Energy Materials and Solar Cells*, *85*(2), 143–152. doi:10.1016/j.solmat.2004.04.013

Olea, J., Toledano-Luque, M., Pastor, D., González-Díaz, G., & Mártil, I. (2008). Titanium doped silicon layers with very high concentration. *Journal of Applied Physics*, *104*(1), 016105–016103. doi:10.1063/1.2949258

Olson, J., Kurtz, S., & Kibbler, K. (1990). A 27.3% efficient $Ga_{0.5}In_{0.5}P$/GaAs tandem solar cell. *Applied Physics Letters*, *56*, 623. doi:10.1063/1.102717

Olson, R. W., Loring, R. F., & Fayer, M. D. (1981). Luminescent solar concentrators and the reabsorption problem. *Applied Optics*, *20*, 2934–2940. doi:10.1364/AO.20.002934

Ong, P. L., Euler, W. B., & Levitsky, I. A. (2010). Hybrid solar cells based on single-walled carbon nanotubes/Si heterojunctions. *Nanotechnology*, *21*(10). doi:10.1088/0957-4484/21/10/105203

Ong, P.-L., & Levitsky, I. (2010). Organic / IV, III-V semiconductor hybrid solar cells. *Energies*, *3*(3), 313–334. doi:10.3390/en3030313

O'Regan, B. C., López-Duarte, I., Martínez-Díaz, M. V., Forneli, A., Albero, J., & Morandeira, A. (2008). Catalysis of recombination and its limitation on open circuit voltage for dye sensitized photovoltaic cells using phthalocyanine dyes. *Journal of the American Chemical Society*, *130*(10), 2906–2907. doi:10.1021/ja078045o

O'Regan, B., & Gratzel, M. (1991). A low-cost, high-efficiency solar cell based on dye-sensitized colloidal TiO_2 films. *Nature*, *353*(6346), 737–740. doi:10.1038/353737a0

Osaka, Japan: WCPEC. Takamoto, T., Yamaguchi, M., Ikeda, E., Agui, T., Kurita, H., & Al-Jassim, M. (1999). Mechanism of Zn and Si diffusion from a highly doped tunnel junction for InGaP/GaAs tandem solar cells. Journal of Applied Physics, 85, 1481.

Oshima, R., Okada, Y., Takata, A., Yagi, S., Akahane, K., Tamaki, R., & Miyano, K. (2011). High-density quantum dot superlattice for application to high-efficiency solar cells. *Physica Status Solidi. C, Current Topics in Solid State Physics*, *8*, 619. doi:10.1002/pssc.201000461

Oshima, R., Takata, A., & Okada, Y. (2008). Strain compensated InAs/GaNAs quantum dots for use in high-efficiency solar cells. *Applied Physics Letters*, *93*, 083111. doi:10.1063/1.2973398

Othonos, A. (1998). Probing ultrafast carrier and phonon dynamics in semiconductors. *Applied Physics Reviews*, *83*, 1789. doi:10.1063/1.367411

Padinger, F., Rittberger, R. S., & Sariciftci, N. S. (2003). Effects of postproduction treatment on plastic solar cells. *Advanced Functional Materials*, *13*(1), 85–88. doi:10.1002/adfm.200390011

Palacios, P., Sánchez, K., Conesa, J. C., Fernández, J. J., & Wahnón, P. (2007). Theoretical modelling of intermediate band solar cell materials based on metal-doped chalcopyrite compounds. *Thin Solid Films*, *515*(15), 6280–6284. doi:10.1016/j.tsf.2006.12.170

Palmaerts, A., Lutsen, L., Cleij, T. J., Vanderzande, D., Pivrikas, A., & Neugebauer, H. (2009). Development of novel processable electron accepting conjugated polymers containing fluoranthene units in the main chain. *Polymer*, *50*(21), 5007–5015. doi:10.1016/j.polymer.2009.08.031

Pana, O., & Giurgiu, L. M., Darabont, et al. (2006). Core-shell effects in granular perovskite manganites. *Journal of Physics and Chemistry of Solids*, *67*(1-3), 624–627. doi:10.1016/j.jpcs.2005.10.148

Paper. (2011). *Website*. Retrieved from http://www.paper.edu.cn/index.php/default/feature/downCount/815

Park, H. M., Kim, K. H., Lee, S. H., Park, D. H., Hong, Y. K., & Joo, J. (2008). Electrochemical polymerization of polypyrrole (PPy) and poly(3-hexylthiophene) (P3HT) using functionalized single-wall carbon nanotubes. *Colloids and Surfaces A: Physicochemical and Engineering Aspects*, *313-314*, 72–76. doi:10.1016/j.colsurfa.2007.04.077

Park, S. H., Roy, A., Beaupre, S., Cho, S., Coates, N., & Moon, J. S. (2009). Bulk heterojunction solar cells with internal quantum efficiency approaching 100%. *Nature Photonics*, *3*(5), 297–303. doi:10.1038/nphoton.2009.69

Park, S., Tatebayashi, J., & Arakawa, Y. (2004). Formation of ultrahigh-density InAs/AlAs quantum dots by metalorganic chemical vapor deposition. *Applied Physics Letters*, *84*, 1877. doi:10.1063/1.1687465

Parmer, J. E., Mayer, A. C., Hardin, B. E., Scully, S. R., McGehee, M. D., & Heeney, M. (2008). Organic bulk heterojunction solar cells using poly(2,5-bis(3-tetradecyllthiophen-2-yl)thieno[3,2,-b]thiophene). *Applied Physics Letters*, *92*(11), 113309–113303. doi:10.1063/1.2899996

Pasquier, A. D., Mastrogiovanni, D. D. T., Klein, L. A., Wang, T., & Garfunkel, E. (2007). Photoinduced charge transfer between poly(3-hexylthiophene) and germanium nanowires. *Applied Physics Letters*, *91*(18), 183501. doi:10.1063/1.2801554

Paxman, M., Nelson, J., Barnham, K. W. J., Braun, B., Connolly, J. P., & Button, C. (1993). Modelling the spectral response of the quantum well solar cell. *Journal of Applied Physics*, *74*, 614. doi:10.1063/1.355275

Paxman, M., Nelson, J., & Braun, B. (1993). Modeling the spectral response of the quantum well solar cell. *Journal of Applied Physics*, *74*, 614–621. doi:10.1063/1.355275

Peng, X., Schlamp, M. C., Kadavanich, A. V., & Alivisatos, A. P. (1997). Epitaxial growth of highly luminescent CdSe/CdS core/shell nanocrystals with photostability and electronic accessibility. *Journal of the American Chemical Society*, *119*, 7019–7029. doi:10.1021/ja970754m

Perdew, J. P., & Wang, Y. (1992). Accurate and simple analytic representation of the electron-gas correlation energy. *Physical Review B: Condensed Matter and Materials Physics*, *45*, 13244. doi:10.1103/PhysRevB.45.13244

Peters, M., Goldschmidt, J. C., Loeper, P., Blasi, B., & Willeke, G. (2008). Light trapping with angular selective filters. In *Proceedings of the 23rd European Photovoltaic Solar Energy Conference*. Valencia, Spain: EU PVSEC.

Phillips, J., Kamath, K., Zhou, X., Chervela, N., & Bhattacharya, P. (1997). Photoluminescence and far-infrared absorption in Si-doped self-organized InAs quantum dots. *Applied Physics Letters*, *71*, 2079. doi:10.1063/1.119347

Platzer-Björkman, C., Zabierowski, P., Pettersson, J., Törndahl, T., & Edoff, M. (2010). Improved fill factor and open circuit voltage by crystalline selenium at the Cu(In,Ga)Se2/buffer layer interface in thin film solar cells. *Progress in Photovoltaics: Research and Applications*, *18*(4), 249–256.

Polo, A. S., Itokazu, M. K., & Murakami Iha, N. Y. (2004). Metal complex sensitizers in dye-sensitized solar cells. *Coordination Chemistry Reviews*, *248*(13-14), 1343–1361. doi:10.1016/j.ccr.2004.04.013

Popescu, V., Bester, G. L., Hanna, M. C., Norman, A. G., & Zunger, A. (2008). Theoretical and experimental examination of the intermediate-band concept for strain-balanced (In,Ga)As/Ga(As,P) quantum dot solar cells. *Physical Review B: Condensed Matter and Materials Physics*, *78*(20), 205321. doi:10.1103/PhysRevB.78.205321

Popescu, V., Bester, G., Hanna, M. C., Norman, A. G., & Zunger, A. (2008). Theoretical and experimental examination of the intermediate-band concept for strain-balanced (In,Ga)As/Ga(As,P) quantum dot solar cells. *Physical Review B: Condensed Matter and Materials Physics*, *78*, 205321. doi:10.1103/PhysRevB.78.205321

Pötz, W., & Kocevar, P. (1983). Electronic power transfer in pulsed laser excitation of polar semiconductors. *Physical Review B: Condensed Matter and Materials Physics*, *28*, 7040. doi:10.1103/PhysRevB.28.7040

Prabakar, K., Seo, H., Son, M., & Kim, H. (2009). CdS quantum dots sensitized TiO_2 photoelectrodes. *Materials Chemistry and Physics*, *117*(1), 26–28. doi:10.1016/j.matchemphys.2009.05.056

Pravettoni, M., Farrell, D. J., Chatten, A. J., Bose, R., Kenny, R. P., & Barnham, K. W. J. (2009). External quantum efficiency measurements of luminescent solar concentrators: A study of the impact of backside reflector size and shape. In *Proceedings of the 24th European Photovoltaic Solar Energy Conference*. Hamburg, Germany: EU PVSEC.

Prażmowska, J., Paszkiewicz, R., Korbutowicz, R., Wośko, M., & Tłaczała, M. (2007). Solar cells conversion efficiency enhancement techniques. *Optica Applicata*, *37*(1-2), 93–99.

Pryce, I. M., Koleske, D. D., Fischer, A. J., & Atwater, H. A. (2010). Plasmonic nanoparticle enhanced photocurrent in GaN/InGaN/GaN quantum well solar cells. *Applied Physics Letters*, *96*(15), 153501. doi:10.1063/1.3377900

Pugnet, M., Collet, J., & Cornet, A. (1981). Cooling of hot electron-hole plasmas in the presence of screened electron-phonon interactions. *Solid State Communications*, *38*, 531–536. doi:10.1016/0038-1098(81)90431-2

Quilitz, J., Koole, R., Slooff, L. H., Chatten, A. J., Bose, R., & Farrell, D. J. (in press). Fabrication and full characterisation of state-of-the-art CdSe quantum dot luminescent solar concentrators. *Solar Energy Materials and Solar Cells*.

Radziemska, E. (2003). The effect of temperature on the power drop in crystalline silicon solar cells. *Renewable Energy*, *28*(1), 1–12. doi:10.1016/S0960-1481(02)00015-0

Raisky, O. Y., Wang, W. B., & Alfano, R. R. (1999). Resonant enhancement of the photocurrent in multiple-quantum-well photovoltaic devices. *Applied Physics Letters*, *74*, 129–131. doi:10.1063/1.122972

Rajeshwar, K., & de Tacconi, N. R. (1997). Electrodeposition and characterization of nanocrystalline semiconductor films. In Prashant, V. K., & Dan, M. (Eds.), *Studies in Surface Science and Catalysis* (*Vol. 103*, pp. 321–351). London, UK: Elsevier. doi:10.1016/S0167-2991(97)81109-3

Rehm, J. M., McLendon, G. L., Nagasawa, Y., Yoshihara, K., Moser, J., & Gratzel, M. (1996). Femtosecond electron-transfer dynamics at a sensitizing dye−semiconductor (TiO_2) interface. *Journal of Physical Chemistry*, *100*(23), 9577–9578. doi:10.1021/jp960155m

Reisfeld, R. (1984). Spectroscopy and nonradiative phenomena of rare earths in glasses: Future applications. *Inorganica Chimica Acta*, *95*, 69–74. doi:10.1016/S0020-1693(00)87369-7

Reisfeld, R. (1987). Industrial applications of rare earths in fiber optics, luminescent solar concentrators and lasers. *Inorganica Chimica Acta*, *140*, 345–350. doi:10.1016/S0020-1693(00)81119-6

Reisfeld, R. (2010). New developments in luminescence for solar energy utilization. *Optical Materials*, *32*, 1–7. doi:10.1016/j.optmat.2010.04.034

Ren, S. F., Cheng, W., & Yu, P. Y. (2004). Microscopic investigation of phonon modes in SiGe alloy nanocrystals. *Physical Review B: Condensed Matter and Materials Physics*, *69*, 235327. doi:10.1103/PhysRevB.69.235327

Reyes-Reyes, M., Kim, K., & Carroll, D. L. (2005). High-efficiency photovoltaic devices based on annealed poly(3-hexylthiophene) and 1-(3-methoxycarbonyl)-propyl-1- phenyl-(6,6)C[sub 61] blends. *Applied Physics Letters*, *87*(8), 083506–083503. doi:10.1063/1.2006986

Riad, S. (2000). Dark and photoelectric conversion properties of p-MgPc/n-Si (organic/inorganic) heterojunction cells. *Thin Solid Films*, *370*(1-2), 253–257. doi:10.1016/S0040-6090(99)00951-7

Richards, B. S. (2006). Ray-tracing simulations of luminescent solar concentrators containing multiple luminescent species. In *Proceedings of the 21st European Photovoltaic Solar Energy Conference*. Dresden, Germany: EU PVSEC.

Richards, B. S., Shalav, A., & Corkish, R. P. (2004). A low escape-cone-loss luminescent solar concentrator. In *Proceedings of the 19th European Photovoltaic Solar Energy Conference.* EU PVSEC.

Ridley, B. K. (1999). *Quantum processes in semiconductors*. Oxford, UK: Oxford University Press.

Rimada, J. C., Hernandez, L., Connolly, J. P., & Barnham, K. W. J. (2007). Conversion efficiency enhancement of AlGaAs quantum well solar cells. *Microelectronics Journal*, *38*, 513–518. doi:10.1016/j.mejo.2007.03.007

Robel, I., Bunker, B. A., & Kamat, P. V. (2005). Single-walled carbon nanotube–CdS nanocomposites as light-harvesting assemblies: Photoinduced charge-transfer interactions. *Advanced Materials (Deerfield Beach, Fla.)*, *17*(20), 2458–2463. doi:10.1002/adma.200500418

Rohr, C., Connolly, J. P., Ekins-Daukes, N., Abbott, P., Ballard, I., & Barnham, K. W. J. (2002). InGaAs/InGaAs strain-compensated quantum well cells for thermophotovoltaic applications. *Physica E, Low-Dimensional Systems and Nanostructures*, *14*(1-2), 158–161. doi:10.1016/S1386-9477(02)00369-7

Rölver, R., Berghoff, B., Bätzner, D., Spangenberg, B., Kurz, H., Schmidt, M., & Stegemann, B. (2008). Si/SiO_2 multiple quantum wells for all silicon tandem cells: Conductivity and photocurrent measurements. *Thin Solid Films*, *516*(20), 6763–6766. doi:10.1016/j.tsf.2007.12.087

Roncali, J. (2009). Molecular bulk heterojunctions: An emerging approach to organic solar cells. *Accounts of Chemical Research*, *42*(11), 1719–1730. doi:10.1021/ar900041b

Roncali, J., & Garnier, F. (1984). Photon-transport properties of luminescent solar concentrators: Analysis and optimization. *Applied Optics*, *23*, 2809. doi:10.1364/AO.23.002809

Rosenwaks, Y., Hanna, M. C., Levi, D. H., Szmyd, D. M., Ahrenkiel, R. K., & Nozik, A. J. (1993). Hot-carrier cooling in GaAs: Quantum wells vs bulk. *Physical Review B: Condensed Matter and Materials Physics*, *48*, 14675. doi:10.1103/PhysRevB.48.14675

Ross, R. T. (1967). Some thermodynamics of photochemical systems. *The Journal of Chemical Physics*, *46*(12), 4590. doi:10.1063/1.1840606

Ross, R. T., & Nozik, A. J. (1982). Efficiency of hot-carrier solar energy converters. *Journal of Applied Physics*, *53*, 3813. doi:10.1063/1.331124

Rowan, B. C., Richards, B. S., Bcrowanhwacuk, E., Robertson, N., Jones, A. C., Richardson, P., & Moudam, O. (2008). Near-infrared emitting lanthanide complexes for luminescent solar concentrators. In *Proceedings of the 23rd European Photovoltaic Solar Energy Conference*. Valencia, Spain: EU PVSEC.

Rowan, B. C., Wilson, L. R., & Richards, B. S. (2009). Visible and near-infrared emitting lanthanide complexes for luminescent solar concentrators. In *Proceedings of the 24th European Photovoltaic Solar Energy Conference*. Hamburg, Germany: EU PVSEC.

Ryan, J. F., Taylor, R. A., Tuberfield, A. J., Maciel, A., Worlock, J. M., Gossard, A. C., & Wiegmann, W. (1984). Time-resolved photoluminescence of two-dimensional hot carriers in GaAs-AlGaAs heterostructures. *Physical Review Letters*, *53*(19), 1841–1844. doi:10.1103/PhysRevLett.53.1841

Rytov, S. M. (1956). Acoustical properties of a thinly laminated medium. *Soviet Physics: Acoustics*, *2*, 69.

Ryvkin, S. M. (1964). *Photoelectric effects in semiconductors*. New York, NY: Consultant Bureau.

Sailor, M. J., Ginsburg, E. J., Gorman, C. B., Kumar, A., Grubbs, R. H., & Lewis, N. S. (1990). Thin films of n-Si/poly-$(CH_3)_3$Si-cyclooctatetraene: Conducting-polymer solar cells and layered structures. *Science*, *249*(4973), 1146–1149. doi:10.1126/science.249.4973.1146

Saraidarov, T., Levchenko, V., Grabowska, A., Borowicz, P., & Reisfeld, R. (2010). Non-self-absorbing materials for luminescent solar concentrators (LSC). *Chemical Physics Letters*, *492*, 60–62. doi:10.1016/j.cplett.2010.03.087

Sariciftci, N. S., Smilowitz, L., Heeger, A. J., & Wudl, F. (1992). Photoinduced electron transfer from a conducting polymer to buckminsterfullerene. *Science*, *258*(5087), 1474–1476. doi:10.1126/science.258.5087.1474

Sarma, S., Das, S. M. A., & Kim, K. W. (1992). Paper. *Semiconductor Science and Technology*, *60*(7).

Sasaki, T., Arafune, K., Lee, H. S., Ekins-Daukes, N. J., Tanaka, S., Ohshita, Y., & Yamaguchi, M. (2006). Effects of thermal cycle annealing on reduction of deficit density on lattice-mismatched InGaAS solar cells. *Physica B, Condensed Matter*, *376-377*, 626. doi:10.1016/j.physb.2005.12.158

Sato, Y., Yamagishi, K., & Yamashita, M. (2005). Multilayer structure photovoltaic cells. *Optical Review*, *12*, 324–327. doi:10.1007/s10043-005-0324-3

Saunders, B. R., & Turner, M. L. (2008). Nanoparticle-polymer photovoltaic cells. *Advances in Colloid and Interface Science*, *138*(1), 1–23. doi:10.1016/j.cis.2007.09.001

Scheblykin, I. G., Yartsev, A., Pullerits, T., Gulbinas, V., & Sundström, V. (2007). Excited state and charge photogeneration dynamics in conjugated polymers. *The Journal of Physical Chemistry B*, *111*(23), 6303–6321. doi:10.1021/jp068864f

Schiff, E. A. (2003). Low mobility solar cells: A device physics primer with applications to amorphous silicon. *Solar Energy Materials and Solar Cells*, *78*, 567–595. doi:10.1016/S0927-0248(02)00452-X

Schmidt-Mende, L., & Grätzel, M. (2006). TiO_2 pore-filling and its effect on the efficiency of solid-state dye-sensitized solar cells. *Thin Solid Films*, *500*(1-2), 296–301. doi:10.1016/j.tsf.2005.11.020

Selberherr, S. (1984). *Analysis and simulation of semiconductor device simulation*. New York, NY: Springer-Verlag. doi:10.1007/978-3-7091-8752-4

Shaheen, S. E., Brabec, C. J., Sariciftci, N. S., Padinger, F., Fromherz, T., & Hummelen, J. C. (2001). 2.5% efficient organic plastic solar cells. *Applied Physics Letters*, *78*(6), 841–843. doi:10.1063/1.1345834

Shah, J., Pinczuk, P., Gossard, A. C., & Wiegmann, W. (1985). Energy-loss rates for hot electron and holes in GaAs quantum wells. *Physical Review Letters*, *18*, 2045. doi:10.1103/PhysRevLett.54.2045

Shan, W., Walukiewicz, W., Ager, J. W., Haller, E. E., Geisz, J. F., & Friedman, D. J. (1999). Band anticrossing in GaInNAs alloys. *Physical Review Letters*, *82*(6), 1221. doi:10.1103/PhysRevLett.82.1221

Shaw, P. E., Ruseckas, A., & Samuel, I. D. W. (2008). Exciton diffusion measurements in poly(3-hexylthiophene). *Advanced Materials (Deerfield Beach, Fla.)*, *20*(18), 3516–3520. doi:10.1002/adma.200800982

Shcherbatyuk, G. V., Inman, R. H., Wang, C., Winston, R., & Ghosh, S. (2010). Viability of using near infrared PbS quantum dots as active materials in luminescent solar concentrators. *Applied Physics Letters*, *96*(19), 191901. doi:10.1063/1.3422485

Shirakawa, H. (2001). The discovery of polyacetylene film: The dawning of an era of conducting polymers (nobel lecture). *Angewandte Chemie International Edition*, *40*(14), 2574–2580. doi:10.1002/1521-3773(20010716)40:14<2574::AID-ANIE2574>3.0.CO;2-N

Shirakawa, H., McDiarmid, A., & Heeger, A. (2003). Twenty-five years of conducting polymers. *Chemical Communications*, *1*, 1–4. doi:10.1039/b210718j

Shockley, W., & Queisser, H. (1961). Detailed balance limit of efficiency of p-n junction solar cells. *Journal of Applied Physics*, *32*, 510. doi:10.1063/1.1736034

Shockley, W., & Queisser, H. J. (1961). Detailed balance limit of efficiency of p-n junction solar cells. *Journal of Applied Physics*, *32*(3), 510–519. doi:10.1063/1.1736034

Shockley, W., & Read, W. T. (1952). Statistics of the recombinations of holes and electrons. *Physical Review*, *87*, 835. doi:10.1103/PhysRev.87.835

Shoji, Y., Oshima, R., Takata, A., Morioka, T., & Okada, Y. (2010a). Multi-stacked InGaAs/GaNAs quantum dot solar cell fabricated on GaAs (311)B substrate. In *Proceedings of the 35th IEEE Photovoltaic Specialists Conference*, (p. 1859). Honolulu, HI: IEEE Press.

Shoji, Y., Oshima, R., Takata, A., & Okada, Y. (2010b). Structural properties of multi-stacked self-organized InGaAs quantum dots grown on GaAs (311)B substrate. *Journal of Crystal Growth*, *312*, 226. doi:10.1016/j.jcrysgro.2009.10.053

Shrotriya, V., Wu, E. H.-E., Li, G., Yao, Y., & Yang, Y. (2006). Efficient light harvesting in multiple-device stacked structure for polymer solar cells. *Applied Physics Letters*, *88*(6), 064104–064103. doi:10.1063/1.2172741

Slooff, L. H., Bende, E. E., & Budel, T. (2009). The non-fluorescent flat plate concentrator. In *Proceedings of the 24th European Photovoltaic Solar Energy Conference*. Hamburg, Germany: EU PVSEC.

Slooff, L. H., Budel, T., Burgers, A. R., Bakker, N. J., Danz, R., Meyer, T., & Meyer, A. (2007). The luminescent concentrator: Stability issues. In *Proceedings of the 22nd European Photovoltaic Solar Energy Conference*. EU PVSEC.

Slooff, L. H., Bende, E. E., Burgers, A. R., Budel, T., Pravettoni, M., & Kenny, R. P. (2008). A luminescent solar concentrator with 7.1% power conversion efficiency. *Physica Status Solidi*, *2*(6), 257–259. doi:10.1002/pssr.200802186

Slooff, L. H., Bende, E. E., Burgers, A. R., Budel, T., Pravettoni, M., & Kenny, R. P. (2008). Supporting information for a luminescent solar concentrator with 7.1% power conversion efficiency. *Physica Status Solidi*, *2*(6).

Smestad, G. P. (2002). *Optoelectronics of solar cells*. Bellingham, UK: SPIE Press. doi:10.1117/3.446028

Smestad, G., Bignozzi, C., & Argazzi, R. (1994). Testing of dye sensitized TiO2 solar cells I: Experimental photocurrent output and conversion efficiencies. *Solar Energy Materials and Solar Cells*, *32*(3), 259–272. doi:10.1016/0927-0248(94)90263-1

Soedergren, S., Hagfeldt, A., Olsson, J., & Lindquist, S. E. (1994). Theoretical models for the action spectrum and the current-voltage characteristics of microporous semiconductor films in photoelectrochemical cells. *Journal of Physical Chemistry*, *98*(21), 5552–5556. doi:10.1021/j100072a023

Solomon, G. S., Trezza, J. A., Marshall, A. F., & Harris, J. S. Jr. (1996). Vertically aligned and electronically coupled growth induced InAs islands in GaAs. *Physical Review Letters*, *76*, 952. doi:10.1103/PhysRevLett.76.952

Song, Y. J., Lee, J. U., & Jo, W. H. (2010). Multi-walled carbon nanotubes covalently attached with poly(3-hexylthiophene) for enhancement of field-effect mobility of poly(3-hexylthiophene)/multi-walled carbon nanotube composites. *Carbon*, *48*(2), 389–395. doi:10.1016/j.carbon.2009.09.041

Springholz, G., Holy, V., Pnczolits, M., & Bauer, G. (1998). Self-organized growth of three-dimensional quantum-dot crystals with fcc-like stacking and tunable lattice constant. *Science*, *282*, 734. doi:10.1126/science.282.5389.734

Srivastava, G. P. (1990). *The physics of phonons*. Bristol, UK: Adam Hilger.

Srivastava, G. P. (2008). Paper. *Physical Review B: Condensed Matter and Materials Physics*, *77*, 155–205.

Stefopoulos, A. A., Chochos, C. L., Prato, M., Pistolis, G., Papagelis, K., & Petraki, F. (2008). Novel hybrid materials consisting of regioregular poly(3-octylthiophene) s covalently attached to single-wall carbon nanotubes. *Chemistry (Weinheim an der Bergstrasse, Germany)*, *14*(28), 8715–8724. doi:10.1002/chem.200800683

Strandberg, R., & Reenaas, T. W. (2009). Photofilling of intermediate bands. *Journal of Applied Physics*, *105*(12), 124512. doi:10.1063/1.3153141

Strandberg, R., & Reenaas, T. W. (2010). Limiting efficiency of intermediate band solar cells with spectrally selective reflectors. *Applied Physics Letters*, *97*(3), 031910. doi:10.1063/1.3466269

Strandberg, R., & Reenaas, T. W. (2011). Drift-diffusion model for intermediate band solar cells including photo-filling effects. *Progress in Photovoltaics: Research and Applications*, *19*, 21. doi:10.1002/pip.983

Sugawara, M. (1999). *Self-assembled InGaAs/GaAs quantum dots*. San Diego, CA: Academic Press.

Sugiura, H., Amano, C., Yamamoto, A., & Yamaguchi, M. (1988). Double heterostructure GaAs tunnel junction for a AlGaAs/GaAs tandem solar cell. *Japanese Journal of Applied Physics*, *27*, 269.

Sun, B., Snaith, H. J., Dhoot, A. S., Westenhoff, S., & Greenham, N. C. (2005). Vertically segregated hybrid blends for photovoltaic devices with improved efficiency. *Journal of Applied Physics*, *97*(1), 014914–014916. doi:10.1063/1.1804613

Swanson, R. M. (2006). A vision for crystalline silicon photovoltaics. *Progress in Photovoltaics: Research and Applications*, *14*, 443.

Swartz, B. A., Cole, T., & Zewail, A. H. (1977). Photon trapping and energy transfer in multiple-dye plastic matrices: An efficient solar-energy concentrator. *Optics Letters*, *1*, 73–75. doi:10.1364/OL.1.000073

Swift, P. D., Smith, G. B., & Franklin, J. B. (1999). Light-to-light efficiencies in luminescent solar concentrators. In *Proceedings of the SPIE Conference*, (pp. 21-28). SPIE.

Swift, P. D., & Smith, G. B. (2003). Color considerations in fluorescent solar concentrator stacks. *Applied Optics*, *42*, 5112–5117. doi:10.1364/AO.42.005112

Sze, S. M. (1981). *Physics of semiconductor devices* (2nd ed.). New York, NY: John Wiley & Sons.

Tablero, C. (2006). Analysis of the optical properties for Ga4P3Ti compound with a metallic intermediate band. *Computational Materials Science*, *36*(3), 263–267. doi:10.1016/j.commatsci.2005.04.005

Tablero, C., & Fuertes Marrón, D. (2010). Analysis of the electronic structure of modified CuGaS2 with selected substitutional impurities: Prospects for intermediate-band thin-film solar cells based on cu-containing chalcopyrites. *The Journal of Physical Chemistry C*, *114*(6), 2756–2763. doi:10.1021/jp909895q

Takamoto, T., Agui, T., Ikeda, T., & Kurita, E. (2000). Paper. In *Proceedings of the 28th IEEE Photovoltaic Specialists Conference*, (p. 976). New York, NY: IEEE Press.

Takamoto, T., Agui, T., Kamimura, K., Kaneiwa, M., Imaizumi, M., Matsuda, S., & Yamaguchi, M. (2003). Paper. In *Proceedings of the 3rd World Conference on Photovoltaic Energy Conversion, WCPEC-3*, (p. 581).

Takamoto, T., Agui, T., Yoshida, A., Nakaido, K., Juso, H., & Sasaki, K. … Takahashi, M. (2010). Paper. In *Proceeding of 35th IEEE Photovoltaic Specialists Conference*, (p. 412). New York, NY: IEEE Press.

Takamoto, T., Ikeda, E., Agui, T., Kurita, E., Tanabe, T., & Tanaka, S. … Yamaguchi, M. (1997). Paper. In *Proceedings of the 26th IEEE Photovoltaic Specialists Conference*, (p. 1031). New York, NY: IEEE Press.

Takamoto, T., Ikeda, E., Kurita, H., Ohmori, M., & Yamaguchi, M. (1997). Two-terminal monolithic $In_{0.5}Ga_{0.5}P$/*GaAs* tandem solar cells with a high conversion efficiency of over 30%. *Japanese Journal of Applied Physics*, *36*, 6215. doi:10.1143/JJAP.36.6215

Takamoto, T., Kaneiwa, M., Imaizumi, M., & Yamaguchi, M. (2005). InGaP/GaAs-based multijunction solar cells. *Progress in Photovoltaics: Research and Applications*, *13*, 495. doi:10.1002/pip.642

Takata, A., Oshima, R., Shoji, Y., Akahane, K., & Okada, Y. (2010). Paper. In *Proceedings of the 35th IEEE Photovoltaic Specialists Conference*, (p. 1877). Honolulu, HI: IEEE Press.

Takeuchi, T., Kageyama, H., Nakazawa, H., Atsumi, T., Tamura, S., & Kamijo, N. (2008). Preparation of fluorine-containing indium tin oxide sputtering targets using spark plasma sintering process. *Journal of the American Ceramic Society*, *91*(8), 2495–2500. doi:10.1111/j.1551-2916.2008.02503.x

Talapin, D. V., Koeppe, R., Gotzinger, S., Kornowski, A., Lupton, J. M., & Rogach, A. L. (2003). Highly emissive colloidal CdSe/CdS heterostructures of mixed dimensionality. *Nano Letters*, *3*(12), 1677–1681. doi:10.1021/nl034815s

Talapin, D. V., Nelson, J. H., Shevchenko, E. V., Aloni, S., Sadtler, B., & Alivisatos, A. P. (2007). Seeded growth of highly luminescent CdSe/CdS nanoheterostructures with rod and tetrapod morphologies. *Nano Letters*, *7*(10), 2951–2959. doi:10.1021/nl072003g

Tanaka, S., Kobayashi, H., Saito, H., & Shionoya, S. (1980). Luminescence of high density electron-hole plasma in GaAs. *Journal of the Physical Society of Japan*, *49*, 1051. doi:10.1143/JPSJ.49.1051

Tang, C. W. (1986). Two-layer organic photovoltaic cell. *Applied Physics Letters*, *48*(2), 183–185. doi:10.1063/1.96937

Tauc, J., Grigorovici, R., & Vancu, A. (1966). Optical properties and electronic structure of amorphous germanium. *Physica Status Solidi*, *15*, 627–637. doi:10.1002/pssb.19660150224

Tenne, R., Rao, C. N. R. (2004). Inorganic nanotubes. *Philosophical Transactions of the Royal Society A, 362*(1823), 2099-2125.

Tian, H., Zhang, J., & Yangjing, Yu. T., & Zou, Z. (2011). Analysis on dye-sensitized solar cell's efficiency improvement. *Journal of Physics: Conference Series, 276*, 012188.

Tobías, I., Luque, A., & Martí, A. (2008). Light intensity enhancement by diffracting structures in solar cells. *Journal of Applied Physics*, *104*(3), 034502–034509. doi:10.1063/1.2960586

Tobías, I., Luque, A., & Martí, A. (2011). Numerical modeling of intermediate band solar cells. *Semiconductor Science and Technology*, *26*, 014031. doi:10.1088/0268-1242/26/1/014031

Tomić, S. (2010). Intermediate-band solar cells: Influence of band formation on dynamical processes in InAs/GaAs quantum dot arrays. *Physical Review B: Condensed Matter and Materials Physics*, *82*, 195321. doi:10.1103/PhysRevB.82.195321

Tomić, S., Jones, T. S., & Harrison, N. M. (2008). Absorption characteristics of a quantum dot array induced intermediate band: Implications for solar cell design. *Applied Physics Letters*, *93*, 263105. doi:10.1063/1.3058716

Tomita, T. (2006). Paper. In *Proceedings of the 4th World Conference on Photovoltaic Energy Conversion*, (p. 2450). New York, NY: IEEE Press.

Tran, D., Vendura, G. J., Jr., Jones, W. L., & Rezek, E. A. (2002). *Solar cell used in satellites and space stations, has intermediate semiconductor layers whose bandgaps transitions from smaller energy state to larger energy state*. Patent US6437233-B1. Washington, DC: US Patent Office.

Tremolet de Villers, B., Tassone, C. J., Tolbert, S. H., & Schwartz, B. J. (2009). Improving the reproducibility of P3HT: PCBM solar cells by controlling the PCBM/cathode interface. *The Journal of Physical Chemistry C*, *113*(44), 18978–18982. doi:10.1021/jp9082163

Trivich, D., & Flinn, P. A. (1955). Maximum efficiency of solar energy conversion by quantum process. *Solar Energy Research*, 143-147.

Tsai, C.-Y., & Tsai, C.-Y. (2009). Effects of carrier escape and capture processes on quantum well solar cells: A theoretical investigation. *IET Optoelectronics*, *3*(6), 300–304. doi:10.1049/iet-opt.2009.0027

Ulbrich, R. (1973). Energy relaxation of photoexcited hot electrons in GaAs. *Physical Review B: Condensed Matter and Materials Physics*, *8*, 5719. doi:10.1103/PhysRevB.8.5719

van de Lagemaat, J., Barnes, T. M., Rumbles, G., Shaheen, S. E., Coutts, T. J., & Weeks, C. (2006). Organic solar cells with carbon nanotubes replacing In_2O_3:Sn as the transparent electrode. *Applied Physics Letters*, *88*(23), 233503–233503. doi:10.1063/1.2210081

Van Driel, H. M. (1979). Influence of hot phonons on energy relaxation of high-density carriers in germanium. *Physical Review B: Condensed Matter and Materials Physics*, *19*, 5928. doi:10.1103/PhysRevB.19.5928

Varghese, O. K., Gong, D., Paulose, M., Ong, K. G., Dickey, E. C., & Grimes, C. A. (2003). Extreme changes in the electrical: Resistance of titania nanotubes with hydrogen exposure. *Advanced Materials (Deerfield Beach, Fla.)*, *15*, 624–627. doi:10.1002/adma.200304586

Varonides, A. C. (2008). Quantum size effects in amorphous Si superlattice solar cells. *Renewable Energy*, *33*(2), 273–276. doi:10.1016/j.renene.2007.05.033

Verbunt, P. P. C., Bastiaansen, C. W. M., Broer, D. J., & Debije, M. G. (2009). The effect of dyes aligned by liquid crystals on luminescent solar concentrator performance. In *Proceedings of the 24th European Photovoltaic Solar Energy Conference*. Hamburg, Germany: EU PVSEC.

Verbunt, P. P. C., Kaiser, A., Hermans, K., Bastiaansen, C. W. M., Broer, D. J., & Debije, M. G. (2009). Controlling light emission in luminescent solar concentrators through use of dye molecules aligned in a planar manner by liquid crystals. *Advanced Functional Materials*, *19*, 2714–2719. doi:10.1002/adfm.200900542

Vietmeyer, F., Seger, B., & Kamat, P. V. (2007). Anchoring ZnO particles on functionalized single wall carbon nanotubes: Excited state interactions and charge collection. *Advanced Materials (Deerfield Beach, Fla.)*, *19*(19), 2935–2940. doi:10.1002/adma.200602773

Vlachopoulos, N., Liska, P., Augustynski, J., & Graetzel, M. (1988). Very efficient visible light energy harvesting and conversion by spectral sensitization of high surface area polycrystalline titanium dioxide films. *Journal of the American Chemical Society*, *110*(4), 1216–1220. doi:10.1021/ja00212a033

Vurgaftman, I., & Meyer, J. R. (2001). Using JPF1 format. *Journal of Applied Physics*, *89*(11), 5815–5875. doi:10.1063/1.1368156

Wagner, J., Gruber, M., Hinderhofer, A., Wilke, A., Bröker, B., & Frisch, J. (2010). High fill factor and open circuit voltage in organic photovoltaic cells with diindenoperylene as donor material. *Advanced Functional Materials*, *20*(24), 4295–4303. doi:10.1002/adfm.201001028

Wahnón, P., & Tablero, C. (2002). Ab initio electronic structure calculations for metallic intermediate band formation in photovoltaic materials. *Physical Review B: Condensed Matter and Materials Physics*, *65*(16), 1–10. doi:10.1103/PhysRevB.65.165115

Walters, R. J., Summers, G. P., Messenger, S. R., Freundlich, A., Monier, C., & Newman, F. (2000). Radiation hard multi-quantum well InP/InAsP solar cells for space applications. *Progress in Photovoltaics: Research and Applications*, *8*(3), 349–354. doi:10.1002/1099-159X(200005/06)8:3<349::AID-PIP326>3.0.CO;2-Z

Wang, Y., Yang, H., Liu, Y., Wang, H., Shen, H., Yan, J., & Xu, H. (2010). The use of Ti meshes with self-organized TiO_2 nanotubes as photoanodes of all-Ti dye-sensitized solar cells. *Progress in Photovoltaics: Research and Applications*, *18*, 285–290.

Wasilewski, R. Z., Fafard, S., & McCaffrey, P. J. (1999). Size and shape engineering of vertically stacked self-assembled quantum dots. *Journal of Crystal Growth*, *20-202*, 1131. doi:10.1016/S0022-0248(98)01539-5

WBGU. (2003). *World in transition – Towards sustainable energy systems*. London, UK: Earthsan.

Weber, W. H., & Lambe, J. (1976). Luminescent greenhouse collector for solar radiation. *Applied Optics*, *15*, 2299. doi:10.1364/AO.15.002299

Wei, D. (2010). Dye sensitized solar cells. *International Journal of Molecular Sciences*, *11*, 1103–1113. doi:10.3390/ijms11031103

Wei, G. D., Shiu, K. T., Giebink, N. C., & Forrest, S. R. (2007). Thermodynamic limits of quantum photovoltaic cell efficiency. *Applied Physics Letters*, *91*(22), 223–507. doi:10.1063/1.2817753

Wei, J., Jia, Y., Shu, Q., Gu, Z., Wang, K., & Zhuang, D. (2007). Double-walled carbon nanotube solar cells. *Nano Letters*, *7*(8), 2317–2321. doi:10.1021/nl070961c

Weiming, W., Albert, S. L., & Jamie, D. P. (2009). Intermediate-band photovoltaic solar cell based on ZnTe:O. *Applied Physics Letters*, *95*(1), 011103. doi:10.1063/1.3166863

Wenger, S. (2010). *Strategies to optimizing dye-sensitized solar cells: Organic sensitizers, tandem device structures, and numerical device modeling*. Retrieved from http://library.epfl.ch/en/theses/?nr=4805

Wenger, S., Schmid, M., Rothenberger, G., Grätzel, M., & Schumacher, J. O. (2009). *Model-based optical and electrical* characterization of dye-sensitized solar cells. Retrieved from http://www.juergenschumacher.de/html/material/veroeffentlichungen/DSC-EUPVSEC-Hamburg.pdf

Wienk, M., Kroon, J. M., Verhees, W. J. H., Krol, J., Hummelen, J. C., Van Haal, P., & Janssen, R. A. J. (2003). Efficient methano[70] fullerene/MDMO-PPV bulk heterojunction photovoltaic cells. *Angewandt Chemie International Edition, 42*(29), 3371-3375.

Wilson, H. R. (1988). Fluorescent quantum yields and long-term stability of silver island/polymer/dye systems, with applications to longer wavelength fluorescent solar concentrators. In *Proceedings of SPIE Conference*. Hamburg, Germany: SPIE.

Wilson, L. R., & Richards, B. S. (2008). High-efficiency dyes for luminescent solar concentrators - Photostability and modeling. In *Proceedings of the 23rd European Photovoltaic Solar Energy Conference*. Valencia, Spain: EU PVSEC.

Wilson, H. R. (1987). Fluorescent dyes interacting with small silver particles: A system extending the spectral range of fluorescent solar concentrators. *Solar Energy Materials*, *16*, 223–234. doi:10.1016/0165-1633(87)90022-0

Wilson, L. R., Rowan, B. C., Robertson, N., Moudam, O., Jones, A. C., & Richards, B. S. (2010). Characterization and reduction of reabsorption losses in luminescent solar concentrators. *Applied Optics*, *49*, 1651. doi:10.1364/AO.49.001651

Wittwer, V., Stahl, W., & Goetzberger, A. (1984). Fluorescent planar concentrators. *Solar Energy Materials*, *11*, 187–197. doi:10.1016/0165-1633(84)90070-4

Wolf, M. (1960). Detailed balance limit of efficient p-n junction solar cells. In *Proceedings of IRE 48*, (pp. 1246). IRE.

Wolf, M. (1960). Limitations and possibilities for improvements of photovoltaic solar energy converters: Part I: Considerations for earth's surface operation. *Proceedings of the IRE*, *48*(7), 1246–1263. doi:10.1109/JRPROC.1960.287647

World Bank. (2008). *World development indicators 2008*. Washington, DC: World Bank.

Wu, J., Walukiewicz, W., & Haller, E. E. (2002). Band structure of highly mismatched semiconductor alloys: Coherent potential approximation. *Physical Review B: Condensed Matter and Materials Physics*, *65*, 233210. doi:10.1103/PhysRevB.65.233210

Würfel, P. (1982). The chemical potential of radiation. *Journal of Physics. C. Solid State Physics*, *15*, 3967–3985. doi:10.1088/0022-3719/15/18/012

Würfel, P. (1997). Solar energy conversion with hot electrons from impact ionization. *Solar Energy Materials and Solar Cells*, *46*, 43. doi:10.1016/S0927-0248(96)00092-X

Würfel, P. (2009). *Physics of solar cells: From basic principles to advanced concepts*. New York, NY: Wiley.

Würfel, P., Brown, A. S., Humphrey, T. E., & Green, M. A. (2005). Particle conservation in the hot-carrier solar cell. *Progress in Photovoltaics: Research and Applications*, *13*, 277. doi:10.1002/pip.584

Wu, Y., & Zhang, G. (2010). Performance enhancement of hybrid solar cells through chemical vapor annealing. *Nano Letters*, *10*(5), 1628–1631. doi:10.1021/nl904095n

Xue, J., Rand, B. P., Uchida, S., & Forrest, S. R. (2005). A hybrid planar-mixed molecular heterojunction photovoltaic cell. *Advanced Materials (Deerfield Beach, Fla.)*, *17*(1), 66–71. doi:10.1002/adma.200400617

Yablonovitch, E. (1980). Thermodynamics of the fluorescent planar concentrator. *Journal of the Optical Society of America*, *70*(11), 1362–1363. doi:10.1364/JOSA.70.001362

Yablonovitch, E. (1993). Photonic band-gap structures. *Journal of the Optical Society of America. B, Optical Physics*, *10*, 283. doi:10.1364/JOSAB.10.000283

Yablonovitch, E., & Cody, G. D. (1982). Intensity enhancement in textured optical sheets for solar cells. *IEEE Transactions on Electron Devices*, *29*, 300–305. doi:10.1109/T-ED.1982.20700

Yamaguchi, M. (2004). Paper. In *Proceedings of the 19th European Photovoltaic Solar Energy Conference* (p. xl). Munich, Germany: WIP.

Yamaguchi, M. (2003). III–V compound multi-junction solar cells: Present and future. *Solar Energy Materials and Solar Cells*, *75*, 261. doi:10.1016/S0927-0248(02)00168-X

Yamaguchi, M., & Amano, C. (1985). Numerical analysis for high-efficiency GaAs solar cells fabricated on Si substrates. *Journal of Applied Physics*, *58*, 3601.

Yamaguchi, M., Nishimura, K., Sasaki, T., Suzuki, H., Arafune, K., & Kojima, N. (2008). Novel materials for high-energy III-V multi-junction solar cells. *Solar Energy*, *82*, 173. doi:10.1016/j.solener.2007.06.011

Yamaguchi, M., Okuda, T., Taylor, S. J., Takamoto, T., Ikeda, W., & Kurita, H. (1997). Superior radiation-resistant properties of InGaP/GaAs tandem solar cells. *Applied Physics Letters*, *70*, 1566. doi:10.1063/1.118618

Yang, M.-J., Yamaguchi, M., Takamoto, T., Ikeda, E., Kurita, H., & Ohmori, M. (1997). III–V compound multi-junction solar cells: Present and future. *Solar Energy Materials and Solar Cells*, *45*, 331. doi:10.1016/S0927-0248(96)00079-7

Yong, V., Ho, S. T., & Chang, R. P. H. (2008). Modeling and simulation for dye-sensitized solar cells. *Applied Physics Letters*, *92*(14), 143506. doi:10.1063/1.2908204

Yoshida, A., Agui, T., Nakaido, K., Murasawa, K., Juso, H., Sasaki, K., & Takamoto, T. (2011). Technical digest. In *Proceedings of 21st International Photovoltaic Science and Engineering Conference*. Fukuoka, Japan: Photovoltaic Science and Engineering.

Yoshida, K., Okada, Y., & Sano, N. (2010b). Self-consistent drift-diffusion approach for analysis intermediate band solar cells with multi-stacked quantum dots. In *Proceedings of 25th European Photovoltaic Solar Energy Conference and Exhibition / 5th World Conference on Photovoltaic Energy Conversion*, (p. 545). Valencia, Spain: WIP.

Yoshida, K., Okada, Y., & Sano, N. (2010c). Self-consistent drift-diffusion analysis of intermediate band solar cell (IBSC): Effect of energetic position of IB on conversion efficiency. In *Proceedings of 35th IEEE Photovoltaic Specialists Conference*, (p. 71). Honolulu, HI: IEEE Press.

Yoshida, K., Okada, Y., & Sano, N. (2010a). Self-consistent simulation of intermediate band solar cells: Effect of occupation rates on device characteristics. *Applied Physics Letters*, *97*, 133503. doi:10.1063/1.3488815

Yu, G., Gao, J., Hummelen, J. C., Wudl, F., & Heeger, A. J. (1995). Polymer photovoltaic cells: Enhanced efficiencies via a network of internal donor-acceptor heterojunctions. *Science*, *270*(5243), 1789–1791. doi:10.1126/science.270.5243.1789

Yu, K. M., Walukiewicz, J. W. A., Bour, D., Farshchi, R., & Dubon, O. D. (2006). Multiband GaNAsP quaternary alloys. *Applied Physics Letters*, *88*(9), 092110. doi:10.1063/1.2181627

Yu, P. Y., & Cardona, M. (2001). *Fundamentals of semiconductors*. Berlin, Germany: Springer-Verlag.

Zhang, X.-T., Liu, H.-W., Taguchi, T., Meng, Q. B., Sato, O., & Fujishima, A. (2004). Slow interfacial charge recombination in solid-state dye-sensitized solar cell using Al_2O_3-coated nanoporous TiO_2 films. *Solar Energy Materials and Solar Cells*, *81*(2), 197–203. doi:10.1016/j.solmat.2003.11.005

Zhang, Y., Aslan, K., Previte, M. J. R., & Geddes, C. D. (2007). Metal-enhanced fluorescence: Surface plasmons can radiate a fluorophores structured emission. *Applied Physics Letters*, *90*(5), 053107. doi:10.1063/1.2435661

Zhao, J., Wang, A., Green, M. A., & Ferrazza, F. (1998). 11.8% efficient "honeycomb" textured multicrystalline and 24.4% monocrystalline silicon solar cells. *Applied Physics Letters*, *73*(14), 1991–1993. doi:10.1063/1.122345

Zhou, X., Kobayashi, Y., Romanyuk, V., Ochuchi, N., Takeda, M., Tsunekawa, S., & Kasuya, A. (2005). Preparation of silica encapsulated CdSe quantum dots in aqueous solution with the improved optical properties. *Applied Surface Science*, *242*(3-4), 281–286. doi:10.1016/j.apsusc.2004.08.022

About the Contributors

Laurentiu Fara is Professor in the Physics Department, Faculty of Applied Sciences, Polytechnic University of Bucharest, Romania. He received his PhD from the Institute of Atomic Physics, Bucharest, Romania, in 1987. His research focuses on PV cells and systems, as well as on Solar Thermal systems. He also works in the modelling and simulation of advanced solar cells, namely Quantum Well Solar Cells, Polymer Solar Cells, and Dye Solar Cells. He received the Romanian Academy Award in Physics for his activity in Solar Energy in 1987. He is the Chairman of Romania ISES Section. He contributed in several research and training projects, funded by both European and National Programmes. In 2008, he was the chairman of the Scientific Committee of the International Workshop dedicated to "New Trends in Photovoltaics," organized in Bucharest, Romania. He is a member of the Academy of Romanian Scientists.

Masafumi Yamaguchi is a Principal Professor at the Toyota Technological Institute (TTI), Nagoya, Japan. He received his Ph.D degree from the Hokkaido University, Japan, in 1978. His research focuses on III-V compound multi-junction solar cells and materials, space and concentrator cells, crystalline Si solar cells and materials, and analysis of defects and impurities in semiconductor materials and devices. He has received several awards such as the William Cherry Award from the IEEE in 2008 and the Becquerel Prize from the European Commission in 2004. Currently, he is the Director of Solar Cells and Modules Division, International Solar Energy Society (ISES), the Research Supervisor in the field of the Creative Research for Clean Energy using Solar Energy, Japan Science and Technology Agency (JST), and the Project Leader of the Next Generation High Performance PV R&D Project, New Energy and Industrial Technology Development Organization (NEDO).

* * *

Elisa Antolín (b. 1977) obtained her Physical Science degree at Universidad Autónoma de Madrid, in 2001, and the Ph.D. degree from the Universidad Politécnica de Madrid (U.P.M.) in 2010. She has been collaborating with the Silicon and Fundamental Studies research group at the Institute of Solar Energy of the U.P.M., lead by Prof. Luque, since 2004. Dr. Antolín is specialized in the field of photovoltaics, and her research topics include theoretical and experimental studies of the intermediate band solar cell.

Keith Barnham is Emeritus Professor of Physics at Imperial College London. His early research career was in Experimental Particle Physics at Birmingham University, CERN Geneva, Berkeley, California, and Imperial. In the 1980s, he changed his research field to the study of photovoltaics, spending

a year as a Royal Society/SERC Industrial Fellow before returning to Imperial to found the Quantum Photovoltaic group. The group developed a new type of high-efficiency solar cell, the quantum well solar cell, and a novel quantum dot concentrator. He has co-founded two solar cell companies. One of these, QuantaSol Ltd. manufactured 40% efficient triple-junction concentrator cells using the quantum well technology and achieved Guardian CleanTech Top 100 positions in 2008 and 2009. The cell passed qualification. Despite a substantial order for cells, the company was sold against the founder's wishes to JDSU in July 2011. He was a founding member of Scientists Against Nuclear Arms (SANA) and is now a sponsor of the successor organisation, Scientists for Global Responsibility (SGR).

Rahul Bose studied Physics at Imperial College London, where he completed his MSci degree with First-Class Honours in 2006 and conducted PhD research on the topic of Luminescent Solar Concentrators under supervision of Prof. Keith Barnham and Dr. Amanda Chatten from 2006 to 2010. Rahul developed a raytrace model of the concentrator, characterised different concentrator configurations, and investigated novel luminescent materials. He has presented his research at several international conferences and been involved in international outreach activities with the Quantum Photovoltaic Group at Imperial. Rahul currently works as a consultant at McKinsey and Company in Berlin.

Amanda Chatten is a Lecturer in the Department of Physics at Imperial College London. She studied for both her BSc, for which she was awarded the University of London Neil Arnott Prize for Chemistry 1992, and her PhD in the Department of Chemistry at University College London. Following her PhD, Amanda carried out postdoctoral research on a novel approach to the intensive structuring of surfactant systems and the effects of heat and mass transfer in two-phase multi-component flowing systems. Between 2000 and 2007, she carried out further postdoctoral research in the Department of Physics at Imperial, developing characterization techniques and models for the luminescent solar concentrator as well as developing models of charge transport in binary blends for organic solar cells. Amanda took up a lectureship in the Experimental Solid State group in 2008 and has published over 30 papers on solar photovoltaics in refereed journals and proceedings.

Corneliu Cincu, PhD obtained in 1975, is Associated Professor at Politehnica University of Bucharest, Faculty of Applied Chemistry and Materials Science. From 1974-2011, he taught at the Faculty of Applied Chemistry and Materials Science of Politehnica University of Bucharest, courses on processing technology of polymers and additives for polymer processing, and at universities in France, as a visiting professor, the course of polymer rheology. He developed the research activity in areas of polymer processing, synthesis, and characterization of polymers materials, biopolymers, and polymer materials for solar cells. He is the author and / or coauthor of 13 books, 18 patents in the field of polymer technology, and over 95 professional articles (over 50 published in ISI journals).

Magdalena Lidia Ciurea received her Ph.D. in Physics from the Central Institute of Physics, Bucharest-Magurele, Romania, in 1981 (Graduate Studies University of Bucharest, Faculty of Physics, Condensed Matter Physics specialty). She is a Senior Researcher 1st Degree from 1996 at the National Institute of Materials Physics, Magurele, Romania, and PhD adviser (Professor) in Condensed Matter Physics at Doctoral School of Physics, University of Bucharest. Prof. Ciurea was head of Low Dimensional Systems Department for many years (2001-2009). She has published more than 100 journal and

conference papers, 2 book chapters (Springer publisher), 3 chapters in 3 books (publishing house of the Romanian Academy), more than 30 invited lectures at international and national conferences, and another 13 invited lectures at prestigious European universities and research institutes. She has research contributions in the field of nanostructured materials based on elements from group IV (Si, Ge, or C): photoluminescent nanocrystalline porous silicon, electrical transport, and phototransport (conduction mechanisms, percolation phenomena in Si, Ge, or C nanotubes-based nanostructures); quantum confinement effects (unified model for energy levels in 0D, 1D, and 2D systems); trapping phenomena, experiment, and modeling (finding of trap parameters that are not directly measurable, identification of stress induced traps).

James Connolly is Senior Researcher at the Nanophotonic Technology Center of the Polytechnic University of Valencia. He is responsible for photovoltaic design and simulation, currently focused on plasmonic and quantum confined structures in silicon nanostructured solar cells. Previously, he developed modelling of multijunction III-V quantum well solar cells at Imperial College London. The high efficiency concepts concerned include hot carrier effects, radiative dominance, and photon recycling. He has also worked with the company Quantasol, adapting the multijunction models he developed to the needs of the industrial design process. Other interests include developing modelling of thin film II-VI chalcopyrite cells with the CNRS in France. Resulting collaborations involve novel tunnel junction design and model development for III-V multijunction cells on silicon developed with the LGEP and the IEF in Paris.

Aurel Diacon, PhD, Assistant Professor at University Politehnica of Bucharest, Faculty of Applied Chemistry and Materials Science, Advanced Polymer Materials Group. He obtained his PhD degree in 2011 in Engineering Sciences/Chemical Engineering at University Politehnica under Prof. Corneliu Cincu. He also received a PhD degree in Organic Chemistry at University of Angers, France, under Prof. Piétrick Hudhomme. His research activity has been related to dye synthesis, solid-state Grätzel solar cells, electroconductive polymers, organic synthesis of functional electroactive molecules, carbon nanotube modifications, photonic crystals manufacturing, and modification.

Pablo García-Linares (b. 1983) obtained his Engineer in Telecommunication degree at the Universidad Politécnica de Madrid (U.P.M.), Spain, in 2006, and his Engineer in Electronics degree at the Ecole Nationale Supérieure de l'Electronique et de ses Applications, France, in 2006. He is currently doing a Ph.D at the Institute of Solar Energy of the U.P.M. on the field of intermediate band solar cells under the supervision of Prof. Martí. He has been collaborating with the Silicon and Fundamental Studies research group at the Institute of Solar Energy, lead by Prof. Luque, since 2006.

Jean Francois Guillemoles, Researcher at CNRS, is presently Deputy Director for Research of IRDEP and Project Leader there of the High Efficiency program. He has been involved in the PV field since 1989, where he contributed to the research and development of fabrication processes of thin film semiconductors for PV applications and the technology transfer to industry. He has been visiting scientist in several high profile institutes in PV and author of more than 100 papers, 7 patents, and over 100 proceedings.

Lunmei Huang obtained her PhD at Uppsala University on Ab Initio Electronic Structure Calculation on Materials in 2007. Then she worked as a post-doc at IRDEP where she modeled vibration spectra of semiconductor nanostructures. After that, she was Visiting Researcher in University of New South Wales and University of Oregon. Since 2010, she is a post-doc Assistant Professor in University of Michigan, and now she is working on semiconducting device modeling.

Sana Laribi is a Researcher Engineer at IRDEP, in charge of semiconductor materials simulation at atomic scale for photovoltaics and PV device modelling. She works within the High Efficiency Photovoltaic program within IRDEP. Before joining EDF, she worked as a Researcher in a startup company, as a photovoltaic project leader. In 2008, she received her PhD from Université Paris VI, in Materials Chemistry and Physics, after PhD studies at Unité Mixte de Physique CNRS/Thales and STMicroelectronics.

Arthur Le Bris, after his Engineer and Master degree at Ecole Centrale Paris, he obtained his PhD at the Institute for Research and Development on Energy from Photovoltaics (IRDEP), a joint laboratory between EDF, CNRS, and Chimie Paristech, in September 2011. He worked on demonstrating the feasibility of the concept of a hot carrier photovoltaic device. Starting from a thermodynamical model of an ideal hot carrier solar cell, he developed a model that takes into account heat losses and non-ideal selective contacts. Specialized in modelling and simulations, he also performed experimental studies of carrier thermalization. He is the first author of three refereed papers and ten conference communications.

Ana-Maria Lepadatu received B.S. and M.S. degrees from Faculty of Physics, University of Bucharest, Bucharest, Romania. She is a PhD student in Condensed Matter Physics at the University of Bucharest, Doctoral School of Physics, Romania. She has a Researcher position at the National Institute of Materials Physics, Magurele, Romania. Her scientific contributions are in topics of electrical transport phenomena and conduction mechanisms in nanocrystalline Si, Ge, C nanotube-based films and structures and quantum confinement effects, and also trapping phenomena (experiment and modelling). She has published 14 journal and conference papers and a book chapter (publishing house of the Romanian Academy).

Antonio Luque (b. 1941) is Dr. Engineer in Telecommunication. He has been Chair Professor of Electronic Technology at the Universidad Politécnica de Madrid, since 1970, and is the founder of the Institute of Solar Energy, in 1979. His research activity is devoted to photovoltaics. He invented the bifacial cell in 1976, which was fabricated by Isofotón, a company he created in 1982. More recently (1997), Prof. Luque proposed the intermediate band solar cell, and his main present research focus is further understanding and developing this new concept. He also inspired the creation of the Institute for Concentrator Photovoltaic Systems, ISFOC, in Castilla La Mancha and the Silicon ultra-purification university-industry joint company, CENTESIL. He has published more than 250 scientific papers in English language as well as some books and holds over 20 patents. He has been honored by several important prizes and distinctions worldwide.

Antonio Martí (b. 1965) obtained his Physical Science degree at Universidad Complutense de Madrid, in 1987, and the Ph.D. degree from the Universidad Politécnica de Madrid (U.P.M.), in 1992. He has been Associate Professor of Electronic Technology at U.P.M. since 1997 and Full Professor since

2007. He has been working on the development of the intermediate band solar cell, which he proposed in 1997 together with Prof. Luque. He has supervised 6 Ph.D theses and 23 Final Projects. Prof. Martí has published more than 60 scientific papers as well as some books and holds 5 patents. He has also led a number of regional, Spanish, and European research projects.

Mihai Razvan Mitroi, PhD, Eng. 1986, Ph.D. in Engineering Sciences, specialty, Electro-technical material, University Politehnica of Bucharest. 1977, Dip. engineer, specialty, University Politehnica of Bucharest, Faculty of Materials Science and Engineering. 1999 – present, Associated Professor at Department of Physics, Faculty of Applied Science, University Politehnica of Bucharest. Member of the Romanian Physics Society, and member of the European Physics Society. Award of Romanian Academy "Consatntin Miculescu," 1987. Member in the Scientific Committee of The 2nd International Colloquium "Physics of Materials" October 7-9, 2010, Bucharest. Member in the Scientific Committee of The 6th International Colloquium "Mathematics and Physics in Engineering, Numerical Physics and Complexity," October 7-9, 2010, Bucharest.

Andrei Galbeaza Moraru is a Junior Researcher at Polytechnic University of Bucharest who contributed to numerous research projects both European and National. The main focus of his research is represented by testing and simulation of PV cells and systems.

Yoshitaka Okada is a Professor at the Research Center for Advanced Science and Technology, the University of Tokyo. He received his B.Sc degree from the University of London in 1984, and M.E and Ph.D degrees in Electronic Engineering from the University of Tokyo, in 1987 and 1990. In 1990, he joined the Institute of Materials Science, University of Tsukuba, as a Research Assistant. He then served as an Assistant Professor and later an Associate Professor at University of Tsukuba, before he moved to the University of Tokyo in 2008, where he is currently a Professor in the Department of New Energy. He was appointed as a Visiting Assistant Professor, at the Department of Electrical Engineering, Stanford University, in 1995-1996, and Visiting Fellow (JSPS-Royal Society Exchange Fellow) at the Department of Physics, Imperial College London, in 2006. His research interests include MBE growth of III-V-N(Sb) dilute nitrides and semiconductor low-dimensional structures and application to next-generation high efficient multi-junction and multi-band solar cells.

Par Olsson obtained his PhD on Ab Initio Modeling at Uppsala University, Sweden, in 2005. He subsequently got a position at EDF R&D, applying DFT-based techniques to modeling of semiconductors for photovoltaic application. Since 2011, he is an Associate Professor at KTH, Stockholm. He has published some 50 refereed papers in international journals.

Yasushi Shoji is a Ph.D student at the Institute of Applied Physics, University of Tsukuba. He received his B.E and M.E degrees from University of Tsukuba in 2008 and in 2010. His thesis is on the MBE growth and fabrication of high efficiency quantum dot intermediate band solar cells.

Ionel Stavarache received B.S. and M.S. degrees in Spectroscopy, Plasma, Optics and Lasers from Faculty of Physics, University of Bucharest, Bucharest, Romania. He also received his Ph.D. in Condensed Matter Physics from University of Bucharest, Doctoral School of Physics, Romania, in 2011. His position

is of Senior Researcher 3rd degree at the National Institute of Materials Physics, Magurele, Romania. His research contributions are in topics of electrical transport and phototransport phenomena and conduction mechanisms in nanocrystalline Si, Ge, C nanotube-based films and structures and trapping processes, including stress induced traps (experiment and modelling). His scientific contributions were published in 22 journal and conference papers and a book chapter (publishing house of the Romanian Academy).

Katsuhisa Yoshida is a Ph.D student at the Department of Electrical Engineering and Information Systems, Graduate School of Engineering, the University of Tokyo. He received his B.Sc in Physics from Tokyo University of Science in 2008, and M.E degree from University of Tsukuba in 2010. His thesis is on the device physics and simulation of high efficiency solar cells.

Catalin Zaharia, PhD, Lecturer at University Politehnica of Bucharest, Faculty of Applied Chemistry and Materials Science, Advanced Polymer Materials Group. He obtained his PhD degree in 2006 in Engineering Sciences/Chemical Engineering at University Politehnica. He also has a PhD degree in Cell Biology at University of Angers, France. His research activity is mainly related to polymers and polymeric materials. He has experience in the synthesis, characterization, and processing of polymers for various applications. During the last years, he has worked in the synthesis and characterization of electroconductive polymers such as polytiophene, polyacetylens, and doped polymers with electroconductive polymers. He has also worked in the field of polymers for medical and biological applications, optical applications, and water-soluble polymeric materials.

Index

H

I

K

L

M

N

O

P

Q

R

S

T

V

W

X